ADVANCES IN POLYMER SCIENCE

223

Volume Editors G. Meller · T. Grasser

# Organic Electronics

**223**
**Advances in Polymer Science**

**Editorial Board:**
**A. Abe · A.-C. Albertsson · K. Dušek · W.H. de Jeu**
**H.-H. Kausch · S. Kobayashi · K.-S. Lee · L. Leibler**
**T.E. Long · I. Manners · M. Möller · O. Nuyken**
**E.M. Terentjev · M. Vicent · B. Voit**
**G. Wegner · U. Wiesner**

# Advances in Polymer Science

Recently Published and Forthcoming Volumes

**Organic Electronics**
Volume Editors: Meller, G., Grasser, T.
Vol. 223, 2010

**Inclusion Polymers**
Volume Editor: Wenz, G.
Vol. 222, 2009

**Advanced Computer Simulation Approaches for Soft Matter Sciences III**
Volume Editors: Holm, C., Kremer, K.
Vol. 221, 2009

**Self-Assembled Nanomaterials II**
Nanotubes
Volume Editor: Shimizu, T.
Vol. 220, 2008

**Self-Assembled Nanomaterials I**
Nanofibers
Volume Editor: Shimizu, T.
Vol. 219, 2008

**Interfacial Processes and Molecular Aggregation of Surfactants**
Volume Editor: Narayanan, R.
Vol. 218, 2008

**New Frontiers in Polymer Synthesis**
Volume Editor: Kobayashi, S.
Vol. 217, 2008

**Polymers for Fuel Cells II**
Volume Editor: Scherer, G. G.
Vol. 216, 2008

**Polymers for Fuel Cells I**
Volume Editor: Scherer, G. G.
Vol. 215, 2008

**Photoresponsive Polymers II**
Volume Editors: Marder, S. R., Lee, K.-S.
Vol. 214, 2008

**Photoresponsive Polymers I**
Volume Editors: Marder, S. R., Lee, K.-S.
Vol. 213, 2008

**Polyfluorenes**
Volume Editors: Scherf, U., Neher, D.
Vol. 212, 2008

**Chromatography for Sustainable Polymeric Materials**
Renewable, Degradable and Recyclable
Volume Editors: Albertsson, A.-C., Hakkarainen, M.
Vol. 211, 2008

**Wax Crystal Control · Nanocomposites Stimuli-Responsive Polymers**
Vol. 210, 2008

**Functional Materials and Biomaterials**
Vol. 209, 2007

**Phase-Separated Interpenetrating Polymer Networks**
Authors: Lipatov, Y. S., Alekseeva, T.
Vol. 208, 2007

**Hydrogen Bonded Polymers**
Volume Editor: Binder, W.
Vol. 207, 2007

**Oligomers · Polymer Composites Molecular Imprinting**
Vol. 206, 2007

**Polysaccharides II**
Volume Editor: Klemm, D.
Vol. 205, 2006

**Neodymium Based Ziegler Catalysts – Fundamental Chemistry**
Volume Editor: Nuyken, O.
Vol. 204, 2006

# Organic Electronics

Volume Editors: Gregor Meller · Tibor Grasser

With contributions by

M.A. Baldo · S.D. Baranovskii · H. Bässler · D. Basu
A. Dodabalapur · E.V. Emelianova · J.G. Grote
A. Herasimovich · G. Horowitz · I. Hörselmann
P.J. Jadhav · F. Jansson · H. Kosina · L. Li · B.N. Limketkai
C. Melzer · R. Österbacka · G. Paasch · O. Rubel
N.S. Sariciftci · S. Scheinert · H. von Seggern · T.B. Singh
A. Troisi

*Editors*
Gregor Meller
TU Wien
Inst. Mikroelektronik
Gußhausstraße 27-29
1040 Wien
E-360
Austria
meller@iue.tuwien.ac.at

Tibor Grasser
TU Wien
Inst. Mikroelektronik
Gußhausstraße 27-29
1040 Wien
E-360
Austria
grasser@iue.tuwien.ac.at

ISSN 0065-3195 e-ISSN 1436-5030
ISBN 978-3-642-04537-0 e-ISBN 978-3-642-04538-7
DOI 10.1007/978-3-642-04538-7
Springer Heidelberg Dordrecht London New York

Library of Congress Control Number: 2009936785

© Springer-Verlag Berlin Heidelberg 2010
This work is subject to copyright. All rights are reserved, whether the whole or part of the material is concerned, specifically the rights of translation, reprinting, reuse of illustrations, recitation, broadcasting, reproduction on microfilm or in any other way, and storage in data banks. Duplication of this publication or parts thereof is permitted only under the provisions of the German Copyright Law of September 9, 1965, in its current version, and permission for use must always be obtained from Springer. Violations are liable to prosecution under the German Copyright Law.
The use of general descriptive names, registered names, trademarks, etc. in this publication does not imply, even in the absence of a specific statement, that such names are exempt from the relevant protective laws and regulations and therefore free for general use.

*Cover design*: WMXDesign GmbH, Heidelberg

Printed on acid-free paper

Springer is part of Springer Science+Business Media (www.springer.com)

# Volume Editors

Gregor Meller

TU Wien
Inst. Mikroelektronik
Gußhausstraße 27–29
1040 Wien, E-360, Austria
*meller@iue.tuwien.ac.at*

Tibor Grasser

TU Wien
Inst. Mikroelektronik
Gußhausstraße 27-29
1040 Wien, E-360, Austria
*grasser@iue.tuwien.ac.at*

# Editorial Board

Prof. Akihiro Abe

Department of Industrial Chemistry
Tokyo Institute of Polytechnics
1583 Iiyama, Atsugi-shi 243-02, Japan
*aabe@chem.t-kougei.ac.jp*

Prof. A.-C. Albertsson

Department of Polymer Technology
The Royal Institute of Technology
10044 Stockholm, Sweden
*aila@polymer.kth.se*

Prof. Karel Dušek

Institute of Macromolecular Chemistry, Czech
Academy of Sciences of the Czech Republic
Heyrovský Sq. 2
16206 Prague 6, Czech Republic
*dusek@imc.cas.cz*

Prof. Dr. Wim H. de Jeu

Polymer Science and Engineering
University of Massachusetts
120 Governors Drive
Amherst MA 01003, USA
*dejeu@mail.pse.umass.edu*

Prof. Hans-Henning Kausch

Ecole Polytechnique Fédérale de Lausanne
Science de Base
Station 6
1015 Lausanne, Switzerland
*kausch.cully@bluewin.ch*

Prof. Shiro Kobayashi

R & D Center for Bio-based Materials
Kyoto Institute of Technology
Matsugasaki, Sakyo-ku
Kyoto 606-8585, Japan
*kobayash@kit.ac.jp*

Prof. Kwang-Sup Lee

Department of Advanced Materials
Hannam University
561-6 Jeonmin-Dong
Yuseong-Gu 305-811
Daejeon, South Korea
*kslee@hnu.kr*

Prof. L. Leibler

Matière Molle et Chimie
Ecole Supérieure de Physique
et Chimie Industrielles (ESPCI)
10 rue Vauquelin
75231 Paris Cedex 05, France
*ludwik.leibler@espci.fr*

Prof. Timothy E. Long

Department of Chemistry
and Research Institute
Virginia Tech
2110 Hahn Hall (0344)
Blacksburg, VA 24061, USA
*telong@vt.edu*

Prof. Ian Manners

School of Chemistry
University of Bristol
Cantock's Close
BS8 1TS Bristol, UK
*ian.manners@bristol.ac.uk*

Prof. Martin Möller

Deutsches Wollforschungsinstitut
an der RWTH Aachen e.V.
Pauwelsstraße 8
52056 Aachen, Germany
*moeller@dwi.rwth-aachen.de*

Prof. Oskar Nuyken

Lehrstuhl für Makromolekulare Stoffe
TU München
Lichtenbergstr. 4
85747 Garching, Germany
*oskar.nuyken@ch.tum.de*

Prof. E. M. Terentjev

Cavendish Laboratory
Madingley Road
Cambridge CB 3 OHE, UK
*emt1000@cam.ac.uk*

Maria Jesus Vicent, PhD
Centro de Investigacion Principe Felipe
Medicinal Chemistry Unit
Polymer Therapeutics Laboratory
Av. Autopista del Saler, 16
46012 Valencia, Spain
*mjvicent@cipf.es*

Prof. Brigitte Voit

Institut für Polymerforschung Dresden
Hohe Straße 6
01069 Dresden, Germany
*voit@ipfdd.de*

Prof. Gerhard Wegner

Max-Planck-Institut
für Polymerforschung
Ackermannweg 10
55128 Mainz, Germany
*wegner@mpip-mainz.mpg.de*

Prof. Ulrich Wiesner

Materials Science & Engineering
Cornell University
329 Bard Hall
Ithaca, NY 14853, USA
*ubw1@cornell.edu*

# Advances in Polymer Sciences Also Available Electronically

*Advances in Polymer Sciences* is included in Springer's eBook package *Chemistry and Materials Science*. If a library does not opt for the whole package the book series may be bought on a subscription basis. Also, all back volumes are available electronically.

For all customers who have a standing order to the print version of *Advances in Polymer Sciences*, we offer the electronic version via SpringerLink free of charge.

If you do not have access, you can still view the table of contents of each volume and the abstract of each article by going to the SpringerLink homepage, clicking on "Chemistry and Materials Science," under Subject Collection, then "Book Series," under Content Type and finally by selecting *Advances in Polymer Sciences*.

You will find information about the

- Editorial Board
- Aims and Scope
- Instructions for Authors
- Sample Contribution

at springer.com using the search function by typing in *Advances in Polymer Sciences*.

*Color figures* are published in full color in the electronic version on SpringerLink.

## Aims and Scope

*Advances in Polymer Sciences* reviews actual trends in modern biotechnology.

Its aim is to cover all aspects of this interdisciplinary technology where knowledge, methods and expertise are required for chemistry, biochemistry, microbiology, genetics, chemical engineering and computer science.

Special volumes are dedicated to selected topics which focus on new biotechnological products and new processes for their synthesis and purification. They give the state-of-the-art of a topic in a comprehensive way thus being a valuable source for the next 3–5 years. It also discusses new discoveries and applications.

In general, special volumes are edited by well known guest editors. The series editor and publisher will however always be pleased to receive suggestions and supplementary information. Manuscripts are accepted in English.

In references *Advances in Polymer Sciences* is abbreviated as *Adv. Polym. Sci.* and is cited as a journal.

Special volumes are edited by well known guest editors who invite reputed authors for the review articles in their volumes.

Impact Factor in 2008: 6.802; Section “Polymer Science”: Rank 2 of 73

# Preface

Dear Readers,

Since the ground-breaking, Nobel-prize crowned work of Heeger, MacDiarmid, and Shirakawa on molecularly doped polymers and polymers with an alternating bonding structure at the end of the 1970s, the academic and industrial research on hydrocarbon-based semiconducting materials and devices has made encouraging progress.

The strengths of semiconducting polymers are currently mainly unfolding in cheap and easily assembled thin film transistors, light emitting diodes, and organic solar cells. The use of so-called "plastic chips" ranges from lightweight, portable devices over large-area applications to gadgets demanding a degree of mechanical flexibility, which would overstress conventional devices based on inorganic, perfect crystals. The field of organic electronics has evolved quite dynamically during the last few years; thus consumer electronics based on molecular semiconductors has gained sufficient market attractiveness to be launched by the major manufacturers in the recent past.

Nonetheless, the numerous challenges related to organic device physics and the physics of ordered and disordered molecular solids are still the subjects of a continuing lively debate.

The future of organic microelectronics will unavoidably lead to new device-physical insights and hence to novel compounds and device architectures of enhanced complexity. Thus, the early evolution of predictive models and precise, computationally effective simulation tools for computer-aided analysis and design of promising device prototypes will be of crucial importance.

With regard to novel developments and challenges, the organizers of the SISPAD 2007 conference decided to organize an "Organic Electronics" Companion Workshop. World leading experts have been invited to Vienna to present their current work on this fascinating and important field of research. Subsequent to the workshop, all participants, together with those scientists who which were regrettably unable to join the conference, have been invited to contribute a chapter to the present volume of the book series "Advances in Polymer Science."

This foreword closes with a sketchy summary of each chapter. Here the chapter summaries have been arranged in the same order in which they appear in the book.

In the opening chapter, Evguenia Emelianova and Heinz Baessler analyze the dissociation of optically generated excitons into pairs of free carriers in the case of pure, blended and doped polymers. The effects of Gaussian disorder, temperature, and electric field on the photocarrier yield are investigated. As the presented analytical examination shows, energetic disorder enhances exciton dissociation. Moreover, the temperature dependence of the yield is weakened and loses the activated shape it exhibits in the case of moderate fields and zero disorder.

Priya Jadhav, Benjie Limketkai and Marc Baldo dedicated Chapter 2 to recapitulate experimental results, effective temperature models, and the percolation theory treatment with special emphasis on the compound $AlQ_3$. The authors discuss the applicability of percolation theory to the calculation of low-field carrier mobilities and debate the strengths and limitations of effective temperature models when being applied to a wider range of electric field strengths, lattice temperatures and carrier concentrations.

In Chap. 3, Sergei Baranovski presents various important theoretical concepts relevant to the transport theory of organic glasses, molecularly doped polymers and conjugated polymers.

Originally developed for amorphous inorganic semiconductors characterized by an exponential density of states, the author discusses the extension of these concepts to Gaussian densities of states under special consideration of state- and carrier-concentrations, electric fields, and temperatures.

In Chap. 4, Debarshi Basu and Ananth Dodabalapur drift velocity and drift mobility measurements in organic field effect transistors. A method is introduced which is based on the time-of-flight of an electron swarm injected into the channel by a voltage pulse. The method also grants an improved understanding of the injection process, the basic working mechanism of an organic transistor, and the nature of trap distributions.

In an organic thin film transistor, the relevant interfaces occur between the gate dielectric and the semiconductor and between the semiconductor and the source and drain contacts. In Chap. 5, Gilles Horowitz investigates the specific problems and sophisticated requirements arising in connection with these interfaces and describes how to characterize them and their effects on the device performance.

Low-cost polymer films are typically realized by solution-based technology. The resulting hole mobilities, however, lie below that of vapor deposited layers. Consequently, the performance of solution-based organic field effect transistors is limited. In Chap. 6, Susanne Scheinert and Gernot Paasch address the problems of low-cost sub-micrometer devices and present experimental results, contact problem simulations, and simulations of short-channel effects, which lead to short-channel design rules.

Birendra Singh and Serdar Sariciftci devoted Chap. 7 to the microelectronic applicability of the promising DNA-based bio-polymer DNA-CTMA. The authors present their work concerning the processing steps leading to feasible DNA-CTMA films and study the various characteristics of this compound. Properties

like transparency, a large bandgap, or a tunable electrical resistance, to name just a few, make this polymer very interesting for the enhancement of numerous types of organic devices.

Christian Melzer and Heinz von Seggern discuss different ways to realize complementary organic CMOS inverters and present their basic design rules in Chap. 8. The authors illustrate several realizations of CMOS-like inverters and demonstrate an inverter based on two identical almost unipolar n- and p-type organic field effect transistors.

In Chap. 9 Alessandro Troisi blocks out disorder effects by focusing on the charge transport in crystalline organic media. In this way, the interplay between a compound's electrical characteristics and the chemical structure of the soft lattice "dressing" of the effective masses and energies by local distortions can be examined from a microscopic point of view by the means of computational chemistry.

In Chap. 10, Ling Li and Hans Kosina present compact models which they have recently derived. The addressed topics range from carrier-concentration dependent mobilities over analytical models describing the doping and trapping characteristics to a current injection model based on multiple trapping theory.

It was a great pleasure for us to cooperate with such outstanding scientists. We want to express our gratitude to all workshop-lecturers, book contributors, peer reviewers and last but not least to Dr. Hertel, Mrs. Samide and Mrs. Kreusel from Springer Verlag for facilitating and coaching the publication in the renowned book series "Advances in Polymer Science".

Vienna, Summer 2009

*Gregor Meller*
*Tibor Grasser*

# Contents

**Steady-State Photoconduction in Amorphous Organic Solids** .............. 1
H. Bässler and E.V. Emelianova

**Effective Temperature Models for the Electric Field Dependence of Charge Carrier Mobility in Tris(8-hydroxyquinoline) Aluminum** .................................. 29
P.J. Jadhav, B.N. Limketkai, and M.A. Baldo

**Description of Charge Transport in Disordered Organic Materials** .............................................................. 45
S.D. Baranovskii, O. Rubel, F. Jansson, and R. Österbacka

**Drift Velocity and Drift Mobility Measurement in Organic Semiconductors Using Pulse Voltage** .................................. 73
Debarshi Basu and Ananth Dodabalapur

**Interfaces in Organic Field-Effect Transistors** ............................ 113
Gilles Horowitz

**Low-Cost Submicrometer Organic Field-Effect Transistors** ................ 155
Susanne Scheinert, Gernot Paasch, Ingo Hörselmann, and Andrei Herasimovich

**Bio-Organic Optoelectronic Devices Using DNA** ............................ 189
Thokchom Birendra Singh, Niyazi Serdar Sariciftci, and James G. Grote

**Organic Field-Effect Transistors for CMOS Devices** ........................ 213
Christian Melzer and Heinz von Seggern

**Theories of the Charge Transport Mechanism in Ordered Organic Semiconductors** .......... 259
Alessandro Troisi

**Charge Transport in Organic Semiconductor Devices** .......... 301
Ling Li and Hans Kosina

**Index** .......... 325

Adv Polym Sci (2010) 223: 1–28
DOI:10.1007/12_2009_11
© Springer-Verlag Berlin Heidelberg 2009
Published online: 19 June 2009

# Steady-State Photoconduction in Amorphous Organic Solids

**H. Bässler and E.V. Emelianova**

**Abstract** By applying various experimental techniques, e.g., transient absorption in a strong electric field and delayed field collection of charge carriers, it has been proven that in neat conjugated polymers singlet excitations can dissociate into pairs of free charge carriers in a strong electric field. Random walk theory has been developed to treat this process analytically. At variance of conventional 3D Onsager theory it is assumed that an exciton with finite lifetime can first transfer endothermically an electron to an adjacent site, thereby generating a charge transfer state whose energy is above the energy of that of the initial exciton. In a second step the latter can fully dissociate in accordance with Onsager's concept Brownian motion. The results indicate that, depending on the energy required for the first jump, the first jump contributes significantly to the field dependence of the dissociation yield. Disorder weakens the temperature dependence of the yield dramatically and precludes extracting information on the exciton binding energy from it. The chapter will also address the problem of photogeneration in donor–acceptor blends used in organic photovoltaic cells and emphasize the crucial role of geminate recombination of the electron–hole pair at the internal interface.

**Keywords** Conjugated polymer · Electron–hole pair · Exciton · Hopping transport · Photogeneration

H. Bässler
Department of Chemistry, Philipps University, Hans-Meerwein-Street, 35032 Marburg, Germany
e-mail:baessler@Staff.Uni-Marburg.DE

E.V. Emelianova (✉)
Laboratory for Molecular Dynamics and Spectroscopy, KU Leuven, Celestijnenlaan 200F, 3001 Heverlee-Leuven, Belgium
e-mail:zhenia.emelianova@fys.kuleuven.be

## Contents

1 Introduction .......... 2
2 Comparison Between Optical and Electrical Properties of Molecular Crystals and Random Organic Solids .......... 3
3 The Onsager Concept for Charge Photogeneration .......... 5
4 Experimental Probes of Photogeneration in Neat Conjugated Polymers .......... 7
5 Photogeneration in Doped and Blended Conjugated Polymers .......... 11
6 Analytic Treatment of Exciton Dissociation .......... 13
6.1 Theory .......... 14
6.2 Results .......... 17
6.3 Discussion .......... 23
7 Conclusions .......... 25
References .......... 26

# Abbreviations

| | |
|---|---|
| 3D | Three dimensional |
| CT | Charge transfer |
| DOS | Density of states |
| *e–h* pair | Electron–hole pair |
| FET | Field effect transistor |
| HOMO | Highest occupied molecular orbital |
| LPPP | Laddertype poly-phenylene |
| LUMO | Lowest unoccupied molecular orbital |
| (MDMO-PPV):PCBM | Poly(2-methoxy, 5-(3′, 7′ dimethyl-octyloxy))-*p*-phenylene vinylene |
| OC1C10-PPV | Poly(2-methoxy-5-(3′, 7′-dimethyloctyloxy)-phenylene vinylene |
| OLED | Organic light emitting diode |
| PCBM | (6,6)-Phenyl $C_{61}$ butyric acid methyl ester |
| PPV | Poly-phenylenevinylene |
| PV | Photovoltaic cell |
| SY | Superyellow |

# 1 Introduction

Conjugated polymers are fashionable objects of current device-oriented solid state research. The advances in exploiting their opto-electronic properties for developing organic light emitting diodes (OLEDs), organic field effect transistors (FETs), and organic photovoltaic cells (PVs) are, indeed, impressive [1–5]. It is the fruit of scientific imagination and in-depth understanding of the properties of the materials. However, the foundation for this development was laid down by both the earlier

work on molecular crystals [6] and the advances in the field of electrophotography [7]. In fact, the latter emerged as one of the key technologies of the twentieth century. It is based upon photoconductivity in a semiconductor acting as a photonic sensor. Early on it has been recognized that photoreceptors of commercial use must be inexpensive and large scale noncrystalline layers. Improvement of the growing technology has been complemented by advances regarding the conceptual understanding of the opto-electronic properties of semiconductors of the chalcogenide family $(As_2S_3, As_2Se_3)$ [8]. One step forward towards a mature technology was the recognition that one can profitably use aromatic molecules embedded in an inert flexible polymeric binder matrix as a photoreceptor. Meanwhile, most of the photocopies and laser printers use these type of receptors but few users will recognize that once they push the printout button they start an experiment of transient photoconductivity in a polymeric photoreceptor. To date this is still the only large scale application of opto-electronic properties of polymers but there is strong hope that organic LEDs, FETs, and PVs are about to meet competition from existing technology based upon inorganic materials.

This chapter focuses on the principles of photoconduction in random, polymeric semiconductors, and notably on optical generation of charge carriers. It is not the intention to present an overview of the current work in this area but rather to highlight elementary processes, their involvement in modern devices, and to address recent developments and achievements.

## 2 Comparison Between Optical and Electrical Properties of Molecular Crystals and Random Organic Solids

The opto-electronic properties of organic and inorganic semiconductors differ in several qualitative as well as quantitative aspects. The underlying reasons are as follows. (1) In an inorganic semiconductor, strong bonding among the atoms leads to the formation of several eV wide valence and conduction bands. Transitions between them control their optical absorption. Strong coupling also implies mobilities of charge carriers of the order of $10^3\,cm^2\,Vs^{-1}$ or even larger and, concomitantly, carrier mean free paths much larger than interatomic spacings. (2) In organic semiconductors strong chemical bonding is confined to a molecular level only while intermolecular coupling is controlled by weak van der Waals forces. As a consequence, the molecular building blocks retain their identity, valence and conduction bands are typically only several 0.1 eV wide [9], charge carrier mobilites are on the order of $1\,cm^2\,Vs^{-1}$, and their mean free paths are comparable to intermolecular spacings. (3) In inorganic semiconductors the dielectric constant is typically $\varepsilon \geq 10$. It implies binding energies of Wannier-like excitons of the order of 10 meV. Excitonic effects become noticeable at low temperatures only, while at room temperature optically generated charge carriers are essentially free. The fact that in organic solids the dielectric constant is typically between 3 and 4 combined with the weakness of intermolecular coupling has a profound effect on their spectroscopy. In a

system with $\varepsilon = 3$ the coulombic radius, i.e., the separation of an electron–hole with a coulombic binding energy comparable to $kT$ at room temperature, is 20 nm. In view of the extremely low oscillator strength for transitions between valence and conductions bands, absorption of a photon usually generates electron–holes confined to individual molecules, i.e., Frenkel excitons of singlet or triplet character depending on their spin. To dissociate them into free charged entities requires overcoming an exciton binding energy of the order of 1 eV [10]. Recall that the coulombic binding energy of an electron–hole $(e–h)$ pair separated by 0.6 nm in a system with $\varepsilon = 3$ is 0.6 eV. Absorption and luminescence spectra resemble those of the molecular building blocks modified by crystal field effects. (4) Electron–electron correlations are a signature of the strength of electronic coupling. In inorganic semiconductors these are unimportant whereas in organic systems they play a major role revealed by, for instance, the magnitude of the splitting between singlet and triplet states [11].

Abandoning the translational symmetry of a crystalline semiconductor generates localized states within the bandgap. In amorphous inorganic systems there is a demarcation energy, the so-called mobility edge separating delocalized and localized states. The localized states usually feature an exponential dependence on energy above/below the valence/conduction bands [12]. In random organic solids, on the other hand, the already narrow valence and conduction bands of the underlying molecular crystal are split into a distribution of localized states. This has a profound effect on the transport of both charge carriers and neutral excitations, i.e., excitons. Since this phenomenon is of key importance it will be elaborated on in greater detail below.

Adopting Lyons classic approach [6] the energy of the valence band of a molecular crystal, i.e., the ionization energy, is determined by the ionization energy of the parent molecule in the gas phase diminished by the predominantly electronic polarization energy of a charge inside the crystal. The essential parameter is the molecular polarizability which is an anisotropic quantity. This implies that the polarization energy of a charge, be it a hole or an electron, depends on the microscopic structure of its surroundings [13]. In a random structure it results in a distribution of polarization energies. Since the interaction energy depends on a large number of variables, each varying randomly, central limit theorem [14] applies and predicts a Gaussian shaped density of states (DOS) distribution. It controls charge transport in a random organic solid such as a molecular glass or a molecularly doped polymer in which the charge carrying moieties are molecules embedded within an inert random polymer matrix that is responsible for the mechanical properties of the material. If polar, however, it can have an effect on the DOS of the transport molecules [15].

Since there is no principle difference between an ion and an optically excited yet neutral molecule embedded within a polarizable medium, the “disorder” concept applies to optical transition to molecular chromophores as well. In fact, the observation of inhomogeneously broadened absorption and photoluminescence spectra is a direct and simple experimental probe of the DOS distribution [14]. For this reason time resolved photoluminescence is a useful analogous tool for checking the validity of concepts for analyzing charge transport in random organics.

It is obvious that the above concept, which is based upon the polarization energy as the essential quantity that determines the DOS distribution of a random organic solid, can only be a zero order approach. It ignores, for instance, any inhomogeneities on a mesoscopic scale such as local phase separation and site correlation effects. In the case of conjugated polymers one has to consider an extra source of level broadening beyond random polarization effects of the environment of a charged or optically excited polymer chain. It relates to the dependence of the energies of excited states as a function of chain length. It is an accepted notion that the "length" of a chromophore in a conjugated polymer is not identical with the actual chain length but is rather the length of a more or less unperturbed segment of the chain confined by topological chain distortions. In qualitative accordance with the classic particle in the box model, energy levels and excitation energies decrease as a chain gets longer although quantitative understanding of this phenomenon has to go beyond the simple particle in the box formalism [16]. It is clear that the so-called effective conjugation length is a statistical quantity and must contribute to inhomogeneous state broadening. Mapping the low energy tail of relevant charged or excitonic states by a Gaussian envelope function is only a convenient practice.

Another possible source for broadening the DOS of charge transporting states in random organic systems is accidental or deliberate doping by charged moieties, for instance electrochemical introduced coulombic centers whose coulombic potentials are superimposed onto the rough energy landscape arising from random polarizabilities [17]. An early simulation study [18] indicated that the presence of extra stationary charges gives rise to deep states in the DOS that feature an exponential distribution which is reminiscent of what has been observed in amorphous chalcogenides. It is a signature of random potential fluctuations that affect charge transport.

## 3 The Onsager Concept for Charge Photogeneration

As mentioned in Sect. 2, the energy of a singlet exciton in a molecular crystal is insufficient to generate a pair of free charges. Its dissociation requires an additional energy of approximately 1 eV. Nevertheless, there is usually photoconduction observed near the excitonic $S_1 \leftarrow S_0$ absorption threshold. It can originate from the dissociation of singlet (or triplet) excitons near an electrode or at a dopant molecule acting as a charge (usually electron) acceptor. Intrinsic photoconduction starts $\geq 1$ eV above the absorption edge. It is caused by autoionization [19] of a higher excited Franck Condon state by which the initially hot electron is transferred to a neutral molecule in the neighborhood, thus generating a transient coulombically bound geminate *e–h* pair. The latter can either escape from the mutual coulombic potential via a field and temperature activated diffusive process or recombine geminately and form a fluorescent or a nonradiative singlet state. This process can be modeled in terms of Onsager's classic theory formulated in 1938 [20]. It assumes that (1) the *e–h* pair with initial pair distance $r_0$ is generated by a photon assisted

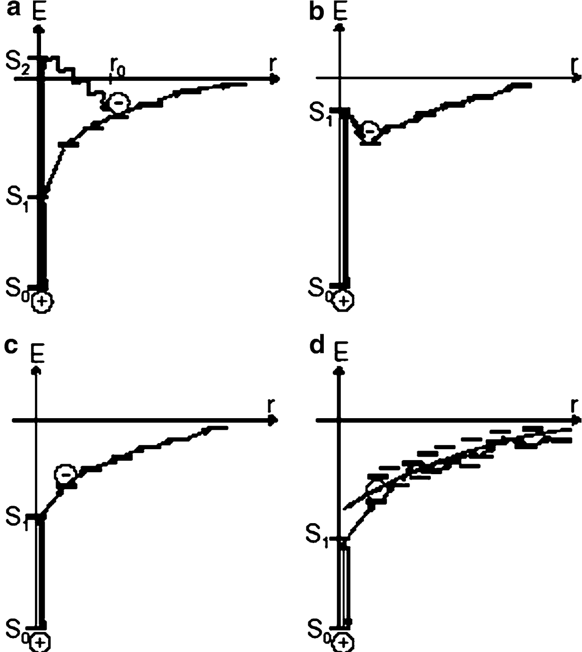


**Fig. 1** Various pathways of photoionization in an organic solid. (**a**) A higher excited molecular Franck–Condon state in a neat solid can autoionize in course of a thermalization process. It generates an electron–hole pair with separation distance $r_0 > a$, $a$ is the lattice constant. It can either dissociate completely executing a temperature and a electric field assisted diffusive random walk or decay geminately to the ground state via the first excited singlet state $(S_1)$. (Onsager 1938 case). (**b**) In a donor/acceptor system an excited donor transfers an electron to the acceptor state thus creating a charge transfer (CT) state that is the lowest excited state of the system. The electron can either dissociate like in case (**a**), or recombine with the ionized donor. The process of the dissociation has a higher probability since the CT state lifetime is longer. (**c**) If in a neat system the energy difference between the CT state and the $S_1$ state is finite but sufficiently small to allow for thermal activation to the CT state, $S_1$ can make several attempts to dissociate during its lifetime. (**d**) This is similar to case (**c**) except for a inhomogeneous broadening of the energy levels in a random system. On average the disorder assists the dissociation since lower energy sites are available for dissociation

process, (2) its escape from the coulombic potential can be described by a field and temperature assisted Brownian motion, and (3) once the *e*–h pair recombines it will do so instantaneously (infinite sink approximation) (see Fig. 1a). The classic experimental work by Braun et al. [21] on anthracene crystals confirms the applicability of Onsager's theory.

Braun [22] extended Onsager's theory to the case that the dissociating *e–h* pair is the lowest excited state of the system, such as the charge transfer (CT) state in a binary molecular solid, for instance a charge transfer crystal composed by donor–acceptor moieties or a molecular solid doped with either donors or acceptors. The essential new element in Braun's theory is the notion that the *e–h* pair has a finite lifetime, determined by its nonradiative decay. This implies that an initially optically

excited pair has many chances for ultimate dissociation before it dies (Fig. 1b). The dissociation yield $\Phi$ is given by

$$\Phi(F,T) = \frac{k_{\mathrm{d}}(F,T)}{k_{\mathrm{f}} + k_{\mathrm{d}}(F,T)}, \quad (1)$$

where $k_{\mathrm{f}}$ is the inverse fluorescence lifetime $\tau$, $k_{\mathrm{d}}(F,T)$ is the rate constant for pair escape formulated by Onsager [22], and $F$ is the external electric field. At low electric fields and, concomitantly, $k_{\mathrm{d}} < 1/\tau$, $\Phi$ increases in proportion to the pair lifetime while in the high field limit Onsager's and Braun's approaches converge. It is important to realize that in both cases the effects of temperature and electric fields on the diffusive escape process superimpose and yield

$$k_{\mathrm{d}}(F,T) = \frac{3\mu e}{4\pi\varepsilon\varepsilon_0 a^3} \exp\left(-\frac{\Delta E}{kT}\right)\left(1 + b + b^2/3 + b^3/18 + \ldots..\right), \quad (2)$$

where $b = e^3F/8\pi\varepsilon\varepsilon_0 k^2T^2$, $\Delta E = e^2/4\pi\varepsilon\varepsilon_0 a$, $\mu$ is the spatially averaged sum of hole and electron mobilities, $e$ the elementary charge, $\varepsilon$ the spatially averaged dielectric constant, $\varepsilon_0$ the permittivity of vacuum, and $a$ the $e$–$h$ pair separation.

In practice, the temperature dependence implied by Eq. (2) is seldom verified, because very often the yield is measured as a function of electric field yet not over a sufficiently large temperature range. Once applicability of the Onsager approach is tacitly accepted, a measured field dependence of the yield can be used to extract the value of the initial $e$–$h$ pair separation $r_0$ and, concomitantly, the coulombic binding energy of the pair. It is important to keep in mind, though, that the Onsager formalism is premised upon to notion that the initial number of $e$–$h$ pairs is independent of both electric field and temperature. Any temperature and field activated step to generate the $e$–$h$ pair is disregarded. Such an effect would, for instance, be the endothermic dissociation of the "cold" $S_1$ state in a molecular crystal/solid into an intermediate geminate $e$–$h$ pair (Fig. 1c). Figure 1d illustrates how disorder effects the dissociation of a singlet exciton via hopping among tail states of the DOS. In Sect. 6 this process will receive particular attention.

## 4 Experimental Probes of Photogeneration in Neat Conjugated Polymers

Dissociation of an excited singlet state in conjugated polymers is a process of particular interest because the semiconductor model postulated that the primary optically excited species is a well separated electron–hole state already. This would imply that the exciton binding energy is of the order $kT$ only [23]. However, it was observed that the action spectrum of photoconduction in systems like polyphenylenevinylene (PPV) and the laddertype poly-phenylene (LPPP) is flat within $S_1 \leftarrow S_0$ transition and increases steeply until the excess energy, relative to the

relaxed $S_1$ energy, reaches about 1 eV [24, 25]. This suggests that conjugated polymers behave very similar to molecular solids, such as an anthracene crystal, rather than inorganic semiconductors. However, this experimental observation neither discloses the origin of the photocurrent generated within the spectral range of the $S_1 \leftarrow S_0$ transition nor proves or disproves the applicability of the Onsager model. The essential question to be solved is whether or not photogeneration of charges within the spectral range of the $S_1 \leftarrow S_0$ transition starts from relaxed singlet excitons or not.

A unique experiment that offers an answer to the above question is based upon the technique of delayed field collection of optically generated charge carriers [26] combined with field dependent fluorescence quenching. It is able to prove or disprove the existence of metastable precursor states for generating a pair of charges and, concomitantly, to identify the rate limiting step in the carrier kinetics. With a short laser pulse one excites an intermediate coulombically bound *e–h* pair at variable electric field. After some time delay a second, collecting field is applied that is strong enough to dissociate any intermediate precursor *e–h* pair with unit efficiency. Simultaneously the fluorescence is recorded. The latter experiment is a measure of the number of optical excitations that are lost for fluorescence as a function of an electric field during excitation.

Experiments that were done on films of MeLPPP show that upon applying an electric field the fluorescence is significantly reduced bearing a super-linear field dependence (Fig. 2). At $F = 2 \times 10^6\,\mathrm{V\,cm^{-1}}$, and dependent on photon energy, between 20% and 50% of fluorescent singlet excitations are quenched. A simultaneous measurement of time delayed photogenerated charge carriers as a function of the electric field applied during excitation, i.e., prior to the application of a collecting field pulse

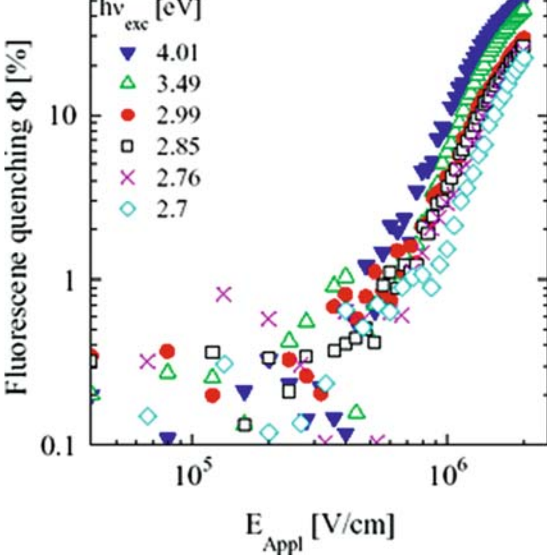


**Fig. 2** The dependence of fluorescence quenching $\Phi$ in the applied electric field of MeLPPP, parametric in excitation energy [26]. Fluorescence quenching is the difference in fluorescence with and without applied field, normalized to fluorescence without field

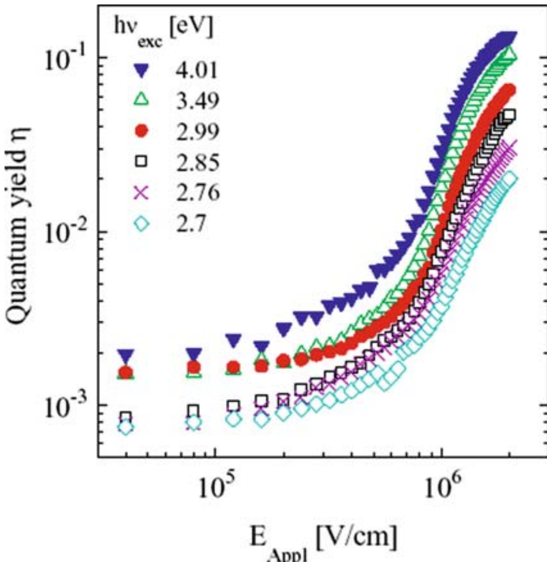


**Fig. 3** Charge generation efficiency vs applied electric field of MeLPPP, parametric in excitation energy [26]. Time delay $t_\mathrm{d}$ and the collection field $(E_\mathrm{coll})$ were set to 100 ns and $1 \times 10^6\,\mathrm{V\,cm^{-1}}$, respectively

of $1\,\mathrm{MV\,cm^{-1}}$ with a delay time of 100 ns, bears out a remarkably similar functional dependence (Fig. 3). A comparison between Figs. 2 and 3 indicates that both fluorescence quenching and carrier generation must have the same origin. Obviously, in the course of a field assisted process one generates an intermediate metastable state, e.g., a coulombically bound *e–h* pair that either dissociates into a pair of free carriers or recombines nonradiatively. Following the work by Graupner et al. [27], Gulbinas et al. [28] went one step further and monitored the growth of intermediate *e–h* pairs by field dependent transient absorption on a time scale from 1 to 150 ps employing a double modulation technique. The energy of the incident photons were either 3.1 eV or 4.6 eV. At 3.1 eV the signal confirms that the number of *e–h* pairs evolves smoothly within the entire time domain and complements the decay of the reservoir of $\mathrm{S}_1$ excitations. However, upon 4.6 eV excitation the *e–h* pair signal shows an instantaneous rise followed by a gradual rise [29]. These experiments lead to the following conclusions: (1) at $F \leq 5 \times 10^5\,\mathrm{V\,cm^{-1}}$ vibrationally relaxed singlet excitons can dissociate during their entire lifetime into metastable *e–h* pair in the course of a field assisted process obeying dispersive kinetics; (2) at lower electric fields there is residual photogeneration, most likely caused by sensitization by impurities; (3) at higher photon energies or by double quantum excitations higher Franck Condon states can autoionize and yield *e–h* pairs requiring less or no assistance by a electric field; (4) the lifetime of the intermediate *e–h* pair prior to complete dissociation is $\sim$100 ns or even longer; and (5) its subsequent dissociation requires escape from their mutual coulombic field that competes with nonradiative recombination.

The above conclusions are supported by several independent studies [30–33]. In summary, they prove that conjugated polymers behave fundamentally no differently

from classic molecular solids but there are important quantitative differences. One of them is the inapplicability of the classic Onsager approach to treat photogeneration of charge carriers. The reason is that the exciton binding energy is the sum of two energy terms that pertain to the initial step to generate a coulombically bound *e–h* pair from a neutral $S_1$ exciton and its subsequent complete dissociation. It is obvious that casting the entire field and temperature dependence of the photogeneration yield into to second step only is erroneous even when data fits might look acceptable. An important message from these results relates to the magnitude to the exciton binding energy. The binding energy is 0.4–0.8 eV [33], i.e., roughly 0.5 eV smaller than in molecular crystals of the acene-type, and permit field assisted dissociation of a vibrationally relaxed singlet exciton. The conceptual reason for this difference is the fact that in classic molecular crystals the lowest excited state is an intramolecular Frenkel exciton while in conjugated polymers it is a less tightly bound *e–h* pair in between Frenkel and Wannier-type with intra pair distance of about 1 nm [34]. Therefore, its expansion into an intermolecular CT state requires less work against the coulombic potential.

A complementary probe of photogeneration in conjugated polymers is THz probing of charge carriers generated by ultra-short light pulses. It permits the study of transient photoconductivity with sub-picosecond temporal resolution in real time. In principle, one measures the pump-induced modulation of the electric field of the transmitted essential single-cycle electromagnetic pulses of about 1 ps FWHM. Since (1) the electric field of the probing radiation is 1 kV cm$^{-1}$ only and (2) probing is on a picosecond time scale, this technique is suitable for monitoring instantaneous photogeneration under essentially field-free condition, not affected by retardation effects such as bimolecular exciton annihilation or energy transfer to accidental impurities that may act as sensitizers. In the course of such studies. The Delft group [35] excited MEH-PPV both in solution and film by 150-fs pulses of 3-eV photons and monitored the complex conductivity up to a delay time of 10 ps between pump and probe pulses. It turned out that in the polymer film up to 1% of the absorbed photons create charges. Most of them recombine geminately after 2 ps but some of them (10%) persist on a time scale of 5 ps or longer and contribute to real conductivity. In solution the efficiency of photogeneration is smaller and the conductivity decays to zero within 1–2 ps. The authors conclude that photogeneration involves ejection of an electron or hole from the initially hot exciton (with excess energy of 0.6 eV) to a neighboring chain. This process is feasible in films but not solution. The experiments moreover prove that charge carriers involved in photoconductivity are only those that result from initial interchain transfer, because the remaining intra-chain pairs recombine geminately and rather quickly. An important message derived from related work on regio-random polythiophene [36] is that morphology has a significant impact on the efficiency of charge carrier generation and their geminate recombination. In general, the results substantiate the notion that in conjugated polymers single photon photogeneration is an inefficient process because it requires an excited electron to work against the coulombic potential in order to escape from its sibling.

## 5 Photogeneration in Doped and Blended Conjugated Polymers

The only way to raise the yield of photoionization in conjugated polymers and other organic systems substantially is doping by electron acceptors or donors. The key requirement for generating an *e–h* pair at a donor–acceptor pair is that its energy be lower than the energy of the lowest excited singlet state of either the donor or acceptor. Otherwise energy transfer would populate the lowest singlet state that can decay radiatively. This is the prerequisite for efficient electroluminescence in light emitting diodes. Conceptually, this is straightforward. However, predicting which system is suitable for a LED or a photovoltaic device is not at all straightforward. The ambiguity is related to the lack of precise knowledge of the energy levels of the e–h pair. This energy is the difference between the energy of a radical cation of the donor, i.e., its ionization energy or, equivalently, the energy of the highest occupied molecular orbital (HOMO), and that of a radical anion as set by the electron affinity or, equivalently, the energy of the lowest unoccupied molecular orbital (LUMO), albeit diminished by the coulombic binding of the pair.

In practice, one often assumes that the energy of pair is solely determined by the oxidation and reduction potentials of both compounds as measures of the HOMO and LUMO levels and ignores the coulombic binding pair of the pair. Even worse, often only one of the potentials of the components is available via cyclic voltammetry and the missing potential is inferred from the optical $S_1 \leftarrow S_0$ 0–0 transition. This ignores the coulombic binding energy of the singlet state that is usually $\geq 0.5\,\text{eV}$. On the other hand, even if both potentials were known from cyclic voltammetry, a systematic error is encountered because these data refer to charge transfer from an electrode into molecule/polymer usually in a polar solvent. However, in a polar solvent the solvation energy of the anion/cation is higher than in a solid, mostly apolar dielectric. Fortunately, the above ambiguity becomes irrelevant if the dopant is highly electronegative, such as $C_{60}$, because its LUMO is at least 1 eV below those of common donors such as PPV or polyfluorenes. In this case, charge transfer is undoubtedly favored over energy transfer.

A prototypical donor–acceptor system is a PPV-type donor blended with $C_{60}$ or a derivative of it, such as (6,6)-phenyl $C_{61}$ butyric acid methyl ester (PCBM). Transient absorption measurements on a thin film of a poly(2-methoxy, 5-($3'$,$7'$ dimethyl-octyloxy))-*p*-phenylene vinylene (MDMO-PPV):PCBM composite demonstrates occurrence of charge transfer. Bleaching of the donor absorption and the simultaneous onset of the absorption of the PCBM radical anion occurs with a time constant of 45 fs [37]. This is equivalent to a charge exchange interaction energy of 0.1 eV, comparable to the strength of electron transfer in a molecular crystal [9]. It implies that every absorbed photon is converted to a pair of donor radical cation and acceptor radical anion which is a prerequisite for using the system as an active layer in an efficient PV. In fact, a power efficiency of several percent (6.5%) has already been realized with such systems [38]. This proves that the majority of photo-induced charges are indeed collected by the built-in electric field and migrate towards the electrodes without major loss by nongeminate recombination.

On the other hand, this raises a fundamental question as to why the initially generated *e–h* pair escapes from its mutual coulombic potential so easily while in a single component system coulombic effects cut down the yield to below $10^{-3}$.

In order to answer this question, Mihailetchi et al. [39] measured photogeneration in a blend of poly(2-methoxy-5-(3′, 7′-dimethyloctyloxy)-phenylene vinylene (OC1C10-PPV) and PCBM as function of applied voltage and temperature. Presuming that the essential intermediate is an optically generated coulombically bound *e–h* pair located at an internal donor–acceptor hetero-junction that can either dissociate completely or recombine geminately, they analyzed their data in terms of Braun's model [22]. Based upon a broad distribution of *e–h* pair distances centered at 1.3 nm and invoking a value of 1 µs for the *e–h* pair lifetime they were able to rationalize their experimental results that include a measured 60% carrier yield at a built-in field of $7.5 \times 10^4\,\mathrm{V\,cm^{-1}}$ at room temperature. However, an open question appears to be their choice of a pair lifetime of 1 µs. Recent experiments on a blend of a polyfluorenecopolymer and PCBM reveal a broad distribution of lifetimes albeit centered at a value as short as 1 ns [40].

Complementary experiments on photogeneration in doped and blended systems were performed by Im et al. [41]. The donors were a copolymer of phenyl-substituted PPV (SY, superyellow) and a alkyl-substituted hexa-benzo-coronene and the acceptors were perylenediimide and tri-nitro-fluorenone. The photocurrent was measured as a function of the external electric field within a broad range of acceptor concentration. It turned out that for concentration ranging between 0.1% (by weight) and a few percent the yield of charge carriers increases only marginally. The reason is that as little as 0.05% of inadvertant impurities of the donor materials is enough the quench 50% of initial optical excitations due to charge transfer. Only a minor fraction of them (<0.1%) dissociate into free charge carriers. However, a dramatic increase by two orders of magnitude is observed beyond 10% doping (Fig. 4).

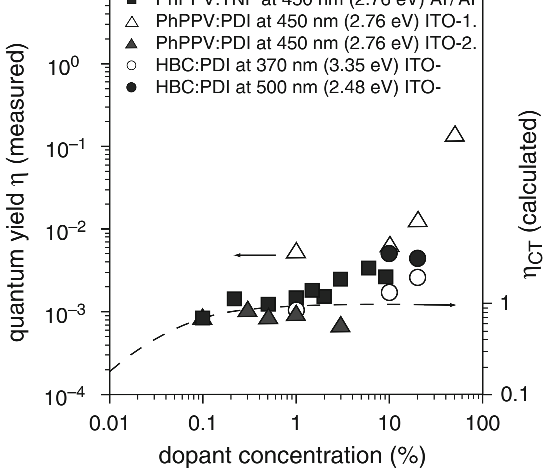


**Fig. 4** Dependence of charge carrier photogeneration quantum yield on the dopant concentration at 293 K [41]. The photoactive materials, the dopant and the sample structure are varied as shown in the legend

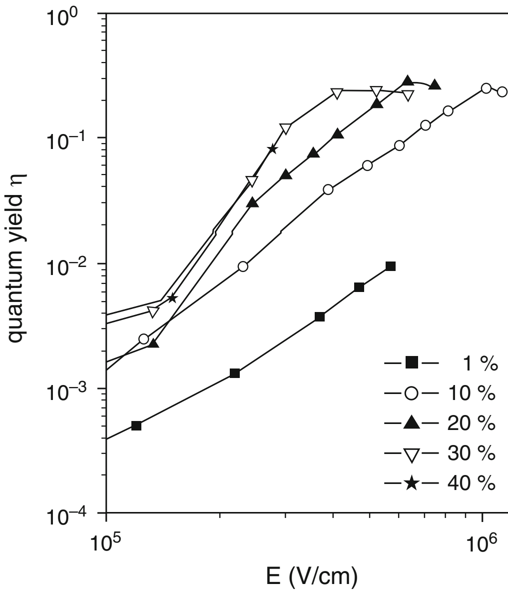


**Fig. 5** Field dependence of the charge carrier photogeneration quantum yield in the device ITO/PhPPV:PDI/Al [41]. The temperature is 293 K at varying dopant concentrations. The photocurrent has been excited with 2.25 eV (550 nm) light

A clue for understanding this effect is provided by the field dependence of the yield. Figure 5 shows, that the yield increases with electric field with tendency towards saturation. Importantly, onset of saturation, which is a measure of how strongly the geminate *e–h* pairs are bound, shifts towards lower fields at increasing acceptor concentration, indicating that the pairs become more loosely bound. Recently, a model by Arkhipov et al. [42] has been advanced that rests on the establishment of an internal, mesoscopic interface between donors and acceptors in the blend. Their difference of electronegativities gives rise to the formation of a dipole layer that exists already prior to optical excitation. This dipolar field counteracts the coulombic field of the *e–h* pair and introduces a screening effect. Obviously, the topology of the interface plays a crucial [43]. The present results substantiate the notion that the rate limiting step in optical charge generation in an organic PV-cell is the dissociation of the geminately bound *e–h* pair rather than nongeminate recombination in the bulk.

## 6 Analytic Treatment of Exciton Dissociation

Below, a conceptual framework to rationalize photogeneration in systems such as conjugated polymers is developed with particular emphasis on their randomness. Because of structural disorder all relevant energy levels, notably the energy of the *e–h* pair state, are associated with inhomogeneous broadening usually featuring

Gaussian-type of distribution functions [14]. This is not only relevant when an *e–h* pair is generated from the parent singlet state but also for its subsequent escape from mutual coulombical potential. From hopping theory [44] it is known that transport occurs close to the so-called transport energy within the DOS distribution that depend on temperature. It is a ubiquitous feature, borne out by both temperature dependent experiments and Monte Carlo simulation studies, that the temperature dependence of the charge carrier mobility deviates from Arrhenius' law [45]. Another example is charge injection from a metal electrode to a conjugated polymer [46, 47]. In the following this concept will be extended to bulk systems. The goal is to obtain an analytic solution for describing the dependence of the exciton dissociation yield as a function of temperature, electric field, and width of the DOS distribution.

In conjugated polymers the primary excitations are singlet excitons with a mean electron–hole separation of about 1 nm. Subsequent transfer of an electron to an adjacent, previously unexcited polymer segment, i.e., formation of a CT state, requires additional energy. Otherwise the photoluminescence spectrum would feature a broad, red-shifted band with a lifetime longer than the usual fluorescence decay time, typically 100…800 ps, contrary to experimental observation. Such electron transfer can, however, be initiated by a strong electric field that can overcompensate the required charge transfer energy. This is evidenced by experiments described in Sect. 4 and by the observation of a temporal fluorescence spike after switching off the stimulating field applied during optical excitation. It indicates that a strong electric field is required to stabilize metastable, nonfluorescent *e–h* pairs [48]. On the other hand, the activation energy of steady state photoconduction is notoriously low, typically less than 0.1 eV, although the photocarrier yield bears out a strong field dependence. This appears to be in contradiction with the notion that the exciton binding energy is comparable to that conventional molecular solids, i.e., on the order of 1 eV.

### *6.1 Theory*

Dissociation of an exciton into a pair of coulombically unbound charge carriers in a conjugated polymer will be treated analytically under premise of (1) that the energy of the nearest neighbor CT state exceeds that of the exciton and (2) that the carrier transport occurs in energetically and positionally disordered systems. We describe it as a two step process in which the first step is charge transfer from the excited singlet state $S_1$ to the CT state and the subsequent event is escape of the *e–h* pair forming the CT state from their mutual coulombic potential well. We also take into account that the $S_1$ state has a finite lifetime. The model system is a cubic array of hopping sites with lattice spacing $a$. An optical excitation of a site, i.e., a molecule or a subunit of a conjugated polymer chain, raises an electron from the HOMO to the LUMO. Complete dissociation of the initial excitation, supposed to be a singlet state, requires supply of the exciton binding energy $E_b$. It is the sum of the energy

to transfer the electron to a neighboring site and the coulombic binding energy of the resulting CT state, $E_{\mathrm{coul}}$, or more generally, the coulombically bound *e–h* pair. Subsequently either the electron or the hole of the CT state executes a random walk within a potential:

$$U(r) = E_{\mathrm{b}} - \frac{e^2}{4\pi\varepsilon\varepsilon_0 r} - eFr\cos\vartheta, \tag{3}$$

where $r$ is the distance between carriers in geminate pair, $F$ the external field, $e$ the elementary charge, $\varepsilon$ the dielectric constant, $\varepsilon_0$ the dielectric permittivity, and $\vartheta$ is an angle between directions of the electric field and the charge transfer. Then

$$E_{\mathrm{CT}} = E_b - \frac{e^2}{4\pi\varepsilon\varepsilon_0 a}, \tag{4}$$

is the energy needed so that the exciton can transfer an electron to a CT state with nearest neighbor distance $a$. If $E_{\mathrm{CT}} > 0$ formation of the CT state is an upward jump in energy. Since the hopping system is an energetically as well as positionally random array of sites, $E_{\mathrm{CT}}$ is a random quantity, tractable in terms of random walk theory. It was shown [49, 50] that in disordered hopping systems the energy of the target site populated by upward jumps does not depend upon the initial energy of the carrier. In order to continue its motion a charge carrier has to be excited to a hopping site from which transfer to a site away from the origin site can compete with a return to the origin. The energy at which this condition is met is the so-called transport energy [44] whose equivalent is the mobility edge in amorphous inorganic semiconductors. If the first carrier jump is an upward jump one can assume that thermal quasi-equilibrium is already established after the first jump, implying that there is no further carrier relaxation within the tail of the DOS.

Let us consider a charge carrier, e.g., electron, being transferred to CT state from excited singlet state across of distance $r$. If the CT state dissociates into free carriers, the electron contributes to the photocurrent unless it returns back to the singlet state. The dissociation probability of CT state is determined by interplay between drift and diffusion within the potential well that is formed by a superposition of an external electric field and the Coulomb field of the geminate *e–h* pair. It can be described in terms of the known 3D Onsager escape probability. On premise of the Miller-Abrahams formalism [51], the rate of this electron transfer from a discrete bulk excited singlet state with energy $E$ into a disorder affected CT state with energy $E'$ is given by

$$\begin{aligned} \nu\left(E,E',r\right) &= \nu_0 \exp(-2\gamma r)\,\mathrm{Bol}\left(E,E'\right) \\ \mathrm{Bol}\left(E,E'\right) &= \begin{cases} 1 & : \quad E' < E \\ \exp\left(-\frac{E-E'}{kT}\right) & : \quad E' > E \end{cases}, \end{aligned} \tag{5}$$

where $\nu_0$ is the attempt-to-jump frequency, $\gamma$ the inverse localization radius, $T$ the temperature, and $k$ the Boltzmann constant. Taking into account the

disorder-effected energy distribution of CT states $g(E)$, the averaged rate of an electron jump from excited singlet state to CT state is

$$\nu(r,\vartheta) = \nu_0 \exp(-2\gamma r) \int_{-\infty}^{\infty} \mathrm{d}E' \mathrm{Bol}(E') g\left[U(r,\vartheta,F) - E'\right]. \quad (6)$$

For simplicity we consider a Gaussian distribution of hopping sites and assume the same width of CT states and coulombically unbound transport sites. It should be emphasized that the averaging over energy in Eq. (6) is automatically taken care of. It implies that the rate of the first electron transfer event does not depend upon the energy of its target site but is governed by the disorder of the system and the value of $E_\mathrm{b}$.

After being transferred to the CT state electron has a probability to escape from the potential well (3) or return back to the excited molecule. The probability for electron to escape from the potential well (3), i.e., the dissociation of the CT state into free carriers, will be described in terms of the framework of 3D Onsager model [20, 52].

$$p(r,\vartheta,F) = \exp(-A-B) \sum_{n=0}^{\infty} \sum_{m=0}^{\infty} \frac{A^m}{m!} \frac{B^{m+n}}{(m+n)!},$$
$$A = e^2/4\pi\varepsilon\varepsilon_0 kTr, \qquad B = (eFr/2kT)(1+\cos\vartheta). \quad (7)$$

In accordance with the model it is assumed that the rate of geminate recombination of the CT state to the first excited singlet state follows Eq. (5) under the constraint that $E' > E$. This implies that the CT state is always above the singlet exciton state. In single component molecular systems this condition is usually fulfilled as evidenced by the observations that (1) the fluorescence spectra are mirror-symmetric with absorption and (2) fluorescence quenching requires a high electric field [53]. Obviously, the present theory is limited to cases in which $E_\mathrm{b} > E_\mathrm{coul}$.

By combining Eqs. (6) and (7) the rate of two step process, i.e., the formation of the CT state and its subsequent full dissociation is

$$\nu_\mathrm{esc}(r,\vartheta) = \nu(r,\vartheta) p(r,\vartheta,F). \quad (8)$$

Integrating Eq. (8) over the dissociation volume yields a total frequency of an exciton dissociation into free carriers:

$$\nu_\mathrm{tot} = \int_V \nu(r,\vartheta)\, p(r,\vartheta,F) \mathrm{d}V. \quad (9)$$

Since the result of the integration depends mainly upon the energy disorder of the hopping system and the value of the energy $E_\mathrm{b}$ and it only weakly depends upon the direction of the first jump or upon the angle $\vartheta$, one can ignore the angular

dependence and assume $\vartheta = 0$. Applying the Que [54] formalism to calculate a total frequency of exciton dissociation one arrives at

$$\nu_{\mathrm{tot}} = 4\pi \int_a^\infty r^2 \mathrm{d}r \nu(r) \exp(-A-B) \sum_{n=0}^\infty \sum_{m=0}^\infty \frac{A^m}{m!} \frac{B^{m+n}}{(m+n)!} =$$

$$\nu_0 4\pi \frac{kT}{eF} \sum_{i=1}^\infty i \left(\frac{4\pi\varepsilon_0\varepsilon F}{e}\right)^{i/2} I_i \left(\frac{2}{kT}\sqrt{\frac{e^3 F}{4\pi\varepsilon_0\varepsilon}}\right) \int_a^\infty \mathrm{d}r r^{i+1} w(r), \tag{10}$$

where $w(r) = \nu_{\mathrm{esc}}(r, \vartheta = 0)/\nu_0$. It is worth mentioning that $\nu_{\mathrm{esc}}(r, \vartheta = 0)/\nu_0$ can be considered as a distribution function for the distance of the first jump for an electron from the exciton state to the CT state, considering that the lower limit in the integration is the intermolecular distance $a$.

Different from the Braun [22] extension to Onsager's theory in which the CT state is considered to have a finite lifetime and Onsager 1934 theory [55] in which the dissociating state is an infinitely lived ion pair, the present treatment is premised upon the notion that the dissociating state is an exciton state with finite lifetime. As a representative value we consider the intrinsic lifetime of a singlet state of an average conjugated polymer, that is about 0.5 ns. Depending on the energy gap between the CT state and the singlet state, the latter can make several attempts to reach the CT state. The probability for an exciton to dissociate into free carriers is

$$\Phi = \frac{\nu_{\mathrm{tot}}}{1/\tau + \nu_{\mathrm{tot}}}. \tag{11}$$

Employing a Gaussian function for the energy distribution of CT states,

$$g(E) = \frac{N_{\mathrm{t}}}{\sqrt{2\pi}\sigma} \exp\left(-\frac{E^2}{2\sigma^2}\right), \tag{12}$$

where $N_{\mathrm{t}}$ is the total density of CT-states and $\sigma$ is a disorder parameter, one can use Eq. (12) to calculate field- and temperature dependencies of photogeneration quantum yield.

### 6.2 Results

Figure 6 shows the field dependence of the dissociation yield $\Phi$ of an optically generated exciton parametric in the exciton binding energy $E_{\mathrm{b}}$. The input parameters are the lattice parameter in a cubic lattice $a = 1$ nm, the minimum electron–hole separation in the CT state $r_0$ is assumed to be identical with $a$, the dielectric constant $\varepsilon = 3.5$, $T = 300$ K, and $\tau = 0.5$ ns is the exciton lifetime which is a representative value for singlet excitons in conjugated polymers [56]. The prefactor rate,

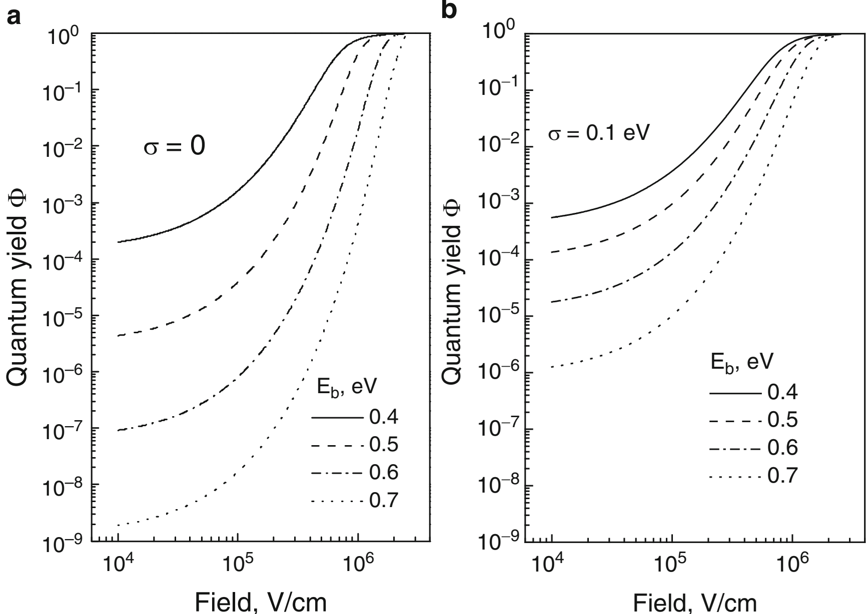


**Fig. 6** Calculated yield $\Phi$ of dissociation of an exciton in a discrete hopping system (**a**), $\sigma = 0$ and in a hopping system in which the hopping sites feature a Gaussian shaped DOS distribution with variance $\sigma = 0.1\,\mathrm{eV}$ (**b**) as a function of electric field. The parameter is the exciton binding energy $E_\mathrm{b}$. The minimum jump distance is $r_0 = 1\,\mathrm{nm}$, the dielectric constant is $\varepsilon = 3.5$, the prefactor hopping rate is $\nu_0 \exp(-2\gamma r_0) = 10^{12}\,\mathrm{s}^{-1}$, the exciton lifetime $\tau$ is taken to be 0.5 ns and the temperature is 300 K. The choice of $r_0$ and $\varepsilon$ implies a maximum coulombic binding energy of the electron–hole pair forming a CT state of 0.4 eV

$\nu_0 \exp(-2\gamma r_0)$, is taken to be $10^{12}\,\mathrm{s}^{-1}$. This estimate is derived from the mobility of charge carriers extrapolated to $T \to \infty$–about $0.1\,\mathrm{cm}^2\,\mathrm{V}^{-1}\,\mathrm{s}^{-1}$–which is the mobility in a hopping system in the absence of disorder making use of Einstein's relation between diffusivity and mobility and assuming isotropic diffusion with a diffusion coefficient $D = (1/6)\,a^2 \nu_0 \exp(-2\gamma r_0)$. The choice of $\varepsilon$ and $r_0$ imply a coulombic binding energy of the CT state of 0.4 eV. A value of $E_\mathrm{b} = 0.4\,\mathrm{eV}$ would, therefore, imply that exciton and CT state are isoenergetic. From Fig. 6a it is obvious that the yield decreases as $E_\mathrm{b}$ increases as it should when additional activation energy is needed to populate the intermediate CT state. A relevant question to ask is whether or not this field dependence is unique, i.e., could one fit an experimentally determined photocarrier yield in terms of the classic 3D version of Onsager's theory disregarding the present theory for field dependent endothermic exciton dissociation. To do this one can compare the $\Phi(F)$ plots in Fig. 6a with optimal 3D Onsager plots using $r_0$ as a fit parameter. Figure 7 shows that one more or less could fit the calculated $\Phi(F)$ dependence within the lower field range yet not in the higher field.

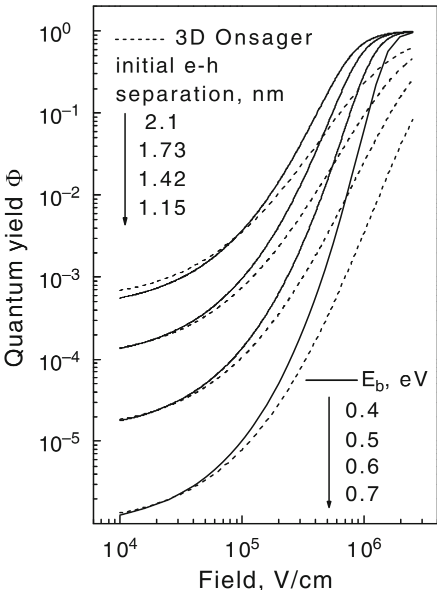


**Fig. 7** Comparison between the calculated dissociation yield $\Phi(F)$ taken from Fig. 6b (*full curves*) and hypothetical Onsager plots (*dashed curves*) in which $r_0$ is varied in a way to obtain optimal agreement in the low to moderate field range

A key result of the current study, evidence by comparing Fig. 6a and 6b, is the recognition that disorder assists exciton dissociation. This is illustrated by Fig. 8 in which the field dependence of the yield is plotted parametric in σ for two values of $E_b$. Figure 9 shows the dissociation yield as a function of $E_b$ at variable disorder, quantified in terms of the variance σ of the DOS distribution. In Fig. 9 the slope $\partial(\ln\Phi)/\partial E_b$ for $\sigma = 0$ and moderate field $F = 10^5\,\mathrm{V\,cm^{-1}}$ is $-1/kT$ in accordance with the expected Arrhenius behavior. Another noteworthy result is the temperature dependence of the yield. While Fig. 10a confirms that for moderate fields the yield bears out simply activated behavior, Fig. 10b,c demonstrates that in the presence of disorder the T-dependence is much weaker and deviates significantly from Arrhenius' law. This difference is even more striking when the electric field is increased to $F = 10^6\,\mathrm{V\,cm^{-1}}$ (Fig. 11). In this case the apparent activation energy for a system with an exciton binding energy $E_b = 0.5\,\mathrm{eV}$, determined at 300 K, is only about 0.04 eV.

The exciton binding energy is the sum of the energy needed to expand the exciton to a CT state $(E_{CT})$ and the coulombic binding energy $E_{coul}$ of the CT state. Since the CT state in a conjugated polymer is experimentally an ill-defined quantity, we explored the effect of varying the $E_{coul}$ while keeping $E_b$ as well as the electronic coupling parameter, $2\gamma a$, fixed. Figure 12 demonstrates that on decreasing $E_{coul}$ from 0.4 eV to 0.25 eV, equivalent to increasing $r_0$ from 1.0 to 1.6 nm, in a system with $E_b = 0.7\,\mathrm{eV}$ and $\sigma = 0.1\,\mathrm{eV}$, the yield increases and the temperature dependence becomes weaker. This demonstrates that the share of the coulombic binding energy to the total exciton binding energy has, indeed, an effect on the $\Phi(F,T)$ dependence.

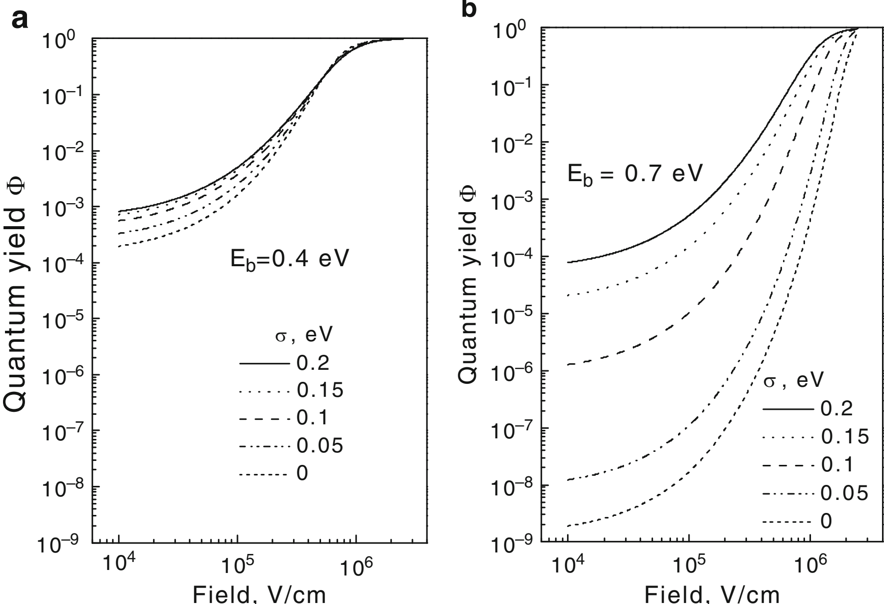


**Fig. 8** Calculated quantum yield $\Phi$ as a function of electric field parametric in σ for $E_b = 0.4$ eV (**a**) and $E_b = 0.7$ eV (**b**). (For parameters see Fig. 6)

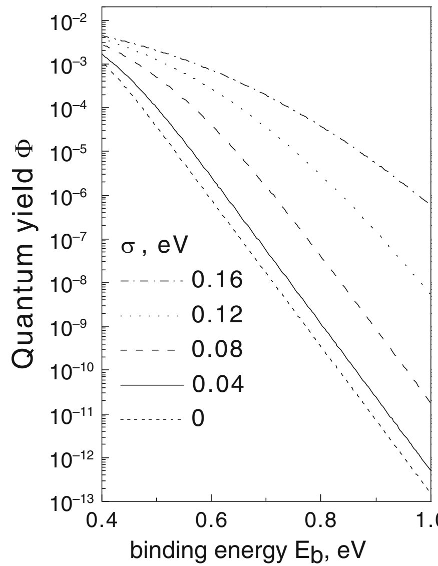


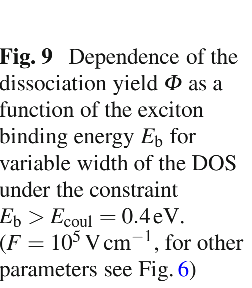

**Fig. 9** Dependence of the dissociation yield $\Phi$ as a function of the exciton binding energy $E_b$ for variable width of the DOS under the constraint $E_b > E_{coul} = 0.4$ eV. ($F = 10^5$ V cm$^{-1}$, for other parameters see Fig. 6)

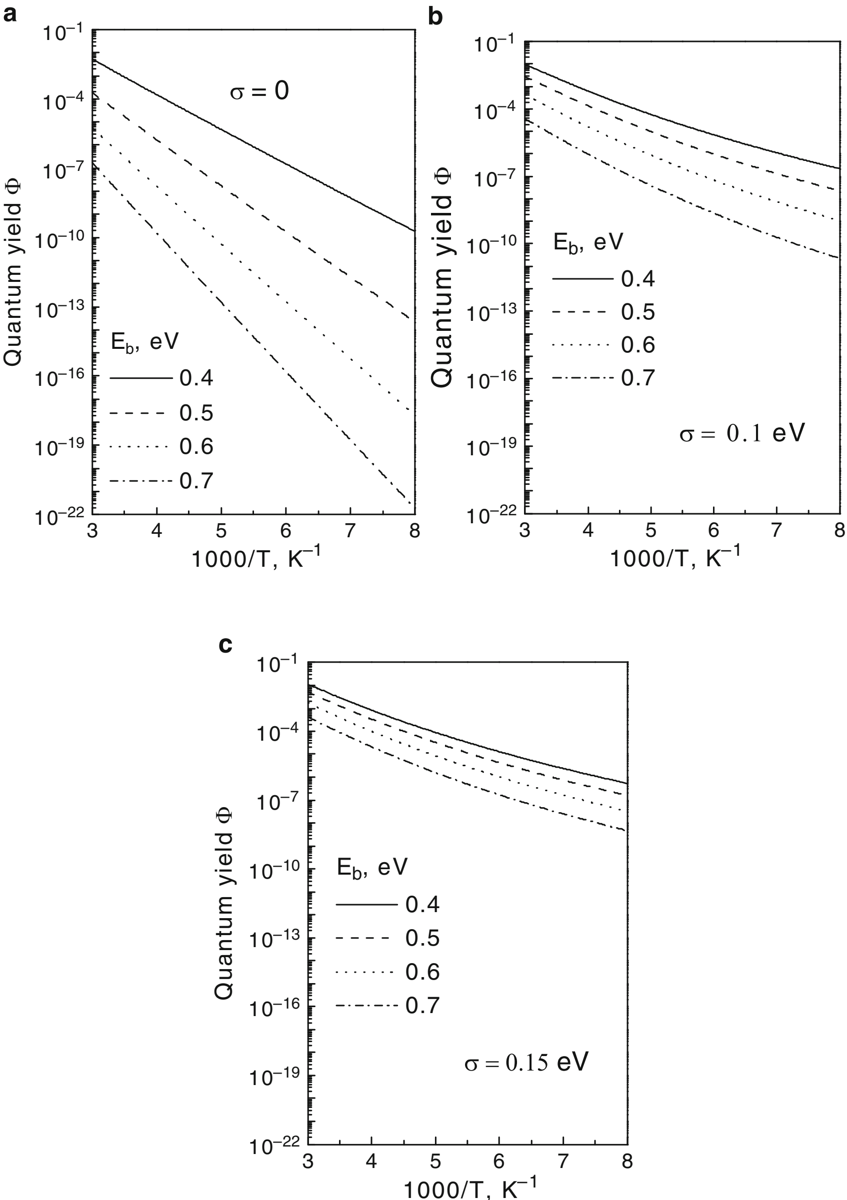


**Fig. 10** Temperature dependence of the calculated dissociation yield $\Phi$ parametric in $E_b$ for $\sigma = 0$ (**a**), $\sigma = 0.1\,\mathrm{eV}$ (**b**), and $\sigma = 0.15\,\mathrm{eV}$ (**c**). The electric field was $10^5\,\mathrm{V\,cm^{-1}}$. For remaining parameters see Fig. 6

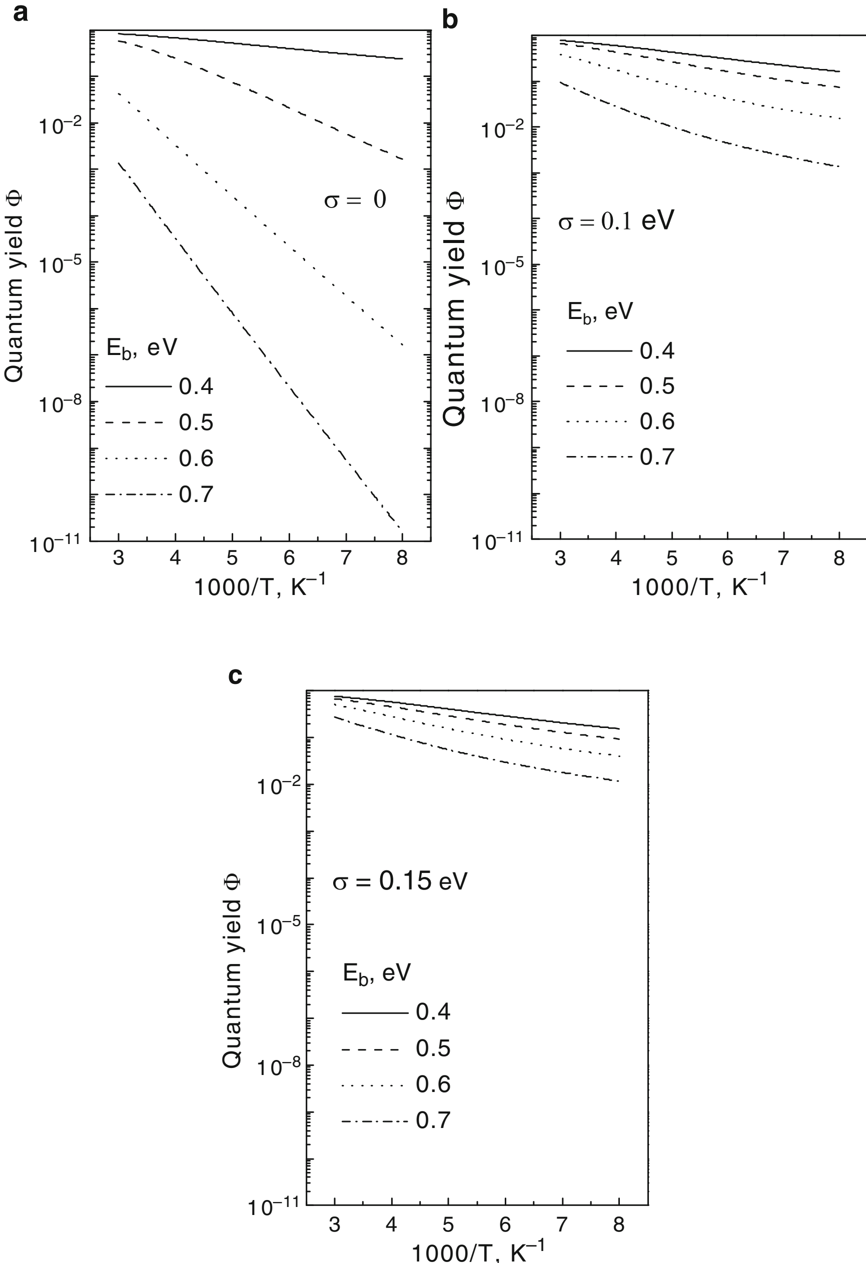


**Fig. 11** Temperature dependence of the calculated dissociation yield $\Phi$ parametric in $E_b$ for $\sigma = 0$ (**a**), $\sigma = 0.1\,\mathrm{eV}$ (**b**), and $\sigma = 0.15\,\mathrm{eV}$ (**c**). The electric field was $10^6\,\mathrm{V\,cm^{-1}}$. For remaining parameters see Fig. 6

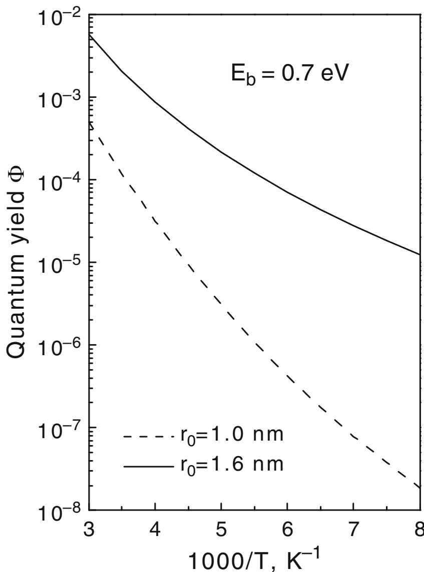


**Fig. 12** Temperature dependence of the yield at constant $E_b$ but for different share between the charge transfer energy and the coulombic binding energy $E_{coul}$ determined by the initial electron–hole separation. ($E_b = 0.7\,eV$, $F = 3 \times 10^5\,V\,cm^{-1}$, for other parameters see Fig. 6)

## *6.3 Discussion*

The present study solves this puzzle regarding the temperature dependence of the photocarrier yield. It indicates that the apparent activation energy, determined from the slope of an Arrhenius plot at a given temperature, can be as small as 10% of the expected value of the exciton binding energy, i.e., $\partial(\ln\mu)/\partial(1/T)$ does not reflect the exciton binding energy. This phenomenon is a signature of hopping transport in a Gaussian DOS. Under normal conditions the transport energy is below the center of a Gaussian DOS. Most important, it shifts towards energies at lower temperatures [44]. Therefore the activation energy needed to transfer an electron from the exciton to LUMO of the CT state decreases as the temperature decreases. This implies that the temperature dependence of the dissociation yield becomes progressively lower. A related phenomenon was observed when studying dissociation of a coulombically bound *e–h* pair by Monte Carlo simulation [57]. In that case an electron was generated at a given distance from its sibling countercharge at an energetically random site. In this case the $T$-dependence of the Onsager-like escape from the coulombic potential deviates from Arrhenius' because the moving carrier has only to be excited to the transport energy rather than to the center of the DOS. Although the result is equivalent, the situation in the current case is conceptually different because here all the disorder is cast into the first jump of the electron from the exciton state to the CT state while subsequent diffusive motion is treated in term of Onsager's 1938 theory.

Strong field dependence of the yield and a simultaneously weak temperature dependence of exciton dissociation is at variance of Onsager's classic description of photogeneration predicting that $\lim_{F\to\infty}\Phi(F) = \lim_{T\to\infty}\Phi(T) = \Phi_0$, $\Phi_0$ being the

primary yield of the precursor *e–h* pairs. Comparing Fig. 6a and 6b demonstrates, however, that this is a generic signature of an energetically random system. This is in accordance with experiment. Photogeneration in conjugated polymers usually bears out a steep field dependence and a notoriously weak temperature dependence. Although the present theory does provide a qualitative explanation of experimental results, quantitative data fits are inevitably ambiguous because there are three adjustable parameters, i.e., the exciton binding energy, the disorder potential, and the minimum distance for exciton to CT state jump. However, there are also conceptual problems. The current theory is based upon the assumption that the real world system can be represented by a cubic array of point sites among which charge carriers can hop. In conjugated polymers there is anisotropy regarding electronic coupling, i.e., within the π-bonded backbone electronic coupling is strong but weak between the chains. Therefore the initial steep in photogeneration will be an on-chain charge transfer step to a CT state involving two neighboring chain segments that are for a short time stabilized by on-chain disorder. Further dissociation requires off-chain hopping. Modeling the transition from the exciton to the CT-state in terms of parameters inferred from charge transport studies that probe inter-site hopping processes can, therefore, be a serious oversimplification. The treatment also neglects the anisotropy of the dielectric permittivity and underestimates the effect of the disorder involving the first jump. When comparing theory with the experimental side one should also consider that at high electric fields the bottom states of the intermediately generated *e–h* pairs can be below the singlet exciton energy [48] and geminate recombination is impeded. Since this effect is disregarded in the theory the experimentally measured yields at high electric field will bear out a weaker field dependence.

Apart from these conceptual problems one has to consider that in a photoconduction experiment there is always an extrinsic contribution to photogeneration such as sensitization due to inadvertent impurities and exciton dissociation at an electrode. The former usually dominates at low to moderate electric fields. It originates from charge transfer from bulk excitons towards mostly acceptor-type of impurities such as oxidation products and can be rationalized in terms of Arkhipov et al.'s theory [58]. It is worth mentioning, though, that at high electric fields, photogeneration is, in fact, intrinsic as evidenced by the concomitant decrease of fluorescence [26].

Having these cautionary remarks in mind we analyze previous data on the field dependence of photocarrier generation in a film of the ladder-type methyl-substituted polyphenylene (MeLPPP) [59] within a field range between 0.1 and $3\,\mathrm{MV\,cm^{-1}}$ (Fig. 13). To compare theory and experiment the parameters $r_0 = 1\,\mathrm{nm}$, $\varepsilon = 4$, $T = 298\,\mathrm{K}$, $2\gamma r_0 = 7$, $\sigma = 0.15\,\mathrm{eV}$, $\tau\nu_0 \exp(-2\gamma r_0) = 1$ or 2 and correspondently either 0.65 or 0.8 eV for $E_\mathrm{b}$ have been used. The value of $\tau\nu_0 \exp(-2\gamma r_0)$, which is the number of attempts an exciton makes towards dissociation, is by a factor of 4 (or 2) less that what one would expect upon on the basis of fluorescence lifetime and hopping rate in a hopping system in the absence of disorder. The latter can be inferred from the infinite temperature intercept of the hole mobility ($3\times10^{-3}\,\mathrm{cm^2\,V^{-1}\,s^{-1}}$ [60]) employing the theoretical μ/D–ratio between mobility and diffusion combined with the assumption of isotropic diffusion $\left(4\times10^{10}\,\mathrm{s^{-1}}\right)$.

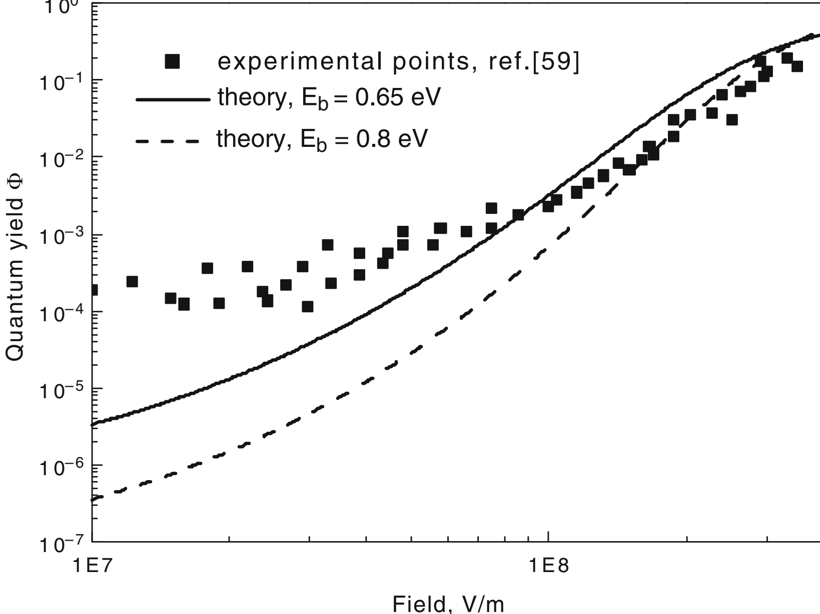


**Fig. 13** Comparison between experimental and calculated field dependence of the photocarrier yield for MeLPPP. Parameters are $r_0 = 1\,\text{nm}$, $\varepsilon = 4$, $T = 298\,\text{K}$, $\sigma = 0.15\,\text{eV}$, $\gamma = 7/(2r_0)$; $\tau\nu_0 \exp(-2\gamma r_0) = 1$, with $E_\text{b} = 0.65\,\text{eV}$ and $\tau\nu_0 \exp(-2\gamma r_0) = 2$ with $E_\text{b} = 0.8\,\text{eV}$. Experimental data are taken from [59]

The fluorescence lifetime of a MeLPPP chain in a glassy matrix is 300 ps (Yu. Romanovskii, private comm.) whereas the estimated lifetime in the film is 100 μs (F. Laquai, private comm.). The crucial quantity introduced in data fitting turns out to be the disorder parameter. Well structured absorption and fluorescence spectra indicate that MeLPPP is weakly disordered. From hole transport $\sigma = 0.05\,\text{eV}$ has been inferred [61]. On the other hand the unusually weak temperature dependence of the photocarrier yield provides strong evidence that $\sigma$ must be significantly larger than 0.05 eV. The probable solution to this puzzle is that a coulombically bound *e–h* pair located at different chains encounters a larger spread of site energies than a single carrier migrating within an entirely empty DOS. The fact that the photocarrier yield at moderate field exceeds the theoretical value is readily accounted for by extrinsic effects such as sensitization by impurities/dopants [59].

## 7 Conclusions

Random walk theory is able to rationalize the experimental observation that (1) in conjugated polymers or related disordered organic solids intrinsic photogeneration

starts at the absorption edge indicating that relaxed singlet excitons can, indeed, dissociate and (2) it features a strong field dependence with a concomitant abnormally weak temperature dependence. It explains why the infinite temperature intercept of $\Phi(T)$ in an Arrhenius plot is significantly less than the asymptotic carrier yield in the $F \rightarrow \infty$ limit and cannot be taken as a measure of the exciton binding energy. It is premised upon the notion that the energy gap between the CT state and the singlet state is supplied by electric field and temperature but is diminished by disorder effects. Upon exciting the sample above the $S_1 \leftarrow S_0$ 0–0 threshold, the excess energy stored in a vibrationally hot Franck Condon state can further assist dissociation. Then autoionization takes over.

Another timely problem relates to the improvement of the efficiency of organic PVs made of donor–acceptor blends. Meanwhile it is becoming clear that the crucial step is the dissociation of the *e–h* pair that has been generated optically at an internal donor–acceptor interface. The challenge is to find a way to overcompensate its mutual coulombic potential so that geminate recombination is suppressed. This is the subject of current experimental and theoretical work.

**Acknowledgments** HB acknowledges valuable discussions with Dirk Hertel and financial support by the Fond der Chemischen Industrie.

## References

1. Forrest SR, Thompson ME (Guest eds) (2007) Organic electronics and optoelectronics. Chem Rev 107:923–1386
2. Friend RH, Gymer RW, Holmes AB, Burroughes JH, Marks RN, Taliani C, Bradley DDC, Dos Santos DA, Bredas JL, Logdlund M, Salaneck WR (1999) Electroluminescence in conjugated polymers. Nature 397:121
3. Forrest SR (2004) The path to ubiquitous and low-cost organic electronic appliances on plastic. Nature 428:911
4. Müllen K, Scherf U (eds) (2006) Organic light emitting devices synthesis, properties and applications. Wiley, Weinheim
5. Yersin H (ed) (2007) Highly efficient OLEDs with phosphorescent materials. Wiley, Weinheim
6. Pope M, Swenberg CE (1999) Electronic processes in organic crystals and polymers. Oxford University Press, New York
7. Borsenberger PM, Weiss DS (1998) Organic photoreceptors for xerography. Marcel Dekker, New York
8. Pfister G (1977) Hopping transport in a molecularly doped organic polymer. Phys Rev B 16:3676
9. Coropceanu V, Cornil J, Da Silva Filho DA, Olivier Y, Silbey R, Bredas J-L (2007) Charge transport in organic semiconductors. Chem Rev 107:926
10. Silinsh EA, Capek V (1994) Organic molecular crystals. AIP Press, New York
11. Romanovskii YuV, Gerhard A, Schweitzer B, Scherf U, Personov RI, Bässler H (2000) Phosphorescence of pi-conjugated oligomers and polymers. Phys Rev Lett 84:1027
12. Rudenko AI (1977) Theory of trap-controlled transient current injection. J NonCryst Solids 22:215
13. Schwoerer M, Wolf HC (2006) Organic molecular solids. Wiley, Weinheim
14. Kador L (1991) Stachastic-theory of inhomogeneous spectroscopic line-shapes reinvestigated. J Chem Phys 95:5574

15. Borsenberger PM, Bässler H (1991) Concerning the role of dipolar disorder on charge transport in molecularly doped polymers. J Chem Phys 95:5327
16. Hertel D, Bässler H (2006) In: Müllen K, Scherf U (eds) Organic light emitting devices synthesis, properties and applications. Wiley, Weinheim, p 95
17. Arkhipov VI, Heremans P, Emelianova EV, Bässler H (2005) Effect of doping on the density-of-states distribution and carrier hopping in disordered organic semiconductors. Phys Rev B 71:045214
18. Silver M, Pautmeier L, Bässler H (1989) On the origin of exponential band tails in amorphous semiconductors. Solid State Commun 72:177
19. Geacintov N, Pope MJ (1967) Generation of charge carriers in antracene with polarized light. Chem Phys 47:1194
20. Onsager L (1938) Initial recombination of ions. Phys Rev 54:554
21. Chance RR, Braun CL (1976) Temperature-dependence of intrinsic carrier generation in anthracene single-crystals. J Chem Phys 64:3573
22. Braun CL (1984) Electric-field assisted dissociation of charge-transfer states as a mechanism of photocarrier production. J Chem Phys 80:4157
23. Heeger AJ, Kivelson S, Schrieffer JR, Su WP (1988) Solitons in conducting polymers. Rev Mod Phys 60:781
24. Chandross M, Mazumdar S, Jeglinski S, Wie X, Vardeny ZV, Kwock EW, Miller TM (1994) Excitons in poly(para-phenylenevinylene). Phys Rev B 50:14702
25. Barth S, Bässler H, Scherf U, Müllen K (1998) Photoconduction in thin films of a ladder-type poly-para-phenylene. Chem Phys Lett 288:147
26. Hertel D, Soh EV, Bässler H, Rothberg LJ (2002) Electric field dependent generation of geminate electron–hole pairs in a ladder-type $\pi$-conjugated polymer probed by fluorescence quenching and delayed field collection of charge carriers. Chem Phys Lett 361:99
27. Graupner W, Cerullo G, Lanzani G, Nisoli M, List EW, Leising G, De Silvestri S (1998) Direct observation of ultrafast field-induced charge generation in ladder-type poly(para-phenylene). Phys Rev Lett 81:3259
28. Gulbinas V, Zaushitsyn Y, Sundström V, Hertel D, Bässler H, Yartsev A (2002) Dynamics of the electric field-assisted charge carrier photogeneration in ladder-type poly(para-phenylene) at a low excitation intensity. Phys Rev Lett 89:107401
29. Gulbinas V, Zaushitsyn Y, Bässler H, Yartsev A, Sundström V (2004) Dynamics of charge pair generation in ladder-type poly(para-phenylene) at different excitation photon energies. Phys Rev B 70:035215
30. Silva C, Dhoot AS, Russell DM, Stevens MA, Arias AC, Mackenzie JD, Greenham N, Friend RH (2001) Efficient exciton dissociation via two-step photoexcitation in polymeric semiconductors. Phys Rev B 64:125211
31. Müller JG, Lemmer U, Feldmann J, Scherf U (2002) Precursor states for charge carrier generation in conjugated polymers probed by ultrafast spectroscopy. Phys Rev Lett 88:147401
32. Gambetta A, Virgili T, Lanzani G (2005) Ultrafast excitation cross-correlation photoconductivity in polyfluorene photodiodes. Appl Phys Lett 86:253509
33. Arkhipov VI, Bässler H (2004) Exciton dissociation and charge photogeneration in pristine and doped conjugated polymers. Phys Stat Sol (a) 201:1152
34. Van der Horst JW, Bobbert PA, Michels MAJ, Bässler H (2001) Calculation of excitonic properties of conjugated polymers using the Bethe-Salpeter equation. J Chem Phys 114:6950
35. Hendry E, Koeberg M, Schins JM, Siebbeles LDA, Bonn M (2004) Ultrafast charge generation in a semiconducting polymer studied with THz emission spectroscopy. Phys Rev B 70:033202
36. Ruseckas A, Theander M, Andersson MR, Svensson M, Prato M, Inganäs O, Sundström V (2000) Ultrafast photogeneration of inter-chain charge pairs in polythiophene films. Chem Phys Lett 322:136
37. Brabec CJ, Zerza G, Cerullo G, De Silvestri S, Luzzati S, Hummelen JC, Sariciftci S (2001) Tracing photoinduced electron transfer process in conjugated polymer/fullerene bulk heterojunctions in real time. Chem Phys Lett 340:232
38. Kim JY, Lee K, Coates NE, Moses D, Nguyen T-Q, Dante M, Heeger AJ (2007) Efficient tandem polymer solar cells fabricated by all-solution processing. Science 317:222

39. Mihailetchi VD, Koster LJA, Hummelen JC, Blom PWM (2004) Photocurrent generation in polymer-fullerene bulk heterojunctions. Phys Rev Lett 93:216601
40. Scheblykin IG, Yartsev A, Pullerits T, Gulbinas V, Sundström VJ (2007) Excited state and charge photogeneration dynamics in conjugated polymers. Phys Chem B 111:6303
41. Im C, Tian W, Bässler H, Fechtenkötter A, Watson MD, Müllen KJ (2003) Photoconduction in organic donor-acceptor system. Chem Phys 119:3952
42. Arkhipov VI, Heremans P, Bässler H (2003) Why is exciton dissociation so efficient at the interface between a conjugated polymer and an electron acceptor? Appl Phys Lett 82:4605
43. Snaith JH, Arias AC, Morteani AC, Silva C, Friend RF (2002) Charge generation kinetics and transport mechanisms in blended polyfluorene photovoltaic devices. Nano Lett 2:1353
44. Arkhipov VI, Emelianova EV, Adriaenssens GJ (2001) Effective transport energy versus the energy of most probable jumps in disordered hopping systems. Phys Rev B 64:125125
45. Arkhipov VI, Fishtchuk II, Kadastchuk A, Bässler H (2006) In: Hadziioannou G, Malliaras GG (eds) Semiconducting polymers. Wiley, Weinheim
46. Arkhipov VI, Wolf U, Bässler H (1999) Current injection from a metal to a disordered hopping system. II. Comparison between analytic theory and simulation. Phys Rev B 59:7514
47. Van Woudenbergh T, Blom PWM, Vissenberg MCJM, Huiberts JN (2001) Temperature dependence of the charge injection in poly-dialkoxy-*p*-phenylene vinylene. Appl Phys Lett 79:1697
48. Schweitzer B, Arkhipov VI, Bässler H (1999) Field-induced delayed photoluminescence in a conjugated polymer. Chem Phys Lett 304:365
49. Conwell EM (1997) Conductive polymeric transport, photophysics and applications. In: Nalwa HS (ed) Handbook of organic conductive molecules and polymers, vol 4. Wiley, Chichester
50. Arkhipov VI, Bässler H (1995) Concentration-dependence of carrier mobility and diffusivity in diluted hopping systems. Philos Mag B 72:505
51. Miller A, Abrahams E (1960) Impurity conduction at low concentrations. Phys Rev 120
52. Pai DM, Enck R (1975) Onsager mechanism of photogeneration in amorphous selenium. Phys Rev B 11:5163
53. Schweitzer B, Arkhipov VI, Scherf U, Bässler H (1999) Geminate pair recombination in a conjugated polymer. Chem Phys Lett 313:57
54. Que W, Rowlands JA (1995) X-ray photogeneration in amorphous selenium – geminate versus columnar recombination. Phys Rev B 51:10500
55. Onsager L (1934) Deviations from Ohm's law in the weak electrolythes. Chem Phys 2:599
56. Im C, Lupton JM, Schouwink P, Heun S, Becker H, Bässler HJ (2002) Fluorescence dynamics of phenyl-substituted polyphenylenevinylene-trinitrofluorenone blend systems. Chem Phys 117:1395
57. Albrecht U, Bässler H (1995) Yield of geminate pair dissociation in an energetically random hopping system. Chem Phys Lett 235:389
58. Arkhipov VI, Emelianova EV, Bässler H (2003) Dopant-assisted charge carrier photogeneration in conjugated polymers. Chem Phys Lett 372:886
59. Weiter M, Bässler H, Gulbinas V, Scherf U (2003) Transient photoconductivity in a film of ladder-type poly-phenylene: failure of the Onsager approach. Chem Phys Lett 379:177
60. Hertel D, Bässler H, Scherf U, Horhold HH (1999) Charge carrier transport in conjugated polymers. J Chem Phys 110:9214
61. Fishchuk II, Hertel D, Bässler H, Kadashchuk AK (2002) Effective-medium theory of hopping charge-carrier transport in weakly disordered organic solids. Phys Rev B 65:125201

Adv Polym Sci (2010) 223: 29–44
DOI:10.1007/12_2009_5
© Springer-Verlag Berlin Heidelberg 2009
Published online: 19 June 2009

# Effective Temperature Models for the Electric Field Dependence of Charge Carrier Mobility in Tris(8-hydroxyquinoline) Aluminum

**P.J. Jadhav, B.N. Limketkai, and M.A. Baldo**

**Abstract** The development of accurate and predictive models of charge carrier mobility is a crucial milestone on the path to the rational design of organic semiconductor devices. In this chapter we review effective temperature models that combine both the temperature and electric field dependence of the charge carrier mobility into a single parameter – the effective temperature. Although effective temperature models were originally developed for use in disordered inorganic semiconductors, here we compare various models to data from the archetype small molecular weight organic semiconductor tris(8-hydroxyquinoline) aluminum ($AlQ_3$). We conclude that it may prove impossible to develop a universal effective temperature model that is valid for all electric fields and temperatures. But several effective temperature models are observed to work well within the typical operational environments of electronic devices. Thus, the effective temperature concept promises to be a practical and useful tool for the development of organic semiconductor technology.

## Contents

1 Introduction .......... 30
2 Percolation Models of Mobility at Low Electric Fields .......... 31
3 Effective Temperature Models .......... 34
4 Comparison to Experiment .......... 37
5 Discussion .......... 41
6 Conclusion .......... 42
References .......... 43

P.J. Jadhav, B.N. Limketkai, and M.A. Baldo (✉)
Department of Electrical Engineering and Computer Science, Massachusetts Institute of Technology, Cambridge, MA 02139, USA
e-mail:baldo@mit.edu

## 1 Introduction

Organic semiconductor-based devices such as organic light emitting devices (OLEDs) are attracting increasing commercial interest. Unlike most conventional semiconductors, however, the molecules in an organic semiconductor are held together by weak van der Waal's forces. Consequently, organic semiconductors possess narrower electronic bands than most conventional covalently-bonded semiconductors. The result is localization of charge carriers [1], especially in the disordered amorphous organic semiconductors typical of applications such as OLEDs.

Localized charge carriers in organic semiconductors move by electric field or temperature-induced charge hopping. There are proven microscopic models for charge hopping between sites under low electric fields [2–4]. But charge transport in thin films of organic semiconductors is complicated by energetic and spatial disorder. For example, the conductivity of a thin film is observed to depend on the charge carrier density as well as the electric field and temperature [5–10]. The absence of an analytical model that explains all these dependencies has complicated the rational design of organic semiconductor devices.

The modeling of charge carrier transport in organic semiconductors has been dominated by quasi-empirical models such as the various Poole Frenkel descriptions for the electric field dependence of mobility [9, 11]. But empirical relations complicate the construction of predictive device models because many parameters are of obscure physical origin and difficult to extrapolate between materials. This chapter reviews an alternative approach: effective temperature models. These modify the distribution of charge carriers, increasing their temperature to represent the effect of an applied electric field. We present comparisons to organic semiconductor data that demonstrate the utility of the effective temperature approach for device engineers. It correctly models device behavior near room temperature, and the physical origin and limits of the approach are clear.

Much of the theory discussed here was originally proposed many years ago for application to disordered conventional semiconductors such as amorphous Si [12–15]. We review effective temperature models that build on the success of percolation theory in understanding the charge density and temperature dependence of charge transport. Percolation theory at low electric field is reviewed in Sect. 2. To summarize: percolation theory in the absence of an electric field predicts that mobility is strongly dependent on the charge carrier density [10]. Given the presence of just a few charge carriers, the current flow is retarded by sparsely distributed low energy sites also known as traps. The mobility of carriers increases dramatically as these deep sites are filled. Because the majority of hops out of a trap are to sites with higher energy, the mobility is also strongly temperature dependent. Given an exponential density of states (DOS), the theory predicts $\mu \sim n^{T_0/T}$ where $\mu$ is the mobility, $n$ the charge carrier density, $T$ the temperature, and $T_0$ the characteristic trap temperature [10]. Interestingly, this solution is almost identical to the successful but controversial trapped charge limited (TCL) model for charge transport in organic semiconductors [5, 16, 17], although percolation theory correctly models

the localized nature of organic semiconductors whereas the TCL models consider an unphysical band edge above an exponential distribution of traps.

Percolation models in the absence of an electric field have previously proven successful in organic thin film transistors where the lateral electric field in the channel can comfortably be neglected due to the large dimensions of the channel [10]. The electric field, however, is typically much larger in thin vertical organic devices such as OLEDs or organic photovoltaics (OPVs). Large electric fields lead to a nonequilibrium distribution of charge carriers that can prove difficult to model. In response, the effective temperature model notes that the effect of electric field on mobility in hopping transport is similar to that of temperature [15, 18, 19]. Increasing the temperature raises the population of charge carriers to higher energies, where the DOS is broader, and hence the mobility improves. Increasing the field has a similar effect – the carriers gain energy by hopping in the direction of the field. So the mobility can be seen as dependent on some quantity $T_{\mathrm{eff}}(F,T)$, which is a function of electric field and temperature. We define $T_{\mathrm{eff}}(F,T)$ as the effective temperature. The form of the function $T_{\mathrm{eff}}(F,T)$ is the subject of Sect. 3 of this chapter.

In Sect. 4 we compare the various effective temperature theories to current–voltage and mobility data for organic semiconductors. We focus particularly on analysis of the current–voltage characteristics of the archetype small molecular weight electron transport material tris(8-hydroxyquinoline) aluminum ($\mathrm{AlQ_3}$) [20]. There is extensive data available on the charge transport characteristics of $\mathrm{AlQ_3}$ [5, 21–23], providing a convenient system to test various approaches to modeling charge transport in disordered organic semiconductors. Finally, in Sect. 5, we conclude by discussing the limits of the effective temperature approach.

## 2 Percolation Models of Mobility at Low Electric Fields

Percolation models of charge conduction were originally applied to charge transport in inorganic amorphous semiconductors [12]. More recently the percolation formalism has also been applied to organic materials [10, 24]. Here, we review the percolation approach. It begins by noting that charge transport in organic semiconductors occurs via electric field or thermally-activated hops between localized states. The hopping motion of charge carriers can be described by the kinetic master equation [25]

$$\frac{\partial P_{\mathrm{d}}(t)}{\partial t} = \sum_{\mathrm{a}\neq\mathrm{d}} \left[R_{\mathrm{da}}P_{\mathrm{d}}(t)\left(1-P_{\mathrm{a}}(t)\right) - R_{\mathrm{ad}}P_{\mathrm{a}}(t)\left(1-P_{\mathrm{d}}(t)\right)\right], \tag{1}$$

where $P_{\mathrm{d}}(t)$ is the occupational probability of site d at time $t$ and $R_{\mathrm{da}}$ is the transition rate from the donor site d to acceptor site a.

Next, we assume that polaronic effects are negligible compared to energetic disorder. The activation energy $\Delta E$ for hopping is then dependent only on the site energy differences and not on the molecular conformation energies required to form activated complexes prior to charge transfer. Under this assumption, the hopping rate

$R_{da}$ from a site with energy $E_d$ to a site with energy $E_a$ at a distance $r_{da}$ apart can be described by the Miller–Abrahams rate model for phonon-assisted tunneling [2]:

$$R_{da} = \begin{cases} \nu_0 \exp(-2ar_{da}) \exp((E_a - E_d)/kT), & E_a - E_d > 0, \\ \nu_0 \exp(-2ar_{da}), & E_a - E_d \leq 0, \end{cases} \tag{2}$$

where $\nu_0$ is the attempt to hop frequency dependent on the phonon DOS and intermolecular overlap. Miller Abrahams is perhaps the simplest solution that satisfies the detailed balance requirement in Eq. (1) at equilibrium.

Under the condition that the system is close to equilibrium (i.e., the difference between donor and acceptor quasi Fermi levels $\mu_d - \mu_a \ll 2kT$), the master equation with Miller–Abrahams transition rates can be linearized to obtain a conductance [26]:

$$G_{da} = \frac{q\nu_0}{4kT} \frac{\exp[-2\alpha r_{da}] \exp[-|E_a - E_d|/2kT]}{\cosh[(E_a - \mu_a)/2kT] \cosh[(E_d - \mu_d)/2kT]}. \tag{3}$$

Here, $\mu_d$ and $\mu_a$ are the quasi-electrochemical potentials that deviate from the equilibrium electrochemical potential as $\mu - qFr$, where $\mu$ is the chemical potential, $F$ is the applied field, and $r$ is the position of the sites.

Equation (3), or a simplified version thereof, can be used to model every possible hop between localized sites in the organic semiconductor as a distinct conductance. Each conductance is characterized by the respective site energies, the intermolecular spacing and the quasi Fermi energies. Unfortunately, the energy distribution of the sites (also known as the DOS) is usually unknown because, until recently, it has not been easy to measure. It is commonly presumed to be a Gaussian distribution [11] with a tail of states that extends into the energy gap between the lowest unoccupied molecular orbital (LUMO) and the highest occupied molecular orbital (HOMO). Recent Kelvin probe measurements of the archetype organic semiconductors $N,N'$-diphenyl-$N,N'$-bis(1-naphthyl)-1,1′-biphenyl–4,4′-diamine (α-NPD) [27], and copper phthalocyanine (CuPC) [28], however, have observed an exponential DOS. In this chapter, we tentatively assume that exponential tails are a universal characteristic of organic semiconductors. Further measurements of other archetype organic semiconductors may confirm this assumption. Disorder in the intermolecular spacing is usually neglected since it is expected to yield a charge carrier mobility that decreases with electric field, in contrast with experimental results [11, 29].

Assuming we know the distribution of site energies, and if we neglect the spatial disorder, the remaining problem is to solve the conductance network. In an organic semiconductor the conductances corresponding to each possible hop are expected to vary by many orders of magnitude. Percolation theory seeks to simplify the determination of the macroscopic conductance in this disordered system [12, 30]. Conceptually, the film is broken into numerous conducting clusters defined relative to a reference conductance $G$. For a given reference conductance $G$, all conductive pathways between sites with $G_{da} \leq G$ are removed from the network, which leaves a collection of spatially disconnected clusters of high conductivity, $G_{da} > G$. As the reference conductance $G$ is decreased, the size of these isolated clusters increases. The critical percolation conductance is defined as the maximum reference

conductance $G = G_c$ at the point when percolation first occurs, meaning the first formation of a continuous, infinite cluster (cluster that spans the whole system). This infinite cluster will be composed of clusters that are all connected by critical conductive links with conductance $G_c$. Since the conductances comprising the infinite cluster are expected to vary by many orders of magnitude, it is assumed that the conductivity of the cluster is that of the most resistive link. The total conductance of the system is then equal to $G_c$. To determine the threshold for percolation, the average number of bonds per site is calculated. A bond is defined as a link between two sites which have a conductance $G_{da} > G$. As the reference conductance $G$ decreases, the average number of bonds per site $B$ increases. A large average number of bonds per site indicates a large average size of a cluster (collection of sites with $G_{da} > G$). Therefore, it is assumed that once the average number of bonds per site $B$ reaches some critical bond number $B_c$, the average cluster sizes will be large enough such that they all touch and form a continuous pathway that spans the whole disordered system (form an infinite cluster). The critical bond number is usually determined using numerical simulations. It has been estimated to be $B_c \simeq 2.8$ in an amorphous three-dimensional system [31].

To apply percolation theory, Eq. (3) is simplified by noting that bonds at the critical conductance involve site energies that are high above the quasi-electrochemical potential $(E_d - \mu_d \gg kT)$. The conductance in Eq. (3) for small applied electric fields can then be approximated in the zero-field limit as [26]

$$G_{da} \approx \frac{q\nu_0}{kT} \exp\left[-2\alpha r_{da}\right] \exp\left[-\frac{|E_a - E_d| + |E_d - \mu_d| + |E_a - \mu_a|}{2kT}\right]. \tag{4}$$

Next, the conductance between sites can be written as $G = G_0 \exp\left[-s_{ij}\right]$ with $G_0 = q\nu_0 / kT$ and [10]

$$s_{da} = 2\alpha r_{da} + \frac{|E_a - E_d| + |E_d - \mu_d| + |E_a - \mu_a|}{2kT}. \tag{5}$$

The critical conductance is written $G_c = G_0 \exp\left[-s_c\right]$. The conductivity of the disordered system is therefore $\sigma = \sigma_0 \exp\left[-s_c\right]$, where $s_c$ is the critical exponent of the critical conductance when percolation first occurs (when $B = B_c$ ).

The average number of bonds $B$ is equal to the density of bonds, $N_b$, divided by the density of sites that form bonds, $N_s$, in the material. At the percolation threshold, when $B = B_c$, the density of bonds is given by

$$N_b = \int d^3 r_{da} \int dE_d \int dE_a g(E_d)\, g(E_a)\, \theta(s_c - s_{da}), \tag{6}$$

where $r_{ij}$ is integrated in three dimensions over the entire material, $g(E)$ is the DOS in the material, and $\theta$ is the Heaviside unit step function. The density of sites that form bonds at the percolation threshold $(B = B_c)$ is given by

$$N_s = \int dE g(E)\, \theta(s_c - s_{da}). \tag{7}$$

Determination of the conductance at the percolation threshold rests on the evaluation of step function. Setting $s_{da} = s_c$ in Eq. (5) yields either (1) a maximum hop distance, $r_{max} = s_c/2\alpha$, obtained when $E_a = E_d = \mu_a = \mu_d$, or (2) a maximum energy, $E_{max} = \mu + s_c kT$ in the limit of $r_{da} \to 0$. The maximum energy is crucial. Because the hops typically take place in the tail of the DOS, the maximum number of density of sites in the percolation cluster occurs at $E_{max}$. Consequently, it characterizes the system and sets the integration limits in Eqs. (6) and (7).

Assuming an exponential DOS with characteristic temperature $T_0$, Vissenberg and Matters [10] obtained

$$B_c = \frac{N_b}{N_s} \approx \pi N_0 \left(\frac{T_0}{2\alpha T}\right)^3 \exp\left[\frac{E_F + s_c kT}{kT_0}\right], \tag{8}$$

where they assumed $E_F \ll kT_0$ and $s_c kT \gg kT_0$ Solving for the critical conductance yields

$$\sigma = \sigma_0 e^{-s_c} = \sigma_0 \left[\frac{\pi}{B_c}\left(\frac{T_0}{2\alpha T}\right)^3 n\right]^{T_0/T}, \tag{9}$$

where $n$ is the charge carrier density. Again, we stress that this result is largely a recapitulation of previous studies. Indeed, Vissenberg and Matters remarked that their result in Eq. (8) is in agreement with previous results up to a numerical factor [10]. Perhaps surprisingly, given their contrasting physical foundations, Eq. (9) is also identical to the TCL model up to a numerical factor [5, 16].

## 3 Effective Temperature Models

The result of the previous section is only valid close to equilibrium. The electric field is limited such that the difference between donor and acceptor quasi Fermi levels $\mu_d - \mu_a \ll 2kT$. Close to equilibrium we can assume that the electron distribution is characterized by the lattice temperature, and we can also linearize the hopping conductivity expression of Eq. (3).

Although the low electric field percolation model is useful in organic field effect transistors, it is not suitable for OLEDs or OPVs due to the much larger electric fields in these devices. Under an applied electric field, charge carriers hop from sites deep in the DOS to higher energy levels where the DOS is broader (see Fig. 1). The effect of the electric field is to create a population of “hot” carriers above the Fermi level [18]. The aim of the effective temperature concept is to model the electric field by a nonequilibrium distribution of electrons characterized by an effective temperature $T_{eff}$.

We expect $T_{eff}$ to be a function of the temperature $T$ and electric field $F$. The simplest cases are $F = 0$ and $T = 0$. The former is trivial: $T_{eff} = T$, and the expression

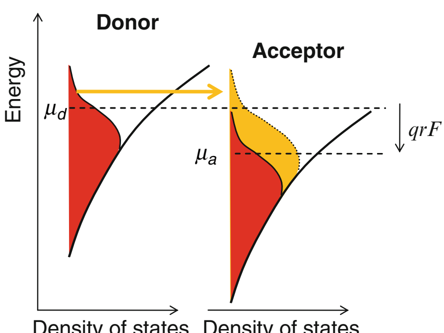


**Fig. 1** Electron hopping within the energetic tail of a distribution of localized sites under an electric field $F$. Due to the potential gradient, electrons from lower energy states can hop into states further from the Fermi energy where the density of states is broader, and hence gaining energy with respect to the local Fermi level

for mobility should reduce to the proven low field percolation model. At $T = 0$, however, $T_{\text{eff}} = T_{\text{F}}$ where $T_{\text{F}} = qF/2\alpha k$, $q$ is the electronic charge, $F$ is the *magnitude* of the electric field, $\alpha$ is the inverse of the decay length of the localized wave functions and $k$ is the Boltzmann constant. Marianer et al. [18] have a simple approach to this result. When an electric field is applied at $T = 0\text{K}$, an electron can increase its local energy $E$ by $\Delta E = qFr$ by hopping against the field over a distance $r$. The hopping mechanism at $T = 0$ is tunneling, and so the hopping rate into the acceptor state is

$$\nu = \nu_0 \exp\left(-2\alpha r\right) = \nu_0 \exp\left(-2\alpha \Delta E \big/ qF\right), \quad \Delta E > 0. \tag{10}$$

Marianer et al. [18] assume that "The energy relaxation rate does not depend exponentially on the energy difference." Consequently, we assume that relaxation from the hot state is independent of energy:

$$\nu = \nu_0, \quad \Delta E < 0. \tag{11}$$

To obtain the carrier distribution, we can label the relaxed state as the donor and the hot state as the acceptor. For steady state current flow between donor and acceptor states, the population of the donor and acceptor states should be invariant in time. Substituting Eqs. (10) and (11) into Eq. (1) is consistent with a Fermi–Dirac distribution with $T = T_{\text{F}} = qF \big/ 2\alpha k$.

Alternatively, we may obtain $kT_{\text{F}} = qF/2\alpha$ by demanding self consistency within a percolation cluster at $T = 0$. At $T = 0$, the percolation limit is given by Eq. (1) assuming no backward hops [24]:

$$f\left(E_{\text{c}}\right) \exp\left[-2\alpha r_{\text{da}}\right] = \exp\left[-s_{\text{c}}\right], \tag{12}$$

where $E_{\text{c}}$ is the maximum donor energy and we have neglected filled acceptor sites in the tail of the distribution.

We are concerned with the carrier distribution $f(E_{\text{c}})$ at energies approaching the maximum possible donor energy $E_{\max}$. From Eq. (12), $f\left(E_{\max}\right) = \exp\left[-s_{\text{c}}\right]$. Because there is no thermal excitation at $T = 0$, carriers at $E_{\max}$ must be excited

by the electric field. Thus, sites at $E_{\max}$ must participate in bonds of length $r_{\mathrm{da}} > 0$. It follows that, for short hops, the maximum acceptor energy cannot be less than $E_{\max}$. The maximum acceptor energy is obtained by hops parallel to the electric field. Thus, for carriers with energy close to $E_{\max}$, the percolation limit is

$$E_{\mathrm{c}} = E_{\max} - q r_{\mathrm{da}} F. \tag{13}$$

For $T = 0$, Eqs. (12) and (13) yield an occupation function $f(E_{\mathrm{c}})$ of the form $A\exp[-E_{\mathrm{c}}/kT_{\mathrm{F}}]$, where $kT_{\mathrm{F}} = \mathrm{qF}/2\alpha$, identical to the result of Marianer et al. [18].

The remaining issue is the determination of the effective temperature for arbitrary electric fields and ambient temperatures. There are two models as follows.

(1) *The linear model*

The gain in potential energy for any hop within the percolation cluster is partly due to thermal energy and partly due to the electric energy. The potential energy gained from thermal energy is maximized for short range hops. But the potential energy gained from the electric field is maximized for long range hops. Under the linear effective temperature model, the maximum potential energy gained from temperature-induced hops is added to the maximum potential energy gained from electric field-induced hops, i.e.,

$$T_{\mathrm{eff}} = T_{\mathrm{F}} + T. \tag{14}$$

To our knowledge, there is no rigorous justification for Eq. (14). Rather, the linear model implicitly treats the electric field in the form of $T_{\mathrm{F}}$ as a perturbation to the lattice temperature, $T$. The above analysis of hot carriers at $T = 0K$ is used to determine the form of the perturbation $T_{\mathrm{F}}$. Given $T_{\mathrm{eff}} = T_{\mathrm{F}} + T$, the expression for conductivity obtained for an exponential DOS is [24]

$$\sigma = \frac{\sigma 0}{q}\left[\frac{\pi}{B_{\mathrm{C}}}\frac{T0^3}{(2\alpha)^3}\frac{16T_{\mathrm{eff}}}{(2T_{\mathrm{eff}}-T_{\mathrm{F}})^2\,(2T_{\mathrm{eff}}+T_{\mathrm{F}})^2}\right]^{T_0/T_{\mathrm{eff}}} n^{T_0/T_{\mathrm{eff}}}. \tag{15}$$

(2) *Non linear models*

Several authors have proposed an effective temperature of the form

$$T_{\mathrm{eff}}^{n} = T^{n} + (\beta T_{\mathrm{F}})^{n}, \tag{16}$$

where $n \approx 2$ and $\beta \approx 1.4$. Marianer et al. [18] and Baranovskii et al. [15] both ran Monte Carlo simulations considering electrons hopping through an exponential DOS. The resulting electron distribution is a Fermi distribution characterized by an effective temperature given by $T_{\mathrm{eff}}^{n} = T^{n} + (\beta T_{\mathrm{F}})^{n}$. Baranovskii et al. [15] found $n = 2$ and $\beta = (1.38 \pm 0.06)$ consistent with the earlier findings of Marianer et al. [18], who fit their distribution to $n = 2$ and $\beta = 1.34$.

Arkhipov et al. [19] derived the effective temperature for an algebraic DOS. Their result was obtained from the low field model of Eq. (5):

$$s_{\mathrm{c}} = 2\alpha r + \frac{E - qrF - \mu}{kT}. \tag{17}$$

Similar to the percolation approach, they required that the number of sites, $N_{\mathrm{s}}$, in Eq. (7) exceeded one (but note [8]). The DOS was taken to be

$$g(E) = g_0 \left(\frac{E-\mu}{E_0}\right)^{\gamma}, \quad E > \mu, \quad -1 < \gamma < \infty. \tag{18}$$

The effective temperature was determined to be

$$T_{\mathrm{eff}}(T,F) = T\left[\frac{4-(4+\gamma)f^{2+\gamma}-(5+\gamma)f^{3+\gamma}+(2+\gamma)f^{4+\gamma}+(3+\gamma)f^{5+\gamma}}{4(1-f^2)^2}\right]^{1/(1+\gamma)}, \tag{19}$$

where $f = T_{\mathrm{F}}/T$. At weak fields where $f \ll 1$, and, where $\gamma > 0$, $T_{\mathrm{eff}}$ reduces to

$$T_{\mathrm{eff}}(T,F) = T\left[1 + \frac{2}{1+\gamma} f^2\right]. \tag{20}$$

At strong fields $T_{\mathrm{eff}}$ is simply proportional to $T_{\mathrm{F}}$:

$$T_{\mathrm{eff}}(T,F) = \left[\frac{3+\gamma}{4}\right]^{1/1+\gamma} T_{\mathrm{F}}. \tag{21}$$

The $T_{\mathrm{eff}}$ derived by Arkhipov et al. [19], though different in precise form to the results of Marianer et al. [18] and Baranovskii et al. [15], is similar to Eq. (16) when $\beta = 1$ and $0 < \gamma < 1$. The various theories discussed in this section are depicted as a plot of $T_{\mathrm{F}}$ vs $T$ at an effective temperature of 300 K in Fig. 2.

## 4 Comparison to Experiment

The effective temperature theories are tested against current–voltage and mobility measurements conducted by Brütting et al. and Limketkai et al. using the archetypical small molecule tris (8-hydroxyquinoline) aluminum ($\mathrm{AlQ_3}$) over a wide range of electric fields and temperatures [22, 23]. The device used for the measurements is a 300 nm thick $\mathrm{AlQ_3}$ film with calcium cathode and aluminum anode. $\mathrm{AlQ_3}$ is an electron transporter, and electrons are injected from the calcium cathode. Calcium has a low work function and so interface effects are minimized. This is important because no injection effects are taken into account in the theory. Figure 3 shows the current–voltage data for the device. The circles represent data, and the solid lines

**Fig. 2** $T_F$ vs $T$ plotted for various effective temperature theories at an effective temperature of 300 K. *Solid line:* $T_{eff} = T + T_F$; *broken line with dots:* $T_{eff}^n = T^n + (\beta T_F)^n$ where $\beta = 1.34$ and $n = 2$; *dotted line:* $\beta = 1.1$ and $n = 1.5$; *broken line:* $T_{eff}$ transformation under the model derived by Arkhipov et al. [19]; from Eq. (19) with $\gamma = 0.7$

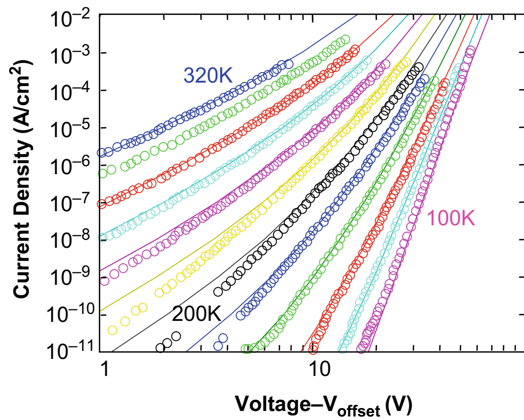


**Fig. 3** Temperature dependence of *I–V* characteristics of an $Al/AlQ_3/Ca$ device, $AlQ_3$ thickness: 300 nm. *Symbols* are data. *Lines* are fits to theory. The offset voltage is $V_{bi} = 2$ V. As can be seen, the data fits the theory over a wide range of temperature and field. From [24]

**Table 1** Fit parameters used in Fig. 3

| | $\sigma_0$ | $\alpha$ | $T_0$ |
|---|---|---|---|
| $V_{offset} = 2$ V | $2 \times 10^3\,\mathrm{S\,m^{-1}}$ | $0.575 \times 10^{10}\,\mathrm{m^{-1}}$ | 450 K |

represent the current calculated using the conductivity expression in Eq. (15) [24]. The parameters used to fit the data to theory are given in Table 1. The parameters have been calculated for an offset voltage of 2 V [24]. As can be seen from the figure, the theory accurately fits the data over a temperature range of 100–320 K.

Mobility data for $AlQ_3$ taken through transient electroluminescence (EL) measurements [23] has also been fitted to the theory [24]. Though the transient mobility measurement may not be exactly comparable to the predictions from the steady state theory, it is useful to compare the trends. The mobility for our theory is obtained from the conductance in Eq. (15) using $\mu = \sigma/qn$. The charge density is not experimentally defined in transient measurements, and consequently a best fit constant value of $2 \times 10^{18}\,\mathrm{cm^{-3}}$ is used.

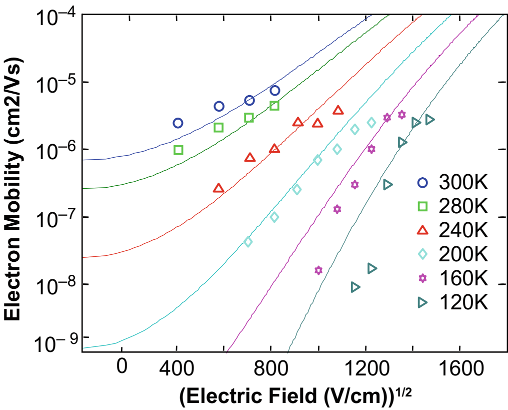


**Fig. 4** Temperature and electric field dependence of charge carrier mobility obtained from transient electroluminescence measurements. Theoretical fits are shown in *solid lines*. From [24]

Figure 4 shows the fit as a log of mobility plotted against the square root of the electric field. Plotting against $\sqrt{F}$ should yield a straight line according to the Poole–Frenkel phenomenological model for mobility [9, 11]:

$$\mu = \mu_0 \exp\left[-\frac{\Theta}{kT}\right] \exp\left[B\left(\frac{1}{kT} - \frac{1}{kT_0}\right)\sqrt{F}\right], \tag{22}$$

where $\Theta$ is a temperature-independent activation barrier, and $\mu_0$, $B$ and $T_0$ are constants. It is evident that neither the data nor the theory exhibit Poole–Frenkel dependencies over a wide range of electric fields.

Next, to show the equivalence of temperature and electric field, we examine the current–voltage data as a plot of voltage vs temperature at constant conductance in Fig. 5a. The mostly straight lines are consistent with the $T_{\text{eff}} = T + T_{\text{F}}$ form of effective temperature within the temperature limits of the theory: from 100 to 300 K, and over an electric field range: of $10^5$–$10^6\,\text{V cm}^{-1}$ over a conductivity range of seven orders of magnitude. At very low fields there is a deviation from the straight line. This is attributed to variation of the charge carrier density, $n$, with current. It is evident in Eq. (15) that the conductance is strongly dependent on $n$. The linear effective temperature theory also matches the data in this regime.

Figure 5b shows the voltage–temperature plot for $\text{AlQ}_3$ devices of 700 Å thickness with different cathodes at a constant conductivity of $0.1\,\text{S m}^{-1}$ [22, 23]. The different cathodes alter the current–voltage characteristics, either by varying the density of free charge within the $\text{AlQ}_3$ or by varying the injection barrier. As the work function of the cathode increases, the plots seem to show a constant voltage shift to higher voltages but again the linear form of $T_{\text{eff}}$ is still observable.

Figure 6 shows a voltage–temperature plot for an $\text{AlQ}_3$ device of thickness 700 Å with a MgAg cathode [22]. The temperature range is wider for this data and a clear deviation from the linear is observed at low temperature. Some uncertainty is introduced by the possibility of an injection barrier at the $\text{MgAg}/\text{AlQ}_3$ interface; however, good agreement at low temperatures is evident for an effective temperature given by $T_{\text{eff}}^n = T^n + (\beta T_{\text{F}})^n$ with $n = 1.41$ and $\beta = 1.24$.

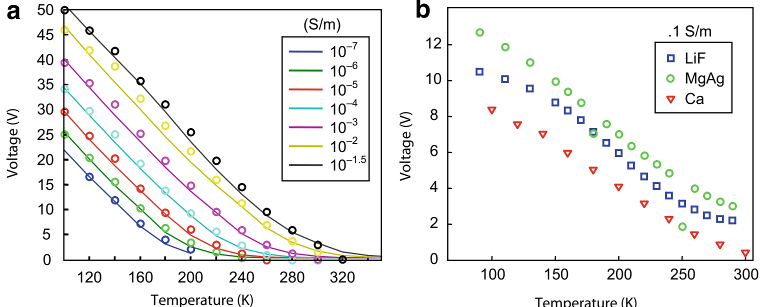


**Fig. 5** **a** Voltage vs temperature as a function of conductivity for the Al/$AlQ_3$/Ca data ($AlQ_3$ thickness 300 nm) collected by Brütting et al. [23]. The *circles* are data and the *lines* are a theoretical fit. The plots are linear over a wide range of conductivity except at very low fields. This fits the linear dependence of effective temperature on field and temperature. **b** The same plot for 70 nm $AlQ_3$ devices with Ca, LiF and MgAg cathodes at a constant conductivity of $0.1\,\mathrm{S\,m^{-1}}$. The Ca plot is not data but a calculation for a 70 nm thick device using a linear extrapolation from thickness dependence studies for $AlQ_3$ in [23] and the current–voltage characteristics of the 300 nm thick $AlQ_3$ device in **a**. The different cathodes seem to add a constant voltage shift but the linear effective temperature dependence on field and temperature still exists. At temperatures lower than 100 K, the data veers to lower voltage values than predicted by theory

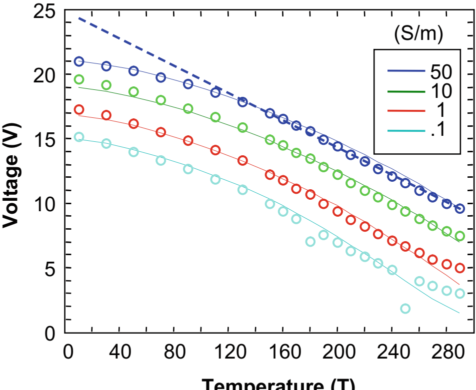


**Fig. 6** Voltage vs temperature as a function of conductivity for a 700 A thick $AlQ_3$ device with a MgAg cathode. The *lines* are fits to theory and the *circles* are data from [19]. The fit parameters used here are ones deduced from the Brütting et al. data [23], except for $T_0 = 500\,\mathrm{K}$, and $V_{\mathrm{offset}} = 1\,\mathrm{V}$. The theoretical fit represents an effective temperature dependence given by $T_{\mathrm{eff}}^n = T^n + (\beta T_{\mathrm{F}})^n$ where $n = 1.41$ and $\beta = 1.24$. The *dashed line* shows the linear effective temperature dependence

The $T_{\mathrm{eff}}^n = T^n + (\beta T_{\mathrm{F}})^n$ form is further explored through the Brütting et al. data [23] for a 3,000 Å thick $AlQ_3$ device with Ca cathode. The transient mobility data (Fig. 4) are transformed under the various effective temperature models discussed in Sect. 3. Figure 7 shows a plot of the transient mobility data for various electric

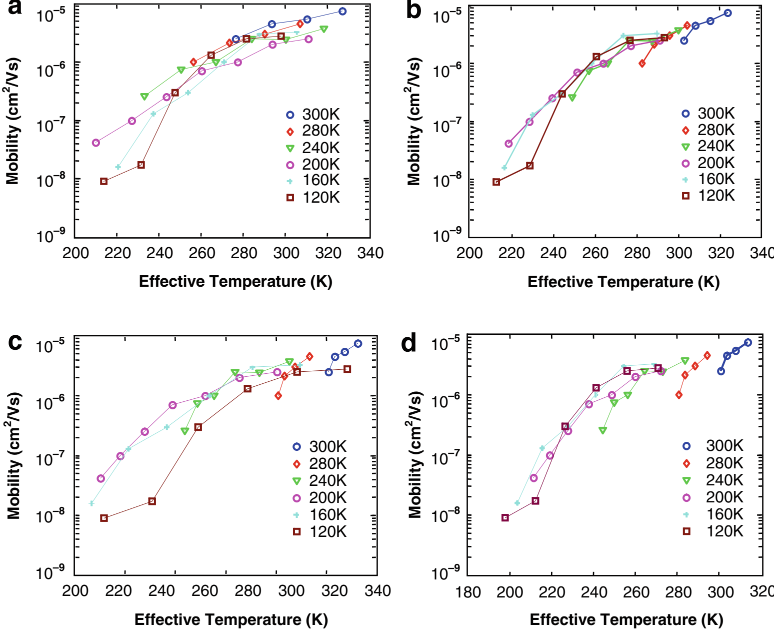


**Fig. 7** The transient mobility data of Fig. 4 under various effective temperature transformations. The first four are given by $T_{\mathrm{eff}}^{n} = T^{n} + (\beta T_{\mathrm{F}})^{n}$ where: **a** $n = 1$, $\beta = 1$; **b** $n = 1.5$, $\beta = 1.1$; **c** $n = 2$, $\beta = 1.3$; **d** Transformation under the model derived by Arkhipov et al. [19]; from Eq. (19) with $\gamma = 0.7$

fields and temperatures vs the effective temperature. Specifically, Fig. 7a–c shows $T_{\mathrm{eff}}^{n} = T^{n} + (\beta T_{\mathrm{F}})^{n}$ with $n = 1$, 1.5 and 2 and optimal $\beta$ values [32]. The $\beta$ has been optimized to fit each transformation, except for $n = 1$, where it is taken as $\beta = 1$. If the mobility is a function of the effective temperature, then all the data (for all temperatures and fields) should collapse onto a single function. Figure 7d shows the transformation under the expression in Eq. (19) derived by Arkhipov et al. [19] with an optimized value of $\gamma = 0.7$.

## 5 Discussion

Comparisons with data demonstrate that the effective temperature model shows promise: both the steady state current–voltage data and the mobility data exhibit universal behavior parameterized by an effective temperature. Data are observed to fit the effective temperature model over a wide range of temperatures, carrier densities, and electric fields. Figure 6 confirms that the $T_{\mathrm{eff}}^{n} = T^{n} + (\beta T_{\mathrm{F}})^{n}$ model with $n \approx 1.5$ provides the best fit over the widest range of temperatures, albeit with the addition of the empirical parameter $n$ [32]. But for engineering purposes, where performance near room temperature is most important, the linear model provides the best fit;

compare Fig. 7a, b. It is observed to work well when $T_F$ is a small perturbation $(T_F \ll T)$. The linear effective temperature model fails at lower temperatures when the electric field temperature, $T_F$, approaches the lattice temperature, $T$.

Despite the success of the effective temperature models in describing charge transport in $AlQ_3$, each model possesses an uncertain physical foundation. The linear theory essentially treats the electric field as a perturbation and is experimentally observed to be valid only above $T \approx 100\,K$. Despite the apparent failure of the model at low temperatures, the form of $T_F$ is determined using arguments at $T = 0\,K$. Its success at room temperature may then be due to the implicit combination of a fit parameter and $\alpha$, the orbital decay constant. Since quantum chemical calculations can be used to determine $\alpha$, further studies should be able to resolve this. The $T_{\text{eff}}^n = T^n + (\beta T_F)^n$ models are closest to universal but they are fundamentally empirical. Numerical studies have also suggested that even $T_{\text{eff}}^n = T^n + (\beta T_F)^n$ models cannot be truly universal because $\beta$ apparently varies when the effective temperature is used to simulate transient or steady state currents [33]. Lastly, the theory of Arkhipov et al. [19] applies only to algebraic densities of states, and provides a relatively poor fit to the data. The later theory is notable, however, for suggesting that the form of the effective temperature may depend on the DOS.

The linear model has also been criticized by Cleve et al. [33] as possessing incorrect asymptotic behavior at low electric fields. They require that

$$\left.\frac{d\sigma}{dF}\right|_{F\to 0} = \left.\frac{d\sigma}{dT_{\text{eff}}}\frac{dT_{\text{eff}}}{dF}\right|_{F\to 0} = 0. \tag{23}$$

Their concern was $dT_{\text{eff}}/dF \neq 0$ in the linear effective temperature model. Physically, we expect that a successful model of conductance should smoothly evolve from electric field-independence at $F = 0$ to increasing electric field-dependent nonlinearity at $F > 0$. Plots of the charge carrier mobility using the linear effective temperature model in Fig. 4 are consistent with the expected behavior. Moreover, we note that the effective temperature depends on the *magnitude* of the electric field. Hence, as required by symmetry arguments,

$$\frac{T_{\text{eff}}\,(\delta/2) - T_{\text{eff}}\,(-\delta F/2)}{\delta F} = 0, \quad \delta F > 0. \tag{24}$$

In any case, comparisons with data show no evidence of failure of the linear model at low electric fields. In fact, the linear model arguably fits the low electric field data better than the $T_{\text{eff}}^n = T^n + (\beta T_F)^n$ models.

## 6 Conclusion

It has been established that percolation theory can successfully explain the mobility in organic semiconductors at low electric fields. Organic semiconductor devices, however, often operate at larger electric fields. The electric field distorts the

distribution of carriers within the organic semiconductor, leading to a substantial change in the charge carrier mobility. Effective temperature models seek to describe such complex hot carrier phenomena with a single effective temperature dependent on the electric field and the lattice temperature. It remains unclear whether a truly universal effective temperature theory is possible [33]. Nevertheless, comparisons to data from the archetype small molecular weight electron transport material $AlQ_3$ yield three important conclusions. First, the most accurate effective temperature model over a wide range of temperatures is the empirical relation $T_{eff}^n = T^n + (\beta T_F)^n$ with $n \approx 1.5$ [32]. Second, the simple linear model is arguably superior to the empirical models near room temperature. It also replaces constants of unclear physical origin with parameters that may potentially be obtained using quantum chemical simulations. Third the linear effective temperature model is simply understood as a first order perturbation in the carrier distribution, i.e., it is expected to be valid for $T_F \ll T$, which typically corresponds to the operating conditions of most organic devices. Thus, for organic semiconductor engineers concerned with the rational design of OLEDs and OPVs, the linear model of effective temperature may provide the most practical description of the electric field dependence of charge carrier mobility.

## References


1. Anderson PW (1958) Absence of diffusion in certain random lattices. Phys Rev 109:1492
2. Miller A, Abrahams E (1960) Impurity conduction at low concentrations. Phys Rev 120:745
3. Holstein T (1959) Studies of polaron motion. Part 1. The molecular-crystal model. Ann Phys 8:325
4. Holstein T (1959) Studies of polaron motion. Part II. The 'small' polaron. Ann Phys 8:343
5. Burrows PE, Shen Z, Bulovic V, McCarty DM, Forrest SR, Cronin JA, Thompson ME (1996) Relationship between electroluminescence and current transport in organic heterojunction light-emitting devices. J Appl Phys 79:7991
6. Tanase C, Blom PWM, de Leeuw DM (2004) Origin of the enhanced space-charge-limited current in poly(*p*-phenylene vinylene). Phys Rev B 70:193202
7. Tanase C, Meijer EJ, Blom PWM, de Leeuw DM (2003) Unification of the hole transport in polymeric field-effect transistors and light-emitting diodes. Phys Rev Lett 91:216601
8. Coehoorn R, Pasveer WF, Bobbert PA, Michels MAJ (2005) Charge-carrier concentration dependence of the hopping mobility in organic materials with Gaussian disorder. Phys Rev B 72:155206
9. Pasveer WF, Cottaar J, Tanase C, Coehoorn R, Bobbert PA, Blom PWM, de Leeuw DM, Michels MAJ (2005) Unified description of charge-carrier mobilities in disordered semiconducting polymers. Phys Rev Lett 94:206601
10. Vissenberg MCJM, Matters M (1998) Theory of the field-effect mobility in amorphous organic transistors. Phys Rev B 57:12964
11. Bässler H (1993) Charge transport in disordered organic photoconductors. Phys Status Solidi B 175:15
12. Ambegaokar V, Halperin BI, Langer JS (1971) Hopping conductivity in disordered systems. Phys Rev B 4:2612
13. Shklovskii BI (1973) Hopping conduction in semiconductors subjected to a strong electric-field. Sov Phys Semiconductors USSR 6:1964
14. Shklovskii BI, Levin EI, Fritzsche H, Baranovskii SD (1990) In: Fritzsche H (ed) Advances in disordered semiconductors, vol. 3, Transport, correlation and structural defects. World Scientific, Singapore, pp 161–191

15. Baranovskii SD, Cleve B, Hess R, Thomas P (1993) Effective temperature for electrons in band tails. J Non Cryst Sol 166:437
16. Lampert MA, Mark P (1970) Current injection in solids. Academic, New York
17. Ioannidis A, Forsythe E, Gao Y, Wu MW, Conwell EM (1998) Current-voltage characteristics of organic light emitting diodes. Appl Phys Lett 72:3038
18. Marianer S, Shklovskii BI (1992) Effective temperature of hopping electrons in a strong electric-field. Phys Rev B 46:13100
19. Arkhipov VI, Emelianova EV, Adriaenssens GJ (2003) Field-dependent effective temperature and variable range hopping: application to dark dc conductivity in doped a-Si: H. J Appl Phys 93:6150
20. Tang CW, VanSlyke SA (1987) Organic electroluminescent diodes. Appl Phys Lett 51:913
21. Baldo MA, Forrest SR (2001) Interface limited injection in amorphous organic semiconductors. Phys Rev B 64:085201
22. Limketkai BN, Baldo MA (2005) Charge injection into cathode-doped amorphous organic semiconductors. Phys Rev B 71:085207
23. Brütting W, Berleb S, Mückl AG (2001) Device physics of organic light-emitting diodes based on molecular materials. Org Electron 2:1
24. Limketkai BN, Jadhav P, Baldo MA (2007) Electric field dependent percolation model of charge carrier mobility in amorphous organic semiconductors. Phys Rev B 75:113203
25. Movaghar B, Grunewald M, Ries B, Bassler H, Wurtz D (1986) Diffusion and relaxation of energy in disordered organic and inorganic materials. Phys Rev B 33:5545
26. Vissenberg MCJM (1999) Opto-electronic properties of disordered organic semiconductors. University of Leiden, The Netherlands
27. Tal O, Rosenwaks Y, Preezant Y, Tessler N, Chan CK, Kahn A (2005) Direct determination of the hole density of states in undoped and doped amorphous organic films with high lateral resolution. Phys Rev Lett 95:256405
28. Celebi K, Jadhav PJ, Milaninia KM, Bora M, Baldo MA (2008) The density of states in thin film copper phthalocyanine measured by Kelvin probe force microscopy. Appl Phys Lett 93:083308
29. Hirao A, Nishizawa H, Sugiuchi M (1995) Diffusion and drift of charge carriers in molecularly doped polymers. Phys Rev Lett 75:1787
30. Sahimi M (1994) Applications of percolation theory. Taylor and Francis, London
31. Pike GE, Seager CH (1974) Percolation and conductivity – Computer study 1. Phys Rev B 10:1421
32. Jansson F, Baranovskii SD, Gebhard F, Osterbacka R (2008) Effective temperature for hopping transport in a Gaussian density of states. Phys Rev B 77:195211
33. Cleve B, Hartenstein B, Baranovskii SD, Scheidler M, Thomas P, Baessler H (1995) High-field hopping transport in band tails of disordered semiconductors. Phys Rev B 51:16705

Adv Polym Sci (2010) 223: 45–71
DOI:10.1007/12_2009_2
© Springer-Verlag Berlin Heidelberg 2009
Published online: 19 June 2009

# Description of Charge Transport in Disordered Organic Materials

**S.D. Baranovskii, O. Rubel, F. Jansson, and R. Österbacka**

**Abstract** In this chapter we present some useful concepts developed to describe theoretically electrical conduction in disordered organic materials such as molecularly doped and conjugated polymers and organic glasses. In such systems electrical conduction is due to incoherent hopping of charge carriers between localised states. We focus on the dependences of the conductivity and the carrier drift mobility on the concentration of localised states, concentration of carriers, temperature and electric field.

**Keywords** Disordered organic semiconductors · Hopping transport

## Contents

1 Introduction .......... 46
 1.1 General Remarks .......... 46
 1.2 The Model for Charge Carrier Transport in Random Organic Semiconductors .......... 50
2 General Concepts for Description of Charge Carrier Transport in Random Organic Materials .......... 51
 2.1 Percolation Approach .......... 51
 2.2 The Concept of the Transport Energy .......... 52
 2.3 Energy Relaxation of Electrons in an Exponential DOS: Dispersive Transport .......... 54
 2.4 Energy Relaxation of Electrons in a Gaussian DOS: Transition from Dispersive to Non-Dispersive Transport .......... 55
 2.5 Calculations of the Mobility $\mu$ and of the Relaxation Time $\tau_{\mathrm{rel}}$ .......... 58
 2.6 Saturation Effects .......... 60
 2.7 Nonlinear Effects at High Electric Fields .......... 63
3 Concluding Remarks .......... 69
References .......... 69

S.D. Baranovskii (✉) and O. Rubel
Department of Physics and Center for Material Sciences, Philipps Universität Marburg, 35032 Marburg, Germany
e-mail:baranovs@staff.uni-marburg.de

F. Jansson and R. Österbacka
Department of Physics and Center for Functional Materials, Åbo Akademi University, Finland

# 1 Introduction

## *1.1 General Remarks*

In this chapter we present basic ideas for description of charge carrier transport in disordered organic materials. So far electrophotographic image recording has been the main technique that exploited the electrical conducting properties of organic solids on a broad industrial scale [1]. The main efforts of researchers are presently focused on the development of organic materials for applications in light-emitting diodes (LEDs), in field-effect transistors as well as in photovoltaics. Materials used for these purposes are mostly random organic, notably conjugated, and/or molecularly doped polymers with semiconductor properties [1, 2]. Therefore we restrict our description in this chapter to considering electrical conduction in these organic semiconducting materials. In such materials charge transport is provided by a sequence of incoherent tunnelling transitions (hopping) of electrons or holes via localised states, randomly distributed in space and energy [1–7]. It is this transport mode which is described in our chapter.

Basic ideas for theoretical description of hopping transport were developed in the late 1960s and early 1970s. In particular it was recognised very early that an essential ingredient of a successful theory for hopping transport in disordered materials is that it takes into account that hopping is not determined by the rate of 'average' hops, but rather by the rate of those hops that are 'most difficult but still relevant': hopping conduction is in fact a percolation problem. The appropriate theoretical description of the hopping transport mode based on the mathematical theory of percolation was proposed independently by Ambegaokar et al. [8], Pollak [9], and Shklovskii and Efros [10]. The result was the comprehensive theory of the variable-range-hopping (VRH). Most of the theoretical treatments performed in the 1990s in order to describe hopping transport in disordered organic materials were based on the averaging of hopping rates (see, for instance, [11–14]). This procedure has been analysed and qualified as erroneous in numerous studies [15–19] and we are not going to repeat this analysis in our chapter, although the ensemble averaging of hopping rates is still often used when dealing with disordered organic systems (see, for instance, [20, 21]).

We would just like to remark here that a rather unlucky situation has been established with respect to the term 'averaging of hopping rates' in the field of organic semiconductors. It is recognised that the ensemble averaging of hopping rates leads to erroneous results, in particular, that it washes out the exponential dependence of hopping rates on distances between localised states and that it also gives a wrong temperature dependence for the hopping conductivity [22]. It is worth noting, however, that the procedure called the averaging of hopping rates in [23–26] is not the procedure noted in [22] and previously in [11–14]. In [23–26], the average hopping rate is simply *redefined* via the following chain of arguments. On one hand, the well-known general expression for the DC conductivity is used in the form [27]

$$\sigma_{\mathrm{DC}} = e \int \mathrm{d}\varepsilon \, \tilde{\mu}(\varepsilon) \, \tilde{n}(\varepsilon) \,, \tag{1}$$

where $e$ is the elementary charge, $\tilde{n}(\varepsilon)\mathrm{d}\varepsilon$ is the concentration of electrons in the states with energies between $\varepsilon$ and $\varepsilon + \mathrm{d}\varepsilon$ and $\tilde{\mu}(\varepsilon)$ is the mobility of these electrons. On the other hand, one uses the general expression for the DC conductivity in the form $\sigma_{\mathrm{DC}} = e\mu n$, where $n$ is the total concentration of the charge carriers:

$$n = \int \mathrm{d}\varepsilon \, \tilde{n}(\varepsilon) \,, \tag{2}$$

and $\tilde{n}(\varepsilon) = g(\varepsilon) \, f(\varepsilon)$ is the product of the density of states (DOS) $g(\varepsilon)$ and the Fermi function $f(\varepsilon)$, dependent on the position of the Fermi level $\varepsilon_{\mathrm{F}}$. The quantity $\mu$ obtained as $\mu = \sigma_{\mathrm{DC}}/en$ is claimed to be proportional to the average hopping rate. This definition is, however, not the same as the averaged hopping rates used in [11–14].

In the late 1960s and early 1970s the main effort of theoreticians was directed at describing hopping transport in doped crystalline semiconductors where localised states for charge carriers (electrons and holes) are created by donors and acceptors. These systems provide a really valuable test field for theoretical description of hopping transport, since the electronic structure of individual localised states in doped semiconductors is well known. For shallow impurities these states are simple hydrogen-like electron states with renormalised Bohr radius. Due to the screening of the core Coulomb potential of the impurity atom by the semiconductor matrix, the wavefunction of the valence electron or hole on shallow donors and acceptors has a much larger spatial extension than that in a hydrogen atom. Nevertheless the structure of the electron state is very similar to that in a hydrogen atom. This well-known electron structure of localised states allows one to develop theoretical description of hopping transport in full detail. Such detailed description of the theory can be found, for instance, in the monograph by Shklovskii and Efros [15]. Among other results it was shown that the shape of the DOS, i.e. the energy distribution of localised states available for hopping charge carriers, is essential for conducting properties of the material under study.

The latter message became particularly important when the attention of the scientific community in the 1970s turned to studying inorganic amorphous semiconductors, such as amorphous silicon (a-Si), amorphous germanium (a-Ge), and their alloys. These materials are usually prepared as thin films by deposition of atomic or molecular species. Particularly, hydrogenated amorphous silicon (a-Si:H), has been attracting much attention, since incorporation of hydrogen essentially improves the conducting properties favourable for device applications of amorphous semiconductors. The density of localised states in the band-tails of inorganic amorphous semiconductors is believed to have a purely exponential energy dependence (see, for instance, [18] and references therein):

$$g(\varepsilon) = \frac{N}{\varepsilon_0} \exp\left(\frac{\varepsilon}{\varepsilon_0}\right), \tag{3}$$

where energy $\varepsilon$ is counted from the mobility edge, $N$ is the total concentration of localised states in the band-tail, and $\varepsilon_0$ determines the energy scale of the tail. We consider in our chapter electrons as charge carriers. The results for holes can be obtained in an analogous way.

Theoretical description of hopping transport in a system with exponential DOS has been suggested in the 1970s and 1980s for all possible transport regimes – equilibrium transport [28], non-equilibrium transient transport [29], and for non-equilibrium steady-state transport [30]. These were essentially the VRH theories, in which the interplay between spatial (localisation length) and energetic factors (DOS function) plays the decisive role. The result of this interplay is in providing a particular energy level within the DOS that dominates all hopping transport phenomena [28–30].

In organic amorphous materials the DOS is not exponential as in their inorganic counterparts, but it is rather described by the Gaussian distribution [1–7]:

$$g(\varepsilon) = \frac{N}{\sigma\sqrt{2\pi}} \exp\left(-\frac{\varepsilon^2}{2\sigma^2}\right), \tag{4}$$

where $\sigma$ is the energy scale of the distribution and the energy $\varepsilon$ is measured relative to the centre of the DOS. The origin of the energetic disorder is the fluctuation in the lattice polarisation energies and the distribution of segment length in the p- or s-bonded main-chain polymer [5]. The Gaussian shape of the DOS was assumed on the basis of the Gaussian profile of the excitonic absorption band and by recognition that the polarisation energy is determined by a large number of internal coordinates, each varying randomly by small amounts [5].

Another argument in favour of the Gaussian DOS is provided by experimental data on the temperature dependence of the carrier drift mobility and conductivity. The temperature dependence of the drift mobility obtained in time-of-flight experiments in random organic solids usually has the form

$$\mu \propto \exp\left\{-\left(\frac{T_0}{T}\right)^2\right\}, \tag{5}$$

where $T_0$ is a parameter [1–7]. This temperature dependence has been reproduced in Monte Carlo computer simulations of the charge carrier hopping transport in a set of localised states with Gaussian energy distribution [31] strongly supporting the validity of Eq. (4). For exponential DOS described by Eq. (3) the temperature dependence of the mobility follows the Arrhenius law [28–30].

It has become a tradition in the field of organic materials to claim that the Gaussian shape of the energy distribution of localised states prevents analytical solution of the hopping transport problem [4–7, 32]. In this chapter we show that such a solution can be easily obtained within the standard set of ideas developed long ago for description of the VRH in inorganic disordered materials with exponential DOS. Furthermore, we will see below that the description of VRH in a system with Gaussian DOS is much easier than in a system with exponential DOS. The reason

for this is rather transparent. For materials with the exponential DOS described by Eq. (3), kinetic coefficients such as the drift mobility and diffusivity of charge carriers are not well defined. Indeed, if some small amount of electrons are inserted into a system with exponential DOS at such temperatures that $kT < \varepsilon_0$, where $k$ is the Boltzmann constant, electrons would continuously relax in energy, diving energetically deeper and deeper in course of time. In such a case their mobility is continuously decreasing with time. Therefore the result of a mobility measurement, for instance in a time-of-flight experiment, would depend on the length of the sample and on the applied electric field, since these parameters determine how long carriers move across the sample. In other words, there is no universal mobility for a particular material with an exponential DOS. This transport mode is known as dispersive transport. The diving of electrons in energy stops when they arrive into the vicinity of the Fermi level $\varepsilon_F$. Therefore the value of the measured mobility would depend on the concentration of electrons that determines the position of $\varepsilon_F$, and hence it is not an intrinsic characteristic for a given material.

In systems with Gaussian DOS the situation with the energy relaxation of electrons is much simpler. Even in a very diluted system, in which electrons behave independently from each other, there exists some limiting energy $< \varepsilon_\infty >$ for the energy relaxation of electrons. After arriving in the vicinity of this limiting energy, electrons would not relax to deeper states anymore. If this energy $< \varepsilon_\infty >$ lies above the Fermi level, one can easily calculate the mobility of electrons, which would be a well-defined quantity independent of the sample size and on the applied field (at low fields in long enough samples) characterising the material itself. As will be shown below, in this regime the temperature dependence of the mobility should be described by Eq. (5). If the concentration of electrons is high, so that the Fermi level is situated above $< \varepsilon_\infty >$, mobility becomes dependent on the concentration of electrons in the system. Furthermore, in the latter regime the temperature dependence of the carrier mobility due to hopping in the Gaussian DOS takes the Arrhenius form [18]

$$\mu \propto \exp\left\{-\frac{\Delta}{kT}\right\}, \tag{6}$$

where $\Delta$ is the activation energy. Usually the latter dependence in organic materials is observed by measurements of the electrical conductivity in systems with a significant concentration of charge carriers, for instance in field-effect transistors [33]. It is often claimed that the temperature dependence (Eq. 5) evidences a Gaussian DOS (Eq. 4), while the Arrhenius law (Eq. 6) favours purely exponential DOS (Eq. 3). We will show below that both temperature dependences described by Eqs. (5) and (6) are predicted theoretically in the frame of the same transport model with the same Gaussian DOS, depending on the total concentration of charge carriers in the system. At low carrier densities the dependence described by Eq. (5) is predicted, while at high carrier densities the dependence described by Eq. (6) should be valid [34, 35].

In the following we consider in parallel the description of the VRH transport in a system with the exponential DOS and that in a system with the Gaussian DOS. We will show that the well-known concepts successfully applied for decades to describe the VRH electrical conduction in the inorganic disordered materials such as

doped crystalline semiconductors and amorphous semiconductors with the exponential DOS are well able to account for the broad variety of experimental observations in disordered organic materials with Gaussian DOS.

## *1.2 The Model for Charge Carrier Transport in Random Organic Semiconductors*

The general model for charge carrier transport in random organic solids could be formulated as follows [1–7]. It is assumed that charge carriers move via incoherent hopping transitions between localised states randomly distributed in space with some concentration $N$. All states are presumed to be localised. The energy distribution of the localised states is described by Eq. (4). The energy scale $\sigma$ of the DOS in most random organic materials is of the order of $\sim 0.1\,\mathrm{eV}$ [1, 2]. In the initial model, no correlations between spatial positions of localised states and their energies were included [1, 2]. For the sake of simplicity we will assume below that this assumption is valid unless the contrary is specified.

A tunnelling transition rate of a charge carrier from a localised state $i$ to a localised state $j$ lower in energy, depends on the spatial separation $r_{ij}$ between sites $i$ and $j$ as $\nu(r_{ij}) = \nu_0 \exp(-2r_{ij}/\alpha)$, where $\alpha$ is the localisation length which we assume equal for all sites. This length determines the exponential decay of the carrier wavefunction in the localised states. The decay length on single sites has been evaluated in numerous studies of the concentration-dependent drift mobility. For example, for trinitrofluorenone in PVK the estimates $\alpha \approx 1.1 \times 10^{-8}\,\mathrm{cm}$ and $\alpha \approx 1.8 \times 10^{-8}\,\mathrm{cm}$ were obtained for holes and electrons, respectively [36]. For dispersions of $N$-isopropylcarbazole in polycarbonate the estimate $\alpha \approx 0.62 \times 10^{-8}\,\mathrm{cm}$ for holes has been obtained [37]. The pre-exponential factor $\nu_0$ depends on the electron interaction mechanism that causes the transition. Usually it is assumed that carrier transitions contributing to charge transport in disordered materials are caused by interactions with phonons. Often the coefficient $\nu_0$ is simply assumed to be of the order of the phonon frequency $\sim 10^{13}\,\mathrm{s}^{-1}$, although a more rigorous consideration is in fact necessary to determine $\nu_0$. Such a consideration should take into account the particular structure of the electron localised states and also the details of the interaction mechanism [38, 39].

When a charge carrier performs a transition upward in energy from a localised state $i$ to a localised state $j$, the transition rate depends on the energy difference between the states. This difference should be compensated, for example, by absorption of a phonon with the corresponding energy [40]. Generally, the transition rate from the occupied site $i$ to an empty site $j$ can be expressed as

$$\nu(r_{ij}, \varepsilon_i, \varepsilon_j) = \nu_0 \exp\left(-\frac{2r_{ij}}{\alpha}\right) \exp\left(-\frac{\varepsilon_j - \varepsilon_i + |\varepsilon_j - \varepsilon_i|}{2kT}\right). \tag{7}$$

If the system is in thermal equilibrium, the contribution of a pair of sites to the conductivity can be calculated by taking into account the occupation probabilities of sites with different energies determined by the Fermi statistics. Taking into account these occupation probabilities one should write the number of electrons making the transition between sites $i$ and $j$ per unit time in the form [40]

$$\Gamma(r_{ij},\varepsilon_i,\varepsilon_j)=\Gamma_0\exp\left(-\frac{2r_{ij}}{\alpha}\right)\exp\left(-\frac{|\varepsilon_j-\varepsilon_i|+|\varepsilon_j-\varepsilon_F|+|\varepsilon_i-\varepsilon_F|}{2kT}\right). \quad (8)$$

The problem of theoretical description of the hopping conduction can be then formulated as follows. One has to calculate the conductivity which is provided by transition events with the rates described by Eqs. (7) or (8) in the manifold of localised states with the DOS described by Eq. (4).

# 2 General Concepts for Description of Charge Carrier Transport in Random Organic Materials

## *2.1 Percolation Approach*

One of the most powerful theoretical tools to account for charge carrier transport in disordered systems is provided by the percolation theory as described in numerous monographs (see, for instance, [15, 18]). According to the percolation theory, one has to connect sites with fastest transition rates in order to fulfil the condition that the average number Z of connected bonds per site is equal to the so-called percolation threshold $B_C$. In the three-dimensional case this threshold is [15, 41, 42]:

$$Z \equiv B_C = 2.7 \pm 0.1. \quad (9)$$

This method has been successfully applied to the theoretical description of hopping transport in doped crystalline semiconductors [15] and also in disordered materials with exponential DOS [43]. A treatment of charge transport in disordered systems with a Gaussian DOS in the framework of the percolation theory can be found in [34, 35, 44]. However, this theory is not easy for calculations. Therefore it is desirable to have a more transparent theoretical description of transport phenomena in disordered systems with a Gaussian DOS. In the next section we present such an approach based on the well-approved concept of the transport energy (TE). This concept was successfully applied earlier to describe transport phenomena in inorganic disordered systems with exponential DOS [28–30]. We show below how this concept works in both cases for exponential and for Gaussian DOS functions.

## *2.2 The Concept of the Transport Energy*

The crucial role of a particular energy level in the hopping transport of electrons via localised band-tail states with the DOS described by Eq. (3) was first recognised by Grünewald and Thomas [28] in their numerical analysis of equilibrium VRH conductivity. This problem was later considered by Shapiro and Adler [45], who came to the same conclusion as Grünewald and Thomas, namely, that the vicinity of some particular energy level dominates the hopping transport of electrons in the band-tails. In addition, they achieved an analytical formula for this level and showed that its position does not depend on the Fermi energy. Independently, a rather different problem of non-equilibrium energy relaxation of electrons by hopping through the band-tail with the DOS described by Eq. (3) was solved at the same time by Monroe [29]. He showed that an electron, starting from the mobility edge, most likely makes a series of hops downward in energy. This character of the relaxation process changes drastically at some particular energy $\varepsilon_t$, which Monroe called TE. The hopping process near and below TE resembles a multiple-trapping type of relaxation with the TE playing the role of the mobility edge. In the multiple-trapping relaxation process [46] only electron transitions between delocalised states above the mobility edge and the localised band-tail states are allowed, while hopping transitions between the localised tail states are neglected. Hence, every second transition brings electron to the mobility edge. The TE of Monroe [29] plays the role of this edge for the hopping relaxation. It coincides exactly with the energy level discovered by Grünewald and Thomas [28] and by Shapiro and Adler [45] for equilibrium hopping transport. Shklovskii et al. [30] have shown that the same energy level $\varepsilon_t$ also determines the recombination and transport of electrons in the non-equilibrium steady-state under continuous photogeneration in a system with the DOS described by Eq. (3). We see, therefore, that the TE, in both equilibrium and non-equilibrium, controls both transient and steady-state transport phenomena. The question then arises as to why this energy level is so universal that hopping of electrons in its vicinity dominates all transport phenomena. Below, we give a derivation of the TE based on consideration of a single hopping event of an electron localised deep in the band-tail. It is the TE that maximises the hopping rate as a final electron energy in the hop, independently of its initial energy [47]. All derivations below are carried out for the case $kT < \varepsilon_0, \sigma$.

Consider an electron in a state with energy $\varepsilon_i$. According to Eq. (7), the typical rate of a downward hop of such an electron to a localised state somewhat deeper in energy is

$$\nu_{\downarrow}(\varepsilon_i) = \nu_0 \exp\left[-\frac{2r(\varepsilon_i)}{\alpha}\right], \tag{10}$$

where

$$r(\varepsilon) = \left[\frac{4\pi}{3}\int_{-\infty}^{\varepsilon} \mathrm{d}x\, g(x)\right]^{-1/3}. \tag{11}$$

The typical rate of an upward hop of such an electron to a localised state with energy $\varepsilon_x > \varepsilon_i$ is

$$\nu_{\uparrow}(\varepsilon_i, \varepsilon_x) = \nu_0 \exp\left[-\frac{2r(\varepsilon_x)}{\alpha} - \frac{\delta}{kT}\right], \quad (12)$$

where $\delta = \varepsilon_x - \varepsilon_i \geq 0$. This expression is not exact. The typical nearest-neighbour distance, $r(\varepsilon_x)$ is based on all states deeper than $\varepsilon_x$. For the exponential or Gaussian DOS this is equivalent to considering a slice of energy with the width of the order $\varepsilon_0$ or $\sigma$, respectively. This works for a DOS that varies slowly compared with $kT$, but not in general. It is also assumed for simplicity that the localisation length $\alpha$ does not depend on energy. The latter assumption can be easily released on the cost of a somewhat more complicated form of the equations. We will analyse the hopping rates at a given temperature $T$, and try to find the energy $\varepsilon_x$, which provides the fastest typical hopping rate for the electron placed initially at energy $\varepsilon_i$. The corresponding energy $\varepsilon_x$ is determined by the condition

$$\frac{\mathrm{d}\nu_{\uparrow}(\varepsilon_i, \varepsilon_x)}{\mathrm{d}\varepsilon_x} = 0. \quad (13)$$

It is easy to show [47, 48] that the final energy $\varepsilon_x$ determined by Eq. (13) does not depend on the initial energy $\varepsilon_i$ and hence it is universal for given parameters $N\alpha^3$, and $\varepsilon_0/kT$ (for exponential DOS) and $\sigma/kT$ for Gaussian DOS.

In the case of exponential DOS one obtains

$$\varepsilon_{\mathrm{t}} = -3\varepsilon_0 \ln \frac{3\varepsilon_0 (4\pi/3)^{1/3} N^{1/3}\alpha}{2kT}, \quad (14)$$

while in the case of Gaussian DOS the TE is determined by the equation

$$\varepsilon_{\mathrm{t}} = \sigma X\left(N\alpha^3, kT/\sigma\right), \quad (15)$$

where $X\left(N\alpha^3, kT/\sigma\right)$ is the solution of the equation [48]

$$\exp\left(\frac{X^2}{2}\right)\left[\int_{-\infty}^{X/\sqrt{2}} \mathrm{d}t\, \exp\left(-t^2\right)\right]^{4/3} = \left[9(2\pi)^{1/2} N\alpha^3\right]^{-1/3} kT/\sigma. \quad (16)$$

It has been shown [48] that at low temperatures, $kT < \varepsilon_0$, $\sigma$, the maximum determined by Eq. (13) is sharp and therefore the introduction of the TE for both exponential and Gaussian DOS functions makes sense.

Unfortunately it is claimed sometimes that there is no TE in the variable-range sense for a Gaussian DOS [49]. Equations (15) and (16) clearly show that this energy does exist. Furthermore, the equation for the TE in a Gaussian DOS literally coinciding with Eq. (16) was later discussed by Arkhipov et al. [50], who claimed that the concept of TE is applicable to practically all realistic DOS distributions.

However, it has been shown in [48] that, for example, in a system with the DOS in the form $g(\varepsilon) \propto \exp\left(-\sqrt{\varepsilon/\varepsilon_0}\right)$ the maximum determined by Eq. (13) is so broad and the position of $\varepsilon_t$ is so deep in the tail of the DOS that introduction of the TE makes no sense. The DOS $g(\varepsilon) \propto \exp\left(-\sqrt{\varepsilon/\varepsilon_0}\right)$ is well known for the mixed crystals with compositional disorder [51]. Furthermore, sometimes the TE approach is applied to a system with a constant, energy-independent DOS [52]. We do not think that such a procedure is meaningful. If the energy dependence of the DOS is weak, the transport path in the equilibrium conditions corresponds to the vicinity of the Fermi level. Concomitantly, the temperature dependence of the conductivity obeys the classical Mott formula: $\sigma_{\mathrm{DC}}(T) \propto \exp\left\{-(T_0/T)^{1/4}\right\}$ [15, 27]. Below we show how one can use the concept of the TE in order to describe the energy relaxation of electrons and to calculate the transport coefficients.

## 2.3 *Energy Relaxation of Electrons in an Exponential DOS: Dispersive Transport*

Consider an electron in some shallow state with the energy close to the mobility edge. Let the temperature be low, so that the TE $(\varepsilon_{\mathrm{t}})$ lies well below the mobility edge, which we consider here as a reference energy $\varepsilon_{\mathrm{C}} = 0$. The problem is to find the energy $\varepsilon_{\mathrm{d}}(t)$, which corresponds to the maximum of the energy distribution of electrons as a function of the time $t$. At early times, as long as $\varepsilon_{\mathrm{d}}(t) > \varepsilon_{\mathrm{t}}$ the relaxation is governed by Eqs. (10) and (11). The depth $\varepsilon_{\mathrm{d}}(t)$ of an electron in the band-tail is determined by the condition

$$\nu_{\downarrow}\left[\varepsilon_{\mathrm{d}}(t)\right] t \cong 1. \tag{17}$$

This leads to the double logarithmic dependence $\varepsilon_{\mathrm{d}}(t) \propto -\varepsilon_0 \ln\left[\ln(\nu_0 t)\right] + C$ with constant $C$ dependent on $\varepsilon_0$, $N$, and $\alpha$. Indeed, Eqs. (10) and (17) prescribe the logarithmic form for the time dependence of the hopping distance $r(t)$ and Eqs. (3) and (11) lead to another logarithmic dependence $\varepsilon_{\mathrm{d}}[r(t)]$. At time

$$t_{\mathrm{C}} \cong \nu_0^{-1} \exp\left(\frac{3\varepsilon_0}{kT}\right), \tag{18}$$

the typical electron energy $\varepsilon_{\mathrm{d}}(t)$ approaches the TE $\varepsilon_{\mathrm{t}}$ and the style of the relaxation process changes. At $t > t_{\mathrm{C}}$, every second hop brings electron into states in the vicinity of the TE from where it falls downward in energy to the nearest in space localised state. For such a relaxation process the typical electron energy is determined by the condition [29]

$$\nu_{\uparrow}\left[\varepsilon_{\mathrm{d}}(t),\ \varepsilon_{\mathrm{t}}\right] t \cong 1, \tag{19}$$

where $\nu_{\uparrow}[\varepsilon_{\mathrm{d}}(t),\ \varepsilon_{\mathrm{t}}]$ is the typical rate of electron hops upward from the demarcation energy towards the TE [29]. This condition leads to the typical energy position of the relaxing electron at time $t$ determined as

$$\varepsilon_{\mathrm{d}}(t) \cong -3\varepsilon_0 \ln\left[\frac{3\varepsilon_0 (4\pi/3)^{1/3} N^{1/3}\alpha}{2kT\,\tilde{e}}\right] - kT\ln(\nu_0 t), \qquad (20)$$

where $\tilde{e}$ is the basis of the natural logarithm. This is a very important result, showing that in a system with purely exponential energy dependence of the DOS, described by Eq. (3), the typical energy of a set of independently relaxing electrons would continuously dive deeper and deeper into the mobility gap. Of course, Eq. (20) is valid for long enough times, so that the demarcation energy $\varepsilon_{\mathrm{d}}(t)$ lies below the mobility edge, i.e. $\varepsilon_{\mathrm{d}}(t) < 0$. This continuous decrease of the charge carrier energy leads to the time dependence of the carrier mobility. The longer is the time, which electrons spend carrying the current, the smaller is their mobility. The latter is determined by the activation of electrons from the demarcation energy $\varepsilon_{\mathrm{d}}(t)$ decreasing with time in accord with Eq. (20) to the time-independent TE $\varepsilon_{\mathrm{t}}$. This is the essence of the so-called dispersive transport in which the mobility of charge carriers depends on the sample length and on the applied electric field, since these two parameters determine the time scale at which electrical current is measured. In such situation the measured or calculated carrier mobility cannot be well defined as a characteristic quantity for a material. In the next section we will see that the situation with energy relaxation of electrons in a Gaussian DOS is much simpler than that for the exponential DOS and that the carrier mobility for a Gaussian DOS can be defined unambiguously. Before showing this, we would like to emphasise once more that one should be cautious with application of theoretical methods traditional for crystalline materials to the description of charge transport phenomena in disordered systems. For example, in some theoretical studies based on the Fokker–Planck equation, it has been claimed that the maximum of the energy distribution of electrons coincides with the TE $\varepsilon_{\mathrm{t}}$ and hence it is independent of time (see, for example [53]). Such statements are in contradiction to the above result with the maximum of the distribution at energy $\varepsilon_{\mathrm{d}}(t)$ given by Eq. (20). One should realise that the Fokker–Planck approach presumes a diffusive style of charge carrier energy relaxation. Hence, it is invalid for description of the energy relaxation in the exponential or Gaussian DOS, in which electron can jump over the full energy range of the DOS (from a very deep energy state towards the TE) in a single hopping event [48].

### *2.4 Energy Relaxation of Electrons in a Gaussian DOS: Transition from Dispersive to Non-Dispersive Transport*

One of the most remarkable results for energy relaxation of charge carriers in a Gaussian DOS is the existence of the so-called equilibration energy $< \varepsilon_{\infty} >$ [4–7].

This situation is in contrast to the case of the exponential DOS, where in the empty system at low temperatures the charge carrier always relaxes downward in energy and the carrier mobility slows down in the course of the energy relaxation, as discussed in the previous section. In the Gaussian DOS the charge carrier on average relaxes from high-energy states downward in energy only until it arrives at the equilibration energy $< \varepsilon_\infty >$, even in an empty system without any interaction between the relaxing carriers [4–7]. In computer simulations [5–7], non-interacting carriers were initially distributed uniformly over the localised states, and their further relaxation via hopping processes with the rates described by Eq. (7) was traced. The temporal evolution of a packet of non-interacting carriers relaxing within a Gaussian DOS is shown in Fig. 1.

Initially the energy distribution of carriers coincides with that of the DOS. In the course of time the carrier energy distribution moves downward until its maximum $< \varepsilon(t) >$ arrives at the energy $< \varepsilon_\infty >= \lim_{t\to\infty} < \varepsilon(t) >= -\sigma^2/kT$ [5–7]. This result can be obtained analytically [54]:

$$< \varepsilon_\infty >= \frac{\int_{-\infty}^{\infty} \varepsilon\, g(\varepsilon) \exp\left(-\varepsilon/kT\right) \mathrm{d}\varepsilon}{\int\limits_{-\infty}^{\infty} g(\varepsilon) \exp\left(-\varepsilon/kT\right) \mathrm{d}\varepsilon} = -\frac{\sigma^2}{kT}. \tag{21}$$

The time required to reach this equilibrium distribution (called the relaxation time) $\tau_{\mathrm{rel}}$ is of key importance for the analysis of experimental results [55]. Indeed at time scales shorter than $\tau_{\mathrm{rel}}$, charge carriers initially randomly distributed over

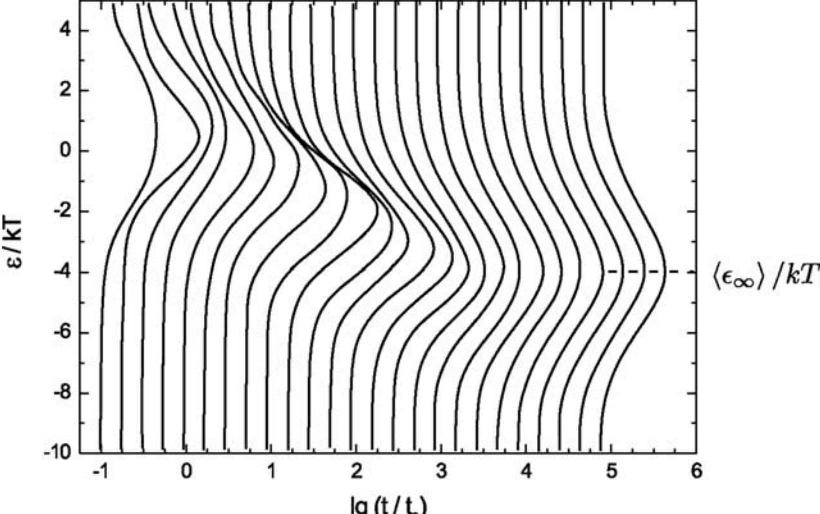


**Fig. 1** Temporal evolution of the distribution of carrier energies in a Gaussian DOS $(\sigma/kT = 2.0)$. $< \varepsilon_\infty >$ denotes the theoretical equilibrium energy determined by Eq. (21) (reproduced with permission from [5]. Copyright 1993, Wiley-VCH)

localised states perform a downward energy relaxation during which transport coefficients, such as the carrier drift mobility, essentially depend on time, and charge transport is dispersive, as described above. At time scales longer than $\tau_{\rm rel}$, the energy distribution of charge carriers stabilises around the equilibration energy $< \varepsilon_\infty >$, even in a very dilute system with non-interacting carriers. In such a regime, transport coefficients are time-independent. In other words, at $t \approx \tau_{\rm rel}$ dispersive transport is succeeded by the non-dispersive (Gaussian) transport behaviour. This is one of the most important results for charge carrier transport in disordered organic media [5]. While at short times dispersive current transients were observed in such materials, at long times transport characteristics are non-dispersive, time-independent and hence they can be well characterised and described, in contrast to analogous quantities in inorganic disordered materials with exponential DOS. In the latter materials, transport coefficients in dilute systems are always dispersive (time-dependent) as shown in the previous section. It has been established by computer simulations that $\tau_{\rm rel}$ strongly depends on temperature [5, 55]:

$$\tau_{\rm rel} \propto \exp\left\{\left(\frac{B\sigma}{kT}\right)^2\right\}, \tag{22}$$

where the numerical coefficient $B$ is close to unity: $B \cong 1.1$. It has also been found by computer simulations that the carrier drift mobility $\mu$ at long times corresponding to the non-dispersive transport regime has the temperature dependence [4–7, 55]

$$\mu \propto \exp\left\{-\left(\frac{C\sigma}{kT}\right)^2\right\}. \tag{23}$$

For the coefficient $C$ the value $C = 2/3$ has become a conventional one [4–7, 55]. In fact, computer simulations [31] give for this coefficient the value $C \cong 0.69$, while rather sophisticated analytical calculations [53, 55] predict a close value $C \cong 0.64$. Equation (23) with $C = 2/3$ is believed to be universal, and it is widely used to determine the energy scale $\sigma$ of the DOS from the experimental measurements of the $\ln(\mu)$ vs $T^{-2}$ [56, 57].

However, it looks rather strange that the coefficients $C$ and $B$ in Eqs. (22) and (23) are considered as the universal ones. In fact, it is the main feature of the VRH transport mode that the spatial and energy parameters are interconnected in the final expressions for transport coefficients [15]. Equations (7) and (8) show that both the energy difference between localised states and the spatial distance between them determine the hopping probability. Hopping transport in a system with spatially and energetically distributed localised states is essentially a VRH process. In such a process, the transport path used by charge carriers is determined by both energy and spatial variables in transition probabilities. It means that the temperature dependence of transport coefficients should include the spatial parameter $N\alpha^3$, while the dependence of transport coefficients on the concentration $N$ of localised states should depend on the temperature normalised by the energy scale of the DOS,

$kT/\sigma$. In computer simulations [31], a particular value of the spatial parameter was taken: $N\alpha^3 = 0.001$, and the magnitude $C \cong 0.69$ was obtained. The question then arises of whether this value of $C$ is stable against variations of $N\alpha^3$.

There is another important question, already raised in the scientific literature [55], that is related to the apparent difference in the temperature dependences of $\tau_{rel}$ and $\mu$ expressed by the difference between coefficients $C$ and $B$ in Eqs. (22) and (23). The relaxation time $\tau_{rel}$ at which a transition from dispersive to non-dispersive transport should take place depends on the ratio $\sigma/kT$ more strongly than the carrier drift mobility $\mu$. This has an important consequence that a time-of-flight signal produced by a packet of charge carriers drifting across a sample of some given length must become dispersive above a certain degree of disorder, i.e. below a certain temperature at otherwise constant system parameters, because eventually $\tau_{rel}$ will exceed the carrier transient time [55]. The early analytical theories [54, 58] already indicated the difference between coefficients $C$ and $B$, although they predicted $C > B$ in contrast to the simulation results. Therefore a consequent analytical theory for description of the VRH transport in a system of random sites with a Gaussian distribution is definitely desirable.

### *2.5 Calculations of the Mobility $\mu$ and of the Relaxation Time $\tau_{rel}$*

Qualitatively, the energy relaxation of carriers in a Gaussian DOS is schematically shown in Fig. 2. At low temperatures, $kT < \sigma$, carriers placed in the high-energy part of the Gaussian DOS perform downward energy transitions until they reach a

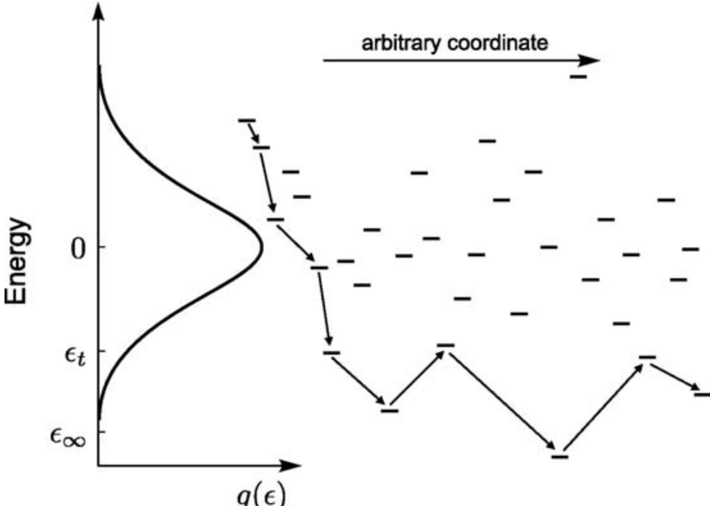


**Fig. 2** Schematic picture of carrier energy relaxation in the Gaussian DOS via the transport energy $\varepsilon_t$ (reproduced with permission from [59]. Copyright 2000 by the American Physical Society)

particular energy level $\varepsilon_t$ called the TE. At $\varepsilon_t$ the character of the relaxation changes. After a hop to a state below $\varepsilon_t$, the carrier hops upward in energy to a state in the vicinity of $\varepsilon_t$. This hopping process near and below $\varepsilon_t$ resembles a multiple-trapping process where $\varepsilon_t$ plays the role of the mobility edge.

After having understood the relaxation kinetics, it is easy to calculate $\tau_{rel}$ and $\mu$ [59]. Let us start with temperature dependences of these quantities. We consider the case $\langle \varepsilon_\infty \rangle < \varepsilon_t < 0$, which corresponds to any reasonable choice of materials parameters $N\alpha^3$ and $kT/\sigma$ [48]. After generation of carriers in a non-equilibrium situation, the carrier energy distribution moves downward in energy with its maximum $< \varepsilon(t) >$ logarithmically dependent on time $t$ [59]. States above $< \varepsilon(t) >$ achieve thermal equilibrium with $\varepsilon_t$ at time $t$, while states below $< \varepsilon(t) >$ have no chance at time $t$ to exchange carriers with states in the vicinity of $\varepsilon_t$, and hence the occupation of these deep energy states does not correspond to the equilibrium occupation. The system of non-interacting carriers comes into thermal equilibrium when the time-dependent energy $< \varepsilon(t) >$ achieves the equilibrium level $< \varepsilon_\infty >$ determined by (21). The corresponding time is the relaxation time $\tau_{rel}$ [59]. At this time, dispersive conduction is replaced by the Gaussian transport [59]. As long as the relaxation of carriers occurs via thermal activation to the level $\varepsilon_t$, the relaxation time $\tau_{rel}$ is determined by the activated transitions from the equilibrium level $< \varepsilon_\infty >$ to the TE $\varepsilon_t$[59].

Hence according to Eq. (7), $\tau_{rel}$ is determined by the expression [59]

$$\tau_{rel} = \nu_0^{-1} \exp\left[\frac{2r(\varepsilon_t)}{\alpha} + \frac{\varepsilon_t - < \varepsilon_\infty >}{kT}\right], \tag{24}$$

where $r(\varepsilon)$ is determined by Eq. (11). From Eqs. (15) and (16) it is apparent that the activation energy of the relaxation time in Eq. (24) depends on both parameters $\sigma/kT$ and $N\alpha^3$ and therefore the coefficient $B$ should depend on the magnitude of the parameter $N\alpha^3$. Solving Eq. (16) numerically, one obtains for $N\alpha^3 = 0.001$ the dependence described by Eq. (22) with $B \cong 1.0$ in good agreement with computer simulations that give $B \cong 1.1$ [5, 54]. Hence the result of the analytic calculation confirms Eq. (22). However, at another value of the parameter $N\alpha^3 = 0.02$, the relaxation time is described by Eq. (22) with another value of the coefficient $B \cong 0.9$. This clearly shows that the temperature dependence in Eq. (22) cannot be universal with respect to the concentration of localised states $N$ and the decay parameter of the carrier wave function $\alpha$.

Now we turn to the calculation of the carrier drift mobility $\mu$. We assume that the transient time $t_{tr}$, necessary for a carrier to travel through a sample is much longer than $\tau_{rel}$, and hence the charge transport takes place in the equilibrium conditions. As described above, every second jump brings the carrier upward in energy to the vicinity of the TE, being succeeded by a jump to the spatially nearest site with deeper energy determined solely by the DOS. Therefore, in order to calculate the drift mobility, it is correct to average the times of hopping transitions over energy states below $\varepsilon_t$ since only these states are essential for charge transport in thermal equilibrium [59, 60]. Hops downward in energy from the level $\varepsilon_t$ occur exponentially

faster than upward hops towards $\varepsilon_t$. Therefore, one can neglect the former in the calculation of the average time $< t >$. The carrier drift mobility can be evaluated as

$$\mu \cong \frac{e}{kT}\frac{r^2(\varepsilon_t)}{< t >}. \tag{25}$$

The average hopping time has the form [60]

$$< t >= \left[\int_{-\infty}^{\varepsilon_t} \mathrm{d}\varepsilon\, g(\varepsilon)\right]^{-1} \int_{-\infty}^{\varepsilon_t} \mathrm{d}\varepsilon\, g(\varepsilon)\, \nu_0^{-1} \exp\left[\frac{2r(\varepsilon_t)\, B_C^{1/3}}{\alpha} + \frac{\varepsilon_t - \varepsilon}{kT}\right], \tag{26}$$

where $B_C$ is the percolation parameter taken from Eq. (9). This numerical coefficient is introduced into Eq. (26) in order to warrant the existence of an infinite percolation path over the states with energies below $\varepsilon_t$. Using Eqs. (4), (15), (16), (25) and (26), one obtains for the exponential terms in the expression for the carrier drift mobility the relation [60]

$$\ln\left[\mu\left(\frac{er^2(\varepsilon_t)\,\nu_0}{kT}\right)^{-1}\right] = -2\left[\frac{4\sqrt{\pi}}{3B_C}N\alpha^3 \int_{-\infty}^{X/\sqrt{\pi}} \mathrm{d}t \exp\left(-t^2\right)\right]^{-1/3} - \frac{\sigma X}{kT} - \frac{1}{2}\left(\frac{\sigma}{kT}\right)^2. \tag{27}$$

It is this equation that determines the dependence of the carrier drift mobility on the parameters $N\alpha^3$ and $\sigma/kT$. Equation (27) gives the temperature dependence of the mobility in the form of Eq. (23) with the coefficient $C$ dependent on the parameter $N\alpha^3$ as inherent for the VRH transport [59, 60].

Note that this solution was obtained considering a single charge carrier in the Gaussian DOS. For exponential DOS such a consideration would not make sense, since the result for the drift mobility would depend on time because if $kT$ is less than the energy scale of the DOS, a single charge carrier in the exponential DOS is continuously decreasing its energy in course of the energy relaxation.

### *2.6 Saturation Effects*

So far we have discussed the drift mobility of charge carriers under the assumption that their concentration is much less than that of the localised states in the energy range essential for hopping transport. In the case of the exponential DOS described by Eq. (3), this transport mode provides kinetic coefficients, which are time-dependent as described above. In the case when the concentration of moving electrons is significant and should be taken into account, the theory of the VRH for the DC conductivity $\sigma_{DC}$ in the exponential DOS has been developed by Vissenberg and Matters [43], using the percolation theory. In the percolation approach one treats

the transition rates between all pairs of sites, taking into account both the quantum mechanical transition probabilities and also the probabilities that one of the sites in a pair is filled by a charge carrier, while the other site is empty, as described by Eq. (8). These probabilities are determined by the energy levels, $\varepsilon_i$ and $\varepsilon_j$ of the involved sites with respect to the position of the Fermi level $\varepsilon_F$. The latter quantity is determined by the concentration of charge carriers $n$. The number of electrons making transition between sites $i$ and $j$ per unit time can be expressed as

$$\Gamma_{ij} = \Gamma_0 \exp\left(-\xi_{ij}\right), \tag{28}$$

where $\xi_{ij}$ denotes the exponent in Eq. (8). Connecting only sites with $\xi_{ij} < \xi$, and increasing $\xi$, one determines the value $\xi = \xi_C$, at which the infinite percolation cluster of interconnected sites first appears. This cluster is responsible for the hopping motion of charged carriers in the DC regime [15]. The critical value $\xi_C$ determines the exponential temperature and concentration dependences of transport coefficients

$$\sigma_{DC} = \sigma_0 \exp\left(-\xi_C\right), \tag{29}$$

where $\sigma_0$ is a prefactor not given by the percolation theory. Vissenberg and Matters [43] calculated $\sigma_{DC}(T,n)$ using the classical percolation criterion with $B_C$ given by Eq. (9). They obtained the following expression:

$$\sigma_{DC}(T,n) = \sigma_0 \left[\frac{\pi\left(\varepsilon_0/kT\right)^3 n}{(2\alpha)^3 B_C \Psi\left(1-kT/\varepsilon_0\right)\Psi\left(1+kT/\varepsilon_0\right)}\right]^{\varepsilon_0/kT}, \tag{30}$$

where $\Psi(z) = \int_0^\infty \mathrm{d}x\ \exp(-x)x^{z-1}$. It is this equation that describes analytically the dependence of the DC hopping conductivity on the concentration of charge carriers $n$ and on temperature. The corresponding temperature dependence can be usually well fitted by the Arrhenius law (Eq. 6), in which the activation energy $\Delta$ is close to the difference between the TE $\varepsilon_t$ and the Fermi energy $\varepsilon_F$. Only if the TE lies below the Fermi level, one could expect the validity of the dependence $\sigma_{DC} \propto \exp\left[-\left(T_0/T\right)^\beta\right]$ with $\beta = 1/4$ (Mott law) or with $\beta = 1/2$ for the case of strong electron–electron interactions (Shklovskii–Efros law) [15].

The approach of Vissenberg and Matters [43] has been checked by straightforward computer simulations and a satisfactory agreement has been reported [61].

For the Gaussian DOS described by Eq. (4) the theoretical treatment is even easier than that for the exponential DOS. If the concentration of electrons is negligibly small, the DC conductivity can be calculated as a product

$$\sigma_{DC} = e\mu n, \tag{31}$$

where $n$ is the concentration of charge carriers in the material and $\mu$ is their drift mobility. The latter is calculated via Eq. (27) under the assumption that the system is empty and a charge carrier is not affected by the possibility that localised states can

be occupied by other carriers. In such a regime, the dependence of the conductivity on the concentration of charge carriers is linear as given by Eq. (31).

If, however, the concentration $n$ of charge carriers is increased so that the Fermi energy $\varepsilon_F$ in thermal equilibrium or the quasi-Fermi energy under stationary excitation is located energetically higher than the equilibrium energy $<\varepsilon_\infty>$ determined by Eq. (21), one should use a more sophisticated theory in order to calculate $\sigma_{DC}$. Analytical theory for the dependence of the hopping conductivity on the concentration of charge carriers in a Gaussian DOS has been developed in [34, 35, 44]. Let us first estimate the critical concentration of charge carriers $n_C$, below which the consideration based on Eqs. (27) and (31) is valid. In order to estimate $n_C$, the value of the Fermi energy $\varepsilon_F$ should first be calculated. The position of the Fermi level is determined by the equation

$$\int_{-\infty}^{\infty} \frac{g(\varepsilon)\,\mathrm{d}\varepsilon}{1+\exp\left[(\varepsilon-\varepsilon_F)/kT\right]} = n. \tag{32}$$

At low $n$ for all energies in the domain giving the main contribution to the integral in Eq. (32), the exponential function in the denominator of the integral is large compared with unity (the non-degenerate case). Then a straightforward calculation [34] gives for the DOS determined by Eq. (4) at low temperatures

$$\varepsilon_F = -\frac{1}{2}\left(\frac{\sigma^2}{kT}\right) - kT\ln\left(\frac{N}{n}\right). \tag{33}$$

From the equation $\varepsilon_F(n_C) =<\varepsilon_\infty>$, where $<\varepsilon_\infty>$ is determined by Eq. (21), one obtains the estimate

$$n_C = N\exp\left[-\frac{1}{2}\left(\frac{\sigma}{kT}\right)^2\right]. \tag{34}$$

At $n < n_C$, the Fermi level is situated below the equilibration energy, $<\varepsilon_\infty>$, and the charge transport can be described for independent carriers via Eqs. (27) and (31). At $n > n_C$, the theory for charge transport should be essentially modified. These arguments can easily be converted in order to consider the case of constant concentration of charge carriers and changing temperature. Then at some particular temperature $T_C$ equation $\varepsilon_F(T_C) =<\varepsilon_\infty>$ will be fulfilled. From Eqs. (21) and (33) one obtains [18, 34]

$$T_C = \frac{\sigma}{2^{1/2}k\ln^{1/2}(N/n)}. \tag{35}$$

At $T > T_C$, the carrier mobility and conductivity can be described by Eqs. (27) and (31), while at $T < T_C$, an essential modification of the theory is needed.

In order to develop a theory for hopping transport at $n > n_C$ (or at $T < T_C$) one should explicitly take into account the filling probabilities of the localised states by charge carriers.

One possibility is to solve the percolation problem with transition rates between localised states described by Eq. (8) that includes the value of the Fermi energy related via Eq. (32) to the concentration of carriers, $n$ [34, 35]. An alternative theoretical approach to describe hopping conductivity in the Gaussian DOS, taking into account the occupation of the essential fraction of localised states by charge carriers, was recently suggested by Schmechel [62, 63]. Schmechel extended the concept of TE described in Sect. 2.2, taking into account the possibility that the localised states can be essentially filled by charge carriers. Another kind of percolation approach to the problem was suggested by Coehoorn et al. [44]. We will not describe these theories in detail; the interested reader can find a comprehensive analysis of some of the theories in [44]. We would like, however, to emphasise one very pronounced result of those theories.

As soon as the Fermi energy determined by Eq. (32) lies essentially above the equilibration energy determined by Eq. (21), the temperature dependence of the electrical conductivity is no longer proportional to $\exp\left[-(C\sigma/kT)^2\right]$ as in the case of low carrier concentrations at which Eqs. (23), (27) and (31) are valid. The conductivity instead closely follows the Arrhenius behaviour [34, 35]. For example, the percolation approach predicts at $n > n_C$ the temperature dependence

$$\sigma_{DC} = \sigma_0 \exp\left(-\frac{\varepsilon_t - \varepsilon_F}{kT}\right), \tag{36}$$

where $\sigma_0$ is the preexponential factor only slightly dependent on temperature [34, 35].

It is worth noting that there are numerous observations of a simple activated temperature dependence of the conductivity in disordered organic materials [64–67]. Particularly the Arrhenius temperature dependence of the conductivity is often observed in field-effect transistors, where charge carrier concentration is usually high (see, for instance, [33]). Often the dependence $\ln(\mu) \propto T^{-2}$ or $\ln(\sigma_{DC}) \propto T^{-2}$ is considered as evidence for a Gaussian DOS, while the Arrhenius temperature dependence $\ln(\mu) \propto T^{-1}$ or $\ln(\sigma_{DC}) \propto T^{-1}$ is claimed to indicate a pure exponential DOS. The important conclusion from the above consideration is the possibility to account successfully for both kinds of temperature dependence of hopping conductivity described by Eqs. (5) and (6) in the framework of the universal theoretical model based on the Gaussian DOS. The temperature dependence of the conductivity is sensitive to the concentration of charge carriers.

### *2.7 Nonlinear Effects at High Electric Fields*

So far we discussed transport phenomena in organic materials at low values of electric fields $F$, at which the conductivity and mobility of charge carriers are independent of the applied electric field. However, at high electric fields the carrier mobility and the conductivity in organic disordered materials depend strongly on

the applied electric field. In this section we describe a model suggested for theoretical treatment of the field-dependent mobility and conductivity.

Two effects are usually discussed with respect to the field dependence of the charge carrier mobility in organic semiconductors [1, 2, 4–7]. One of them is the apparent decrease of the drift mobility with rising field at relatively high temperatures [1, 2, 4–7, 68–70]. The other is the strong increase of the drift mobility with rising field at low temperatures.

It has been shown experimentally [71, 72] and theoretically [73] that the apparent decrease of the mobility with rising field is an artefact. Indeed the experimental data are obtained by the time-of-flight technique, in which charge carriers are created close to one surface of a sample with a given thickness $L$ and the transient time $\tau_{tr}$ is measured, which is needed for charge carriers to reach the opposite surface of the sample at a particular strength of the applied electric field $F$. Then the drift mobility is calculated as

$$\mu = \frac{L}{\tau_{tr} F}. \tag{37}$$

However, at high temperatures and low electric fields the current transients in the time-of-flight experiments are determined mostly by diffusion of charge carriers rather than by their drift. Therefore use of the drift formula (Eq. 37) strongly overestimates the mobility. It is the presence of the field strength in the denominator of Eq. (5) that leads to apparent 'increase' of the mobility at decreasing $F$ [71, 73]. If one uses diffusion formula instead of Eq. (37) at low fields $F$ and high temperatures, then no increase of the mobility with decreasing field is seen [73].

This observation does not exclude the possibility of the negative differential conductivity in the hopping regime. Böttger and Bryksin [74] and Shklovskii et al. [75, 76] have suggested the detailed theory for the hopping mobility and conductivity decreasing with increasing electric field in various systems, particularly with a Gaussian DOS [76]. The analytical theory has been recently confirmed by computer simulations [95]. The effect of the negative differential conductivity is however to expect at very high fields. This regime succeeds the very strong increase of the mobility with rising field [75, 76], and does not precede it at lower field as claimed on the basis of Eq. (37) [1, 2, 4–7, 68–70]. Therefore we turn now to the real effect, namely to the very strong increase of the carrier drift mobility with rising field at high values $F$.

We start with a description of this effect for disordered materials with an exponential DOS described by Eq. (3), which is typical for inorganic amorphous materials. Li, Meller and Kosina [77] recently approached this problem by inserting the dependence of transition rates on the electric field and that of the percolation threshold into the percolation theory of Vissenberg and Matters [43]. We describe below another approach based on a very useful concept of the so-called field-dependent effective temperature. Then this concept will be extended to organic disordered materials with a Gaussian DOS.

Transport phenomena under the influence of high electric fields in inorganic non-crystalline materials, such as amorphous semiconductors, has been the object of intensive experimental and theoretical study for decades. This is implied by observations of strong nonlinearity in the field dependences of the dark conductivity [78, 79],

of the photoconductivity [80] and of the charge carrier drift mobility [78, 81, 82] at high electric fields. This effect is most pronounced at low temperatures, when charge transport is determined by electron hopping via localised band-tail states.

While the field-dependent hopping conductivity at low temperatures was always a challenge for theoretical description, the theories for the temperature dependence of the hopping conductivity at low electric fields were successfully developed for all transport regimes: for the dark conductivity [28, 43], for the drift mobility [29], and for the photoconductivity [30]. In all these theories, hopping transitions of electrons between localised states in the exponential band-tails play a decisive role, as described above.

Shklovskii was the first who recognised that a strong electric field plays, for hopping conduction, a role similar to that of temperature [83]. In order to obtain the field dependence of the conductivity $\sigma_{DC}(F)$ at high fields, Shklovskii replaced the temperature $T$ in the well-known dependence $\sigma_{DC}(T)$ for low fields by a function $T_{eff}(F)$ of the form [83]

$$T_{eff} = \frac{eF\alpha}{2k}. \tag{38}$$

A very similar result was obtained later by Grünewald and Movaghar in their study of the hopping energy relaxation of electrons through band-tails at very low temperatures and high electric fields [84]. The same idea was also used by Shklovskii et al. [30], who suggested that, at $T = 0$, one can calculate the field dependence of the stationary photoconductivity in amorphous semiconductors by replacing the laboratory temperature $T$ in formulas for the low-field finite-temperature theory by an effective temperature $T_{eff}(F)$ given by Eq. (38).

It is easy to understand why electric field plays a role similar to that of temperature for the energy relaxation of electrons. In the presence of the field, the number of sites available for charge transport at $T = 0$ is essentially enhanced in the direction prescribed by the field, as shown in Fig. 3. Hence, electrons can relax faster at higher fields. From the figure it is seen that an electron can increase its energy with respect to the mobility edge by the amount $\varepsilon = eFx$ in a hopping event over a distance $x$ in the direction prescribed by the electric field. The process resembles thermal activation. The analogy becomes closer when we express the transition rate for the hop as

$$\nu(x) = \nu_0 \exp\left(-\frac{2x}{\alpha}\right) = \nu_0 \exp\left(-\frac{2\varepsilon}{eF\alpha}\right) \equiv \nu_0 \exp\left[-\frac{\varepsilon}{kT_{eff}(F)}\right], \tag{39}$$

where $T_{eff}(F)$ is given by Eq. (38). This effective activation induced by electric field produces at $T = 0$ a Boltzmann tail in the energy distribution function of electrons via localised states, as shown by numerical calculations [86, 87].

However, experiments are usually carried out not at $T = 0$, but at finite temperatures, and the question arises on how to describe the transport phenomena in the presence of both factors, finite $T$ and high $F$. By studying the steady-state energy distribution of electrons in numerical calculations and computer simulations [86, 87] and by straightforward computer simulations of the steady-state hopping

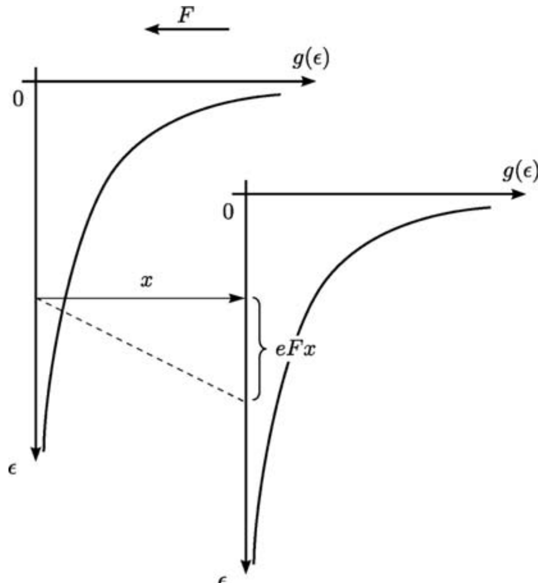


**Fig. 3** Tunnelling transition of a charge carrier in the band-tail affected by a strong electric field. Travelling the distance $x$, the carrier acquires energy $eFx$, where $F$ is the strength of the electric field, and $e$ is the elementary charge (reproduced with permission from [85]; copyright 1995 by the American Physical Society)

conductivity and the transient energy relaxation of electrons [85], the following result has been found. The whole set of transport coefficients can be represented as a function of a single parameter $T_{\text{eff}}(T,F)$

$$T_{\text{eff}}(T,F) = \left[T^{\beta} + \left(\gamma \frac{eF\alpha}{k}\right)^{\beta}\right]^{1/\beta} \tag{40}$$

with $\beta \approx 2$ and values of $\gamma$ in the range 0.5–0.9, depending on which transport coefficient is considered [85]. For instance, in Fig. 4 simulation results are shown for the charge carrier drift mobility once as a function of the electric field $F$ and different temperatures $T$ (Fig. 4a), once as a function of temperature at different fields (Fig. 4b) and once as a function of the effective temperature given by Eq. (40) with parameters $\beta = 2$ and $\gamma = 0.89$ [85]. We are aware of no analytical theory that can support this numerical result.

Recently, Limketkai et al. [88] did exploit the concept of the effective temperature in order to account for the strong field nonlinearity of the conductivity and carrier mobility observed in organic semiconductors [89]. Unfortunately, Limketkai et al. have chosen the expression for the effective temperature $T_{\text{eff}}(T,F)$ in the form of Eq. (8) with $\beta = 1$ and $\gamma = 0.5$, although it has been proven [85] that such an expression for the effective temperature with $\beta = 1$ cannot be valid. Indeed, suppose the conductivity $\sigma_{\text{DC}}$ is dependent on $T_{\text{eff}}(T,F)$ solely. Then

$$\frac{\mathrm{d}\sigma_{\text{DC}}}{\mathrm{d}F} = \frac{\mathrm{d}\sigma_{\text{DC}}}{\mathrm{d}T_{\text{eff}}} \frac{\mathrm{dT}_{\text{eff}}}{\mathrm{d}F}. \tag{41}$$

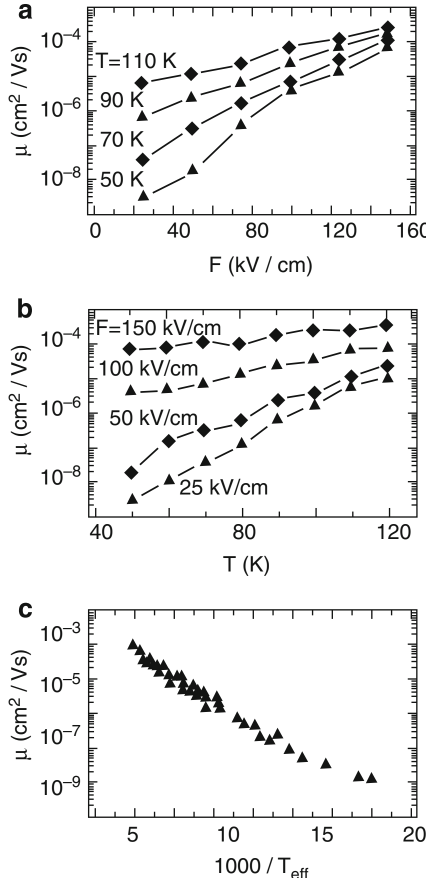


**Fig. 4** **a** Field dependences of the mobility at different temperatures. **b** Temperature dependences of the mobility at different fields. **c** The same data as in **a** and **b** represented as a function of a single quantity $T_{\text{eff}}$ described by Eq. (40) with $\beta = 2$ and $\gamma = 0.89$ (reproduced with permission from [85]; copyright 1995 by the American Physical Society)

In the ohmic transport regime at $F \ll kT/e\alpha$, the conductivity $\sigma_{\text{DC}}$ must be field-independent, implying that

$$\frac{\mathrm{dT_{eff}}}{\mathrm{d}F} \rightarrow 0\,\mathrm{as}\,F \rightarrow 0. \tag{42}$$

The function described by (40) with $\beta = 1$ obviously does not fulfil this condition. However, any function of this kind with $\beta > 1$ is in accord with Eq. (42) along with the necessary condition $T_{\text{eff}} = T$ at $F = 0$ and $T_{\text{eff}} \propto F$ at $T = 0$ [83].

A challenging problem arises to find out whether the concept of the effective temperature is applicable to systems with a Gaussian DOS, and if yes, what is the expression for $T_{\text{eff}}(T, F)$. We show below that the concept of the effective temperature is valid also for such systems. Furthermore, Eq. (40) for the effective temperature is valid also in the case of a Gaussian DOS, though the values of the parameters $\beta$ and $\gamma$ in this expression can be slightly different from those for the exponential DOS.

Following the ideas of Marianer and Shklovskii [86], and using numerical methods presented by Yu et al. [90–93], the mobility and steady-state energy distribution of charge carriers in a system with a Gaussian DOS were investigated [94]. Even at high fields, the energy distribution of charge carriers follows, to a good approximation, a Fermi–Dirac distribution, with the temperature $T$ replaced by the effective temperature $T_{\text{eff}}(T,F)$. In this case, $T_{\text{eff}}(T,F)$ is given by Eq. (40), with the parameters $\beta \approx 1.54$ and $\gamma \approx 0.64$. An example of steady-state carrier distributions and fitted Fermi–Dirac functions is shown in Fig. 5. The effective temperature described by Eq. (40) is independent of the concentration of charge carriers. The

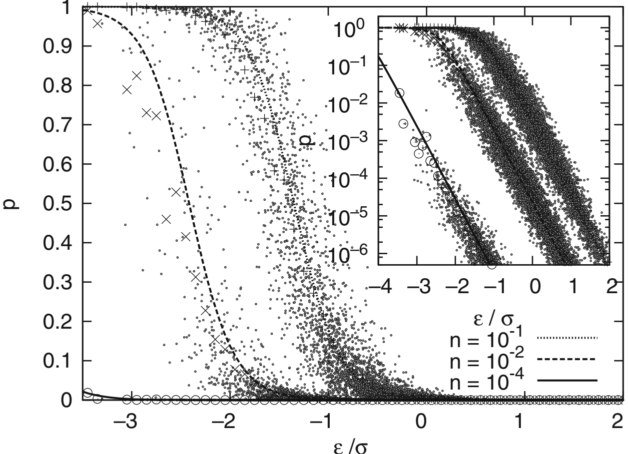


**Fig. 5** The steady-state occupation probability as a function of site energy, for sites with a Gaussian energy distribution. The *curves* show the fitted Fermi–Dirac functions. The *inset* shows the same data on a logarithmic scale

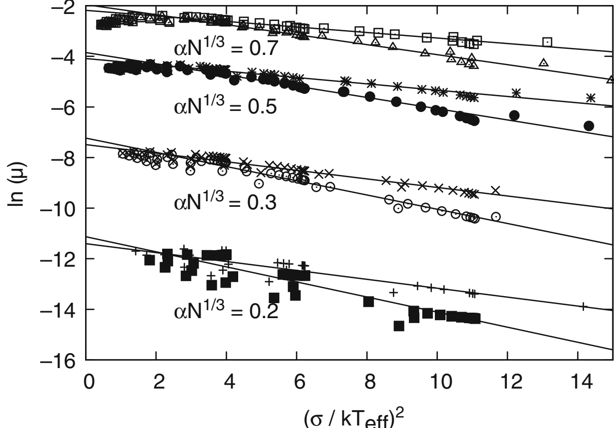


**Fig. 6** Mobility as a function of the effective temperature, for different localisation lengths. In each pair of lines, the higher is for the concentration $n = 10^{-2}$ while the lower is for $n = 10^{-5}$ charges per site

carrier mobility can well be described as a function of the effective temperature, carrier concentration and localisation length. This means, that the field dependence of the mobility can be described completely via the effective temperature. Equation (23), that is valid for low electric fields, can be used also at high fields, if $T$ is replaced by $T_{\text{eff}}\left(T,F\right)$, see Fig. 6. The parameter $C$ in Eq. (23) is dependent on both the carrier concentration $n$ and the localisation length $\alpha$.

## 3 Concluding Remarks

In this chapter we have presented several basic concepts developed for description of charge carrier transport in organic disordered semiconductors, such as molecularly doped, conjugated polymers, and organic glasses. These concepts are, to a great extent, analogous to the theoretical concepts developed earlier for description of charge transport in inorganic disordered materials such as amorphous and microcrystalline semiconductors. Therefore, we tried to keep the presentation of these ideas for systems with a Gaussian DOS typical for organic disordered materials parallel to that for systems with exponential DOS typical for inorganic amorphous semiconductors. Particular emphasis was given to the dependences of the transport coefficients on the concentration of localised states, concentration of carriers, temperature and electric field. We focussed in this chapter only on the description of the motion of charge carriers through the disordered material. Such important topics as the injection of charge carriers from the contacts into the system as well as the description of the space-charge-limited currents remained beyond our scope. Readers interested in these topics can find comprehensive descriptions, for example, in the review article of Bässler [1].

## References

1. Bässler H (2000) Charge transport in random organic semiconductors. In: Hadziioannou G, van Hutten PF (eds) Semiconducting polymers. Wiley, New York, p 365
2. Hadziioannou G, van Hutten PF (eds) (2000) Semiconducting polymers. Wiley, New York
3. Roth S (1991) Hopping conduction in electrically conducting polymers. In: Pollak M, Shklovskii BI (eds) Hopping transport in solids. Elsevier, Amsterdam, p 377
4. Pope M, Swenberg CE (1999) Electronic processes in organic crystals and polymers. Oxford University Press, Oxford
5. Bässler H (1993) Phys Stat Sol B 175:15
6. Borsenberger PM, Magin EH, van der Auweraer M, de Schryver FC (1993) Phys Stat Sol A 140:9
7. van der Auweraer M, de Schryver FC, Borsenberger PM, Bässler H (1994) Adv Matter 6:199
8. Ambegaokar V, Halperin BI, Langer JS (1971) Phys Rev B 4:2612
9. Pollak M (1972) J Non Cryst Solids 11:1
10. Shklovskii BI, Efros AL (1971) Sov Phys JETP 33:468
11. Arkhipov VI, Bässler H (1993) Phil Mag Lett 67:343
12. Arkhipov VI, Bässler H (1994) Phil Mag Lett 69:241

13. Arkhipov VI, Bässler H (1993) Phil Mag B 68:425
14. Arkhipov VI, Bässler H (1994) Phil Mag B 70:59
15. Shklovskii BI, Efros AL (1984) Electronic properties of doped semiconductors. Springer, Berlin Heidelberg New York
16. Baranovskii SD, Faber T, Hensel F, Thomas P, Adriaenssens GJ (1996) J Non Cryst Solids 198/200:214
17. Baranovskii SD, Cordes H, Kohary K, Thomas P (2001) Phil Mag B 81:955
18. Baranovskii S, Rubel O (2006) Description of charge transport in disordered organic materials. In: Baranovski S (ed) Charge transport in disordered solids with applications in electronics. Wiley, Chichester, 221p
19. Baranovskii S, Rubel O (2006) Description of charge transport in amorphous semiconductors. In: Baranovski S (ed) Charge transport in disordered solids with applications in electronics. Wiley, Chichester, p 49
20. Roichman Y, Tessler N (2003) Synth Met 135/136:443
21. Roichman Y, Preezant Y, Tessler N (2004) Phys Stat Sol A 201:1246
22. Arkhipov VI, Emelianova EV, Adriaenssens GJ (2001) Phys Rev B 64:125125
23. Arkhipov VI, Emelianova EV, Bässler H (2001) Phil Mag B 81:985
24. Arkhipov VI, Emelianova EV, Bässler H (2002) J Non Cryst Solids 299/302:1047
25. Arkhipov VI, Heremans P, Emelianova EV, Adriaenssens GJ, Bässler H (2002) J Phys Condens Matter 14:9899
26. Arkhipov VI, Heremans P, Emelianova EV, Adriaenssens GJ, Bässler H (2003) Appl Phys Lett 82:3245
27. Mott NF (1969) Phil Mag 19:835
28. Grünewald M, Thomas P (1979) Phys Stat Sol B 94:125
29. Monroe D (1985) Phys Rev Lett 54:146
30. Shklovskii BI, Levin EI, Fritzsche H, Baranovskii SD (1990) Hopping photoconductivity in amorphous semiconductors: dependence on temperature, electric field and frequency. In: Fritzsche H (ed) Advances in disordered semiconductors, vol 3. World Scientific, Singapore, p 161
31. Schönherr G, Bässler H, Silver M (1981) Phil Mag B 44:369
32. Mozer AJ, Sariciftci NS, Pivrikas A, Österbacka R, Juska G, Brassat L, Bässler H (2005) Phys Rev B 71:035214
33. Horowitz G (2000) Physics of organic field-effect transistors. In: Hadziioannou G, van Hutten PF (eds) Semiconducting polymers. Wiley, New York, p 463
34. Baranovskii SD, Zvyagin I, Cordes H, Yamasaki S, Thomas P (2002) Phys Stat Sol B 230:281
35. Baranovskii SD, Zvyagin I, Cordes H, Yamasaki S, Thomas P (2002) J Non Cryst Solids 299–302:416
36. Gill WD (1972) J Appl Phys 43:5033
37. Santos Lemus SJ, Hirsch J (1986) Phil Mag B 53:25
38. Holstein T (1978) Phil Mag B 37:49
39. Scher H, Holstein T (1981) Phil Mag 44:343
40. Miller A, Abrahams E (1960) Phys Rev 120:745
41. Dalton NW, Domb C, Sykes MF (1964) Proc Phys Soc 83:496
42. Domb C, Dalton NW (1966) Proc Phys Soc 89:859
43. Vissenberg MCJM, Matters M (1998) Phys Rev B 57:12964
44. Coehoorn R, Pasveer WF, Bobbert PA, Michels MAJ (2005) Phys Rev B 72:155206
45. Shapiro FR, Adler D (1985) J Non Cryst Solids 74:189
46. Orenstein J, Kastner MA (1981) Solid State Commun 40:85
47. Baranovskii SD, Thomas P, Adriaenssens GJ (1995) J Non Cryst Solids 190:283
48. Baranovskii SD, Faber T, Hensel F, Thomas P (1997) J Phys C 9:2699
49. Hartenstein B, Bässler H (1995) J Non Cryst Solids 190:112
50. Arkhipov VI, Wolf U, Bässler H (1999) Phys Rev B 59:7514
51. Baranovskii SD, Efros AL (1978) Sov Phys Semicond 12:1328
52. Martens HCF, Hulea IN, Romijn I, Brom HB, Pasveer WF, Michels MAJ (2003) Phys Rev B 67:121203

53. Zherzdev AV, Karpov VG, Pevtsov AB, Pilatov AG, Feoktistov NA (1992) Sov Phys Semicond 26:421
54. Movaghar B, Grünewald M, Ries B, Bässler H, Würtz D (1986) Phys Rev B 33:5545
55. Bässler H (1990) Transport and relaxation of excitations in random organic solids: Monte Carlo simulation and experiment. In: Pollak M, Fritzsche H (eds) Advances in disordered semiconductors, vol 2. World Scientific, Singapore, p 491
56. Borsenberger PM, Pautmeier L, Bässler H (1991) J Chem Phys 94:5447
57. Ochse A, Kettner A, Kopitzke J, Wendorff JH, Bässler H (1999) Phys Chem Chem Phys 1:1757
58. Grünewald M, Pohlmann B, Movaghar B, Würtz D (1984) Phil Mag B 49:341
59. Baranovskii SD, Cordes H, Hensel F, Leising G (2000) Phys Rev B 62:7934
60. Rubel O, Baranovskii SD, Thomas P, Yamasaki S (2004) Phys Rev B 69:014206
61. Baranovskii SD, Rubel O, Thomas P (2005) Thin Solid Films 487:2
62. Schmechel R (2002) Phys Rev B 66:235206
63. Schmechel R (2003) Appl J Phys 93:4653
64. Borsenberger PM, Weiss DS (1998) Organic photoreceptors for xerography. Marcel Dekker, New York
65. Pai DM (1970) J Chem Phys 52:2285
66. Schein LB, Glatz D, Scott JC (1990) Phys Rev Lett 65:472
67. Pautmeier LT, Scott JC, Schein LB (1992) Chem Phys Lett 197:568
68. Abkowitz M (1992) Phil Mag B 65:817
69. Peled A, Schein LB (1988) Chem Phys Lett 153:422
70. Schein LB (1992) Phil Mag B 65:795
71. Hirao A, Nishiwawa H, Sugiuchi M (1995) Phys Rev Lett 75:1787
72. Juska G, Geneviius K, Arlauskas K, Österbacka R, Stubb H (2002) Phys Rev B 65:233208
73. Cordes H, Baranovskii SD, Kohary K, Thomas P, Yamasaki S, Hensel F, Wendorff JH (2001) Phys Rev B 63:094201
74. Böttger H, Bryksin VV (1979) Phys Stat Sol B 96:3219
75. Lien NV, Shklovskii BI (1981) Solid State Commun 38:99
76. Levin EI, Shklovskii BI (1988) Solid State Commun 67:233
77. Li L, Meller G, Kosina H (2007)Microelectron J 38:47
78. Nebel CE, Street RA, Johanson NM, Tsai CC (1992) Phys Rev B 46:6803
79. Nagy A, Hundhausen M, Ley L, Brunst G, Holzenkämpfer E (1993) J Non Cryst Solids 164–166:529
80. Stachowitz R, Fuhs W, Jahn K (1990) Phil Mag B 62:5
81. Antoniadis H, Schiff EA (1991) Phys Rev B 43:13957
82. Murayama K, Oheda H, Yamasaki S, Matsuda A (1992) Solid State Commun 81:887
83. Shklovskii BI (1973) Sov Phys Semicond 6:1964
84. Grünewald M, Movaghar B (1989) J Phys C Condens Matter 1:2521
85. Cleve B, Hartenstein B, Baranovskii SD, Scheidler M, Thomas P, Bässler H (1995) Phys Rev B 51:16705
86. Marianer S, Shklovskii BI (1992) Phys Rev B 46:13100
87. Baranovskii SD, Cleve B, Hess R, Thomas P (1993) J Non Cryst Sol 164/166:437
88. Limketkai BN, Jadhav P, Baldo MA (2007) Phys Rev B 75:113203
89. Brütting W, Berleb S, Mückl AG (2001) Org Electron 2:1
90. Yu ZG, Smith DL, Saxena A, Martin RL, Bishop AR (2001) Phys Rev B 63:085202
91. Yu ZG, Smith DL, Saxena A, Martin RL, Bishop AR (2000) Phys Rev Lett 84:721
92. Pasveer WF, Cottaar J, Bobbert PA, Michels MAJ (2005) Synth Met 152:157
93. Cottaar J, Bobbert PA (2006) Phys Rev B 74:115204
94. Jansson F, Baranovskii SD, Gebhard F, Österbacka R (2008) Phys Rev B 77:195211
95. Nenashev AV, Jansson F, Baranovskii SD, Österbacka R, Dvurechenskii AV, Gebhard F (2008) Phys. Rev. B 78:165207

Adv Polym Sci (2010) 223: 73–112
DOI:10.1007/12_2009_4
© Springer-Verlag Berlin Heidelberg 2009
Published online: 19 June 2009

# Drift Velocity and Drift Mobility Measurement in Organic Semiconductors Using Pulse Voltage

**Debarshi Basu and Ananth Dodabalapur**

**Abstract** This chapter is focused on the electrical characterization of organic field effect transistors. Conventional methods for characterizing mobility in organic semiconductors include field-effect mobility measurement and optical time-of-flight measurement of drift mobility. In his presentation this chapter describes a new method that combines the advantages of both these methods. It involves the injection of carriers at the source of a transistor using a voltage pulse followed by their subsequent extraction at the drain. The delay between the two events is used to extract the velocity of carriers. The electronic time-of-flight method is a fast, simple and direct method to determine the charge transport properties of the semiconductor. In combination with the prevalent methods the electronic time-of-flight method presents itself as a source of information for understanding injection into the semiconductor and determining the trap distribution.

**Keywords** Time-of-flight · Organic semiconductor · Mobility · Charge transport

## Contents

1 Introduction ........ 74
2 Mobility Extraction by Pulse Voltage Method ........ 75
2.1 Distinction Between Optical and eTOF ........ 76
2.2 Mathematical Description ........ 76
2.3 Analysis and Solution ........ 76
2.4 Simulation of Transport ........ 85
3 Measurement of Drift Velocity Using Pulse Voltage Method ........ 88
3.1 Materials Used for Fabrication ........ 88
3.2 Fabrication Details ........ 94
3.3 Experimental Setup ........ 96

D. Basu and A. Dodabalapur (✉)
Ashley H. Priddy Centennial Professor of Engineering, June and Gene Gillis Fellow,
Department of Electrical and Computer Engineering, Microelectronics Research Center,
The University of Texas at Austin, 10100 Burnet Road, Bldg 160, Room 2.206E, Austin, TX 78758

3.4 Results ... 97
3.5 Field Dependence ... 100
3.6 Channel Length Dependence ... 102
4 Extension of Time Scale: Channel Charge Buildup and Bias Stress Effects ... 105
4.1 Displacement Current ... 106
4.2 Delay ... 107
4.3 Channel Formation ... 107
4.4 Bias-Stress/Trapping ... 108
5 Conclusion ... 110
References ... 111

## 1 Introduction

Organic and polymer transistor based circuits are being investigated for a number of low-cost, large-area applications, particularly those that are compatible with flexible plastic circuits [1–3]. The organic materials that have been used as active semiconductor materials include both sublimed and solution processed semiconductors such as pentacene [3], oligothiophenes [4], hexadecafluoro copper-phthalocyanine [5], polythiophene [6], etc. This choice of materials opens up several possibilities to develop integrated circuit technologies based on organic transistors for various large-area low-cost applications. However, the future of printed electronic displays and circuit applications utilizing organic transistors is dependent on the performance of solution processible semiconducting polymers. Therefore it is necessary to obtain a detailed understanding of charge transport in polymers such as poly(3-hexyl)thiophene.

Most studies of charge transport in polymers employ field-effect mobility measurements [7–9]. Temperature-dependent measurement of the field effect transistor (FET) mobility has provided numerous insights on the characteristics of the charge carriers and nature of transport phenomena. Temperature-dependent measurements of FET mobility have highlighted the role of disorder in transport. A percolation model for hopping applied to a slowly decaying exponential band-tail have been used with success to describe movement of carriers in solution processed amorphous polymers and small molecules [9]. However, in a disordered semiconductor such as organic polymers, the FET mobility $\mu_{\mathrm{FET}}$ is different the trap-free mobility $\mu$ as most of the carriers remain trapped in the band-tail states [7–9]. In such systems, determining the drift mobility becomes very important.

This work is focused on the electrical characterization of polymer field effect transistors. We have introduced a method to measure the drift mobility that combines the advantages of the two prevalent methods of extracting mobility namely field-effect mobility measurement and optical time-of-flight measurement of drift mobility [10, 11]. It involves the injection of carriers at the source of a transistor using a voltage pulse followed by their subsequent extraction at the drain. The delay between the two events is used to extract the velocity of carriers. The electronic time-of-flight (eTOF) method is a fast, simple, and direct method to determine the charge transport properties of the semiconductor. The method we employ is based upon the technique first demonstrated in silicon by Burns in the 1960s [12]. In this

chapter we have demonstrated this new technique on p-channel semiconductors; however, by reversing the polarity of the applied voltage, it can also be used to extract the mobility of an n-channel semiconductor.

Preliminary modeling of transport was performed to capture the effects of channel geometry and applied voltage on mobility. The solution of the equation of motion for the traveling carrier density set into motion by the pulse voltage was approached using two methods. The first is a transmission line approach which approximates the channels to a network of resistors and capacitors while the second method uses classical electrodynamics with simplifying assumptions to reduce the complexity of the problem. It was also shown that both these methods are equivalent in the sense that they describe the same differential equation. Time-of-flight measurements of drift mobility were performed in organic transistors with different semiconductors and dielectrics. It was observed that the eTOF mobility lies in the range of the field-effect mobility. Variation in drift mobility was also observed with the applied pulse voltage. This was explained to be caused due to a combination of the increase in mobility with gate voltage and the increase in drift mobility at high lateral fields. Finally, mobility measurements were done on transistors with varying channel length which established the validity of Poole–Frenkel like effect on mobility at high fields.

By extending the time for which the pulse is applied we have been able to show the initial decay of displacement current, the intermediate delay caused due to the movement of charges in the channel, the buildup of charges to form the channel, and finally the bias-stress causing the gradual decay in current; all in the same experiment. Hence the pulse voltage method cannot just extract the drift mobility of the transistor, it provides a window to the functioning of the transistor, and gets us one step closer in our goal of elucidating the charge transport mechanisms in polymer transistors.

## 2 Mobility Extraction by Pulse Voltage Method

The objective of the experiment is to study transport in p-type semiconductors by extracting the carrier velocity and hence the mobility of carriers in these materials. Carriers inside the semiconductor move in response to an electric field. The electric field is created by applying a voltage bias between two metal contacts, one kept nominally at ground. The contact at higher potential is the terminal where the carriers are injected. This contact therefore serves a dual purpose. First it helps establish the field and second it acts as an injection point. The other electrode is tied to the ground through a small resistor, so that the exiting carrier current produces a voltage that can be used to identify the time of their transit.

In an FET geometry the higher potential is applied to the source electrode and the drain electrode is connected to the resistor. The third gate electrode is kept at ground so that a low carrier concentration is maintained in the channel initially. A low carrier concentration is needed initially so as to reduce the initial displacement current flowing through the channel. Another advantage of this method is that the electric-field can be varied to study its effect on the mobility.

## 2.1 Distinction Between Optical and eTOF

Although eTOF technique shares some similarities with the optical time-of-flight, it differs markedly in the conditions that govern transport. First, in an optical TOF the displacement component of the total current is equally important to the conduction current. However in an eTOF the displacement current is orders of magnitude smaller than the conduction current and hence can be neglected. Second, the carriers that transit in an optical TOF experiment are created by optical excitation; therefore the density of carriers in electronic states depends on the spectrum of the optical source used. The distribution of excess carriers does not follow the equilibrium statistics dictated by Fermi–Dirac distribution. On the other hand, injection of carriers in an eTOF flight is through a combination of field-aided thermionic emission, and tunneling through the energy barrier [13]. The injection process depends nontrivially on the distribution of band gap state, interface dipoles, and phonon distribution [14]. The transit-times in an eTOF contain critical information about the injection process which cannot be obtained from the optical TOF data.

Charge extraction by linearly increasing voltage (CELIV) [15, 16] is another important technique to extract the drift mobility of transistors; however it is applicable to organic LEDs and provides information about mobility in the perpendicular direction similar to optical time-of-flight.

## 2.2 Mathematical Description

The mathematical description of the problem and its solution is adapted from a study of large-signal transit time effect in silicon transistor by Burns [12]. The problem deals with obtaining the time dependent carrier distribution $\rho(x,t)$ flowing through the channel in response to a voltage $V(x=0,t)$ applied to the source $(x=0)$ of a transistor, the gate and drain $(x=L)$ being connected to ground. The voltage waveform $V(x=0,t)$ is assumed to be a step function $U(t)$ with the step occurring at the initial instant:

$$\begin{aligned} &V(x=0,t) = V_0 U(t), \\ &V(x=L,t) = 0, \\ &V_{\mathrm{GATE}} = 0. \end{aligned} \tag{1}$$

## 2.3 Analysis and Solution

The problem of pulse voltage technique can be approached in one of two equivalent ways. The first method involves the transmission line approach which considers the channel as an infinite resistance–capacitance ladder. The current flowing through the channel divides up into these two branches at every point, one that charges up

the channel and the other that flows towards the drain. The second method uses classical electrodynamics equations formulated by Maxwell with the assumption that the charge in the channel is controlled by the gate–substrate voltage difference. This helps in isolating this two-dimensional problem into a set of two independent linear differential equations along the two directions. Hence the name quasi-one-dimensional approach.

### 2.3.1 Transmission Line Approach

This approach is useful for both the small- and large-signal picture. As shown in Fig. 1, the channel can be assumed to be composed of a series of resistor–capacitor network. An elemental portion of the channel is represented as a series resistor and a parallel capacitor connecting to the gate electrode. The capacitance per unit length $C$ is constant and is proportional to the insulator capacitance where as the resistance per unit length is a function of the charge induced by the gate-substrate voltage difference, hence it is a function of the channel voltage $V(x,t)$.

$$C = \frac{\varepsilon_0 \varepsilon_{\mathrm{I}}}{T_{\mathrm{I}}} W, \tag{2}$$

where $W$ is the channel width, $\varepsilon_0$ is the permittivity of free space, $\varepsilon_{\mathrm{I}}$ is the relative dielectric constant of the gate insulator and $T_{\mathrm{I}}$ is the insulator thickness.

$$G = R^{-1} = \mu C \left(V_G - V_{\mathrm{T}} - V(x,t)\right), \tag{3}$$

where $\mu$ is the hole mobility in the channel. $G$ is the conductance per unit length which is inverse of the resistance $R$ per unit length, and $V_{\mathrm{T}}$ is the turn on voltage of the organic semiconductor channel. At a time $t$ and a distance $x$ from the source, the displacement current that flows through the capacitor results in reduction of $I(x,t)$ given by

$$-\frac{\partial I(x,t)}{\partial x} = C\frac{\partial \left(V(x,t) - V_{\mathrm{GATE}}\right)}{\partial t}. \tag{4}$$

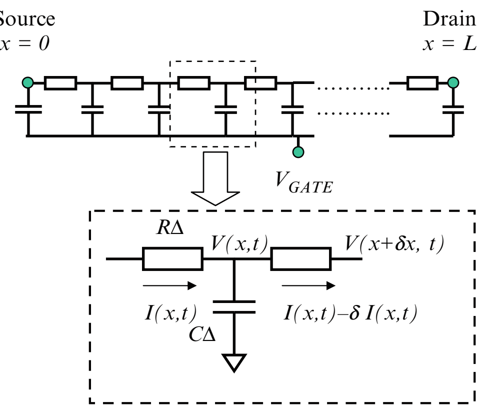


**Fig. 1** Schematic representation of RC transmission network approach to the pulse voltage problem

This helps in charging up the channel and reducing the resistance that causes more current to flow. The current flowing through the resistor reduces the voltage as given by

$$\frac{\partial V(x,t)}{\partial x} = -I(x,t)\,R. \quad (5)$$

This results in the voltage wavefront moving forward along the channel. The current $I(x,t)$ can therefore be written in terms of $V(x,t)$ as

$$I(x,t) = -\mu C\left(V_{\mathrm{GATE}} - V_{\mathrm{T}} - V(x,t)\right)\frac{\partial V(x,t)}{\partial x}. \quad (6)$$

Therefore Eqs. (4) and (6) form a simultaneous differential equation pair that can be solved to obtain the equation for the voltage $V(x,t)$.

The equation pair can be simplified by the following substitution:

$$V'(x,t) = V_{\mathrm{GATE}} - V_{\mathrm{T}} - V(x,t). \quad (7)$$

Hence the simultaneous equation pair reduces to

$$\begin{aligned}\frac{\partial I(x,t)}{\partial x} &= C\frac{\partial V'(x,t)}{\partial t},\\ I(x,t) &= \mu C V'(x,t)\frac{\partial V'(x,t)}{\partial x}.\end{aligned} \quad (8)$$

By eliminating $I(x,t)$ from the equation pair (Eq. 8) we get

$$\mu\frac{\partial}{\partial x}\left(V'(x,t)\frac{\partial V'(x,t)}{\partial x}\right) = \frac{\partial V'(x,t)}{\partial t}. \quad (9)$$

This equation must be solved for $V'(x,t)$ subject to the boundary conditions:

$$\begin{aligned}V'(0,t) &= -V(0,t) = V_0 U(t),\\ V'(L,t) &= -V(L,t) = 0,\\ V'(x,0) &= -V(x,0) = 0.\end{aligned} \quad (10)$$

In deriving the boundary condition the gate voltage is taken a zero, and the turn on voltage which is usually small is neglected.

### 2.3.2 Quasi-One-Dimensional Approach

Figure 2 shows the schematic representation of the problem. The two-dimensional problem of transiting voltage wavefront is a complicated one without any additional

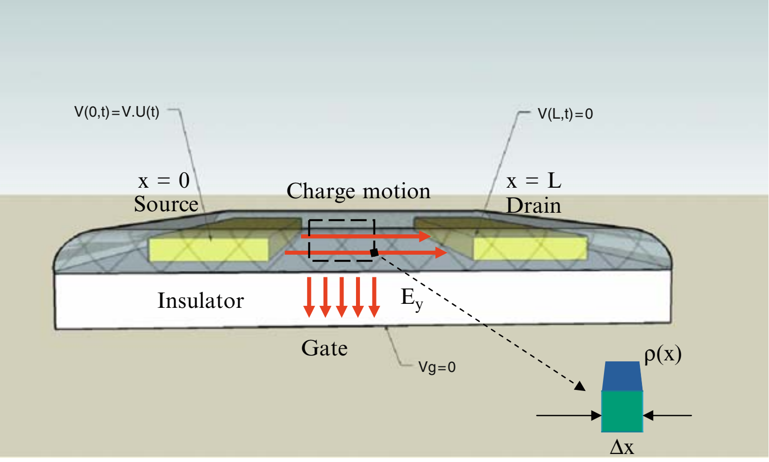


**Fig. 2** Schematic representation of the quasi-one-dimensional approach for solving the pulse voltage problem

simplifying assumptions. By introducing the condition that the charge in the channel is controlled only by the gate voltage we reduce the complex problem into a set of two independent differential equations. The assumption is justified by the fact that the transverse electric field due to gate, at any point in the channel, exceeds the longitudinal electric field due to the applied source-drain bias. The charge concentration which depends on the electric field by the Gauss law is therefore dependent mainly on the gate voltage. It has been shown by Alam et al. that the transport in an organic channel takes place in the first few monolayers from the semiconductor–insulator interface [17]. Hence we further assume that the channel is two-dimensional rather than three-. Hence the charge density can be expressed as a sheet of charge that changes from point to point along the length of the channel while remaining uniform along the width of the channel. The continuity equation is therefore given by

$$\frac{\partial J}{\partial x} + \frac{\partial \rho}{\partial t} = 0,$$
$$\rho = ep\left(x,t\right). \tag{11}$$

By eliminating $\rho$ from the above equation we get

$$\frac{\partial J}{\partial x} = -\frac{e\partial p}{\partial t}. \tag{12}$$

Current is conducted chiefly by holes. Since one of the carriers (electrons) gets trapped in these p-channel devices, the hole mobility is overwhelmingly larger [18]. Also the drift component of the hole current is orders of magnitude larger than its

diffusion and displacement counterparts. These assumptions therefore lead to the current expression given in Eq. (13):

$$\begin{aligned}
&J = J_{\mathrm{N}} + J_{\mathrm{P}},\\
&J_{\mathrm{P}} \gg J_{\mathrm{N}} \;\; J \cong J_{\mathrm{P}},\\
&J_{\mathrm{P}} = -\mu e p \frac{\partial V}{\partial x} - e D_{\mathrm{P}} \frac{\partial p}{\partial x},\\
&J_{\mathrm{P,Drift}} \gg J_{\mathrm{P,Diffusion}},\\
&J = J_{\mathrm{P}} = -\mu e p \frac{\partial V}{\partial x}.
\end{aligned} \tag{13}$$

By eliminating $J$ from Eqs. (12) and (13), we get

$$\frac{\partial}{\partial x}\left(\mu\, p \frac{\partial V}{\partial x}\right) = \frac{\partial p}{\partial t}. \tag{14}$$

The channel charge is given by Poisson's equation:

$$\begin{aligned}
&\nabla^2 V = \frac{\rho}{\varepsilon_0 \varepsilon_S},\\
&\rho = e\left(\mathrm{p} - \mathrm{n}\right),\\
&p \gg \mathrm{n},\\
&\frac{\partial^2 V}{\partial x^2} + \frac{\partial^2 V}{\partial y^2} = \frac{ep}{\varepsilon_0 \varepsilon_S}.
\end{aligned} \tag{15}$$

Since the injected hole concentration is much higher than the electron concentration the resulting charge concentration can be assumed to be consisting entirely of hole. The Poisson's equation in integral form transforms into the Gauss law:

$$\int \varepsilon \vec{E} \bullet \partial \overrightarrow{A} = Q_{\mathrm{enc}} = \rho \left|\overrightarrow{A}\right|. \tag{16}$$

For a long channel the $x$-component of the electric field can be neglected with respect to its $y$-component; this is also known as the long channel or the gradual channel approximation. Therefore Eq. (16) yields

$$\begin{aligned}
&E_y \gg E_x \;\; \vec{E} = E_y \hat{y},\\
&E_y = \frac{ep}{\varepsilon_{ox}}.
\end{aligned} \tag{17}$$

The $y$-component of the electric field can be written in terms of the electric field as

$$E_y = \frac{V_{\mathrm{GATE}} - V_{\mathrm{ON}} - V\left(x,t\right)}{T_{\mathrm{I}}}. \tag{18}$$

Hence the charge concentration can be written in terms of the voltage as

$$\rho = e\,p(x,t) = e\,\varepsilon_0 \varepsilon_\mathrm{I} \frac{V_\mathrm{GATE} - V_\mathrm{ON} - V(x,t)}{T_\mathrm{I}}. \tag{19}$$

and $p$ can be replaced in Eq. (14) to obtain the differential equation for the system

$$\frac{\partial}{\partial x}\left(\mu\,(V_\mathrm{GATE} - V_\mathrm{ON} - V)\frac{\partial V}{\partial x}\right) = \frac{\partial (V_\mathrm{GATE} - V_\mathrm{ON} - V)}{\partial t}. \tag{20}$$

### 2.3.3 Equivalence of Both Techniques

The introduction of the long channel approximation essentially reduces the differential equation for the quasi-one-dimension approach to the same differential equation. It can be seen that by applying the substitution in Eq. (7) with the following conditions.

$V_\mathrm{GATE}$ equals zero and the turn on voltage is small enough to be neglected; we arrive at the following differential equation:

$$\frac{\partial}{\partial x}\left(\mu\,V'\frac{\partial V'}{\partial x}\right) = \frac{\partial V'}{\partial t}. \tag{21}$$

which is same as Eq. (9) for the RC transmission line approach. This can be further simplified into

$$\frac{\partial^2}{\partial x^2}\left(V'\right)^2 = \frac{2}{\mu}\frac{\partial V'}{\partial t}. \tag{22}$$

This is the equation of transport for the pulse voltage problem.

### 2.3.4 Solution of Differential Equation

To solve the equation we make the simplifying substitution result of which is to normalize the variables:

$$\begin{aligned} v &= \frac{V'(x,t)}{V_o}, \\ z &= 1 - \frac{x}{L}, \\ \tau &= \frac{t}{T} \text{ where } T = \frac{L^2}{\mu V_0}. \end{aligned} \tag{23}$$

Equation (22) then reduces to

$$\frac{\partial v}{\partial \tau} = \frac{\partial}{\partial z}\left(v\frac{\partial v}{\partial z}\right) \tag{24}$$

with the following boundary condition:

$$\begin{aligned} v(1,\tau) &= 1; \text{Gate to source voltage constant} = \mathrm{V_0} \\ v(0,\tau) &= 0; \text{Gate to source voltage constant} = 0 \\ v(z,0) &= 0; \text{channel initially uncharged.} \end{aligned} \tag{25}$$

From Eq. (24) it is apparent that the rate of change of voltage is extremely slow at low voltages and identically zero at zero voltage. This characteristic is different from a linear resistor–capacitor circuit where the voltage is never identically zero at any finite distance or time. The solution can therefore be intuitively compared to a traveling wave and at a given time the voltage will be identically zero for distances greater than the wavefront.

The particular problem at hand belongs to a class of problems dealing with diffusion into a semiinfinite medium that have been discussed in depth by Wagner [19]. Following a similar approach the problem can be divided into two sections:

1. For the duration of time before the wave front reaches the drain $(t < t_\mathrm{d})$, the solution is similar to that of diffusion into semiinfinite medium. During this period of time the boundary condition at the drain electrode is always satisfied because of the wave propagation behavior.
2. After the wavefront reaches the drain electrode, it stops progressing further and tries to settle down to its steady state value. $v = \sqrt{z}$.

The partial differential equation can be transformed into an ordinary differential equation by the substitution

$$y = \frac{1-z}{2\sqrt{\tau}}, \tag{26}$$

which converts Eq. (24) into

$$v\frac{\partial^2 v}{\partial y^2} + \left(\frac{\partial v}{\partial y}\right)^2 + 2y\frac{\partial v}{\partial y} = 0. \tag{27}$$

Equation (27) cannot be solved analytically; hence the numerical solution is presented in Fig. 3. As can be seen from Fig. 3, the values of $v$ with $y$ greater than 0.81 are identically equal to zero. This implies for a particular point in the channel given by $z_0$, $v(z_0 \tau_0)$ is zero for a certain time in the beginning before the wave front reaches $z_0$. For the drain $z_0$ equals zero hence the time for the wave front to reach the drain is given by

$$\begin{aligned} z_0 &= 0 = 1 - 2 \cdot 0.81 \cdot \sqrt{\tau_0}, \\ \tau_0 &= (1/1.62)^2 = 0.38. \end{aligned} \tag{28}$$

Hence the time for the carriers to reach the drain can be derived from Eq. (28) to be

$$t_\mathrm{d} = 0.38\frac{L^2}{\mu V_0}. \tag{29}$$

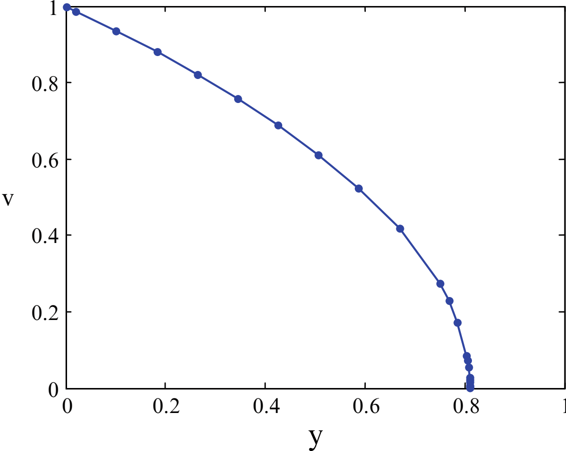


**Fig. 3** Numerical solution of Eq. (27). It is evident that the variable $v$ is identically equal to zero for values of $y > 0.81$ which implies that there is a finite amount of time for which there is no current at the drain

For $t > t_{\mathrm{d}}$ the voltage distribution tries to attain its equilibrium distribution given by

$$v = \sqrt{z} = \sqrt{1 - \frac{x}{L}}. \tag{30}$$

The second part of this diffusion problem can be solved by making an approximation that the diffusion coefficient is a function of distance rather than voltage. This results in linearization of the partial differential equation (Eq. 24) which then becomes

$$\frac{\partial v}{\partial t} = \frac{\partial v}{\partial x} + x\frac{\partial^2 v}{\partial x^2}. \tag{31}$$

Later in this chapter we have simulated the transport and it will be seen that the above approximation is justified due to the linear profile of the voltage distribution after it reaches the drain. It will also be seen in Fig. 4 that the distribution does not change much after the wave front reaches the drain electrode; therefore it is reasonable to approximate the solution as a sum of the steady state and an error term as in Eq. (32):

$$v\,(z,\tau) = \sqrt{z} + \frac{1}{2}\varepsilon\,(z\tau)\,. \tag{32}$$

Substituting this into Eq. (27) the following linear partial differential equation is obtained:

$$z^2\frac{\partial^2 \varepsilon}{\partial z^2} + z\frac{\partial \varepsilon}{\partial z} - \frac{\varepsilon}{4z^{3/2}} = \frac{\partial \varepsilon}{\partial \tau}. \tag{33}$$

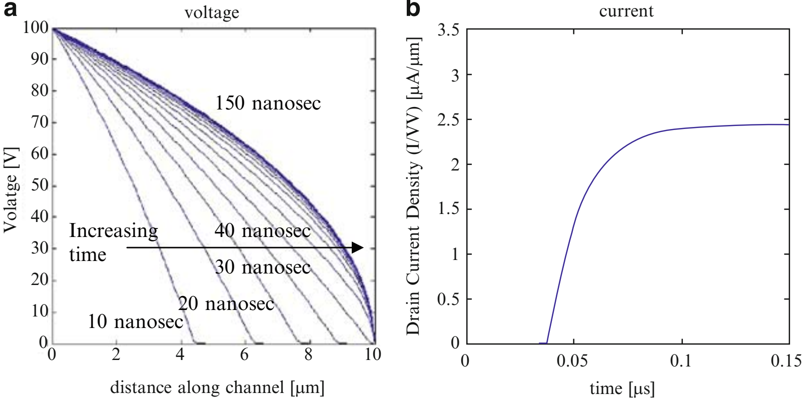


**Fig. 4** Simulation of transport of carriers along the channel of a transistor ($L = 10\,\mu\text{m}$, $\mu = 0.1\,\text{cm}^2\,\text{V}^{-1}\text{s}^{-1}$) in response to a step voltage ($V_0 = 100\,\text{V}$) applied at the source. (**a**) The voltage distribution along the channel at intervals of 10 ns. (**b**) The plot of drain current as a function of time

This can be solved by standard separation of variables yielding a general solution of the form

$$\varepsilon\left(z, \tau - \tau_0\right) = \sum_{n=1}^{\infty} C_n J_{2/3}\left(\frac{4}{3} k_n Z^{3/4}\right) \exp\left(-k_n^2\left(\tau - \tau_0\right)\right), \tag{34}$$

where $k_n$ is the separation constant and $\tau > \tau_0$. $J$ is a Bessel function of order 2/3 which ensures that the second boundary condition in Eq. (25) is met since $J_{2/3}(0) = 0$.

The first boundary condition can be realized by choosing $k_n$ appropriately so that

$$\begin{aligned} J_{2/3}\left(\frac{4}{3} k_n\right) &= 0, \\ \frac{4}{3} k_n &= \alpha_n, \end{aligned} \tag{35}$$

where $\alpha_n$ are the zeros of Bessel function $J_{2/3}$. Following the analysis of Burns [12] the constant factor $C_n$ is chosen so that the best agreement between Eq. (34) and the solution of Eq. (31) is obtained. As shown in Fig. 5, a factor of 0.53 results in the best fit. Substituting Eq. (34) with appropriate values of constants into Eq. (32) and using Eq. (4), the defining relation of current, we obtain

$$\begin{aligned} I_{\text{Drain}}(\tau) &= 0 \qquad \tau < 0.38, \\ I_{\text{Drain}}(\tau) &= \frac{\mu C_I W}{L} V_0^2 \{1 - 0.83 \exp\left(-6.406\left(\tau - 0.38\right)\right) \\ &\qquad -0.17 \exp\left(-2 \cdot 6.406\left(\tau - 0.38\right)\right)\}, \\ &\qquad \tau \geq 0.38, \\ \tau &= \frac{t}{L^2/\mu V_0}. \end{aligned} \tag{36}$$

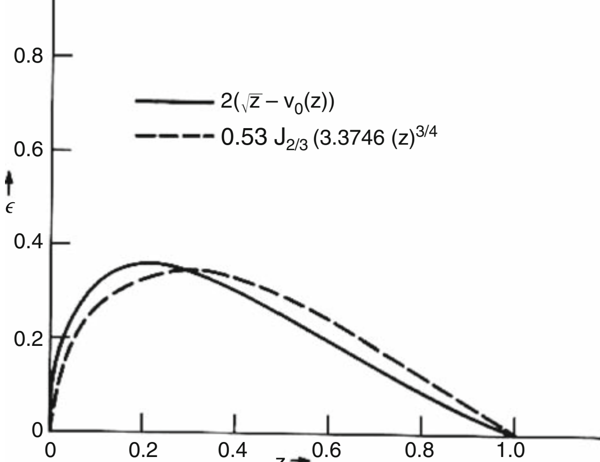


**Fig. 5** The *solid curve* represent the exact solution to the pulse voltage problem obtained numerically; the *dashed curve* is an approximate solution to the problem shown by Eq. (33). This solution is weighted by a factor of 0.53 to obtain the best match to the exact solution. (Reprinted from [12], we have been unable to trace or contact the copyright holder. If notified the publisher will be pleased to rectify any errors or omissions at the earliest opportunity)

## *2.4 Simulation of Transport*

Equation (36) provides an approximate solution to the problem of pulse voltage measurement of eTOF mobility. It is helpful in understanding the dynamics of the transport and extracting parameters of the semiconductor that affect transport of charge carriers. It is nevertheless essential to have an exact solution to the problem. Since it cannot be solved analytically we have to resort to numerical analysis.

We have simulated the movement of carriers in the channel in response to the application of a step voltage in MATLAB®, the results of which are presented in Fig. 4. There is a finite amount of time when the drain current is identically equal to zero, and the time delay is inversely proportional to the mobility of the transistor. The inverse of the delay time gives the characteristic frequency of the transistor operating as an amplifier. Determination of this parameter, therefore, specifies both the small-signal frequency and large-signal transient response of the device.

The simulation of Fig. 4 is done assuming ideal step voltage, constant mobility, trap-less semiconductor, and ideal contacts. These ideal conditions do not exist in reality because, first there is always a finite amount of rise time for the pulse to go to its maximum, and second the mobility of an organic semiconductor is dependent on a variety of conditions including the local field, the charge concentration etc. Third, traps in an organic semiconductor dominate transport, and finally nonideal injection from contacts can adversely affect transport of charge carriers. In the following subsections we have tried to incorporate these effects into the simulation.

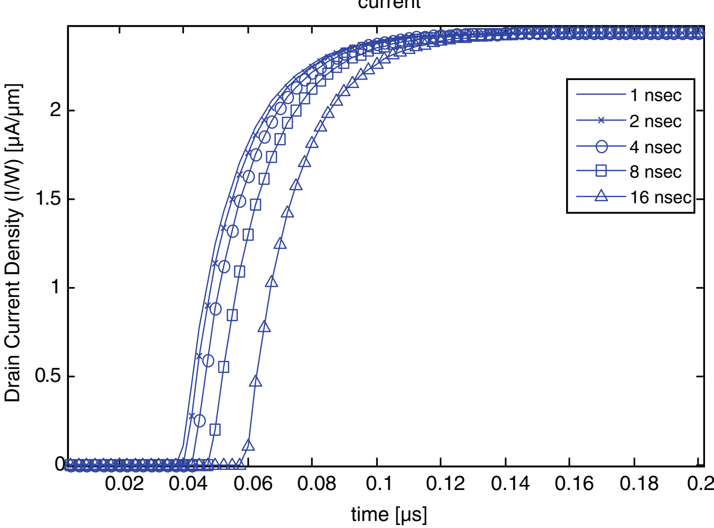


**Fig. 6** Effect of finite rise time on initial delay for the drain current to appear, Pulse applied to the source begins rise at $t = 0$. $\left(L = 10\,\mu\text{m}, V_0 = 100\,\text{V}, \mu = 0.1\,\text{cm}^2\,\text{V}^{-1}\,\text{s}^{-1}\right)$

### 2.4.1 Rise-Time Correction

Assuming a linear rise from zero to maximum value $V_0$ of the voltage pulse, we have simulated the transient response. Figure 6 shows the effect of finite rise time on the initial delay. As can be seen, the curve shifts with increasing rise time, the shift being equal to half the rise time. Therefore the expression for the initial from which the mobility is extracted needs to be modified as

$$t_{\text{Delay}}^{\text{Ramped}} = t_{\text{Delay}}^{\text{unramped}} + \frac{T_{\text{ramp}}}{2},$$
$$t_{\text{Delay}}^{\text{unramped}} = 0.38\frac{L^2}{\mu V_0}. \tag{37}$$

In the case of a nonlinear rise, half of the rise time (10–90%) can also be used as an approximate correction factor. Alternatively, the delay time can be measured from the time where the voltage is half of the maximum value. It will be seen later that for practical purposes it is always advisable to use a sharper pulse.

### 2.4.2 Effect of Field Dependence of Mobility

Investigation of *J*–*V* characteristics as a function of temperature has shown that the mobility of an organic semiconductor, under high fields, tends to follow a Poole–Frenkel-like behavior [20] given as

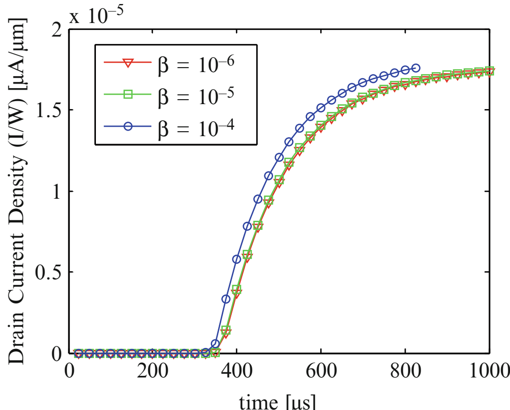


**Fig. 7** Simulation of electric field dependence of mobility at room temperature with $L = 1\,\mu m, V_0 = 1\,\mathrm{V}, \mu_0 = 0.1\,\mathrm{cm}^2\,\mathrm{V}^{-1}\mathrm{s}^{-1}$

$$\mu = \mu_{\mathrm{i}} \exp\left(\frac{\beta\sqrt{E} - \Delta}{kT}\right), \tag{38}$$

where $k$ is Boltzmann's constant, $T$ is the temperature, $E$ is the electrical field, $\Delta$ is zero field hopping barrier of the carriers, $\mu_{\mathrm{i}}$ is intrinsic mobility without a hopping barrier, and $\beta$ is the field-dependent coefficient. The expression of field dependence of mobility given in Eq. (38) was originally proposed by Poole and Frenkel [21] based on modification of columbic potential by high electric field. Gill [22] later obtained a similar expression for mobility in amorphous TNF:PVK films. The value of $\beta$ originally proposed in the Poole–Frenkel model was $\mathrm{e}/\pi\varepsilon_0\varepsilon_{\mathrm{r}}$. However, in later literature it has been used as a fitting parameter [23]. On introducing the field dependence of mobility (Eq. 38) in Eq. (21) we get the field dependent transport equation

$$\frac{\partial}{\partial x}\left(\mu_0 \exp\left(\frac{\beta\left(\frac{\partial V'}{\partial x}\right)^{1/2}}{kT}\right) V' \frac{\partial V'}{\partial x}\right) = \frac{\partial V'}{\partial t}. \tag{39}$$

Simulations were done for room temperature transient response with $\beta$ varying between $10^{-6}$ and $10^{-4}\mathrm{eV}/\left(\mathrm{V/cm}\right)^{1/2}$, the results of which are shown in Fig. 7. As is evident, the initial delay is not affected although the field dependence changes the final steady state value of the current. This is because the simulations were done at room temperature where the effect is less prominent than at low temperatures. The electric field is also not high enough to cause appreciable difference. Hence the delay time is given by the zero field mobility of the semiconductor.

### 2.4.3 Effect of Injection Time

For an ideal ohmic contact in an inorganic semiconductor the time for carriers to be injected from the metal to the semiconductor is much less than the dielectric

relaxation time of the semiconductor [24], which is of the order of picoseconds. However the injection in organics is complicated and takes place through a combination of field-aided thermionic emission and tunneling through the energy barrier. Baldo and Forrest [14] have recently proposed that injection is limited by charge hopping out of interfacial molecular sites whose energy distribution is broadened by disorder in the presence of the interfacial dipoles. The exact nature of trap distribution must be known to determine accurately the time it takes for carriers to be injected.

For the purpose of determining the delay in transient response at the drain of an organic transistor, we have added a correction term $t_{\mathrm{inj}}$ in the expression for delay to account for the delays in injection and extraction at the contacts

$$t_{\mathrm{d}}^{\mathrm{total}} = t_{\mathrm{inj}} + t_{\mathrm{d}}^{\mathrm{channel}}. \tag{40}$$

# 3 Measurement of Drift Velocity Using Pulse Voltage Method

So far we have engaged ourselves with the theoretical description of the pulse voltage method. As described previously, the delay in the response of the drain waveform is a direct indicator of the drift velocity of the carriers in the semiconductor. In the following sections we will describe the experimental details of the extraction of the drift velocity in organic transistors using the pulse voltage measurement. The setup has been described following a short discussion of the fabrication of transistors used for the experiments. The results of the experiments are then explained before concluding with the summary. The pulse voltage method has been employed on multiple semiconductor–dielectric combinations; to study the effect of dielectric–semiconductor interface on the mobility we have compared the mobility of each of the semiconductors on multiple dielectrics. We have also characterized the dependence of mobility on both the channel length of the transistor and the voltage of the pulse waveform to explain the field-dependence of drift mobility.

## *3.1 Materials Used for Fabrication*

We have used the bottom contact structure with the gate at the bottom and source-drain contact at the top. The fabrication of the structure is explained in detail in Sect. 3.2 after a short discussion of the organic semiconductor, insulators, and self-assembled monolayers (SAMs) for surface treatment in that order.

### 3.1.1 Organic Semiconductors

The most important material required for fabricating an organic transistor is the organic semiconductor which forms the active layer for transporting carrier. It usually

comes in two varieties, small molecules and polymers. Small molecules are usually deposited under vacuum by sublimation, whereas polymers are dispersed from solution. The crystallinity of the semiconductor is the principal factor in determining the mobility of the semiconductor, a high mobility enhances current density and increases switching speed, and reducing voltages of operation permits organic circuits to meet realistic specifications. For our experiment we have used a small molecule and another polymer semiconductor, both of which have high mobility due to their relatively crystalline structure.

### Pentacene

Pentacene is a polycyclic aromatic hydrocarbon molecule consisting of five linearly-fused benzene rings (Fig. 8a) and has the appearance of a dark-blue powder. The chemical names with other details are listed in Table 1. Pentacene is one of the most commonly used organic semiconductors with the highest mobilities recorded till date. Pentacene, mobilities of $1.5\,\mathrm{cm^2V^{-1}s^{-1}}$ were reported by Lin et al. [25]. High performance pentacene devices have also been fabricated using polymer dielectrics with carrier mobilities of $3\,\mathrm{cm^2V^{-1}\,s^{-1}}$ [26]. Recent literature shows mobilities greater than $3\,\mathrm{cm^2V^{-1}\,s^{-1}}$ [27]. However, it is highly sensitive to light and oxygen and deteriorates in performance unless passivated. Most commercial samples of pentacene appear dark purple due to ambient oxidization. Vacuum sublimation has been used to purify pentacene for fabricating our devices; other methods for purification include adsorption chromatography.

Pentacene is sublimed, at low pressures, onto the substrate, which is maintained at a relatively high temperature (75°C), by heating pentacene above 350°C. A smooth hydrophobic surface aids the formation of bigger grains and hence results in higher mobilities.

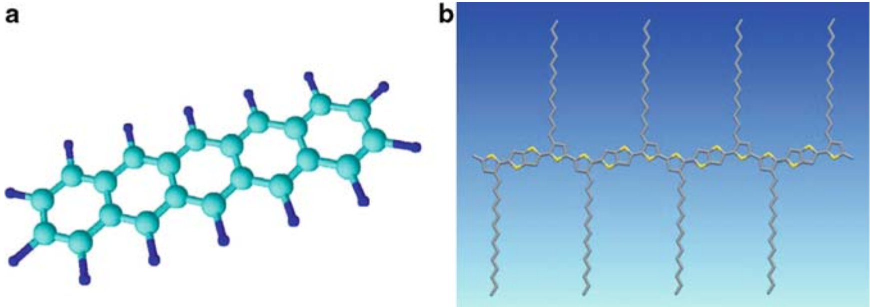


**Fig. 8** (**a**) Pentacene molecule consisting of five fused benzene ring. Pentacene is one of the most common organic semiconductor with high mobilities. (**b**) Structure of pBTTT, a high crystallinity polymer

**Table 1** Properties of pentacene and pBTTT

| Name | Pentacene | pBTTT |
|---|---|---|
| Structure | | |
| Chemical formula | $C_{22}H_{14}$ | Poly(2,5-bis(3-alkylthiophen-2-yl) thieno[3,2- b]thiophene |
| Type of semiconductor | Small molecule | Polymer |
| Highest recorded mobility $cm^2 V^{-1} s^{-1}$ | 3 | 0.8 (3.5 with electrolyte dielectric) |

Poly(2,5-bis(3-tetradecylthiophen-2yl)thieno[3,2-b]thiophene)

A polymer poly(2,5-bis(3-tetradecylthiophen-2yl)thieno[3,2-*b*]thiophene) (pBTTT) which stands for poly(2,5-bis(3-tetradecylthiophen-2yl)thieno[3,2-*b*]thiophene) was also used for our experiments. It belongs to a class of polymers composed of regiosymmetric 2,5-bis(3-alkylthiophen-2yl)thieno[3,2-*b*]thiophene monomeric units. The chemical structure is shown in Fig. 8b and chemical names with other details are listed in Table 1. These polymers are marked by excellent self organization in ordered lamellar domain, and high pi orbital overlap resulting in high mobilities. The pBTTT polymer has been shown to achieve high charge-carrier field-effect mobilities of up to $0.8\,cm^2\,V^{-1}\,s^{-1}$ [28]. Its high mobility has been ascribed to its crystalline structure. Recently, mobility of $3.5\,cm^2\,V^{-1}\,s^{-1}$ has also been obtained using an electrolyte dielectric which induces extremely large carrier densities in the channel [29].

A 5-mM solution was prepared by mixing pBTTT in 1,2-dichlorobenzenethiol. Once dissolved, the solution becomes gelatinous at room temperature. It was heated to convert it into its liquid form. The liquid was subsequently spin coated on the substrate in a nitrogen filled chamber. The substrate with the polymer film was then annealed by heating it into a liquid crystalline state and then cooled down to room temperature at $5^{\circ}C\ min^{-1}$. Annealed pBTTT films exhibit unusually high degree of order [30].

### 3.1.2 Dielectric

The second most important material that affects the charge carrier mobility of an FET is the gate insulator. The surface roughness of the dielectric at the semiconductor insulator interface is a determining factor for the ordering of the semiconductor

molecules or polymer strands. A higher roughness results in multiple nucleating sites which reduces the grain size of the semiconductor thus yielding low field-effect mobility [31]. This is also known that higher transverse gate field results in higher charge concentration leading to higher charge carrier mobilities. Smaller effective oxide thickness (EOT) of the insulator helps in producing a higher electric field. Reducing the physical thickness of the dielectric often leads to reliability issues due to higher leakage current through the dielectric. Therefore a lower EOT can be achieved using a high K dielectric; in addition, use of high K dielectrics reduces voltages of operation to permit organic circuits to meet realistic specifications for transistor applications.

#### Silicon Dioxide

Silicon dioxide is the most common insulator that has been used in the semiconductor industry. It is one of the most well characterized insulators present. Hence it was an obvious choice when fabricating an organic transistor. Due to its low surface roughness, it presented itself as an excellent candidate for making high mobility transistors.

#### Tantalum Oxide

Tantalum oxide $(Ta_2O_5)$ is a high refractive index, low absorption material useful for coatings in the near-UV to IR spectra regions; it decomposes only at temperatures $>1470°C$. $Ta_2O_5$ is used to make capacitors in automotive electronics, cell phones and pagers, electronic circuitry, thin-film components, and high-speed tools. In the 1990s, there was a very strong interest to carry out research on tantalum oxide as a high-k dielectric for DRAM capacitor applications. Subsequently, in the 2000s, this strong interest has dropped very significantly. Due to its high index of refraction, $Ta_2O_5$ has been utilized in the fabrication of the glass of many photographic lenses.

Tantalum oxide is a high k dielectric that can be vacuum deposited. However, due to problems of leakage through the insulator, tantalum metal was deposited instead of its oxidized form, followed by anodization of the tantalum thin film [32] at room temperature using a 0.01 M solution of citric acid as electrolyte, thereby obtaining 1,700-Å high-$k$ $Ta_2O_5$ $(\varepsilon_r : 25.0)$. The roughness of anodized $Ta_2O_5$ measured by AFM was around 22.9 Å, which was much larger than that of commonly-used thermally-grown $SiO_2$2.6 Å [33].

#### Poly(Vinyl Phenol)

PVP or poly(vinyl phenol) is a polymer dielectric. The advantage of using a polymer dielectric over an inorganic one is the ability to formulate a process which completely relies on solution processible materials. This process can potentially be

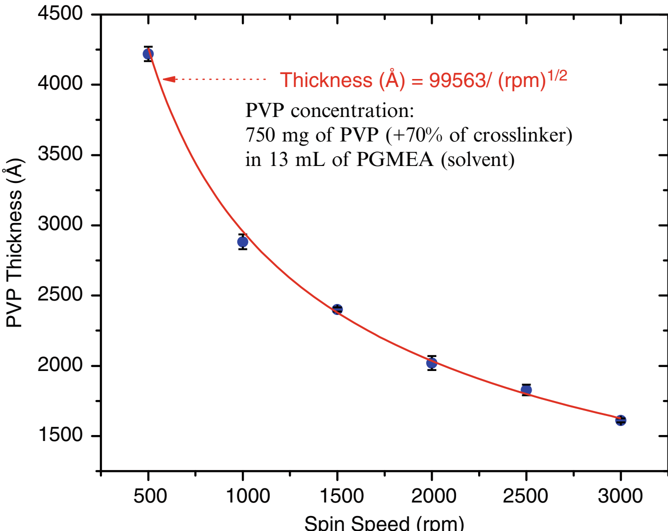


**Fig. 9** Thickness of PVP dielectric as a function of spin speed. The lowest possible thickness of 1,700 Å is used for fabricating transistors

used to print low-cost circuits on plastic. However, the polymeric dielectrics like PVP differ from inorganic dielectrics with respect to its surface energy and reactivity to organic solvents. In addition, PVP can be easily patterned by etching in oxygen plasma, thus providing a method to fabricate multilayered integrated circuits using organic semiconductors such as pentacene [34].

The solution was formed by mixing PVP (30 wt%) and a cross-linker methylated poly(melamine-*co*-formaldehyde) (70 wt%) in propylene glycol methyl ether acetate (PGMEA). The cross-linker is generally mixed in the solution to increase the chemical resistivity of the dielectric to organic solvents by connecting PVP molecules via covalent bonds. It also reduces the free volume of the dielectric as the dielectric shrinks after cross-linking. The solution is then spun on the substrate and the desired thickness is determined by the spin speed. In order to obtain a high gate control we have used the smallest possible thickness of the dielectric, approximately 1,700 Å, by spinning at a speed of 3,000 rpm. The thickness vs spin speed curve is shown in Fig. 9.

### Surface Treatment of Insulator

The semiconductor insulator interface is the primary factor that determines the field-effect mobility of charge carriers in an organic field effect transistor (OFET). Vapor phase or solution based treatments with an alkyl silane or silazine group forms a self-assembled monolayer on the surface of the insulator. Such treatments prior to the deposition of the semiconductor reduces the surface energy which improves the

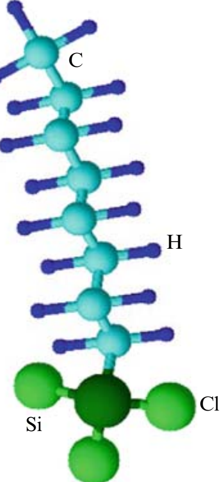


**Fig. 10** Structure of octyltrichlorosilane molecule. On treatment with OTS, it forms a self assembled monolayer on the surface of the oxide that aids the formation of crystalline domains

mobility and hence the electrical performance of the transistor. Compounds that can be used for improving the surface for transistor fabrication include hexamethyldisilazine (HMDS), octyltrichlorosilane (OTS), and octadecyltrichlorosilane. Structure of OTS molecule is shown in Fig. 10. OTS treatment has shown reduction in the surface nucleation density of bare oxide, resulting in micron-scale terraced pBTTT films with improved charge transport [31]. Figure 11b shows the improved morphology of the OTS treated oxide surfaces as opposed to the surface of bare silicon dioxide Fig. 11a. The strong dependence of morphology on the surface chemistry plays an important role in the large hole mobility of this polymer semiconductor.

### Surface of Contacts

Nonideal contacts can adversely affect the performance of OFETs by limiting the charge carrier injection, this results in superlinear behavior near the origin in transistor characteristics. This can be modeled as a high resistance in series to the transistor, the value of which depends on the applied voltage. The effect of this series resistance is a reduction in the mobility of the transistor which ultimate affects its performance. Treatment with an organic thiol has been shown to improve injection at the contacts [35]. Such compounds include nitrobenzenethiol, octadecanethiol, and 2, 4-dichlorobenzenethiol. The exact reason is not understood; however it has been proposed that formation of an organic layer over the gold electrode reduces its surface energy and help formation of ordered domains in the semiconductor, which improves the injection and transport of carriers [36]. Formation of a SAM has also been purported to reduce the energy barrier for injection thus increasing the efficiency and hence the mobility of the transistor [37].

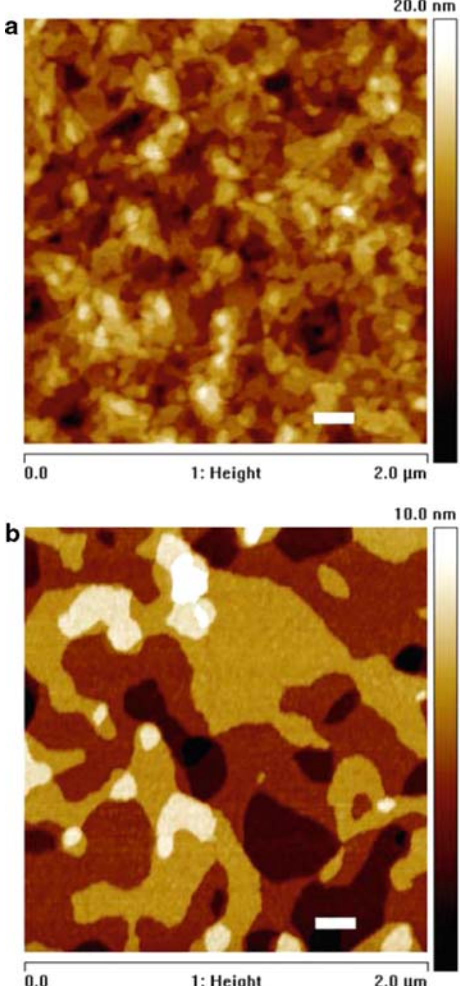


**Fig. 11** AFM images of (**a**) bare silicon surface and (**b**) surface of oxide treated with OTS. Reprinted with permission from [31]. Copyright 2007 American Institute of Physics

## *3.2 Fabrication Details*

We have used a bottom-contact geometry with a bottom gate structure for fabricating our field effect transistor. Using the various combinations of gate dielectric and metal contacts we have used three different structures as discussed below.

### 3.2.1 Fabrication Scheme A

This is the simplest of the three structures. It consists of degenerately doped silicon acting as the gate contact. The gate dielectric consisted of 1,000 Å of thermally

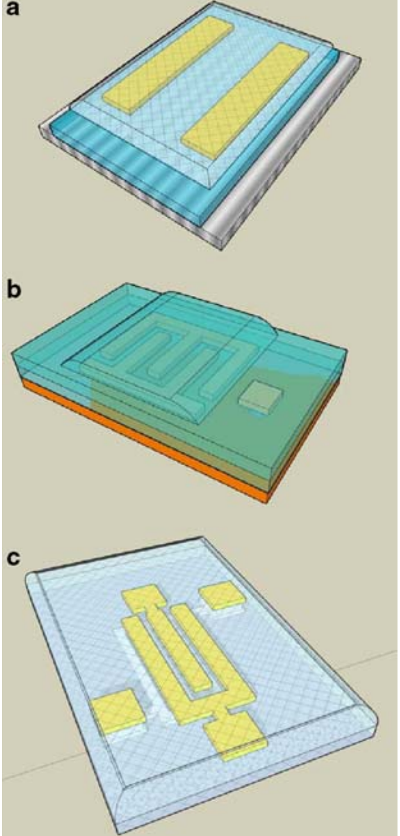


**Fig. 12** (**a**) Fabrication scheme A – being the simplest of the three it involves the least amount of processing. (**b**) Fabrication scheme B – the gate is patterned but exists below the source and drain contacts. (**c**) Fabrication scheme C – gate is patterned and does not exist below the semiconductor

grown silicon dioxide on top. The gold source and drain contacts were deposited photolithographically by a process of image reversal using photoresist AZ 5214 E. Surface treatments were performed to increase the mobility of the semiconductor that was finally deposited on top of the structure. A schematic of the structure is shown in Fig. 12a. The main disadvantage of this structure with respect to pulse voltage measurement was a high gate to source overlap which resulted in a high capacitive charging current at the beginning of the experiment that limits the ability to correctly extract the delay time.

### 3.2.2 Fabrication Scheme B

A schematic of the structure is shown in Fig. 12b. This structure was prefabricated by Lucent Technologies [5]. The channel width and length of the transistors were

2,000 and 7.5 µm, respectively. The dielectric consisted of 2,000 Å of $Si_3N_4$ under 1,000 Å of $SiO_2$, with an estimated gate dielectric capacitance of 17 nF cm$^{-2}$. Aluminum was used as the interconnect metal and the source and drain metals used was gold.

#### 3.2.3 Fabrication Scheme C

This scheme of fabrication improves upon the previous two by using a patterned gate and therefore reducing the overlap between the gate and the source. The channel lengths used are from 5, 10, and 20 µm. In order to connect t the bottom gate the dielectric was patterned. A schematic of the structure is shown in Fig. 12c. The source and drain were composed of titanium and gold.

### *3.3 Experimental Setup*

The circuit configuration used to measure the transient response of the device is shown in Fig. 13. The assembly consists of a pulse voltage generator (HP/Agilent 214B), an oscilloscope (LeCroy 6030 Waverunner), and a resistor (750 Ω). The gate of the OFET was grounded, and a square wave from an HP/Agilent 214B voltage pulse generator was applied to the OFET source that switched between 0 V and a maximum positive voltage $V_0$. The duty cycle of the square wave voltage pulse was 0.1 with a pulse width of 300 µs. The rise time of the pulse was approximately 100 ns for all the voltage values. The input of the LeCroy 6030 oscilloscope was coupled to DC 1 MΩ. The resistor was connected to the drain contact of the OFET the other end of which was shorted to ground.

Due to the inherent instability of characteristics of OFET caused by bias stress effect, the response of the pulse is recorded at the first instant the pulse is applied. The

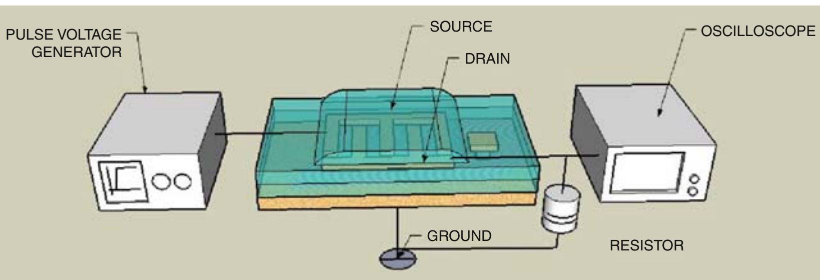


**Fig. 13** Experimental setup consisting of an impulse voltage generator, an oscilloscope, and a resistor

resulting waveform is then analyzed using MATLAB® and fitted to the following expression:

$$I = I_0 \left\{ 1 - \alpha \exp\left( -\frac{t - t_{\mathrm{D}}}{\tau_1} \right) - \beta \exp\left( -\frac{t - t_{\mathrm{D}}}{\tau_2} \right) \right\}, \tag{41}$$

where $t_{\mathrm{D}}$ is the delay in response and $I_0$, $\alpha$, $\beta$, $\tau_1$, $\tau_2$, are fitting parameters.

## *3.4 Results*

The results of the pulse voltage measurement on different semiconductor are discussed in this section. Each semiconductor has been used on more than one dielectric to observe the effect of insulators on the mobility of the semiconductor.

### 3.4.1 Transient Response of Pentacene

Pentacene OFETS were characterized on silicon dioxide as well as tantalum oxide dielectrics. The silicon dioxide sample was made using fabrication scheme A. Before depositing pentacene, it was purified via vacuum sublimation, the silicon dioxide surface was treated with a 10-mM solution of octadecyltrichlorosilane dissolved in toluene for 50 min, and the gold contacts were treated with a 10-mM solution of nitrobenzenethiol dissolved in acetonitrile for 1 h. A film of 400 Å of pentacene was thermally deposited at a base pressure $<4 \times 10^{-7}$ torr at 0.3 Å $s^{-1}$ for the first 50 Å, and then 1 Å $s^{-1}$ for the remaining 350 Å. All measurements were carried out under a vacuum $<2 \times 10^{-3}$ torr at room temperature. Figure 14a shows the $I_d - V_{ds}$ characteristics obtained from an HP/Agilent 4145B semiconductor parameter analyzer. The pulse voltage response of pentacene is shown in Fig. 14b. The maximum voltage of the pulse, $V_0$, was varied from 20 to 50 V in increments of 5 V. A nonzero delay between the application of the source pulse and the drain waveform is seen. The transient mobility was calculated and plotted against the field-effect mobility in Fig. 14c. Both the transient and the DC mobility increases with the voltage of the pulse from a value of 0.04 and 0.03 $cm^2V^{-1}s^{-1}$, respectively at 20 V to a value of 0.07 and 0.06 $cm^2 V^{-1}s^{-1}$, respectively at 50 V. A possible explanation is the increase in mobility with gate voltage.

Transient experiments were also performed on pentacene OFETs with tantalum oxide as the dielectric. The channel length used was 50 µm, so that the effect of the initial displacement current can be eliminated. Fabrication scheme A was used in making the OFETs. The substrates were treated with vapors of HMDS. The HMDS treatment resulted in decreased threshold voltage, and an increase in $I_{on}/I_{off}$ ratio by more than an order of magnitude [33]. The steady state characteristics of the transistor are shown in Fig. 15a. The saturation region mobility obtained from the FET

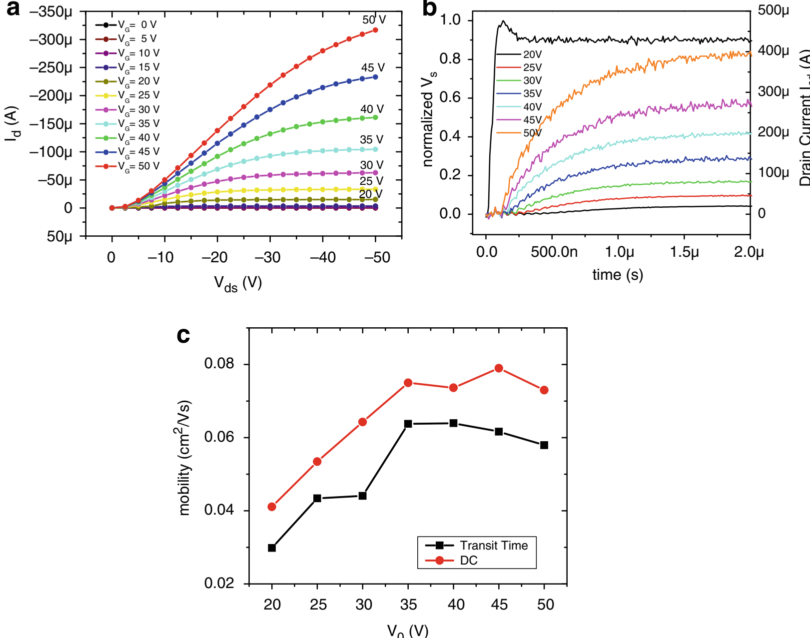


**Fig. 14** (**a**) Steady state characteristics of pentacene transistors on silicon dioxide dielectric. (**b**) Transient response of pentacene transistors on silicon dioxide dielectric. (**c**) Pentacene drift and DC mobilities for fabrication scheme B ($L = 7.5\,\mu$m)

curve is $0.2\,cm^2V^{-1}s^{-1}$. The maximum voltage of the pulse, $V_0$, was varied from 15 to 35 V in increments of 2.5 V. The reduction in the range of operating voltage is due to an increase in the dielectric constant of the insulator that enables higher current densities at lower operating voltages. Figure 15b shows the fitting of the transient response for 35 V to the expression in Eq. (41); the fit is in good agreement to the data. The plot of the drift mobility obtained from the transient time extracted by fitting to data for different pulse voltages is plotted in Fig. 15c along with the delay times. In the case of tantalum oxide dielectric the FET mobility lies within the range of the FET mobility. The drift mobility of pentacene almost doubles with applied voltage for the silicon dioxide dielectric; however the drift mobility for the sample with tantalum oxide dielectric does not show a clear trend with voltage. This may be because of its large channel length which results in reduced electric field.

### 3.4.2 Transient Response of pBTTT

Scheme B for fabrication of transistors was used for making pBTTT OFETs. The surface of silicon dioxide, the insulator, was cleaned with oxygen plasma (25 W, 5 min) followed by treatment with a 0.1 M solution of octyltrichlorosilane in toluene

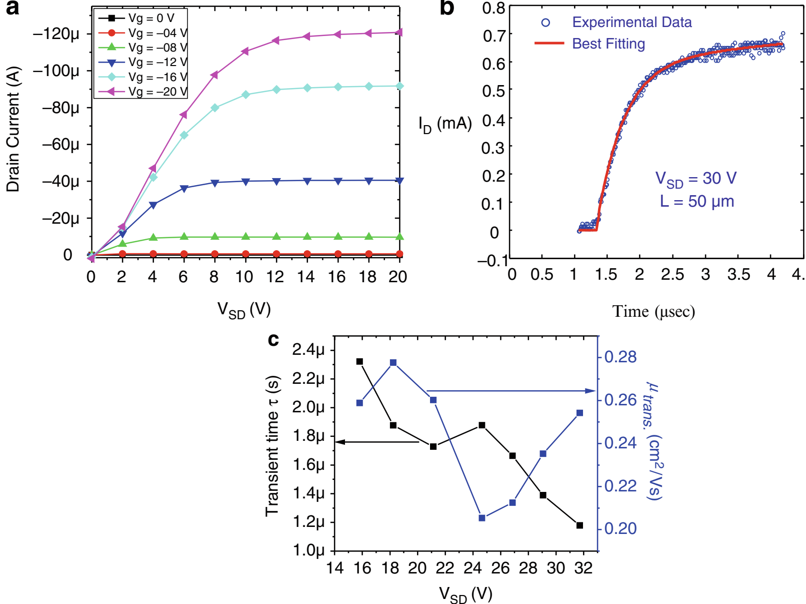


**Fig. 15** (**a**) Steady state characteristics of pentacene transistors on tantalum dioxide dielectric. (**b**) Transient response of pentacene transistors on tantalum dioxide dielectric. The *dots* represent experimental data while the *red line* is the fit to the expression at Eq. (36). The fit is in agreement with the data. (**c**) Plot of transient TOF mobility and delay times for pentacene on tantalum oxide ($L = 50\,\mu\text{m},\ \mu_{\text{FET}} = 0.2\,\text{cm}^2\,\text{V}^{-1}\,\text{s}^{-1}$ at $V_G = -20\,\text{V}$)

to improve the ordering of the polymer chains. The pBTTT solution is then spin coated. The substrate is annealed from 120°C to room temperature at a slow rate in nitrogen ambient. The transistor characteristics are shown in Fig. 16a. The solid lines represent simulation using a two-dimensional device simulator called MEDICI® which simulated the device characteristics using a drift–diffusion model. The dots represent experimentally obtained data points. Simulation of the device characteristics is done assuming an ordered semiconductor with ideal contacts; however an OFET is far from an ideal device. This is the reason deviation is observed between the simulation and data. Pulse voltage measurements were also performed the maximum voltage of the pulse, $V_0$, ranging from 30 to 100 V in increments of 10 V. The pulse voltage response of pBTTT is shown in Fig. 17a, along with the pulse voltage applied to the source (normalized by its maximum voltage $V_0$). The response is fitted to the expression given in Eq. (41) to extract the delay time (Fig. 17b); the delay time was then used to calculate the transient mobility. The graph of transient TOF mobilities vs the pulse voltage is shown in Fig. 17c along with the extracted delay times. The DC mobility and the drain current for the condition

$$V_{\text{Source-Gate}} = V_{\text{Source-Drain}} = V_0\,(\text{ maximum voltage of pulse}) \qquad (42)$$

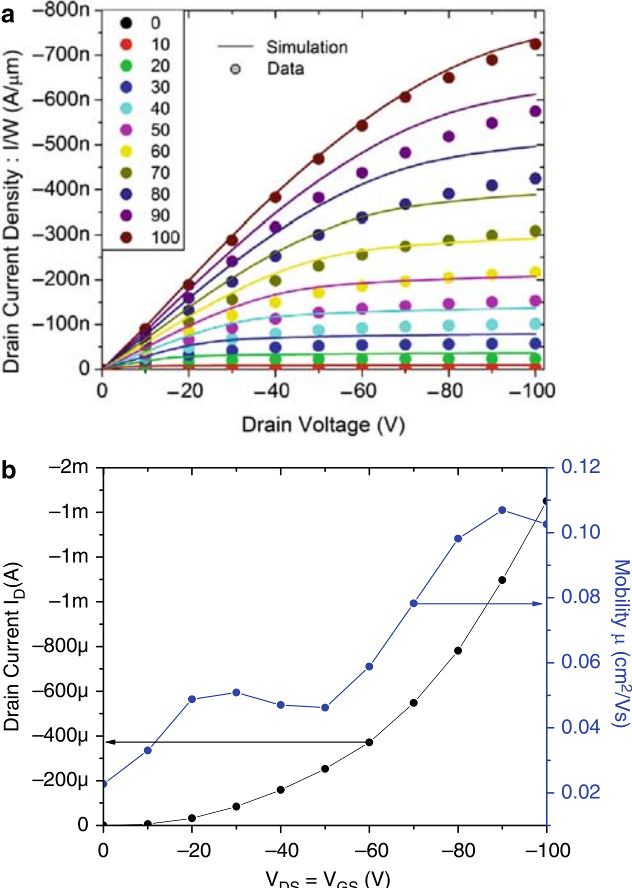


**Fig. 16** (**a**) Transistor characteristics of pBTTT OFET with silicon dioxide gate dielectric. The *dots* represent experimental data while the *solid lines* represent simulation in MEDICI® a drift–diffusion simulator. (**b**) Plot of DC saturation mobility and drain currents for pBTTT on silicon dioxide $(L = 7.5\,\mu\text{m})$

is plotted in Fig. 16b. Both the DC and the transient mobility show an increasing trend with the voltage of the pulse. The DC mobility lie within the range of the transient mobility for the various pulse voltages applied.

## *3.5 Field Dependence*

It can be seen from Figs. 14c and 17c that the drift mobility increases with the voltage of the pulse applied. An exact dependence of the mobility on the pulse voltage cannot be predicted; however it can be explained along the following line of argument.

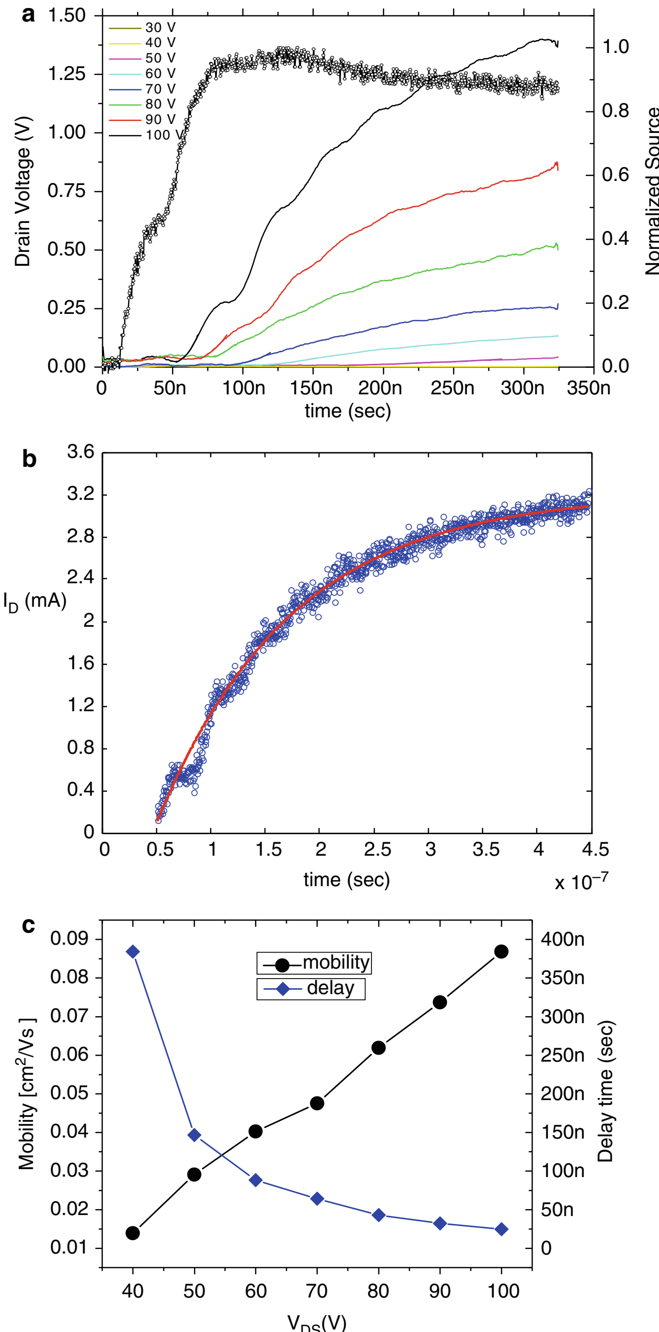


**Fig. 17** (**a**) Transient response of pentacene transistors on silicon dioxide dielectric. (**b**) Fitting of transient response data for pBTTT transistors on silicon dioxide insulator. The *dots* represent experimental data while the *red line* is the fit for $V_0 = 100\,\mathrm{V}$. (**c**) Plot of transient TOF mobility and delay times for pBTTT on silicon dioxide ($L = 7.5\,\mu\mathrm{m}, \mu_{\mathrm{FET}} = 0.1\,\mathrm{cm}^2\,\mathrm{V}^{-1}\,\mathrm{s}^{-1}$ at $-100\,\mathrm{V}$)

In the pulse voltage measurement, the gate and drain of an OFET are maintained at or very near to ground potential. Hence an applied source voltage not only creates a source to drain field but also a source-gate bias which is equal to the source-drain bias. Therefore the variation of TOF mobility with pulse voltage can be due to the dependence of mobility on the source-gate bias or the source-drain bias or due to combination of both these biases.

An increase in field-effect mobility of carriers with increasing gate voltage has been observed and explained in terms of multiple trap and release (MTR) with a distribution of traps located in the grain boundaries [38]. According to the MTR model, the initial increase corresponds to the filling of the traps in the grain boundaries, thereby reducing the barrier for transport. Increased gate voltage results in increased density of carriers in the accumulation region. The variable range hopping model proposed by Vissenberg and Matters [39] has shown on the basis of the previous argument that increased gate voltage can lead to an increased mobility. The source-drain field provides the drive for carriers in the channel of a FET. An increase in field-effect mobility has been observed in optical time-of-flight methods [40]. At high fields, a log $\mu \sim E^{1/2}$ relationship was observed with a slope that approaches zero at high temperatures (Fig. 18). The results were explained within the framework of the disorder transport formalism proposed by Bässler [41] and modified by Kenkre [42]. However, it should be noted that at high temperatures the mobilities decreased with increasing field at low fields.

Thus the increased in mobility with pulse voltage observed can be either a effect of source-gate voltage or the source-drain bias or a combination of both. Since the exact nature of the dependence would not only be extremely complicated but also dependent on the density of states which is not known precisely, separation of these two phenomena in the information available would be nearly impossible. To investigate the mobility behavior further, independent control of gate and drain biases are necessary.

In the following section we have discussed an experiment which displays the variation of TOF mobility on the channel length of the transistor. By changing the channel length while keeping the pulse voltage constant, the transverse electric field can be varied independent of the gate source voltage.

### *3.6 Channel Length Dependence*

Transistors are fabricated with pBTTT as the semiconductor according to scheme C. The bottom gate metal consists of chromium which is also the interconnect metal. A via is formed by etching through the PVP dielectric to contact the bottom gate. OTS treatment is performed on the substrate and the contacts are treated with 2,4-dichlorobenzenethiol. The channel lengths used in this scheme were 5, 10, and 20µm. The widths of the transistors increase proportionally so that the W/L ratio is the same for all the transistors.

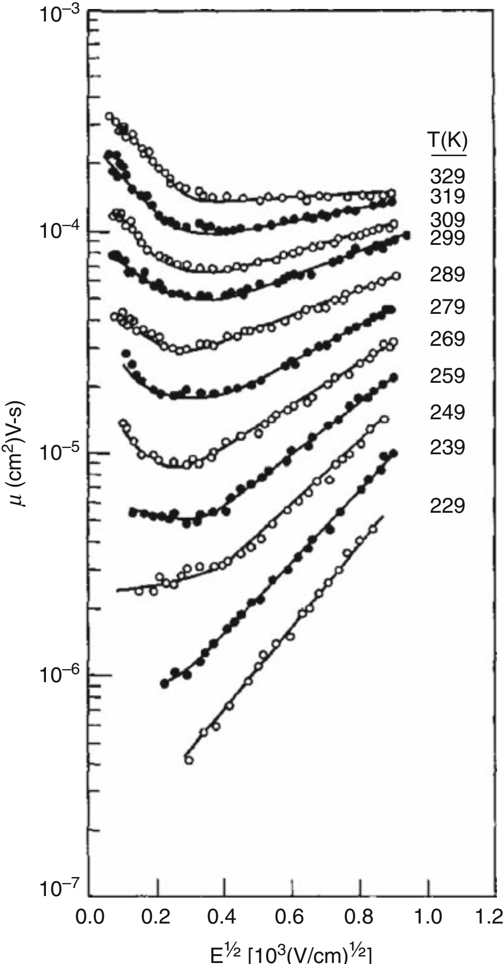


**Fig. 18** Plot of optical TOF mobilities as a function of the electric field for various temperatures. The mobility follows exponential square root dependence with the electric field. Reprinted with permission from [40]. Copyright 1991 American Institute of Physics

The DC characteristics of the three transistors are plotted together in Fig. 19. A field-effect mobility of 0.13, 0.16, and 0.22 $\mathrm{cm}^2/\mathrm{Vs}$ was obtained in the saturation region for 5, 10 and 20 µm channel lengths respectively. The fact that the 5 µm channel length transistor has lower mobility can be ascribed to a nonideal contact for injection into the electrodes.

The transient responses for the three channel lengths are shown in Fig. 20a for the same pulse voltage of 35 V, the slowest being the 20-µm channel. The delay times are calculated by fitting the responses at various pulse voltages and the mobilities are plotted in Fig. 20b. The smallest mobility is observed for the 5-µm channel. The TOF mobilities are also plotted with square root of the average electric field in the channel in Fig. 21. It is observed that for higher electric fields existing in the 5-µm channel the mobilities tend to increase with applied voltage, whereas for

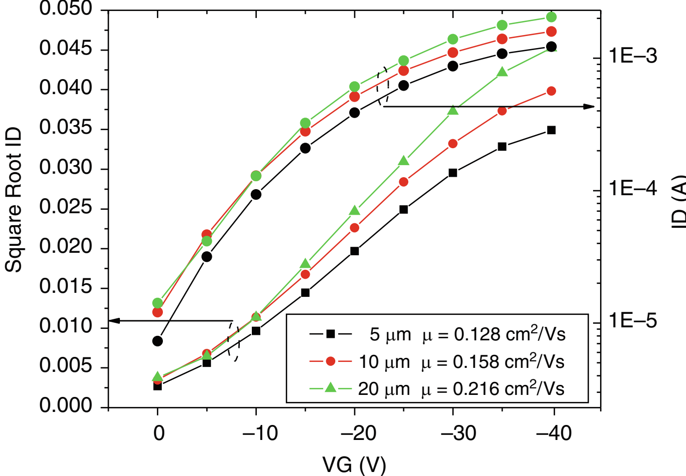


**Fig. 19** Plot of square root of drain current in linear scale and drain current in logarithmic scale against gate voltage. The field-effect mobilities are also reported

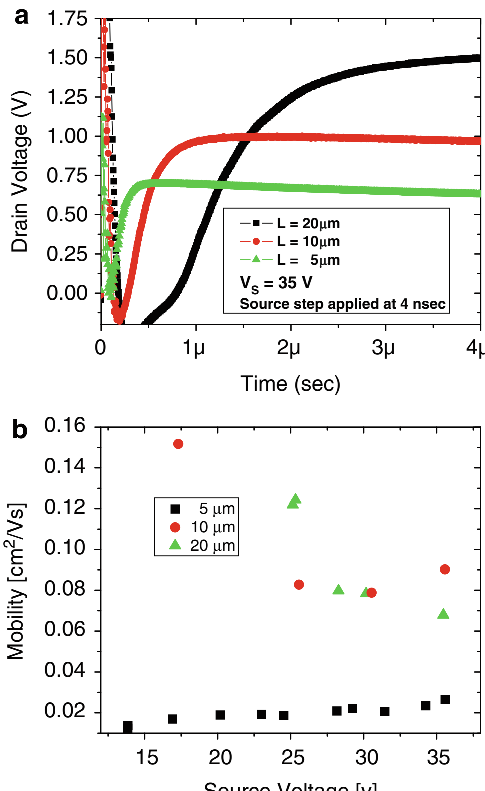


**Fig. 20** (**a**) Transient response of pBTTT on PVP for varying channel length transistors. The pulse voltage is constant at 35 V. (**b**) Plot of transient TOF mobility for pBTTT on PVP for three different channel lengths

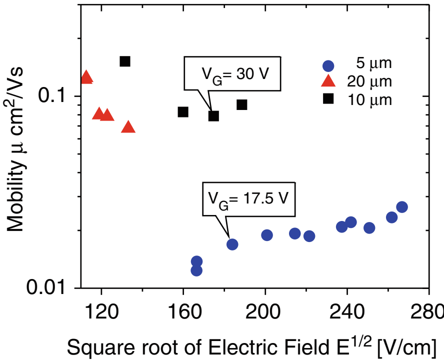


**Fig. 21** Plot of transient TOF in logarithmic scale as a function of the square root of electric field

larger channel lengths the TOF mobility reduces with increasing voltage. A smaller channel length implies a higher electric field for the same applied voltage. It can also be seen that the increase of mobility for the smaller channel length is linear, indicating exponential square root dependence on the applied voltage. So it can be concluded that mobilities decrease at lower electric field and increase proportional to the square root of the electric field at higher fields. The mobilities of the smaller channel length transistor are lower compared to the higher channel length ones. This reduction in mobilities can be due to a lower gate voltage for the same lateral electric field. Nonideal injection can also reduce the value of mobility by affecting the time to inject through the contacts.

## 4 Extension of Time Scale: Channel Charge Buildup and Bias Stress Effects

Time-of-flight measurement of drift mobility was performed in organic transistors with varying dielectrics fabricated by different methods of fabrication; the TOF mobility lies in the range of the DC mobility. Variation in drift mobility was also observed with the applied pulse voltage. This was explained to be due to a combination of following two phenomena: the increase in mobility with gate voltage and the increase in drift mobility at high lateral fields. Finally, TOF measurements were done on transistors with varying channel lengths and it was observed that the mobility reduces at low electric field and increase proportional to the exponential square root of the source-drain bias. By changing the timescales for which the pulse is applied, we can look into various phenomena that influence transistor current in response to the pulse.

Figure 22 illustrates the various influences/current components the transistor experiences as the time duration for the application of the pulse voltage is extended. On application of the pulse voltage the displacement current starts to flow and decays quickly. Then there is a time duration for which no current flows through the drain. This is followed by the appearance of the conduction current which causes charges

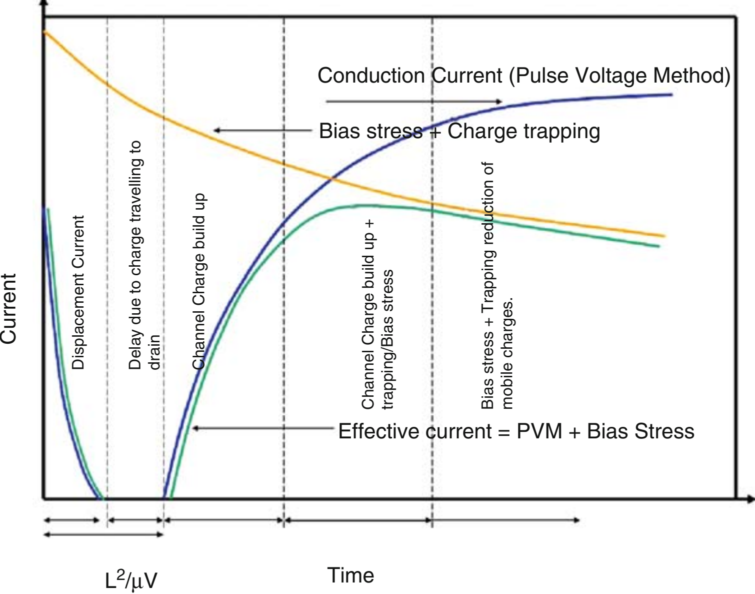


**Fig. 22** By extending the duration of the pulse, various phases of transformations of the transistor are revealed

to buildup and form the channel. The charges that travel through the channel also interact with the localized energy states and get trapped. This causes reduction in the number of mobile charges and therefore the current. This can be seen as the decay in current after it reaches its highest value.

## *4.1 Displacement Current*

As soon as the pulse is applied to the source, the electric field in the channel changes, which results in an almost instantaneous displacement current. The displacement current does not lead to movement of carriers, it is just reestablished with the electric field in response to the applied voltage. The decay of the displacement current is essential in order to measure the drift mobility by the pulse voltage method because otherwise it would conceal the actual time at which the conduction current starts rising. In our experiments above we have tried to minimize the displacement current by grounding the gate which redirects part of the displacement current through the grounded gate. The rate of decay of the displacement current is related to the dielectric relaxation time of the material which is given by Eq. (43):

$$\tau_{\mathrm{Dielectric}} = \frac{\varepsilon_0 \varepsilon_{\mathrm{r}}}{e \mu p}, \tag{43}$$

where $\varepsilon_0 = 8.854 \times 10^{-14}(\mathrm{F\,cm^{-1}})$ is the permittivity of free space and $\varepsilon_r$ is the relative dielectric constant for the organic semiconductor. It can be seen from Eq. (43) that the dielectric relaxation time is inversely proportional to the carrier concentration. This sets a lower limit to the channel length of the transistor that can be used to perform pulse voltage measurement.

### *4.2 Delay*

For a long channel transistor, there is finite time after the decay of the displacement current during which the current flowing out of the drain is identically equal to zero. During this interval the charges injected through the source traverse the channel. The delay is therefore related to the finite amount of time spent by the charge carriers in traversing the channel. It is the basis of the pulse voltage measurement which extracts the drift velocity of the carriers based on this delay time.

### *4.3 Channel Formation*

Our main focus previously had been on the delay time as it indicated the drift velocity of the carriers in the channel. However, by extending the duration of the pulse it became apparent that the pulse voltage method contains information about the charge transport beyond the drift velocity of the charge carriers. In order to demonstrate this, a pulse voltage of 100 V with duration varying from 1 μs up to 3.5 ms is applied on a pBTTT transistor fabricated on a structure described in fabrication scheme B. Figure 23a shows that after the initial delay the drain current builds up quickly, almost saturating to a steady state value at about 1 μs. This increase in the current is a result of the formation of the channel by the injected carriers. All the charge carriers injected at the source do not flow out of the drain, some accumulate at the dielectric semiconductor interface to form the channel. The exact charge distribution depends on the biases applied at the terminals (given by Eq. 42); however, due to the nature of the experiment, the transistor is inherently biased in the saturation region. As a result the charge distribution gets concentrated towards the source. This increase in charge density reduces the effective resistance of the channel which results in the current increasing, the increased current further contributing to the formation of the channel. This process continues until a steady state charge carrier distribution is achieved in the channel. Figure 23b shows that the drain current remains steady at about 1.8 mA from 1 to 10 μs. There is a slight increase, which may be due to the fact that the fast rise in current is partially nullified by bias stress effect which is described in the following section.

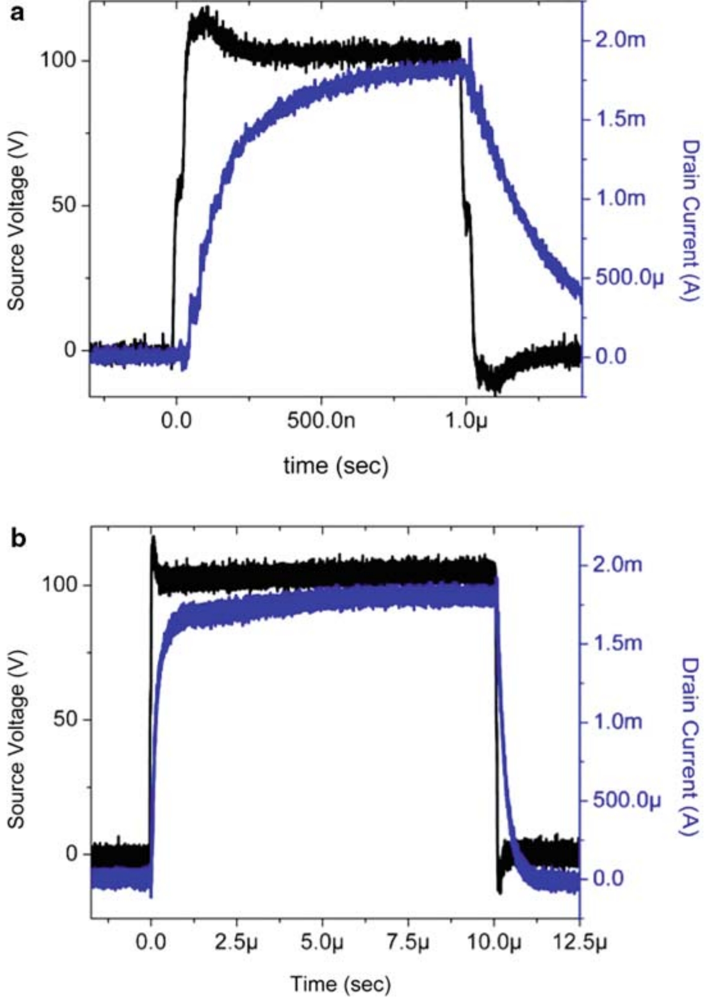


**Fig. 23** The pulse voltage applied to the source is shown in *black* while the drain voltage waveform is shown in *blue*. (**a**) Extension of duration of the pulse shows the formation of channel taking place after the initial delay in the appearance of the drain current. (**b**) Once the channel is formed the current more or less remains constant. A pulse of 100 V was applied to a pBTTT transistor with $L = 7.5\,\mu\text{m}$ and $W = 2{,}000\,\mu\text{m}$

## *4.4 Bias-Stress/Trapping*

Bias stress effect resulting in long term instability has been of the biggest concerns in the field of organic transistors. Even with improved processing and passivation of active layer, organic devices exhibit shift in threshold voltages and consequent reduction in current due to this effect. The exact reason for the bias stress is still

unclear; however it has been widely attributed to traps [43, 44]. Irrespective of the cause of bias stress effect, its effect is visible in the pulse voltage measurement as a decrease in the drain current after it reaches its maximum value. As shown in Fig. 24a, after reaching its maximum value at about 10 μs the drain current starts reducing slowly. The effect is more pronounced in Fig. 24b where the time duration has been extended to 3.5 ms. This decrease in steady state current is a signature of bias stress effect.

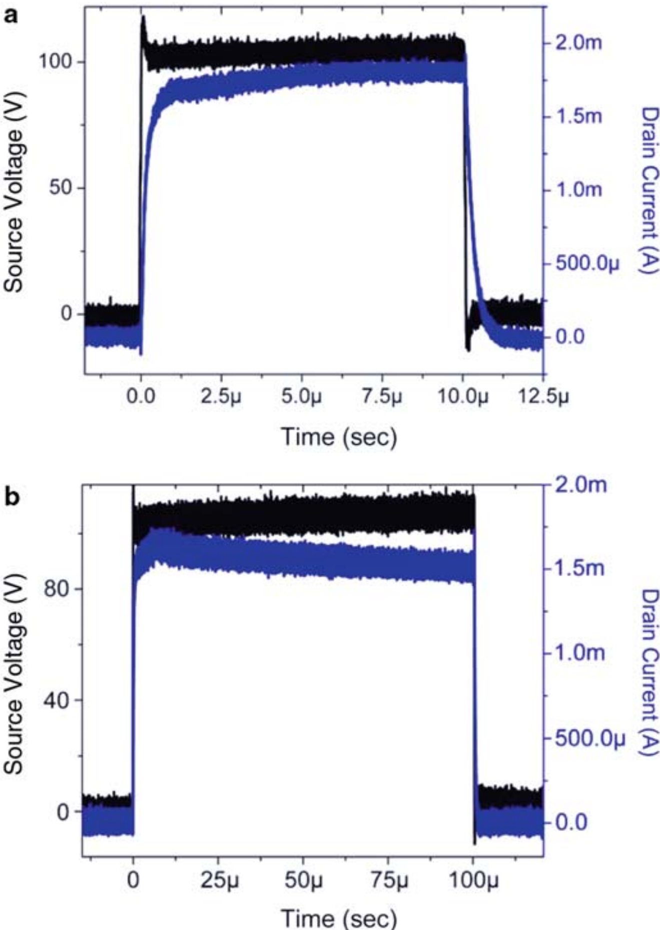


**Fig. 24** Bias-stress effect result in (**b**) decrease of the drain current after (**a**) it reaches its maximum value at about 10 μs. A pulse of 100 V was applied to a pBTTT transistor with $L = 7.5\,\mu\text{m}$ and $W = 2{,}000\,\mu\text{m}$

## 5 Conclusion

Organic semiconducting polymers are endowed with qualities such as easy processibility and variety of materials. Their potential for use in low-cost electronics and photovoltaic applications has prompted technological and scientific interest in these materials. Although the electrical characteristics of organic semiconducting polymers have improved tremendously over recent years, the performance of organic circuit are hindered by low speeds of operation. This is due to the fact that the majority of the carriers in a polymeric semiconductor are trapped in localized states, resulting in low field-effect mobility. Therefore it is important to understand how charge carriers interact with traps as they drift through polymers. There have been multiple attempts to understand charge transport in organic semiconductors, most of which have involved either characterizing the field effect or the optical time-of-flight mobility.

We have introduced a new method that combines the advantages of both of these methods. It uses the time-of-flight of a charge packet injected by a voltage pulse to calculate the drift velocity and mobility of carriers. This technique can help to improve our understanding of charge transport by providing a new method to characterize the mobility. This technique is a fast and simple way to determine the charge transport properties of the semiconductor. In addition it also presents itself as a source of information for understanding injection into the semiconductor and determining the trap distribution.

Theoretical modeling of the experiment was carried out using two approaches that led to the same solution. Simulations were also performed to include non-idealities like finite rise time that are exceedingly difficult to solve analytically. Time-of-flight measurement of drift mobility was performed in organic transistors with varying semiconductors and dielectrics that were produced by different methods of fabrication.

It was observed that the eTOF mobility lies in the range of the field-effect mobility. Variation in drift mobility was also observed with the applied pulse voltage. This was shown to be a combined effect of two phenomena: the increase in mobility with gate voltage and the increase in drift mobility at high lateral fields. Time-of-flight measurements carried out on transistors with varying channel length concluded that the mobility increases at high electric field and the increase is proportional to the exponential square root of the source-drain bias.

Finally the duration of the pulse voltage method was extended to reveal the phases of transformation that the transistor undergoes in order to reach steady state. Therefore the pulse voltage measurement not only provides valuable information about the drift velocity of the charge carriers; it also describes the working of the transistor. The pulse voltage method is thus a precious source of information in understanding charge transport in organic semiconductors.

**Acknowledgments** The authors would like to thank Dr. Soumya Dutta for critical review of the manuscript. They also thank Yeon Taek Jeong, Lawrence Dunn, Brian Cobb, and Dharmendar Reddy for helpful discussions.

## References


1. Loo Y-L, Someya T, Baldwin K, Bao Z, Ho P, Dodabalapur A, Katz HE, Rogers JA (2002) PNAS 99:10252
2. Klauk H, Halik M, Zschieschang U, Eder F, Schmid G, Dehm C (2003) Appl Phys Lett 82:4175
3. Dimitrakopoulos CD, Purushothaman S, Kymissis J, Callegari A, Shaw JM (1999) Science 283:822
4. Horowitz G, Fichou D, Peng X, Garnier F (1991) Synth Met 45:163
5. Crone B, Dodabalapur A, Lin Y, Filas RW, Bao Z, LaDuca A, Sarpeshkar R, Katz HE, Li W (2000) Nature 403:521
6. Bao Z, Dodabalapur A, Lovinger AJ (1996) Appl Phys Lett 69:4108–4110
7. Horowitz G, Hajlaoui R, Fichou D, El Kassmi A (1999) J Appl Phys 85(6):3202–3206
8. Street RA, Northrup JE, Salleo A (2005) Phys Rev B 71:16
9. Vissenberg MCJM, Matters M (1998) Phys Rev B 57(20):12964–12967
10. Dunn L, Basu D, Wang L, Dodabalapur A (2006) Appl Phys Lett 88:063507
11. Yang Y, Lee JY, Miller P, Li L, Kumar J, Tripathy SK (1991) Solid State Commun 77:10
12. Burns JR (1969) RCA Review 30:15
13. Scott JC (2003) J Vac Sci Technol 21:521
14. Baldo MA, Forrest SR (2001) Phys Rev B 64:085201
15. Juška G, Arlauskas K, Viliunas M, Genevicius K, Österbacka R, Stubb H (2000) Phys Rev B 62:R16235
16. Mozer AJ, Sariciftci NS, Pivrikas A, Österbacka R, Juška G, Brassat L, Bässler H (2005) Phys Rev B 71:035214
17. Alam MA, Dodabalapur A, Pinto M (1997) IEEE Trans Electron Dev 44(8):1332–1337
18. Chua L-L, Zamusell J, Chang J-F, Ou EC-W, Ho PK-H, Sirringhaus H, Friend RH (2005) Nature 434:194
19. Wagner C (1950) J Chem Phys 18:1227
20. Wang L, Fine D, Basu D, Dodabalapur A (2007) J Appl Phys 101:054515
21. Frenkel J (1938) Phys Rev 54:647
22. Gill WD (1972) J Appl Phys 43:5033
23. Simmons JG (1967) Phys Rev 155:657
24. Sze SM (1981) Physics of semiconductor devices, 2nd edn. Wiley, New York p 252
25. Lin Y-Y et al. (1997) IEEE Trans Electron Dev Lett 18:606
26. Klauk H et al. (2002) J Appl Phys 92:5259
27. Kelley TW (2006) Organic electronics. In: Klauk H (ed) Materials, manufacturing and applications. Wiley, Weinheim
28. McCulloch I, Heeney M, Bailey C, Genevicius K, MacDonald I, Shkunov M, Sparrowe D, Tierney S, Wagner R, Zhang W, Chabinyc ML, Kline RJ, McGehee MD, Toney MF (2006) Nat Mater 5:328
29. Dhoot AS, Yuen JD, Heeney M, McCulloch I, Moses D, Heeger AJ (2006) Proc Natl Acad Sci U S A 103:11834
30. DeLongchamp DM et al. (2006) AIChE Session T6001
31. Kline RJ, DeLongchamp DM, Fischer DA, Lin EK, Heeney M, McCulloch I, Toney MF (2007) Appl Phys Lett 90:062117
32. Tate J, Rogers JA, Jones CDW, Vyas B, Murphy DW, Li W, Bao Z, Slusher RE, Dodabalapur A, Katz HE (2000) Langmuir 16:6054
33. Jeong Y-T, Yoo B, Dodabalapur A (2007) MRS Session O5.2
34. Klauk H, Halik M, Zschieschang U, Eder F, Schmid G, Dehm C (2003) Appl Phys Lett 82:4175
35. Gundlach DJ, Li Li J, Jackson TN (2001) IEEE Electron Dev Lett 22:571
36. Dimitrakopoulos C, Mascaro DJ (2001) IBM J Res Dev 45:1
37. Kim SH, Lee JH, Lim SC, Yang YS, Zyung T (2003) Jpn J Appl Phys 43:L60
38. Mottaghi M, Horowitz G (2006) Organic Electron 7:528
39. Matters M, Vissenberg MCJM (1998) Phys Rev B 57:12964
40. Borsenberger PM, Pautmeier L, Bässler H (1991) J Chem Phys 94:5447

41. Bässler H (1993) Phys Stat Sol B 175:15
42. Kenkre V, Dunlap DH (1992) Phil Mag B 65:831
43. Salleo A, Street RA (2003) J Appl Phys 94:471
44. Torres I, Taylor DM, Itoh E (2004) Appl Phys Lett 85:314

Adv Polym Sci (2010) 223: 113–153
DOI:10.1007/12_2009_7
© Springer-Verlag Berlin Heidelberg 2009
Published online: 19 June 2009

# Interfaces in Organic Field-Effect Transistors

**Gilles Horowitz**

**Abstract** Interfaces play a crucial role in all solid-state electronic devices. In organic transistors there are two kinds of interfaces: between the gate dielectric and the semiconductor layer, and between the semiconductor and the source and drain contacts. The former is the very place where charge transport in the conducting channel occurs, while the latter governs charge injection and removal to and from the external circuit. Because of the importance of the insulator–semiconductor interface, the choice of the dielectric is at least as critical as that of the semiconductor. On the other hand, charge injection is currently considered as at least as crucial as charge transport in the organic semiconductor. In this chapter, the relevant issues associated with the interfaces are developed. Particular attention is paid to the characterization of the interfaces and to models developed to understand and improve their properties.

**Keywords** Charge transport · Contact resistance · Dielectric materials · Parameters extraction · Self-assembled monolayers

## Contents

1 Introduction .... 114
2 Basic Concepts .... 114
  2.1 Operating Mode of the Organic Thin-Film Transistor .... 114
  2.2 Calculating the Drain Current .... 116
  2.3 Parameters Extraction .... 117
  2.4 Charge Transport in Organic Semiconductors .... 119
3 The Insulator–Semiconductor Interface .... 125
  3.1 Dielectric Materials for Organic Transistors .... 126
  3.2 Physics of the Insulator–Semiconductor Interface .... 129
4 The Interface Between Electrodes and Semiconductor .... 133
  4.1 Measuring the Contact Resistance .... 133

G. Horowitz (✉)
ITODYS, Université Paris Diderot, CNRS-UMR 7086, 75205 Paris cedex 13, France
e-mail:horowitz@univ-paris-diderot.fr

4.2 Origin of Contact Resistance ........ 137
4.3 SAM Modified Electrodes: Injection vs Morphology ........ 146
5 Concluding Remarks ........ 147
References ........ 148

## 1 Introduction

The operation of solid-state microelectronic devices largely depends on specific electrical responses occurring at the interface between materials of different nature. A representative example for this statement is the rectifying property of the metal–semiconductor contact, which has been identified as early as the end of the nineteenth century (the semiconductor properties of galena were identified by Karl Ferdinand Braun in 1874; 32 years later, Greenleaf Whittier Pickard patented a crystal radio receiver [1], which used a "crystal detector" that was actually a metal–semiconductor diode made of galena). As a consequence, the performance of these devices critically depends on the quality and reliability of their interfaces. Organic electronic devices do not escape this universal rule.

The organic thin-film transistors (OTFTs) [2–4] are particularly reliant on this general issue. OTFTs are fabricated by stacking layers of three different qualities: conducting, insulating, and semiconducting. Accordingly, there exist in an OTFT at least two kinds of interface: that between the gate dielectric and the semiconductor layer, and that between the semiconductor and the two electrodes that inject from and retrieve charge carriers.

The object of this chapter is to investigate the current state of the art in organic thin-film transistors under the outlook of the specific problem of interfaces. Both classes of interfaces identified above will be taken into consideration, with their own issues. Methods to characterize the interfaces and their effect on the performance of the device will be described, together with particular solutions to work around the encountered problems.

The chapter is divided into three parts. In the first part, the operation of the transistor is described. Special attention is devoted to the problem of parameter extraction. The second and third parts focus on the specific problems related to the insulator–semiconductor and metal–semiconductor interfaces, respectively.

## 2 Basic Concepts

### *2.1 Operating Mode of the Organic Thin-Film Transistor*

A thin-film transistor can be viewed as a parallel plate capacitor, where one of the plates constitutes the *gate* electrode, while the other plate is made of a semiconductor film which is equipped with two additional electrodes, the *source* and the *drain,*

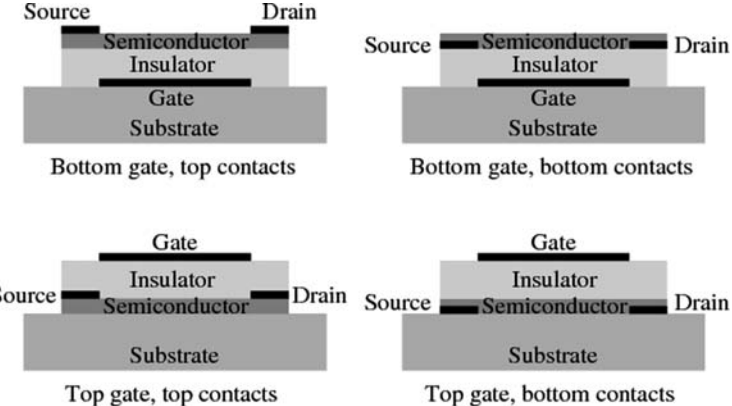


**Fig. 1** Various configurations of organic thin-film transistors

that are in direct contact with the semiconductor. The function of these two additional electrodes is to inject in and retrieve charges from the semiconductor film. As will be detailed below, the role of the third electrode (the gate), which is isolated from the semiconductor by a dielectric layer, is to modulate the current that flows between the source and the drain.

The modulation of the current occurs through the charging of the capacitor, leading to the formation of a conducting channel between source and drain. In electronic circuits this property is used to amplify a signal; alternatively, the transistor also serves as a controllable switch in logical circuits.

In essence, the OTFT is made of three components: a dielectric, a semiconductor film, and three electrodes. The respective arrangement of the three components may vary, as displayed in Fig. 1.

Electrically speaking, organic semiconductors essentially behave as insulators. That is, the density of thermally induced free carriers in these solids is very low, much lower than that found in conventional inorganic semiconductors, which are most usually used under their so-called extrinsic (doped) form. Because of that, in the absence of a gate electrode, practically no current flows when a voltage $V_D$ is applied between the source and the drain electrodes. The presence of a gate and the application of a voltage $V_G$ to this electrode changes the situation. When $V_G$ goes beyond a given threshold, equal charges but of opposite sign appear at both sides of the parallel plate capacitor formed by the gate, the dielectric, and the semiconductor layer, resulting in the formation of a conducting channel between source and drain. The sign of the charge carriers in the channel is opposite to that of the voltage applied to the gate (i.e., n-channel for a positive gate bias, p-channel for a negative one). The drain current is now proportional to the charge density in the channel, which in turn varies linearly with the gate bias. Of course, a requisite for that to occur is that charges can be injected from the source electrode into the semiconductor.

## 2.2 Calculating the Drain Current

The principle of the calculation is illustrated in Fig. 2. The first step is to estimate the charge d$q$ induced by applying a voltage $V_G$ to the gate in an elemental strip of width d$x$ at a distance $x$ from the source. Below threshold, the charge is zero. Above threshold, it becomes

$$\mathrm{d}q = -C_{\mathrm{i}}\left[V_{\mathrm{G}} - V_{\mathrm{T}} - V(x)\right] W \mathrm{d}x. \tag{1}$$

Here, $V_T$ is the threshold voltage and $V(x)$ the potential at the position $x$ of the channel induced by the application of the drain bias; $V(x) = 0$ at the source and $V(x) = V_D$ at the drain. $C_i$ is the capacitance per unit area of the dielectric layer and $W$ the channel width, so that $W\mathrm{d}x$ represents the area of the elemental strip. The minus sign at the right hand side of Eq. (1) arises from the fact that $V_G$ is applied to the gate (one of the plate of the capacitor), while we are interested in the charge on the other plate (the conducting channel).

The current $I_D$ that flows between source and drain corresponds to the passage of the elemental charge d$q$ during the elemental time d$t$:

$$I_{\mathrm{D}} = \frac{\mathrm{d}q}{\mathrm{d}t} = \frac{\mathrm{d}q}{\mathrm{d}x}\frac{\mathrm{d}x}{\mathrm{d}t}. \tag{2}$$

The mobility $\mu$ is defined as the ratio between the mean velocity $v = \mathrm{d}x/\mathrm{d}t$ of the charge carriers and the electric field $E = -\mathrm{d}V/\mathrm{d}x$, so that $\mathrm{d}x/\mathrm{d}t = -\mu(\mathrm{d}V/\mathrm{d}x)$. Making use of Eq. (1), Eq. (2) can be rearranged as [5]

$$I_{\mathrm{D}}\mathrm{d}x = W C_{\mathrm{i}}\mu\left[V_{\mathrm{G}} - V_{\mathrm{T}} - V(x)\right]\mathrm{d}V. \tag{3}$$

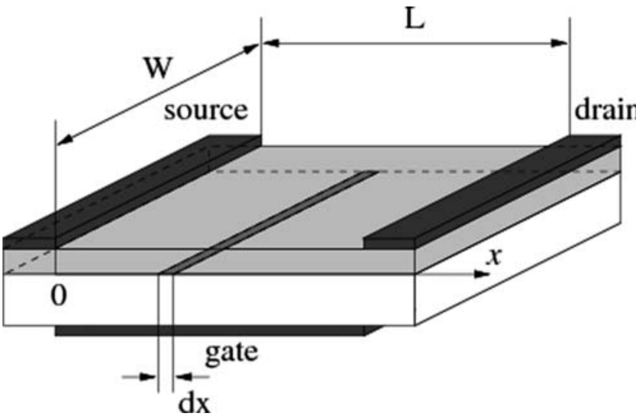


**Fig. 2** Derivation of the drain current

The drain current is now obtained by integrating Eq. (3) from source $(x=0, V(x)=0)$ to drain $(x=L, V(x)=V_D)$. Assuming constant mobility, this leads to

$$I_D = \frac{W}{L} C_i \mu \left( V_G - V_T - \frac{V_D}{2} \right) V_D. \tag{4}$$

Equation (4) corresponds to the so-called *linear regime*, where $V_D < V_G - V_T$.

As $V_D$ increases, the voltage at the drain electrode gradually decreases, up to a point where it falls to zero. This occurs at the so-called *pinch off* point, when $V_D = V_G - V_T$. Beyond pinch off, a narrow depletion zone forms next to the drain because the local potential there drops below threshold. Further increase of $V_D$ leads to a slight extension of the depletion zone and a subsequent shift of the pinch off point towards the source. Because the potential at the pinch off point remains equal to $V_G - V_T$, the drain current becomes independent of the drain voltage; this is the *saturation regime*. Here, the current is obtained by equating $V_D$ to $V_G - V_T$ in Eq. (4):

$$I_{Dsat} = \frac{W}{2L} C_i \mu \left( V_G - V_T \right)^2. \tag{5}$$

Because there are two independent voltages, the current–voltage curves of a transistor are of two sorts: in the *output* characteristic, a set of drain current vs drain voltage curves are drawn for various gate voltages; conversely, *transfer* characteristics are those in which the drain current is plotted as a function of the gate voltage for a given drain voltage. As will be seen in the following, parameter extraction is carried out from the latter set of curves. Representative examples of output and transfer characteristics are shown in Fig. 3.

## *2.3 Parameters Extraction*

Besides its technological interest, the thin-film transistor is also a tool of choice to analyze charge injection and transport in organic semiconductors. In that respect, methods for extracting the basic parameters are of crucial importance.

Equations (4) and (5) are the premise for the most popular methods for mobility extraction. The probably most widespread one makes use of the transfer characteristic in the saturation regime. More precisely, the square root of the drain current is plotted as a function of the gate voltage. The principle of the method can be illustrated by rewriting Eq. (5) as

$$\sqrt{I_{Dsat}} = \sqrt{\frac{W}{2L} C_i \mu} \left( V_G - V_T \right). \tag{6}$$

Equation (6) predicts a straight line; the mobility is obtained from the slope of the line, while the threshold voltage corresponds to the extrapolation of the line to zero current.

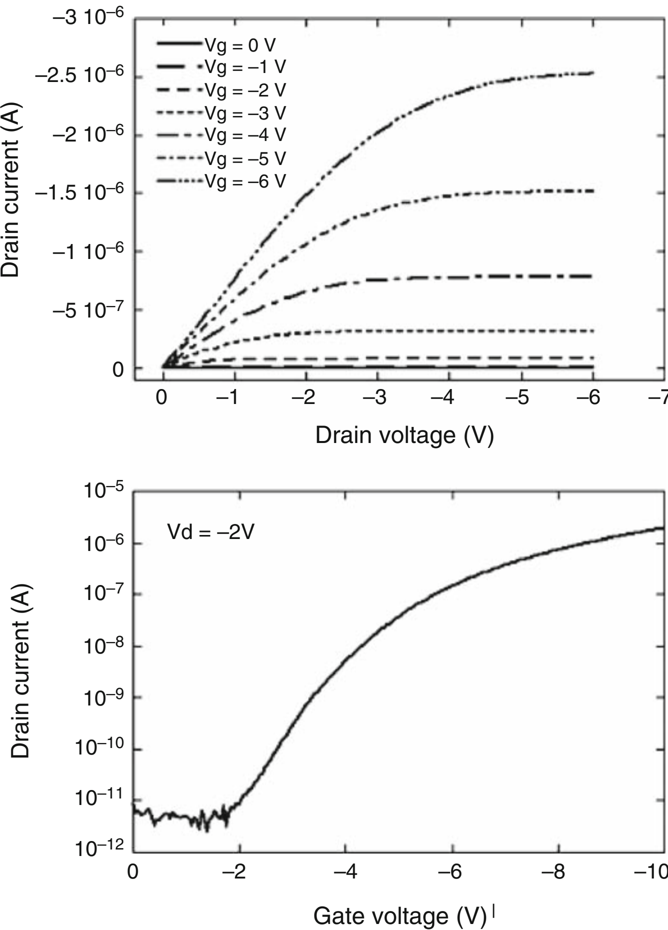


**Fig. 3** Representative output (*top*) and transfer (*bottom*) characteristics of an organic transistor

However, this method presents a critical drawback. In the saturation regime, the density of charge varies considerably along the conducting channel, from a maximum near the source to practically zero at the drain. As will be seen in the following, the mobility in organic semiconductors is not constant; rather, it largely depends on various parameters, including the density of charge carriers. A direct consequence of this is that in the saturation regime, the mobility is not constant along the channel, and the extracted value only represents a mean value. For this reason, it is often more judicious to extract the mobility in the linear regime, where the density of charge is more uniform. This is usually done through the so-called *transconductance* $g_m$ [6], which follows from the first derivative of Eq. (4) as a function of the gate voltage:

$$g_{\mathrm{m}} = \frac{\partial I_{\mathrm{D}}}{\partial V_{\mathrm{G}}} = \frac{W}{L} C_{\mathrm{i}} \mu V_{\mathrm{D}}. \tag{7}$$

However, it must be stressed that the validity of the transconductance method is limited to the case where the mobility varies slowly with the gate voltage. Moreover, the method is very sensitive to limitations of charge injection and retrieval at source and drain electrodes. Ways to work around these issues will be addressed in the following.

## *2.4 Charge Transport in Organic Semiconductors*

The important topic of charge transport in organic materials is outside the scope of this chapter, and for that we refer the reader to excellent review papers and book chapters [7–11]. Suffice here to recall a few basic concepts that will help in dealing with the problem of interfaces.

### 2.4.1 Band Transport

Band transport refers to the mechanism occurring in crystalline conducting and semiconducting inorganic solids. Energy bands form in these solids because when a large number of interacting atoms are brought together, their energy levels become so closely spaced that they become indistinct. Any solid has a large number of bands, but not all of these bands are filled with electrons. The likelihood of any particular band being filled is given by the Fermi–Dirac statistics, Eq. (8), where $k$ is the Boltzmann constant and $T$ the absolute temperature, so that at zero temperature, bands are filled up to the so-called Fermi energy $E_\mathrm{F}$:

$$f(E)=\left(1+\exp\frac{E-E_\mathrm{F}}{kT}\right)^{-1}. \tag{8}$$

On this basis, solids can be divided into insulators, in which the highest occupied band (the valence band) is completely filled, while the lowest unoccupied band (the conduction band) is completely empty, and metals that present a partly filled band (the conduction band). Semiconductors are a particular case of insulators where the energy gap between the top of the valence band and the bottom of the conduction band is small enough that, at nonzero temperature, the smoothing out of the Fermi–Dirac distribution causes an appreciable number of states at top of the valence band to be empty and an equivalent number of states at bottom of the conduction band to be filled.

One of the earliest models for charge transport in delocalized bands is the Drude model [12], which assumes the charge carriers as free to move under the influence of an applied electric field, but subject to damping forces due to collisions. This model is valid in semiconductors, where the density of carriers is much lower that the atomic density; in metals, where the density of carriers is much higher, it leads to inconsistencies that were removed by taking quantum effects into account.

A statistical equation for estimating the mean drift velocity of the carriers in the direction of the electric field $F_x$ can be written as

$$\frac{\mathrm{d}}{\mathrm{d}t}\langle v_x \rangle = \frac{q}{m^*}F_x - \frac{1}{\tau}\langle v_x \rangle, \qquad (9)$$

where $q$ is the elemental charge, $m^*$ the effective mass, and $\tau$ the mean time between two collisions (relaxation time). Steady state occurs when the left hand side of Eq. (9) is 0; under such circumstances, the solution of this equation gives

$$\langle v_x \rangle = \frac{q\tau}{m^*}F_x = \mu F_x, \qquad (10)$$

which defines the mobility $\mu$. It is worth noting at this stage that the model is only valid when the mean free path $\lambda = v_{\mathrm{th}}\tau$ (the mean distance between two collisions) is larger than the distance between two atoms in the solid. Here, $v_{\mathrm{th}} = \sqrt{3kT/m^*}$ is the electron thermal velocity. The mobility can be written as

$$\mu = \frac{q\lambda}{m^* v_{\mathrm{th}}}. \qquad (11)$$

Its variation with temperature depends on the nature of the scattering centers. However, in all cases it is found that it follows a power law, that is, $\mu \propto T^{-n}$, where $n > 0$, so the mobility increases when temperature decreases.

### 2.4.2 Polaron Transport

In organic solids, the domination of molecular over crystalline properties, due to the weakness of van der Walls intermolecular interactions, leads to a tendency to localization of charge carriers on individual molecules. During a typical residence time, the localized charge manages to polarize the surrounding electronic and nuclear subsystems. As a result, charge carriers move in the solid not as free particles, but "dressed" by a polarization cloud. Such entities are called "polarons".

In the formalism developed by Silinch and Cápek [11], the main polarization effect in solids formed of conjugated molecules is that on the clouds formed by the π-electrons, the so-called *electronic* polarization. In order to estimate the stability of the polaron, two characteristic times are defined: (1) the residence time $\tau_{\mathrm{res}}$ corresponds to the average time a charge resides on a given molecule; (2) the electronic polarization time $\tau_{\mathrm{el}}$ is the time it takes for the polarization cloud to form around the charge. An order of magnitude of both times can be estimated by using Heisenberg's uncertainty principle $\tau \geq \hbar/\Delta E$. Here, $\Delta E$ is a characteristic energy that will be the width of the allowed energy band, typically 0.1 eV in organic semiconductors, for the residence time and the energy of an electron transition, that is,

the energy gap ($\sim$1 eV), for the polarization process. Accordingly, $\tau_{res} \approx 10^{-14}$ s and $\tau_{el} \approx 10^{-15}$ s, which implies that electronic polarization always takes place in organic semiconductors.

Complementary to electronic polarization, a charge carrier in a molecular solid also polarizes the vibration modes of the molecule on which it resides as well as dipole active modes of the neighboring molecules, thus forming an extended ionic state. The corresponding relaxation time $\tau_v$ is estimated from the frequency of the vibration mode $\left(\sim 1{,}000\,\mathrm{cm}^{-1}\right)$ to ca. $10^{-14}$ s, comparable to the residence time $\tau_{res}$. The quasi-particle associated with this process is the *molecular polaron*.

An alternative approach to polaron transport in organic solids is in terms of electron transfer (ET). The process can be viewed as a special case of the non-radiative decay of an electronic state. The derivation of the theory is developed in various books or review papers [13–15]. The parameter of importance here is the transition probability per unit time (or transition rate) $k_{if}$ between an initial and a final state. The rate is estimated within the Franck–Condon approximation. In the high-temperature regime $(\hbar\omega_{if} < kT)$ the Franck–Condon-weighted density (FCWD) reduces to a standard Arrhenius equation, so the rate takes its semiclassical Marcus theory expression [16]:

$$k_{if} = \frac{2\pi}{\hbar} \frac{|V_{if}|^2}{\sqrt{4\pi\lambda kT}} \exp\left[-\left(\Delta G^0 + \lambda\right)^2 / 4\lambda kT\right]. \tag{12}$$

Here, $V_{if} = \langle \psi_i | V | \psi_f \rangle$ is the electronic coupling matrix element (overlap integral), $\lambda$ the reorganization energy induced by the charge transfer, and $\Delta G^0$ the variation of the Gibbs free energy during the reaction.

Equation (12) was established in the framework of perturbation theory; its application is therefore restricted to the limiting case of weak electronic coupling (nonadiabatic ET regime). In a more general case, the thermal activation energy also depends on the electronic coupling, while the prefactor depends on both the attempting nuclear frequency $\nu_n$ (frequency of nuclear motion along the reaction coordinate) and the electronic frequency $\nu_e$ that is actually the prefactor in Eq. (12) $\left(\nu_e = 2\pi \left|V_{ij}\right|^2 / \hbar\sqrt{4\pi\lambda kT}\right)$. The other limiting case when the electronic coupling is dominant $(\nu_e \ll \nu_n)$ is referred to as the adiabatic ET regime, in which the hopping rate for self-exchange reaction $\left(\Delta G^0 = 0\right)$ is given by

$$k_{if} = \nu_n \exp\left[-(\lambda - 2|V_{if}|)^2 \big/ 4\lambda kT\right]. \tag{13}$$

The ET approach establishes an important criterion for discriminating between activationless ("band-like") and localized transport, namely, the former dominates for large overlap integral and low reorganization energy, while the converse leads to localization. At this stage, a connection can be established with the polaron model, by pointing out a link between the overlap integral and the residence time on the one hand, and between the reorganization energy and the polarization time on the other hand.

### 2.4.3 Hopping Transport

Charge transport in disordered organic semiconductors, such as polymers, is dominated by localized states. In order to participate in the transport, the charge carriers must hop between these localized states, leading to very low mobility. As first suggested by Conwell [17] and Mott [18], to overcome the energy difference between two states, the carrier absorbs or emits one phonon. As discussed by Mott, in the case of a constant density of states (DOS) at low temperature, hopping over long distances becomes energetically more favorable than hopping to high energies. Under such circumstances, the conductivity σ varies with temperature as $\sigma \propto \exp\left[-\left(T_0/T\right)^{1/4}\right]$. This is the well-known variable-range hopping (VRH) model.

One of the easiest ways to model charge transport in a random distribution of localized states is via Monte Carlo simulation [7, 8]. The essential input parameter is the width $\sigma$ of the DOS, which is usually assumed to be of Gaussian shape:

$$N(E) = \frac{N_\mathrm{t}}{\sqrt{2\pi}\sigma} \exp\left(-\frac{E^2}{2\sigma^2}\right). \tag{14}$$

Here, $N_\mathrm{t}$ is the total density of localized states. The Monte Carlo simulation reveals that carriers tend to relax to an equilibrium level located $\sigma^2/kT$ below (for electrons) or above (for holes) the center of the DOS. This results in a temperature dependent mobility $\mu = \mu_0 \exp\left[-\left(2\sigma/3kT\right)^2\right]$. The mobility must also depend on the electric field because the average barrier height for uphill jumps is reduced in the direction of the field. However, in transistors the field along the source to drain direction is low because the distance is large, so this effect can be ignored in most cases.

A much more significant effect resulting from the density of localized states is the gate voltage dependence of the mobility. This can be understood as follows. By applying a voltage to the gate, charge carriers are injected in the channel, and there they fill the lower states of the DOS. Any additional charge injected in the system will therefore occupy states at higher energies, which means that they will need less energy to jump to other sites, leading to enhanced mobility. On this basis, Vissenberg and Matters [19] have developed a model based on a percolation mechanism. Unlike the Monte Carlo simulation evoked above, which is a one-particle model, this transport model also accounts for the filling of localized states. It predicts that at low carrier density, the transport is governed by the tail states of the Gaussian DOS, which is approximated by an exponential distribution:

$$N(E) = \frac{N_\mathrm{t}}{kT_0} \exp\left(-\frac{E}{kT_0}\right), \tag{15}$$

where $T_0$ represents the width of the distribution. The resulting mobility in the linear regime is given by the following expression:

$$\mu = \frac{\sigma_0}{q}\left(\frac{\pi\,(T_0/T)^3}{(2\alpha)^3 B_c \Gamma(1-T/T_0)\Gamma(1+T/T_0)}\right)^{T_0/T}\left[\frac{C_i^2\,(V_G-V_T)^2}{2kT_0\varepsilon_s}\right]^{T_0/T-1}. \quad (16)$$

Here, $\sigma_0$ is a prefactor for the conductivity, $\alpha$ an effective overlap parameter that intervenes in the hopping of charges from site to site and $B_c$ the critical number for the onset of percolation. $q$ is the elemental charge and $\varepsilon_s$ the permittivity of the semiconductor. A major outcome of the model is that it predicts a gate voltage dependent mobility that follows a power law, a behavior that has been indeed observed in polymeric transistors.

### 2.4.4 Multiple Trapping and Release

An alternative model to the hopping model of Vissenberg and Matters is the multiple trapping and release (MTR) model [20, 21]. The starting point of the model is a distribution of localized levels in the vicinity of a delocalized transport band edge. Note that a Gaussian distribution of localized levels into which charge transport occurs through hops can also be regarded as a transport band; in that case, the maximum of the charge carrier distribution represents the equivalent of the band edge. During their transit in the transport band, the charge carriers interact with the localized levels through trapping and thermal release (Fig. 4). The basic assumptions of the model are: (1) carriers arriving at a trap are instantaneously captured with a probability close to one and (2) the release of trapped charges is a thermally activated process.

An important outcome of the MTR model is that, in the case of an energy distributed DOS, the mobility is gate voltage dependent. When a bias is applied to the gate, a potential $V_s$ develops at the semiconductor–insulator interface, which results in shifting the Fermi level towards the band edge, thus partly filling the DOS. Accordingly, any additional charge carrier has its energy closer to the band edge, so its thermal release becomes easier, and the effective mobility increases. The form of the gate voltage dependence relies on that of the DOS. In the case of the exponential distribution evoked above, the effective mobility is given by

$$\mu_{eff} = \mu_0 \frac{N_c}{N_t}\left(\frac{C_i\,(V_G-V_T)}{qN_t}\right)^{T_0/T-1}. \quad (17)$$

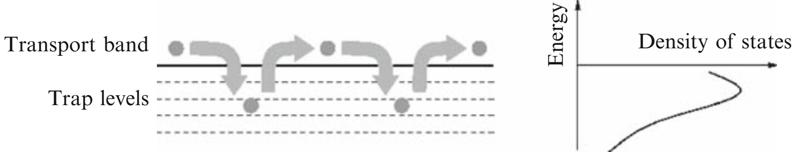


**Fig. 4** Principle of the multiple trapping and thermal release limited charge transport

Here, $N_c$ is the effective DOS at the transport band edge. Note the very similar gate voltage and temperature dependences as for the Vissemberg and Matters model. The reason is that both models derive from an exponential distribution of localized states.

### 2.4.5 Gate Voltage Dependent Mobility and Parameter Extraction

Both the hopping transport and MTR model predict a gate voltage dependent mobility. This has dramatic consequences on parameter extraction, because Eqs. (6) and (7) are no longer valid. For this reason, it is of importance to recall here a few rules that should be followed for a safe parameter extraction:

- It should always be kept in mind that in the saturation regime, the potential in the channel substantially varies from source to drain (see Eqs. 1 and 3). A direct consequence of gate voltage dependent mobility is therefore that parameters extracted in this regime correspond to uncontrolled average values. For this reason, extraction in the linear regime should always be preferred.
- Besides mobility, the other parameter of importance in transistors is the threshold voltage. However, due to the problems evoked above, the extraction of $V_T$ from Eq. (6) appears inappropriate.

Because a reliable knowledge of $V_T$ is also of vital importance in silicon microelectronics, numerous methods have been developed to extract its value. In organic transistors, $V_T$ may be fundamentally understood as the transition point between depletion, where no current flows between source and drain, and accumulation; in other words, $V_T$ is the starting point of the formation of the conducting channel. In the linear regime $(V_D \ll V_G - V_T)$ Eq. (4) reduces to

$$I_D = \begin{cases} 0, & \text{if } V_G < V_T, \\ \frac{W}{L} C_i \mu \left(V_G - V_T\right) V_D, & \text{if } V_G > V_T. \end{cases} \tag{18}$$

The transfer curve of an ideal device that would exactly follow these equations is drawn in Fig. 5, together with its first and second derivative. The first derivative is a step function, while the second derivative reduces to a sharp peak at $V_G = V_T$, thus allowing a precise and reliable estimation of the threshold voltage [22–24]. A major interest of the method is that it is not sensitive to both gate voltage dependence and contact resistance.

It is also worth pointing out that, once the threshold voltage is known, the gate voltage dependent mobility can be safely extracted from Eq. (18) without any further derivation that would introduce additional uncontrollable terms [22].

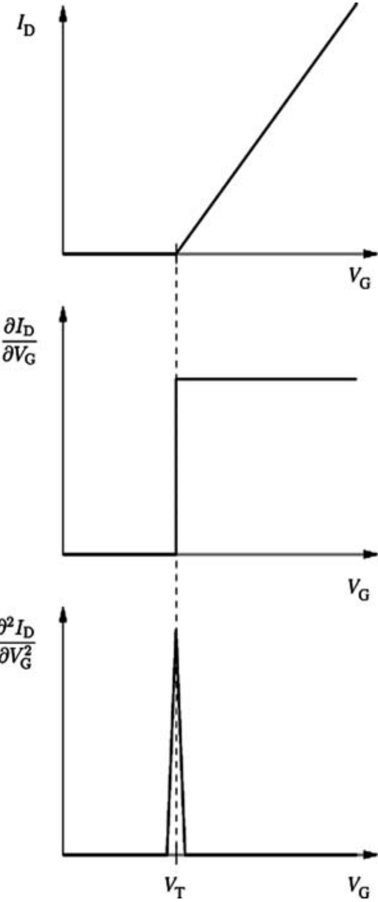


**Fig. 5** Transfer characteristic of an ideal organic transistor in the linear regime, and its first and second derivative. $V_T$ is the threshold voltage

## 3 The Insulator–Semiconductor Interface

The conducting channel where charges are driven from source to drain consists of a very thin layer close to the insulator–semiconductor interface. Accordingly, charge transport there is highly dependent on the quality of this interface. In that respect, the choice of the dielectric is at least as important as that of the semiconductor. More details on the issues linked to the dielectric in organic field-effect transistors can be found in recent reviews [25–27].

## *3.1 Dielectric Materials for Organic Transistors*

Most of the early organic transistors used silicon oxide $SiO_2$ thermally grown on crystalline silicon as the gate dielectric. The reason for this choice is that this structure is readily available from conventional microelectronic technology, and also the very good quality of this dielectric.

Motivations to search for alternatives to $SiO_2$ are: (1) the use of high dielectric constant materials to reduce the operating voltage of the transistor, an alternative way being the use of ultrathin dielectrics; (2) the use of low energy surfaces that are prone to reduce the density of defects in the semiconductor layer; (3) the reduction of surface charges that may induce large shifts of the threshold voltage; (4) $SiO_2$ is known to present a large amount of surface OH groups that act as electron traps, thus rendering n-channel devices very difficult to achieve [28].

As shown by Eqs. (4) and (5), low operating voltage requires high gate dielectric capacitance per area $C_i = k\varepsilon_0 / d_i$, where $k$ is the dielectric constant, $\varepsilon_0$ the permittivity of vacuum and $d_i$ the thickness of the dielectric layer. Hence, there are two methods to increase the current: increase the dielectric constant or decrease the thickness [26].

Another motivation for searching alternate dielectrics is that silicon oxide also presents several drawbacks in terms of the quality of the insulator–semiconductor interface. Also, the realization of more complex circuits than individual transistors is not possible with thermally oxidized silicon wafers, because in that case the gate electrode cannot be patterned.

### 3.1.1 Inorganic Dielectrics

To work around the above-mentioned drawbacks issued by thermally grown $SiO_2$, the group at Penn State University made use of ion-beam sputtered silicon oxide. The process can be conducted at temperatures compatible with organic materials (80°C) and can be carried out on flexible substrates [29]. An alternative low temperature technique is plasma enhanced chemical vapor deposition (PECVD), which has been put into practice with silicon nitride by several groups [30, 31].

Commonly used inorganic dielectrics are displayed in Table 1. Probably the most appealing inorganic dielectrics are high dielectric constant (high-$k$) materials because of their ability to induce low operating voltage devices. Among others, inorganic oxides such as $Al_2O_3$ [32, 33], $TiO_2$ [34, 40], BZT [Ba(ZrTi)O] [35], BST [Ba(SrTi)O] [35], $Ta_2O_5$ [36, 37] and $Bi_{1.5}ZnNb_{1.5}O_7$ (BZN) [39] have been tested either as pure materials or in combination with polymers [38]. However, these oxides suffer from expensive deposition methods (mostly sputtering) and poor film quality, requiring relatively thick depositions to avoid leaks. Another problem with high-$k$ dielectric is that they are suspected to induce charge transport degradation, as will be detailed in the following.

**Table 1** Deposition technique and dielectric constant of some inorganic dielectrics

| Dielectric | Deposition method | Temperature (°C) | k | Refs |
|---|---|---|---|---|
| $SiO_2$ | Ion beam sputtered | 80 | 3.9 | [29] |
| $Al_2O_3$ | Sputtered | na | 5.1 | [32] |
| $Al_2O_3$ | Anodized | r.t. | $4.2 \pm 0.7$ | [33] |
| $TiO_2$ | Anodized | r.t. | 21 | [34] |
| BZT | r.f. sputtered | r.t. | 17.3 | [35] |
| BST | r.f. sputtered | r.t. | 16 | [35] |
| $Ta_2O_5$ | e-Beam evaporation | r.t. | 21 | [36] |
| $Ta_2O_5$ | Anodized | r.t. | na | [37] |
| $Ta_2O_5$ + PMMA | e-Beam evaporation | r.t. | 21–22 | [38] |
| BZN | Sputtered | r.t. | 51–55 | [39] |



**Fig. 6** Chemical structure of polymers used as gate dielectrics: polyvinylphenol (PVP), polystyrene (PS), polymethylmethacrylate (PMMA), polyvinylalcohol (PVA), and polyvinylidene-fluoride (PVDF)

### 3.1.2 Polymeric Dielectrics

Solution-processable polymers are attractive as alternative dielectrics because of their capability to be patterned with low cost techniques such as spin coating, casting, or printing. Polymers with various chemical structures and physical properties are readily available. Some of them are already largely used as photolithography resins in silicon microelectronics. The chemical structure of representative polymers is given in Fig. 6. Most of the polymeric dielectrics are deposited from a solution. Additional heat or irradiation treatments are required to initiate cross-link or cyclization reactions.

Polymer dielectrics were first investigated by Garnier's group [41], with a systematic study on cast films of PVA, PVC, PS, PMMA and a high dielectric constant (high-*k*) polymer, cyanoethylpululane (CYEPL). The semiconductor was sexithiophene (6 T). A strong correlation was reported between the measured field-effect mobility and the dielectric constant, which is reminiscent of what observed later on oxides.

The first all polymer printed OTFT was reported by Bao and coworkers with polyimide (PI) as the gate insulator [42]. This was followed by the report of the first polymer integrated circuit (IC) by a group at Philips [43]. In this case, the dielectric was melamine-crosslinked PVP, and the electrodes were made of a conducting

polymer, polyaniline (PANI). More recently, the Cambridge group demonstrated an ink-jet printed all-polymer IC [44]. This time, the conducting polymer used for electrodes was polystyrenesulfonate-doped polyethyleneoxythiophene (PEDOT:PSS).

Because of their many benefits in terms of performance and adaptability for printing (ink-jet and roll-to-roll) deposition techniques, polymer dielectrics seem to have gained the advantage over inorganic dielectrics. Among the most used polymers, typical examples are cross-linked PVP [45, 46] and the commercial lithography resin benzocyclobutene (BCB) [47, 48].

Another example is poly-*para*-xylylene (Parylene), which is obtained by the generation, through pyrolysis, of radicals of a *para*-xylylene dimmer that readily polymerize on a substrate held at room temperature. This is a solvent free process so that the polymer can be deposited on any kind of substrate, including organic ones. Although the main application of parylene remains encapsulation [49], its dielectric properties have also been put into profit to use it as a gate dielectric [50, 51].

### 3.1.3 Ultrathin Dielectrics

A critical issue in organic transistors is the large operating voltage resulting from poor capacitive coupling due to thick gate dielectric associated with low dielectric constant. This is particularly true in the case of organic insulators. One way to work around this problem is the use of high dielectric (mostly inorganic) materials. However, this may lead to reduction of the mobility of charge carriers in the conducting channel of the transistor, as will be demonstrated in the following. The other way is to reduce the thickness of the dielectric. A promising approach to such a reduction is the use of self-assembled monolayers (SAM), which are monomolecular layers that spontaneously form when putting a surface in contact with a reactive molecule, either in solution or in gas phase [52]. The formation of a SAM results from a complex interplay between the interactions between the reactive group with the surface and the intermolecular forces acting between the molecules.

Alkoxysilane SAMs deposited on oxidized silicon as ultrathin dielectrics in thin film transistors were first explored by the group of Vuillaume in both inorganic [53] and organic devices [54]. The SAM consisted of vinyl-terminated molecules that were subsequently oxidized to obtain a carboxyl-terminated monolayer. In the organic case, the authors combined electron beam lithography and lift-off of both the source drain electrodes and semiconductor layer. The source drain distance was as low as 30 nm. The device functioned at low voltage (2 V), but the overall performance remained modest, partly because of the nature of the semiconductor (sexithiophene).

More recently, a group at Infenion has prepared SAMs through direct grafting of a modified alkoxysilane molecule on an activated surface. When pentacene was used as the semiconductor, a mobility of $1\,\mathrm{cm}^2\,\mathrm{V}^{-1}\,\mathrm{s}^{-1}$ was reported, and the operating voltage was less than 2 V [55]. Given the small thickness of the monolayer, a highly dense film is required to prevent leakage through the dielectric. This was achieved by adding a phenoxy end group to the alkoxysilane molecule. An alternative solution is the use of phosphonic acid based SAMs [56, 57].

### 3.2 Physics of the Insulator–Semiconductor Interface

There has been considerable debate in the literature regarding the exact role of the insulator–semiconductor interface on the performance of the device. We will here restrict our discussion to devices where the semiconductor is deposited on top of the gate dielectric (bottom gate architecture). Basically, the physical features that intervene may be of electrical or morphological nature. These two aspects will now be dealt with in sequence.

#### 3.2.1 Morphology

One of the earliest approaches to interfacial modification of the dielectric was from the Penn State group involving devices made of pentacene, the now most widely known p-type organic semiconductor used in organic transistors. Pentacene crystallizes in a herringbone structure that has been resolved long ago [58]. More recently, a second crystal phase was identified in thin films deposited from the vapor phase, the so-called *thin-film* phase [59]. The thin-film phase is characterized by a lower tilt angle of the molecule with respect to the normal to the substrate on which they are deposited. The implication of this new structure is a bigger compactness, which in turn would favor charge transport through higher bond strength. What the Penn State group showed is that modifying the surface of the gate dielectric (here thermally grown silica $SiO_2$) with vapor deposited silanes resulted in a substantial increase of the effective mobility [60].

Further works from this group and others included the use of various SAMs, resulting in mobility values within the range of $1\,cm^2\,V^{-1}\,s^{-1}$ or slightly above [31, 32, 61]. Even higher mobility values have been reported to result from the deposition of a very thin polymeric film on top of the oxide dielectric [62, 63]. In all cases, the marked effect of this kind of surface treatment is a reduction of the surface energy (as clearly indicated by the subsequent increase of the contact angle), which in turn alters the morphology of the pentacene layer deposited on top of the dielectric. We note that a similar impact is also observed by heating the substrate during the deposition of the semiconductor layer [64].

The exact nature of the improvement is still highly controversial. The role of the thin-film phase is now well accepted. On the other hand, the literature is full of conflicting data concerning the effect of the surface treatment on the size and shape of the crystal grains that compose the polycrystalline organic film. As shown in Fig. 7, atomic-force microscopy (AFM) can be used to study grain size and morphology in vapor deposited organic films [65]. Here, the semiconductor is pentacene and the substrate alumina ($Al_2O_3$). The column at the left hand side corresponds to bare $Al_2O_3$, while the surface was modified with a SAM made of a carboxylic acid in the right column. The most obvious effect of the treatment is the reduction of the size of the grain. Another effect can be inferred when comparing the top images (0.5 nm, that is, 0.3 monolayer) and the subsequent ones. On bare alumina, the growth abruptly changes from two-dimensional to three-dimensional, with an

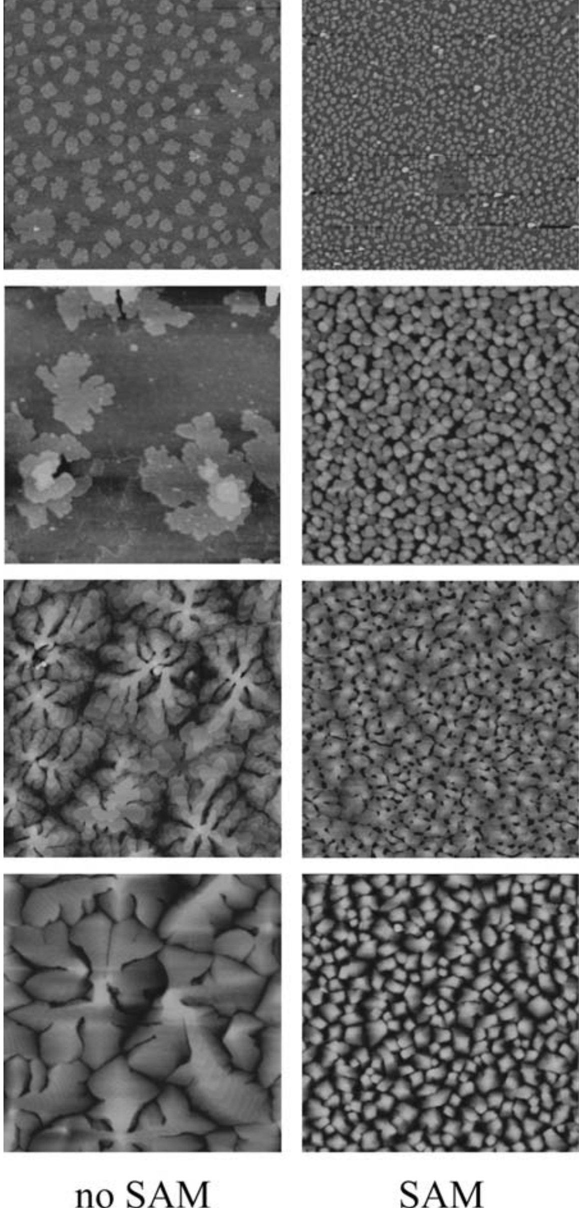


**Fig. 7** AFM images of pentacene films vapor deposited on bare (*left column*) and SAM modified (*right column*) alumina substrate. The thickness of the films are top down: 0.5, 3, 6 and 30 nm. The size of the images is $4 \times 4\,\mu\text{m}^2$

associated increase of the grain size, after completion of the first monolayer. A drastically different situation is observed on the modified substrate, with a deposition that starts three-dimensional and remains so all along the process.

Surprisingly, higher mobility was reported in small grain devices (grown on the modified alumina) than on large grain ones, which is at variance with theoretical models of charge transport in polycrystalline media that state that the effective mobility should increase with grain size [64, 66]. However, many groups working with modified oxide dielectric, mainly silicon oxide, have indeed observed decreasing mobility with increasing grain size [31, 67, 68]. A rationale to this counter-intuitive observation can be found by reasoning in terms of surface energy [68]. Nucleation and growth models teach us that the size of the grains is directly correlated to the surface energy; that is, the higher the surface energy, the larger the grain size. On the other hand, large surface energy is liable to induce two-dimensional growth; more importantly, it may also cause the deposition of pentacene molecules flat on the surface, which is detrimental for charge transport along the insulator–semiconductor interface. In conclusion, the key parameter appears to be surface energy. Bare oxides have large surface energy that concomitantly induces large grains and poor charge transport at the dielectric interface. Higher mobility can be obtained by reducing the surface energy with the help of surface modification; in turns, this reduction leads to a lowering of the grain size.

### 3.2.2 Electrical Effects

The interplay between the dielectric and the organic semiconductor is complex, and there are clearly other effects not solely related to the morphology of the semiconductor layer. This can be illustrated here by two representative examples.

The first example involves amorphous polymers based on a series of triarylamine derivatives (PTAA). Early works on amorphous polymers suggested that the mobility in these materials might be limited to low values. However, amorphous solids offer some appealing features, among which the absence of local defects such as grain boundaries, resulting in materials of great homogeneity. PTAA, which has first been found in xerographic application, offers mobility up to the $0.01\,\mathrm{cm^2\,V^{-1}\,s^{-1}}$ range, good air stability and low threshold voltage. On these bases, Veres and coworkers have conducted a comprehensive study on the effect of the polarity of the dielectric on the performance of the device [69]. The salient result of this work is that the performance of the device is improved when using a low $k$ gate dielectric. The improvement results in both increased mobility and reduced threshold voltage. This result was interpreted within the framework of localized charge transport in disordered materials. It is stated that the random dipole field generated at the surface of dielectrics with high dielectric constant is liable to enhance the localization of charge carriers. Another way to rationalize this concept is through the Gaussian DOS depicted in Eq. (14). The effect of the dipole field is a broadening of the distribution, which according to the model results in a decrease of the mobility.

These statements are at variance with earlier results, which started from the observation that most organic semiconductors show an increase of the mobility with increasing gate voltage [20, 70], which is usually interpreted in terms of an exponential density of localized states, as demonstrated above through Eqs. (16) and (17). Because the density of charge carriers induced in the conducting channel equals $C_i(V_G - V_T)$, it can also be stated that the mobility increases with the induced charge. In connection with this, a group at IBM demonstrated a substantial rise of the mobility upon using high dielectric constant (high *k*) gate dielectrics [35]. An additional interest of high-*k* insulators is the correlated reduction of the operating gate voltage of the device.

The second example is more related to n-channel organic transistors. In the early days of organic electronics, a largely widespread belief was that conduction by electrons was much more difficult in organic semiconductors than conduction by holes. Several rationales have been invoked to account for such a feature, including the fact that radical-anions, the ions that form when molecules release an electrons, are much more sensitive to the ambient than radical-cations. This belief was seriously blown apart when the Cambridge group reported that, by simply changing the almost universal gate dielectric, silicon oxide, to polymer dielectrics, n-type channel transistors could be made with numerous polymeric semiconductors [28]. The absence of n-type conduction in devices using $SiO_2$ gate dielectric can be attributed to the presence of a large amount of hydroxyl group at the surface of the dielectric. These groups act as very efficient electron traps, while their effect on holes passes unnoticed. Covering the silica with alkyl SAM of various lengths brought further evidence for electron trapping. Although the SAM cannot completely eliminate the detrimental effect of the hydroxyl groups, there is a partial recovering of electron mobility, which increases with increasing alkyl chain length.

Further evidence for the crucial role of the dielectric was brought by reports on n-channel operation with pentacene through the use of PVA as gate dielectric [71, 72]. Hence the concept of *ambipolar* semiconductor, where the type of the charge carriers (electrons or hole) is not dictated by the nature of the semiconductor; instead, it will depend on the nature of the gate dielectric and of the contacts.

At this point it should be stressed that ambipolar devices are not good candidates for complementary circuits. Complementary architecture (often designated by the acronym CMOS, which makes reference to the conventional silicon MOSFET) consists of designing circuits that associate n-channel and p-channel transistors. Its key advantage is that, because one of the transistor types is passing while the other is blocking, the circuit only consumes power when the circuit is switching. Because an ambipolar transistor is always passing (either through electrons or through holes), except in the narrow voltage range where the charge transport switches from n- to p-conduction, a circuit made of ambipolar transistors will not retain this ability to exhibit very low power consumption.

# 4 The Interface Between Electrodes and Semiconductor

As charge transport within the conducting channel of the transistor improves, the issue of limitations due to charge injection at the source and charge retrieval at the drain becomes more and more crucial. In that respect, the thin-film transistor offers the advantage of being a tool to examine injection by discriminating between the contact resistance and the channel resistance. We will thus first expose the various methods that can have been developed to differentiate between charge injection and charge transport.

## *4.1 Measuring the Contact Resistance*

### 4.1.1 Analyzing Single Devices

The first attempts to get access to the contact resistance were by analyzing the current–voltage characteristics of single devices. It has been soon recognized that the transfer characteristics of organic transistors could not be satisfactorily described by the simple Eqs. (6) and (7), which are generally used to extract the mobility and threshold voltage, as stated above. The problem manifests itself by a downward curvature of the $\sqrt{I_{\mathrm{Dsat}}}$ curve, or alternatively a decrease of the mobility with increasing gate voltage [73].

Extracting a contact resistance from the characteristics of single devices can only be achieved by assuming a simple equivalent circuit where the transistor is in series with a resistor [70]. Because in this method the respective estimations of the mobility in the conducting channel and the series resistance (also known as *parasitic* resistance) are tightly entangled, assumptions have to be made on their respective dependence on various variables, among which the gate voltage appears to be the most relevant one. As a result, choosing which of the parameter is taken as constant may lead to very different results, with no real possibility to discriminate the good one [73, 74]. As will be shown in the following, the issue resides in that both the mobility and the contact resistance are gate voltage dependent, making a direct analysis of the current–voltage characteristics of single devices unable to clarify the actual situation. The merit of these early analyses was to point out the problem of contact resistance. However, more sophisticated parameter extraction techniques were needed to get deeper insight in the physical situation. We will now present three of these techniques.

### 4.1.2 Gated Four-Probe Measurements

The use of the gated four-probe technique has readily extended to the organic transistor [75–77]. The basic principle of the method is illustrated in Fig. 8. It consists of introducing two additional electrodes within the space separating the source and

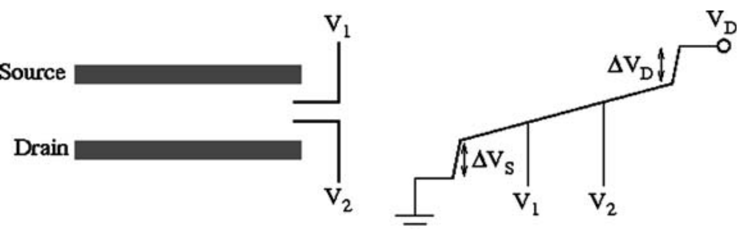


**Fig. 8** Electrode pattern for four-probe measurements. The corresponding voltage profile along the conducting channel is shown on the *right hand side*

the drain. The respective voltage $V_1$ and $V_2$ of these two electrodes is measured together with the current flowing from source to drain when the drain is biased. Assuming a linear voltage profile between source and drain, and because the voltage drop between the two additional electrodes is independent of the contact resistance, the source–drain voltage drop through the channel is given by

$$\Delta V_{\text{ch}} = (V_2 - V_1)\,\frac{L}{L_2 - L_1}. \tag{19}$$

Here, $L_1$ and $L_2$ are the distance between source and additional electrode 1 and 2, respectively.

Additionally, the respective voltage drops at the source and drain electrode can be calculated by

$$\Delta V_{\text{S}} = V_1 - (V_2 - V_1)\,\frac{L_1}{L_2 - L_1}, \tag{20}$$

$$\Delta V_{\text{D}} = V_{\text{D}} - \frac{V_1\,(L_2 - L) - V_2\,(L_1 - L)}{L_2 - L_1}. \tag{21}$$

The corresponding channel, source, and drain contact resistances are obtained by dividing the respective voltage drop by the drain current.

However, the implementation of the four-probe method is subject to several technical issues that should not be underestimated. First, the additional electrode must be placed in a location where they do not interfere with the electrical potential distribution established during the operation of the device. With that in mind, the electrodes are usually located at the rim of the conducting channel. This requires a careful patterning of the four electrodes during the fabrication of the device. Next, recent finite element calculations performed by the group of Frisbie showed that patterning the semiconductor layer is a crucial issue [78]. Failing to do so may lead to inaccurate estimation of the contact voltage drop, so it is important to make sure that the semiconductor rims fit the contact edges. Another difficulty is the measurement of the voltage drop between the two additional electrodes, which requires a highly sensitive voltmeter with very high input impedance.

It should also be stressed that Eqs. (19)–(21) are only valid when the voltage profile between source and drain is linear. That is, the use of the four-probe technique should be limited to the linear regime.

### 4.1.3 Transfer Line Method

The transfer line method (TLM) was initially developed in the case of the hydrogenated amorphous silicon thin-film transistor [79]. The method is simple to implement, and it has become the most widely used technique to extract contact resistance in OTFTs [80–85]. The principle of the method is illustrated by Eq. (22), which directly derives from the current in the linear regime, that is, when $V_D \ll V_G - V_T$.

$$R_{ON} = R_{ch} + R_c = \frac{L}{W\,C_i\,\mu\,(V_G - V_T)} + R_c. \tag{22}$$

Here, $R_{ON} = V_D / I_D$ is the input resistance of the device; $R_{ch}$ and $R_c$ are the channel and contact resistance, respectively. It can be seen in Eq. (22) that the channel resistance is proportional to the length of the channel, while the contact resistance is independent of it. In consequence, the method consists of measuring the input resistance of a series of devices with various channel length that have been fabricated in the same run. By plotting the resistance as a function of $L$, one obtains a straight line whose extrapolation to zero length corresponds to the contact resistance. In addition, the mobility can in principle be extracted from the slope of the line.

The method is simple and easy to put into practice. Many research groups have carried out measurements with this technique, so that some convergent aspects of the contact resistance can now be put forward. This will be done in a subsequent section.

### 4.1.4 Surface Potential Microscopy

Surface potential microscopy derives from the local probe techniques that came to light in the early 1980s. Also known as Kelvin probe force microscopy (KPFM) or scanning Kelvin probe microscopy (SKPM), it is a noncontact variant of AFM. Bürgi has recently provided a detailed theoretical analysis of KPFM [86]. In surface potential microscopy, a conducting cantilever is scanned at a constant height over a surface in order to map the work function of the surface. The determination of the work function is based on the measurement of the electrostatic forces between the AFM tip and the sample. When both elements are brought into contact, a net electric current flows between them until the Fermi level are aligned. Resulting from the net charge transfer, an electrostatic force between the tip and the surface builds up. For the measurement, a voltage is applied to the tip that is regulated by a feedback loop such that the force between the tip and the surface is minimized.

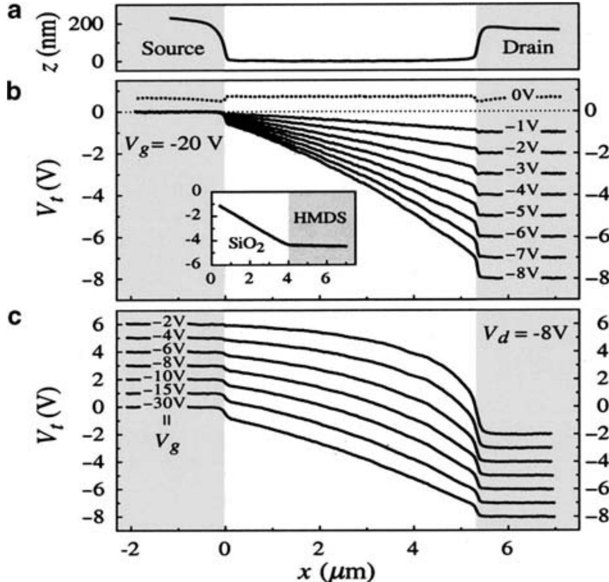


**Fig. 9** KPFM profile along the channel of an organic transistor for various drain and gate voltages. (**a**) AFM profile. (**b**) KPFM profile at $V_G = -20$ V and various drain voltages. (**c**) KPFM profile at $V_D = -8$ V and various gate voltages. Taken from [87]

In principle, surface potential microscopy is only usable on conductive substrates. However, the accumulation layer at the insulator–semiconductor interface can be viewed as a conductive layer, whereas the bulk of the semiconductor film is just part of the gap dielectric. In other words, KPFM is capable of imaging the actual potential in the conducting channel with a 100 nm lateral resolution [87–91]. A representative example of the potential profile across the conducting channel is shown in Fig. 9.

Unlike the gated four-point and transfer line techniques, KPFM does not directly give access to the contact resistance. Rather, it allows a direct visualization of the barrier heights at the source and drain contacts. For this reason, it is an essential complementary technique.

### 4.1.5 Ohmic vs Non-Ohmic Contact

In principle, the extraction of contact resistance with four-probe or TLM can only be performed in the case where the resistance is purely ohmic. However, non-ohmic contact resistance is frequently encountered in organic transistors. Direct evidence for non-ohmic contact resistance is brought by the output characteristic, which presents an upward curvature at low drain voltage, as shown in Fig. 10.

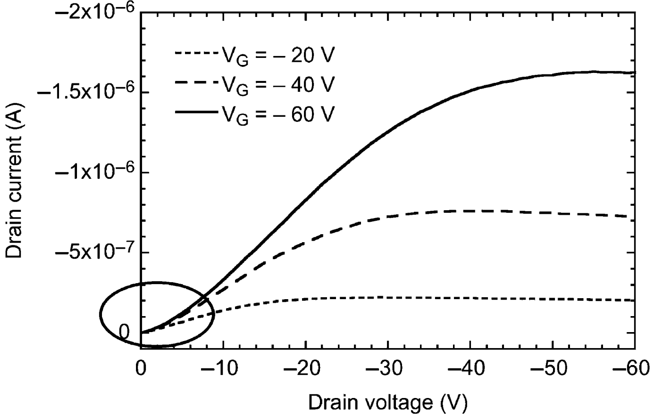


**Fig. 10** Typical output curve with a non-ohmic contact resistance

This difficulty can be worked around by introducing the concept of contact voltage drop. Both gated four-probe and surface potential measurements tend to show that most of the voltage-drop occurring at contacts takes place at the source; in other words, the limiting step is the injection, not the removal of the charges. Starting from this, the model assumes that (1) all the contact voltage drop $V_C$ occurs at the source and (2) the voltage drop extends over a thin layer of thickness $d$. The current in the conducting channel can now be estimated by integrating Eq. (3) from $(x = d, V(x) = V_C)$ to the drain $(x = L, V(x) = V_D)$:

$$I_D = \frac{W}{L-d} C_i \mu \left[ (V_G - V_T)(V_D - V_C) - \frac{V_D^2 - V_C^2}{2} \right]. \tag{23}$$

Equation (23) can be used to infer $V_C$ for each $I_D$. For this, $V_T$ and $\mu$ must be independently estimated. Ways for estimating the threshold voltage have been exposed in the first part of this chapter. More difficult seems to be the estimation of the mobility. Natelson and coworkers have recently developed a method using the TLM approach [92]. Data are collected from identical devices with various channel lengths; $I_D V_D$ data are then used with some assumed $\mu$ to infer the corresponding $I_D V_C$ data. The correct value of the mobility is the one for which the characteristics collapse in one curve.

## 4.2 *Origin of Contact Resistance*

Being probably the most decisive factor in organic electronics, charge injection from electrodes into organic semiconductors has been the subject of an unprecedented

amount of research effort. To be simple, there are two aspects that govern charge injection: energy alignment and morphology. They will now be addressed in sequence.

### 4.2.1 Energy Level Alignment

At metal–semiconductor interfaces, the hole and electron injection barrier heights ($E_{\mathrm{bp}}$ and $E_{\mathrm{bn}}$ in Fig. 11) depend on the position of the highest occupied molecular orbital (HOMO) and lowest unoccupied molecular orbital (LUMO) with respect to the Fermi level of the metal. Ever since the early days of organic electronics, barriers for charge injection have commonly been described by assuming that energy levels at both sides of metal–organic semiconductor interfaces follows a *vacuum level* alignment rule [93–95], also known as Mott–Schottky (MS) limit, in which $E_{\mathrm{bh}}$ corresponds to the difference between the semiconductor ionization potential IP and metal work function $W_{\mathrm{m}}$, while $E_{\mathrm{bh}}$ is given by the difference between $W_{\mathrm{m}}$ and the semiconductor electron affinity EA. Assuming vacuum level alignment is equivalent to suppose that the energy levels at both sides of the interface keep the same value as in the bulk of each material involved. There are now numerous pieces of evidence for the fact that in the real world such an assumption is rarely fulfilled [96–100], so that a more realistic energy diagram of the interface is that given by the left and right sides in Fig. 11. The difference between the ideal case and the realistic case is the presence of an interface layer where a significant shift of the energy levels is taking place. It is now widely recognized that the origin of this shift is to be sought in the presence of an interface dipole, hence the designation of the interface energy shift as *interface dipole barrier* Δ.

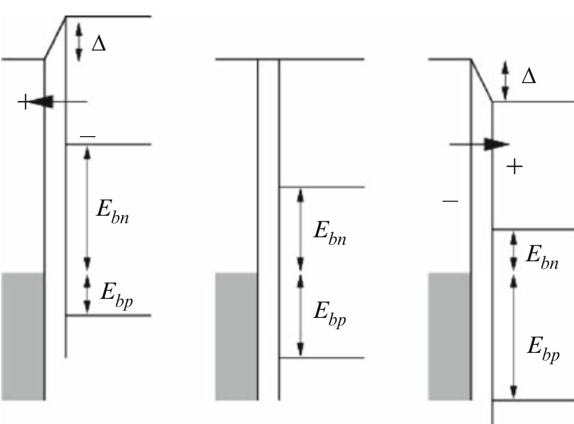


**Fig. 11** Energy barrier scheme at the metal–semiconductor interface. *Center*: Mott–Schottky limit (vacuum level alignment). $E_{\mathrm{bn}}$ and $E_{\mathrm{bp}}$ are the electron and hole injection barriers, respectively; *left* and *right*: with an interface dipole Δ

### 4.2.2 Methods for Measuring the Barrier Height

Photoelectron Spectroscopy

Ultraviolet photoelectron spectroscopy (UPS) is the method of choice to estimate the HOMO level in organic solids and energy barrier heights at interfaces [101]. The technique consists of impinging the surface of a solid with a monochromatic source of photons of sufficient energy as to extract valence electrons from the solid. The distribution of the kinetic energy KE of the extracted electrons is then measured with an appropriate detector. Because of energy conservation, the kinetic energy is the difference between the binding energy BE of the electron and the energy of the impinging photon:

$$\mathrm{KE} = h\nu - \mathrm{BE}. \tag{24}$$

The basic requirements for a photoemission experiment are (1) a source of fixed energy radiation (typically, a He discharge lamp), (2) an electron energy analyzer, and (3) ultrahigh vacuum (UHV) environment to enable the emitted electrons to be detected without interference from gas phase collisions.

A typical UPS spectrum of a metal is displayed in Fig. 12. The salient features of the spectrum can be depicted as follows. At low binding energy (high kinetic energy) there is a small step that corresponds to the Fermi energy, that is, the maximum energy of the free electrons in the solid. This is followed by features that can be put in correspondence with the DOS of the metal. The broad feature that comes after is correlated to secondary electrons, that is, electrons that are ejected by other electrons rather than directly emitted by the impinging photons. The abrupt fall off of the signal (cutoff energy) corresponds to electrons with zero kinetic energy; these electrons have a binding energy equal to that of the incident photons. Thus, by translating the cutoff energy by the energy of the photon, one gets the vacuum energy. In turn, the work function $W_{\mathrm{m}}$ is given by the difference between the vacuum level and the Fermi level.

Because the density of electrons at the Fermi energy is zero in a semiconductor, the respective UPS spectrum does not present the initial step. In this case, UPS is essentially used to estimate the ionization potential, that is, the difference between

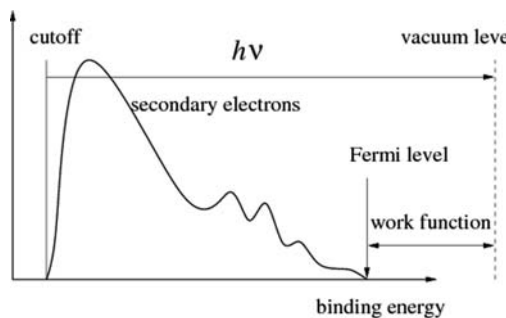


**Fig. 12** Ultraviolet photoelectron spectrum of a metal

the HOMO level and the vacuum level. There are several other issues when dealing with organic semiconductors. The front of the sample must be maintained in electrical contact with the metallic substrate. The use of very thin films can prevent any surface charge from building up during the course of the measurements by allowing electrons to tunnel from the substrate.

#### Kelvin Probe

The Kelvin probe does not directly give access to the work function. Instead, it measures the contact potential difference (CPD) between a tip and the sample being analyzed. As such, it necessitates the knowledge of the work function of a given solid that can be either the tip itself or a reference solid. It is a noncontact technique and unlike UPS, the measurement can be carried out in air as well as under vacuum.

The principle of the measurement is illustrated in Fig. 13. The top panel shows two metals in close proximity that are not in electrical contact. The respective Fermi level is separated from the vacuum level by a distance corresponding to the respective work function $W_{m1}$ and $W_{m2}$. In the center panel, the two metals are connected through an external conducting wire; electrons flows from the metal with lower work function until equilibrium, which takes place when the Fermi levels are aligned. At equilibrium, the potential associated with the electric field created by the opposite charging of both metals exactly cancels out the work function difference. This can be utilized to measure the CPD. Applying a counter potential between the electrodes and monitoring the charge on one of them allows the determination of the charge free point. The counter potential that exactly achieves this state equals – CPD.

In his original experiment, Lord Kelvin used a gold-leaf electroscope to monitor the charge of the metals. In modern set-ups, one of the metals (the Kelvin probe) is vibrating at a frequency $\omega$. Due to the varying distance, the amount of charge necessary to maintain the electric field between the surfaces varies; a lock-in amplifier is used to monitor the current generated by the oscillation. Through gradual ramping of the counter potential, the CPD is found by detecting the point of zero current.

### 4.2.3 Physics of the Metal–Semiconductor Interface

#### Bardeen's Model

Experimental deviations from the MS limit have been found since the early days of microelectronics. As early as 1947, Bardeen proposed that if a large density of surface states were present at the metal–semiconductor interface, then the barrier height would be independent of the metal work function [102]. This can be understood in terms of equilibrium between the surface states and the bulk of the semiconductor. Bardeen's model rests on the existence of a thin insulating layer

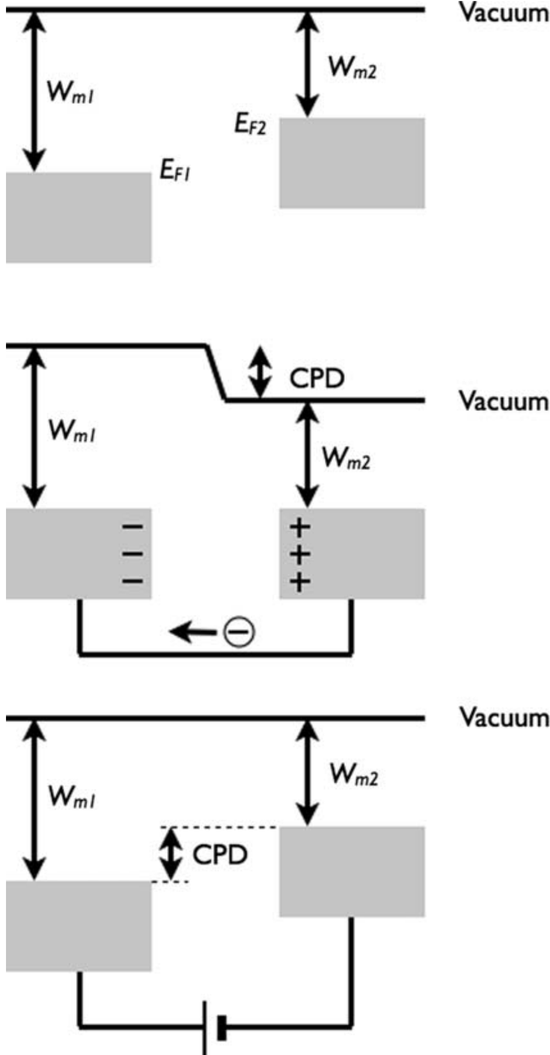


**Fig. 13** Measurement of the contact potential with the Kelvin probe. *Top*: metals before contact; *center*: metals after electrical contact; *bottom*: after applying a counter potential

that separates the metal from the semiconductor. The interfacial layer is assumed to be thin enough as to be transparent to electron flow, yet able to withstand a potential difference across it. If the density of surface states is large, then the Fermi level at the surface will establish at a value $W_0$ located within the energy gap. Under such circumstances, the potential difference between the work function of the metal $W_m$ and that of the semiconductor $W_s$ will appear entirely across the interfacial layer. Accordingly, no change in the charge of the depletion layer in the semiconductor is

necessary, and the barrier height is independent of $W_m$. The barrier height is simply given by

$$E_b = E_g - W_0, \tag{25}$$

where $E_g$ is the band gap. The Fermi level is pinned by the surface states to an energy $W_0$ above the valence band edge.

In the most general case, the metal–semiconductor contact is somewhere between the MS and the Bardeen limits [103]. Consider an n-type semiconductor; the interface layer has a thickness $\delta$ and a permittivity $\varepsilon_i$, and the density of surface states is $N_{ss}$ (per unit area and unit energy). The barrier height is then given by

$$E_b = S(W_m - EA) + (1 - S)\left(E_g - W_0\right), \tag{26}$$

where

$$S = \frac{\varepsilon_i}{\varepsilon_i + qN_{ss}\delta}. \tag{27}$$

The dimensionless parameter $S$ (also called *slope* or *screening* parameter) varies between zero and unity. If the density of surface states is low, $S = 1$ and Eq. (26) reduces to the MS limit. The reverse case, $S = 0$, corresponds to the Bardeen limit.

### Induced Density of Interface States

The van der Walls forces that bond organic semiconductors do not involve sharing of electrons between nearest-neighbor molecules. For this reason, molecules at the surface of the solid do not experience the same dissymmetrical forces as in elemental crystals, thus making the formation of dangling bonds and the associated high density of surface states assumed in Bardeen's model unlikely. Several alternative models have been proposed to rationalize the deviation from the vacuum level alignment at the metal–organic semiconductor interface [93, 104]: (1) chemically reactive interfaces; (2) the orientation of permanent molecular dipoles; (3) charge transfer between the metal and the organic layer; (4) the compression of the metal electron tail (the so-called pillow effect). The origin of the latter effect is illustrated in Fig. 14.

Of importance under that respect is the induced density of interface state (IDIS) model [105, 106] that states that when an organic material is put into contact with a metal surface, the tails of the metal orbitals tunnel into the HOMO–LUMO gap of the organic solid, which has the effect of broadening the molecular levels. As a result, the initial discrete distribution turns to a continuum DOS with, in particular, a nonzero DOS in the HOMO–LUMO gap. This DOS can play the same role as the surface states in the model of Bardeen.

The central quantity in the IDIS model is the charge neutrality level (CNL), the position of which is such that the integrated induced DOS up to the CNL equals the number of electrons of the isolated molecule:

$$N = \int_{-\infty}^{\mathrm{CNL}} \rho_{\mathrm{IDIS}} \mathrm{d}E. \tag{28}$$

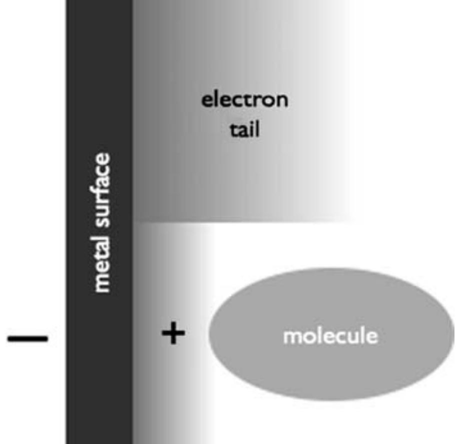


**Fig. 14** Pillow effect. *Upper part*: the surface of a metal is characterized by an electronic tail that extends a fraction of a nanometer outside the surface. *Lower part*: placing a molecule on the surface results in compressing the tail, thus creating a positive charge outside the surface and a counterbalancing negative charge inside. These two charges form a surface dipole

If the CNL of the organic layer is higher than the metal work function, electrons will be transferred from the organic material to the metal, thus giving rise to an interface dipole. Like in the case of the Bardeen model, the CNL plays the role of an effective Fermi level at the interface.

The amount of charge transferred is quantified through the above-defined screening parameter $S = \mathrm{d}E_\mathrm{F} / \mathrm{d}W_\mathrm{m}$, which can be theoretically calculated from the DOS induced at the interface $D(E_\mathrm{F})$:

$$S = \frac{1}{1 + 4\pi e^2 D(E_\mathrm{F})\delta / A}. \tag{29}$$

Here, $e$ is the elemental charge, $\delta$ the thickness of the interface layer and $A$ the projected area of the molecule that constitute the organic material. The Fermi level and induced dipole are given by

$$E_\mathrm{F} - \mathrm{CNL} = S(W_\mathrm{m} - \mathrm{CNL}), \tag{30}$$

and

$$\Delta^{\mathrm{IDIS}} = (1 - S)(W_\mathrm{m} - \mathrm{CNL}). \tag{31}$$

### The Case of Polymeric Semiconductors: Additional Fermi Level Pinning

While most molecular organic semiconductors experience the formation of an interface dipole when deposited on a clean metal surface, polymeric semiconductors usually follow vacuum level alignment. These different behaviors may originate

from the way organic materials are deposited into thin films: molecular materials are usually transferred from the vapor phase, while polymers are cast from solutions.

On this basis, a group at Linköping University has conducted a series of measurements of the injection barrier at the interface between conducting substrates and various polymeric semiconductors [107, 108]. In order to extend the range of the work function towards high values, they also used conducting polymers (CP) as the conducting substrate.

CP can be used as electrodes in organic electronic devices in two ways: as stand alone films or by inserting a CP layer between a conducting electrode and the semiconductor layer. It is worth pointing out that, in a majority of organic light-emitting diodes, the transparent indium tin oxide (ITO) anode is covered with polystyrenesulfonate-doped poly(3,4-ethylenedioxythiophene) (PEDOT:PSS). In this mixture, positive charges on the PEDOT are stabilized by negative charges in the PSS. Interestingly, the work function $W_{\mathrm{m}}$ of CPs is greatly dependent on the preparation of the film. In the case of PEDOT:PSS, it has been demonstrated that $W_{\mathrm{m}}$ largely depends on the residual water content. Work functions up to 5.6 eV have been reported, which is substantially higher than the work function of noble metals, thus potentially rendering CPs highly efficient hole injecting systems.

The group did observe the vacuum-level rule $(S = 1)$ as long as the work function of the electrode fell between upper and lower limits. However, out of these limits, complete Fermi level pinning $(S = 0)$ took place. The overall behavior is illustrated in Fig. 15.

The origin of this additional pinning is still controversial. Due to a (maybe coincidental) good agreement between the pinning levels and the polaron energy of electron and holes, the pinning was attributed by the Linköping group to polaron or bipolaron states, located at an energy of a few tenths of eV above the HOMO or below the LUMO level. However, such an interpretation does not account for the fact that, because of the high speed of the formation of polaron, HOMO and LUMO levels in the solid state already include the polaron binding energy [94].

#### 4.2.4 Effect of Morphology

Energy alignment is the leading characteristic that controls charge injection in organic electroluminescent diodes (OLEDs) and photovoltaic cells. This is because, in a diode structure, the area of the contacts largely dominates the thickness of the device, so that charge injection prevails over charge transport within the bulk of the device. Things are different in a transistor, where the channel length is much larger than the area of the contacts. Under such circumstances, it has been claimed that the prevailing aspect that determine contact resistance is the morphology of the semiconductor film in the region of the contacts rather than energy alignment.

Direct evidence for the role of morphology is given by the importance of device architecture on the final performance of the device. Top-contact transistors

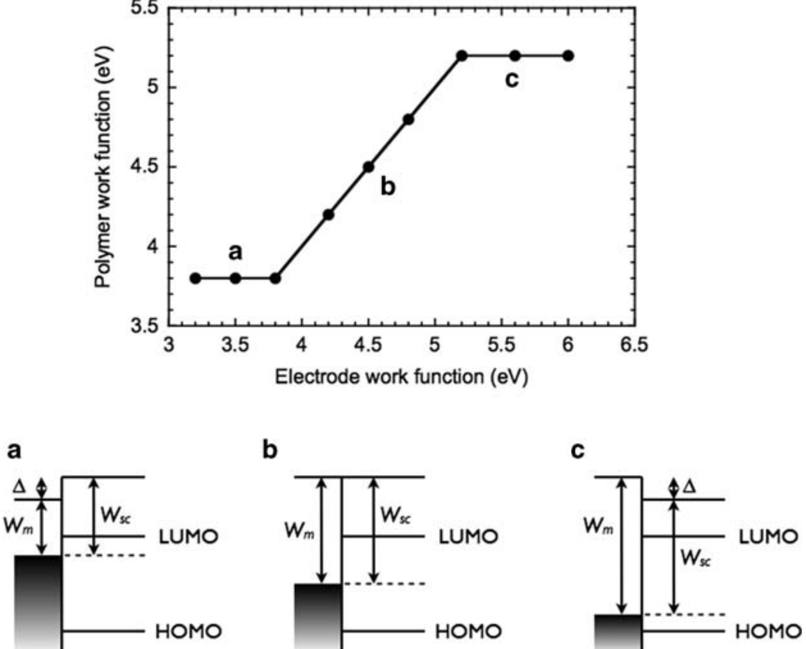


**Fig. 15** Variations of the work function of a typical polymeric semiconductor as a function of the work function of the underneath electrode. The three regimes are illustrated by the corresponding energy diagram. (**a**) Fermi level pinning near the HOMO level. (**b**) Vacuum level alignment. (**c**) Fermi level pinning near the LUMO level

(see Fig. 1) usually have better performance in term of mobility and threshold voltage over bottom contact devices [83]. This can be understood by thinking of depositing a layered crystal structure such as that of pentacene over a substrate that present different surface properties. Figure 16 illustrates the dramatic effect the transition between the electrode and the dielectric can induce in a bottom contact configuration. The diagram shows two types of disorder introduced in a short molecule layer as its growth is confronted with a discontinuity in the surface energy of the substrate. On the low-energy-surface dielectric, the molecules tend to align straight on the surface, while they lay down on the metal high-energy surface [109]. The step existing at the metal–dielectric transition reinforces this tendency to disorder. There are two ways to work around this issue: (1) realizing a planar structure where the electrode and the insulator would be on the same level – such a solution poses big technological problems, but successful attempts have been reported recently [89]; (2) modifying the electrode surface to decrease its surface energy – this has been done with the help of SAM [110–112]. Note that the latter technique closely resembles that used with the insulator–semiconductor interface.

The top-contact configuration does not suffer this problem. Here, the organic semiconductor is deposited on a homogeneous planar surface where the molecules

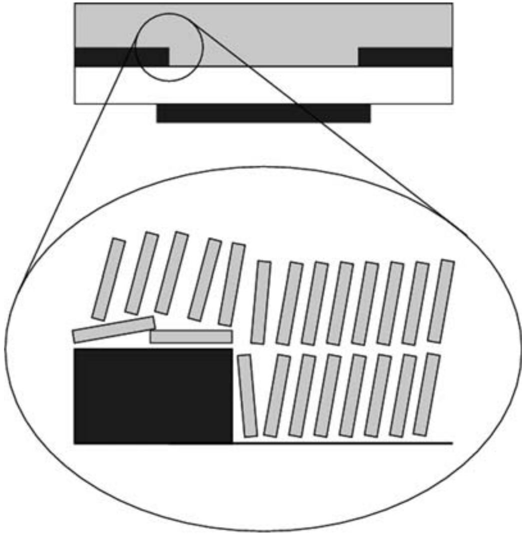

**Fig. 16** Illustration of the morphology of an organic semiconductor near the source electrode

can adopt a well-ordered configuration over the whole area. However, this architecture most often limits to large channel distances because the use of photolithography is problematic, because of the sensitivity of the organic semiconductor to process chemicals.

### *4.3 SAM Modified Electrodes: Injection vs Morphology*

To conclude the part devoted to contacts, we present a critical review of data on OTFTs with SAM modified electrodes. As stated at the beginning of the previous subsection, charge injection in organic diodes is essentially controlled by the energy level alignment at the metal–semiconductor interface. In turn, the presence of an interface dipole most often prevents easy tuning of the injection barrier height. Early work by Campbell and coworkers has shown that an elegant way to work around this issue is to purposely introduce on top of the metal electrode a SAM bearing a counter-balancing dipole [113]. Kelvin probe was used to estimate the work function of a silver electrode modified with thiol SAMs terminated with various end groups. A decrease of the work function was observed with $CH_3$ and $NH_2$ end groups, while $W_m$ increased with $CF_3$. These results were in agreement with the calculated dipole moment of the respective molecules. Later, another group confirmed these predictions by fabricating and characterizing diodes made of the modified Ag electrode and MEH–PPV, a derivative of polyphenylenevinylene, as semiconductor [114]. With the $CH_3$ terminated SAM, the work function of silver

was lowered down to 3.8 eV, and the hole current of the diode was completely blocked, while with the $CF_3$ end group, the work function of the electrode rose up to 5.5 eV and the current of the diode increased by six orders of magnitudes at a 5 V bias.

No such improvement has been reported in organic transistors, which we have attributed to the very different geometry as compared to that of the diode. Instead, the effect of SAM is generally attributed to morphological effects. Recent works by Bock and coworkers seem to corroborate the early results depicted in the previous subsection [110, 111]. In this case, the SAMs were made of thiols with an anthracene end group. Interestingly, TLM measurements did not show any improvement of charge injection; instead, the *channel* resistance decreased by a factor of ten. On the basis of temperature dependent data, the authors went to the conclusion that the improved charge transport had to be attributed to a strong reduction of the density of traps.

However, other results seem to indicate that barrier lowering through the mechanism described by Campbell does also lead to a reduction of contact resistance in transistors. First, a Dutch group reported on transistors made of MEH–PPV and regio-regular polyhexylthiophene (rr-P3HT) with gold electrodes modified by decanethiol SAMs with $CH_3$ and $CF_3$ end groups [115]. This time, TLM measurements indicated that the channel mobility only depends on the nature of the semiconductor, not on that of the contact. As for the contact resistance, it was found to be one order of magnitude larger for the SAM-modified devices with respect to the untreated electrodes. However, the contact resistance was lower with the $CF_3$ terminated SAMs than with the $CH_3$ terminated SAMs.

More recently, a group in Paris reported on a similar work with pentacene as the semiconductor [116]. In this case, the TLM extracted contact resistance showed a clear increase of the contact resistance with $CH_3$ terminated SAMs and an improved injection with the fluorinated SAMs, which is exactly what expected from the respective work functions of the modified gold electrode. Interestingly, the morphology of the pentacene on the electrode did not follow the same trend. Instead, the film showed a fibrillar structure on bare gold, indicative of molecules lying down on the substrate [109], while the structure characteristic of standing molecules was observed on both SAM-modified electrodes. In other words, there was no correlation between morphology and contact resistance. All the effect could be attributed to dipole-induced barrier tuning.

## 5 Concluding Remarks

In this chapter, we have reviewed the role of the two interfaces in the operation of the organic transistor. The interface between the semiconductor and the insulator is crucial because it is the very place where the conducting channel emerges. Because its thickness does not exceed a few monolayers, charge transport in the conducting channel is mainly dictated by the quality of this interface. Under that respect, the

nature of the insulator is at least as important as that of the semiconductor. Two contradictory requirements are demanded to the dielectric. On the one hand, high dielectric constant would favor low voltage operation; this would require the use of inorganic oxides. On the other hand, high quality (i.e., defect free) interfaces are easier to achieve with polymeric dielectrics, which present low energy surfaces, but also low dielectric constants. A way to work around this difficulty would be the use of ultrathin insulating films.

As the performance of the transistor improves, the need for good injecting contacts becomes more imperative. Problems linked to charge injection at the metal–organic semiconductor interface has largely been identified in the field of organic diodes. It mainly relies on the energy level alignment. With small molecules, vacuum level alignment, that states that the barrier height for charge injection is simply given by the difference between the work function of the metal and the energy difference between the frontier orbital levels and vacuum, can be ruled out. Instead, the alignment is controlled by a DOS arising at the interface, which is reminiscent of the Bardeen model for inorganic semiconductors. Probably because of their different deposition technique, polymeric semiconductors do follow the MS rule. However, an additional pinning process takes place when the Fermi level of the electrode comes close to the band edges, so that the barrier height cannot be reduced under a minimum value of the order of a few tenths of eV.

Due to the reduced area of contacts in organic transistors, energy alignment issues are not the only aspect that controls charge injection; the morphology of the semiconductor near the contacts also plays a major role. In that respect, the techniques that have been developed to improve the insulator–semiconductor interface can also be used for the metal–semiconductor interface, e.g., surface energy reduction by modification of the surface.

**Acknowledgments** The author gratefully acknowledges his past and present collaborators and PhD students Abderrahim Yassar, Philippe Lang, Nicolas Battaglini, Nadia Karsi, Wolfgang Kalb, Mohammad Mottaghi, Patrick Marmont, Daniele Braga, and Hyeok Kim. He is indebted to Philippe Delannoy, Jérôme Cornil, Xavier Crispin, Fabio Biscarini, Antoine Kahn, Jean-Noël Chalzaviel, Martin Knupfer, and Yvan Bonnassieux for stimulating discussions and fruitful collaborations.

## References

1. Pickard GW (1906) Means for receiving intelligence communicated by electric waves. U.S. Patent 836,531
2. Dimitrakopoulos CD, Malenfant PRL (2002) Organic thin film transistors for large area electronics. Adv Mater 14:99–117
3. Horowitz G (2004) Organic thin film transistors: from theory to real devices. J Mater Res 19:1946–1962
4. Sirringhaus H (2005) Device physics of solution-processed organic field-effect transistors. Adv Mater 17:2411–2425
5. Shur M (1990) Physics of semiconductor devices. Prentice-Hall, Englewood Cliffs
6. Sze SM (1981) Physics of semiconductor devices. Wiley, New York

7. Arkhipov VI, Fishchuk II, Kadashchuk A, Bässler H (2007) Charge transport in neat and doped random organic semiconductors. In: Hadziioannou G, Malliaras GG (eds) Semiconducting polymers. Chemistry, physics and engineering, 2nd, completely revised and enlarged edn. Wiley, Weinheim, pp 275–383
8. Bässler H (1993) Charge transport in disordered organic photoconductors. Phys Stat Sol B 175:15–56
9. Cornil J, Beljonne D, Calbert JP, Brédas JL (2001) Interchain interactions in organic pi-conjugated materials: impact on electronic structure, optical response, and charge transport. Adv Mater 13:1053–1067
10. Coropceanu V, Cornil J, da Silva DA, Olivier Y, Silbey R, Bredas JL (2007) Charge transport in organic semiconductors. Chem Rev 107:926–952
11. Silinsh EA, Cápek V (1994) Organic molecular crystals: interaction, localization, and transport phenomena. AIP, New York
12. Ashcroft NW, Mermin ND (1976) Solid state physics. Holt, New York
13. Brédas J-L, Beljonne D, Coropceanu V, Cornil J (2004) Charge-transfer and energy-transfer processes in p-conjugated oligomers and polymers: a molecular picture. Chem Rev 104:4971–5003
14. Brédas JL, Calbert JP, Da Silva Filho DA, Cornil J (2002) Organic semiconductors: a theoretical characterization of the basic parameters governing charge transport. Proc Natl Acad Sci 99:5804–5809
15. da Silva Filho DA, Olivier Y, Coropceanu V, Brédas J-L, Cornil J (2007) Theoretical aspects of charge transport in organic semiconductors: a molecular perspective. In: Bao Z, Locklin J (eds) Organic field-effect transistors. CRC, Boca Raton, pp 1–26
16. Marcus RA (1993) Electron-transfer reactions in chemistry – theory and experiment. Rev Mod Phys 65:599–610
17. Conwell EM (1956) Impurity band conduction in germanium and silicon. Phys Rev 103:51–61
18. Mott NF (1956) On the transition to metallic conduction in semiconductors. Can J Phys 34:1356–1368
19. Vissenberg MCJM, Matters M (1998) Theory of the field-effect mobility in amorphous organic transistors. Phys Rev B 57:12964–12967
20. Horowitz G, Hajlaoui ME, Hajlaoui R (2000) Temperature and gate voltage dependence of hole mobility in polycrystalline oligothiophene thin film transistors. J Appl Phys 87:4456–4463
21. Le Comber PG, Spear WE (1970) Electronic transport in amorphous silicon films. Phys Rev Lett 25:509–511
22. Mottaghi M, Horowitz G (2006) Field-induced mobility degradation in pentacene thin-film transistors. Org Electron 7:528–536
23. Ortiz-Conde A, Garcia Sanchez FJ, Liou JJ, Cerdeira A, Estrada M, Yue Y (2002) A review of recent MOSFET threshold voltage extraction methods. Microelectron Reliab 42:583–596
24. Wong H-S, White MH, Krutsick TJ, Booth RV (1987) Modeling of transconductance degradation and extraction of threshold voltage in thin oxide MOSFETs. Solid-State Electron 30:953–968
25. Facchetti A, Yoon M-H, Marks TJ (2005) Gate dielectrics for organic field-effect transistors: new opportunities for organic electronics. Adv Mater 17:1705–1725
26. Halik M (2006) Gate dielectrics. In: Klauk H (ed) Organic electronics. Materials, manufacturing and applications. Wiley, Weinheim, pp 132–162
27. Veres J, Ogier S, Lloyd G, de Leeuw D (2004) Gate insulators in organic field-effect transistors. Chem Mater 16:4543–4555
28. Chua L-L, Zaumseil J, Chang J-F, Ou ECW, Ho PKH, Sirringhaus H, Friend RH (2005) General observation of n-type field-effect behavior in organic semiconductors. Nature 434:194–199
29. Klauk H, Gundlach DJ, Bonse M, Kuo CC, Jackson TN (2000) A reduced complexity process for organic thin film transistors. Appl Phys Lett 76:1692–1694

30. Hamilton MC, Martin S, Kanicki J (2004) Field-effect mobility of organic polymer thin-film transistors. Chem Mater 16:4699–4704
31. Knipp D, Street RA, Volkel AR (2003) Morphology and electronic transport of polycrystalline pentacene thin-film transistors. Appl Phys Lett 82:3907–3909
32. Kelley TW, Boardman LD, Dunbar TD, Muyres DV, Pellerite MJ, Smith TP (2003) High-performance OTFTs using surface-modified alumina dielectrics. J Phys Chem B 107:5877–5881
33. Majewski LA, Schroeder R, Grell M, Glarvey PA, Turner ML (2004) High capacitance organic field-effect transistors with modified gate insulator surface. J Appl Phys 96:5781–5787
34. Majewski LA, Schroeder R, Grell M (2005) One volt organic transistor. Adv Mater 17:192–196
35. Dimitrakopoulos CD, Purushothaman S, Kymissis J, Callegari A, Shaw JM (1999) Low-voltage organic transistors on plastic comprising high-dielectric constant gate insulators. Science 283:822–824
36. Bartic C, Jansen H, Campitelli A, Borghs S (2002) $Ta_2O_5$ as gate dielectric material for low-voltage organic thin-film transistors. Org Electron 3:65–72
37. Iino Y, Inoue Y, Fujisaki Y, Fujikake H, Sato H, Kawakita M, Tokito S, Kikuchi H (2003) Organic thin-film transistors on a plastic substrate with anodically oxidized high-dielectric-constant insulators. Jpn J Appl Phys 1 42:299–304
38. Deman AL, Tardy J (2005) PMMA-Ta2O5 bilayer gate dielectric for low operating voltage organic FETs. Org Electron 6:78–84
39. Choi Y, Kim I-D, Tuller HL, Akinwande AI (2005) Low-voltage organic transistors and depletion-load inverters with high-K pyrochlore BZN gate dielectric on polymer substrate. IEEE Trans Electron Device 52:2819–2824
40. Majewski LA, Schroeder R, Grell M (2005) Low-voltage, high-performance organic field-effect transistors with an ultra-thin $TiO_2$ layer as gate insulator. Adv Funct Mater 15:1017–1022
41. Peng XZ, Horowitz G, Fichou D, Garnier F (1990) All-organic thin-film transistors made of alpha-conjugated sexithienyl semiconducting and various polymeric insulating layers. Appl Phys Lett 57:2013–2015
42. Bao ZN, Feng Y, Dodabalapur A, Raju VR, Lovinger AJ (1997) High-performance plastic transistors fabricated by printing techniques. Chem Mater 9:1299
43. Gelinck GH, Geuns TCT, de Leeuw DM (2000) High-performance all-polymer integrated circuits. Appl Phys Lett 77:1487–1489
44. Sirringhaus H, Kawase T, Friend RH, Shimoda T, Inbasekaran M, Wu W, Woo EP (2000) High-resolution inkjet printing of all-polymer transistor circuits. Science 290:2123–2126
45. Klauk H, Halik M, Zschieschang U, Schmid G, Radlik W, Weber W (2002) High-mobility polymer gate dielectric pentacene thin film transistors. J Appl Phys 92:5259–5263
46. Mäkelä T, Jussila S, Kosonen H, Baecklund TG, Sandberg HGO, Stubb H (2005) Utilizing roll-to-roll techniques for manufacturing source-drain electrodes for all-polymer transistors. Synth Met 153:285–288
47. Chua L-L, Ho PKH, Sirringhaus H, Friend RH (2004) High-stability ultrathin spin-on benzocyclobutene gate dielectric for polymer field-effect transistors. Appl Phys Lett 84:3400–3402
48. Singh TB, Marjanovic N, Matt GJ, Gunes S, Sariciftci NS, Ramil AM, Andreev A, Sitter H, Schwodiauer R, Bauer S (2005) High-mobility n-channel organic field-effect transistors based on epitaxially grown C-60 films. Org Electron 6:105
49. Zhou L, Park S, Bai B, Sun J, Wu S-C, Jackson TN, Nelson S, Freeman D, Hong Y (2005) Pentacene TFT driven AM OLED displays. IEEE Electron Device Lett 26:640–642
50. Podzorov V, Pudalov VM, Gershenson ME (2003) Field-effect transistors on rubrene single crystals with parylene gate insulator. Appl Phys Lett 82:1739–1741
51. Stassen AF, de Boer RWI, Iosad NN, Morpurgo AF (2004) Influence of the gate dielectric on the mobility of rubrene single-crystal field-effect transistors. Appl Phys Lett 85:3899–3901
52. Ulman A (1991) An introduction to ultrathin organic films: from Langmuir-Blodgett to self-assembly. Academic, San Diego

53. Collet J, Vuillaume D (1998) Nano-field effect transistor with an organic self-assembled monolayer as gate insulator. Appl Phys Lett 73:2681–2683
54. Collet J, Tharaud O, Chapoton A, Vuillaume D (2000) Low-voltage, 30 nm channel length, organic transistors with a self- assembled monolayer as gate insulating films. Appl Phys Lett 76:1941–1943
55. Halik M, Klauk H, Zschieschang U, Schmid G, Dehm C, Schuetz M, Maisch S, Effenberger F, Brunnbauer M, Stellacci F (2004) Low-voltage organic transistors with an amorphous molecular gate dielectric. Nature 431:963–966
56. Klauk H, Zschieschang U, Pflaum J, Halik M (2007) Ultralow-power organic complementary circuits. Nature 445:745–748
57. Ma H, Acton O, Ting G, Ka JW, Yip HL, Tucker N, Schofield R, Jen AKY (2008) Low-voltage organic thin-film transistors with pi-sigma-phosphonic acid molecular dielectric monolayers. Appl Phys Lett 92:113303
58. Campbell RB, Robertson JM, Trotter J (1961) The crystal and molecular structure of pentacene. Acta Crystallogr 14:705–711
59. Fritz SE, Martin SM, Frisbie CD, Ward MD, Toney MF (2004) Structural characterization of a pentacene monolayer on an amorphous $SiO_2$ substrate with grazing incidence X-ray diffraction. J Am Chem Soc 126:4084–4085
60. Lin YY, Gundlach DJ, Nelson SF, Jackson TN (1997) Stacked pentacene layer organic thin-film transistors with improved characteristics. IEEE Electron Device Lett 18:606–608
61. Sheraw CD, Zhou L, Huang JR, Gundlach DJ, Jackson TN, Kane MG, Hill IG, Hammond MS, Campi J, Greening BK, Francl J, West J (2002) Organic thin-film transistor-driven polymer-dispersed liquid crystal displays on flexible polymeric substrates. Appl Phys Lett 80:1088–1090
62. Kelley TW, Muyres DV, Baude PF, Smith TP, Jones TD (2003) High performance organic thin film transistors. Mater Res Soc Symp Proc 771:169–179
63. Kelley TW (2006) High-performance pentacene transistors. In: Klauk H (ed) Organic electronics. Materials, manufacturing and applications. Wiley, Weinheim, pp 35–57
64. Horowitz G, Hajlaoui ME (2000) Mobility in polycrystalline oligothiophene field-effect transistors dependent on grain size. Adv Mater 12:1046–1050
65. Kalb W, Lang P, Mottaghi M, Aubin H, Horowitz G, Wuttig M (2004) Structure-performance relationship in pentacene/$Al_2O_3$ thin-film transistors. Synth Met 146:279–282
66. Kang SJ, Noh M, Park DS, Kim HJ, Whang CN, Chang CH (2004) Influence of postannealing on polycrystalline pentacene thin film transistor. J Appl Phys 95:2293–2296
67. Shtein M, Mapel J, Benziger JB, Forrest SR (2002) Effects of film morphology and gate dielectric surface preparation on the electrical characteristics of organic-vapor-phase-deposited pentacene thin-film transistors. Appl Phys Lett 81:268–270
68. Yang SY, Shin K, Park CE (2005) The effect of gate-dielectric surface energy on pentacene morphology and organic field-effect transistor characteristics. Adv Funct Mater 15:1806–1814
69. Veres J, Ogier SD, Leeming SW, Cupertino DC, Khaffaf SM (2003) Low-k insulators as the choice of dielectrics in organic field- effect transistors. Adv Funct Mater 13:199–204
70. Necliudov PV, Shur MS, Gundlach DJ, Jackson TN (2000) Modeling of organic thin film transistors of different designs. J Appl Phys 88:6594–6597
71. Guo TF, Tsai ZJ, Chen SY, Wen TC, Chung CT (2007) Influence of polymer gate dielectrics on n-channel conduction of pentacene-based organic field-effect transistors. J Appl Phys 101:124505
72. Singh TB, Meghdadi T, Gunes S, Marjanovic N, Horowitz G, Lang P, Bauer S, Sariciftci NS (2005) High-performance ambipolar pentacene organic field-effect transistors on poly(vinyl alcohol) organic gate dielectric. Adv Mater 17:2315–2320
73. Horowitz G, Hajlaoui R, Fichou D, El Kassmi A (1999) Gate voltage dependent mobility of oligothiophene field-effect transistors. J Appl Phys 85:3202–3206
74. Street RA, Salleo A (2002) Contact effects in polymer transistors. Appl Phys Lett 81:2887–2889

75. Chwang AB, Frisbie CD (2000) Field effect transport measurements on single grains of sexithiophene: role of the contacts. J Phys Chem B 104:12202–12209
76. Goldmann C, Haas S, Krellner C, Pernstich KP, Gundlach DJ, Batlogg B (2004) Hole mobility in organic single crystals measured by a "flip-crystal" field-effect technique. J Appl Phys 96:2080–2086
77. Yagi I, Tsukagoshi K, Aoyagi Y (2004) Direct observation of contact and channel resistance in pentacene four-terminal thin-film transistor patterned by laser ablation method. Appl Phys Lett 84:813–815
78. Pesavento PV, Puntambekar KP, Frisbie CD, McKeen JC, Ruden PP (2006) Film and contact resistance in pentacene thin-film transistors: dependence on film thickness, electrode geometry, and correlation with hole mobility. J Appl Phys 99:094504
79. Luan S, Neudeck GW (1992) An experimental study of the source/drain parasitic resistance effects in amorphous silicon thin film transistors. J Appl Phys 72:766–772
80. Blanchet GB, Fincher CR, Lefenfeld M, Rogers JA (2004) Contact resistance in organic thin film transistors. Appl Phys Lett 84:296–298
81. Gundlach DJ, Zhou L, Nichols JA, Jackson TN, Necliudov PV, Shur MS (2006) An experimental study of contact effects in organic thin film transistors. J Appl Phys 100:024509
82. Klauk H, Schmid G, Radlik W, Weber W, Zhou L, Sheraw CD, Nichols JA, Jackson TN (2003) Contact resistance in organic thin film transistors. Solidstate Electron 47:297–301
83. Necliudov PV, Shur MS, Gundlach DJ, Jackson TN (2003) Contact resistance extraction in pentacene thin film transistors. Solidstate Electron 47:259–262
84. Stadlober B, Haas U, Gold H, Haase A, Jakopic G, Leising G, Koch N, Rentenberger S, Zojer E (2007) Orders-of-magnitude reduction of the contact resistance in short-channel hot embossed organic thin film transistors by oxidative treatment of Au-electrodes. Adv Funct Mater 17:2687–2692
85. Zaumseil J, Baldwin KW, Rogers JA (2003) Contact resistance in organic transistors that use source and drain electrodes formed by soft contact lamination. J Appl Phys 93:6117–6124
86. Bürgi L, Richards T, Chiesa M, Friend RH, Sirringhaus H (2004) A microscopic view of charge transport in polymer transistors. Synth Met 146:297–309
87. Bürgi L, Sirringhaus H, Friend RH (2002) Noncontact potentiometry of polymer field-effect transistors. Appl Phys Lett 80:2913–2915
88. Bürgi L, Richards TJ, Friend RH, Sirringhaus H (2003) Close look at charge carrier injection in polymer field-effect transistors. J Appl Phys 94:6129–6137
89. Luo Y, Gustavo F, Henry JY, Mathevet F, Lefloch F, Sanquer M, Rannou P, Grevin B (2007) Probing local electronic transport at the organic single-crystal/dielectric interface. Adv Mater 19:2267–2273
90. Nichols JA, Gundlach DJ, Jackson TN (2003) Potential imaging of pentacene organic thin-film transistors. Appl Phys Lett 83:2366–2368
91. Puntambekar KP, Pesavento PV, Frisbie CD (2003) Surface potential profiling and contact resistance measurements on operating pentacene thin-film transistors by Kelvin probe force microscopy. Appl Phys Lett 83:5539–5541
92. Hamadani BH, Natelson D (2005) Nonlinear charge injection in organic field-effect transistors. J Appl Phys 97:064508
93. Ishii H, Sugiyama K, Ito E, Seki K (1999) Energy level alignment and interfacial electronic structures at organic metal and organic organic interfaces. Adv Mater 11:605–625
94. Kahn A, Koch N, Gao W (2003) Electronic structure and electrical properties of interfaces between metals and p-conjugated molecular films. J Polym Sci B Polym Phys 41:2529–2548
95. Koch N (2007) Organic electronic devices and their functional interfaces. ChemPhysChem 8:1438–1455
96. Koch N, Kahn A, Ghijsen J, Pireaux JJ, Schwartz J, Johnson RL, Elschner A (2003) Conjugated organic molecules on metal versus polymer electrodes: demonstration of a key energy level alignment mechanism. Appl Phys Lett 82:70
97. Narioka S, Ishii H, Yoshimura D, Sei M, Ouchi Y, Seki K, Hasegawa S, Miyazaki T, Harima Y, Yamashita K (1995) The electronic-structure and energy-level alignment of porphyrin/metal interfaces studied by ultraviolet photoelectron-spectroscopy. Appl Phys Lett 67:1899–1901

98. Peisert H, Knupfer M, Schwieger T, Auerhammer JM, Golden MS, Fink J (2002) Full characterization of the interface between the organic semiconductor copper phthalocyanine and gold. J Appl Phys 91:4872–4878
99. Schroeder PG, France CB, Park JB, Parkinson BA (2002) Energy level alignment and two-dimensional structure of pentacene on Au(111) surfaces. J Appl Phys 91:3010–3014
100. Watkins NJ, Yan L, Gao Y (2002) Electronic structure symmetry of interfaces between pentacene and metals. Appl Phys Lett 80:4384–4386
101. Salaneck WR, Stafström S, Brédas JL (1996) Conjugated polymer surfaces and interfaces. Cambridge University Press, Cambridge
102. Bardeen J (1947) Surface states and rectification at a metal-semiconductor contact. Phys Rev 71:717–727
103. Cowley AM, Sze SM (1965) Surface states and barrier height of metal-semiconductor systems. J Appl Phys 36:3212–3220
104. Knupfer M, Paasch G (2005) Origin of the interface dipole at interfaces between undoped organic semiconductors and metals. J Vac Sci Technol A 23:1072–1077
105. Vazquez H, Dappe YJ, Ortega J, Flores F (2007) A unified model for metal/organic interfaces: IDIS, ‘pillow’ effect and molecular permanent dipoles. Appl Surf Sci 254:378–382
106. Vazquez H, Dappe YJ, Ortega J, Flores F (2007) Energy level alignment at metal/organic semiconductor interfaces: “Pillow” effect, induced density of interface states, and charge neutrality level. J Chem Phys 126:144703
107. Crispin A, Crispin X, Fahlman M, Berggren M, Salaneck WR (2006) Transition between energy level alignment regimes at a low band gap polymer-electrode interfaces. Appl Phys Lett 89:213503
108. Tengstedt C, Osikowicz W, Salaneck WR, Parker ID, Hsu CH, Fahlman M (2006) Fermi-level pinning at conjugated polymer interfaces. Appl Phys Lett 88:053502
109. Hu WS, Tao YT, Hsu YJ, Wei DH, Wu YS (2005) Molecular orientation of evaporated pentacene films on gold: alignment effect of self-assembled monolayer. Langmuir 21:2260–2266
110. Bock C, Pham DV, Kunze U, Kafer D, Witte G, Woll C (2006) Improved morphology and charge carrier injection in pentacene field-effect transistors with thiol-treated electrodes. J Appl Phys 100:114517
111. Bock C, Pham DV, Kunze U, Kafer D, Witte G, Terfort A (2007) Influence of anthracene-2-thiol treatment on the device parameters of pentacene bottom-contact transistors. Appl Phys Lett 91:052110
112. Kymissis I, Dimitrakopoulos CD, Purushothaman S (2001) High-performance bottom electrode organic thin-film transistors. IEEE Trans Electron Device 48:1060–1064
113. Campbell IH, Rubin S, Zawodzinski TA, Kress JD, Martin RL, Smith DL, Barashkov NN, Ferraris JP (1996) Controlling Schottky energy barriers in organic electronic devices using self-assembled monolayers. Phys Rev B Cond Matter 54:14321–14324
114. de Boer B, Hadipour A, Mandoc MM, Van Woudenbergh T, Blom PWM (2005) Tuning of metal work functions with self-assembled monolayers. Adv Mater 17:621–625
115. Asadi K, Gholamrezaie F, Smits ECP, Blom PWM, de Boer B (2007) Manipulation of charge carrier injection into organic field-effect transistors by self-assembled monolayers of alkanethiols. J Mater Chem 17:1947–1953
116. Marmont P, Battaglini N, Lang P, Horowitz G, Hwang J, Kahn A, Amato C, Calas P (2008) Improving charge injection in organic thin-film transistors with thiol-based self-assembled monolayers. Org Electron 9:419–424

Adv Polym Sci (2010) 223: 155–188
DOI:10.1007/12_2009_8
© Springer-Verlag Berlin Heidelberg 2009
Published online: 19 June 2009

# Low-Cost Submicrometer Organic Field-Effect Transistors

**Susanne Scheinert, Gernot Paasch, Ingo Hörselmann, and Andrei Herasimovich**

**Abstract** Low-cost fabrication of circuits with organic field-effect transistors (OFETs) as basic devices requires solution-based technologies. However, then the carrier mobility values can hardly exceed 0.01–0.1 $cm^2 V^{-1} s^{-1}$. For a cut-off frequency above 100 kHz to 1 MHz, relevant for broader applications, and an operation voltage below 10 V, the channel length of the transistors should be smaller than 1–10 μm. Considering inevitable parasitic capacitances one must envisage submicrometer channel lengths. Demonstrations of different patterning have so far realized neither resolution nor alignment accuracy desired, and photolithography is too costly for the submicrometer regime. Here, an overview is given of short-channel OFETs based on the definition of the submicrometer structures by undercutting, and preparation of the devices using additional simple steps of well established microelectronics technology without any of the costly steps such as high temperature treatments, high resolution lithography, and ion implantation.

**Keywords** OFET (organic field effect transistor) · Short channel transistor · Short channel effect · Underetching

## Contents

1 Introduction .......... 156
2 Analytical Estimates and Scaling .......... 157
3 Short-Channel OFETs .......... 162

S. Scheinert (✉), I. Hörselmann, and A. Herasimovich
Ilmenau Technical University, Institute of Solid State Electronics, PF 100565, D-98684 Ilmenau, Germany
e-mail:susanne.scheinert@tu-ilmenau.de

G. Paasch
Leibniz Institute for Solid State and Materials Research IFW Dresden, PF 270116, D-01171 Dresden, Germany
e-mail:g.pasch@ifw-dresden.de

4 Simulation Study of Short-Channel Effects ........ 163
5 Fabrication and Characterization of Low-Cost Short-Channel OFETs ........ 165
5.1 Technology Scheme with Definition of Submicrometer Channel Length by Undercutting ........ 165
5.2 Basic Experimental Results ........ 169
5.3 Characterization and Improvement of the Contact Structures ........ 172
5.4 Surface Modified Gate Insulator and TPD(4M)–MEH–PPV as Active Layer ........ 175
5.5 Future Prospects ........ 177
6 Conclusions ........ 181
References ........ 185


## 1 Introduction

In organic transistors on the basis of the field-effect at least the active layer is made from an organic semiconductor. The appearance of the field-effect in organic materials had already been proven in 1983–1984 [1, 2]. Soon the first transistors were reported with an organic layer on a $Si/SiO_2$-substrate [3–5]. Whereas in other work [3, 4] the active layer had been prepared by spin coating of the polymer polythiophene, an active layer of $\alpha -$ sexithienyl ($\alpha -$ 6T) has been prepared in [5] by evaporation. The transistors were designed as thin-film transistors (TFT), either with the source and drain contacts deposited directly onto the gate insulator ("bottom contact" structure – BOC, Fig. 1a), or after deposition of the active organic layer on top of this layer ("top contact" structure – TOC, Fig. 1b). Both types of structures are currently used. Differences in their performances have been clarified recently in both pure theoretical simulation studies [6] and simulations of prepared transistors [7]. In the first organic transistors the drain current increased with increasingly negative gate-source ($V_{GS}$) and drain-source ($V_{DS}$) voltages. Thus both materials are p-semiconductors. Already these first prepared organic transistors indicated a general trend: the hole mobility values are lower in the polymer layers deposited in a solution based technology than those in vapor deposited layers, $\approx 10^{-5}\,cm^2\,V^{-1}\,s^{-1}$ for polythiophene and $\approx 10^{-3}\,cm^2\,V^{-1}\,s^{-1}$ for $\alpha -$ 6T. Subsequently, fast progress has been achieved, especially in increasing the mobility, development of organic n-semiconductors, refinements of technological steps, and "all-polymer" variants, described in several review articles [8–16].

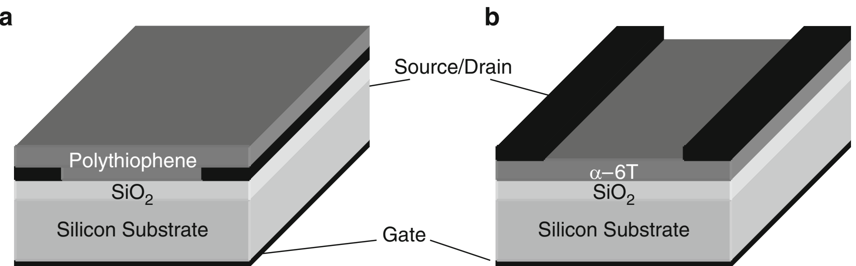


**Fig. 1** Schematic representation of the BOC structure applied in [3, 4] (**a**) and TOC structure applied in [5] (**b**)

Apart from the scientific interest in studying and understanding the properties of organic semiconductors, the widespread work on OFETs is motivated (and justified) by the expectation of polymer electronics-based products. Mechanical flexibility could be one advantage. However, a broader break-through can be expected only if production costs far below those for silicon devices can be achieved. From this point of view only solution-based technologies are of interest for application relevant developments. Thus the transistor performance will be limited by the mobility values which can be obtained in such layer deposition. Even with special surface modifications of the gate insulator, the upper limit for the mobility in a spin coated or printed layer will be of the order of $\mu \approx 0.01$ to $0.1\,\mathrm{cm^2\,V^{-1}\,s^{-1}}$. Another possibility to increase the drain current and the cut-off frequency of the transistor is the reduction of the channel length *L*. But again, relevance for real application also requires a method for patterning which is extremely cheap.

In order to quantify the expectations on the transistor, one should set some requirements. The most important ones are the following: (1) a low supply voltage is needed, at least below 10 V, which implies that (2) the threshold voltage should not exceed a few V, and (3) in addition the inverse subthreshold slope should be smaller than $1\,\mathrm{V\,dec^{-1}}$ for the desired on-off ratio larger than $10^4$. Moreover, the threshold voltage should be negative (positive) for p- (n-) channel transistors in order to avoid additional circuitry. Finally transistor operation requires a fairly good saturation behavior.

Thus, the goal of low-cost submicrometer channel length preparation must be seen in the context of all these requirements. Therefore, we summarize first in Sect. 2 analytical estimates, before giving in Sect. 3 a short literature survey on short-channel OFETs. Then in Sect. 4 a simulation study of short-channel effects is presented leading to guidelines for the short-channel design. In Sect. 5 a technology scheme is developed using undercutting as the basic step to define submicrometer channel length and employing inexpensive standard steps of microelectronics. Basic experimental results (with poly-(3-hexylthiophene) (P3HT) as the active layer) are presented and contact problems are analyzed by simulation and reduced by improved layer deposition. With another polymer (a modified poly(phenylene-vinylene)) and surface modification by hexamethyldisilazane (HMDS) a significantly higher mobility is achieved. Two methods for self aligned gate preparation have been realized experimentally. A complete "all-polymer" variant is not yet possible due to the lack of a suitable organic insulator thin enough to prevent short-channel effects.

## 2 Analytical Estimates and Scaling

Analytical approximations are helpful in order to estimate achievable device properties and to analyze measured current–voltage characteristics. Although MIS (metal insulator semiconductor) capacitors are also of interest, here only the basic analytical dependencies for OFETs, more specifically for TFTs, are compiled.

Starting at the beginning with a thick semiconductor layer and neglecting short-channel effects, one obtains the areal charge in the semiconductor with the Gauss law from the surface electric field (actually the field at the interface to the gate insulator) $E_s$ according to $Q'' = -\varepsilon_0 \varepsilon_s E_s$. It has been shown in [17] that even for Gaussian or exponential density of states the areal charge is given to a rather good approximation in the nondegenerate approximation. The dependence of the surface electric field $E_s$ on the surface potential $\varphi_s$ follows from the solution of the one-dimensional Poisson equation (perpendicular to the interface between semiconductor and gate insulator) as

$$E_s = \mathrm{sgn}(\varphi_s - \varphi_b)\sqrt{2}\frac{V_T}{L_D}\left(\cosh\frac{\varphi_s - \varphi_F}{V_T} - \cosh\frac{\varphi_b - \varphi_F}{V_T} + \frac{\varphi_s - \varphi_b}{V_T}\frac{N_A}{2n_i}\right)^{\frac{1}{2}} \tag{1}$$

with the temperature voltage $V_T = \mathrm{k}T/\mathrm{e}$, $L_D = \sqrt{\varepsilon_0 \varepsilon_s V_T / 2\mathrm{e} n_i}$ as the intrinsic Debye-length where $\varepsilon_s$ is the semiconductor dielectric constant, the intrinsic density $n_i = \sqrt{N_C N_V} \exp -E_G/2\mathrm{k}T$, and the bulk potential $\varphi_b$, which is connected with the doping by $\varphi_b = -V_T \ln N_A/n_i$. Here $E_G$ is the gap energy, $\varphi_F$ is the Fermi potential, $N_C$, $N_V$ are in the case of organics, instead of the effective densities of states, the monomer densities, and $N_A$ is the effective ionized acceptor doping level. A further equation follows from the voltage drop $V_{GS}$ over the full MIS structure as

$$E_s = \frac{\varepsilon_{is}}{\varepsilon_s}\frac{V_{GS} - V_{FB} - (\varphi_s - \varphi_b)}{d_{is}}. \tag{2}$$

Here, $\varepsilon_{is}$ and $d_{is}$ are the insulator dielectric constant and the thickness of the gate insulator, respectively. From both equations one obtains for a given gate voltage both the surface potential and the surface electric field (at the interface to the insulator). The flat band voltage $V_{FB}$ follows from the work function difference $\Phi_{MS}$ between the gate and semiconductor materials. In addition one has to take into account fixed interface charges (per unit area) $Q''_{if}$. Thus one has with the insulator capacitance per unit area $C''_{is}$ and $N''_{if}$ as the areal density of interface charges

$$V_{FB} = \Phi_{MS} - \frac{Q''_{if}}{C''_{is}} = \Phi_{MS} - \frac{\mathrm{e} N''_{if} d_{is}}{\varepsilon_0 \varepsilon_{is}}. \tag{3}$$

Organic transistors are thin-film transistors. In contrast to the most common inorganic field-effect transistors they operate in depletion (off-state) and accumulation (on-state). The current is determined by the gradient of the quasi-Fermi potential $\varphi_{Fp}$ along the channel. Thus, one can write, e.g., for a p-channel transistor of width $w$

$$I = -\mu_p w Q''_p(x)\frac{d\varphi_{Fp}}{\mathrm{d}x} \qquad \text{with} \qquad Q''_p(x) = Q''(x) + \mathrm{e} N_A d, \tag{4}$$

where $\mu_\mathrm{p}$ is the hole mobility. In this equation the areal charge $\mathrm{e}N_\mathrm{A}d$ corresponds to the hole concentration as determined by the doping in the layer of thickness $d$, which is by $Q''(x)$ according to Eq. (4) enhanced (accumulation) or reduced (depletion). This leads to

$$Q''_\mathrm{p}(x) \approx -C''_\mathrm{is}\{(V_\mathrm{GS}-V_\mathrm{th})-\varphi_\mathrm{Fp}(x)\} \qquad \text{with} \qquad V_\mathrm{th} = V_\mathrm{FB} + \frac{\mathrm{e}N_\mathrm{A}d}{C''_\mathrm{is}} - 2\varphi_\mathrm{b}\,. \quad (5)$$

With this equation in Eq. (4) and integrating from source to drain one obtains the Shockley-model

$$I_\mathrm{D} = \mu\frac{w}{L}C''_\mathrm{is}\left[(V_\mathrm{GS}-V_\mathrm{th})V_\mathrm{DS} - \frac{1}{2}V_\mathrm{DS}^2\right] \qquad V_\mathrm{DS} < V_\mathrm{GS} - V_\mathrm{th},$$

$$I_\mathrm{D} = \mu\frac{w}{L}C''_\mathrm{is}\frac{1}{2}(V_\mathrm{GS}-V_\mathrm{th})^2 \qquad V_\mathrm{DS} > V_\mathrm{GS} - V_\mathrm{th}\,. \quad (6)$$

$V_\mathrm{DS}$ and $V_\mathrm{th}$ are the drain-source voltage drop and the threshold voltage, respectively. However, for a layer thickness $d > l_\mathrm{dep}$ (the depletion length $l_\mathrm{dep} = \sqrt{2\varepsilon_0\varepsilon_s 2|\varphi_\mathrm{b}|/\mathrm{e}N_\mathrm{A}}$ is determined by the doping) one has to take into account that the layer is not completely depleted and the remaining ohmic contribution to the current

$$I_\Omega = \mathrm{e}\,\mu_\mathrm{p}N_\mathrm{A}^- \frac{w(d-l_\mathrm{dep})}{L}V_\mathrm{DS} \quad (7)$$

determines the device. Thus, for achieving the off-state and the saturation region of the transistor the layer thickness must be smaller than the depletion length determined by the (unintentional) doping. Moreover, in the design of the transistor one has to take into account that for many applications supply voltages below 10 V and clock frequencies in the region of 100 kHz ... 10 MHz are of interest. The resulting requirements on the material and device parameters will be estimated in the following. A more detailed model for the thin-film transistor is given in the Appendix.

In order to realize low control (5 ... 10 V) voltages one needs both a low threshold voltage and a low inverse subthreshold slope. In the determination of the threshold voltage for a thin layer, $d < l_\mathrm{dep}$, one has to consider that neutrality ($\varphi = \varphi_\mathrm{b}$) cannot be achieved. This modifies of course the operation of the transistor and especially the threshold voltage Eq. (5) will be modified. The derivation in the Appendix leads to

$$V_\mathrm{th} = V_\mathrm{FB} + \frac{\mathrm{e}N_\mathrm{A}d}{C''_\mathrm{is}} - 2\varphi_\mathrm{b}\left(\frac{d}{l_\mathrm{dep}}\right)^2 \qquad \text{for} \qquad d < l_\mathrm{dep}\,. \quad (8)$$

The validity of this expression is proven in the Appendix by comparison with numerical 2D simulations. The dependence of the threshold voltage on different parameters is depicted in Fig. 2 for a transistor with the organic insulator poly-(4-vinylphenol) (P4VP) ($\varepsilon_\mathrm{P4VP} = 2.56$), P3HT as the active layer ($E_\mathrm{G} = 2\,\mathrm{eV}$, $\chi = 3\,\mathrm{eV}$, $\varepsilon_\mathrm{P3HT} = 3.24$) and a gate with the work function $\Phi_\mathrm{M} = 5\,\mathrm{eV}$. For the determination

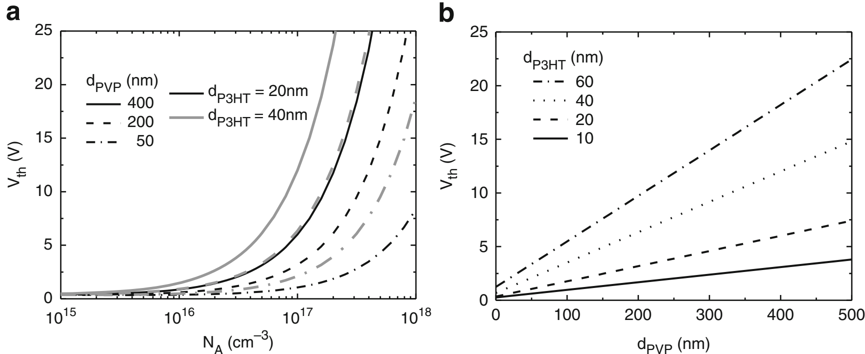


**Fig. 2** Threshold voltage (8) as a function of doping concentration (**a**) and thickness of the organic insulator for a doping concentration of $N_A = 10^{17}\,\text{cm}^{-3}$ (**b**)

of the flat band voltage it has been assumed that $N''_{\text{if}} = 0$. It is visible that the threshold voltage is positive for all chosen parameters since a negative contribution in Eq. (8) can arise only from the flat band voltage. Since in the p-channel transistor accumulation is achieved by applying a negative gate voltage, $V_{\text{th}} \approx 0\,V$ would be favorable, which requires (see Fig. 2a) low doping $N_A < 10^{16}\,\text{cm}^{-3}$. Such low values can be achieved usually only with low molecular weight materials. Polymers as deposited from solution exhibit often an (unintentional) doping of the order $10^{17}\,\text{cm}^{-3}$. Then the threshold voltage can be reduced only by reducing the layer thicknesses of both the active layer and the gate insulator (see Fig. 2b). In addition, one has to consider the influence of fixed interface charges on the threshold voltage. For negative (positive) charges of the concentration $N''_{\text{if}} = 10^{12}\,\text{cm}^{-2}$ one obtains from Eq. (3) a positive (negative) shift of the flat band voltage of $3.5\,\text{V}\,(21\,\text{V})$ for a thickness of the organic insulator of $50\,\text{nm}\,(300\,\text{nm})$. This demonstrates clearly the importance of realizing rather thin insulators.

For the optimal thickness of the active layer one has essentially the requirement that full depletion can be achieved, $d < l_{\text{dep}}$. For the usually high doping level this is already a strong requirement. A lower limit for the thickness of the active layer cannot be given formally. It is mainly determined by the necessity to achieve in the deposition a closed layer.

In the range $V_{\text{GS}} < V_{\text{th}}$, the inverse subthreshold slope $S$ is defined as the variation of the gate voltage for a variation of the current by one decade. From the current equation in this region one obtains [18]

$$S = \frac{\partial V_{\text{GS}}}{\partial \lg(I_D/\text{A})} = V_T \ln 10 \left(1 + \frac{C_d + C_{\text{it}}}{C_{\text{is}}}\right), \tag{9}$$

where $C_d = \varepsilon_0 \varepsilon_s A / l_{\text{dep}}$ is the depletion capacitance which is determined by the doping and rechargeable bulk traps, $C_{\text{is}}$ is the insulator capacitance, and $C_{\text{it}}$ is the capacitance due to rechargeable interface traps. For thin active layers and thin gate

insulators the minimum value at room temperature is $S \approx V_\mathrm{T} \ln 10 = 60\,\mathrm{mV\,dec}^{-1}$. But for organic thin-film transistors one often has experimental values in the region of several $\mathrm{V\,dec}^{-1}$ [19–22]. According to Eq. (9) this strong deviation will be caused either by bulk or by interface traps. This has been proven directly by numerical simulations [21, 22].

As a measure for the achievable working frequency one can use the cut-off frequency $f_\mathrm{T} = g_\mathrm{m}/(2\pi C_\mathrm{GS})$ as the frequency at which the current gain becomes unity. The maximum value is determined by the transconductance $g_\mathrm{m} = \partial I_D/\partial V_\mathrm{GS}|_{V_\mathrm{DS}}$ of the transistor, and the gate-source capacitance $C_\mathrm{GS}$, which is larger than the insulator capacitance due to parasitic capacitances, i.e., $C_\mathrm{GS} \geq C''_\mathrm{is} wL$. One obtains

$$f_\mathrm{T} \leq \frac{1}{2\pi} \frac{g_\mathrm{m}}{C''_\mathrm{is} wL} = \frac{\mu}{2\pi L^2} V_\mathrm{GS,eff}, \qquad V_\mathrm{DS} = V_\mathrm{GS,eff} = V_\mathrm{GS} - V_\mathrm{th}\,. \tag{10}$$

Requirements for the transistor following from this equation are clearly visible in Fig. 3. Frequencies in the desired range for a channel length of $L < 1\,\mu\mathrm{m}$ can only be realized for mobility values $\mu > 0.1\,\mathrm{cm}^2\,\mathrm{V}^{-1}\,\mathrm{s}^{-1}$. Active layers prepared from solution usually have mobilities in the range $10^{-4}\,\mathrm{cm}^2\,\mathrm{V}^{-1}\,\mathrm{s}^{-1} < \mu < 10^{-2}\,\mathrm{cm}^2\,\mathrm{V}^{-1}\,\mathrm{s}^{-1}$. Even refined treatments of the insulator interface yield slightly larger values but only under special preparation conditions which can hardly be achieved under low-cost conditions. Therefore, realistically, channel length in the submicrometer range will be needed. Apart from the problems of low-cost fabrication of circuits with submicrometer transistors, there occurs in addition the problem that short-channel effects

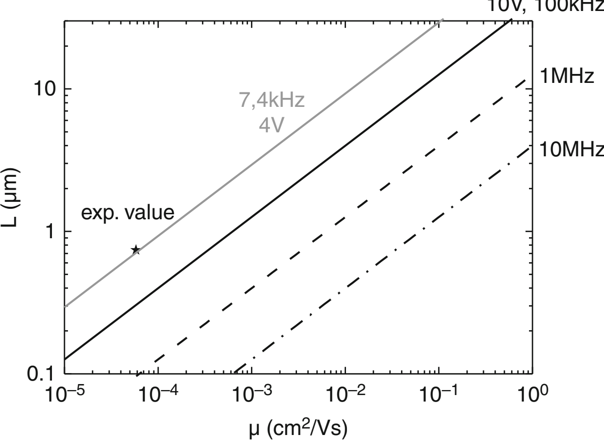


**Fig. 3** Channel length as function of the mobility leading for a given effective voltage of 10V to three different cut-off frequencies-100 kHz, 1 MHz, and 1 MHz. Also one experimental value for our fabricated submicrometer OFET is depicted together with the dependence Eq. (10) for the corresponding voltage and maximum cut-off frequency. Figure taken from [15]

become increasingly important. This problem will be analyzed in Sect. 4. But before, in Sect. 3 a short overview is given of published attempts to overcome the problems outlined earlier.

## 3 Short-Channel OFETs

It has been demonstrated in the preceding section that large cut-off frequencies require either an active material with a high carrier mobility or transistors with a short channel. Organic short-channel transistors with $SiO_2$ or surface-modified $SiO_2$ as gate insulator have been described in [23–36]. However, most of the groups used the costly electron beam lithographic process for the patterning of the source/drain electrodes [26–28, 30, 32–36]. Rogers et al. applied near-field photolithography combined with microcontact printing to realize an OFET and inverter with a channel length of 0.1 µm. Extreme short-channel lengths of 70 nm [25] have been prepared by using nanoimprint lithography (NIL). However, the patterning of the mold requires high resolution electron beam lithography. The advantage of this technique is the possibility of large area, parallel, and arbitrarily complex submicron patterning [25]. In [29] the channel length of 500 nm was prepared by a Si-etching method. However, the output characteristics do not show saturation because of the relative great thickness of the gate insulator ($d_{ox} = 100$ nm). As described in [33], to achieve saturation a ratio of channel length to oxide thickness of 5:1 is necessary.

Alternative insulators have been used for short-channel transistors in [37–41]. Self-assembled monolayers (SAM) with thicknesses in the range of 1.9–2.6 nm serve as insulator in [37]. But the channel is prepared by using electron beam lithography. In [38] an inexpensive embossing technique is presented and transistors with a channel length of approximately 900 nm and a 700 nm thick organic gate insulator have been prepared. But the measured output characteristics do not approach saturation even at rather high drain-source voltages. It will be demonstrated in the next section that such behavior is a result of so-called short-channel effects. Transistors with channel lengths down to 250 nm were prepared with a 1-µm dielectric P4VP combining nanoimprint lithography and inkjet printing [39]. But, as in the previous case, there is no saturation for the transistor with the shortest channel with such a thick insulator. To reduce the short-channel effects an additional $SiO_2$ barrier in between source and drain electrodes was incorporated [40], resulting in better behavior. Nevertheless, the inverse subthreshold increase is very high in both cases. The nanoimprint lithography was also applied for the preparation of 500-nm transistors with an 85 nm thick benzocyclobutene (BCB) insulator [41]. The relatively high temperature necessary for the baking process of the insulator is a problem. Nevertheless, a perfect saturation could be observed for the prepared transistors with evaporated pentacene.

We fabricated organic transistors with channel lengths $L < 1$ µm using only a few simple technological steps which are used in microelectronics [42, 43]. In order to avoid short-channel effects from the very beginning, necessary design parameters have been estimated by numerical two-dimensional simulations.

## 4 Simulation Study of Short-Channel Effects

Two-dimensional simulations have been carried out using the standard drift-diffusion model implemented in the numerical program DESSIS [44]. The program solves simultaneously the Poisson equation for the electrical potential and the continuity equations for the hole and electron densities. Generally, any low-cost preparation route for short-channel transistors should use a gate dielectric also made from a solution processable organic material. Therefore, in the simulations for the BOC structure (see Fig. 1b) we used the material parameters of the organic insulator P4VP, i.e., a dielectric constant of $\varepsilon_{\mathrm{P4VP}} = 2.56$. The material parameters used for P3HT are the effective densities of states $N_\mathrm{C} = N_\mathrm{V} = 10^{21}\,\mathrm{cm}^{-3}$ [15], a relative dielectric constant $\varepsilon_\mathrm{r} = 3.24$, an affinity of $\chi = 3\,\mathrm{eV}$, and a gap of $E_\mathrm{G} = 2\,\mathrm{eV}$. For the mobility we use here a constant value of $\mu = 10^{-3}\,\mathrm{cm}^2\,\mathrm{V}^{-1}\,\mathrm{s}^{-1}$. Recent theoretical work has been concentrated on the dependence of the mobility on the carrier concentration and on the field [45–49]. Indicative of the dependence on the carrier concentration is a stronger than linear increase of the transfer characteristics in the active region. Such dependence was untypical for the prepared short channel transistors. Therefore we preferred to use a constant mobility. Moreover, our recent simulation study [50] comparing different kinds of such mobility models for different transistor designs has shown the difficulty in deciding which of the models is relevant for a given material. Nevertheless, future simulations of short-channel transistors should include the field dependence of the mobility. The thickness of the active P3HT layer has been chosen sufficiently small ($d_{\mathrm{P3HT}} = 30\,\mathrm{nm}$) in order to ensure full depletion for the assumed doping concentration of $N_\mathrm{A} = 10^{16}\,\mathrm{cm}^{-3}$ leading to a real off-state and to saturation at higher drain voltages. The work functions of source, drain, and gate has been chosen as 5 eV. The channel length has been varied between $L = 5\,\mu\mathrm{m}$ and $L = 300\,\mathrm{nm}$. Simulated current–voltage characteristics for such variations are depicted in Fig. 4 for an insulator thickness

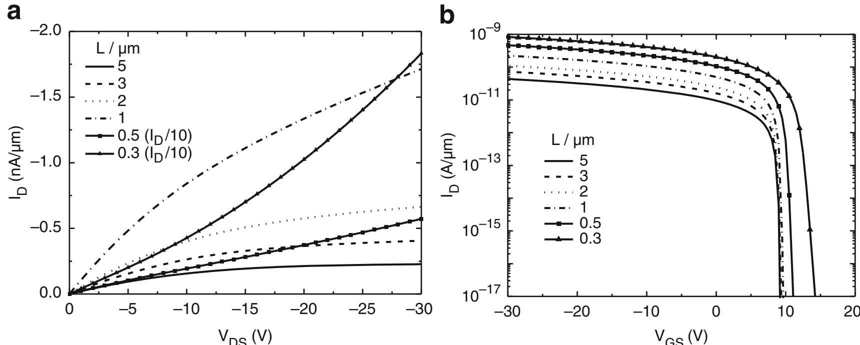


**Fig. 4** Simulated current–voltage characteristics (current per unit channel width) for $-10\mathrm{V}$ gate-source voltage in the output characteristics (**a**) and $-1\mathrm{V}$ drain-source voltage in the transfer characteristics (**b**) for a doping concentration of $N_\mathrm{A} = 10^{17}\,\mathrm{cm}^{-3}$. For a 400 nm thick P4VP gate insulator the channel length is varied as indicated. Figure taken from [15]

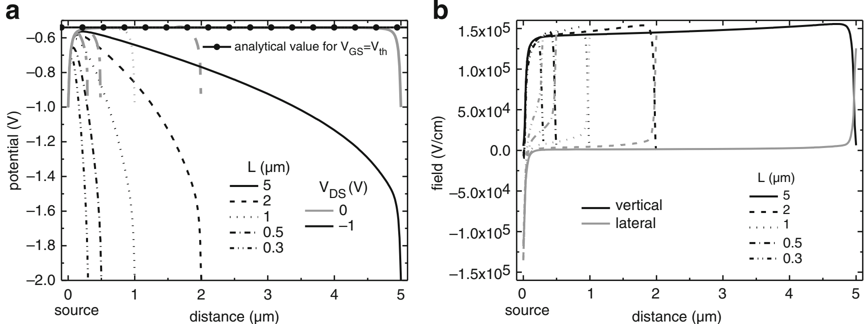


**Fig. 5** Potential profiles for two drain voltages $V_{DS} = 0$V and $V_{DS} = -1$ V (**a**) and the field components for $V_{DS} = -1$ V (**b**) from source to drain 1nm below the interface to the insulator for a gate voltage of $V_{GS} = 8$ V for the devices of Fig. 4. Figure 5a taken from [15]

of $d_{P4VP} = 400$ nm. The output characteristics show a transition into saturation for channel length $L > 1$ µm. But the current increases more strongly than linearly for the two shortest channels. From the transfer characteristics for the transistors with channel lengths 5 ... 1 µm one can extract a threshold voltage of about $V_{th} = 9$ V, a value which is close to the 8.9 V obtained from Eq. (8). With a further reduction in the channel length the simulated threshold voltage increases and reaches $V_{th} \approx 13$ V for the 0.3-µm long-channel transistor.

The origin of such behavior can be understood from the profiles of potential and electric field which are depicted in Fig. 5 for a gate voltage near the threshold voltage. For transistors with the longer channels the potential remains constant along the channel for $V_{DS} = 0$V except for variation near the contact caused by the high contact work functions. The value of the potential within the channel $\varphi_s = -0.541$V corresponds to the value following from inserting Eq. (8) into Eq. (17), with the assumption $Q_p'' = 0$ for $V_{GS} = V_{th}$, resulting in

$$\varphi_s^{th} = \varphi_b - 2\varphi_{bp}\left(\frac{d_{P3HT}}{l_{dep}}\right)^2 . \tag{11}$$

In contrast, for shorter channels, $L < 1$ µm, the potential maximum is reduced leading to an enhanced hole concentration in the channel. For longer channels, the potential maximum is reduced only slightly to $\varphi_s \approx -0.56$ V with increasing drain voltage. That means the source-bulk barrier is almost independent of the drain voltage. But for the transistor with the channel length $L = 0.3$ µm this barrier is significantly lowered ($\varphi_s \approx -0.73$ V in the maximum). Hence one needs a much higher voltage for switching off the transistor. The origin of this effect, known as DIBL- (drain induced barrier lowering), can be understood from the vertical and lateral electrical field strengths. Whereas the maximum vertical field of about $10^5$ V cm$^{-1}$ is almost independent of the channel length, this is not the case for the lateral field. For the longer channels the lateral field has an almost constant value of the order $10^3$ V cm$^{-1}$. In the shortest transistor the lowest value of the lateral field in the

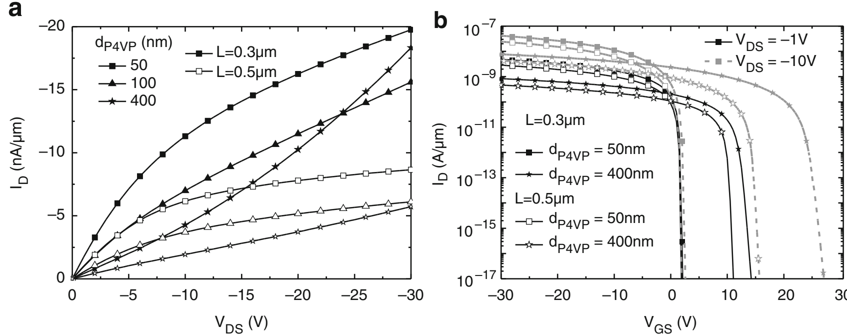


**Fig. 6** Simulated output characteristics for $V_{GS} = -10$V (**a**) and transfer characteristics for the given drain voltages (**b**) for the two channel length 0.5 μm (*open symbols*) and 0.3 μm (*filled symbols*). The gate insulator thickness is varied as indicated. Further parameters: *p*-doping $10^{17}$ cm$^{-3}$ of the 30 nm P3HT layer, mobility $\mu = 10^{-3}$ cm$^2$ V$^{-1}$ s$^{-1}$. Figure 6 a taken from [15]

middle of the channel of about $10^4$ V cm$^{-1}$ is already comparable with the vertical field. Therefore, in contrast to the idealized assumptions, the potential and hence the hole concentration depend not only on the gate voltage but also on the drain voltage.

In order to avoid this short-channel effect, one has to increase the vertical field. This can be achieved by using a thinner gate insulator. The influence of the insulator thickness on the transistor performance is demonstrated in Fig. 6 for the two transistors with submicrometer channel length. With decreasing thickness of the P4VP insulator the transition into saturation is achieved again in the output characteristics, now at higher currents, although the current is still increasing for the 0.3 μm transistor. It becomes clear from the logarithmic representation of the transfer characteristics that, for the thin insulator of $d_{P4VP} = 50$ nm, the threshold voltage becomes independent of the channel length and of the drain voltage. This way one can avoid the DIBL effect.

Another way to avoid the short-channel effect is to use a Schottky contact at drain, as proposed in [51]. However, our simulation has shown that this is connected with a strong reduction of the drain current [52]. Therefore, this approach must be excluded for practical applications.

## 5 Fabrication and Characterization of Low-Cost Short-Channel OFETs

### *5.1 Technology Scheme with Definition of Submicrometer Channel Length by Undercutting*

Since in solution-based preparations the mobility in the active polymer layer cannot be increased above some limit, the aim of higher cut-off frequencies requires a drastic reduction of the channel length below 1 μm. As has been shown in the numerical

simulations in the preceding Sect. 4, the thickness of the gate insulator should then be below about 50 nm (for the value of the dielectric constant of a typical organic insulator). But in spite of much effort, such thin organic insulators with a high breakthrough electric field of the order $10^6\,\mathrm{V\,cm^{-1}}$ at sufficiently low leakage currents, as needed in the field-effect transistor, are even now not available. Consequently, instead of an "all-polymer" submicrometer OFET, the decision in [42] was to begin with a hybrid design. A highly doped $n^+$-silicon wafer was used as the gate with a 30 nm thick $SiO_2$-layer as insulator and BOC-transistors of the schematic cross section depicted in Fig. 1b were prepared. The main effect used for the definition of submicrometer channel length is undercutting which is a well known phenomenon in microelectronics (leading there to an increased effective channel length). It is combined with low-resolution photolithographic steps and a few simple standard processes of microelectronics. The preparation is carried out without any of the expensive microelectronics processes. In particular, no high-temperature processes, no ion implantation, and no high-resolution photolithography are used.

The technological steps are sketched schematically in Fig. 7 [42, 43]. As a first step a large-area gold layer of about 50 nm thickness is sputtered onto the $SiO_2$ insulator covering the highly doped oxidized silicon wafer. Then a positive photoresist is spin coated and structured with low resolution photolithography (Fig. 7a). Next the gold is removed by a wet chemical etching and undercutting (underetching) (Fig. 7b) using potassium iodide/iodine ($KII_2$). Since the undercutting will determine the channel length this process has been investigated in detail. The etch rate has been investigated not only on the wafer covered with silicon dioxide but also on plastic substrates. With the $SiO_2$ surface short etching times $<10\,\mathrm{s}$ were needed in order to realize channel length below 1 μm; details will be presented below. The following step is a large-area evaporation of a 10 nm thick chromium and a 40 nm

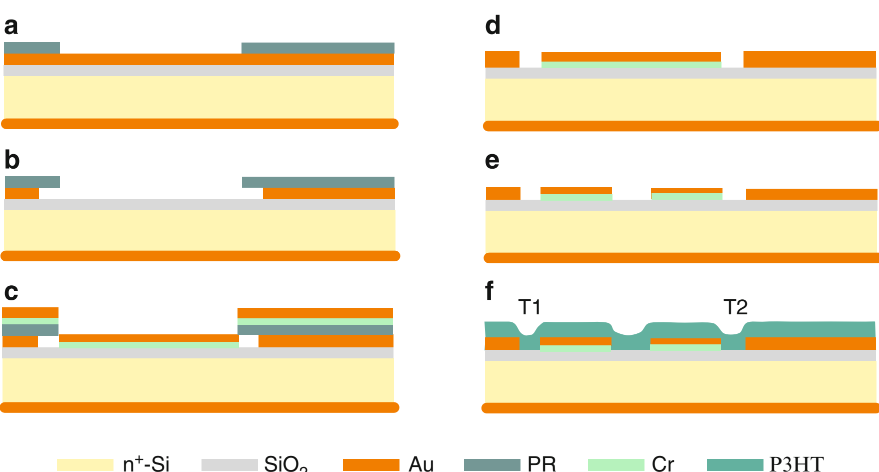


**Fig. 7** Fabrication steps for the short-channel OFET (**a**)–(**e**) and cross section of two transistors T1 and T2 (**f**). Figure taken from [42]

thick gold layer (Fig. 7c) whereby the first one is used to improve the adhesion of the gold layer on the $SiO_2$ surface. The following lift-off process removes the remaining photoresist and the chromium–gold layer on top of it. This leads to the structure shown in Fig. 7d. The depicted detail shows two channels of the transistors T1 and T2 with the contacts (the contacts are alternately made from the sputtered gold and from the evaporated chromium–gold layer) and the channel length determined by the undercutting. The chromium–gold contact in the middle is separated into two contacts by applying again low-resolution photolithography and a subsequent etch step. This leads to the structure shown in Fig. 7e with separate source and drain contacts for both transistors T1 and T2. Then as the active layer of the transistor a polymer is spin coated onto the whole structured surface (Fig. 7f). In the first experiments an approximately 30 nm thick P3HT-layer has been used. The final separation of the transistors T1 and T2 is possible with reactive ion etching (RIE). But in the first phase of the experiments, in order to avoid a possible influence of this process, separation has been achieved simply by mechanical scratching. The final position of source and drain contacts and of the channel, in this case of a width of 200 μm, is demonstrated in an optical micrograph (Fig. 8; [42]). The mask layout for the photolithographic processes was such as to realize channel widths in the range between 200 and 2,000 μm.

A prepared source-drain structure with a channel of the length 800 nm in between the contacts is visible in the scanning electron microscopy (SEM) image (Fig. 9a). The uniformity of the channel is remarkable and the variation of the prepared channel length remains small over the channel width. However, it is also visible that the contact prepared by the undercutting process shows some roughness which might influence the transistor performance. Corresponding modifications of the preparation route will be presented below in Sect. 5.3. The SEM image of Fig. 9b shows a cross section of a prepared structure and is taken after a focused ion beam cut. The lower part of this figure shows a schematic view of this image. On the image one can clearly identify (from bottom to top) the silicon wafer, the silicon dioxide layer, and the two contacts separated from each other by the channel. Visualizing the active polymer (P3HT) layer is difficult in the SEM image. Therefore the complete structure has been covered with an additional evaporated gold layer. The thin gray line in the image separates clearly the upper gold layer from both the gold contacts and the silicon dioxide in the channel region, proving the presence of the closed P3HT

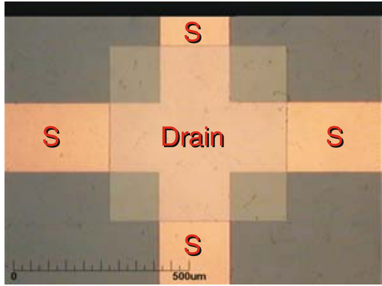


**Fig. 8** Optical micrograph of the transistors with $L = 1$ μm. In the figure, four channels are situated between the drain and source (S) regions. Figure taken from [42]

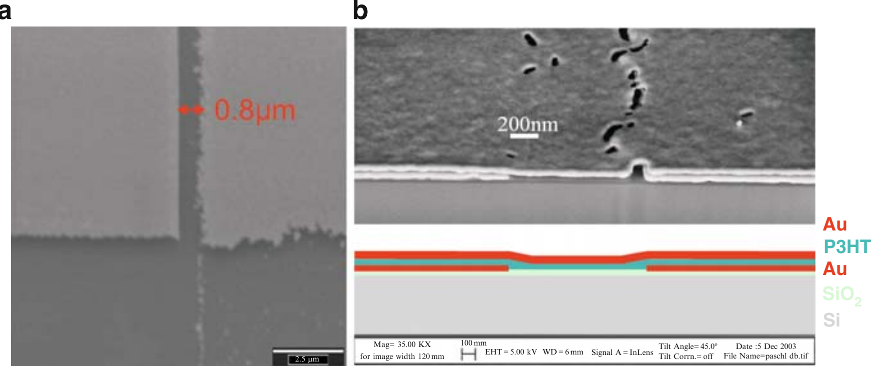


**Fig. 9** SEM image of a transistor with a channel length of 800 nm (**a**) and of a transistor after a focused ion beam cut (**b**). The lower part of (**b**) shows the layers schematically; the top gold layer has been deposited additionally in order to visualize the presence of the P3HT layer

**Fig. 10** Channel length as a function of the etching time for different substrates

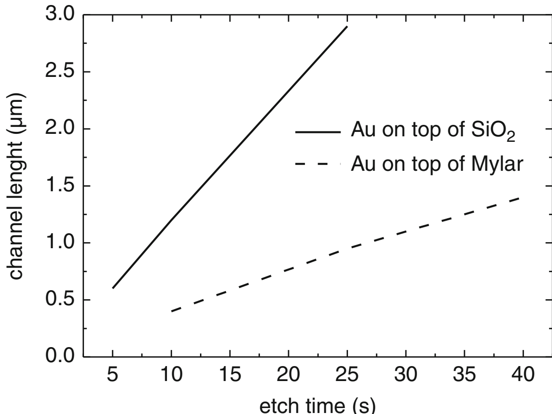


layer. It should be mentioned that this transistor has been electrically characterized showing a good performance, before the further preparation with the FIB cut has been carried out.

Before presenting electrical characterizations of prepared transistors, we return briefly to the etching process. For a wider application one has to be sure that the channel length resulting from undercutting can be controlled precisely. This is indeed the case. For the hybrid structure with the silicon dioxide covered silicon wafer serving as gate the dependence of the resulting channel length in the range from ≈600 nm to ≈3 µm is depicted in Fig. 10. Even for the shorter channel an etching time of about 5 s can be controlled precisely. Although an "all-polymer" type of transistor could not yet be completely prepared (lacking a sufficiently thin solution processed organic insulator), it is important to check whether the undercutting process is also working in this case. Here, the desired structure is based on a plastic substrate, with source and drain on it, and subsequently deposited active layer,

organic gate insulator, and gate. Thus the undercutting process was investigated on mylar as the plastic substrate. As seen in Fig. 10, the process can be even better controlled since larger etching times are needed.

## 5.2 Basic Experimental Results

In this section two examples of the output and transfer characteristics of prepared transistors will be discussed. Both transistors have been prepared independently with different masks on different wafers.

In Fig. 11 the measured output and transfer characteristics are depicted for a short-channel transistor with channel length $L = 880\,\text{nm}$, width $w = 2{,}000\,\mu\text{m}$, and an active 30 nm P3HT layer. These dependencies indicate a high performance. In particular, it should be mentioned that the transistor operates at the desired low voltage below 5 V. The clear transition of the output characteristics into saturation in this voltage range shows that short-channel effects are successfully suppressed in the device by the chosen design. The transfer characteristics show in the active region an almost linear dependence, indicating that contact resistances are negligible. The on–off ratio is larger than $10^4$ and the inverse subthreshold slope of $\approx 400\,\text{mV}\,\text{dec}^{-1}$ is rather small. Often in OFETs, observed large values of several $\text{V}\,\text{dec}^{-1}$ cannot be caused solely by the insulator thickness. Trap recharging is a possible reason for large values of the inverse subthreshold slope [21, 22]. The small value obtained here may indicate that trap recharging is less important. Indeed the regioregular P3HT used was a purified one (Dr. S. Janietz, IAP Golm, Germany). On the other hand, purification also reduces the mobility. This has been repeatedly shown experimentally by us. Examples can be found in [53]. The origin lies in the reduction of the

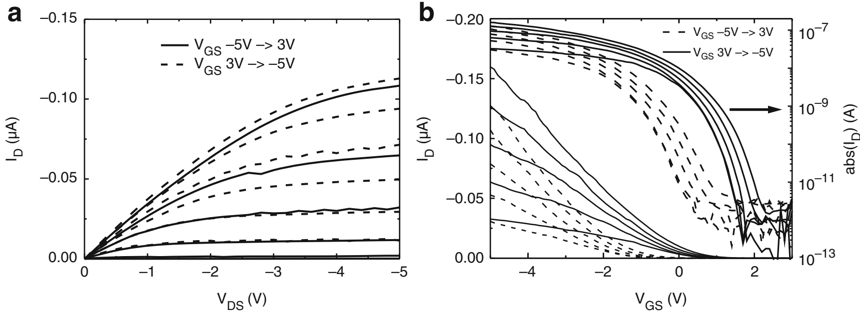


**Fig. 11** Output (**a**) and transfer characteristics on a linear and logarithmic scale (**b**) for a P3HT OFET with $L = 0.88\,\mu\text{m}$, $w = 2{,}000\,\mu\text{m}$. For the output characteristics the gate-source voltage is varied as $-5\,(1)\,3$ V and back as $3\,(-1)-5$ V; depicted are the curves between $-5$ and 0 V. For the transfer characteristics the drain-source voltage is varied as $-7\,(1)-1$ V. For each $V_{\text{DS}}$ the gate-source voltage is varied from $V_{\text{GS}} = -5$ to 3 V and back from 3 to $-5$ V. Figure taken from [42]

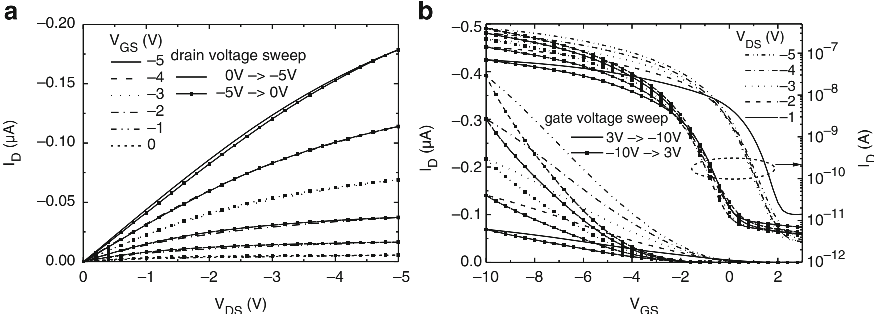


**Fig. 12** Output (**a**) and transfer characteristics on a linear and logarithmic scale (**b**) for a P3HT OFET with $L = 740$ nm, $w = 1{,}000\,\mu$m and the given sweep directions. Figure 12a taken from [42]

unintentional doping occurring during the syntheses. The change of the doping level has been determined by analyzing capacitance–voltage measurements. A short theoretical consideration is given in [15]. In addition, no special treatments for higher order of the active polymer layer have been used. This explains the relatively low mobility of $3 \times 10^{-5}\,\text{cm}^2\,\text{V}^{-1}\,\text{s}^{-1}$. Both the output and transfer characteristics show a clear hysteresis which is often observed in OFETs. A detailed analysis of the present knowledge of this type of hysteresis is given in [15, 54].

In Fig. 12 the output and transfer characteristics are shown for a short-channel transistor with channel length $L = 740\,\text{nm}$ and width $w = 1{,}000\,\mu\text{m}$ and an active layer made from P3HT. The output characteristics show a clear saturation behavior for low drain voltages consistent with the considerations in the preceding sections, though it is less pronounced than in the former case. The drain currents for the different sweep directions indicate that in this case practically no hysteresis occurs when the drain voltage is varied. In contrast, the variation of the gate voltage leads in the transfer characteristics to a clearly visible hysteresis. Furthermore, the linear dependence on the drain voltage in the output characteristics and on the gate voltage in the transfer characteristics in the active transistor region indicates an almost ideal performance which is not strongly influenced by source/drain contact problems. We mention here that this is not the case in all prepared transistors. Though the mobility, estimated from the active transistor region is rather low, $5.8 \times 10^{-5}\,\text{cm}^2\,\text{V}^{-1}\,\text{s}^{-1}$, due to the high $w/L$-ratio one can achieve currents which are relevant for practical applications. In addition, the apparent mobility can be increased by a silanization of the insulator interface which will be discussed below. From the logarithmic representation of the transfer characteristics one gets the rather low inverse subthreshold slope of $0.73\,\text{V}\,\text{dec}^{-1}$ and at the same time the high on–off-ratio of about $10^4$. Moreover, this representation also shows clearly (with the exception of the first measurement, full line for $V_{DS} = -1\,\text{V}$) that the currents in the subthreshold regime do not depend on the drain voltage, short-channel effects are suppressed by the thin insulator, and variations in the subthreshold region should be connected with hysteresis.

For practical applications in circuits, besides a well defined off-state one also needs a high cut-off frequency. As outlined in Sect. 2, this frequency is

approximately given by $f_T = g_m/2\pi C_{GS}$. From the derivative of the transfer characteristic one obtains for $V_{DS} = -4$ V the maximum transconductance of $g_m = 3.96 \times 10^{-8}$ S. With the simplified assumption that $C_{GS} = C_{is}$, one obtains a cut-off frequency of 7.4 kHz. This is the reason why in Fig. 3 the theoretical curve for this frequency is also shown. The value following from channel length and mobility of this transistor lies near the curve for 7.4 kHz. This result shows clearly that one can indeed estimate the needed channel length for a known mobility from the simple equation. However, the measurable cut-off frequency is determined not only by the insulator capacitance but in addition by parasitic capacitances. In the first design of the short-channel transistors the large source/bulk and drain/bulk overlap capacitances lead to a drastic reduction of the cut-off frequency. Possibilities to reduce these capacitances will be discussed below in Sect. 5.5.

In the two examples presented above, in the output characteristics the current increases linearly for low drain voltages as in an ideal transistor. This was not the case in all prepared transistors. In the next example a deviation from this behavior will be demonstrated which is connected with the Cr/Au double layer of one of the contacts. Figure 13 shows the measured output characteristics and the resulting drain conductance of a transistor with $L = 1$ µm and the Cr/Au-contact either as source or as drain. The drain current is higher if the double layer contact acts as drain. Moreover, in both cases one has for low drain voltages a nonlinear increase of the current with a positive curvature. This leads in the drain conductance to a maximum at finite drain voltages. It can be seen in Fig. 13b that the maximum occurs at higher drain voltages if the Cr/Au contact serves as source. Such a nonlinearity is known for organic transistors from the literature [25, 56, 57] although in [56] Cr/Au-electrodes are described as good contacts for source and drain in P3HT transistors. In [57] Ti/Au-contacts with different thickness of the titanium layer have been investigated. The resulting variations of the increase of the current were attributed to an additional series resistance between the gold layer and the channel. Simulations were carried

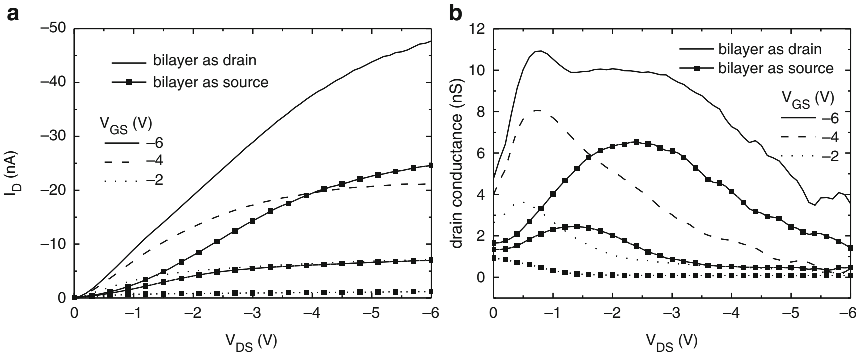


**Fig. 13** Measured output characteristics (**a**) and drain conductance (**b**) for a P3HT transistor with $L = 1$ µm and $w = 500$ µm and the bilayer contact as drain and interchanged contacts. Figure taken from [55]

out in order to clarify the observed peculiarity and will be presented in the following section. The resulting modification of the preparation will also be discussed.

### 5.3 *Characterization and Improvement of the Contact Structures*

Numerical two-dimensional simulations have been carried out in order to understand the origin of the nonlinear increase of the current for small drain voltages [55]. The prepared transistors are of the BOC structure (see Fig. 1b). Thus the simulations have been carried out just for this structure with a channel length $L = 1\,\mu\text{m}$. Parameters are the doping level $N_A = 10^{16}\,\text{cm}^{-3}$, the hole mobility $\mu = 10^{-5}\,\text{cm}^2\,\text{V}^{-1}\,\text{s}^{-1}$, and the material parameters for P3HT. The gate work function is $\Phi_G = 4.17\,\text{eV}$. In the first example the Cr/Au double layer is not yet taken into account. Instead, different work functions were used for the source and drain contacts (Fig. 14). If both source and drain are hole-accumulation contacts (with the high work function $\Phi_S = \Phi_D = 5\,\text{eV}$), the simulation yields the ideal behavior, i.e., a linear increase of the current for low drain voltages and the maximum of the drain conductance at zero drain voltage. When the work function of the drain contact is reduced ($\Phi_D = 4.5\,\text{eV}$) such that the contact is of depletion type, one obtains a nonlinear increase and the maximum of the drain conductance at finite drain voltage. On the other hand, if one reduces in a similar manner the work function of the source contact to $\Phi_S = 4.7\,\text{eV}$, the drain current is drastically reduced, but the maximum of the drain conductance remains at zero drain voltage. One can understand the origin of these differences by inspecting the profile of the hole quasi-Fermi potential in channel direction near the interface to the gate oxide (Fig. 14b). Whereas a Schottky contact at drain is forward biased by the drain voltage, the Schottky contact at source is reverse biased. In the latter case one has consequently a large voltage drop immediately near source and the potential is almost constant in the remaining channel. This leads to the reduction

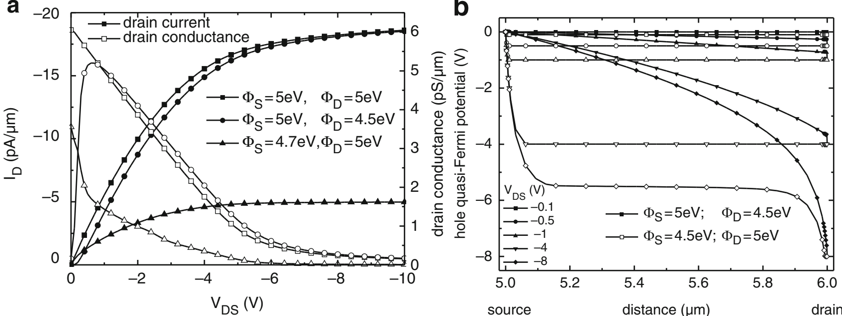


**Fig. 14** Simulated output characteristics and drain conductance (**a**) and potential profiles from source to drain 1 nm below the interface to the insulator for different drain voltages (**b**) for $V_{GS} = -6\,\text{V}$ and different source- and drain work functions

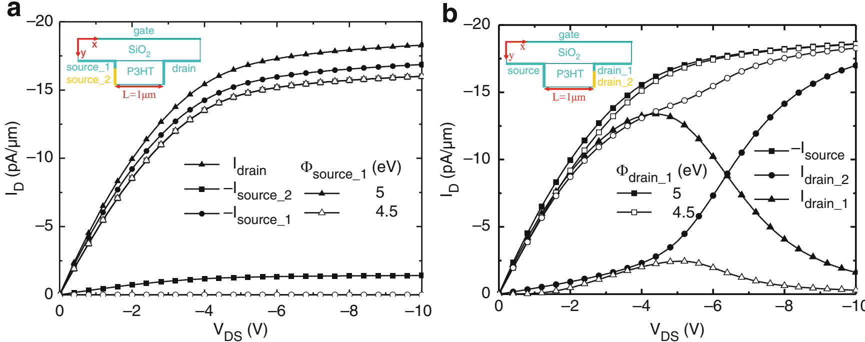


**Fig. 15** Simulated output characteristics (total current and the current components for the bilayer contact) for $V_{GS} = -6\,V$ with the bilayer as source (**a**) and drain (**b**)

of the current. For the Schottky contact at drain one has only to exceed the diffusion voltage until the potential and the current are practically the same as in the ideal transistor.

For the simulations with the Cr/Au contact the structures used are shown as inset in Fig. 15. The thickness of the Cr layer (source 1 or drain 1) is 10 nm and that of the gold layer (source 2 or drain 2) 40 nm. The current contributions are depicted for a variation of the work function of the contact source 1 or drain 1 and $\Phi = 5\,eV$ at the other contacts for a gate voltage of $-6\,V$. If the work function is 5 eV for all contacts one obtains of course the same total current if the double layer contact is either at source or at drain. However, the contributions from the two parts of the double layer contact are different. If this contact acts as source, the current $I_{source_1}$ dominates in both the active and the saturation region. On the other hand, if this contact acts as drain the current is dominated in the active region by the contact drain 1, and in the saturation region $I_{drain_2}$ dominates due to the depletion zone. For the reduced work function (4.5 eV) at source 1 the total current is practically given by the contribution $I_{source_2}$. The larger distance of this contact to the channel and the resulting enhanced series resistance cause the reduction of the current. If the double layer contact acts as drain, the current $I_{drain_2}$ also dominates. Compared to the case with $\Phi_D = 5\,eV$, the current is reduced in the active region due to the larger series resistance. In saturation there are less differences since, due to the space charge layer at the depletion contact, the current is flowing anyway more at depth.

In Fig. 16 the simulated output characteristics and drain conductances are depicted at a gate voltage $V_{GS} = -6\,V$ for different contact conditions. It can be seen that a nonlinear drain current increase and the resulting maximum of the drain conductance at finite drain voltage occur always if at least one contact has a work function $\Phi < 4.7\,eV$. The drain current is lower when the double layer contact acts as source. From these results one can conclude that the low chromium work function causes the nonlinear increase of the drain current. But, in contrast to the measurements, the maximum of the drain conductance occurs at almost the same drain voltage for the double layer contact as source or as drain. Additional simulations

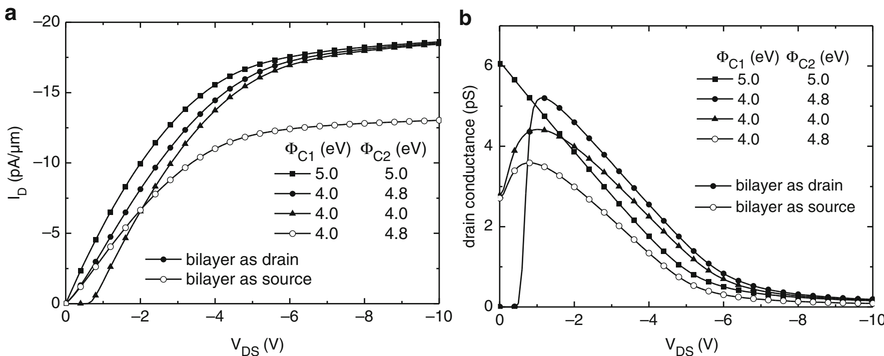


**Fig. 16** Simulated output characteristics (**a**) and drain conductance (**b**) for $V_{GS} = -6$ V and different work functions at the bilayer contact for a transistor with $L = 1\,\mu$m. The work function of the simple contact is 5 eV. Figure taken from [55]

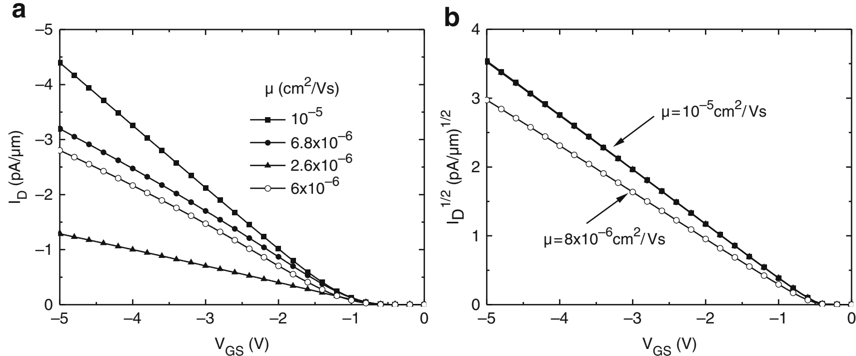


**Fig. 17** Simulated transfer characteristics for $V_{DS} = -1$ V (active region) (**a**) and $V_{DS} = -10$ V (saturation region) (**b**) for the contact conditions of Fig. 16. The given values for the mobility has been estimated using the simple Shockley equation. Figure 17a taken from [55]

have shown that a fixed interface charge at the double layer contact shifts the maximum to higher drain voltages. This effect is more pronounced for the Cr/Au contact as source.

Another important aspect is the influence of the contact conditions on the estimation of the mobility from the current–voltage characteristics. This is customarily done by using the simple Shockley equation for the current. In Fig. 17 simulated transfer characteristics are depicted in the active and in the saturation regions. In the saturation region the representation $\sqrt{I_D} = f(V_{GS})$ is chosen which is better suited for estimating the mobility in this region. In the simulation the mobility has been chosen as $\mu = 10^{-5}\,\mathrm{cm}^2\,\mathrm{V}^{-1}\,\mathrm{s}^{-1}$. Therefore, differences in the currents are caused solely by the different contact conditions. The estimation in the linear region (Fig. 17a) leads only to the correct value of the mobility, if all the contacts are ohmic ones. On the other hand, in saturation, the estimate leads only to an incorrect value for the mobility if the Cr/Au contact is the source. In the other case, Cr/Au as drain,

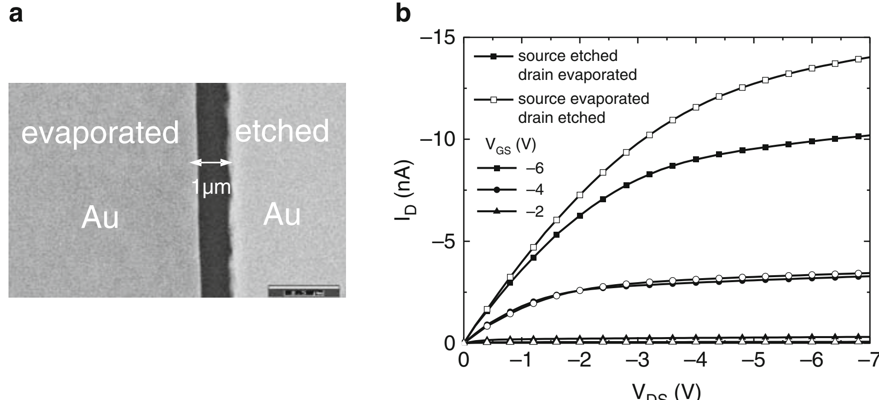


**Fig. 18** SEM image (**a**) and the measured output characteristics (**b**) of a transistor with a channel length of $L = 1\,\mu\text{m}$ and $w = 1{,}000\,\mu\text{m}$ without bilayer contact. Figure taken from [55]

one obtains the same current as for ohmic contacts and hence the estimation of the mobility yields the correct value.

As a result of these simulations we prepared short-channel transistors without the chromium adhesion layer. Thereby the deposition of the gold contact has been optimized such that, even without the chromium layer, good adhesion is achieved. In addition, the sputter process of the first gold layer has been varied in order to reduce the roughness of the underetched contact. Figure 18 shows the SEM-image and measured output characteristics of the transistor prepared with the modified fabrication scheme. Comparison with the SEM image of Fig. 9a shows clearly that the modified sputtering led to an improved underetched contact. The output characteristics were again measured for interchanged contacts. They show now a linear increase of the drain current for low drain voltages. Correspondingly, the maximum of the drain conductance (not shown here) is now at $V_{DS} = 0\,\text{V}$. These two results confirm that the chromium layer was the origin of the nonlinearity. Nevertheless, these measurements also show differences in the drain current when the contacts source and drain are interchanged. But this effect is connected with the variation of the current in repeated measurements which is until now typical for organic transistors and which is connected with the hysteresis effects.

### 5.4 Surface Modified Gate Insulator and TPD(4M)–MEH–PPV as Active Layer

Until now, silicon dioxide dominates as gate insulator and it is also used by us due to the lack of an organic insulator which can be solution processed and which has even for thin layer thickness a sufficiently high breakthrough field strength. But as described in [58, 59], the hydrophilic surface of $SiO_2$ makes the layer formation difficult with the result of low mobilities of the order $10^{-4} \ldots 10^{-6}\,\text{cm}^2\,\text{V}^{-1}\,\text{s}^{-1}$ in

the case of polythiophene. In a treatment of the $SiO_2$ surface with HMDS, polar hydroxyl groups are replaced in a chemical reaction by methyl and alkyl groups. Thereby the surface becomes hydrophobic. This enables a better order of the subsequently spin coated polymer layer resulting in an increase of the mobility of P3HT by a factor of 2–10. This effect was also confirmed by other groups [60, 61]. In [62–65] higher mobility values were achieved by a treatment of the $SiO_2$ surface with octadecyltrichlorosilane (OTS).

We investigated the improvement of the mobility by a HMDS treatment for different polymers. The procedure is based on an optimization of the process developed by Prof. Neher (Universität Potsdam). At first the silicon dioxide surface is treated with an oxygen plasma (2 min, $P = 300\,\text{W}$). Then the sample is deposited into the HMDS vapor for 26 h at 60°C. The last step of this surface modification is rinsing (3 min toluol, 3 min diethylether).

The following preparation of the two gold contacts separated from each other by the short-channel is carried out as described before. The device to be discussed below has a channel length of $L = 1\,\mu\text{m}$ and a width of $w = 250\,\mu\text{m}$. In this device the polymer used is poly[1,4-phenylene-(4-methylphenyl)imino-4,48-diphenylene-(4-methylphenyl) imino- 1,4-phenylenevinylene-2-methoxy-5-(2-ethylhexyloxy)-1,4-phenylene-vinylene] TPD(4M)–MEH–PPV. Results with this polymer obtained with long-channel transistors in BOC and TOC geometry have been published recently [7].

The characteristics of the short-channel transistor are shown in Fig. 19. The transfer characteristics are depicted in Fig. 19a and the output characteristics and the drain conductance $g_d$ in Fig. 19b. Due to the surface modification, the hole mobility is enhanced in the channel (i.e., parallel to the interface) and it is lower perpendicular to the interface which is not of interest for the transistor. From the transfer characteristics, the mobility in the channel has been determined in both the active and the saturation regions. The value extracted from the active region is $1.6 \times 10^{-3}\,\text{cm}^2\,\text{V}^{-1}\,\text{s}^{-1}$ at a drain voltage of $-1\,\text{V}$. From the saturation region one obtains $2.8 \times 10^{-3}\,\text{cm}^2\,\text{V}^{-1}\,\text{s}^{-1}$ at $-8\,\text{V}$. The extraction of different

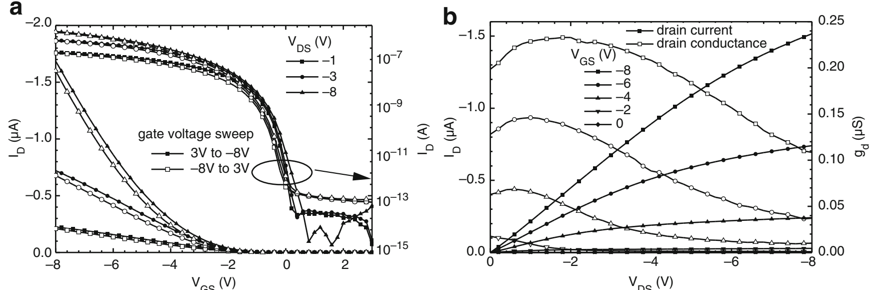


**Fig. 19** Transfer characteristics on a linear and logarithmic scale for different drain voltages and gate voltage sweep directions (**a**) and output characteristics and drain conductance for different gate voltages (**b**) for the TPD(4M)–MEH–PPV transistor with $L = 1\,\mu\text{m}$ and $w = 250\,\mu\text{m}$

values shows only that the current deviates from the description by the simple Shockley equation. Contact problems may be important, but later investigations on long-channel transistors gave no unique explanation [7]. Nevertheless, values of $1\ldots3\times10^{-3}\,\mathrm{cm^2\,V^{-1}\,s^{-1}}$ are near to realistic expectations for solution processing. From both representations of the transfer characteristics a threshold voltage is visible already at a negative voltage as required for a p-channel device. The off state is reached almost at 0 V. Since the threshold voltage can be shifted strongly be the surface modification [66] an optimization (threshold voltage slightly more negative) seems to be possible by variation of details of the surface modification. From the transfer characteristics one obtains in addition the inverse subthreshold slope $S = 160\ldots240\,\mathrm{mV\,dec^{-1}}$ and the on–off ratio of larger than $10^5$, values which are advantageous for low-voltage operation. In the transfer characteristics there is again a hysteresis, but the shift between the two gate voltage sweep directions is already rather small. In the output characteristics the hysteresis with the drain voltage sweep direction is almost negligible. But here one has again the nonlinearity of the output characteristics at low drain voltages which is clearly seen in the position of the maximum of the drain conductance at finite drain voltage. Recent experiments with long channel transistors and TPD(4M)–MEH–PPV as the material of the active layer have shown that this effect does occur also. However, after storing 1 day in air, the nonlinearity disappears and the current is significantly enhanced (corresponding to a higher effective mobility). A possible explanation given in [7] connects this change with traps.

As a result, the surface modification with HMDS improves the short-channel transistor performance considerably, and usage of the chosen polymer seems to be rather promising.

## *5.5 Future Prospects*

There are three prerequisites for the realization of an "all-polymer" variant of this short-channel transistor. At first, the preparation of the source and drain contacts based on the undercutting technology must be carried out on a plastic substrate. It has already been shown in Sect. 5.1 that this is possible. Next, parasitic capacitances must be reduced in order to achieve high cut-off frequencies. Especially in the case of short-channel devices mask adjustment for the gate contact becomes complicated and is therefore not suited for a low-cost fabrication. Thus a self-aligned deposition of the gate contact is desired, compatible with the undercutting method. The third requirement is a sufficiently thin organic insulator needed to avoid short-channel effects and for a low threshold voltage. In this section the problem of a self aligned gate will be treated.

In [67] a method for the preparation of a self aligned gate is described for long-channel transistors ($L = 20\,\mu\mathrm{m}$). Bonfiglio et al. realized the illumination of the photoresist for structuring the gate through a mylar foil which is used as gate insulator. In this process, the source and drain contacts act as mask. For the

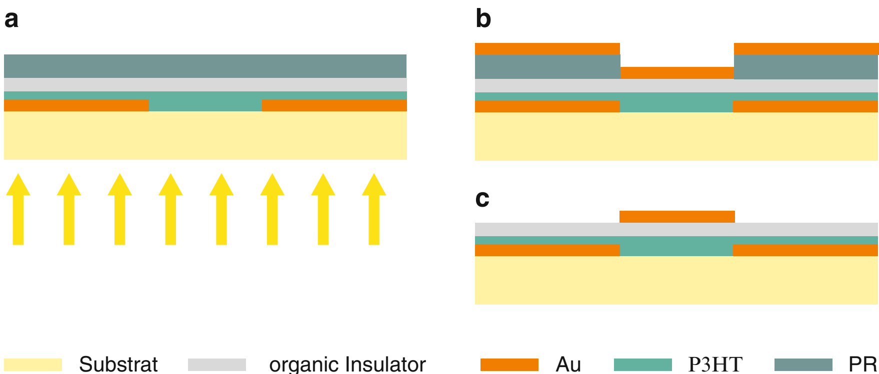


**Fig. 20** Back side illumination for the preparation of self aligned gate contacts

short-channel transistor the mylar foil is too thick to be used as gate insulator. Therefore, the method to use source and drain as masks for the illumination of the photoresist has been applied in a modified manner, which is shown schematically in Fig. 20. Source and drain were prepared onto a plastic and transparent substrate using the undercutting method described in Sect. 5.1. Then the active polymer, the organic insulator, and a positive photoresist were spin coated. It follows an illumination from the back side (arrows in Fig. 20a) whereby the nontransparent source and drain contacts act as mask. For this step the organic materials and the substrate must be transparent for the used light wave length of 365 nm. Moreover, the organic gate insulator has to be a negative photoresist since otherwise it would be removed together with the other (negative) photoresist. The structuring of the photoresist is followed by a large-area evaporation of a gold layer (Fig. 20b). The remaining photoresist with the gold layer on it is removed by a lift-off process and only in the channel region does one now have the gate contact which is adjusted to source and drain (Fig. 20c) with drastically reduced parasitic capacitances.

First investigations of the proposed technology were done with a polyethylene terephthalate (PET)-substrate. This material has been used since it is transparent in the desired wavelength region. Also, it can be used for tempering at the needed temperatures and it is not destroyed by the chemicals used in processing [68]. For the beginning, instead of the short-channel transistors, an interdigital source/drain structure has been used for which the self aligned gate was made employing the back illumination method. As the active polymer, P3HT has been used again. Then the negative photoresist SU8 was spin coated as insulator onto the active layer; however no sufficient adhesion on the P3HT has been achieved. Therefore poly-(allyloxyphenylene) PAOP has been used although its insulating properties are inferior to SU8. Also in this case there were some problems in achieving a closed layer. But the quality was sufficient to test the proposed structuring schema. For the back side illumination of the positive photoresist, an additional large area kapton mask has been used in order to separate the gate contacts of the different transistors from each other. For this purpose a 1 mm adjustment is not critical. Figure 21 shows

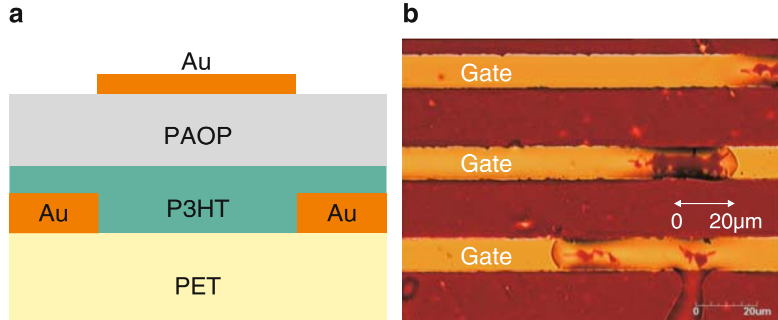


**Fig. 21** Schematic cross section (**a**) and optical micrograph (**b**) of a transistor prepared with back side illumination leading to the self aligned gate (the top Au layer in (**a**)). Figure 21b taken from [68]

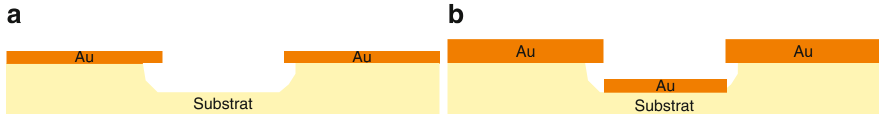


**Fig. 22** Schematic cross section created by the RIE process (**a**) and the result of the subsequent gold evaporation (**b**) for the preparation of self aligned gate contacts

the schematic cross section of one transistor and an optical micrograph of the prepared structure. The micrograph shows clearly that the fabrication of self aligned gate contacts is possible with this method. Problems to be solved concern the compatible selection of organic materials for the active layer and the insulating layer.

Another way to prepare a self-aligned gate was investigated by us using the RIE process. In a first step the source and drain contacts were prepared by the undercutting technology. These two contacts act as masks for the subsequent RIE deep etching process resulting also in a lateral etching of the substrate. This leads to the structure depicted in Fig. 22a. The next step is a large-area gold evaporation leading to the gate contact in the depth created by the RIE process (Fig. 22b). The lateral undercutting prevents a short cut between the gate contact and source and drain. Figure 23 depicts SEM images of prepared structures with source, drain and gate. These images demonstrate clearly that no short cut occurs between the gate and source and drain. This was confirmed by electrical measurements between the different contacts. In order to complete the OFET one has at first to spin coat the organic insulator and then the active polymer. These steps were not yet optimized due to the lack of a well suited organic insulator with a high breakthrough field at low thickness. Another problem to be solved is to prevent the covering of source and drain by the organic insulator. Furthermore, the gate has to be contacted by a via. Consequently, this RIE based method for the fabrication of the self aligned gate is more complex than the back side illumination described before and it is connected with other requirements on the organic insulator. On the one hand, the

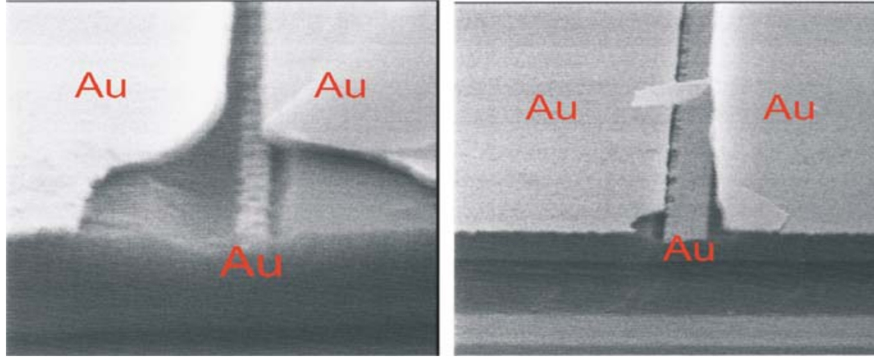


**Fig. 23** SEM images of a short-channel structures with self aligned gate contact prepared by RIE process; the gate is situated in the trench between the source and drain contacts. *Right hand side figure* taken from [42]

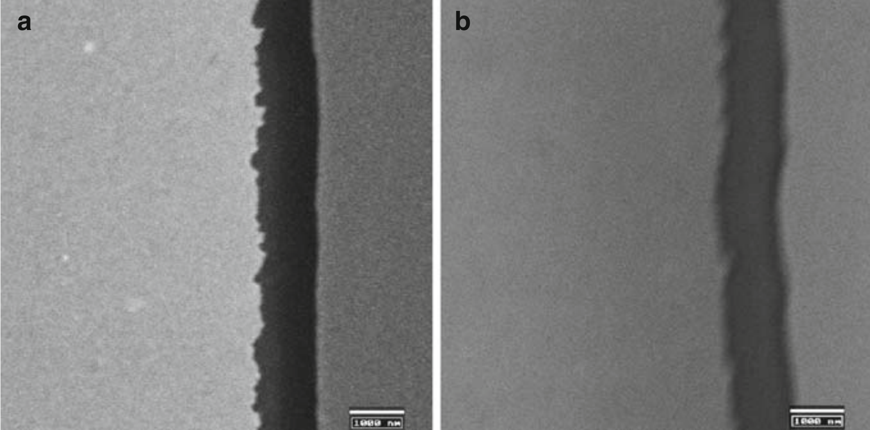


**Fig. 24** SEM image of the cannel for an evaporated (**a**) and sputtered (**b**) gold layer and an etching time of 60 s. Figure taken from [68]

active polymer will be spin coated onto the insulator. On the other hand one can use both positive and negative photoresists. A final decision will depend on the choice of the insulator.

Independent from the method for the gate contact preparation, technological conditions to realize the short-channel structure onto the PET foil have been investigated. This means that one has to optimize the first step of the large-area vapor deposition (or sputtering) of the gold layer such that the edge roughness can be minimized. On the other hand the parameters of the etching process are decisive for the resulting channel length. In [68] both the technological parameters for the vapor deposition and for the sputtering process have been investigated. Figure 24 shows the comparison of short-channel structures with the first gold layer (in both cases on the left hand side) either evaporated or sputtered. For the evaporation the

substrate was heated to 120°C. Sputtering with a LAB500 was carried out at 35 W, gas flow 4 Sccm (Sccm=standard-cm$^3$ per min) for 3 min. The channel lengths of both structures are similar. The edge of the evaporated layer has a larger roughness. The etching times determining the channel length are larger for plastic substrates than by using $SiO_2$. For evaporated gold layers one gets with an etching rate of 15 nm s$^{-1}$ within 40 s a channel length of $700 \pm 100$ nm.

The results obtained indicate clearly that the short-channel technology based on undercutting is rather promising. The future development of a variant with active layer, gate insulator, and substrate made from polymers depends on the availability of suitable organic insulators.

## 6 Conclusions

Solution-based technology is required in order to realize low-cost fabrication of organic field-effect transistors as the basic device of forthcoming organic electronics. Such technology restricts the achievable maximum mobility values of both holes and electrons of the active polymer layer to values which in a mass production will lie clearly below 0.1 cm$^2$ V$^{-1}$ s$^{-1}$. Analytical estimates show that for broader application a reasonable cut-off frequency above 1 MHz and a reasonable supply voltage (below 10 V) can be achieved only with channel length in the submicrometer region.

Further requirements to be fulfilled are the following. The low supply voltage also implies a threshold voltage of only a few volts. The threshold voltage should be negative (positive) for p- (n-) channel transistors in order to avoid additional circuitry. In addition, an inverse subthreshold slope smaller than 1 V dec$^{-1}$ is required in order to realize at the low operation voltage an on–off ratio larger than $10^4$. Of course, transistor operation requires a fairly good saturation behavior. One has also to consider that the active polymers in question, most promising at present modified P3HT and modified PPV, are usually unintentionally doped at a level higher than $10^{16}$ cm$^{-3}$. This is not only due to oxidation connected with the deep lying valence band but also the purity of the chemicals used to synthesize the polymers and remnants of catalysts.

In order to meet such different requirements it is useful to base design and technology on analytical estimates and, concerning short-channel effects, on numerical 2D simulations. As a consequence, active layers of a thickness less than the depletion length (determined by the doping) and extreme thin insulators (roughly speaking less than one tenth of the channel length) are needed.

Source/drain structures separated from each other by a channel in the submicrometer region can be fabricated with a technology based on undercutting which is well know from microelectronics technology. This method works well on both silicon dioxide as gate insulator and on plastic foils as substrate. At present, due to the absence of a suitable thin organic insulator, completion of transistors is possible with a laboratory hybrid design with a highly doped silicon wafer as gate and silicon dioxide as gate insulator. Apart from undercutting, only a few simple and

inexpensive technological steps common in microelectronics are needed. Even without any refinements one can fabricate OFETs with submicrometer channel length showing a remarkable performance. It is characterized by a low operation voltage below 5 V, a clear transition into saturation indicating that short-channel effects are suppressed, an on–off ration larger than $10^4$, and a low inverse subthreshold slope of $\approx$400 mV dec$^{-1}$. With a purified (purification lowers the mobility) P3HT and without special treatment of the silicon dioxide surface one obtains a relatively low mobility of the order of $3 \times 10^{-5}\,\mathrm{cm^2\,V^{-1}\,s^{-1}}$ and especially the transfer characteristics show a clear hysteresis which is often observed in OFETs.

In some cases contact problems do occur. A simulation-aided analysis has shown that chromium as adhesion layer for one of the gold contacts causes such problems due to its low work function. Thus, contact problems can be reduced by improved deposition methods for the gold contact. One can overcome the disadvantage of a low mobility by an HMDS surface modification of the silicon dioxide surface. Together with using the polymer TPD(4M)–MEH–PPV, an increased hole mobility of about $3 \times 10^{-3}\,\mathrm{cm^2\,V^{-1}\,s^{-1}}$ can be achieved and at the same time the hysteresis in the transfer characteristics is significantly reduced. Remaining contact problems are visible in a nonlinear increase of the drain current for small drain voltages, but later investigations with the same material used in long-channel transistors have shown that storing in air increases the current and removes the nonlinearity, an effect which can be attributed to traps.

Finally, two variants of preparing a self-aligned gate needed to prevent parasitic capacitances have been realized experimentally. The final realization of an "all-polymer" variant depends on the development of an organic insulator which can be solution deposited with a thin layer thickness and large breakthrough field strength, and which obeys additional requirements as photoresist and concerning solvents orthogonal to those used for the active layer.

# Appendix: Analytical Model of the Thin-Film Transistor

## *Basic Relations*

Starting point for the derivation of the model is the general Eq. (4). In the expression for the surface electric field, which follows from the voltage drop Eq. (2) over the whole MIS structure, one has to replace the bulk potential $\varphi_\mathrm{b}$ by the potential $\varphi_\mathrm{v}$ at the outer surface of the layer. This leads to

$$E_\mathrm{s} = \frac{\varepsilon_\mathrm{is}}{\varepsilon_\mathrm{s}} \frac{V_\mathrm{GS} - V_\mathrm{FB} - (\varphi_\mathrm{s} - \varphi_\mathrm{v})}{d_\mathrm{is}} = \frac{\varepsilon_\mathrm{is}}{\varepsilon_\mathrm{s}} \frac{V_\mathrm{GS} - V_\mathrm{FB} - \Delta\varphi_\mathrm{p}}{d_\mathrm{is}} . \qquad (12)$$

The voltage drop $\Delta\varphi_\mathrm{p}$ over the layer follows from approximations for Eq. (1) as the first integral of the Poisson equation in the semiconducting layer. In accumulation one has for the surface potential (at the interface to the insulator) $\varphi_\mathrm{s} \leq \varphi_\mathrm{b}$ and at the

outer surface $\varphi_v = \varphi_b$. Thus one can neglect in the solution of the Poisson equation the minority carrier contribution and one obtains for the surface electric field

$$E_s = \frac{V_T}{L_D} \exp - \frac{\varphi_b}{2V_T} \left\{ \exp - \frac{\Delta\varphi_p}{V_T} - 1 \right\}^{\frac{1}{2}} = \left\{ \frac{2eN_A V_T}{\varepsilon_0 \varepsilon_s} \left( \exp - \frac{\Delta\varphi_p}{V_T} - 1 \right) \right\}^{\frac{1}{2}} . \quad (13)$$

Inserting this into Eq. (12) and supposing $\Delta\varphi_p \ll V_{GS} - V_{FB}$ one obtains the voltage drop over the layer as

$$\Delta\varphi_p = -V_T \ln \left\{ 1 + \frac{1}{V_T} \left( \frac{V_{GS} - V_{FB}}{a} \right)^2 \right\} \quad (14)$$

with the constant $a = \sqrt{2\varepsilon_0 \varepsilon_s e N_A} / C''_{is}$. Analogously, in depletion one can neglect the contribution of the mobile carriers which leads to

$$E_s = \left\{ \frac{2eN_A \Delta\varphi_p}{\varepsilon_0 \varepsilon_s} \right\}^{\frac{1}{2}} \quad (15)$$

and thus the variation of the potential over the layer is given by

$$\Delta\varphi_p = V_{GS} - V_{FB} + \frac{a^2}{2} - a\sqrt{V_{GS} - V_{FB} + \frac{a^2}{4}} . \quad (16)$$

Considering in addition the variation of the potential in channel direction one can express the areal charge needed in Eq. (4) as

$$Q''_p(x) = -C''_{is} \left\{ V_{GS} - V_{FB} - \varphi_{Fp}(x) - \frac{eN_A d}{C''_{is}} - \Delta\varphi_p(x) \right\} . \quad (17)$$

With Eq. (14) one gets in accumulation

$$\begin{aligned} Q''_p(x) \quad &= -C''_{is} \left\{ V_{GS} - V_{FB} - \varphi_{Fp}(x) - \tfrac{eN_A d}{C''_{is}} \right. \\ &\left. + V_T \ln \left[ 1 + \tfrac{1}{V_T} \left( \tfrac{V_{GS} - V_{FB} - \varphi_{Fp}(x)}{a} \right)^2 \right] \right\} \end{aligned} \quad (18)$$

and with Eq. (16) in depletion

$$Q''_p(x) = -C''_{is} \left\{ -\frac{eN_A d}{C''_{is}} - \frac{a^2}{2} + a\sqrt{V_{GS} - V_{FB} - \varphi_{Fp}(x) + \frac{a^2}{4}} \right\} . \quad (19)$$

With these two expressions one can integrate Eq. (4) from source ($x = 0$, $\varphi_{Fp}(0) = 0$) to drain ($x = L$, $\varphi_{Fp}(0) = V_{DS}$). But in accumulation, one has to

take into account that the integration from source to drain is only possible for $|V_{DS}| < |V_{GS} - V_{FB}|$, that is when the whole channel from source to drain is in accumulation. For larger drain voltage, $|V_{DS}| > |V_{GS} - V_{FB}|$, the channel becomes depleted near drain and then the integration from source to drain has to be split in two regions. In the first one, up to reaching flat band condition somewhere in the channel, on has to use Eq. (18) for the charge, whereas in the region near drain one has to use Eq. (19). The resulting analytical current equations are given completely in [69, 70]. The advantage of these equations compared to the simple Shockley model is that, by taking into account the position dependence of the voltage drop over the layer, one does not ignore the diffusion component of the current.This is the origin of the agreement of this model with current–voltage characteristics with numerical 2D simulations for the same transistor [69, 70].

Analytical models are especially of interest for circuit design and for estimation of tendencies. On the other hand, for the investigation of the mode of operation, numerical 2D simulations are preferable. Here we will consider only one consequence of the analytical model, namely the threshold voltage which is decisive for the transistor operation. Another advantage of the analytical model is the possibility of extensions. Thus, it has been generalized [69, 70] such that the existence of bipolarons as doubly charged states of polymer chains can be taken into account.

### *Threshold Voltage of the Thin-Film Transistor*

In a thin-film transistor, the threshold voltage $V_{th}$ is the gate voltage leading to complete depletion of the layer. Analogously to the definition for the inversion transistor [18] one also has for the depletion type $Q'' = 0$ and $\varphi_s = -\varphi_b$ for $V_{GS} = V_{th}$. From Eq. (19) one obtains with $l_{dep} = \sqrt{\frac{2\varepsilon_0\varepsilon_s|-2\varphi_b|}{eN_A}}$ just Eq. (8), i.e.,

$$V_{th} = V_{FB} + \frac{eN_A d}{C''_{is}} - 2\varphi_b \left(\frac{d}{l_{dep}}\right)^2 . \tag{20}$$

For extremely thin layers, $d \ll l_{dep}$ the threshold voltage approaches

$$V_{th} = V_{FB} + \frac{eN_A d}{C''_{is}} , \tag{21}$$

i.e., the potential drop over the layer becomes negligible. The maximum is achieved for $d = l_{dep}$. In Fig. 25 the dependencies following from these equations are compared with results from numerical 2D simulations. The simulation results show clearly that the dependence of the threshold voltage on the layer thickness must be taken into account. Comparison of the dependencies following from Eqs. (5), (8), and (21) shows the influence of the different assumptions on the potential drop over the layer. Only for $d \approx l_{dep}$ one has $\Delta\varphi_p = -2\varphi_b$ and Eq. (5) can be used. For thinner

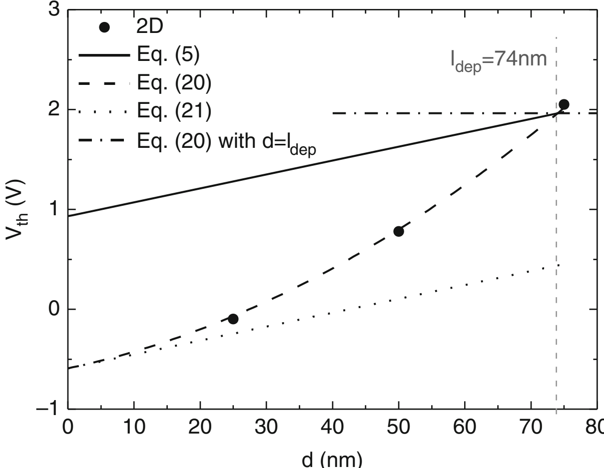


**Fig. 25** Threshold voltage as a function of the layer thickness for the different models. The assumed parameters are the flat band voltage of $-0.59\,\mathrm{V}$ for the system $n^+$-silicon-P3HT, doping concentration of $N_A = 10^{17}\,\mathrm{cm}^{-3}$ and the insulator thickness $d_{SiO_2} = 30\,\mathrm{nm}$

layers one has already complete depletion for $\varphi_s < -\varphi_b$, and therefore only Eq. (8) describes the threshold voltage correctly. For a layer thickness less than 8 nm one already obtains the correct value from Eq. (21), which means that the potential drop over the layer is already negligible and hence the hole concentration is constant across the layer.

## References

1. Ebisawa F, Kurokawa T, Nara S (1983) Electrical properties of polyacetylene/polysiloxane interface. J Appl Phys 54:3255–3259
2. Kudo K, Yamashina M, Moriizumi T (1984) Field effect measurement of organic dye films. Jpn J Appl Phys 23:130
3. Tsumura A, Koezuka H, Ando T (1986) Macromolecular electronic device: field-effect transistor with a polythiophene thin film. Appl Phys Lett 49:1210–1212
4. Assadi A, Svensson C, Willander M, Inganäs O (1988) Field-effect mobility of poly(3-hexylthiophene). Appl Phys Lett 53:195–197
5. Horowitz G, Fichou D, Peng X, Xu Z, Garnier F (1989) A field-effect transistor based on conjugated alpha-sexithienyl. Solid State Commun 72:381–384
6. Lindner Th, Paasch G, Scheinert S (2004) Influence of distributed trap states on the characteristics of top and bottom contact organic field-effect transistors. J Mater Res 19:2014–2027
7. Herasimovich A, Scheinert S, Hörselmann I (2007) Influence of traps on top and bottom contact field-effect transistors based on modified poly(phenylene-vinylene). Appl Phys Lett 102:054509
8. Horowitz G (1998) Organic field-effect transistors. Adv Mater 10:365–377
9. Shaw JM, Seidler PF (2001) Organic electronics: introduction. IBM J Res Dev 45:3–9
10. Dimitrakopoulos CD, Mascaro DJ (2001) Organic thin-film transistors: a review of recent advances. IBM J Res Dev 45:11–27

11. Dimitrakopoulos CD, Malenfant PRL (2002) Organic thin film transistors for large area electronics. Adv Mater 14:99–117
12. Forrest StR (2004) The path to ubiquitous and low-cost organic electronic appliances on plastic. Nature 428:911–918
13. Reese C, Roberts M, Ling M, Bao Z (2004) Organic thin film transistors. Mater today 7:20–27
14. Sirringhaus H (2005) Device physics of solution-processed organic field-effect transistors. Adv Mater 17:2411–2425
15. Scheinert S, Paasch G (2004) Fabrication and analysis of polymer field-effect transistors. Phys Stat Sol A 201:1263–1301
16. Scheinert S, Paasch G (2005) Fabrication and analysis of polymer field-effect transistors. In: W. Brütting (ed) Physics of organic semiconductors. Wiley, New York, pp 343–391
17. Paasch G, Scheinert S (2007) Space charge layers in organic field-effect transistors with Gaussian or exponential semiconductor density of states. J Appl Phys 101:024514
18. Sze SM (1981) Physics of semiconductor devices, 2nd edn. Wiley, New York
19. Lin Y-Y, Gundlach DJ, Nelson SF, Jackson ThN (1997) Pentacene-based organic thin-film transistors. IEEE Trans Electron Dev 44:1325–1331
20. Sirringhaus H, Tessler N, Thomas DS, Brown PJ, Friend RH (1999) High-mobility conjugated polymer field-effect transistors. Adv Solid State Phys 39:101–110
21. Scheinert S, Paasch G, Schrödner M, Roth H-K, Sensfuß S, Doll Th (2002) Subthreshold characteristics of field effect transistors based on poly(3-dodecylthiophene) and an organic insulator. J Appl Phys 92:330–337
22. Scheinert S, Paasch G, Doll Th (2003) The influence of bulk traps on the subthreshold characteristics of an organic field effect transistor. Synth Met 139:233–237
23. Bao Z, Feng Y, Dodabalapur A, Raju VR, Loviger AJ (1997) High-performance plastic transistors fabricated by printing techniques. Chem Mater 9:1299–1301
24. Rogers J, Bao Z, Makhija A, Braun P (1999) Printing process suitable for reel-to-reel production of high-performance organic transistors and circuits. Adv Mater 11:741–745
25. Austin MD, Chou StY (2002) Fabrication of 70 nm channel length polymer organic thin-film transistors using nanoimprint lithography. Appl Phys Lett 81:4431–4433
26. Komoda T, Kita K, Kyuno K, Toriumi A (2003) Performance and degradation in single grain-size pentacene thin-film transistors. Jpn J Appl Phys 42:3662–3665
27. Zhang Y, Petta JR, Ambily S, Shen Y, Ralph DC, Malliaras GG (2003) 30 nm channel length pentacene transistors. Adv Mater 15:1632–1635
28. Wang L, Fine D, Jung T, Basu D, von Seggern H, Dodabalapur A (2004) Pentacene field-effect transistors with sub 10-nm channel lengths. Appl Phys Lett 85:1772–1774
29. Chen Y, Zhu WW, Xiao S, Shih I (2004) Fabrication of short channel organic thin film transistors by Si-etching method. J Vac Sci Technol A 22:768–770
30. Lee JB, Chang PC, Liddle A, Subramanian V (2005) 10-nm channel length pentacene transistors. IEEE Trans Electron Dev 52:1874–1879
31. Haddock JN, Zhang X, Zheng S, Zhang Q, Marder SR, Kippelen B (2006) A comprehensive study of short channel effects in organic field-effect transistors. Org Electron 7:45–54
32. Tsukagoshia K, Shigeto K, Yagi I, Aoyagi Y (2006) Interface modification of a pentacene field-effect transistor with a submicron channel. Appl Phys Lett 89:113507
33. Tulevski GS, Nuckolls C, Afzali A, Graham TO, Kagan CR (2006) Device scaling in sub-100 nm pentacene field-effect transistors. Appl Phys Lett 89:183101
34. Fujimori F, Shigeto K, Hamano T, Minari T, Miyadera T, Tsukagoshi K, Aoyagi Y (2007) Current transport in short channel top-contact pentacene field-effect transistors investigated with the selective molecular doping technique. Appl Phys Lett 90:193507
35. Minari T, Miyadera T, Tsukagoshi K, Hamano T, Aoyagi Y, Yasuda R, Nomoto K, Nemoto T, Isoda S (2007) Scaling effect on the operation stability of short-channel organic single-crystal transistors. Appl Phys Lett 91:063506
36. Hoppe A, Seekamp J, Balster T, Götz G, Buerle P, Wagner V (2007) Tuning the contact resistance in nanoscale oligothiophene field effect transistors. Appl Phys Lett 91:132115

37. Collet J, Tharaud O, Chapoton A, Vuillaume D (2000) Low-voltage, 30 nm channel length, organic transistors with a self-assembled monolayer as gate insulating films. Appl Phys Lett 76:1941–1943
38. Stutzmann N, Friend RH, Sirringhaus H (2003) Self-aligned, vertical-channel, polymer field-effect transistors. Science 299:1881–1884
39. Wang JZ, Gu J, Zenhausern F, Sirringhaus H (2006) Low-cost fabrication of submicron all polymer field effect transistors. Appl Phys Lett 88:133502
40. Wang JZ, Gu J, Zenhausern F, Sirringhaus H (2006) Suppression of short-channel effects in organic thin-film transistors. Appl Phys Lett 89:083513
41. Haas U, Gold H, Haase A, Jakopic G, Stadlober B (2007) Submicron pentacene-based organic thin film transistors on flexible substrates. Appl Phys Lett 91:043511
42. Scheinert S, Scherer A, Doll T, Paasch G, Hörselmann I (2004) Organic field-effect transistors with nonlithographically defined submicrometer channel length. Appl Phys Lett 84:4427–4429
43. Doll T, Scheinert S, Scherer A, Paasch G (2004) Verfahren zur Herstellung von elektronischen Bauelementen. Patent PCT/EP2004/009729
44. ISE-TCAD (1995–1999) Integrated Systems Engineering AG, Zurich, Switzerland
45. Vissenberg MCJM, Matters M (1998) Theory of the field-effect mobility in amorphous organic semiconductors. Phys Rev B 57:12964–12967
46. Coehoorn R, Pasveer WF, Bobbert PA, Michels MAJ (2005) Charge-carrier concentration dependence of the hopping mobility in organic materials with Gaussian disorder. Phys Rev B 72:155206
47. Pasveer WF, Cottaar J, Tanase C, Coehoorn R, Bobbert PA, Blom PWM, de Leeuw DM, Michels MAJ (2005) Unified description of charge-carrier mobilities in disordered semiconducting polymers. Phys Rev Lett 94:206601
48. Limketkai BN, Jadhav P, Baldo MA (2007) Electric-field-dependent percolation model of charge-carrier mobility in amorphous organic semiconductors. Phys Rev B 75:113203
49. Li L, Meller G, Kosina H (2007) Carrier concentration dependence of the mobility in organic semiconductors. Synth Met 157:243–246
50. Scheinert S, Paasch G (2009) Interdependence of contact properties and field- and density-dependent mobility in organic field-effect transistors. J Appl Phys 105:014509
51. Shannon JM, Gerstner EG (2003) Source-gated thin-film transistors. IEEE Electron Dev Lett 24:405–407
52. Lindner T, Paasch G, Scheinert S (2005) Simulated operation and properties of source-gated thin-film transistors. IEEE Trans Electron Dev 52:47–55
53. Scheinert S (2006) Technologie und Eigenschaften organischer Halbleiterbauelemente, Habilitationsschrift, Technische Universität Ilmenau
54. Paasch G, Scheinert S, Herasimovich A, Hörselmann I, Lindner Th (2008) Characteristics and mechanisms of hysteresis in polymer field-effect transistors. Phys Stat Sol A 205:534–548
55. Scheinert S, Paasch G, Hörselmann I, Herasimovich A (2005) Influence of source/drain contacts on sub-micrometer organic field-effect transistors. Phys Stat Sol A 202:R82–R84
56. Bürgi L, Richards TJ, Friend RH, Sirringhaus H (2003) Close look at charge carrier injection in polymer field-effect transistors. J Appl Phys 94:6129–6137
57. Yoneya N, Noda M, Hirai N, Nomoto K, Wada M, Kasahara J (2004) Reduction of contact resistance in pentacene thin-film transistors by direct carrier injection into a-few-molecular-layer channel. Appl Phys Lett 85:4663–4665
58. Sirringhaus H, Tessler N, Friend RH (1998) Integrated optoelectronic devices based on conjugated polymers. Science 280:1741–1744
59. Sirringhaus H, Tessler N, Friend RH (1999) Integrated, high-mobility polymer field-effect transistors driving polymer light-emitting diodes. Synth Met 102:857–860
60. Gorjanc TC, Lévesque I, D'Iorio M (2004) Organic field effect transistors based on modified oligo-p-phenylevinylenes. Appl Phys Lett 84:930–932
61. Yagi I, Tsukagoshi K, Aoyagi Y (2005) Modification of the electric conduction at the pentacene/$SiO_2$ interface by surface termination of $SiO_2$. Appl Phys Lett 86:103502

62. Gundlach DJ, Klauk H, Sheraw CD, Kuo CC, Huang JR, Jackson TN (1999) High-mobility, low voltage organic thin film transistors. IEDM Tech Dig 1999:111
63. Salleo A, Chabinyc ML, Yang MS, Street RA (2002) Polymer thin-film transistors with chemically modified dielectric interfaces. Appl Phys Lett 81:4383–4385
64. Song Ch-K, Koo B-W, Lee S-B, Kim D-H (2002) Characteristics of pentacene organic thin film transistors with gate insulator processed by organic molecules. Jpn J Appl Phys 41:2730–2734 (2002)
65. Kang SJ, Yi Y, Kim CY, Whang CN, Callcott TA, Krochak K, Moewes A, Chang GS (2005) Analysis of octadecyltrichlorosilane treatment of organic thin-film transistors using soft X-ray fluorescence spectroscopy. Appl Phys Lett 86:232103
66. Scheinert S, Pernstich KP, Batlogg B, Paasch G (2007) Determination of trap distributions from current characteristics of pentacene field-effect transistors with surface modified gate oxide. Appl Phys Lett 102:104503
67. Bonfiglio A, Mameli F, Sanna O (2003) A completely flexible organic transistor obtained by a one-mask photolithographic process. Appl Phys Lett 82:3550–3552
68. Weber J (2005) Diplomarbeit, TU Ilmenau
69. Tecklenburg R, Paasch G, Scheinert S (1998) Theory of organic field effect transistors. Adv Mater Opt Electron 8:285–294
70. Tecklenburg R (1998) Theorie und Modellierung organischer Feldeffekttransistoren. Thesis, TU Ilmenau

Adv Polym Sci (2010) 223: 189–212
DOI:10.1007/12_2009_6
© Springer-Verlag Berlin Heidelberg 2009
Published online: 19 June 2009

# Bio-Organic Optoelectronic Devices Using DNA

**Thokchom Birendra Singh, Niyazi Serdar Sariciftci, and James G. Grote**

**Abstract** Biomolecular DNA, as a marine waste product from salmon processing, has been exploited as biodegradable polymeric material for photonics and electronics. For preparing high optical quality thin films of DNA, a method using DNA with cationic surfactants such as DNA–cetyltrimethylammonium, CTMA has been applied. This process enhances solubility and processing for thin film fabrication. These DNA–CTMA complexes resulted in the formation of self-assembled supramolecular films. Additionally, the molecular weight can be tailored to suit the application through sonication. It revealed that DNA–CTMA complexes were thermostable up to 230°C. UV–VIS absorption shows that these thin films have high transparency from 350 to about 1,700 nm. Due to its nature of large band gap and large dielectric constant, thin films of DNA–CTMA has been successfully used in multiple applications such as organic light emitting diodes (OLED), a cladding and host material in nonlinear optical devices, and organic field-effect transistors (OFET). Using this DNA based biopolymers as a gate dielectric layer, OFET devices were fabricated that exhibits current–voltage characteristics with low voltages as compared with using other polymer-based dielectrics. Using a thin film of DNA–CTMA based biopolymer as the gate insulator and pentacene as the organic semiconductor, we have demonstrated a bio-organic FET or BioFET in which the current was modulated over three orders of magnitude using gate voltages less than 10 V. Given the possibility to functionalise the DNA film customised for specific purposes viz. biosensing, DNA–CTMA with its unique structural, optical and electronic properties results in many applications that are extremely interesting.

T.B. Singh (✉) and N.S. Sariciftci
Linz Institute of Organic Solar Cells (LIOS), Institute of physical chemistry, Johannes Kepler University, A 4040 Linz, Austria
e-mail:birendra.singh@CSIRO.Au;serdar.sariciftci@jku.at

J.G. Grote
Air Force Research Laboratory, Materials and Manufacturing Directorate, AFRL/MLPS, Wright-Patterson Air Force Base, OH 45433-7707, USA

**Keywords** Bioelectric phenomena · BioFET · BioLED · Biomolecular electronics · OFET · OLED · Organic electronics · Photonic devices · Plastic electronics

**Contents**

1 Introduction ........ 190
2 DNA–CTMA as Optoelectronic Material ........ 193
3 DNA–CTMA Films in Nonlinear Optics ........ 195
4 DNA–CTMA in Organic Light Emitting Diodes ........ 195
5 DNA–CTMA in Organic Field Effect Transistors ........ 199
6 Dielectric Spectroscopy of DNA–CTMA Thin Films ........ 205
7 Transient Response of BioFETs ........ 208
8 Summary and Outlook ........ 209
References ........ 211

## Abbreviations

| | |
|---|---|
| $Alq_3$ | Tris-(8-hydroxyquinoline) aluminum |
| BCP | 2,9-Dimethyl-4,7-diphenyl-1,10-phenanthroline |
| BioFET | Bio-organic field-effect transistors |
| BioLED | Bio-organic light emitting diodes |
| CTMA | Hexadecyltrimethylammonium chloride |
| EBL | Electron blocking layer |
| EIL | Electron injection layer |
| ETL | Electron transport layer |
| HBL | Hole blocking layer |
| $I_{\mathrm{Drain,Sat}}$ | Saturated drain current |
| LCD | Liquid crystal displays |
| NPB | ($N,N'$-Bis(naphthalene-1-yl)-$N,N'$-bis(phenyl)benzidine) |
| PCBM | 1-(3-Methoxycarbonyl)propyl-1-phenyl (66]$C_{61}$ |
| PEDOT | [Poly(3,4-ethylenedioxythiophene)] |
| PSS | Poly(4-styrenesulfonate) |
| $T$ | Temperature |
| $V_{\mathrm{Drain}}$ | Drain voltage |
| $V_{\mathrm{Gate}}$ | Gate voltage |
| $V_{\mathrm{t}}$ | Threshold voltage |

## 1 Introduction

The progress made in the field of organic electronics in the last two decades have resulted in the demonstration of prototype devices such as a 4.7-in. QVGA active matrix display containing 76,800 organic transistors [1], mechanical sensors [2]

and chemical sensors [3]. Devices such as organic light emitting diodes (OLEDs), which is a part of display technology is now used in consumer electronics in place of LCD (see www.sony.com). All these have been possible with the availability of a variety of organic materials, conducting polymers, insulators, semiconductors and metals. Apart from conventional organic materials, biomaterials are of particular interest. Biomaterials often show unusual properties which are not easily replicated in conventional organic or inorganic materials. In addition, natural biomaterials are from renewable resources and are inherently biodegradable. Among natural biodegradable materials, the science community has shown interest in DNA for various reasons, such as potential use of DNA assembly in molecular electronic devices [4], nanoscale robotics [5] and DNA-based computation [6].

The molecular structure of DNA (double helix) consists of two inter-twined spirals of sugar and phosphate molecules linked by hydrogen-bonded base pairs (see Fig. 1). The phosphate backbone is negatively charged with H+ or Na + to balance the neutrality. The width of the double helix is about two nanometres and the length of the DNA molecule depends on the number of base pairs (about a third of a nanometre per base pair). For practical use, natural DNA, derived from salmon milt, which is normally a waste product of the salmon-fishing industry is attractive

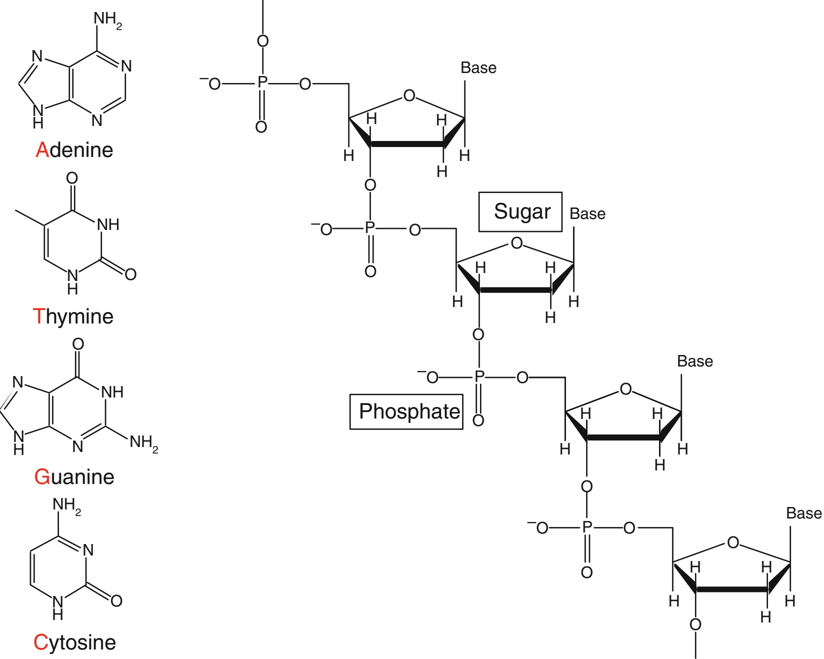


**Fig. 1** Phosphate–sugar backbone of single strand DNA. The phosphate back bone is negatively charged with $H^+$ or $Na^+$ to balance the neutrality. In the early years scientists had already known the phosphate backbone and sugar groups, also the four base groups, adenine, thymine, guanine, cytosine

(see Figs. 2 and 3). Although there is a wealth of knowledge on the nature of the transport properties of synthetic DNA, in this chapter we shall focus only on DNA materials derived from salmon milt. The reader may also pay attention to the fact that there is an ongoing debate on the insulating [7–12], semiconducting [13, 14] as well as highly conducting [15] and even superconducting nature [16] of the transport in DNA molecules.

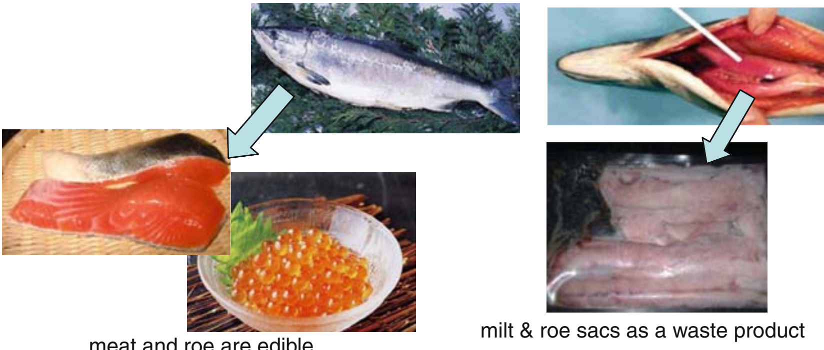


**Fig. 2** Illustration of salmon as an edible meat and as a source of natural biomaterials (salmon DNA)

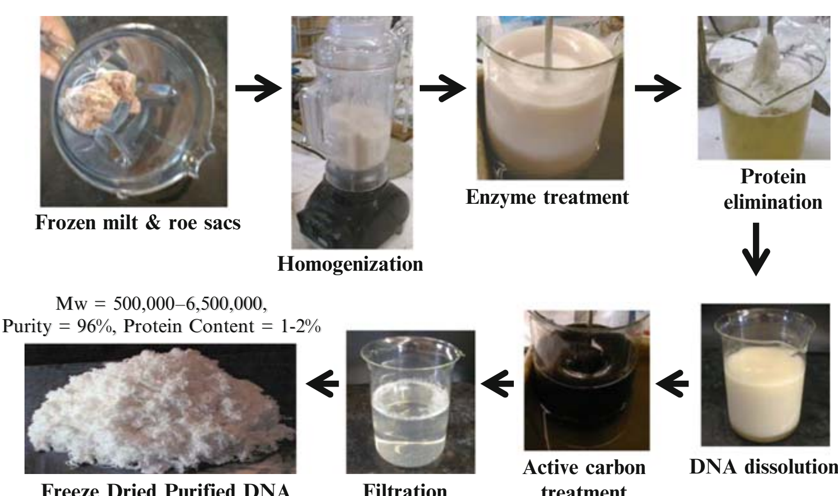


**Fig. 3** Illustration of purifying steps of salmon DNA from its frozen milt and roe sacs

## 2 DNA–CTMA as Optoelectronic Material

The DNA used for research in optoelectronic devices was purified DNA provided by the Chitose Institute of Science and Technology (CIST) [17, 18]. The processing steps involved are summarised in Figs. 2 and 3. The starting point was marine-based DNA, first isolated from frozen salmon milt and roe sacs through a homogenisation process. It then went through an enzymatic treatment to degrade the proteins by protease. Resulting freeze dried purified DNA has molecular weight ranging from 500,000 to 8,000,000 Da with purity as high as 96% and protein content of 1–2%. The average molecular weight of DNA provided by CIST is, on average, greater than 8,000,000 Da. If necessary, the molecular weight of DNA supplied by CIST can be tailored and cut using an ultrasonic procedure [19] which gives rise to lower molecular weight of 200,000 Da depending the sonication energy as shown in Fig. 4. It was found that the purified DNA was soluble only in water, the resulting films are too water sensitive and have insufficient mechanical strength, so are not compatible with typically fabrication processes used for polymer based devices. It has also been observed that many particulates are present in the DNA films. Therefore, additional processing steps are performed to render DNA more suitable for device fabrication with better film quality. From the knowledge of stoichiometric combination of an anionic polyelectrolyte with a cationic surfactant, it has been shown that DNA which is an anionic polyelectrolyte could be quantitatively precipitated with cationic surfactant in water [20]. This processing was accomplished by precipitating the purified DNA in water with a cationic surfactant complex, hexadecyltrimethylammonium chloride (CTMA), by an ion exchange reaction [19, 21–25] (see Fig. 5). This surfactant was selected for the following reasons [17]. First, cationic surfactants having longer (>16) alkyl chains are water-insoluble, and chains shorter than $C_{16}$ might induce poor mechanical property of the materials. Second, DNA complexes made with longer alkyl chains might damage the double helix structure of DNA as the strong association and aggregation among alkyl chains might break the hydrogen bonds of the nucleobase pairs. The third reason is that these surfactants are commercially available. The resulting DNA–lipid complex became water insoluble

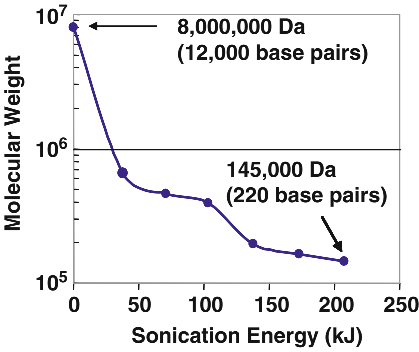


**Fig. 4** Molecular weight of DNA as a function of total sonication energy. The DNA was sonicated on ice in 10 s long pulses with a 20 s rest period between pulses to prevent overheating of the sample. (Reproduced with permission from American Institute of Physics, and [19])

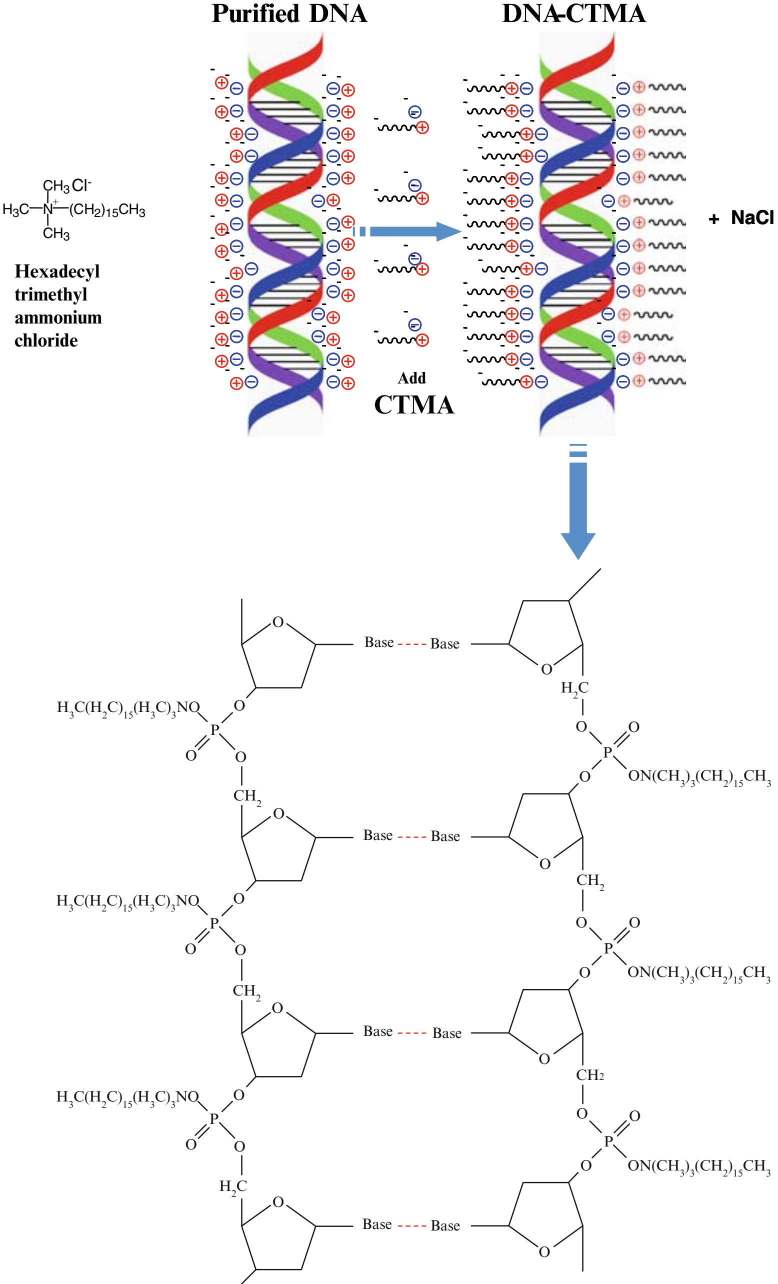


**Fig. 5** DNA–CTMA is formed by adding surfactant groups of CTMA to the back bone of DNA. The main goal of this process is to change the DNA solubility from water soluble to chemical solvent soluble. Chemical structure of CTMA: hexadecyl trimethyl-ammonium chloride or cetyltrimethylammonium chloride is also shown. The 2D schematic diagram shows how surfactants are added to the DNA structure

and more mechanically stable due to the alkyl chain of the CTMA. Adding the CTMA complex, DNA–CTMA could now be dissolved using solvents more compatible with device fabrication, such as chloroform, ethanol, methanol, butanol or a chloroform/alcohol blends. When dissolved in the organic solvent the DNA–CTMA was passed through a 0.2-μm filter to remove any large particulates.

DNA–CTMA films can be cast by standard methods like spin coating, doctor blading, dip coating, drop casting, etc. and exhibit excellent transmission over a broad wavelength range as shown in Fig. 6. DNA–CTMA is also a very low loss optical material applicable over a broad range of wavelengths with refractive index ranging from 1.526 to 1.540 (see Fig. 7). The electrical resistivity of DNA–CTMA films with molecular weights of 500,000 and 6,500000 as a function of temperature are in the range of $10^9$–$10^{14}\,\Omega$-cm depending on the molecular weight (see Fig. 8). Dielectric constant of DNA–CTMA is 7.8–6 at the frequency range of 1–1,000 KHz (see Fig. 9). Thermo-gravimetric analysis (TGA) of the DNA–CTMA complex shows stability up to 230°C and 10% water absorption in air at room temperature (see Fig. 10).

## 3 DNA–CTMA Films in Nonlinear Optics

Thin films of DNA–CTMA exhibits optical losses as low as 0.05 dB $cm^{-1}$ at 800 nm and 0.2 dB $cm^{-1}$ at 1,550 nm [19, 23–25]. This very low optical attenuation makes DNA films promising candidates applicable as waveguides. Improved poling efficiency can be achieved from combining of DNA–CTMA films with polymers that have large nonlinear optical coefficients. All-DNA–CTMA based waveguide was also demonstrated by cross-linking the DNA–CTMA [24]. Cross-linking of DNA–CTMA causes the material to become resistant to its initial solvents upon curing; this allows a core layer of cross-linked DNA–CTMA-chromophores to be spin coated directly on top of a cladding layer of cross-linked DNA–CTMA. The chromophore dye provides for the electro-optic effect to be induced through contact poling. The chromophore also raises the index of refraction of the core layer above that of the cladding needed for waveguiding. Research has shown that DNA–CTMA films also used in microwave applications. Characterisation of DNA–CTMA film at microwave frequencies has yielded low dielectric-loss values, ranging from 0.11 dB at 10 GHz to 0.5 dB at 30 GHz, and a loss tangent of less than 0.1 [26].

## 4 DNA–CTMA in Organic Light Emitting Diodes

DNA can also play a vital role in enhancing light emission in OLEDs. This stems from the fact that DNA–CTMA has large band gap of 4.7 eV for potential use as *electron blocking layer* (EBL) as illustrated in Fig. 11. Hagen et al. [27] have reported that incorporating DNA–CTMA as an EBL into fluorescent type OLEDs

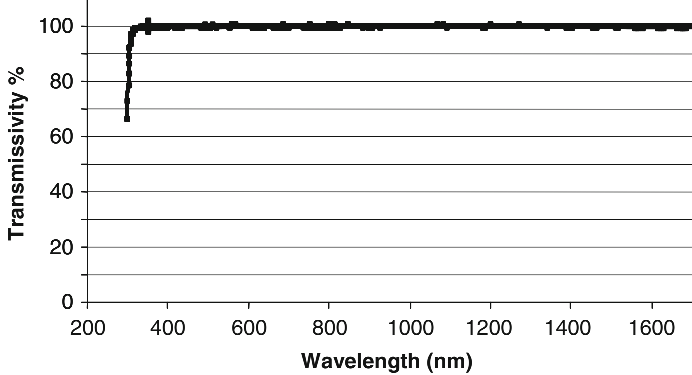


**Fig. 6** Transmissivity of a 3 μm thick DNA–CTMA thin film. (Reproduced with permission from [19])

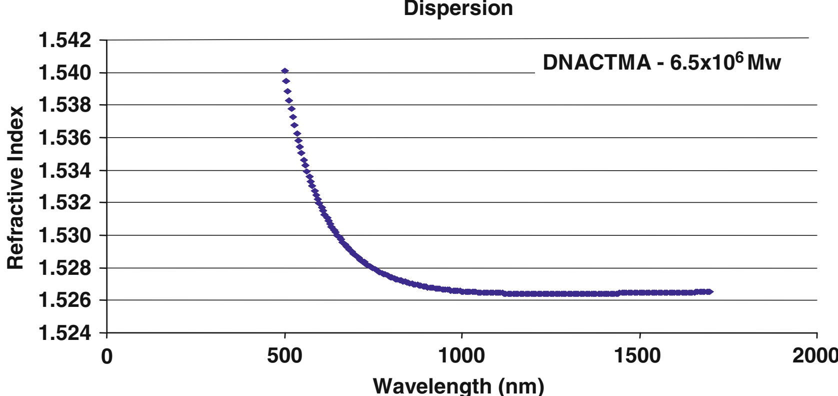


**Fig. 7** Refractive index of DNA–CTMA. (Reproduced with permission from SPIE and [25])

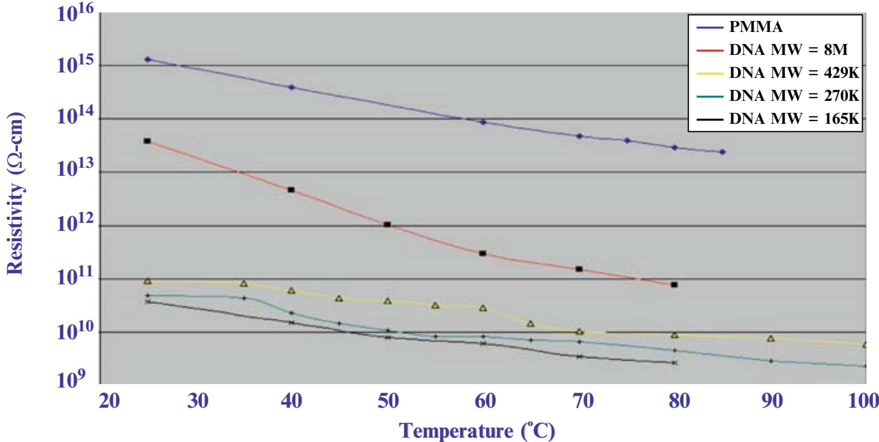


**Fig. 8** Resistivity vs temperature for DNA–CTMA complexes with varying molecular weight and PMMA as a reference. (Reproduced with permission from SPIE and [25])

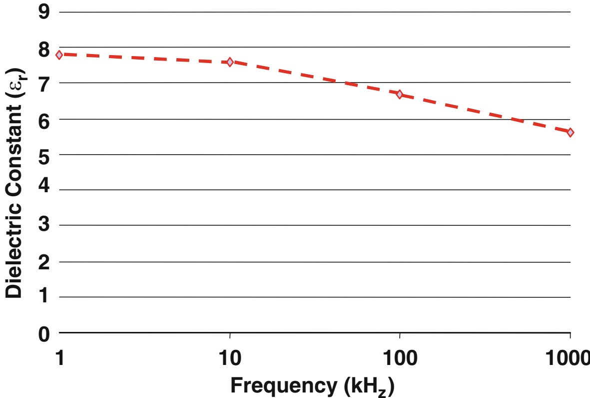


**Fig. 9** Dielectric constant vs frequency for DNA–CTMA complex. (Reproduced with permission from SPIE and [25])

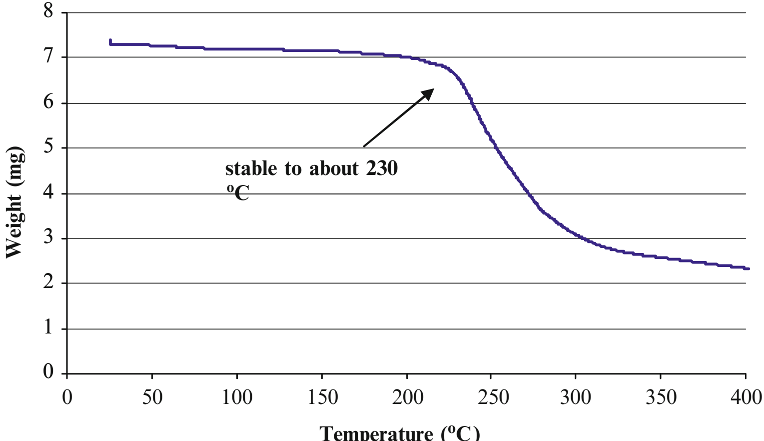


**Fig. 10** Thermo-galvometric analysis (TGA) of DNA–CTMA material. (Reproduced with permission from SPIE and [25])

resulted in BioLEDs that are as much as 10 times more efficient and 30 times brighter than their OLED counterparts (see Fig. 12). In Fig. 12 light emission from green and blue-emitting conventional OLEDs is compared to DNA-containing BioLEDs operated under the same bias conditions and processing conditions including active area. The role of blocking electron flow is to enhance the probability of radiative electron-hole recombination, leading to increased device efficiency and luminance. The resulting green and blue BioLEDs showed a maximum efficiency of about 8 and 1 cd $A^{-1}$, respectively. Typical turn-on and operating voltages for these devices were about 4–5 V and about 10–25 V, respectively. The green BioLED achieved the highest luminance of about 21,000 cd $m^{-2}$, whereas the blue BioLED showed a maximum luminance of about 1,500 cd $m^{-2}$. Figure 11 shows the

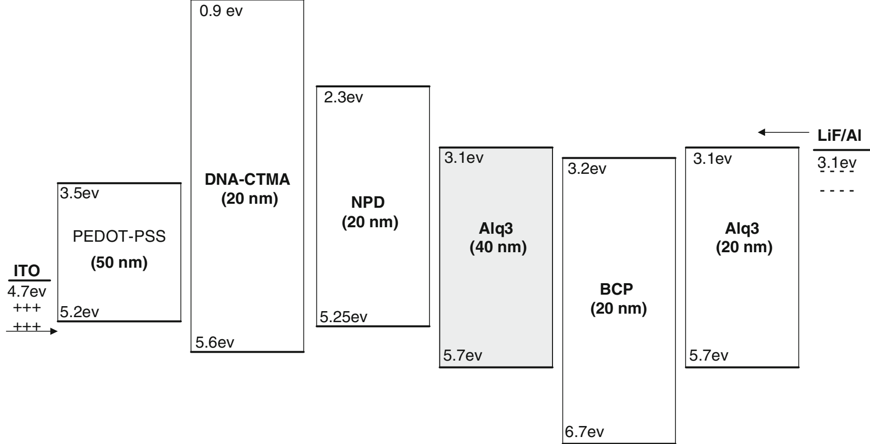


**Fig. 11** Energy levels in the green-emitting ($Alq_3$) DNA–CTMA BioLED structure. In the blue-emitting DNA–CTMA BioLED structure the $Alq_3$ EML was replaced with a single 40 nm NPB EML. Alternative structure evaluated replaced the DNA–CTMA with other EBL materials (PVK and PMMA). 'Baseline' green and blue emitting OLED structures were also fabricated with the same structure, except without the EBL. (Reproduced with permission from American Institute of Physics, and [27])

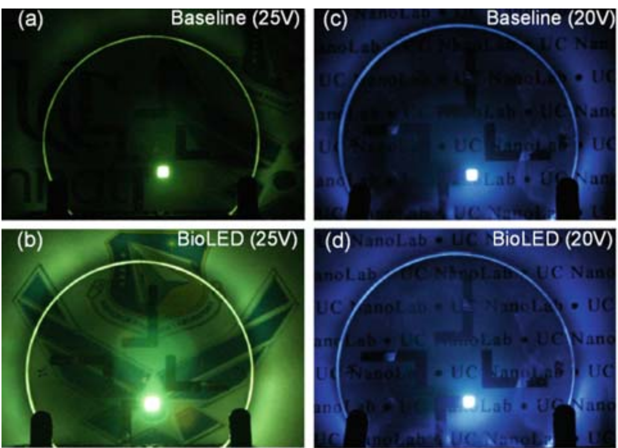


**Fig. 12** Photographs of EL emission from several devices. **a** Green $Alq_3$ baseline OLED at 25 V (707 mA $cm^{-2}$) −590 cd $m^{-2}$, 0.35 cd $A^{-1}$. **b** Green $Alq_3$ BioLED with DNA–CTMA EBL at 25 V (308 mA $cm^{-2}$) −21, 100 cd $m^{-2}$, 6.56 cd $A^{-1}$. **c** Blue NPB baseline OLED at 20 V (460 mA $cm^{-2}$) −700 cd $m^{-2}$, 0.14 cd $A^{-1}$. **d** Blue NPB BioLED with DNA-CTMA EBL at 20 V (200 mA $cm^{-2}$) −1, 500 cd $m^{-2}$, 0.76 cd $A^{-1}$. The device emitting area is $2 \times 2\,mm^2$. (Reproduced with permission from American Institute of Physics, and [27])

energy-level diagrams for green-emitting (Alq3) BioLEDs, with photographs of the devices in operation which was shown in Fig. 12. The highest occupied molecular

orbital (HOMO) and lowest unoccupied molecular orbital (LUMO) energy levels of the organic materials are shown along with the work functions of the metal layers. The green BioLED structure consists of the following layers: indium tin oxide (ITO) metal *anode*; PEDOT [poly(3,4-ethylenedioxythiophene)] doped with PSS [poly(4-styrenesulfonate)] *hole injection layer* (HIL); DNA–CTMA *electron blocking layer* (EBL); NPB [($N,N'$-bis(naphthalene-1-yl)-$N,N'$-bis(phenyl)benzidine)] *hole transport layer* (HTL); $Alq_3$ [tris-(8-hydroxyquinoline) aluminum] *emitter layer* (EML); BCP (2,9-dimethyl-4,7-diphenyl-1,10-phenanthroline] *hole blocking layer* (HBL); $Alq_3$ *electron transport layer* (ETL); LiF *electron injection layer* (EIL); Al *cathode*. The blue BioLED structure did not contain the $Alq_3$ EML, thus forcing the electron-hole recombination and related photoemission to occur in the NPB layer. Reference OLEDs were fabricated which were identical to the BioLEDs except that the DNA–CTMA EBL layer was replaced with organic EBL materials (PMMA – polymethylmethacrylate or PVK – polyvinyl carbazole). The reason for increases in the device efficiency and luminance are primarily due to the low DNA–CTMA LUMO level (0.9 eV) that allows for more efficient electron-hole recombination in the emitting layer of the device by reducing electron flow into the anode region.

## 5 DNA–CTMA in Organic Field Effect Transistors

DNA–CTMA films have been successfully used as gate dielectric in organic field effect transistors (OFETs). OFETs have been fabricated with various device geometries as depicted in Fig. 13. The most commonly used device geometry are bottom gate with top contact and bottom gate with bottom contact partly because of borrowing the concept of thin-film silicon transistor (TFT) using thermally grown $Si/SiO_2$ oxide as gate dielectric as substrate. Due to the advantage of having commercially available high quality $Si/SiO_2$ substrate, it has dominated the whole community in the last decades. Recently, selected organic dielectrics (see Fig. 14) have also been successfully employed for high performance OFETs [28–37]. Organic dielectrics have the following common properties:

1. Can be solution-processed
2. Provide smooth films on transparent glass and plastic substrates
3. Are suitable for optoelectronics like photo-responsive OFETs due to their high optical transparency
4. Can be thermally stable up to 200°C with a relatively small thermal expansion coefficient

It was very recently demonstrated that thin films of DNA–CTMA can be employed as a dielectric for low voltage operating OFETs [38]. This stems from the fact that thin films of DNA–CTMA are relatively smooth depending on the molecular weight as shown in Fig. 15a, b. A smooth film of dielectric layer is a prerequisite to enable deposition of smooth organic semiconductor forming a better interface for charge transport. Another important property is the large capacitive coupling

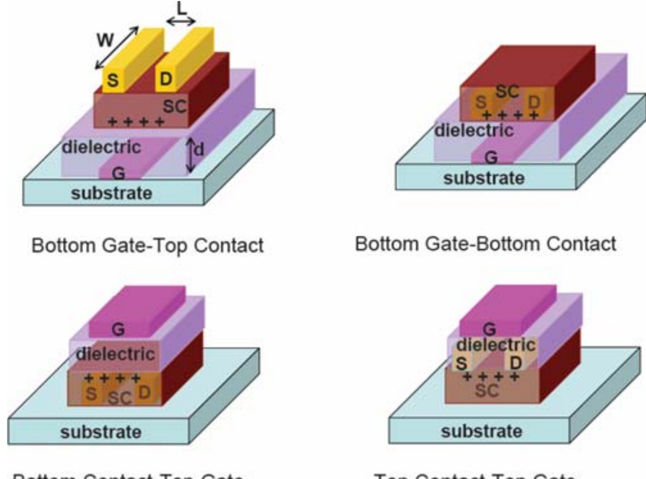


**Fig. 13** Schematic of the bottom-gate organic field-effect transistors (OFETs) with (**a**) top contact and (**b**) bottom contact structures. Schematic diagram of a (**c**) top-gate/bottom contact OFETs using a standard TFT device structures and (**d**) top-gate/top contact is also shown. (Reproduced with permission from Annual Reviews, and [28])

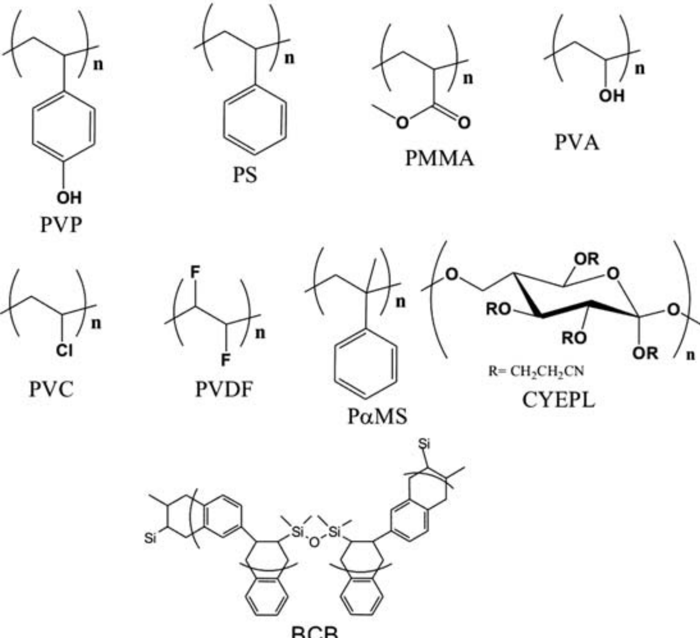


**Fig. 14** Chemical structure of some commonly used organic dielectric. PVP: poly(4-vinyl phenol); PS: polystyrene; PMMA: polymethyl-methacrylate; PVA: polyvinyl alcohol; PVC: polyvinylchloride; PVDF: polyvinylidenfluoride; PαMS: poly(α-methylstyrene], CYEPL: cyano-ethylpullulan and BCB: divinyltetramethyldisiloxane-bis(benzocyclobutene). (Reproduced with permission from Annual Reviews, and [28])

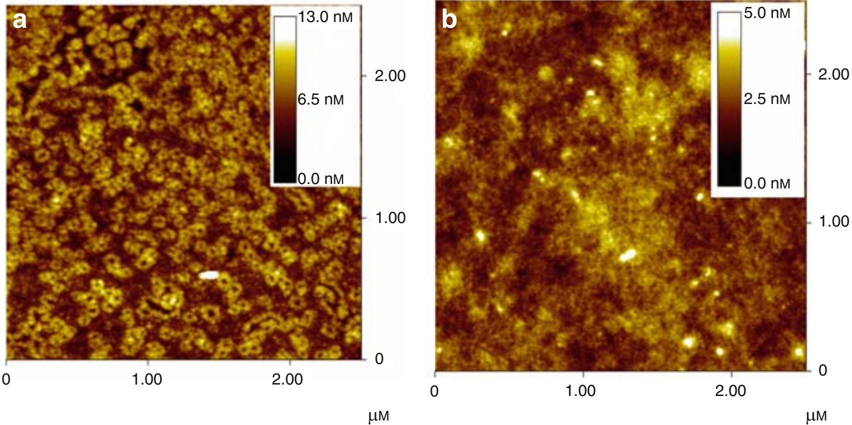


**Fig. 15** AFM topographical images ($2.5 \times 2.5\,\mu m^2$) of spin-coated film of (**a**) 200 nm film of 8 MDa mol wt DNA–CTMA and (**b**) 1 µm thick film of 300 kDa mol wt DNA–CTMA

enabled due to relatively large dielectric constant of 7.8 for DNA–CTMA. A study on the thin film morphology of DNA–CTMA reveals formation of self-organised structures in DNA–CTMA thin-films with higher molecular of 8 MDa mol wt. These self-assembled DNA–surfactant complex materials, with good processability, will have promising applications in molecular optoelectronic fields. It was proposed (see Fig. 16) that such a self-organised structure arises because the alkyl chains are oriented perpendicular to film plane, and chiral DNA helices were oriented in the direction parallel to the film plane [17].

In an effort to demonstrate low voltage operating BioFETs, two organic semiconductors, pentacene and 1-(3-methoxycarbonyl) propyl-1-phenyl (6, 6]$C_{61}$ (PCBM), were employed as an active semiconductor. Both are well known in the field as a benchmark high mobility p-type and n-type semiconductors respectively. Energy level diagrams of respective materials used for p-channel as well an n-channel BioFETs are depicted in Fig. 17. Various devices, such as metal–insulator–metal (MIM) and metal–insulator–semiconductor (MIS) devices were also fabricated using DNA–CTMA as an insulator and PCBM as semiconductor. Surface morphology studies of as deposited organic semiconductor film on top of a DNA indicate a surface roughness of 80 nm for room temperature evaporated pentacene film with an average pentacene crystallites ca. 200 nm (see Fig. 18a), whereas a surface roughness of about 2 nm for solution deposited PCBM on top of DNA. For comparison, larger crystallites of pentacene are usually obtained when using more common organic dielectrics as bottom gate layer. Smoother surfaces of PCBM thin films can be attributed to its highly soluble nature and tendency to form nanocrystalline films [37]. The scheme of p-channel BioFET device is shown in Fig. 19a. Typical output characteristics of the p-channel BioFET are shown in Fig. 19b. With a 200 nm thick film of DNA–CTMA dielectric layer and a 50 nm thin film of pentacene semiconductor, the saturated drain current, $I_{\mathrm{Drain,Sat}}$ was able to modulate

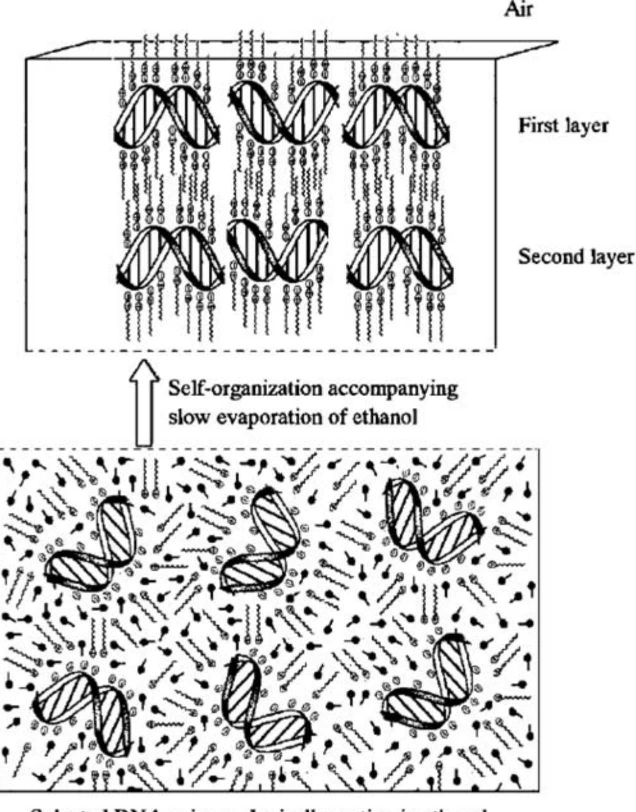


**Fig. 16** Idealised model for self-assembly process of DNA–surfactant cation complexes. (Reproduced with permission from American Chemical Society and [17])

over three orders of magnitude using gate voltages less than 10 V. Figure 19c is a plot of the transfer characteristics for p-channel BioFET. Pronounced hysteresis in the transfer characteristics can be observed in these devices, as indicated by the direction of arrows. Similarly, n-channel BioFET characteristic are shown in Fig. 20. Figure 20a shows the output characteristics of n-channel BioFETs with PCBM as a semiconductor with LiF/Al source-drain electrodes. Since LiF/Al was employed as source drain electrode, which is favourable for electron-injection, a p-channel BioFET with PCBM as a semiconductor is not likely, due to large hole injection barrier ($\phi_b(h^+) = 1.2$ eV] from these electrodes into PCBM [39]. As can be seen in Fig. 20a, $I_{Drain,Sat}$ can be as high as 4–5 μA, for a device with channel length of 35 μm and width of 3 mm and for $V_{Drain} = 20$ V and $V_{Gate} \approx 10$ V. This is promising when compared to standard organic dielectric based PCBM OFETs with an operating voltage in the range of >60 V with the same geometry [37]. The lower operating voltage of the n-channel BioFET is even clearer from its transfer characteristics as shown in Fig. 20b. The threshold voltage, $V_{th}$, is found to be different from standard PCBM OFETs using other organic gate dielectrics, even though the thickness of the

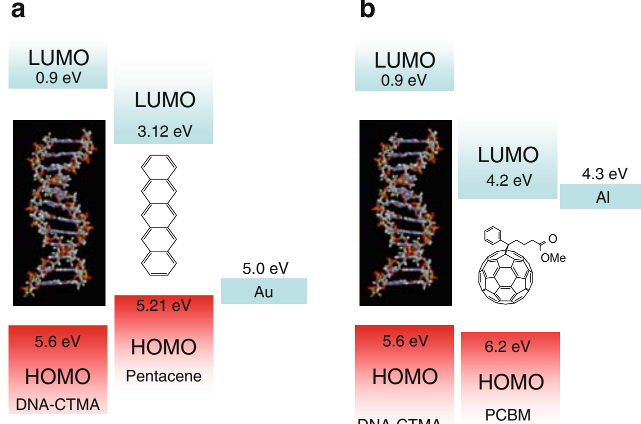


**Fig. 17** Energy level diagram without taking into account of interface dipole layers of the respective materials for use in fabrication of (**a**) p-type BioFET with pentacene as a semiconductor and using Au as source-drain contact (**b**) for a n-type BioFET with PCBM as a semiconductor and using Al and source-drain contact

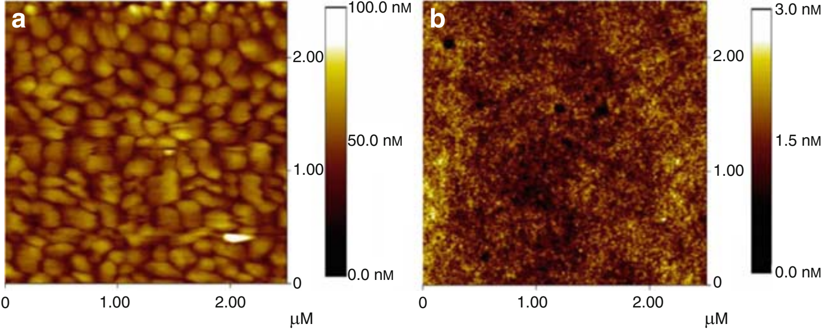


**Fig. 18** **a** AFM topographical images ($2.5 \times 2.5\,\mu m^2$) of 50 nm film of pentacene evaporated on DNA–CTMA. **b** AFM topographical images ($2.5 \times 2.5\,\mu m^2$) of 100 nm spin-coated film of PCBM on DNA–CTMA, (Reproduced with permission from Elsevier and [39])

dielectrics and other device parameters are similar [39]. A lower observed $V_{th}$ is an indication of excellent dielectric coupling between DNA–CTMA and PCBM. Forward and reverse scans, with scan rate of $12.4\,mVs^{-1}$, give rise to hysteresis with a shift in $V_{th}$ by 7 V.

Possible reasons for this observation of hysteresis in OFETs have been investigated extensively in the past couple of years. They are mainly attributed to:

1. Charge trapping and release in the bulk of the semiconductor [40]
2. Polarisable gate dielectric [41]
3. Dipole polarisation [42]
4. Electret effect due to mobile ions in the dielectric [35, 37]
5. Bipolarons [43]

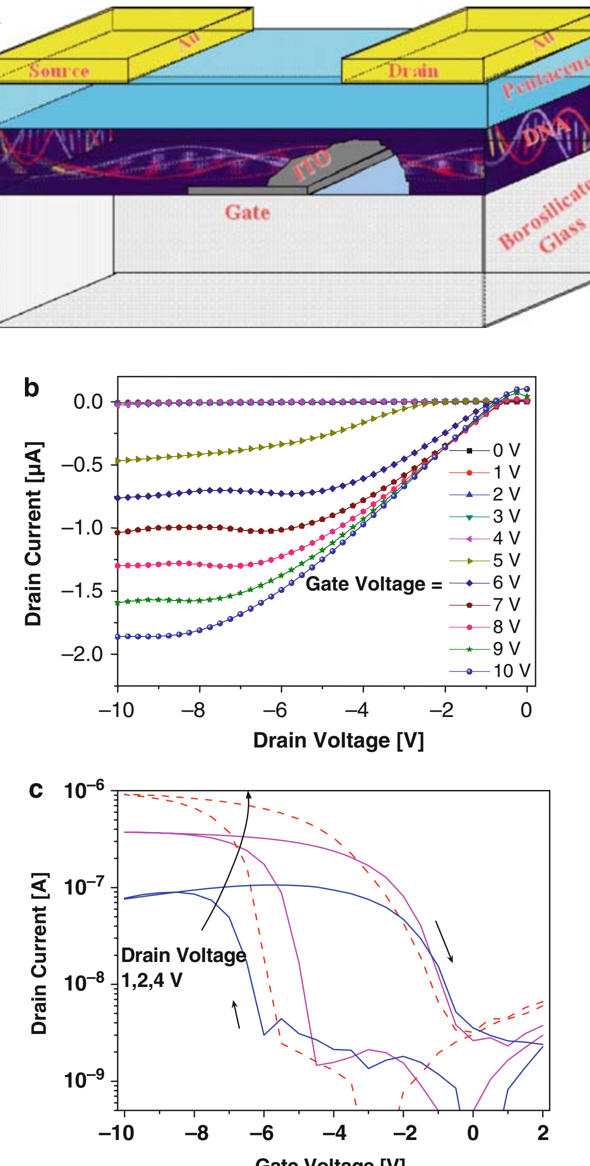


**Fig. 19** **a** Schematic of the top contact BioFET device employing pentacene as a semiconductor and 8 M mol wt DNA–CTMA as a dielectric. **b** Corresponding BioFET output characteristics; drain current, $I_{ds}$ vs drain voltage, $V_{ds}$ for different gate voltages, $V_{gs}$. **c** Transfer characteristics; $I_{ds}$ vs $V_{gs}$ for drain voltages, $V_{ds} = 1$, 2 and 4 V. (Reproduced with permission from American Institute of Physics, and [38])

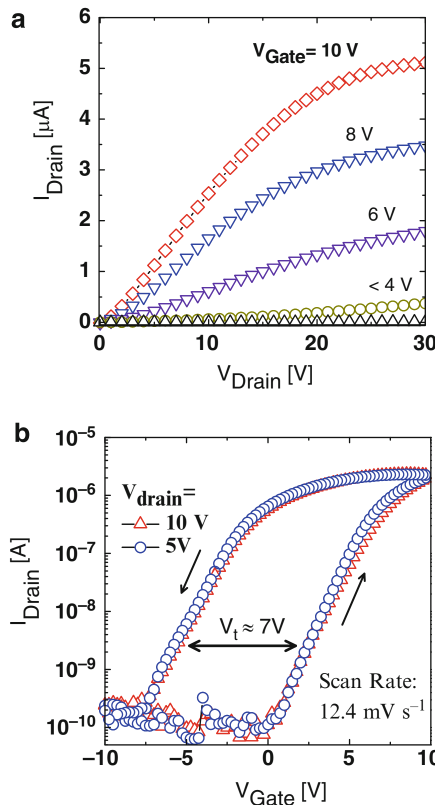


**Fig. 20** **a** Output characteristics of solution-processed low voltage operating n-channel BioFET with voltage step of 1 V s$^{-1}$. **b** Transfer characteristics of BioFET. All measurements are performed with steps of 12.4 mV s$^{-1}$. Note: gate current characteristics of the BioFET, also plotted, correspond to the right scale of the graph. (Reproduced with permission from Elsevier and [39])

Compared to a conventional dielectric material, polarisable gate dielectric and electret effects are well known for the large hysteresis.

## 6 Dielectric Spectroscopy of DNA–CTMA Thin Films

Studies of capacitance–voltage characteristics were done on metal insulator semiconductor (MIS) structures. The MIS structure consists of PCBM spin-coated on top of DNA–CTMA. For the metal electrode in the MIS device Cr/Au was chosen as the bottom as well as top electrode. Similarly, MIM devices were also fabricated and studied. For the MIM devices characteristics of capacitance vs frequency show no significant change in capacitance throughout the measured frequency range (see Fig. 21). On the other hand, MIS devices show rise in capacitance between frequency ranges of $10^1$ to $10^{-2}$ Hz, corresponding to the dielectric relaxation of the PCBM semiconductor. At lower frequencies, capacitance further increases to an

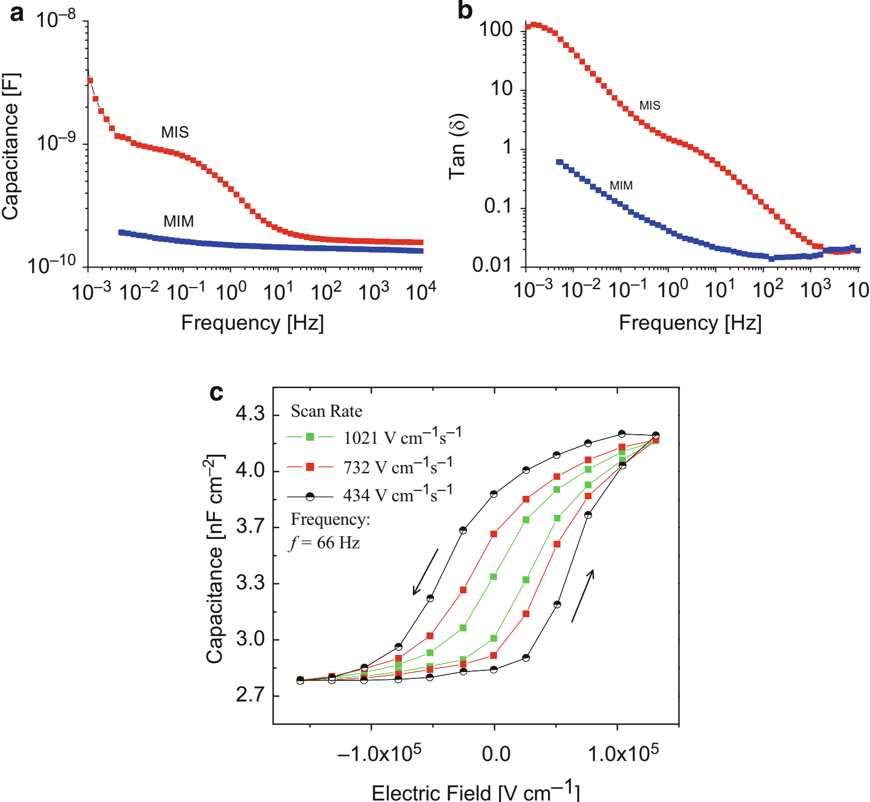


**Fig. 21** Room-temperature capacitance–frequency characteristics. **a** MIM and MIS structure devices (with applied a.c. voltage of 0.5 V). **b,c** Tan (δ)-frequency characteristics (**b**) and quasi-static capacitance–electric field curves (**c**) for the MIS structures (at 66 Hz) at different sweep/scan rate ($dV_{\text{Gate}}/dt$) as indicated. Larger hysteresis with slower scan rates are found. (Reproduced with permission from Elsevier and [39])

unrealistic value, considering the series capacitance of DNA–CTMA and PCBM layer. This sharp rise in capacitance can be attributed to trap charges or impurities, such as ions, which are most likely in the bulk of DNA–CTMA, as well as at the interface. Studies of dielectric loss (tan δ) reveal more vital information about DNA–CTMA as a rather lossy dielectric, as shown in Fig. 21b. A strong increase of tan δ values, on the order of 1 for MIM and 100 for MIS, at low frequencies, can be an indication of the Maxwell–Wagner effect [44].

Studies of capacitance vs electric field at different sweeping rates were also carried out for MIS devices (see Fig. 21c). As evident from the Fig. 21c, the slower the scan rate, the larger is the hysteresis. Further, from the studies of the real part of impedance [45], Z′ and imaginary part of Z″ of the MIS devices, it was found that a simple model based on series connection of two capacitors and resistors for the two layers cannot explain the observed phenomena (see Fig. 22). It gives an impression

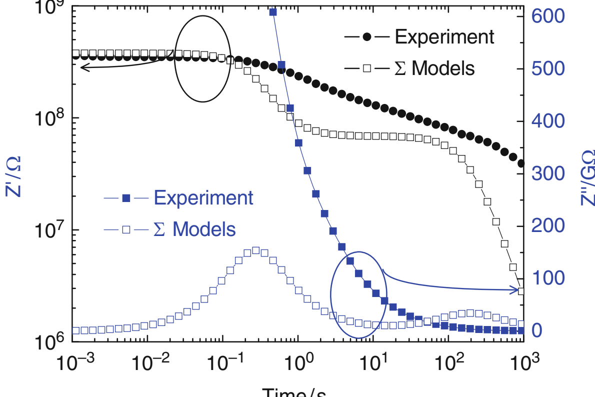


**Fig. 22** Plot of experimentally measured $Z'$ and $Z''$ vs frequency. Data fit using a model is also shown

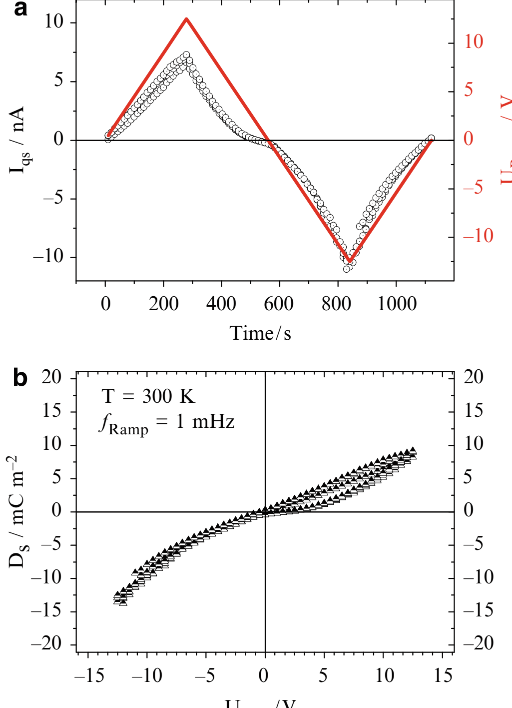


**Fig. 23** Quasi-static current measured (**a**) as a function of an applied slow cyclic voltage ramp and (**b**) surface charge density as a function of a voltage ramp showing quasi-linear charge polarisation at frequency of 1 mHz

that interfacial layer formation between the DNA–CTMA and PCBM layers can be crucial. This observation raises question whether DNA–CTMA possesses the property of a nonlinear charge polarisation effect. The nature of polarisation can be obtained from the quasi-static measurement on MIM devices. As shown in Fig. 23,

the shape of the current–voltage characteristics, for a slowly varying ramp voltage, is quasi-linear, which indicates that DNA–CTMA has a quasi-linear polarisation effect. Furthermore, a plot of the surface charge density vs applied voltage shows that all the curves pass through the origin, which rules out the possibility for nonlinear charge polarisation.

## 7 Transient Response of BioFETs

As mentioned before, charge trapping and release time can be a strong function of applied voltage, as well as device temperature. Transient decay of the $I_{\mathrm{Drain,Sat}}$ was carried out at different temperatures. As shown in Fig. 24, when $I_{\mathrm{Drain,Sat}}$ was measured at $T = 320\,\mathrm{K}$, there exists a remnant behaviour. This remnant behaviour seems to reduce at lower temperatures. However, there is also a decrease in the magnitude of $I_{\mathrm{Drain,Sat}}$, due to lowering of mobility of PCBM at lower temperatures. In all of the cases, at lower temperatures, it is clear that remnant $I_{\mathrm{Drain,Sat}}$ at $V_{\mathrm{Gate}} = 0\,\mathrm{V}$ reduces, indicating no charged species are available to give rise to remnant behaviour.

On the other hand, one can also realise benefit by utilising the observed remnant behaviour for use as a memory element. In Fig. 25, $I_{\mathrm{Drain,Sat}}$ is measured for a $V_{\mathrm{Gate}}$ pulse applied for a longer duration of 200 s. Note that level of the pulse voltage is only around 20 V, thereby demonstrating that voltage levels can be reduced to values of practical interest. However, the programming time is still an obstacle to be addressed in further work. After switching off the voltage pulse, the current decays; after 800 s the *Ids* current is still more than one order of magnitude larger than the off current. It is also evident in Fig. 20a that the relaxation of the current slows down, so we expect a sizable memory even after much longer times. The inset of

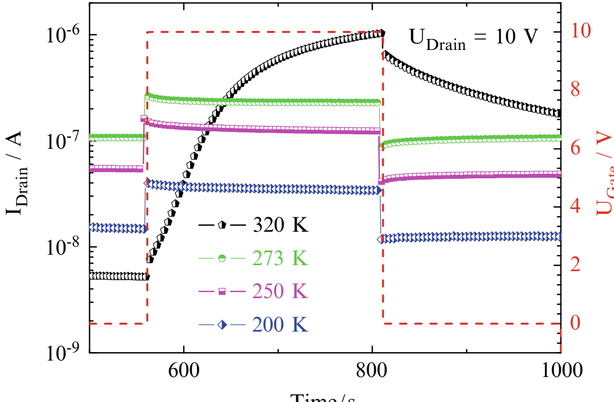


**Fig. 24** Temperature dependent transient decay characteristics of $I_{\mathrm{Drain,Sat}}$ of BioFET when a pulse of $V_{\mathrm{Gate}}$ with pulse height as shown in *right-hand scale*

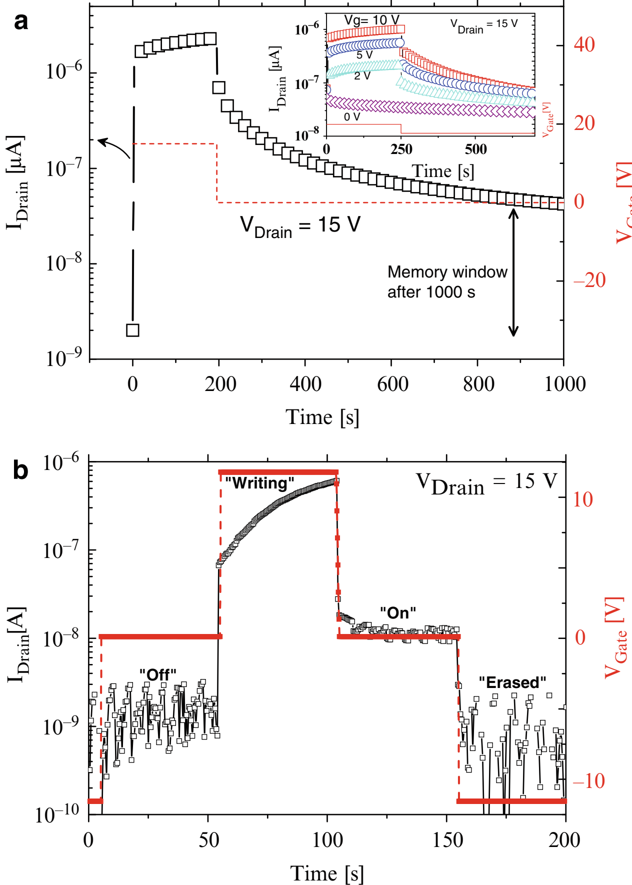


**Fig. 25** Transient response characteristics of BioFETs (**a**) indicating a long retention time. *Inset:* Transient decay characteristics of BioFET with different gate bias condition (**b**) as a memory element with an applied gate voltage pulse showing memory 'off', 'on', 'write' and 'erase'. Note: Gate voltage pulse height is shown in *right-hand scale* of each graph. (Reproduced with permission from Elsevier and [39])

Fig. 25a shows the retention time measurement as a function of $V_{Gate}$. $I_{Drain,Sat}$ can be depleted upon applying a depletion voltage as shown in Fig. 25b. For the measured $I_{Drain,Sat}$ one can define four states: 'off', 'write', 'on' and 'erase'.

## 8 Summary and Outlook

Optoelectronic devices, employing DNA-based biopolymers as either EBL or dielectric layers, can significantly enhance the performance of these devices, compared to their counterparts. In addition, biopolymers, such as salmon based DNA,

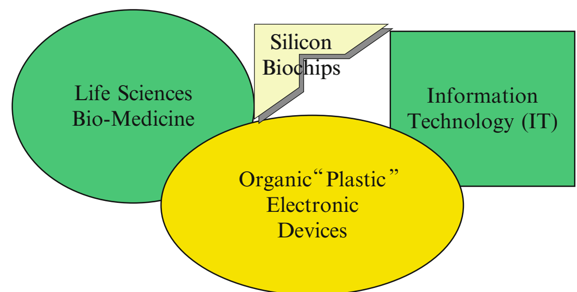


**Fig. 26** Interfacing the life sciences with electronic technology (cybernetics) as future mission for organic semiconductor devices. (Reproduced with permission from Annual Reviews, and [28])

are renewable resources and are inherently biodegradable. Additionally, the molecular weight of DNA can be tailored, with the help of a sonication procedure, to realise molecular weights ranging from 200,000 to 8,000,000 Da, which correspond to 220–12,000 base pairs, respectively. DNA-surfactant complexes render excellent thin films using common organic solvents. This process also enhances the mechanical properties of the resulting thin films and neutralises the charge of DNA. Large band gap, dielectric constant (7.8), fully transparent through the visible regime of the spectrum, tunable electrical resistivity and thermal stability (up to 230°C) make DNA–CTMA suitable for numerous electronic and optoelectronic devices. Although the mechanisms are not yet completely understood, it is proposed that charged species, present in bulk of DNA–CTMA and at the interface of DNA–CTMA and the organic semiconductor layer, are likely to be responsible for the hysteresis in the transistor characteristics. Another possible explanation is related to the formation of an electrical double layer between DNA–CTMA and the semiconductor layer, which is reflected in the measurement of an unusually high capacitance at low frequency, as shown in Fig. 21. Furthermore, due to the compatibility of carbon/hydrogen-based organic semiconductors with organic biomolecules, there can be a great opportunity to integrate such bio-organic semiconductor devices with living organisms.

In general the largely independent bio/lifesciences and information technologies of today can thus be bridged in an advanced cybernetic approach using organic semiconductor devices (Fig. 26). This field of bio-organic electronic devices is proposed to be the future mission of organic semiconductor devices.

**Acknowledgment** The authors would like to acknowledge the work done by Professor Naoya Ogata, CIST in making salmon DNA available for our BioFET research. We also wish to acknowledge the support of the Air Force Research Laboratory, Materials and Manufacturing Directorate (AFRL/RX),the Air Force Office of Scientific Research (AFOSR) and the European Office of Aerospace Research & Development (EOARD) The authors would also like to thank Dr. Joshua Hagen for his technical assistance and fruitful discussions. Excellent work done by DI P. Stadler is also acknowledged. This work is also supported by Austrian Funds for Advancement of Science FWF (NFN S9711-N08).

## References

1. Huitema HE, Gelinck GH, Van Veenendaal E, Cantatore E, Touwslager FJ et al. (2003) A flexible QVGA display with organic transistors. IDW (Informations-dienst-wissenschaft) 1663
2. Darlinski G, Böttger U, Waser R, Klauk H, Halik M, Zschieschang U, Schmid G, Dehm C (2005) J Appl Phys 97:093708
3. Crone B, Dodabalapur A, Gelperin A, Torsi L, Katz HE, Lovinger AJ, Bao Z (2001) Appl Phys Lett 78:2229
4. Robinson BH, Seaman NC (1987) Protein Eng 295:1
5. Yan H, Zhang X, Shen Z, Seeman NE (2002) Nature 62:415
6. Turberfield A (2003) Phys World 43:16
7. Braun E, Eichen Y, Sivan U, Yoseph GB (1998) Nature 291:775
8. de Pablo PJ, Moreno-Herrero F, Colchero J, Gómez Herrero J, Herrero P, Baró AM, Ordejón P, Soler JM, Artacho E (2000) Phys Rev Lett 85:4992
9. Cai L, Tabata H, Kawai T (2000) Appl Phys Lett 77:3105
10. Storm AJ, van Noort J, De Vries S, Dekker C (2001) Appl Phys Lett 79:3881
11. Hwang JS, Kong KJ, Ahn D, Lee GS, Ahn DJ, Hwang SW (2002) Appl Phys Lett 1134:81
12. Zhang Y, Austin RH, Kraeft J, Cox EC, Ong NP (2002) Phys Rev Lett 89:198102
13. Porah D, Bezrydin A, de Vries S, Dekker C (2000) Nature 403:635
14. Yang Y, Yin P, Li X, Yan Y (2005) Appl Phys Lett 203901
15. Fink H, Schönenberger C (1999) Nature 398:407
16. Yu Kasumov A, Kociak M, Guéron S, Reulet B, Volkov VT, Klinov DV, Bouchiat H (2001) Science 291:5502
17. Wang L, Yoshida J, Ogata N, Sasaki S, Kajiyama T (2001) Chem Mater 13(4):1273
18. Zhang G, Wang L, Yoshida J, Ogata N (2001) In: Wang Q, Lee T (eds) SPIE Proceedings of Optoelectronic, Materials and Devices for Communications, vol 337, p 4580
19. Heckman EM, Hagen JA, Yaney PP, Grote JG, Hopkins FK (2005) Appl Phys Lett 87:211115
20. Ghirlando R, Wachtel EJ, Arad T, Minsky A (1992) Biochem 31:7110
21. Tanaka K, Okahata Y (1996) J Am Chem Soc 118:10679
22. Kimura H, Machida S, Horie K, Okahata Y (1998) Polym J 30:708
23. Grote J, Ogata N, Hagen J, Heckman E, Curley M, Yaney P, Stone M, Diggs D, Nelson R, Zetts J, Hopkins F, Dalton L (2003) In: Yates A, Belfield K, Kajzar F, Lawson C (eds) SPIE Proceedings of Nonlinear Optical Transmission and Multiphoton Processes in Organics, vol 53, p 5221
24. Heckman EM, Yaney PP, Grote JG, Hopkins F, Tomczak MM (2006) Proc SPIE 6117:61170K
25. Grote JG et al. (2005) Proc SPIE 5934:593406
26. Subramaniam G, Heckman E, Grote J, Hopkins F (2005) IEEE Microwave Wireless Comput Lett 15:232
27. Hagen JA, Li WX, Grote JG, Steckl AJ (2006) Appl Phys Lett 88:171109
28. For a review article on OFET: Singh ThB, Sariciftci NS (2006) Annu Rev Mater Res 36:199
29. Klauk H, Halik M, Zschieschang U, Schmid G, Radlik W (2002) J Appl Phys 92:5259
30. Parashkov R, Becker E, Ginev G, Riedl T, Johannes HH, Kowalsky W (2006) J Appl Phys 95:1594
31. Park J, Park SY, Shim S, Kang H, Lee HH (2004) Appl Phys Lett 85:3283
32. Schroeder R, Majewski LA, Grell M (2003) Appl Phys Lett 83:3201
33. Knipp D, Street RA, Krusor B, Ho J, Apte RB (2002) Mater Res Soc Symp Proc 708:BB 10
34. Schroeder R, Majewski LA, Grell M (2004) Adv Mater 16:633
35. Singh ThB, Marjanovi N, Matt GJ, Sariciftci NS, Schwödiauer R, Bauer S (2004) Appl Phys Lett 85:5409
36. Naber RCG, Tanase C, Blom PWM, Gelinck GH, Marsman AW, Touwslager FJ, Setayesh S, De Leeuw DM (2005) Nat Mater 4:243
37. Singh ThB, Marjanovi N, Stadler P, Auinger M, Matt GJ, Günes S, Sariciftci NS, Schwödiauer R, Bauer S (2005) J Appl Phys 97:083714
38. Singh ThB, Sariciftci NS, Grote J, Hopkins F (2006) J Appl Phys 100:024514

39. Stadler P, Oppelt K, Singh B, Grote J, Schwödiauer R, Bauer S, Piglmayer-Brezina H, Bäuerle D, Sariciftci NS (2007) Org Electron 8:648
40. Goldmann C, Krellner C, Pernstich KP, Haas S, Gundlach DJ, Batlogg B (2006) J Appl Phys 99:034507
41. Katz HE, Hong XM, Dodabalapur A, Sarpeshkar R J Appl Phys (2002) 91:1572
42. Veres J, Ogier S, Lloyd G, de Leeuw D (2004) Chem Mater 16:4543
43. Street R, Salleo A, Chabinyc M (2003) Phys Rev B 68:085316
44. Kremmer F, Schönhals A (eds) (2003) Broadband dielectric spectroscopy. Spinger, Berlin Heidelberg New York, p 87
45. Stadler P (2007) Master thesis, Linz Institute of Organic Solar Cells (LIOS), Johannes Kepler University of Linz, Austria

Adv Polym Sci (2010) 223: 213–257
DOI:10.1007/12_2009_9
© Springer-Verlag Berlin Heidelberg 2009
Published online: 30 July 2009

# Organic Field-Effect Transistors for CMOS Devices

**Christian Melzer and Heinz von Seggern**

**Abstract** Organic field-effect transistors (OFETs) are the key elements of future low cost electronics such as radio frequency identification tags. In order to take full advantage of organic electronics, low power consumption is mandatory, requiring the use of a complementary metal oxide semiconductor (CMOS) like technique. To realize CMOS-devices p-type and n-type organic field-effect transistors on one substrate have to be provided. Here, the latest concepts to produce in a straightforward way complementary acting OFETs for CMOS-like elements are illustrated on basis of the inverter. Starting from a simple description of thin-film transistors, the basic design rules for the development of complementary OFETs are given and some realizations of CMOS-like inverters are discussed. A CMOS-like inverter based on two identical field-effect transistors disclosing almost unipolar p-type and n-type behavior is presented.

**Keywords** CMOS · Charge carrier injection · Charge carrier transport · Field-effect transistor · Organic semiconductor

## Contents

1 Introduction ........ 214
2 The Organic Field-Effect Transistor ........ 218
2.1 A Simple OFET Model ........ 219
2.2 The Unipolar Organic Field-Effect Transistor ........ 224
2.3 The Insulator ........ 227
2.3.1 Insulator and Semiconductor Morphology ........ 228
2.3.2 Dielectric Properties of the Insulator ........ 228
2.3.3 Electronic States at the Insulator Surface ........ 229

C. Melzer and H. von Seggern (✉)
Institute of Materials Science, Technische Universität Darmstadt, Petersenstraße 23, 64287 Darmstadt, Germany
e-mail:seggern@e-mat.tu-darmstadt.de

2.4 The Source and Drain Contacts ... 237
2.4.1 Contact Resistance in Unipolar Devices ... 238
3 Organic Field-Effect Transistors and CMOS Inverters ... 240
3.1 CMOS Inverters Through Selected Source/Drain Metals ... 243
3.2 CMOS Inverters Through $SiO_2$ Passivation ... 244
3.3 The Ambipolar CMOS Inverter ... 245
3.4 CMOS Inverters Through Dielectric Interface Modification ... 247
4 Conclusion ... 251
References ... 253

# 1 Introduction

Since its first realization by Bardeen, Shockley and Brattain in 1951 [1], the transistor has become one of the key elements in modern day electronics. Its widespread implementation is at last the result of the capability to modulate the electric current by an electric quantity. Even though many transistor concepts have been developed over the years, they can mainly be subdivided into the two groups of bipolar (1) and field-effect transistors (FETs) (2):

1. Bipolar transistors are realized using either an npn- or pnp-junction sequence. The different segments of the device are named as collector, base, and emitter electrode, respectively. In order to operate the transistor, one of the junctions is forward biased, while the other is biased in reverse. Using a small control current over the base electrode, a significant current between the collector and emitter electrodes is enabled.
2. As for the bipolar transistor, the field-effect transistor incorporates an electrode (gate) by which the current between two other electrodes (source and drain) can be modulated. However, for this type of transistor the control electrode is isolated from the transistor channel by a gate dielectric. The conductivity in the transistor channel is altered by applying a voltage between the gate and the source electrode resulting in a change in charge carrier density at the dielectric semiconductor interface as a consequence of the so called field-effect. In contrast to the bipolar transistors, the field-effect transistor is voltage controlled.

A cross section of the respective transistor types is depicted in Fig. 1. While the fields of application for both bipolar and field-effect transistors differ, both concepts

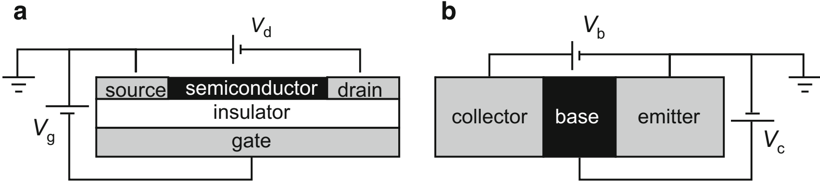


**Fig. 1** Cross section of **a** a bottom gate field-effect transistor and **b** a bipolar transistor as grounded emitter circuits

are equally important for today's electronic applications. Due to their large dielectric strength, their nonsensitive characteristic with respect to electrostatic interference, as well as their high transconductance, bipolar transistors are generally used for the realization of high and low frequency, as well as power amplifiers. Due to their short switching times and excellent spatial integrability, high-density integrated circuits such as microprocessors and semiconductor memories are typical fields of application for field-effect transistors [2]. With respect to the display industry, the FET has also gained significant importance. For most active-matrix liquid crystal, electrophoretic, or organic light-emitting diode (OLED) based displays, FETs are used as the switching element of the respective pixels. However, for such applications a special type of FET, the thin-film field-effect transistor (TFT) is used. Due to its device configuration, which is based on a thin amorphous or polycrystalline semiconducting layer, the TFT can be realized by common thin-film techniques such as chemical/physical vapor deposition (PVD) or maybe, in the near future, by printing or spin coating techniques. These types of production processes are less restricted to a specific substrate and can be realized on large area and flexible substrates. While the sheer substrate size is important to lower the production cost, the attribute flexibility is a key element for aspired future applications such as rollable displays or low cost roll to roll processed electronics such as radio frequency identification (RFID) tags envisioned as replacement for the commonly utilized barcode.

Whereas inorganic polycrystalline or amorphous silicon technologies are well established for the realization of TFTs, high process temperatures [3–5] are required during their production and are one of the reasons for a limited compatibility with flexible plastic substrates. Here, organic field-effect transistors (OFETs) are of special interest since the usual production at low temperature allows for the realization of flexible electronic devices, while still being comparably inexpensive.

Despite the fact that π-conjugated polymers or small molecules have been known as organic semiconductors since the 1940s [6], and OLEDs [7–10] as well as the field-effect in organic semiconductors [11, 12] have been studied in the following three decades, the first organic field-effect transistors were not demonstrated until the mid 1980s [13, 14]. Those early OFETs were implemented using organic dyes such as merocyanine, or polymeric semiconductors such as polythiophene. Since these early days, the OFET performance ($\mu \sim 10^{-6}\,\mathrm{cm^2\,V^{-1}\,s^{-1}}$, On/Off $\sim 10^{2-3}$) has significantly improved over the years, even challenging today's electrical performance of a-Si:H TFT ($\mu \sim 1\,\mathrm{cm^2\,V^{-1}\,s^{-1}}$, On/Off $\sim 10^6$). Illustrated in Fig. 2 is the improvement in the field-effect hole mobility of p-type OFETs, summarizing the development from 1984 to 2007. The respective references are listed in Table 1. A steep increase in charge carrier mobility of over six orders of magnitude was gained in this time period, thus increasing the switching speed of organic electronics in general. This device development is in part ascribed to an optimized semiconductor morphology through improved process parameters as well as an adequate choice in smooth (rms roughness$\sim$ 1 nm) functionalized or nonfunctionalized gate-dielectrics [15–20]. Properly adjusted semiconductor morphology is mandatory, because a strong π-π overlap in the current direction is required to assure an efficient intermolecular charge carrier transport without a substantial amount of electron

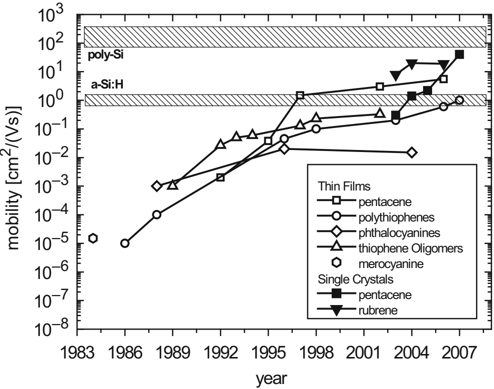


**Fig. 2** The evolution of the hole field-effect mobility of various organic semiconductors in time. The data of Table 1 are grouped into families of molecules with similar main chain. Additionally, hole field-effect mobilities of rubrene and pentacene in single crystals are depicted. For comparison, the electron mobilities of a-Si:H and poly-Si are shown

traps in the transistor channel. Therefore, crystalline materials such as pentacene are preferably used as polycrystalline thin films or even as single crystals.

While p-type OFETs have been intensely studied since the first OFET implementation, fewer reports have been published about n-type organic transistors. Literature takes us just back to the early 1990s where first reports on phthalocyanines appeared [15]. This indicates the fact that the realization of n-type OFETs appeared to be not as easy as the realization of p-type transistors. As prominent examples, $C_{60}$ and its derivative [6,6]-phenyl $C_{61}$-butyric acid methyl ester (PCBM) being well known as electron transporting acceptor moieties in organic bulk heterojunction photovoltaic cells [21, 22] have proven to act as excellent electron conducting materials in organic TFTs [23, 24]. By the use of such fullerene based thin films, electron field-effect mobilities of $1\,cm^2\,V^{-1}\,s^{-1}$ have been reported. These moieties have the advantage of low-lying LUMO (lowest unoccupied molecular orbital) and HOMO (highest occupied molecular orbital), promoting the n-channel behavior in respective OFETs.

Because the HOMO level of many organic semiconductors is in the range of 5 eV, aligning well with the work function of the typically used gold source/drain contacts (4.8–5.1 eV), the injection of holes in p-channel transistors can be easily achieved. In the contrary, the LUMO level typically lies much higher at around 2–3 eV and thus, the use of gold electrodes leads to large injection barriers in the order of electron volts impeding any n-channel behavior of the OFET. Hence, for n-channel transistors the injection of electrons into the LUMO level of the organic semiconductor has to be realized using appropriate electrode materials such as the highly reactive, low workfunction metal calcium. Unfortunately, organic radical anions are mostly present in an n-type channel of an OFET having a rather strong reducing strength, which leads to a reaction with interdiffused oxygen or water [25]. Hence, specially designed semiconductors are often utilized for n-type OFET applications, mostly comprising strong electron-withdrawing groups such as –F or –CN. By employing moieties of electron-withdrawing groups the electron affinity (EA) can be increased, thus allowing for a promoted electron injection even via stable high workfunction metals such as gold. At the same time, the environmental stability of the used organic semiconductor is improved. However, organic compounds such as $C_{60}$, PCBM, or perylene diimide derivatives lacking strong electron-withdrawing groups

**Table 1** The evolution of the hole field-effect mobility of various organic semiconductors in time and the associated references. Additionally, hole field-effect mobilities of rubrene and pentacene in single crystals are listed. The data are summarized in Fig. 2

| Year | Hole mobility $\left(\mathrm{cm}^2\,\mathrm{V}^{-1}\,\mathrm{s}^{-1}\right)$ | Material | References |
|---|---|---|---|
| 1984 | $1.5 \times 10^{-5}$ | Merocyanine | [13] |
| 1986 | $10^{-5}$ | Polythiophene | [14] |
| 1988 | 0.001 | Phthalocyanine | [83] |
| 1988 | $10^{-4}$ | Poly(3-hexylthiophene) | [84] |
| 1989 | $10^{-3}$ | α-Sexithiophene | [85] |
| 1992 | 0.002 | Pentacene | [86] |
| 1992 | 0.027 | Oligothiophene | [86] |
| 1993 | 0.05 | α-ω-Dihexyl-sexithiophene | [87] |
| 1994 | 0.06 | Oligothiophene | [88] |
| 1995 | 0.038 | Pentacene | [89] |
| 1996 | 0.02 | Copper phthalocyanine | [90] |
| 1996 | 0.045 | Poly(3-hexylthiophene) | [91] |
| 1997 | 1.5 | Pentacene | [17] |
| 1997 | 0.13 | α-ω-Dihexyl-sexithiophene | [92] |
| 1998 | 0.1 | Poly(3-hexylthiophene) | [93] |
| 1998 | 0.23 | α-ω-Dihexyl-quaterthiophene | [94] |
| 2002 | 3 | Pentacene | [95] |
| 2002 | 0.33 | 8T-Oligothiophene | [96] |
| 2003 | 0.2 | Poly(3-hexylthiophene) | [97] |
| 2004 | 0.015 | Copper phthalocyanine | [98] |
| 2006 | 5.5 | Pentacene | [99] |
| 2006 | 0.6 | Poly(thieno[3,2-*b*] thiophene) | [100] |
| 2007 | 1 | Poly(2,5-bis(3-tetradecylthiophen-2-yl)thieno[3,2-*b*] thiophene) | [101] |
| | | *Single crystal* | |
| 2003 | 0.3 | Pentacene | [102] |
| 2003 | 8 | Rubrene | [103] |
| 2004 | 1.4 | Pentacene | [104] |
| 2004 | 20 | Rubrene | [105] |
| 2005 | 2.2 | Pentacene | [106] |
| 2006 | 19 | Rubrene | [107] |
| 2007 | 40 | Pentacene | [108] |

but unveiling low-lying LUMOs also allow for good n-type field-effect behavior, and even environmental stability [23–26].

With respect to complementary metal oxide semiconductor (CMOS) technology, where p- and n-type semiconductors with balanced charge carrier transport properties are required on a single substrate, the diverging material properties of organic compounds suited for n-type and p-type conduction cause technological difficulties. Since organic semiconductors cannot easily be structured by classical lithography without significant degradation of the charge carrier transport properties, complicated and costly approaches for the realization of organic CMOS devices have to be applied. The prevailing degradation of the organic material is

due to an intolerance of most organic semiconductors to UV radiation, water, and oxygen. The most frequently implemented technique to realize CMOS-like organic devices is the deposition of spatially separated semiconductor materials with complementary charge carrier transport and injection properties [27–30] by PVD using shadow masks. Another approach to deposit organic materials in a laterally separated pattern is, for example, inkjet printing [31–33]. Unfortunately, both of the techniques mentioned do not meet the requirements for mass production in a continuous roll-to-roll process.

Due to the complexity of the structured implementation of several different organic materials on one substrate, up to now cost efficient organic logic circuits are only realized by employing unipolar acting elements. Unipolar acting inverters in ring oscillators [34] are prominent examples of such circuits. From today's viewpoint of inexpensive organic electronics, more elegant and more economic ways have to be employed to bring organic electronics into application. In this regard, some of the recently developed concepts leading to organic CMOS-like devices are outlined in this chapter. As an alternative to spatial separation of the used substrate in n- and p-type segments by simply texturing specific organic semiconductors, blends of n- and p-conducting moieties have been employed, circumventing a complex structuring [35]. These blends exhibit ambipolar behavior, meaning that in related OFETs, electron as well as hole conduction is possible. Even simpler, single low-bandgap semiconductors have been employed that show ambipolar character and thus can be used for n-type and p-type OFETs simultaneously [35]. However, all these developments exhibited one major drawback: CMOS devices, e.g., inverters, using these semiconductors exhibit substantial electrical losses especially in the final logical states discarding the actual advantage of CMOS technology. It is therefore reasonable to develop new concepts, which allow for a simple device preparation but yield improved CMOS operation. In this chapter, it is shown that alternative ways exist to fabricate easily such enhanced CMOS-like devices. It is argued that ambipolar acting field-effect transistors are suitable precursors for improved CMOS devices prepared with a simplified method since they are the source of any unipolar-acting OFET. To tune ambipolar OFETs to either n-type or p-type the charge carrier transport properties in the transistor channel as well as the source/drain contacts can be engineered, which is discussed below on basis of pentacene OFETs. The adjustment of the contacts and the insulator/semiconductor interface allows for the realization of full pentacene-based CMOS inverters. Furthermore, it is demonstrated that fully functioning CMOS inverters can be obtained using an identical device design for the employed unipolar p- and n-type OFET [36].

## 2 The Organic Field-Effect Transistor

Organic field-effect transistors are three terminal devices that have the capability to modulate the conductance between the metallic source and drain terminal by changing the potential of a third metal terminal, the gate. The layout of a typical field-effect transistor is depicted in Fig. 1a. The organic semiconductor which

carries the current between source and drain is separated from the gate terminal by a dielectric layer providing a capacitive coupling between the gate metal and the semiconductor. Naturally, the conductivity of the employed organic semiconductor is limited by the low intrinsic charge carrier density that results from the large energy difference of several electron volts between the HOMO and the LUMO. However, the charge carrier density and therefore the conductivity are increased by diffusion of excess charge carriers from the source and drain contacts into the semiconductor. Since these excess charge carriers are either electrons or holes, they are repulsed by their self-induced electric field and therefore cannot penetrate deep into the semiconductor. A charge carrier penetration deeper into the semiconductor can be promoted by applying a bias between source and gate electrodes. In this case, the injected excess charge carriers are attracted by and drift towards the gate electrode and finally accumulate at the semiconductor dielectric interface. This process continues until the surface charge at the gate is fully compensated and the surface potentials at the insulator/semiconductor interface and the source/drain contacts have become equal. The accumulation layer and the gate electrode form a charged capacitor and the charged region of the semiconductor at the surface of the gate insulator is called channel. Depending on the applied gate voltage $V_{\mathrm{g}}$, electrons $\left(V_{\mathrm{g}} > 0\,V\right)$ or holes $\left(V_{\mathrm{g}} < 0\,V\right)$ can be accumulated in the channel. Due to the accumulation of charge carriers in the channel, the conductivity in the organic semiconductor is locally increased and a substantial current can flow from source to drain once a bias $V_{\mathrm{d}}$ is applied between them.

## 2.1 A Simple OFET Model

The general current voltage characteristic of an OFET can be easily understood in terms of a simple equivalent circuit of a resistor–capacitance network as depicted in Fig. 3 [37]. The basis of the calculation is the so-called gradual channel approximation which assumes that the field perpendicular to the current flow generated by the gate voltage is much larger than the field driving the current. This is feasible for long channels $(L > 10 \times d_{\mathrm{diel}})$, but fails for the description of short channel transistors. $L$ relates to the channel length and $d_{\mathrm{diel}}$ to the dielectric layer thickness [38]. For simplicity, charge carrier diffusion and specific properties of organic semiconductors such as a charge carrier density dependent mobility will be not taken into account but have been reported in highly disordered organic semiconductors [39–41]. Due to the dependence of the charge carrier mobility on the charge carrier density, the field-effect mobility is in general dependent on the spatial position [42]. Possible contact resistances at source and drain electrodes are ignored as well. This is only reasonable as long as ohmic contacts develop at both electrodes.

At a given gate bias $V_{\mathrm{g}}$ charges are accumulated near the source contact leading to a surface charge density $\hat{Q}$ so that the resulting channel potential equals the source potential, in the present case chosen to be zero. At the source we obtain

$$\hat{Q}(0) = -\hat{C}V_{\mathrm{g}}, \tag{1}$$

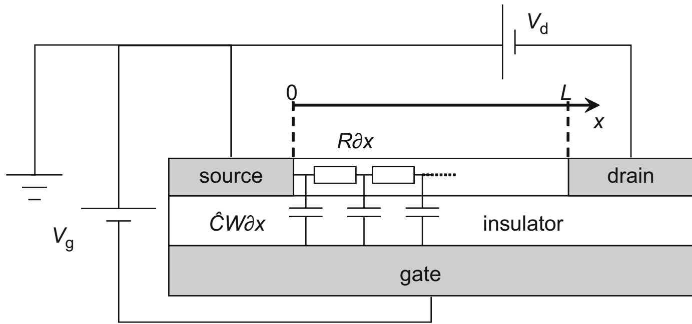


**Fig. 3** Scheme of an OFET model based on a resistor–capacitance network circuit

where $\hat{C}$ is the areal capacitance $\varepsilon_0\varepsilon_{\text{diel}}/d_{\text{diel}}$ determined by the gate dielectric thickness $d_{\text{diel}}$ and its relative permittivity $\varepsilon_{\text{diel}}$. $\varepsilon_0$ is the permittivity of free space. Due to a finite differential resistivity a continuous potential drop $V(x)$ occurs along the channel and hence, at the position $x$ from the source electrode the surface density of accumulated charges is given by

$$\hat{Q}(x) = \hat{C}\left(V(x) - V_{\text{g}}\right). \tag{2}$$

An unambiguous boundary condition at the drain electrode is

$$\hat{Q}(L) = \hat{C}\left(V_{\text{d}} - V_{\text{g}}\right). \tag{3}$$

Assuming that electrons and holes do not exist simultaneously at the same position in the channel since they annihilate due to strong recombination, either electrons $\left(\hat{Q} = -|q|\,\hat{n}\right)$ or holes $\left(\hat{Q} = |q|\,\hat{p}\right)$ are accumulated at the position $x$, depending on $V(x) - V_{\text{g}}$. Here $q$ is the elementary charge and $\hat{n}$ and $\hat{p}$ are the electron and hole surface charge densities, respectively. Thus, in the vicinity of the source terminal the gate voltage determines which charge carrier species dominates. On the other hand, whether electrons or holes are accumulated close to the drain electrode depends on $V_{\text{d}} - V_{\text{g}}$. For $V_{\text{g}} < 0\,\text{V}$ and $V_{\text{d}} > V_{\text{g}}$ holes prevail in the entire channel (or for $V_{\text{g}} > 0\,\text{V}$ and $V_{\text{d}} < V_{\text{g}}$ electrons) and the OFET operates in the unipolar regime. Yet, once $V_{\text{g}} < 0\,\text{V}$ and $V_{\text{d}} < V_{\text{g}}$ hold, electrons are accumulated at the drain (or holes as long as $V_{\text{g}} > 0\,\text{V}$ and $V_{\text{d}} > V_{\text{g}}$ holds) while holes (electrons) still predominate at the source. Since electrons and holes exist in the channel at the same time, the OFET is called to operate in the ambipolar regime.

The differential resistivity $\partial R(x)$ of the transistor channel is determined by the local surface charge density either determined by holes $\left(V(x) > V_{\text{g}}\right)$ or electrons $\left(V(x) \leq V_{\text{g}}\right)$:

$$\partial R(x) = \begin{cases} +\dfrac{\partial x}{W\mu_{\text{p}}\hat{Q}(x)} & \text{for } V(x) > V_{\text{g}} \\ -\dfrac{\partial x}{W\mu_{\text{n}}\hat{Q}(x)} & \text{for } V(x) \leq V_{\text{g}} \end{cases}. \tag{4}$$

Here $W$ is the channel width and $\mu_{p,n}$ are the constant mobilities of the holes and electrons in the transistor channel, respectively. In reality a correction of the gate bias is necessary since only moveable charges can participate in the current while, for instance, accumulated charge carriers located in electronic trap states do not. In general, charge carrier transport in most OFETs is along localized states distributed in energy due to prevailing disorder and thus low tail states of the resulting density of states distribution have to be considered as effective electronic traps reducing the density of free carriers. To take this into account, it is simplest to introduce threshold voltages for holes and electrons which correct the gate bias to an effective gate bias $V_g^{eff} = \left(V_g - V_{th}\right) \cdot \Theta\left(V_g - V_{th}\right)$ and thus the total accumulated surface charge density to a surface charge density of mobile charges. Here $\Theta(x)$ is the Heaviside-step function. At this point it is worth mentioning that the threshold voltage is simply an auxiliary quantity adapting the calculated device characteristics to the measured ones irrespective the physical origin behind it. In principle there are many reasons for a threshold voltage correction of the gate bias. Beside the already mentioned existence of traps reducing the amount of free charge carriers, surface charges might be compensated by complementary charge carriers in the channel, thus leading to an increased channel conductivity and therefore to a threshold voltage. In this contribution it will be shown that the control of the density of interfacial trap states as well as a metastable surface charge can be used to tune the device characteristics of OFETs even allowing for a switch from one transport mode to another.

The ratio between $V(\mathrm{x})$ and the total voltage drop $V_d$ along the channel is given by the ratio of the channel resistivity $R(x)$ at the position $x$ and the total channel resistivity $R_{tot}$. Thus, $\partial\hat{Q} = CV_d / R_{tot}\partial R$ holds and with Eq. (4) a first-order differential equation in $\hat{Q}$ is obtained:

$$\hat{Q}\partial\hat{Q} = \begin{cases} +\dfrac{\hat{C}V_d}{R_{tot}W\mu_p}\partial x & \text{for } \hat{Q} > 0 \\ -\dfrac{\hat{C}V_d}{R_{tot}W\mu_n}\partial x & \text{for } \hat{Q} \leq 0 \end{cases}. \tag{5}$$

This differential equation can be solved for the boundary condition given in Eq. (1). With Eq. (3) the solution provides the possibility to calculate the total resistivity across the entire transistor channel and hence, the current between drain and source terminal $I_d$ since $I_d = V_d / R_{tot}$.

In a general form, the drain current for the same sign of $V_d$ and $V_g$ is then given by

$$|I_d| = \frac{\hat{C}W}{2L} \begin{cases} \mu_1\left(2V_g - V_d\right)V_d & \text{for } |V_d| \leq \left|V_g\right| \\ \left[\mu_1 V_g^2 + \mu_2\left(V_d - V_g\right)^2\right] & \text{for } |V_d| > \left|V_g\right| \end{cases}. \tag{6}$$

In Eq. (6) $L$ is the channel length while $\mu_{1,2}$ are either the mobility of electrons $(1 \rightarrow \mathrm{n})$ and holes $(2 \rightarrow \mathrm{p})$, respectively, or vice versa that of holes $(1 \rightarrow \mathrm{p})$ and electrons $(2 \rightarrow \mathrm{n})$. The former holds for OFETs driven in electron accumulation mode ("electron accumulation mode" we define as $V_g > 0\,\mathrm{V}$ following the

nomenclature used for unipolar OFETs) while the latter is valid for the hole accumulation mode ("hole accumulation mode" we define as $V_g < 0\,\mathrm{V}$).

As long as the applied drain voltage $|V_d|$ is smaller than the gate voltage $|V_g|$ only one charge carrier type is accumulated and the current increases linearly with $V_d$ and $V_g$. When $|V_d|$ approaches $|V_g|$ the channel depletes more and more in the vicinity of the drain electrode; $\hat{Q}(L) \to 0\,\mathrm{Cm}^{-2}$. As a consequence, the current tends to saturate with increased $V_d$ and is fully saturated at $V_d = V_g$. Once $|V_d| > |V_g|$, the electric field between gate and drain is inverted and, hence, the complementary charge carrier species is injected from the drain. This leads to a further increase of the current, given by the second term in Eq. (6) being proportional to the mobility of the complementary charge carrier type [37]. The calculated output $\left(I_d|_{V_g} \text{vs.}\, V_d\right)$ and transfer $\left(I_d|_{V_d} \text{vs.}\, V_g\right)$ characteristics of such an ambipolar field-effect transistor is shown in Fig. 4 for different gate and drain bias, respectively.

As long as the transistor is operating in the ambipolar range $\left(|V_d| > |V_g|\right)$, the channel can be divided into two regions where essentially either electron or hole accumulation prevails and thus one can described the OFET as two serial transistors (n-type and p-type) with varying channel lengths operated in saturation where the sum of the respective channel lengths of the partial n- and p-type OFETs equals the total channel length $L$ of the entire ambipolar OFET. The current through the channel is no longer caused by injection and ejection of one type of the charge carrier, but

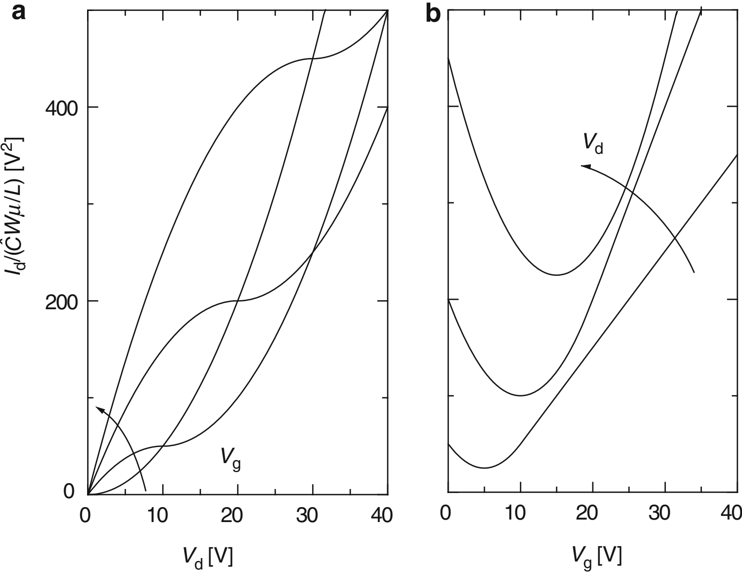


**Fig. 4** Simulated current/voltage characteristics of an ambipolar OFET using the solution of the resistor–capacitance network model depicted in Fig. 3. **a** The output $\left(V_g = 0, 10, 20, 30\,\mathrm{V}\right)$ and **b** the transfer characteristic $(V_d = 10, 20, 30\,\mathrm{V})$. The electron and hole field-effect mobilities are assumed to be equal

by injection and recombination of both charge carrier types. Thereby charge carrier recombination occurs at the merged pinch-off point of both serial transistors with a vanishing lateral extension. The position of the recombination zone $x_r$ that separates the complementary channel regions is given by $V(x_r) = V_g$ and yields

$$x_r = \frac{LV_g^2}{V_g^2 + \frac{\mu_2}{\mu_1}\left(V_d - V_g\right)^2}. \tag{7}$$

At $x_r/L = 0$ the recombination zone is located at the source electrode, while for $x_r/L = 1$ it is found at the drain electrode. Apparently, the position of the recombination zone in the transistor channel can be spatially controlled by the applied voltages. For $V_d = V_g$ the recombination zone is located at the drain electrode and moves at given $V_g$ towards the source electrode once $V_d$ is increased.

The ambipolar character of an organic OFET is most illustratively demonstrated in field-effect transistors utilizing strongly luminescent organic semiconductors. In this case the recombination of electrons and holes is accompanied by light emission. As a consequence the position $x_r$ of the recombination zone emerges as a sharp light-emitting line between source and drain which can easily be detected by optical microscopy. In Fig. 5 a photograph of the channel region of an ambipolar light-emitting OFET is shown [43]. Additionally, the measured transfer characteristic and the related position of the recombination zone are depicted. In this example the used

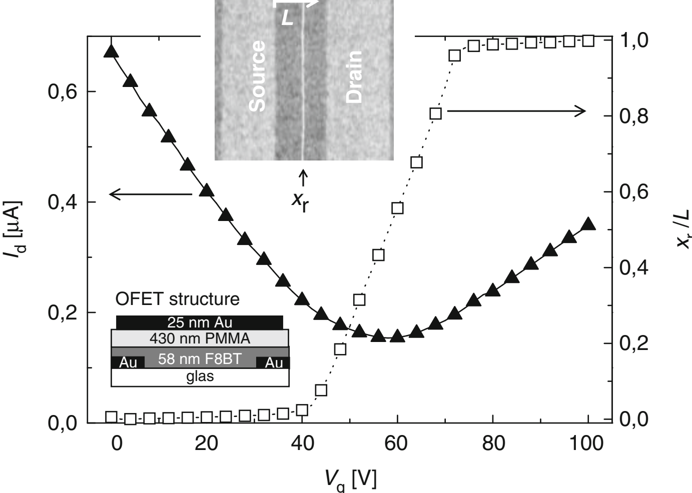


**Fig. 5** The transfer characteristic and the position of the recombination zone relative to the source contact of a light-emitting field-effect transistor. The transistor has been measured at $V_d = 100$ V. The device scheme and a micrograph of the channel of the OFET driven in the ambipolar regime are depicted as insets. The device consists of: poly(methylmethacrylate) (PMMA), poly(9,9-di-*n*-octyl-fluorene-*alt*-benzothiadiazole) (F8BT), and Au source/drain terminals. The source drain metallization was 40 nm thick and the channel length was 100 µm ($L$). The optical micrograph was taken at $V_g = 55$ V and $V_d = 100$ V. The recombination zone appears as a narrow luminescent line in the middle of the channel. With permission reprinted from [43], copyright © 2008 Oldenbourg Wissenschaftsverlag GmbH

top gate OFET is comprised of poly(9,9-di-*n*-octylfluorene-*alt*-benzothiadiazole) (F8BT) as semiconductor, Au source/drain contacts and poly(methyl methacrylate) (PMMA) as polymer dielectric. In comparison to the channel length $L$ the recombination zone appears extremely narrow, underlining the assumption of strong recombination and thus approving the model assumptions of simply splitting the channel in exclusively electron and hole dominated regions. The transfer characteristic of the organic light-emitting OFET proves that ambipolar behavior prevails being accompany by a change in the position $x_r$ of the recombination zone, shifting from the source to the drain electrode for increasing gate bias.

The first field-effect transistor showing light emission and ambipolar character and thus a movable recombination region upon bias change was based on the above-mentioned system where indeed balanced injection as well as transport properties of electrons and holes prevail [44]. However, light emission from organic field-effect transistors has been demonstrated for the first time on tetracene OFETs [45], which did not show the pronounced ambipolar characteristic discussed above. The fact that these tetracene transistors exhibited exclusive p-channel behavior while still emitting light seems unintuitive in the first place. The p-channel behavior was attributed to the use of gold source/drain contacts which hinder an efficient injection of electrons into the channel. Yet, in the saturation regime of the transistor, strong electric fields at the drain electrode emerge which might lead to a field-enhanced injection of the complementary charge carrier species and thus to light emission. Hepp et al. argued that this field enhancement is promoted by an under-edged drain electrode in the bottom contact OFET geometry, resulting in a virtual organic light-emitting diode (OLED) driven at high fields. As a result, the recombination zone appeared for different bias values always in the vicinity of the drain electrode and did not move into the transistor channel leading to a field-effect transistor with pronounced unipolar current/voltage behavior.

## *2.2 The Unipolar Organic Field-Effect Transistor*

Even though the ambipolar OFET constitutes the most general form of an OFET, unipolar FETs are technologically much more important since they can be switched off by setting $V_g = 0\,\mathrm{V}$ while the ambipolar OFET cannot. In general, unipolar field-effect transistors are special cases of ambipolar OFETs as will be illustrated in the following. According to Eqs. (6) and (7) the current and the position of the recombination zone in the ambipolar regime depends on the involved charge carrier mobilities. Figure 6 shows the influence of the hole mobility on the drain current in the ambipolar regime of an OFET driven in electron accumulation mode [43]. The calculation shows that both charge carrier mobilities must be equal to obtain balanced ambipolar transport. This indeed appears to be mandatory for the realization of ambipolar light-emitting OFETs. With decreasing hole mobility but constant electron mobility the transistor characteristic turns to an unipolar behavior, being well reflected in the pinned position of the recombination zone at the drain

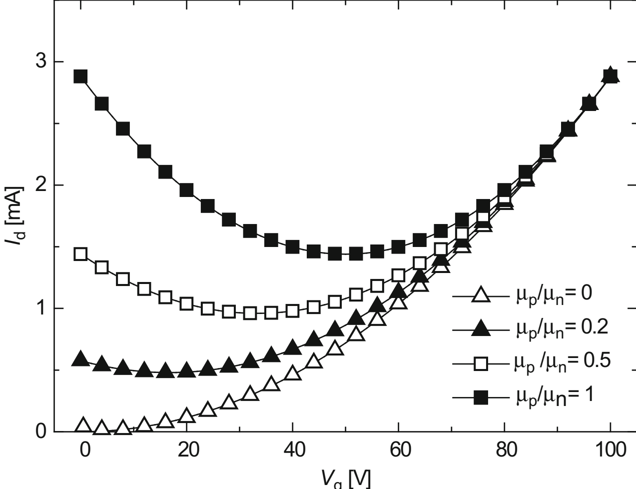


**Fig. 6** Simulated transfer characteristic in electron accumulation mode at $V_{\mathrm{d}} = 100\,\mathrm{V}$ for different ratios of the electron and hole mobility: $\mu_n = 10^{-4}\,\mathrm{m}^2\,\mathrm{V}^{-1}\,\mathrm{s}^{-1}$, $W = 8\,mm$, $L = 100\,\mu\mathrm{m}$, $V_{\mathrm{th,n}} = V_{\mathrm{th,p}} = 0$ V, $\hat{C} = 7.2 \times 10^{-5}\mathrm{F\ m}^{-2}$. With permission adapted from [43], copyright © 2008 Oldenbourg Wissenschaftsverlag GmbH

electrode. From Eq. (7) one can see that the recombination zone becomes independent of bias and remains at the drain electrode once $\mu_2 = \mu_{\mathrm{p}} \rightarrow 0\,\mathrm{cm}^2\,\mathrm{V}^{-1}\mathrm{s}^{-1}$. By varying the electron mobility while the hole mobility is fixed, a similar effect can be observed for electron dominated currents. Even though the potential drop at the drain electrode for $|V_{\mathrm{d}}| > |V_{\mathrm{g}}|$ allows for the accumulation of the complementary charge carrier species, a further transport into the transistor channel is hindered and the recombination zone cannot move into the channel. Alternatively, unbalanced threshold voltages lead to pronounced unipolar behavior. A high threshold voltage associated with the charge carrier species 2 shifts the onset of the ambipolar regime to higher drain bias and thus extends the saturation regime. Thus, by employing organic semiconductors with highly unbalanced charge carrier transport properties unipolar acting OFETs are obtainable and initially the realization of n- and p-type OFETs was attributed to the either pronounced electron or hole transport properties of the selected organic semiconductors, respectively [15].

Besides the transport properties, the contact formation between the source/drain electrodes and the organic semiconductor is crucial for the OFET performance. To illustrate this, balanced charge carrier transport properties $\mu_1 = \mu_2$ in the above evaluated model are assumed and the injection of the complementary charge carrier species is hindered, e.g., by a pronounced injection barrier at the drain/semiconductor contact. The source contact is supposed to inject freely charge carriers of type 1 and out of simplicity they are assumed to be ejected freely at the drain electrode as well. For $|V_{\mathrm{d}}| \rightarrow |V_{\mathrm{g}}|$ the channel depletes more and more in the vicinity of the drain electrode and for $|V_{\mathrm{g}}| < |V_{\mathrm{d}}|$ the charge carriers of type 1

are pushed out of the channel and flow across the semiconductor bulk to the drain. However, simultaneously the charge carriers of type 2 can be injected from the drain contact and, therefore, recombination of both charge carrier species has to be considered. The assumption of strong recombination implies that the currents of both charge carrier species annihilate each other without any mixing in the recombination zone. As a consequence, the recombination zone can only detach from the drain contact moving into the channel once the injection current of the charge carrier type 2 equals the saturated current of the charge carrier type 1. Thus, taking a constant contact resistance $R_{2,\mathrm{d}}$ for the injection of the complementary charge carrier species 2 into account, the drain current is given by

$$I_\mathrm{d} = \frac{\hat{C}W}{2L} \begin{cases} \mu_1 \left(2V_\mathrm{g} - V_\mathrm{d}\right) V_\mathrm{d}, & |V_\mathrm{d}| \le \left|V_\mathrm{g}\right| \\ \mu_1 V_\mathrm{g}^2, & \left|V_\mathrm{g}\right| < |V_\mathrm{d}| \le \left|V_\mathrm{g}\right| + |I_\mathrm{d}| R_{2,\mathrm{d}}. \\ \mu_1 V_\mathrm{g}^2 + \mu_2 \left(V_\mathrm{d} - I_\mathrm{d} R_{2,\mathrm{d}} - V_\mathrm{g}\right)^2, & \text{else} \end{cases} \quad (8)$$

In general, $I_\mathrm{d} R_{2,\mathrm{d}}$ is the potential drop at the drain required to drive an injection current $I_\mathrm{d}$ across the contact. In Fig. 7 calculated transfer characteristics for different $R_{\mathrm{p,d}}$ (substitute 2 → p) are depicted [43]. The charge carrier species 1 and 2 in Eq. (8) correspond again to electrons and holes, respectively. While a contact resistance of 0 Ω is essentially an ohmic contact, an increase in $R_{\mathrm{p,d}}$ can be seen as an increase in the hole injection barrier at the drain contact, i.e., by the choice of another metal. The contact resistance acts twofold on the transfer characteristic. On one hand the hindered injection of the complementary charge carriers results in a delayed onset of the ambipolar behavior. On the other hand, the characteristic in the ambipolar region is influenced by the reduced injection rate at the drain contact itself. Apparently, for a very high contact resistance the ambipolar behavior is fully eliminated and the device turns to an essentially unipolar behavior.

These examples illustrate that balanced injection and transport properties for electrons and holes are of crucial importance for the realization of ambipolar

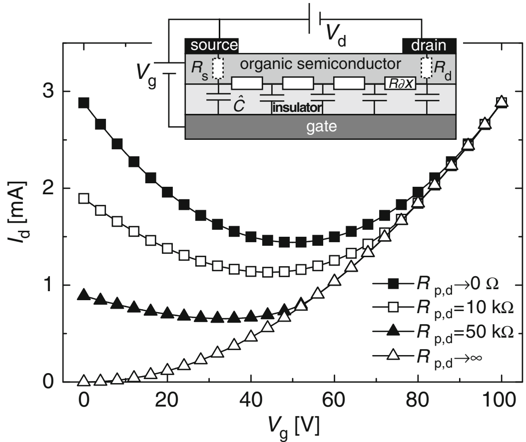


**Fig. 7** Simulated transfer characteristics in electron accumulation mode at $V_\mathrm{d} = 100\,\mathrm{V}$ for different contact resistances $R_{\mathrm{d,p}}$ at the drain terminal. $R_{\mathrm{d,p}}$ simply acts on the injection of holes (p) but not on the extraction of electrons (n). The parameters match those of Fig. 6. Furthermore, $\mu_\mathrm{p} = \mu_\mathrm{n} = 10^{-4}\,\mathrm{m^2\,V^{-1}\,s^{-1}}$ holds. With permission adapted from [43], copyright © 2008 Oldenbourg Wissenschaftsverlag GmbH

OFETs. On the other hand, unipolar n- or p-type transistors can be seen as ambipolar OFETs where the fragile balance in the hole and electron injection and/or transport properties is sufficiently disturbed. Hence, a controlled engineering of the transport and injection properties starting from ambipolar acting OFETs appears to be a promising route to obtain complementary OFETs for CMOS devices. Whether a field-effect transistor acts ambipolar, unipolar p-type or unipolar n-type depends beside the applied voltages on:

- The metals used for the charge carrier injecting and ejecting source and drain contacts, because the existence of high injection barriers hinders the efficient deliverance of charge carriers to the channel region
- The organic semiconductor, because the intrinsic transport properties of the respective organic compound may hinder any transport of injected charge carriers
- The insulator used as gate dielectric, because its surface energy, dielectric properties and electronic structure codetermine the charge transport properties in the organic semiconductor along the semiconductor/insulator interface

So it seems to be the task to identify an appropriate and easily applicable modification of a suited organic semiconductor/insulator combination together with the right choice of the source/drain metals in order to convert an ambipolar OFET to either a p-type or n-type OFET and/or even to an organic CMOS device.

## 2.3 *The Insulator*

Beside the organic semiconductor, the insulator plays a central role for the charge carrier transport in the transistor channel. This is because the majority of charge carriers flow in the immediate vicinity of the insulator/organic interface. The following estimate given in [46] will provide an indication for the spatial extend of the accumulated charge carriers into the organic semiconductor. Assuming $V_g = 10\,\mathrm{V}, \varepsilon_{\mathrm{diel}} = 4$ and $d_{\mathrm{diel}} = 100\,\mathrm{nm}$, the charge carrier areal density accumulated in the organic semiconductor can be approximated to $2 \times 10^{12}\,\mathrm{cm}^{-2}$. Since the wavefunction overlap between molecules is weak, one can assume that each molecule in the organic semiconductor provides an electronic transport state. Thus, the density of states is in the order of $10^{14}\,\mathrm{cm}^{-2}$ [47] being comparable to the density of molecules. This estimation shows that the entire accumulated charge will be located in the first monolayer of the organic semiconductor. For a carrier hop from the first monolayer to the second monolayer against the electric field generated by the gate an energy of $\sim$80 meV is required assuming an approximate distance of 0.8 nm between both layers. If compared to the mean thermal energy at room temperature such a hop would be rather unlikely. Thus it is plausible that the main charge transport will take place within the first few monolayers of the organic semiconductor from the insulator. Indeed, it has been proven by thickness dependent measurements [48–51] that the transistor channel extends only a few nanometers into the organic semiconductor [52]. It was shown that an increase of the semiconductor

thicknesses above 3 nm does not essentially affect the transistor characteristics. The fact that the charge carrier transport occurs essentially in close vicinity of the gate dielectric suggests that different gate dielectrics should lead to different charge carrier transport properties even though the same organic semiconductor is applied.

The gate dielectric affects the electrical characteristics of OFETs mainly by its influence on the morphology of the organic semiconductor, its dielectric properties, and by electronic states existing at the dielectric surface.

### 2.3.1 Insulator and Semiconductor Morphology

The relation between the employed dielectric and the semiconductor morphology is perhaps the most intensively investigated issue. Yang et al. demonstrated for instance that the surface energy of a surface energy controllable poly(imide–siloxane) influences the morphology of a pentacene based semiconducting layer and thus the electrical characteristics of respective organic field-effect transistors [53]. While Stranski–Krastanov growth with large and dendritic grains prevailed at high surface energies, a three-dimensional island growth leading to small grains was observed for lower surface energies. In spite of the small grain size and a decreased ordering of the pentacene molecules, the field-effect mobility in OFETs employing a low surface energy polymeric dielectric was found to be superior if compared to a high surface energy counterpart. This was explained by the fact that the small grains growing on the low surface energy dielectric interconnect upon the subsequent lateral growth of pentacene and thus lead to a filling of the vacant space between them.

Such results show that in first place the morphology in the transistor channel has to be tuned in order to gain suited field-effect characteristics. One goal is therefore to obtain a smooth interface without morphological defects to lower the interface roughness. Another goal is to control the orientation of the semiconductor molecules because the charge transport is known to be highly nonisotropic and requires a strong π–π overlap between the molecules along the transport direction. To control the grain growth and the molecular orientation, self-assembled monolayers (SAMs) can be used to optimize the dielectric interfaces [17–20, 54]. Recent studies by Halik et al. [55] and Klauk et al. [56] have shown that such ultra thin ($d_{\text{diel}} = 2.5\,\text{nm}$) SAMs can even be used as single gate dielectric allowing for low power OFETs and circuit applications.

### 2.3.2 Dielectric Properties of the Insulator

The impact of the mere dielectric properties on the device performance appears to be less investigated. Yet there are examples for a lowering of the charge carrier mobility with an increasing dielectric constant of the used gate insulator [57–59]. It is very likely that a higher dielectric constant of the insulating layer causes a broader distribution of the electronic states in the adjacent organic semiconductor. This can be understood as follows. The Gaussian density of state distribution in

amorphous organic semiconductors is mainly due to the electronic polarization of molecules within the vicinity of the organic molecule carrying the charge carrier. Since the molecular environment is changing from molecule to molecule due to the amorphous nature of the organic solid, the electronic polarization is changing from charged molecule to charged molecule, too. Thus, in general, in amorphous organic semiconductors a broad density of states can be expected. In the vicinity of the gate dielectric, however, a charged semiconductor molecule can polarize an adjacent gate insulator molecule too, and thus the width of the DOS in the transistor channel will differ from the width prevailing in the bulk. A broadening of the density of states in the transistor channel can be expected when a polymeric dielectric with a higher dielectric constant than that of the semiconductor is used since the local electronic polarization will be partially stronger. This leads to a widened density of states and thus to deeper electronic states from where charge carriers have to be activated to participate in the transport. This results directly in a reduced charge carrier mobility.

### 2.3.3 Electronic States at the Insulator Surface

Only recently it has been discovered that electronic states at the dielectric interface substantially determine the charge carrier transport in organic field-effect transistors. Pentacene is a prominent example where the unique p-type behavior of pentacene based OFETs has been attributed to the organic semiconductor alone and where the influence of electronic interface states at the pentacene/insulator surface has been overseen. The reason for this was the belief that organic semiconductors are unable to form dangling bonds at the interface, which are the main cause for interface states in inorganic semiconductors. However, there are other forms of interface states which can act as efficient charge carrier traps.

A pentacene OFET where a $SiO_2$ gate dielectric has been implemented, shows typically decent p-channel behavior with field-effect mobilities exceeding $0.1\,cm^2\,V^{-1}\,s^{-1}$ [60] while a lack of any electron conduction is usually observed. This disparity in the n- and p-type behavior is also mirrored in Fig. 8 where exemplarily the evalution of the electron and hole field-effect mobilities of pentacene over the last 15 years is depicted. Respective data are listed in Table 2. While from the year 1992 up to now the hole field-effect mobility in pentacene steadily increased from 0.002 to $5\,cm^2\,V^{-1}\,s^{-1}$, the first signature of electron transport in field-effect transistors was not found before 2003 [35]. Nowadays, comparable field-effect mobilities for electrons and holes are obtained in transistors comprising polycrystalline pentacene [60, 61].

To understand the reason for the initial absence of electron transport in pentacene based OFETs let us consider the results of impedance measurements on MIS-diodes based on a Ca/pentacene$/SiO_2/p^{++}$–Si layer stack analog to the typically used OFET device structure [46, 62]. In Fig. 9 a differential capacitance measurement is shown where $C_{diel}$ is the capacitance of the $SiO_2$ dielectric, while $C_{tot}$ stands for the total device capacitance of the organic semiconductor/insulator bilayer.

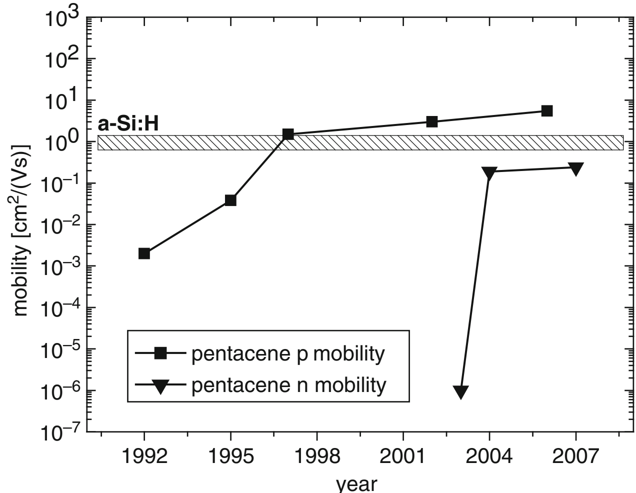


**Fig. 8** The evolution of the electron and hole field-effect mobility of pentacene in time. For comparison, the electron mobility of a-Si:H is shown. The data are listed in Table 2

**Table 2** The evolution of the electron and hole field-effect mobilities of pentacene-based TFTs in time and the associated references. The data are summarized in Fig. 8

| Year | Hole mobility $(cm^2 V^{-1} s^{-1})$ | Electron mobility $(cm^2 V^{-1} s^{-1})$ | References |
|---|---|---|---|
| 1992 | 0.002 | - | [86] |
| 1995 | 0.038 | - | [89] |
| 1997 | 1.5 | - | [17] |
| 2002 | 3 | - | [95] |
| 2003 | - | $10^{-6}$ | [35] |
| 2004 | - | 0.19 | [62] |
| 2006 | 5.5 | - | [99] |
| 2007 | - | 0.24 | [61] |

Apparently, the MIS diode capacitance measured at 100 Hz is independent of $V_g$ and close to $C_{tot}$, suggesting that no charge carriers reach the semiconductor/insulator interface. For reverse biases the mismatch in metal work function and the semiconductor ionization potential (IP) of $\sim$2.2 eV suppresses the hole injection and thus charge carriers cannot reach the $SiO_2$/pentacene interface during one oscillation period. Since in principle electrons should be easily injected in forward bias from the low workfunction metal Ca into the LUMO of pentacene, it appears that electrons are not transported through the pentacene layer at a measurement frequency of 100 Hz. Yet, a dc charging of a pristine MIS diode at a bias of $V_g = 40$ V as depicted in the inset of Fig. 9, yields an accumulated charge of 172 nC translating to a device capacitance of 4.3 nF. Since this capacitance is close to the value for the $SiO_2$ dielectric alone ($d_{diel} = 200$ nm), electron injection from Ca into pentacene must

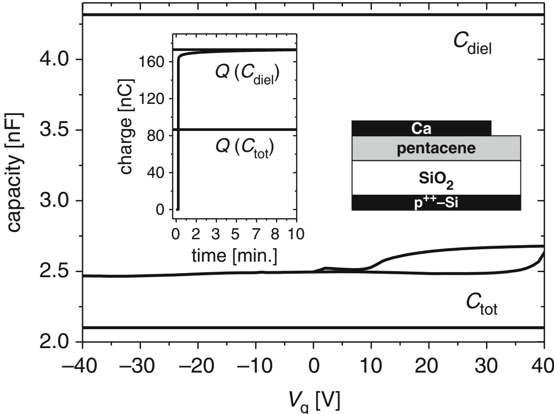


**Fig. 9** Impedance measurement for a Ca/pentacene (50 nm)/$SiO_2$ (200 nm)/$p^{++}$–Si layer stack. *Inset*: MIS diode electron charging in time at a sample dc-bias of 40 V. With permission adapted from [46]

be possible, and the injected electrons can traverse the pentacene layer reaching the $SiO_2$/pentacene interface where they are accumulated. Since, however, no change in the recorded differential device capacitance has been observed, the accumulated negative charge carriers apparently cannot follow the applied ac electric field in the impedance measurement. This could be due to a too small mobility of electrons in the pentacene bulk or due to charge carrier traps at the interface that, when filled, impede the electron transport through the pentacene layer by Coulombic repulsion. In combination with the results of impedance spectroscopy on Ca-modified interfaces discussed below it is most plausible that charge carrier traps at the $SiO_2$/pentacene interface are the cause of the missing electron transport. Transforming this finding to a pentacene OFET, the absence of n-channel behavior is comprehensible.

The suggested interpretation of the MIS diode results was confirmed by Chua et al. [63]. They showed that hydroxyl groups in the form of silanols, normally terminating the $SiO_2$ dielectric surface, act as efficient electron traps and therefore hinder electron transport in n-type OFET structures. On the basis of ATR–FTIR spectroscopy the trapping mechanism depicted in Fig. 10 has been suggested. In the n-channel regime Si–OH groups are reduced and the interface becomes charged by a layer of immobile anions. The gate field is thus compensated by the charged layer leading to a threshold voltage shift beyond the typical voltage range applicable to an OFET. Thus any electron current is suppressed. However, the quenching of the n-channel behavior by silanol groups requires organic semiconductors with sufficiently low electron affinities. Chua et al. claimed that only organic semiconductors comprising EAs larger than 3.85 eV show n-type field-effect behavior on pristine $SiO_2$ interfaces.

In order to compensate the initially proposed interfacial electron traps on the $SiO_2$ dielectric, Ahles et al. [62] introduced traces of Ca to the $SiO_2$ dielectric interface. As a low work function metal, Ca was believed to act as an electron donor saturating traps in the interface near pentacene layer. The capability to accumulate mobile charge carriers at the newly engineered interface can again be examined by MIS diode experiments. The result of impedance measurements on a MIS diode

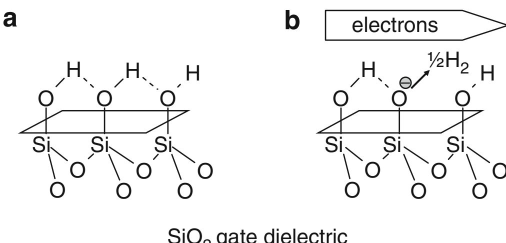


**Fig. 10** **a** Hydroxyl groups terminating the $SiO_2$ surface. **b** Proposed mechanism of electron trapping at the hydroxyl groups terminating the $SiO_2$. Adapted with permission from Macmillan Publishers Ltd: Nature [63], copyright (2005)

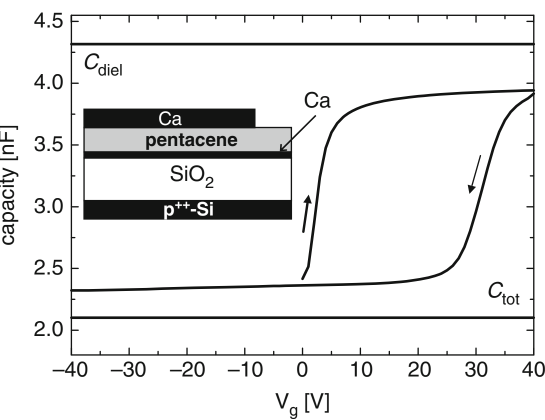


**Fig. 11** Impedance measurements for a Ca/pentacene/Ca(0.6 nm)/$SiO_2$(200 nm)/$p^{++}$–Si layer stack. *Inset*: Device structure of the investigated MIS diode. With permission adapted from [46]

now comprising a 0.6-nm Ca-interlayer between the pentacene and the $SiO_2$ dielectric is shown in Fig. 11 [46]. Due to the large energy barrier for hole injection the accumulation of holes is hindered, and thus a differential capacitance close to $C_{\mathrm{tot}}$ was found for reverse biases $\left(V_{\mathrm{g}} < 0\,\mathrm{V}\right)$. For positive bias a differential capacitance close to $C_{\mathrm{diel}}$ was measured, indicating that an accumulation of mobile electrons at the pentacene $/\mathrm{SiO}_2$ interface is possible under these circumstances. Therefore it was concluded that traces of Ca on the $SiO_2$ dielectric significantly reduce the electron trap density at the $SiO_2$/pentacene interface even though the strong hysteresis indicated that electron trapping still prevails. These results proved that neither the contacts nor the electron transport properties in the bulk of the semiconductor prevent the electron conduction in OFETs employing Ca source/drain contacts and pentacene as organic semiconductor. It is the trapping of accumulated electrons at the dielectric interface which determines the overall performance of such OFETs. Indeed, depositing 0.6 nm of Ca on a pristine $SiO_2$ surface allowed for electron conduction in respective OFETs as can be seen in Fig. 12 providing field-effect mobilities of $0.19\,\mathrm{cm}^2\,\mathrm{V}^{-1}\,\mathrm{s}^{-1}$, comparable to those of holes [62]. Even though it has already been demonstrated in 2003 that electrons can be transported in pentacene field-effect transistors [35] the results confirmed for the first time that pentacene acts as an ambipolar material in which the transport properties of both charge carrier species are indeed balanced.

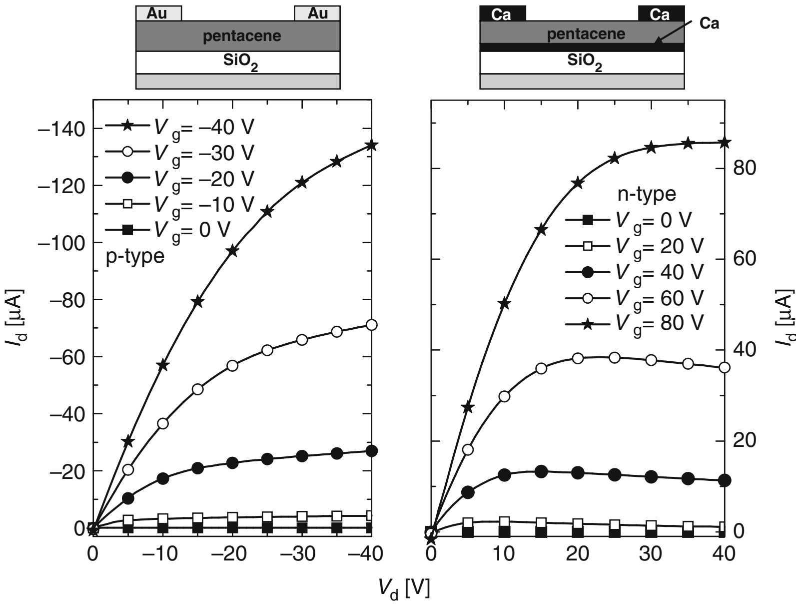


**Fig. 12** Comparison of the n-channel and the p-channel output characteristics measured on pentacene-based OFETs. The respective device structures are depicted as *insets*. While for the p-type transistor $SiO_2$ and Au served as gate dielectric and source/drain metal, respectively, the electron traps terminating the $SiO_2$ surface were passivated by traces of Ca that also served as source/drain metal for the n-type OFET

To study the chemical nature of the newly engineered $Ca/SiO_2$ bilayer, used as gate dielectric, surface sensitive techniques such as XPS have been used [46, 64]. Depicted in Fig. 13 are the respective Ca2p core level emission spectra for several Ca layer thicknesses on a $SiO_2$ substrate in ascending order. For low adsorbate thicknesses only oxidized instead of metallic Ca was found at respective binding energies of 346.5–348.5 eV ($Ca2p_{3/2}$) and 351–353 eV ($Ca2p_{1/2}$). Considering the O1s emission spectrum (not displayed here) the composition of the oxidized Ca layer could be unveiled to consist of –CaOH as well as –CaO components. The appearance of oxidized Ca containing –CaO and –CaOH on the $SiO_2$ substrate under UHV condition suggests that a chemical reaction between atomic Ca and the oxygen substrate component as well as the terminating –OH groups must occur. Indeed, on the basis of the Si2p emission spectrum a reduced Si-substrate component could be proclaimed. The present understanding is that the elimination of the inherent interfacial silanol by an interface reaction in conjunction with the growth of a decorating new Ca oxide reduces the available electron traps and thus promotes electron conduction in the channel. However, with an increase in Ca film thickness, the adsorbate starts to develop a metallic fraction in the oxide between layer thicknesses of 5–12 Å as can be seen from Fig. 13. The fully developed metallic phase did not occur until the adsorbate thickness exceeded 115 Å and an occurrence of a closed metallic layer

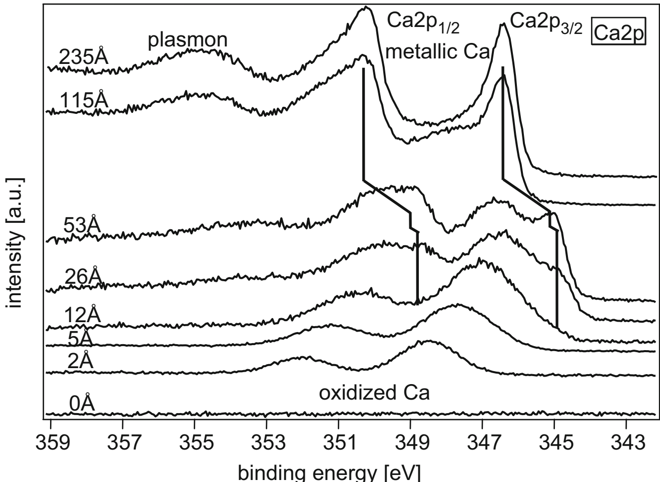


**Fig. 13** Ca2p emission spectra for different layer thicknesses of Ca on a $SiO_2$ gate dielectric in ascending order. Metallic Ca is only detected for higher nominal thicknesses, while oxidized Ca, containing –CaOH and CaO, is obtained for low film thicknesses. With permission reprinted from [46]

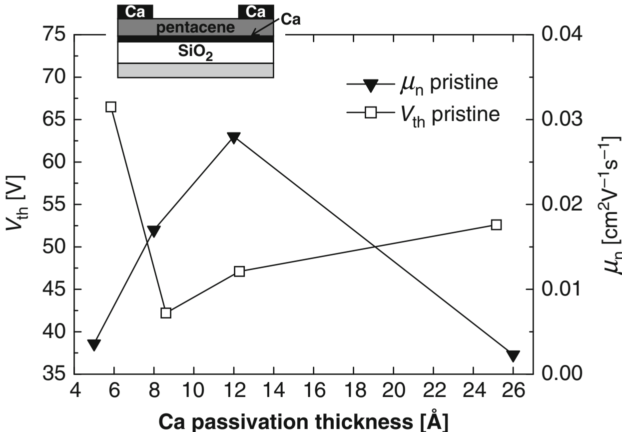


**Fig. 14** Electron field-effect mobility and threshold voltage in dependence on the Ca interlayer thickness. The inset shows the layout of the measured devices. The values have been obtained for devices unexposed to thermal or electrical stress. A cyclic electrical stress leads to an improvement of the device characteristics with a maximal electron field-effect mobility of $0.17\,cm^2\,V^{-1}\,s^{-1}$ and a threshold voltage of 36 V. The electrical stress is believed to stimulate the interface reaction of Ca with $SiO_2$, leading to a trap-free, oxidized Ca overlayer

could be confirmed for an adsorbate thickness of 235 Å, by a complete attenuation of the Si2p and O1s substrate emission lines. The existence of a metallic phase at the insulator surface has naturally severe consequences on the OFET performance [64]. In Fig. 14 the electron field-effect mobility in dependence on the Ca thickness is

depicted. The electron field-effect mobility rises up to $0.028\,\mathrm{cm}^2\,\mathrm{V}^{-1}\,\mathrm{s}^{-1}$ for an increased Ca thickness up to $\sim$12 Å. Afterwards, the mobility begins to decline until it almost completely vanishes at thickness of 26 Å. Thus the availability of metallic Ca at the dielectric interface even in small quantities negatively affects the electron transport, disturbing or even fully screening the electric field in the transistor channel. A short circuit between source and drain electrodes was obtained for Ca layer thicknesses exceeding 25 nm, which correlates well with the value for a closed metallic Ca layer as derived from the XPS measurements (24 nm).

Ahles et al. also showed that in Ca passivated devices the performance improves once the OFET has been subject to an electrical cyclic stress [62]. The stress was applied by a drain voltage of $V_\mathrm{d} = 80\,\mathrm{V}$ for a duration of 50 min, while the gate voltage was pulsed in 5 s intervals between $V_\mathrm{g} = 0\,\mathrm{V}$ and 80 V. For such cyclic conditioned transistors, the device performance increased irreversibly and the Ca layer thickness for an optimal device performance shifted from $\sim$12 to $\sim$8 Å. Ca passivated n-channel transistors which showed electron mobilities comparable to hole mobilities obtained from p-type OFETs with untreated $SiO_2$ have been subject to such a cyclic electrical stress.

Analogous to the electrical conditioning, the characteristics can be improved by a thermal treatment prior to the deposition of the source/drain metallization. On the basis of XPS measurements it could be shown that a heat treatment of the $SiO_2/Ca$ double layer results in a promoted interface reaction reducing the interfacial silanol density and the metallic fraction in the Ca overlayer. The former results in a reduction of the electron trap density and the latter in a reduction of screening effects by the metallic Ca. Since a cyclic electrical stress of an already annealed transistor does not yield a significant additional improvement in device performance, it was concluded that the observed OFET improvement for both device treatments, have the same origin. This implies that the oxidation of the metallic fraction in the Ca overlayer is promoted by the electrical cyclic stress as well as by the heat treatment.

Alternatively to a passivation of the $SiO_2$ dielectric surface by Ca traces, SAMs can be used to create an inert dielectric surface. Kumaki et al. prepared n-channel field-effect transistors with a thiazolothiazole derivative as organic semiconductor on $SiO_2$ gate dielectrics which have been treated with alkyl-substituted silanes of varying length [65]. With increasing alkyl lengths an improvement of the electron field-effect mobility was observed. The authors related these improvements to a spatial separation of the transistor channel from residual electron traps on the $SiO_2$ surface. The improvement of the device performance saturated when silanes with alkyl chains longer than 14 carbon atoms (tetradecyl-trichlorosilane) were employed.

Benson et al. on the other hand achieved electron transport in pentacene based OFETs by employing hydroxyl-free polymeric gate dielectrics [61]. For example, polymethylethacrylate (PMMA), polycarbonate (PC) and polystyrol (PS) allowed for a pronounced electron and hole conduction in the transistor channel. The chemical structure of the used polymers and the schematic device setup are depicted in Fig. 15. The field-effect mobilities obtained are plotted in Fig. 16. The results prove that the charge carrier transport properties of both charge carrier species are rather

**Fig. 15** Different polymeric gate dielectrics: polymethylethacrylate (PMMA), polycarbonate (PC), and polystyrol (PS), poly4̃-vinyl phenol (P4VP) and the structure of the investigated OFETs. The resulting field-effect mobilities are depicted in Fig. 16

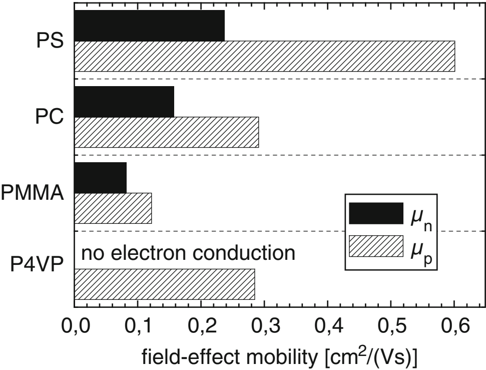


**Fig. 16** Electron and hole field-effect mobilities of pentacene-based OFETs for different polymeric gate dielectrics depicted in Fig. 15. The respective mobilities have been extracted from transfer characteristics of either unipolar p-channel or unipolar n-channel transistors. For one gate dielectric gold or Ca source/drain metals have been used to define the polarity of the field-effect transistors

balanced and that field-effect mobilities in the order of $10^{-1}\,\text{cm}^2\,\text{V}^{-1}\,\text{s}^{-1}$ can be obtained without optimizing the material morphologies.

In comparison, poly(4-vinyl phenol) (P4VP) with only 5.9 at% hydroxyl groups in the polymer structure suppresses totally the electron transport in the respective devices while a hole related field-effect mobility of $0.29\,\text{cm}^2\text{V}^{-1}\,\text{s}^{-1}$ could be reached. Analogously, it was shown that the hydroxyl-free gate dielectric divinyltetramethylsiloxane-bis(benzocyclobutene) (BCB) yields n-channel field-effect conduction in a large variety of conjugated polymers [63]. Electron field-effect mobilities of the order of $10^{-3}$to $10^{-2}\,\text{cm}^2\,\text{V}^{-1}\,\text{s}^{-1}$ were measured in several polyfluorene copolymers and dialkyl-substituted poly(*p*-phenylene vinylene)s. This indicates that more organic semiconductors are actually intrinsically ambipolar than unipolar.

The unveiled strong impact of dielectric interface states on the OFET charge carrier transport properties leads to the question if directed dielectric interface engineering can be utilized to modify the ambipolar charge carrier transport for organic CMOS applications.

### *2.4 The Source and Drain Contacts*

Whether an organic field-effect transistor acts ambipolar, unipolar p-type, or unipolar n-type depends first on the employed source and drain contacts. Ambipolar field-effect transistors also require, besides balanced transport properties in the transistor channel, balanced injection properties of electrons and holes. This means that the contact resistance stemming from the injection of one charge carrier species at the source contact should be comparable to the contact resistance of the other charge carrier species at the drain. Certainly, optimal conditions are obtained, when ohmic contacts at both terminals exist. As shown in Sect. 2.2, the ambipolarity fades once the fragile balance of the hole and electron injection properties is disturbed. When finally an ohmic contact is formed for holes at the source and at the drain terminal, the injection of electrons is efficiently blocked since high injection barriers for electron injection prevail. If the hole conduction in the transistor channel is not impeded due to interface states or insufficient semiconductor morphology, one typically observes unipolar p-type behavior. This restricts the choice of the source/drain metals to high workfunction materials such as Au or Pd. Analogously, a match of the source/drain metal workfunction to the EA of the used semiconductor is mandatory for the realization of unipolar n-type OFETs. Thus, the realization of unipolar n-channel OFETs unfortunately requires the use of low workfunction metals such as Ca or Mg being extremely unstable in ambient conditions. In order to create more robust and efficient terminals one has tried to adapted concepts developed for organic light-emitting diodes (OLEDs) to organic field-effect transistors. In this respect, the use of LiF/Al bilayers as source and drain terminals indeed improves the performance of n-channel transistors [66], although the charge carrier injection in OLEDs does not mimic the process of charge carrier deliverance in the transistor channel completely [67].

Since pentacene proved to act as ambipolar organic semiconductor in conjunction with suited gate dielectrics, it is only a matter of a proper metallization of the source and drain terminals to define complementary acting unipolar field-effect transistors. Considering Fig. 16, the electron and hole transport properties in a pentacene channel are most balanced for a PMMA gate dielectric. As a consequence, ambipolar pentacene OFETs can be fabricated once Ca source and Au drain contacts are in use. Shown in Fig. 17 is the transfer characteristic of such an ambipolar transistor driven in electron accumulation mode, which proves that the injection and the transport of electrons and holes are indeed balanced [43]. Using such an ambipolar transistor a n-channel OFET can be obtained by exchanging the Au drain contact to Ca, thus blocking the hole injection in the ambipolar range of the transistor so that a

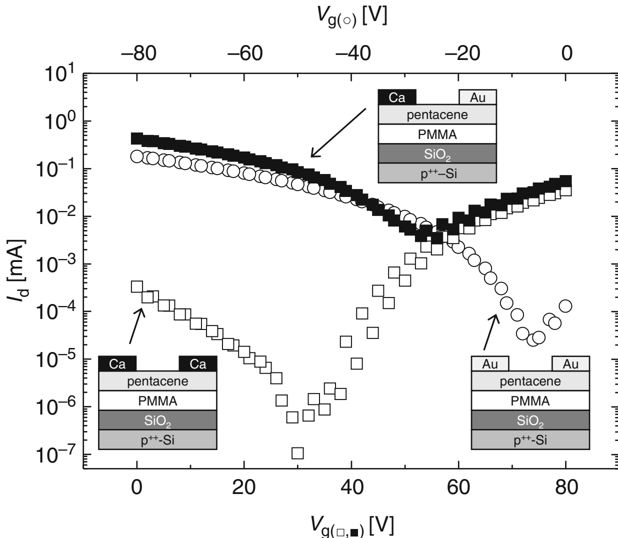


**Fig. 17** Transfer characteristics of pentacene-based OFETs differing by the used source/drain metallization only. Device structure: $p^{++}$–Si/200 nm $SiO_2$/120 nm PMMA/50 nm pentacene/50 nm source/drain metal. $V_g$ (*open squares, filled squares*) is the gate voltage for the n-type and the ambipolar transistor measured in electron accumulation mode at $V_d = 80\,V$; $V_g$ (*open circles*) is the gate voltage for the p-type transistor measured in hole accumulation mode at $V_d = -80\,V$. The *insets* show the respective device structure. With permission reprinted from [43], copyright © 2008 Oldenbourg Wissenschaftsverlag GmbH

saturation regime develops. Indeed, by using a Ca drain terminal, a substantial current suppression in the order of $10^3$ is observed in the low gate voltage regime even though the hole conduction was not fully inhibited (Fig. 17). Vice versa, the ambipolar field-effect transistor can be transformed to an unipolar p-type OFET by simply exchanging the Ca source terminal with Au. From Fig. 17, where the transfer characteristic in hole accumulation mode of such a transistor is depicted, it can be seen that the electron current is efficiently inhibited, leaving the hole contribution nearly unchanged. A unipolar p-channel OFET has been obtained.

### 2.4.1 Contact Resistance in Unipolar Devices

It is important to realize that emerging contact resistances for the injection and ejection of the majority charge carrier species strongly determine the device characteristic of unipolar devices and this in the linear as well as the saturated regime of the OFET [68]. Calculated transfer and output characteristic considering a unipolar OFET with constant contact resistances at the source and the drain contacts are depicted in Fig. 18. Assuming a constant contact resistance $R_s$ for the injection of charge carriers, voltage has to drop at the source contact and therefore the applied $V_d$ and $V_g$ are effectively reduced by $R_s I_d$. As a consequence the current in the linear

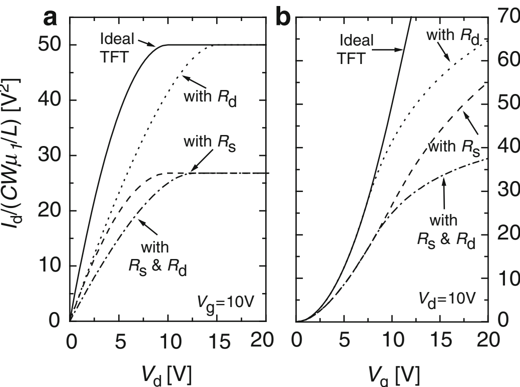


**Fig. 18** Calculated output (**a**) and transfer (**b**) characteristics of an unipolar OFET considering constant contact resistances at the source $R_s$ and the drain $R_d$ terminal. The assumed normalized resistances $R_{s/d} \cdot \hat{C}W\mu_1/L$ were $0.1\,V^{-1}$

and saturated regime is attenuated while the crossover from the linear to the saturation regime still occurs at $V_d = V_g$. Assuming a constant contact resistance for the ejection of the transported charge carrier species at the drain contact, solely the drain voltage $V_d$ is effectively reduced by $R_s I_d$, while the gate voltage $V_g$ remains unchanged. Hence, the current in the linear regime is suppressed while the saturation current remains unchanged so that the crossover from the linear to the saturated transistor regime occurs at $V_d - R_s I_d = V_g$ and thus at larger $V_d$.

It is of crucial importance that the extracted field-effect mobility and threshold voltage obtained from transistor characteristics are therefore not exclusively channel properties but influenced by the contact formation at the source and drain electrodes. Commonly, the transfer line method (TLM) is used to extract the contact resistance from the OFET current/voltage dependence [69]. The method stems from a conventional technique to estimate contact resistances, and was developed for amorphous silicon TFTs. The prevailing contact resistance is determined by varying the channel length $L$ of the transistor. Since the total resistance is the sum of the channel resistance $V_d/I_d$ and the total contact resistance $R\,(= R_{1s} + R_{1d})$, the total resistance $R_{tot}$ in the linear region can be written as

$$R_{tot} = \frac{2}{\hat{C}W\mu_1\left(2V_g - V_d\right)} L + R. \tag{9}$$

The contact resistance is extracted by plotting the total resistance as a function of $L$ yielding a linear dependence with a slope giving access to the field-effect mobility. An extrapolation to zero channel length delivers the entire contact resistance. Unfortunately, this method has the disadvantage that no separate information about $R_s$ and $R_d$ can be obtained which would, however, be important in order to deconvolve their impact on the device characteristic.

Alternatively, a local non-contact potentiometry of the transistor channel allows one to measure the potential distribution $V(x)$ across the entire OFET [70], unveiling thereby possible contact resistances. Due to the local determination of the surface potential, the voltage drops at the source and drain electrodes are accessible. By

correcting the applied bias for the measured voltage drop at the contacts the contact resistance corrected field-effect mobility and threshold voltages can be obtained. The local non-contact potentiometry is, however, a much more powerful method, because the knowledge of $V(\mathrm{x})$ allows one to determine the charge carrier density and electric field dependence of the field-effect mobility. In the transistor channel $\hat{Q}(x) = \hat{C}\left(V(x) - V_{\mathrm{g}}\right)$ relates the potential distribution $V(x)$ to the surface charge (carrier) density distribution $\hat{Q}(x)$ and the electric field $F(x)$ driving the current $I_{\mathrm{d}}$ at the position $x$ in the channel can be calculated by $F(x) = -\partial V(x)/\partial x$. Since $I_{\mathrm{d}} = W\mu_1\hat{Q}(x)F(x)$, the field-effect mobility $\mu_1$ can be determined as a function of the electric field $F$ and the charge (carrier) density $\hat{Q}$.

## 3 Organic Field-Effect Transistors and CMOS Inverters

On the basis of unipolar n-type and p-type OFETs, organic CMOS devices, i.e., inverters, can be constructed. The inverter represents a non-gate and is therefore a basis device type for today's logic circuits. Therefore, inverters are commonly used to demonstrate the usefulness of organic TFTs in future electronics [71, 72]. In Fig. 19 two inverters are depicted, the first acting unipolar and the second working on the basis of the CMOS technology. For both inverters, the input bias $V_{\mathrm{in}}$ can vary from 0 V to the supply voltage $V_{\mathrm{dd}}$. An input voltage of 0 V at the gate yields nearly the supply voltage $V_{\mathrm{dd}}$ at the output and vice versa, an input voltage of $V_{\mathrm{dd}}$ results approximately in $V_{\mathrm{out}} \approx 0\,\mathrm{V}$. The output potential of 0 V is hence an analog of the logical 0 and the potential $V_{\mathrm{dd}}$ that of the logical 1.

In the configuration depicted in Fig. 19 the unipolar inverter has the disadvantage that its switching time is limited by the prevailing $RC$ time. $R$ is the series resistance

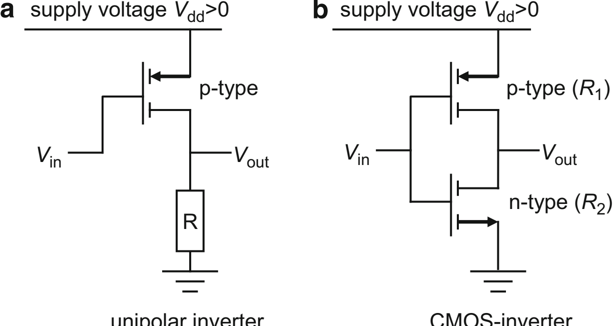


**Fig. 19** Circuit of an unipolar inverter (**a**) and an inverter based on a CMOS-like circuit (**b**). Electrical losses in the ON state of the unipolar inverter exist, since the OFET is open and hence, a substantial current flows due to the finite resistivity of the resistor. For the CMOS inverter on the other hand only little current can flow at each logical state since one of the employed OFETs is always closed. The resistivities of the involved unipolar p- and n-type OFETs are named $R_1$ and $R_2$ respectively

whereby the capacitance is given by the capacitance of the employed OFET and the input capacitance of the subsequent logic element. Moreover, electrical losses in the ON state of the inverter exist, since in this case the OFET is open and hence, a substantial current flows from the supply voltage source to the ground due to the finite resistivity of the employed resistor. The unipolar inverter works as follows. Since the resistivity of the resistor is much larger than the resistivity of the open transistor, nearly all the $V_{dd}$ drops across the resistor and $V_{out} \approx V_{dd}$. On the other hand, when the transistor is closed $(V_{in} = V_{dd})$ and its resistivity exceeds by far the resistivity of the resistor, the output potential will be approximately 0 V.

The problems mentioned can be circumvented by the use of a CMOS inverter. The advantage of CMOS inverters is that at each logical state one of the employed OFETs is closed and, hence, only little current will flow. Therefore, electrical losses are essentially restricted to the switching of the inverter and the inverter output voltage indeed reaches 0 V and $V_{dd}$ in the respective logical states. Moreover, a superior switching time prevails, since the resistivity of the used open transistor is typically very low, providing an effective sink for excess charge carriers.

On the basis of the evaluated description of OFETs in Sect. 2.1, the CMOS inverter can be modeled, namely the output voltage $V_{out}$ as a function of the input voltage $V_{in}$. The CMOS inverter acts as a voltage divider with the output bias of

$$V_{out} = V_{dd} \frac{R_2}{R_1 + R_2}. \tag{10}$$

Here $R_1$ and $R_2$ are the resistors of the two involved OFETs as depicted in Fig. 19. For the transistor, represented by the resistor 1, the gate voltage is given by $V_g = V_{dd} - V_{in}$ and the drain voltage is $V_d = V_{dd} - V_{out}$, while for the other transistor $V_g = V_{in}$ and $V_d = V_{out}$ holds. Ignoring in the first place possible contact resistances and threshold voltages the solution is given by

$$V_{out} = V_{in} \pm \begin{cases} \sqrt{(V_{dd} - V_{in})^2 \frac{\mu_p^p}{\mu_p^p + \mu_p^n} - V_{in}^2 \frac{\mu_n^n}{\mu_p^p + \mu_p^n}} & \text{for } V_{in} < V_{out} \\ \sqrt{V_{in}^2 \frac{\mu_n^n}{\mu_n^n + \mu_n^p} - (V_{dd} - V_{in})^2 \frac{\mu_p^p}{\mu_n^n + \mu_n^p}} & \text{for } V_{in} > V_{out} \end{cases}. \tag{11}$$

Here $\mu_i^m$ is the mobility of the charge carrier type i prevailing in the OFET marked as m-type $(i,\ m \in \{n,\ p\})$. The characteristic of an CMOS-like inverter as depicted in Fig. 19 is shown in Fig. 20 for different electron and hole mobilities. $\mu_p^n$ and $\mu_n^p$ are set to zero, meaning that both involved transistors act unipolar. For balanced electron and hole transport properties of the n-type and p-type transistor, respectively, the switching voltage is half the supply voltage $V_{dd}$. For unbalanced charge carrier transport properties the switching voltage shifts to higher $V_{in}$ when the hole mobility exceeds the electron mobility and vice versa to lower $V_{in}$ for a superior electron mobility. This shows that complementary OFETs with balanced charge carrier transport properties should be employed for optimal functioning CMOS inverters.

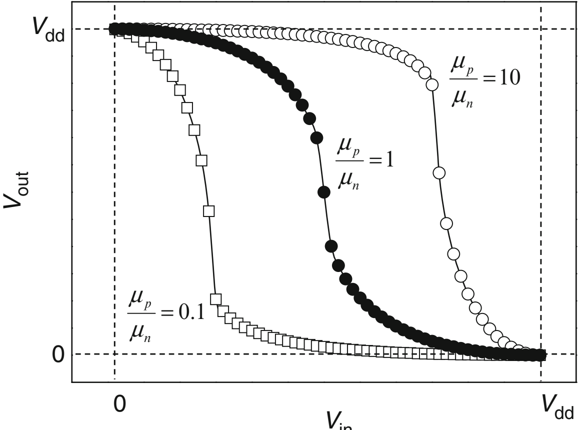


**Fig. 20** Simulated inverter characteristics of a CMOS inverter for different field-effect mobility ratios. In Eq. (11), $\mu_p^n$ and $\mu_n^p$ are set to zero and thus truly unipolar OFETs have been considered

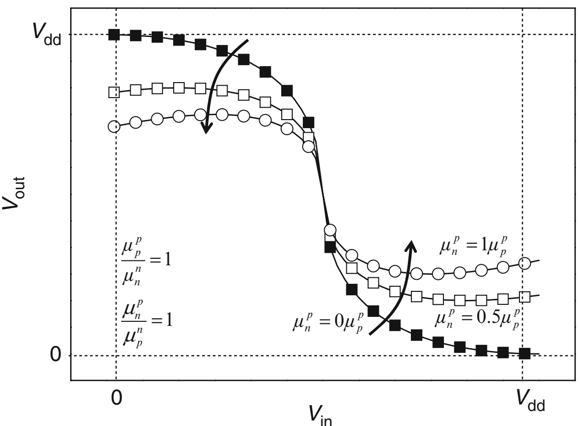


**Fig. 21** Simulated inverter characteristics of a CMOS inverter where ambipolar OFETs have been considered. While $\mu_p^p = \mu_n^n$ and $\mu_p^n = \mu_n^p$ have been assumed, the ratio $\mu_n^p/\mu_p^p$ varies from 0 to 1 in order to consider OFETs with different extent of ambipolarity. For balanced electron and hole mobilities in both involved transistors, a substantial current flows in the final logical states

Apparently, for $V_{in} = 0\,V$ the entire potential $V_{dd}$ determines $V_{out}$ and $V_{out} = 0\,V$ is calculated for $V_{in} = V_{dd}$. This is only possible as long as truly unipolar OFETs have been employed with a rather low off current. Then, at the logical 1 and the logical 0, evanescent voltage losses prevail. The situation changes if the used OFETs show weak ambipolar character since the field-effect transistors lose their ability to close completely. This is when $\mu_p^n$ and/or $\mu_n^p$ are not zero. In Fig. 21 simulated characteristics from an inverter are depicted, where ambipolar transistors have been

considered. Out of simplicity $\mu_\mathrm{n}^\mathrm{n} = \mu_\mathrm{p}^\mathrm{p}$ was assumed. $\mu_p^n$ as well as $\mu_n^p$ varies from zero for unipolar devices to $\mu_\mathrm{p}^\mathrm{n} = \mu_\mathrm{n}^\mathrm{p} = \mu_\mathrm{n}^\mathrm{n}$ to model inverters based on truly ambipolar OFETs. Since the considered ambipolar transistors show no ideal blocking property for the complementary charge carrier species, the full inversion is never reached and thus voltage losses have to be accepted. Even at $V_\mathrm{in} = 0\,\mathrm{V}$ or $V_\mathrm{in} = V_\mathrm{dd}$ a substantial current flows and, hence, electrical losses are still registered at the logical 0 and 1. Thus, truly unipolar acting OFETs are essential and necessary to take full advantage of the CMOS-technology.

## 3.1 CMOS Inverters Through Selected Source/Drain Metals

In order to realize an organic CMOS inverter, unipolar complementary OFETs have to be realized showing balanced charge transport properties of electrons and holes. This requires the use of organic semiconductor/gate insulator combinations, which exhibit equal charge transport properties for electrons and holes in the channel, and the use of source and drain electrodes for either efficient electron or hole injection. The most straight forward design of a CMOS inverter is the utilization of the OFET results displayed in Fig. 17. Here unipolar n- and p-type charge transport was realized with pentacene fabricated on a $SiO_2$/PMMA dielectric applying suited metals as source and drain electrodes. As shown in Sect. 2.3.3 PMMA acts as an electron-trap free dielectric and therefore electron transport can be realized in the vacuum deposited pentacene without influencing the hole transport properties. The incorporated metals are Ca/Ca for the n-type OFET and Au/Au for the p-type OFET for the source and drain contacts, respectively. Figure 22 displays the utilized setup and the achieved CMOS inverter characteristics. The individual transistor characteristics were similar to the ones displayed in Fig. 17. The transition in the output voltage

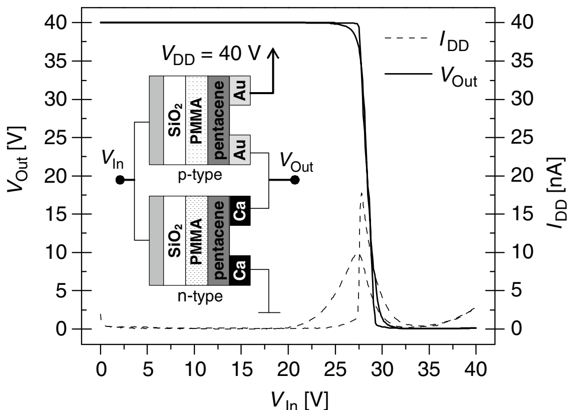


**Fig. 22** Schematic setup and characteristics of a CMOS inverter consisting of OFETs both fabricated by vacuum-deposition of pentacene on a PMMA/$SiO_2$ dielectric. The transport character is achieved by proper choice of source- and drain contact metals

occurs at $V_{out} = 27\,V$ far below the device driving voltage of $V_{DD} = 40\,V$. The device indicates an almost ideal characteristic with a gain of 21.6. It should, however, be mentioned that the ideal characteristic is obtained for low cycling frequencies of $\sim 8\,mHz (V_{in} = 0\,V \Rightarrow 40\,V \Rightarrow 0\,V)$ and that already a frequency of $\sim 80\,mHz$ generates a sizable hysteresis indicating some residual electron and hole trapping.

### 3.2 CMOS Inverters Through $SiO_2$ Passivation

In Sect. 2.3.3 it was demonstrated that pentacene OFETs with Au source and drain terminals and a $SiO_2$ gate dielectric show p-channel behavior. The lack of any electron conduction in the channel could be attributed to interfacial electron traps, so that a passivation of the $SiO_2$ surface by the use of traces of calcium in combination with Ca contacts leads to a pronounced n-type behavior. Thus, it is straightforward to pattern n-type and p-type pentacene OFETs on one substrate to produce organic CMOS inverters. This was first performed by Ahles et al. [60]. They selectively passivated spatially separated areas on a $SiO_2$ dielectric using traces of Ca. This procedure defines the p-type transistor in the region of the pristine $SiO_2$ and the n-type OFET in the region of the Ca passivated $SiO_2$ as long as Au source/drain terminals were used for the former and Ca contacts for the latter OFET. To improve the electron transport properties the n-type OFET had to be exposed to cyclic electrical stress. Such OFETs exhibit balanced electron and hole mobility of $\mu_n = 0.11\,cm^2\,V^{-1}s^{-1}$ and $\mu_p = 0.10\,cm^2\,V^{-1}\,s^{-1}$ as well as On/Off ratios $> 10^5$ and respective threshold voltages of $V_{th,n} = 34\,V$ and $V_{th,p} = -20\,V$. The obtained balanced charge carrier transport properties for electrons and holes allow for the realization of an organic CMOS inverter stage. The inverter characteristic is depicted in Fig. 23, demonstrating a stable operation below its supply voltage of $V_{dd} = 60\,V$ as well as a

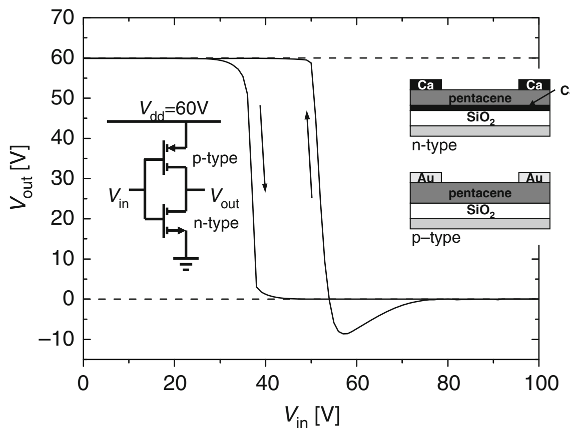


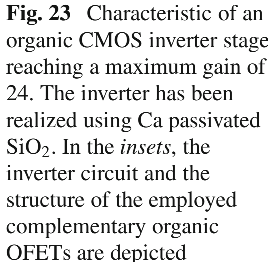

**Fig. 23** Characteristic of an organic CMOS inverter stage reaching a maximum gain of 24. The inverter has been realized using Ca passivated $SiO_2$. In the *insets*, the inverter circuit and the structure of the employed complementary organic OFETs are depicted

maximum gain of 24. The fast switching and the lack of voltage losses in the logical states show that such an CMOS-like inverter operates almost ideal. The observed hysteresis is due to the n-channel OFET, which still exhibits some electron trapping.

### *3.3 The Ambipolar CMOS Inverter*

Organic logic is proclaimed to be cheap in production but at the same time weak in performance. However, at present the realization of logic elements on the basis of OFETs requires a rather complex structuring if truly unipolar OFETs have to be employed which counteracts the aim of being a cheap technology. The CMOS inverter stage discussed in Sect. 3.2 is such an example since it requires a structured interface treatment of the used common insulator and a different source/drain metallization for the employed OFETs. It would be much easier and therefore less expensive to implement organic logic by a network of identical field-effect transistors.

Ambipolar transistors allow for such kinds of CMOS-like logic. The implemented OFETs should consist of an inert dielectric/semiconductor interface, an ambipolar organic material and an identical source/drain metallization to facilitate device production. The main difficulty is to enable balanced hole and electron injection into a single semiconductor from the same metal requiring in an ideal case electron and hole injection barriers of half the bandgap energy of the used organic semiconductor. Hence, a metal has to be found with the Fermi level in between the HOMO and the LUMO of the employed organic semiconductor. Yet, in view of injection efficiency, low injection barriers are mandatory, requiring a semiconductor system with low energy difference between hole transporting and electron transporting states. Since typical organic semiconductors comprise bandgaps of at least 2 eV, high injection barriers and thus an attenuated device performance are expected. Alternatively, a blend of a hole and an electron transporting moiety can be used to lower the injection barriers and to tune the field-effect mobilities of holes and electrons in the active material. Such blends are already known in the field of organic bulk-heterojunction solar cells where, for example, [6,6]-phenyl $C_{61}$-butyric acid methyl ester (PCBM) as electron conductor and poly[2-methoxy-5-(3′,7′-dimethyloctyloxy)]-*p*-phenylene vinylene ($OC_1C_{10}$-PPV) as hole conductor are used [22]. Meijer et al. implemented this blend in a field-effect transistor structure where Au metallization and hexamethyldisilazane passivated $SiO_2$ gate dielectric were used [35]. A scheme of the involved energy levels is depicted in Fig. 24. While the wide bandgap materials PCBM and $OC_1C_{10}$-PPV exclusively showed unipolar n-channel and unipolar p-channel behavior, respectively, the blending of both materials led to a pronounced ambipolar character because the energy gap between the electron transporting states in the PCBM and the hole transporting states in the $OC_1C_{10}$-PPV is small ($\sim$1.3 eV). Since, however, the workfunction of Au (5.1 eV) matches the IP of $OC_1C_{10}$-PPV but is 1.3 eV above the EA of PCBM, unbalanced injection properties disturb the ambipolar characteristic. Similarly, mixtures of soluble

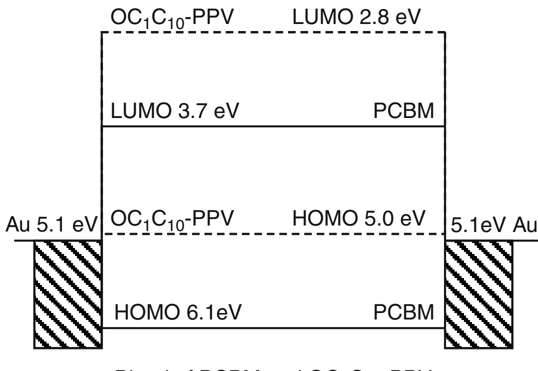


**Fig. 24** Band diagram of a blend of $OC_1C_{10}$-PPV and PCBM sandwiched in between two gold contacts. Due to the blending of both materials an effectively reduced transport gap is obtained leading to more balanced electron and hole injection properties. Adapted with permission from Macmillan Publishers Ltd: Nature Materials [35], copyright (2003)

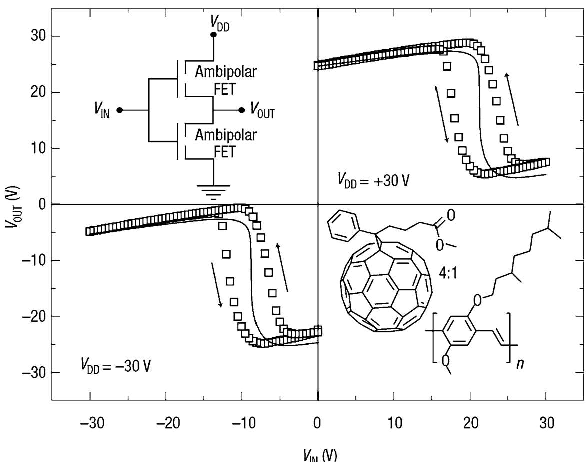


**Fig. 25** Characteristic of a CMOS-like inverter based on ambipolar transistors, operating in the first and the third quadrant. The inverter comprises two identical ambipolar OFETs with a blend of $OC_1C_{10}$-PPV and PCBM as active material. The *solid lines* are simulated inverter characteristics. Reprinted with permission from Macmillan Publishers Ltd: Nature Materials [35], copyright (2003)

oligomers [73] as well as more complex layer structures have been reported [74–76]. Alternatively, low bandgap materials such as poly(3,9-di-*tert*-butylindeno[1,2-*b*] fluorene) (PIF) lead to ambipolar behavior [35].

Using such ambipolar OFETs, complementary logic can be realized since both polarities of charge can be induced in the transistor. Employing two identical ambipolar acting transistors in an inverter structure, decent switching behavior below the supply voltage can be observed. Exemplarily, such inverter characteristics are depicted in Fig. 25 from [35]. Even so, a switching with a gain of 10 can be observed, a strong dependence on the output voltage at low and high input voltages is obtained which is typical for inverters based on ambipolar OFETs. Due to the

ambipolar character, both transistors cannot be switched off and thus a substantial leakage current flows permanently through the inverter. Thus, even though ambipolar complementary logic has the advantage of simple device preparation, severe losses in the device performance have to be accepted and make such a device not attractive for electronic applications.

### *3.4 CMOS Inverters Through Dielectric Interface Modification*

In Sect. 2.3.3 it was substantiated that electronic states at the organic semiconductor/dielectric interface can harm the charge carrier transport in organic field-effect transistors. In principle, the trapping of charges in interface trap states results in a compensated gate field due to the charged interface and thus in a threshold voltage shift to outside the window of operation. Therefore, metastable charged trap states can be used to engineer the threshold voltage in OFETs [77]. On the one hand this allows for the realization of nonvolatile memory elements, [78, 79] but on the other it provides a tool to adjust OFET characteristics for CMOS applications.

Benson et al. have shown that the introduction of charged interface trap states can lead to an inversion of the charge transport type while maintaining the OFET layout [36]. To realize this, pentacene based OFETs with a $PMMA/SiO_2$ gate dielectric were used, since such a material combination provides ambipolar behavior as long as proper source/drain metals are used. The implementation of Ca source/drain terminals yields on the other hand a unipolar n-type OFET as was discussed in Sect. 2.4. The output characteristic of a pentacene OFET with PMMA gate-dielectric and Ca source/drain terminals is depicted in Fig. 26 [43]. However, by selectively treating the PMMA surface with UV light in ambient atmosphere prior to the pentacene deposition, the PMMA surface is essentially modified. Holländer et al. [80] claimed that the exposure of organic polymers to UV radiation leads to breaking of C–C or C–H bonds in a near-surface layer. Illuminated in air, –COH as well as –COOH functional end groups form due to the dissociation of the polymer [81, 82]. By means of a conducted XPS study, an increase in keto-groups relative to singly bonded carbon groups was observed by Benson et al. upon UV exposure [46]. Hence, the UV treatment of a PMMA dielectric is supposed to generate electron traps at the pentacene/PMMA interface, influencing the charge carrier transport properties of the pentacene based OFET. Indeed comparing the output characteristics of the two pentacene OFETs (with and without UV treatment of the PMMA dielectric) in electron accumulation mode a substantial attenuation of the current is observed for the UV-treated OFET (see Fig. 26). For the pentacene OFET with Ca source/drain electrodes and UV modified PMMA dielectric no current is detected in the entire measurement window no matter if driven in electron or hole accumulation mode. This is due to both the hole blocking contact Ca and the electron traps in the PMMA, hindering any electron transport in the transistor channel.

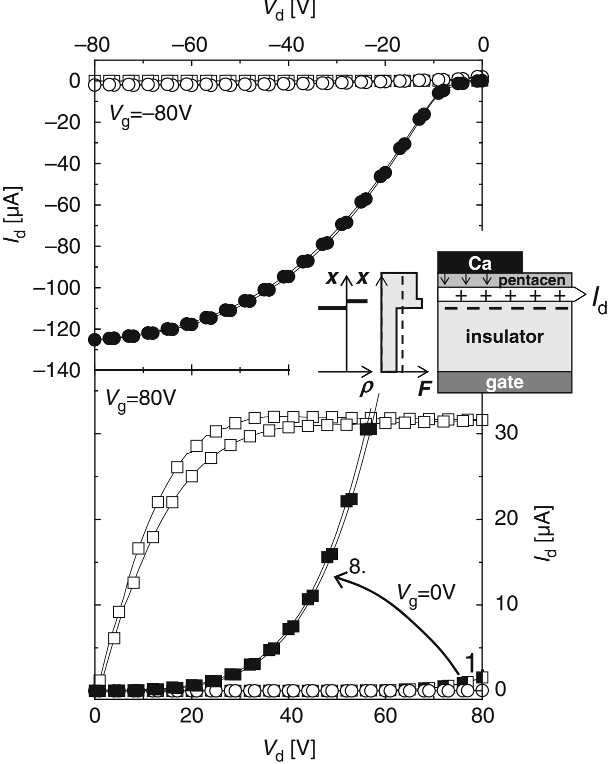


**Fig. 26** Output characteristics of pentacene-based OFETs measured in electron and hole accumulation mode [36, 43, 61]. The transistor structures were: $p^{++}$–Si/SiO$_2$(200 nm)/PMMA (120 nm)/pentacene (50 nm)/Ca (50 nm) source/drain metal. In principle, n-channel behavior prevails in such OFETs (*open squares*). However, the current $I_d$ (*open circles*) of OFETs where the PMMA dielectric has been irradiated with UV light prior to the pentacene deposition is attenuated completely. Once the UV-treated OFET was driven several times in electron accumulation (one cycle: $V_g = 0 \leftrightarrow 80$ V in 20 V steps and respective $V_d$ sweeps from $0 \leftrightarrow 80$ V) the output characteristic measured at $V_g = 0$ V (*filled squares*) recovers. After the eighth cycle a saturation of the current improvement can be observed. Now, the OFET behaves like a unipolar p-type OFET (*filled circle*). The *inset* illustrates the field enhancement at the terminals due to stored negative charges in the PMMA dielectric. With permission reprinted from [43], copyright © 2008 Oldenbourg Wissenschaftsverlag GmbH

However, the trapping of negative charges leading to the suppression of any electron current also has consequences for the hole conduction. Since the negative charges are trapped close to the PMMA/pentacene interface but are sufficiently separated from the transistor channel, recombination processes are circumvented and the developed negative charged region in the PMMA gate dielectric is stable even during the accumulation of holes. The presence of the negatively charged layer in the vicinity of the transistor channel leads to a compensation by positive charge carriers and thus to a reduced threshold voltage for holes. The improved hole conductivity in the

transistor channel and the suppressed accumulation of mobile electrons manifests itself in a device characteristic which is the one of an ambipolar transistor operated below the threshold voltage for electron conduction. In Fig. 26 output characteristics subsequently measured at $V_g = 0\,\text{V}$ in forward bias are depicted, but in between each measurement the OFET has been driven in strong electron accumulation (from $V_d = 0-80\,\text{V}$ for $V_g$ sweeps between 0 and 80 V in 20 V steps). This treatment of the OFET results in a subsequent filling of the interface trap states induced by UV light and thus in an increase of the current from measurement to measurement. After the eighth measurement cycle the device improvement saturated. The obtained characteristic is well described by an unsaturated hole current in the ambipolar regime of the transistor. Using Eq. (6) with $\mu_n = 0\,\text{cm}^2\,\text{V}^{-1}\,\text{s}^{-1}$ and $V_g = 0\,\text{V}$ the improvement in the current can be indeed understood by a positive threshold voltage shift while the hole mobility remains unchanged.

Subsequently, measuring the transistor in the hole accumulation mode, the output characteristic shows a saturated p-type characteristic with no signature of an ambipolar regime proving that the electron conduction is substantially inhibited. The lack in hysteresis indicates the absence of recombination of the mobile positive charge carriers with the trapped electrons. Thus, the UV treatment of the PMMA gate dielectric and the filling of the resulting interfacial electron traps lead to a metastable conversion of the unipolar n-type transistor to a unipolar p-type transistor without further altering the device structure. The device layout of the n- and the p-channel transistors and the essential difference in their production are summarized in Fig. 27.

Puzzling is that p-channel behavior can be obtained even though Ca is used as source/drain metal. Apparently, the presumed high hole injection barrier of $\sim 2\,\text{eV}$ plays hardly any role. Taking into account that the current measured for $V_d > 0\,\text{V}$ is dominated by holes $\left(\mu_n = 0\,\text{cm}^2\,\text{V}^{-1}\text{s}^{-1}\right)$, Eq. (8) reduces to $I_d \approx \frac{\hat{C}W}{2L}\mu_p\left(V_d - V_{p,d}\right)^2$

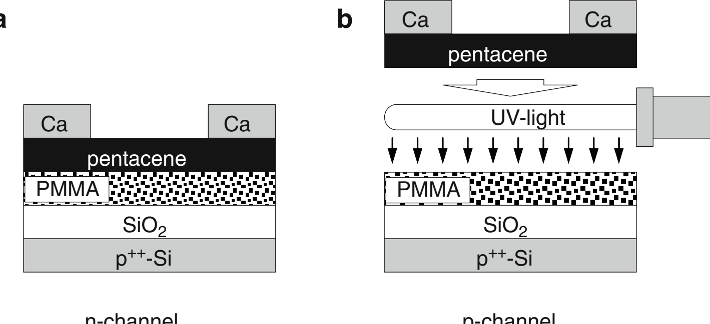


**Fig. 27** Device layout of an n- and p-channel OFET with identical device structure. As gate-dielectric a double layer $SiO_2$/PMMA was used, while pentacene and Ca served as semiconductor and source/drain metal respectively. Both transistors merely differ in a UV-modification of the employed PMMA gate-dielectric. The negative charging of the thus induced electron traps leads to a suppression of electron current and to enhanced hole transport properties

for $V_g = 0\,V$. Here $V_{p,d}$ is the required voltage drop across the drain contact to maintain the current. Thus one can interpret the observed threshold voltage shift induced by the trap filling as a change in contact voltage. This is also shown in Fig. 18 where a high contact resistance at the charge carrier injecting terminal leads to a substantial reduction of the saturation current in unipolar transistors.

Since charge is the source for the electric field and the total potential drop is determined by the externally applied voltage, a field enhancement in the vicinity of the Ca contact occurs once a metastable negative charge is stored in the PMMA. If a UV modified and negatively charged transistor is driven in hole accumulation mode the negative charge helps to inject holes and on the other hand circumvents the accumulation of electrons. The transistor shows unipolar p-channel behavior. The pronounced s-shape in the linear regime of the output characteristic in Fig. 26 indicates, however, that the characteristic is still significantly affected by the hole injection barrier.

The obtained complementary OFETs were connected to form an organic CMOS inverter stage [36]. The transfer characteristic of this inverter is depicted in Fig. 28. The inverter works reliably within the range of the supply voltage ($V_{dd} = 60\,V$), as can be seen from its stable switching behavior below an input voltage of $V_{in} = 60\,V$. The steep transition between high and low state of the inverter for both sweep directions of $V_{in}$ results in a maximum gain of 17.

From Fig. 28 it can be concluded, that the voltage losses in the final logical states are rather low, since truly unipolar complementary OFETs have been used (see Fig. 27). This is an advantage if compared to CMOS-like inverters based on ambipolar OFETs because those disclose in the contrary substantial voltage losses.

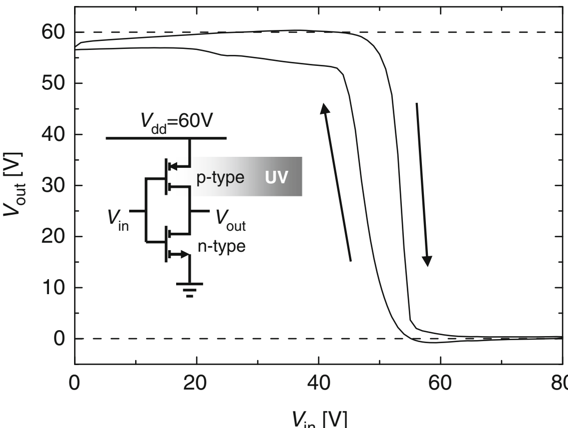


**Fig. 28** CMOS inverter transfer characteristic at $V_{dd} = 60\,V$ showing a maximum gain of 17 for the scan of $V_{in}$ from 0 to 80 V. Identical OFETs, depicted in Fig. 27 were employed. The inverter characteristic shows little electrical losses in the logical states, since truly unipolar OFETs have been used

In addition, however, the device layouts of the employed OFETs are identical and differ simply by the selective UV treatment of the PMMA gate dielectric. This simplifies the manufacturing of logic elements and thus reduces the production cost, being an advantage if compared to inverters were field-effect transistors with different functional materials have been employed.

# 4 Conclusion

In the present state of organic electronics, where a restricted performance level still prevails, it is essential to present circuit and device solutions that can be fabricated at sufficiently low cost. This article offers different strategies to fabricate organic CMOS inverters as fundamental devices for electronics based on organic field-effect transistors in different stages of complexity. After the introduction of function and theory of organic unipolar and ambipolar transistors, it is demonstrated that besides the conventional way of using two different organic semiconductors and two different source and drain metals, requiring thus four deposition steps, ambipolar organic transistors can be used to easily fabricate logic elements. The simplest way is to just implement identical ambipolar transistors in logic elements like inverters. Unfortunately, the performance of such CMOS-like inverters is poor, since the involved transistors cannot be switched off. However, by the use of appropriate device engineering the employed ambipolar transistors can be selectively turned into unipolar transistors with either pronounced n-channel or p-channel behavior leading to an improved operation in respective logic devices while only few production steps are added. This chapter highlights recently developed concepts allowing for such a selective polarity adjustment.

A first possibility to convert ambipolar transistors to unipolar transistors is to use suited source and drain electrodes that, by their position of workfunction in relation to the HOMO and LUMO of the involved organic semiconductor, do not allow for an efficient injection of one charge carrier sign. Although the charge carrier could in principle be transported in the device, the suppression of injection discards its function. Exemplarily, an ambipolar transistor consisting of a PMMA gate insulator, pentacene and calcium source and Au drain electrodes can be turned into an n-channel transistor by simply exchanging the Au drain electrode by a calcium electrode, and to a p-type transistor by choosing Au source/drain metals. The disadvantage of this approach is that for the realization of unipolar n- and p-type transistors for CMOS applications two metal depositions are still required even though a single organic semiconductor/insulator combination can be used.

Beside the suppression of charge carrier injection, another possibility is highlighted in the present chapter, which is the adjustment of the charge carrier transport in the OFET channel. It was shown that by a suitable modification of the gate insulator surface transport of one sign can be either completely suppressed or fully activated. For instance, a pentacene OFET based on a $SiO_2$ insulator known to be

solely p-conducting has been activated for n-conduction by depositing traces of calcium in the channel region of the OFET prior to the deposition of pentacene. By this treatment, electron traps at the oxide interface are eliminated by a chemical reaction providing pathways of calcium oxide and calcium hydroxide where electrons can move freely. Thus an ambipolar acting transistor channel is obtained. By the choice of a proper electrode material, a unipolar electron current can flow in pentacene OFETs. These results show that pentacene is truly an ambipolar material and that the operation mode of OFETs is strongly codetermined by the insulator.

The advantage for the fabrication of an inverter or a more complex circuit design by using Ca-traces would be that one could predetermine the areas of p- and n-conduction by a single Ca-deposition step converting the usual p-areas to n-areas. However, disadvantages are still the necessity for different source and drain metals and a structured deposition of the Ca passivation layer. Nonetheless, full pentacene inverters comprising in such a way engineered $SiO_2$ gate dielectrics showed satisfactory CMOS-like behavior.

An alternative way to adjust the charge carrier transport in OFETs is to introduce charge carrier traps in the transistor channel. The starting point is a semiconductor/insulator combination that allows for ambipolarity such as pentacene and PMMA. By simply choosing calcium electrodes, unipolar n-type OFETs can be prepared being mandatory for a true CMOS operation of inverters. To achieve unipolar p-conduction, the same device structure as for the n-channel OFETs is used except for electron traps being generated in PMMA by UV exposure under ambient condition. Such traps efficiently capture electrons leading to a substantial threshold voltage shift of about 60 V, thereby suppressing any electron current through the device but at the same time stimulating hole injection from the calcium electrodes and thus, efficient hole accumulation. Indeed, respective CMOS inverters exhibit satisfactory characteristics with negligible voltage losses in the 0 and 1 state.

Concerning the fabrication of the CMOS inverters, areas of desired p-conduction are easily defined by simply selectively treating the PMMA gate dielectric with UV light. Thereafter, we have the favourable situation of depositing a common pentacene layer and common calcium source/drain electrodes for both n- and p-type OFETs requiring only two fabrication steps. At present these devices are, however, clearly hampered by the use of calcium electrodes, which are known to corrode at ambient atmosphere. But possibilities may exist to turn the process around, starting with Au electrodes and trapped holes to allow for an efficient electron injection from gold electrodes. Work in this direction is presently in progress. Since the exposure to UV light can easily be achieved by already established semiconductor processes, the proposed technique would allow for a simplified fabrication of more complex circuits.

**Acknowledgments** The authors thank the Deutsche Forschungsgemeinschaft (DFG) and the Bundesministerium für Bildung und Forschung (BMBF) for funding.

## References


1. Shockley W, Sparks M, Teal GK (1951) p-n junction transistor. Phys Rev 83:151–162
2. Sze SM (1981) Physics of semiconductor devices. Wiley, New York
3. Bauer H, Jelting S, Benson N, Fruehauf N (2006) An LTPS active-matrix process with PECVD doped N+ drain/source areas. J SID 14:119–126
4. Cuscunà M, Bonfiglietti A, Carluccio R, Mariucci L, Mecarini F, Pecora A, Stanizzi M, Valetta A, Fortunato G (2002) A novel fabrication process for polysilicon thin film transistors with source/drain contacts formed by deposition and lift-off of highly doped layers. Solid-State Elektron 46:1351–1358
5. Sera K, Okumura F, Uchida H, Itoh S, Kaneko S, Hotta K (1989) High-performance TFT's fabricated by XeCl excimer laser annealing of hydrogenated amorphous-silicon film. IEEE Trans Electron Device 36:2868–2872
6. Pope M, Swenberg CE (1982) Electronic processes in organic crystals. Clarendon, New York
7. Dresner J, Goodman AM (1970) Anthracene electroluminescent cells with tunnel-injection cathode. Proc IEEE 58:1868–1869
8. Helfrich W, Schneider WG (1965) Recombination radiation in anthracene crystals. Phys Rev Lett 14:229–231
9. Pope M, Magnante P, Kallman HP (1963) Electroluminescence in organic crystals. J Chem Phys 38:2042
10. Vincett PS, Barlow WA, Hann RA, Roberts GG (1982) Electrical conduction and low voltage blue electroluminescence in vacuum-deposited organic films. Thin Solid Films 94:171–183
11. Barbe DF, Westgate CR (1970) Surface state parameters of metal-free phthalocyanine single crystals. J Phys Chem Solids 31:2679–2687
12. Heilmeier GH, Zanoni LA (1964) Surface studies of alpha-copper phthalocyanine films. J Phys Chem Solids 25:603
13. Kudo K, Yamashina M, Moriizumi T (1984) Field effect measurement of organic dye films. Jpn J Appl Phys 23:130
14. Tsumura A, Koezuka H, Ando T (1986) Macromolecular electronic device: field-effect transistor with a polythiophene thin film. Appl Phys Lett 49:1210–1212
15. Dimitrakopoulos CD, Malenfant RL (2002) Organic thin film transistors for large area electronics. Adv Mater 14:99–117
16. Knipp D, Street RA, Völkel A, Ho JJ (2003) Pentacene thin film transistors on inorganic dielectrics: morphology, structural properties, and electronic transport. J Appl Phys 93:347–355
17. Lin YY, Gundlach DJ, Nelson SF, Jackson TN (1997) Stacked Pentacene layer organic thin-film transistors with improved characteristics. IEEE Electron Device Lett 18:606–608
18. Salleo A, Chabinyc ML, Yang MS, Street RA (2002) Polymer thin-film transistors with chemically modified dielectric interfaces. Appl Phys Lett 81:4383–4385
19. Shankar K, Jackson TN (2004) Morphology and electrical transport in pentacene films on silylated oxide surfaces. J Mater Res 19:2003–2007
20. Sirringhaus H, Brown PJ, Friend RH, Nielsen MM, Bechgaard K, Langeveld-Voss BMW, Spiering AJH, Janssen RAJ, Meijer EW, Herwig P, de Leeuw DM (1999) Two-dimensional charge transport in self-organized, high-mobility conjugated polymers. Nature 401:685–688
21. Sariciftci NS, Braun D, Zang C, Srdanov V, Heeger AJ, Stucky G, Wudl F (1993) Semiconducting polymer-buckminsterfullerene heterojunctions: diodes, photodiodes, and photovoltaic cells. Appl Phys Lett 62:585–587
22. Shaheen SE, Brabec CJ, Sariciftci NS, Padinger F, Fromherz T, Hummelen JC (2001) 2.5% efficiency organic plastic solar cells. Appl Phys Lett 78:841–843
23. Haddon RC, Perel AS, Morris RC, Palstra TTM, Hebard AF, Fleming RM (1995) C60 thin film transistors. Appl Phys Lett 67:121–123
24. Waldauf C, Schilinsky P, Perisutti M, Hauch J, Brabec CJ (2003) Solution-processed organic n-type thin-film transistor. Adv Mater 15:2084–2088
25. de Leeuw DM, Simenon MMJ, Brown AR, Einerhand REF (1997) Stability on n-type doped conducting polymers and consequences for polymeric microelectronic devices. Synth Met 87:53–59

26. Ling M-M, Erk P, Gomez M, Könemann M, Locklin J, Bao Z (2007) Air-stable n-channel organic semiconductors based on perylene diimide derivatives without strong electron withdrawing groups. Adv Mater 19:1123–1127
27. de Vusser S, Steudel S, Myny K, Genoe J, Heremans P (2006) Low voltage complementary organic inverters. Appl Phys Lett 88:16116
28. Kitamura M, Arakawa Y (2007) Low-voltage-operating complementary inverters with C60 and pentacene transistors on glass substrates. Appl Phys Lett 91:053505
29. Klauk H, Zschieschang U, Pflaum J, Halik M (2007) Ultralow-power organic complementary cricuits. Nature 445:745–748
30. Ling M-M, Bao Z, Erk P, Koenemann M, Gomez M (2007) Complementary inverter using high mobility air-stable perylene di-imide derivatives. Appl Phys Lett 90:093508
31. Kawase T, Shimoda T, Newsome C, Sirringhaus H, Friend RH (2003) Inkjet printing of polymer thin film transistors. Thin Solid Films 438–439:279–287
32. Knobloch A, Manuelli A, Bernds A, Clemens W (2004) Fully printed integrated circuits from solution processable polymers. J Appl Phys 96:2286–2291
33. Subramanian V, Chang PC, Lee JB, Molesa SE, Volkman SK (2005) Printed organic transistors for ultra-low-cost RFID applications. IEEE Trans Components Packaging Technol 28:742–747
34. Clemens W, Fix W, Ficker J, Knobloch A, Ullmann A (2004) From polymer transistors towards printed electronics. J Mater Res 19:1963–1973
35. Meijer EJ, De Leeuw DM, Setayesh S, van Veenendaal E, Huisman B-H, Blom PWM, Hummelen JC, Scherf U, Klapwijk TM (2003) Solution-processed ambipolar organic field-effect transistors and inverters. Nat Mater 2:678–682
36. Benson N, Schidleja M, Melzer C, Schmechel R, von Seggern H (2006) Complementary organic field effect transistors by utraviolet dielectric interface modification. Appl Phys Lett 89:182105
37. Schmechel R, Ahles M, von Seggern H (2005) A pentacene ambipolar transistor: experiment and theory. J Appl Phys 98:084511
38. Zaumseil J, Sirringhaus H (2007) Electron and ambipolar transport in organic field-effect transistors. Chem Rev 107:1296–1323
39. Schmechel R (2002) Gaussian disorder model for high carrier densities: theoretical aspects and application to experiment. Phys Rev B 66:235206
40. Schmechel R (2003) Hopping transport in doped organic semiconductors: a theoretical approach and its application to p-doped zinc-phthalocyanine. J Appl Phys 93:4653–4660
41. Vissenberg MCJM, Matter M (1998) Theory of the field-effect mobility in amorphous organic transistors. Phys Rev B 57:12964–12967
42. Tanase C, Blom PWM, de Leeuw DM, Meijer EJ (2004) Charge carrier density dependence of the hole mobility in poly(p-phenylene vinylene). Phys Stat Solidi A 201:1236–1245
43. Melzer C, von Seggern H (2008) Field-effect transistors for organic CMOS technology. Inform Technol 50:(3), 158–166
44. Zaumseil J, Friend RH, Sirringhaus H (2006) Spatial control of the recombination zone in an ambipolar light-emitting organic transistors. Nat Mater 5:69–74
45. Hepp A, Heil H, Weise W, Ahles M, Schmechel R, von Seggern H (2003) Light-emitting field-effect transistor based on a tetracene thin film. Phys Rev Lett 91:157406
46. Benson N, Melzer C, Schmechel R, von Seggern H (2008) Electronic states at the dielectric/semiconductor interface in organic field effect transistors. Phys Stat Solidi A 205:475–487
47. Silinsh EA, Capek V (1994) Organic molecular crystals. AIP, New York
48. Dodabalapur A, Torsi L, Katz HE (1995) Organic transistors – 2-dimensional transport and improved electrical characteristics. Science 268:270–271
49. Kline RJ, Mc Gehee MD, Toney MF (2006) Highly oriented crystals at the buried interface in polythiopene thin-film transistors. Nat Mater 5:222–228
50. Ruiz R, Papadimitratos A, Mayer AC, Malliaras GG (2005) Thickness dependence of mobility in pentacene thin-film transistors. Adv Mater 17:1795–1798

51. Sandberg HGO, Frey GL, Shkunov MN, Sirringhaus H, Friend RH, Nielsen MM, Kumpf C (2002) Ultrathin regioregular poly (3-hexyl thiophene) field effect transistor. Langmuir 18:10176–10182
52. Li T, Balk JW, Ruden PP, Campbell IH, Smith DL (2002) Channel formation in organic field-effect transistors. J Appl Phys 91:4312–4318
53. Yang SY, Shin K, Park CE (2005) The effect of gate-dielectric surface energy on pentacene morphology and organic field-effect transistor characteristics. Adv Funct Mater 15: 1806–1814
54. Meyer zu Heringdorf F-J, Reuter MC, Tromp RM (2001) Growth dynamics of pentacene thin films. Nature 412:517–520
55. Halik M, Klauk H, Zschieschang U, Schmid G, Dehm C, Schutz M, Maisch S, Effenberger F, Brunnbauer M, Stellacci F (2004) Low-voltage organic transistors with an amorphous molecular gate dielectric. Nature 431:963–966
56. Klauk H, Zschieschang U, Pflaum J, Halik M (2007) Ultralow-power organic complementary circuits. Nature 445:745–748
57. Hulea IN, Fratini S, Xie H, Mulder CL, Iossad NN, Rastelli G, Ciuchin S, Morpurgo AF (2006) Tunable Fröhlich polaron in organic single-crystal transistors. Nat Mater 5:982–986
58. Veres J, Ogier S, Lloyd G, de Leeuw D (2004) Gate insulators in organic field-effect transistors. Chem Mater 16:4543–4555
59. Veres J, Ogier SD, Leeming SW, Cupertino DC, Khaffaf SM (2003) Low-k insulators as the choice of dielectrics in organic field-effect transistors. Adv Funct Mater 13:199–204
60. Ahles M, Schmechel R, von Seggern H (2005) Complementary inverter based on interface doped pentacene. Appl Phys Lett 87:113505
61. Benson N, Schidleja M, Siol C, Melzer C, von Seggern H (2007) Dielectric interface modification by UV irradiation: a novel method to control OFET charge carrier transport properties. Proc SPIE 6658:0W1–9
62. Ahles M, Schmechel R, von Seggern H (2004) n-Type organic field-effect transistor based on interface-doped pentacene. Appl Phys Lett 85:4499–4501
63. Chua LL, Zaumseil J, Chang JF, Ou ECW, Ho PKH, Sirringhaus H, Friend RH (2005) General observation of n-type field-effect behaviour in organic semiconductors. Nature 434:194–199
64. Benson N, Gassmann A, Mankel E, Mayer T, Melzer C, Schmechel R, von Seggern H (2008) The role of Ca traces in the passivation of silicon dioxide dielectrics for electron transport in pentacene organic field effect transistors. J Appl Phys 104:054505
65. Kumaki D, Ando S, Shimono S, Yamashita Y (2007) Significant improvement of electron mobility in organic thin-film transistors based on thiazolothiazole derivative by employing self-assembled monolayer. Appl Phys Lett 90:053606
66. Hoshino S, Nagamatsu S, Chikamatsu M, Misaki M, Yoshida Y, Tanigaki N, Yase K (2002) Device performance of an n-channel organic thin-film transistor with LiF/Al bilayer source and drain electrodes. Jpn J Appl Phys 41:808–810
67. Gundlach DJ, Pernistich KP, Wilckens G, Gruter M, Haas S, Batlogg B (2005) High mobility n-channel organic thin-film transistor and complementary inverters. J Appl Phys 98:064502
68. Schmechel R, Hepp A, Heil H, Ahles M, Weise W, von Seggern H (2003) Light emitting field-effect transistor: simple model and underlying functional mechanisms. Proc SPIE 5217:101–111
69. Zaumseil J, Baldwin KW, Rogers JA (2003) Contact resistance in organic transistors that use source and drain electrodes formed by soft contact lamination. J Appl Phys 93:6117–6124
70. Bürgi L, Sirringhaus H, Friend RH (2002) Noncontact potentiometry of polymer field-effect transistors. Appl Phys Lett 80:2913–2915
71. Anthopoulos TD, de Leeuw DM, Cantatore E, Setayesh S, Meijer EJ, Tanase C, Hummelen JC, Blom PWM (2004) Organic complementary-like inverters employing methanofullerene-based ambipolar field-effect transistors. Appl Phys Lett 85:4205–4207
72. Katz HE, Lovinger AJ, Johnson J, Kloc C, Siegrist T, Li W, Lin Y-Y, Dodabalapur A (2000) A soluble and air-stable organic semiconductor with high electron mobility. Nature 404: 478–481

73. Locklin J, Shinbo K, Onishi K, Kaneko F, Bao ZN, Advincula RC (2003) Ambipolar organic thin film transistor-like behavior of cationic and anionic phthalocyanines fabricated using layer-by-layer deposition from aqueous solution. Chem Mater 15:1404–1412
74. Opitz A, Bronner M, Brütting W (2007) Ambipolar charge carrier transport in miced organic layers of phthalocyanine and fullerene. J Appl Phys 101:063709
75. Wang J, Wang HB, Yan XJ, Huang HC, Yan DH (2005) Organic heterojunction and its application for double channel field-effect transistors. Appl Phys Lett 87:093507
76. Ye RB, Baba M, Oishi Y, Mori K, Suzuki K (2005) Air stable ambipolar organic thin-film tarnsistors based on an organic homostructure. Appl Phys Lett 86:253505
77. Scharnberg M, Zaporojtchenko V, Adelung R, Faupel F (2007) Tuning the threshold voltage of organic field-effect transistors by an electret encapsulation layer. Appl Phys Lett 90:013501
78. Singh TB, Marjanovic N, Matt GJ, Sariciftci NS, Schwödiauer R, Bauer S (2004) Nonvolatile organic field-effect transistor memory element with a polymeric gate electret. Appl Phys Lett 85:5409–5411
79. Singh TB, Marjanovic N, Stadler P, Auinger M, Matt GJ, Günes S, Sariciftci NS, Schwödiauer R, Bauer S (2005) Fabrication and characterization of solution-processed methanofullerene-based organic field-effect transistors. J Appl Phys 97:083714
80. Holländer A, Klemberg-Sapieha JE, Wertheimer MR (1994) Vacuum-ultraviolet-induced oxidation of polyethylene. Macromolecules 27:2893–2895
81. Torikai A, Ohno M, Fueki K (1990) Photodegradation of poly(methyl methacrylate) by monochromatic light – quantum yield, effect of wavelength, and light-intensity. J Appl Polym Sci 41:1023
82. Wei SY, Vaidya B, Patel AB, Soper SA, Mc Carley RL (2005) Photochemically patterned poly(methyl methacrylate) surfaces used in the fabrication of microanalytic devices. J Phys Chem B 109:16988–16996
83. Clarisse C, Riou MT, Gauneau M, Le Contellec M (1988) Field-effect transistor with diphthalocyanine thin film. Electron Lett 24:674–675
84. Assadi A, Svensson C, Willander M, Inganaes O (1988) Field-effect mobility of poly(3-hexylthiophene). Appl Phys Lett 53:195–197
85. Horowitz G, Fichou D, Peng X, Xu Z, Garnier F (1989) A field-effect transistor based on conjugated alpha-sexithienyl. Solid Stat Commun 72:381–384
86. Horowitz G, Peng XZ, Fichou D, Garnier F (1992) Role of the semiconductor insulator interface in the characteristics of Pi-conjugated-oligomer-based thin-film transistors. Synth Met 51:419–424
87. Garnier F, Yassar A, Hajlaoui R, Horowitz G, Deloffre F, Servet B, Ries S, Alnot P (1993) Molecular engineering of organic semiconductors: design of self-assembly properties in conjugated thiophene oligomers. J Am Chem Soc 115:8716–8721
88. Garnier F, Hajlaoui R, Yassar A, Srivastava P (1994) All-polymer field-effect transistor realized by printing techniques. Science 265:1684–1686
89. Dimitrakopoulos CD, Brown AR, Pomp A (1996) Molecular beam deposited thin films of pentacene for organic field effect transistor applications. J Appl Phys 80:2501–2508
90. Bao Z, Lovinger AJ, Dodabalapur A (1996) Organic field-effect transistors with high mobility based on copper phthalocyanine. Appl Phys Lett 69:3066–3068
91. Bao Z, Dodabalapur A, Lovinger AJ (1996) Soluble and processable regioregular poly(3-hexylthiophene) for thin film field-effect transistor applications with high mobility. Appl Phys Lett 69:4108–4110
92. Dimitrakopoulos CD, Furman BK, Graham T, Hegde S, Purushothaman S (1998) Field-effect transistors comprising molecular beam deposited alqha, omega-di-hexyl-hexathienylene and polymeric insulator. Synth Met 82:47–52
93. Sirringhaus H, Tessler N, Friend RH (1998) Integrated optoelectronc devices based on conjugated polymers. Science 280:1741–1744
94. Katz HE, Lovinger AJ, Laquindanum JG (1998) Alpha, omega-dihexylquaterthiophene: a second thin film single-crystal organic semiconductor. Chem Mater 10:457–459
95. Klauk H, Halik M, Zschieschang U, Schmid G, Radlik W (2002) High-mobility polymer gate dielectric pentacene thin film transistors. J Appl Phys 92:5259–5263

96. Hajlaoui ME, Granier F, Hassine L, Kouki F, Bouchriha H (2002) Growth conditions effects on morphology and transport properties of an oligothiophene semiconductor. Synth Met 129:215–220
97. Wang G, Swensen J, Moses D, Heeger AJ (2003) Increased mobility from regioregular poly(3-hexylthiophene) field-effect transistor. J Appl Phys 93:6137–6141
98. Okuda T, Shintoh S, Terada N (2004) Copper-phthalocyanine field-effect transistor with a low driving voltage. J Appl Phys 96:3586–3588
99. Lee S, Koo B, Shin J, Lee E, Park H (2006) Effects of hydroxyl groups in polymeric dielectrics on organic transistor performance. Appl Phys Lett 88:162109
100. Mc Culloch I, Heeney M, Bailey C, Genevicius K, Mac Donald I, Shkunov M, Sparrowe D, Tierney S, Wagner R, Zhang WM, Chabinyc ML, Kline RJ, Mc Gehee MD, Toney MF (2006) Liquid-crystalline semiconductor polymer with high charge-carrier mobility. Nat Mater 5:328–333
101. Hamadani BH, Gundlach DJ, Mc Culloch I, Heeney M (2007) Undoped polythiophene field-effect transistor with mobility of 1cm2/(Vs). Appl Phys Lett 91:243512
102. Butko VY, Chi X, Lang DV, Ramirez AP (2003) Field-effect transistor on pentacene single crystal. Appl Phys Lett 83:4773–4775
103. Podzorov V, Sysoev SE, Loginova E, Pudalov VM, Gershenson ME (2003) Single-crystal organic field effect transistor with the hole mobility ∼8 cm2/ Vs. Appl Phys Lett 83: 3504–3506
104. Goldmann C, Haas S, Krellner C, Pernstich KP, Gundlach DJ, Batlogg B (2004) Hole mobility in organic single crystals measured by a “flip-crystal” field-effect technique. J Appl Phys 96:2080–2086
105. Podzorov V, Menard E, Borissov A, Kiryukhin V, Rogers JA, Gershenson ME (2004) Intrinsic charge transport on the surface of organic semiconductors. Phys Rev Lett 93:086602
106. Roberson LB, Kowalik J, Tolbert LM, Kloc C, Zeis R, Chi X, Fleming R, Wilkins C (2005) Pentacene disproportionation during sublimation for field-effect transistors. J Am Chem Soc 127:3069–3075
107. Reese C, Chung W-J, Ling M-M, Roberts M, Bao Z (2006) High-performance microscale single-crystal transistors by lithography on an elastomer dielectric. Appl Phys Lett 89:202108
108. Jurchescu OD, Popinciuc M, van Wees BJ, Palstra TTM (2007) Interface-controlled, high-mobility organic transistor. Adv Mater 19:688–692

Adv Polym Sci (2010) 223: 259–300
DOI:10.1007/12_2009_10
© Springer-Verlag Berlin Heidelberg 2009
Published online: 19 June 2009

# Theories of the Charge Transport Mechanism in Ordered Organic Semiconductors

**Alessandro Troisi**

**Abstract** The traditional theories of charge transport in ordered organic semiconductors are reviewed and their limitations discussed. The recent contributions of computational chemistry to the understanding of the parameters that determine the charge mobility in bulk semiconductors are analyzed in detail. The effect of thermal motions on the electronic wavefunction and the effect of strong off-diagonal electron–phonon coupling are identified as essential ingredients for the proper description of the charge dynamics. The development of suitable methods to compute the charge mobility taking into account these new computational results is reviewed, with special emphasis on the models that allow the prediction of the structure–property relationship. The available experimental evidence is compared with the predictions made by the most recent models.

**Keywords** Molecular crystal · Polaron · Electron transport · Quantum chemistry · Pentacene · Disorder

## Contents

1 The Role of Theory in Organic Semiconductor Research ........ 260
2 Traditional Views on Charge Transport Mechanism in Molecular Crystals and their Limitations ........ 264
2.1 Delocalized Transport in Simple Electronic Band ........ 265
2.2 Delocalized Transport in Polaronic Band ........ 266
2.3 Hopping Transport ........ 268
2.4 Experimental Evidence ........ 269
2.5 A More General Hamiltonian ........ 269

A. Troisi
Department of Chemistry and Centre of Scientific Computing, University of Warwick, CV4 7AL, Coventry, UK
e-mail:a.troisi@warwick.ac.uk

3 The Contribution of Computational Chemistry ... 270
3.1 Hopping Integral and Band Structure ... 271
3.2 Local Electron–Phonon Coupling ... 273
3.3 Computational Data and Conventional Theories ... 274
4 The Extreme Sensitivity of the Hopping Integral to the Intermolecular Geometry ... 276
5 The Effect of Thermal Motions on the Electronic Eigenfunction ... 278
5.1 Molecular Dynamics/Quantum Chemical Studies ... 278
5.2 Dynamic Localization Effects ... 280
5.3 Rationalization ... 281
6 Models for the Charge Transport in the Presence of Strong Nonlocal Electron Phonon Coupling ... 283
6.1 Elementary Semiclassical Model: Diffusion Limited by Thermal Off-Diagonal Disorder ... 283
6.2 Generalized Semiclassical Model ... 286
6.3 Revised Polaronic Band Models ... 287
6.4 Localization Theory Models ... 288
6.5 Extension to Polymers and Liquid Crystals ... 289
7 Recent Experimental Evidence of Relevance to the Transport Mechanism ... 291
8 Conclusion ... 293
References ... 294

## 1 The Role of Theory in Organic Semiconductor Research

Semiconductors based on organic compounds have been proposed as substitutes for silicon or germanium since the beginning of the electronics era [1], but they found only a limited group of applications until the beginning of the 1990s. Since then, interest toward organic electronics has grown because of the many successful demonstrations of organic light emitting diodes (LED) [2–5], thin film transistors (TFT) [6–10], and organic photovoltaic cells (OPC) [11–16]. In the near future, organic electronics materials are expected to play an important role in applications that require low-cost, large-area, and flexible electronic devices. Organic LEDs are now used for some commercial displays while, for the other applications (TFT, OPC, lighting), the performances of organic devices are approaching the desired level [17–19]. Organic materials for electronics are based on polymers or molecular solids such as pentacene or rubrene (Fig. 1). Isotropic polymers are more used in the LED development (e.g., polytriaryamine), while highly ordered (anisotropic) compounds are considered more suitable for TFTs (e.g., poly(3-hexylthiophene) or P3HT [20]).

It is generally acknowledged [17, 19] that one of the greatest limitations for the advancement of organic electronics is the lack of a solid theoretical framework to rationalize the structure–property relations of organic materials. Without such a deeper understanding, most of the advantages of having materials easily modifiable with organic synthesis are lost and, as a result, the selection of suitable materials proceeds mostly by trial and error. Several important aspects of the device physics such as the role of the dielectric in TFTs or the charge injection mechanism need further theoretical studies [21], but probably the most puzzling open question concerns the mechanism of charge transport in organic semiconductors, the topic of this

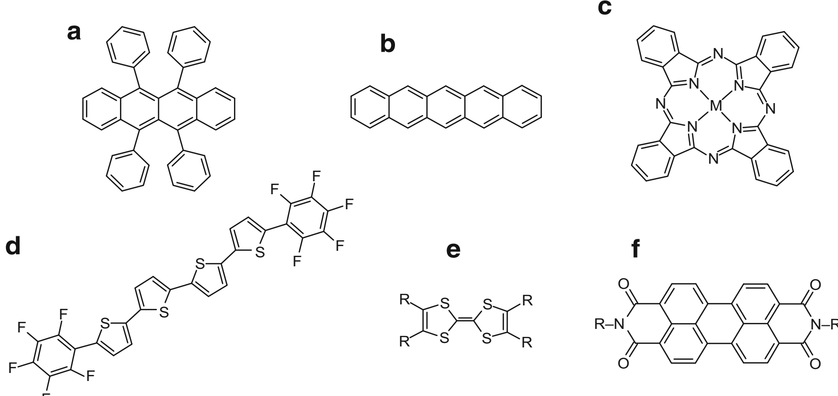


**Fig. 1** A few example molecules which form semiconducting crystals with high mobility. **a** Rubrene. **b** Pentacene. **c** Metal phthalocyanine. **d** One of the perfluoroarene–thiophene oligomer synthesized in T. Marks' group. **e** Tetrathiafulvalene derivative. **f** PTCDI derivative

review. The absolute charge mobility of organic solids cannot be computed from first principles and the relative mobilities measured for a set of similar materials cannot be rationalized on the basis of their structure. Our knowledge of the transport mechanism of these materials is incomplete because there is no link between phenomenological transport theories and microscopic description of the electronic and vibrational structure of the material.

In a phenomenological theory, a simplified model of transport is assumed and a relation between observable quantities (current or mobility, voltage or electric field, temperature) is derived analytically or from numerical simulations. The results of these theories are mathematical expressions with a few parameters that can be used to fit the experimental results. The *Gaussian Disorder Model* (GDM) [22] and its recent improvements [23–25] are prototypes of this modeling paradigm. They derive from the early work of Mott [26] on transport in disordered materials and they focus on the identification of universal relations in the transport characteristics [27]. Charge transport in disordered organic semiconductors is thought to proceed by hopping in an energetically disordered environment. The energy of the localized sites for the electron is assumed to have a Gaussian distribution, the length of each hopping step is consistent with tunneling models, and the relative hopping rates satisfy the principle of detailed balance. The GDM model assumes that the charge carriers are always localized by static disorder, while alternative models have been developed assuming that the charge carriers can be thermally activated into delocalized states (*multiple trapping model*) [28]. These models, when applied to a set of experimental data, lead ultimately to a fitting procedure; they do not provide a structure–property relation and do not suggest any means for improving the charge mobility of the material. This can be seen as a general paradigm of solid state science: the more general, elegant and "universal" is a physical law, the less information it provides to the chemists and engineers that are willing to improve one particular property

of the materials. These phenomenological models are often used for the study of highly disordered solids [29, 30] (e.g., Alq3) for which the atomistic details of the Hamiltonian are unknown and they are particularly useful for the (mesoscale) electric device modeling [31–33]. Two recent overviews on the field of charge transport in soft materials are presented in [34, 35].

In a microscopic description of the charge transport the elementary processes are described in terms of parameters related to the system Hamiltonian which include electronic and phononic states together with the relevant electron–phonon couplings. The parameters of this Hamiltonian can be accessed through computational techniques (and a few experiments) so that, in principle, one can compute the desired mobility starting from the knowledge of the morphology of the solid. Microscopic theories are largely concerned with the structure/property relation and can be thought as the connecting link between chemistry and material science. Traditionally, they have been applied to crystalline solids for which it is easier to compute the Hamiltonian from first principles or to evaluate in an approximate way its main terms. Although it can be argued that the absence of static disorder in crystalline solids make them unlikely model for the transport in polymers, the most promising classes of polymeric materials display a high level of ordering and the correlation between high order and high mobility has been established many times [36–38]. The difference in transport mechanism between ultrapure pentacene and highly ordered P3HT can be more subtle then previously thought and it is likely that the microscopic description can be applied to weakly disordered solids bridging the gap between atomistic and phenomenological theories. Ideally, these microscopic models should be able to offer a rationalization to a constantly growing volume of mobility data on a variety of new compounds prepared by synthetic chemists [39–47].

The use of crystalline solids as model compounds for the understanding of charge transport in all types of organic semiconductors have grown in importance during the past few years thanks to the availability of new experimental techniques and crystal growth methodologies which allowed the study of crystalline molecular semiconductors virtually in the absence of electronic traps. The recent experimental work in very purified pentacene [48–50] and rubrene [51–54] (see Fig. 2) provided an ideal set of experimental data to be compared with the available models, in addition to the earlier ground-breaking works on smaller organic molecule such as naphthalene [55, 56] or stilbene [57]. It soon became apparent that the transport theories developed for inorganic solids were unsuitable for describing the transport in organic crystals and that a new physics was associated with this new class of compounds.

In this contribution we describe how the current understanding of the microscopic charge transport mechanism in crystalline organic semiconductors is developing through a combination of computational and theoretical methods. We will focus on bulk conductance, ignoring the effect of carrier–carrier interaction. In Sect. 2 we will briefly review the limiting cases of charge transport that have been traditionally used for organic semiconductors and we discuss their use and limitations. In Sect. 3 we describe how computational chemistry methods have been used

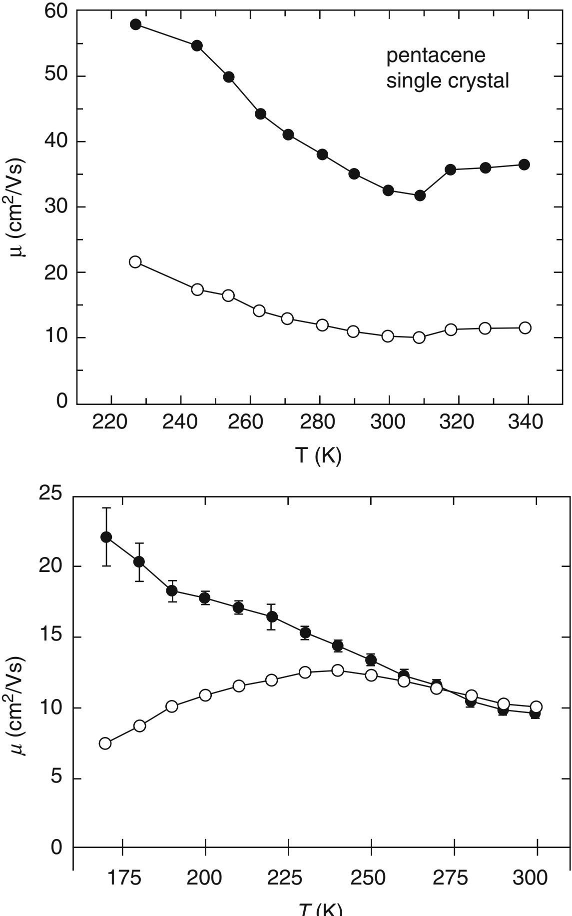


**Fig. 2** (*Top*) Temperature dependence of the mobility in pentacene (reprinted from [46]) showing a band-like mobility up to room temperature. (*Bottom*) Temperature dependence of the Hall mobility of holes in rubrene (*full circles*), essentially due to the free holes in the solid (reprinted from [50]). The total mobility (*empty circles*) is similar to the Hall mobility beyond 230 K. At lower temperature a fraction of carriers are trapped and the initial increase of total mobility with temperature is due to detrapping

to provide a quantitative description of the Hamiltonian for organic semiconductors and in Sects. 4 and 5 we illustrate how some of these computational studies have disclosed the main limitation of the conventional transport models. Few possible transport models can take into account all the "computational observations" and the available experimental data are presented and compared in Sect. 6. Some recent experiments that have shed light on the transport mechanism in organic solids are outlined in Sect. 7. The last section presents a summary and provides an outlook for the field.

## 2 Traditional Views on Charge Transport Mechanism in Molecular Crystals and their Limitations

Any charge transport model is always based on an idealized representation of the system under investigation (which takes the mathematical form of a model Hamiltonian) followed by a set, or hierarchy, of approximations which make the problem treatable. The possible idealizations of the organic crystal are fairly standard and agreed upon. It is reasonable to ignore initially the interaction between charge carriers and between the carrier and the external electric field. The minimalist model used to describe the basic transport mechanisms is a one dimensional array of molecules, with one electronic state per molecule (for the hole or the electron) and one optical phonon per molecule (a more general case will be considered at the end of this section). It is usually written as

$$H = H_{\mathrm{el}}^{0} + H_{\mathrm{phon}}^{0} + V_{\mathrm{el}} + V_{\mathrm{el-phon}}^{\mathrm{local}} + V_{\mathrm{impurities}} \tag{1a}$$

$$H_{\mathrm{el}}^{0} = \sum_{j} \varepsilon_j a_j^{\dagger} a_j \tag{1b}$$

$$V_{\mathrm{el}} = -\tau \sum_{j} a_j^{\dagger} a_{j+1} \tag{1c}$$

$$H_{\mathrm{phon}}^{0} = \sum_{j} \hbar\omega_0 \left( b_j^{\dagger} b_j + \tfrac{1}{2} \right) \tag{1d}$$

$$V_{\mathrm{el-phon}}^{\mathrm{local}} = \sum_{j} g\hbar\omega_0 \left( b_j^{\dagger} + b_j \right) a_j^{\dagger} a_j \tag{1e}$$

where $H_{\mathrm{el}}^{0}$ and $H_{\mathrm{phon}}^{0}$ are the electronic and nuclear Hamiltonians of the non-interacting molecules, $a_j^{\dagger}$ and $a_j$ are the creation and annihilation operators of a charge carrier on site $j$, and $b_j^{\dagger}$ and $b_j$ are the creation and annihilation operators for the phonon. Each localized state interacts with its neighbors via the electronic coupling term $V_{\mathrm{el}}$ ($\tau$ is the hopping integral or electronic coupling between states localized on adjacent molecules). It is customary to assume that the phonons are dispersionless so that they can be considered as localized on each site. The local (or Holstein) electron phonon coupling $V_{\mathrm{el-phon}}^{\mathrm{local}}$ has a simple intuitive meaning: when a charge carrier is localized on state $j$, the molecule is deformed and its energy reduced by $\frac{1}{2}\hbar\omega_0 g^2$. In the chemistry literature, the reorganization energy $\Lambda = \hbar\omega_0 g^2$ is often used to quantify the same effect. Even adopting the minimalist model of Eq. (1), it is not possible to compute the mobility without approximation. The two limit cases of charge transport in organic semiconductors (band and hopping mechanisms, see also Fig. 3) can be seen as two opposite strategies to the approximate solution of the Hamiltonian in Eq. (1).

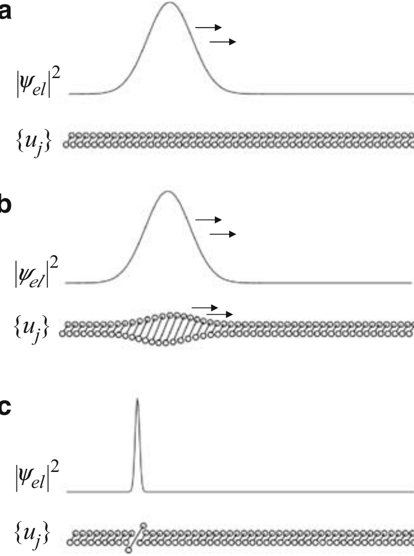


**Fig. 3** An illustration of the transport mechanisms described in Sect. 2 for the one dimensional model of Eq. (1). The *continuous line* represents the density profile of the charge carrier at a given time and the lattice is idealized as an array of diatomic molecules whose bond distance $u_j$ can be modulated by the presence of the charge. In pure band transport (**a**) the carrier travels as a delocalized wavepacket without deforming the underlying lattice. In polaronic band transport (**b**), the carrier and a deformation of the lattice form a quasiparticle that behaves as a "heavier" (and slower) charge carrier. In pure hopping (**c**), the charge is localized in one site and hops with a given rate to the neighboring sites. The intermediate case between (**a**) and (**b**) is studied by large polaron theories, while the transition between (**b**) and (**c**) is studied by small polaron theories

## *2.1 Delocalized Transport in Simple Electronic Band*

If $V_{\text{el-phon}}^{\text{local}}$ is neglected altogether the charge carriers and phonons are completely decoupled. The carrier wavefunction is described by a simple band with dispersion relation given by $\varepsilon(k) = -2\tau\cos(kL)$ ($k$ is the wavevector and $L$ the intermolecular distance). The carriers are completely delocalized and their motion is usually described semiclassically by the Boltzmann equation [58]. Carrier with wavevectors $k$ are scattered to a new state $k'$ by impurities or phonons. In the simplest possible case, the average time between two collisions can be taken as a constant $t_\text{s}$ independent from the initial state $k$. It can be further assumed that the distribution of final states $k'$ after a collision is simply the equilibrium distribution. The mobility under all these assumptions can be written as

$$\mu = et_\text{S}/m^* \tag{2}$$

where $m^*$ is the effective mass, which, for the one dimensional case of Eq. (1) is $m^* = 2|\tau|L^2/\hbar^2$. For a more general system (three dimensional and possibly many states per molecule) the mobility tensor $\upmu$ under the same set of assumptions is

$$\upmu = et_S\mathbf{M}^{-1} \tag{3}$$

with the elements of the inverse mass tensor given by

$$\left(\mathbf{M}^{-1}\right)_{\mu\nu} = -\frac{1}{\hbar^2}\left(\frac{\partial^2 E(\mathbf{k})}{\partial k_\mu \partial k_\nu}\right)_{\mathbf{k}_0} \tag{4}$$

where $\mu$ and $\nu$ are one of the Cartesian coordinates $x, y, z$ and $\mathbf{k}_0$ is the wavevector at which the lowest unoccupied (highest occupied) band energy of the electron (hole) is minimum (maximum).

There are many band structure computations of organic solids and most of them present the effective mass tensor as the quantity most closely related to the experimental mobility [59–65]. It should be noted, however, that the number of assumptions made to relate the effective mass to the mobility is quite considerable so that any possible correlation between high effective mass and high charge mobility should be taken with great caution. The effective mass approximation based on simple bands is truly excellent for the most studied inorganic semiconductors (Si, Ge, GaAs) for which the scattering probabilities due to different scattering mechanisms (impurities, optical and acoustical phonons) have been investigated in great detail and the Boltzman equation has been used beyond the limit of the constant relaxation time approximation [66–68]. A typical signature of band transport is given by the temperature dependence of the mobility which follows the power law $\mu \sim T^{-\alpha}$ (mobility decreases with increasing temperature) because the scattering by phonons is more efficient at higher temperatures. We will discuss in Sect. 6 under what conditions band transport offers a good description of the charge dynamics in molecular crystals.

## *2.2 Delocalized Transport in Polaronic Band*

### 2.2.1 Weak Electron–Phonon Coupling

A step forward in the formulation of a model more general than a simple band model can be made incorporating the effect of $V_{\text{el-phon}}^{\text{local}}$. A group of approximation schemes (weak electron phonon coupling or *large polaron* theories) assume that $V_{\text{el-phon}}^{\text{local}}$ can be considered a small perturbation and that the wavefunction is slightly modified by the interaction with the phonons. The problem has been treated using ordinary Rayleigh–Schrödinger perturbation theory, Brillouin–Wigner perturbation theory or several more advanced methods [69]. One simple and sufficiently accurate result from Rayleigh–Schrödinger theory is that the electron phonon coupling modifies the effective mass of the carrier to a renormalized value $\bar{m}^*$ which is related to the purely electronic effective mass $m^*$ as [70]

$$\bar{m}^* = \frac{m^*}{1-\alpha/6} \tag{5}$$

where $\alpha = \Delta E / \hbar\omega$ and $\Delta E$ is the stabilization energy of the polaron due to the lattice deformation. When $\alpha$ approaches 6, the polaronic mass goes to infinity, indicating a breakdown of the large polaron model (and perturbation theory) and the localization of the charge. As long as the carriers are delocalized, the charge dynamics can be described using the semiclassical theory and the renormalized effective mass. These theories were developed in the 1950s and were based on the idea that a carrier moving in a ionic crystal can carry with itself a polarization cloud (know in this context as Frölich polaron) which increases (slightly) its effective mass. Because of the small polarity of organic crystals, Frölich polaron theories have not been applied in this context, but, as we will see in Sect. 7, they have been recently revived to describe the transport in an organic thin film at the interface with an inorganic polar insulator.

### 2.2.2 Strong Electron–Phonon Coupling

Another approximation scheme (strong electron–phonon coupling theory) starts from the opposite assumption that the electronic coupling $V_{\mathrm{el}}$ is a small perturbation, i.e., the molecular crystal can be seen as a collection of isolated molecules. Molecule $j$ is deformed by the presence of a carrier and the set of vibronic states localized on $j$ form the basis for a transformed Hamiltonian [69, 71, 72]. In second quantization the transformed Hamiltonian can be written as

$$\tilde{H} = e^{S} H e^{-S} \tag{6}$$

where the unitary operator $e^{S}$ is defined such that $S = -g \sum_j \left(b_j^{\dagger} - b_j\right) a_j^{\dagger} a_j$. This transformation diagonalizes the Hamiltonian of the noninteracting molecules (with $\varepsilon_j = 0$):

$$\begin{aligned} e^{S} \left( \sum_j \hbar\omega_0 \left(b_j^{\dagger} b_j + \tfrac{1}{2}\right) + \sum_j g\hbar\omega_0 \left(b_j^{\dagger} + b_j\right) a_j^{\dagger} a_j \right) e^{-S} \\ = \sum_j \hbar\omega_0 \left(\tilde{b}_j^{\dagger} \tilde{b}_j + \tfrac{1}{2}\right) - g^2 \sum_j \tilde{a}_j^{\dagger} \tilde{a}_j \end{aligned} \tag{7}$$

and the transformed operators combine fermionic and bosonic components:

$$\tilde{b}_j = b_j + g a_j^{\dagger} a_j \tag{8a}$$

$$\tilde{a}_j = a_j \exp\left(g\left(b_j^{\dagger} - b_j\right)\right) \tag{8b}$$

The electron phonon interaction is carried by the transformed electronic coupling interaction, $\tilde{V}_{\mathrm{el}} = e^{S} V_{\mathrm{el}} e^{-S}$, which still contains a complicated combination of fermionic and bosonic operators.

The transformed problem is treatable only if one can assume that the carrier is still delocalized. In this case the bosonic component of $\tilde{V}_{\rm el}$ can be eliminated approximating $\tilde{V}_{\rm el} = e^S V_{\rm el} e^{-S}$ with its thermal average $\langle \tilde{V}_{\rm el} \rangle_T$. This is equivalent to the assumption that the phonon occupation number does not change during the transport, i.e., that inelastic processes are not important. In this limit we have for the Hamiltonian in Eq. (1):

$$\tilde{V}_{\rm el} = \tau \mathrm{e}^{-2g^2\left(N_\omega + \frac{1}{2}\right)} \sum_i a_j^\dagger a_{j+1} \tag{9}$$

with $N_\omega = [\exp(\hbar\omega/k_{\rm B}T) - 1]^{-1}$. This result is qualitatively simple to understand: the effect of the phonons in the delocalized limit is to reduce the effective hopping integral to a renormalized value (compare Eq. (9) with Eq. (1c)). The factor $\mathrm{e}^{-2g^2\left(N_\omega + \frac{1}{2}\right)}$ is the (temperature dependent) reduction factor of the bandwidth and of the inverse effective mass. The effect of the phonons is similar to that resulting from large polaron theories and the charge dynamics can also be described, in this case, using the semiclassical approach where the *polaronic band* takes the place of simple band [71]. Since the inverse effective mass decreases with increasing temperature the mobility of carriers in polaronic bands should decrease more markedly with increasing temperature.

## 2.3 Hopping Transport

The approximation leading to Eq. (9) is not valid if the charge is localized on one molecule and can hop to the neighboring molecules (while the phonon occupation number of the two molecules changes). In this case, the rate of charge hopping between two neighboring molecules is computed directly from the Hamiltonian in Eq. (1) but considering only two molecules. The rate of the hopping process between two close molecules is computed from the Fermi Golden rule assuming a Boltzman distribution of the initial vibrational states and in the limit of small coupling $\tau$. The result is expressed more simply if we consider also the limit of high temperatures $(k_{\rm B}T \gg \hbar\omega_0)$:

$$k_{\rm hop} = \frac{\tau^2}{\hbar} \left( \frac{\pi}{k_{\rm B}T\Lambda} \right)^{1/2} \mathrm{e}^{-\Lambda/4k_{\rm B}T} \tag{10}$$

This is of course also the rate expression for a nonadiabatic charge transfer reaction between two identical molecules [73–76] written in the form more common to the physical chemistry literature with the electron–phonon coupling $g$ expressed in terms of the reorganization energy $\Lambda$.

The charge mobility due to hopping can be estimated from the rate constant in Eq. (10), through the Einstein relation $\mu = eD/k_{\rm B}T$ and the relation $D = k_{\rm hop}L^2$. If $\Lambda$ is sufficiently larger than $k_{\rm B}T$ and the model is valid, the mobility increases with temperature following an approximate Arrhenius law $\mu \sim \exp(-E_{\rm B}/k_{\rm B}T)$.

### 2.4 Experimental Evidence

Because of the opposite temperature dependence of the mobility in the delocalized and localized regimes, several researchers have also attempted a more general formulation of the model to describe the transition between the two regimes. This effort has led to elegant theories including the dynamical mean field approach of Fratini and Ciuchi [77], the interpolation scheme proposed by Loos et al. [78] and the general path integral method [79] originally introduced by Feynmann [80]. However, the most recent experiments carried out by different research groups on the molecular solids with the highest mobility (pentacene and rubrene) have shown that the charge transport mechanisms described above cannot be fully consistent with the observations even if intermediate regimes are taken into account [50, 53], i.e., the important mathematical problem of describing the Holstein Hamiltonian in the intermediate localized–delocalized regime is less relevant to organic semiconductors than previously thought. Several groups have reported a "band-like" mobility decreasing with temperature over the broad range between 0 and 300 K. The analysis of the experimental mobilities in these systems (see for example [81]) indicates that the semiclassical transport theories can be fitted to the experiment only assuming unphysical mean free paths much shorter than the intermolecular distances.

It may be surprising that several papers appeared in the past few years assuming opposite transport mechanisms (delocalized or localized) for the same type of material. The confusion is largely justified by the lack of reliable data for ultrapure crystals before the more recent experimental works [82]. The initial experimental reports of activated transport in several solids were affected by the presence of impurities in the sample and the activation energy corresponded actually to the detrapping energy.

### 2.5 A More General Hamiltonian

The reduced number of degrees of freedom and dimensionality in the Hamiltonian of Eq. (1) do not affect the phenomenology of the localized or delocalized transport. However, in order to link the realistic system with the theoretical models, it is necessary to write a more general expression:

$$H = H_{\mathrm{el}}^{0} + H_{\mathrm{phon}}^{0} + V_{\mathrm{el}} + V_{\mathrm{el-phon}}^{\mathrm{local}} + V_{\mathrm{el-phon}}^{\mathrm{nonlocal}} + V_{\mathrm{impurities}} \tag{11a}$$

$$H_{\mathrm{el}}^{0} + V_{\mathrm{el}} = \sum_{j} \varepsilon_j a_j^{\dagger} a_j + \sum_{ij} \tau_{ij} a_i^{\dagger} a_j \tag{11b}$$

$$H_{\mathrm{phon}}^{0} = \sum_{\mathbf{q}l} \hbar\omega_{\mathbf{q}l} \left( b_{\mathbf{q}l}^{\dagger} b_{\mathbf{q}l} + \tfrac{1}{2} \right) \tag{11c}$$

$$V_{\mathrm{el-phon}}^{\mathrm{local}} = \sum_{\mathbf{q}l} \sum_{j} \hbar \omega_{\mathbf{q}l} g_{jj,\mathbf{q}l} \left( b_{\mathbf{q}l}^{\dagger} + b_{-\mathbf{q}l} \right) a_j^{\dagger} a_j \tag{11d}$$

$$V_{\mathrm{el-phon}}^{\mathrm{nonlocal}} = \sum_{\mathbf{q}l} \sum_{i \neq j} \hbar \omega_{\mathbf{q}l} g_{ij,\mathbf{q}l} \left( b_{\mathbf{q}l}^{\dagger} + b_{-\mathbf{q}l} \right) a_i^{\dagger} a_j \tag{11e}$$

The electronic part of the Hamiltonian at Eq. (11b) allows the coupling between any two states, i.e., the system is not necessarily one dimensional or with one state per site. $b_{\mathbf{q}l}^{\dagger}$ and $b_{\mathbf{q}l}$ in Eq. (11c) are the creation and annihilation operators for a phonon (not necessarily dispersionless) with wavevector $\mathbf{q}$ in mode $l$. Apart from these straightforward extensions, the main additional term of this Hamiltonian is the nonlocal Peierls coupling (11e), which corresponds to the modulation of the hopping integral induced by the phonons. This latter component has been neglected for a long time in organic semiconductors but recent computations have shown that it plays an especially important role for the transport mechanism. Hannewald et al. [83] derived an expression (analogous to Eqs. 6–9) that allows the computation of renormalized polaronic bands also in the presence of nonlocal coupling. This and alternative ways of describing the charge dynamics in organic crystals will be presented in Sect. 6 after discussing the precious information provided by various computational studies for the solution of this problem.

## 3 The Contribution of Computational Chemistry

In parallel with the development of theoretical models of transport, the community of computational chemists have developed and validated the methodologies to evaluate all the parameters of the Hamiltonian of Eq. (11). This work is not just necessary to link the theory with the experimental observation but it can be useful to suggest the best strategies to study the charge dynamics from a general Hamiltonian. As we have seen in the previous section, in fact, the transport mechanism is essentially determined by the most suitable hierarchy of approximations and it is certainly convenient to be aware of the magnitude of all matrix elements of Eq. (11) before attempting any approximated treatment.

The group of Brédas and coworkers [84, 85] has pioneered the computation of the parameters of the Hamiltonian adapting the techniques used in other spectroscopic and physico-chemical problems (high resolution electronic spectra, non linear optics, liquid phase electron transfer reactions). The availability of alternative experiments to test the quality of the computed matrix elements makes them particularly useful since their accuracy had undergone independent validation. Even in the absence of an established transport mechanism it is possible with these computations to attempt a semiquantitative correlation between the magnitude of the matrix elements and the measured mobility. Regardless of the adopted model, the carrier mobility increases with the increase of the hopping integral and decreases with the increase of the local electron phonon coupling. It will be briefly reviewed

how these two quantities can be computed, what is the achievable accuracy and the eventual trend emerging from the comparison of computational results across families of compounds.

### *3.1 Hopping Integral and Band Structure*

For a molecular crystal the hopping integral can be defined as

$$\tau_{ij} = \left\langle \varphi_i \left| H_{\text{el}} \right| \varphi_j \right\rangle \tag{12}$$

where $\varphi_i$ and $\varphi_j$ correspond to the molecular orbitals computed for the isolated molecule and $H_{\text{el}}$ is the effective one electron Hamiltonian of the crystal. Usually, only the hopping integral between molecular orbitals belonging to molecules in contact is taken into account and, in this case, the effective Hamiltonian can be approximated to the Hamiltonian of the two molecules that are considered (this approximation is justified if the molecules in the crystal are non polar and long range electrostatic interactions can be neglected). The effective one electron Hamiltonian can be identified with the Fock operator (defined in Hartree–Fock theory) or the Kohn–Sham–Fock operator (defined in Kohn–Sham DFT) [86, 87].

The integral in Eq. (12) can be computed explicitly using the integrals in the atomic basis set provided by any quantum chemistry software [88]. It is also very common to evaluate $\tau_{ij}$ from the energy splitting of a dimer computation [89]. For example, the energy difference between the HOMO-1 and HOMO levels of a dimer is twice the absolute value of the hopping integral between the molecular pair, if the overlap integral between the localized basis can be neglected. For many situations (e.g., the computation of the band structure) it is also important to know the sign of the hopping integral which can be deduced from the phases of the HOMO orbitals of the dimer computation. The dimer method works as long as the splitting energy is smaller than the energy difference between orbitals in the isolated molecules, a case which appears to be relatively frequent but needs to be checked for every system. Valeev et al. [90] discuss how to take into account properly the effect of the overlap between localized MOs and pointed out another possible source of error. The dimer method gives incorrect results if the two molecules in the dimer (which might be equivalent by symmetry in the crystal) are not equivalent by symmetry in the isolated dimer, an effect that needs to be taken into account when the results from the dimer computations are transferred to the crystal. An alternative way to correct this error is based on an embedding technique and was proposed by Lipparini and Mennucci [91].

The most accurate computations of the intermolecular coupling are carried out at the DFT level of theory (usually involving hybrid functionals such as B3LYP) with the molecular orbital expanded in a medium to large atomic basis set. Less accurate but very fast computations are done using the semiempirical ZINDO Hamiltonian which has been optimized for electronic spectroscopy and has been validated against DFT a number of times [92]. More elementary extended Hückel computations were

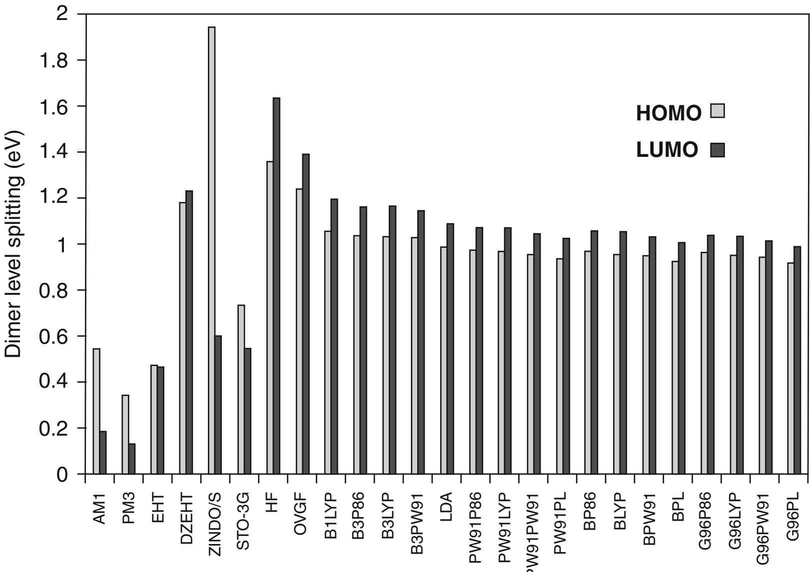


**Fig. 4** Energy splitting of the HOMO and LUMO levels of ethylene from dimer computation compared by Huang and Ketsetz at different levels of theory (from [93])

more popular a few years ago [93, 94] while DFT based tight binding approaches are growing in importance among the most approximate methods [95, 96]. The dependence of the intermolecular coupling on the basis set was studied by Huang and Ketsetz [97] which found the 6–31G* basis set [87] a good compromise for routine computation. The basis set convergence was tested against plane wave computations [98] which allow a more systematic increase in basis set accuracy but are less commonly used and therefore less tested for the prediction of molecular properties. A systematic comparison between various computational methods (from semiempirical to several flavors of DFT) for the evaluation of $\tau_{ij}$ are also presented by the same authors (see Fig. 4) [99]. These methodological works are very useful to assess the degree of confidence that one can put into the computed hopping integrals. Different methods reproduce well the relative magnitudes of the hopping integrals between related materials while the difference in absolute values rarely exceed 10% among a large family of DFT methods.

The hopping matrix elements between frontier orbitals are very similar across different organic solids and they are invariably in the 50–1,200 $\mathrm{cm}^{-1}$ range. It appears to be no simple rationalization of the hopping integral across families of similar compounds for reasons that will be detailed in the next section. As a consequence of this – maybe disappointing – result, the synthesis of compounds with large hopping integral is still a matter of trial and error. An attempt to rationalize the hopping integral results was made by Hutchison et al. [100] who employed a multivariate analysis to describe orientation dependent hopping integrals for a series of oligoheterocycles.

Information equivalent to that contained in the hopping integrals is provided by band structure calculations of organic solids, many of which appeared in the past few years [59, 62, 101–105] for the most promising organic semiconductors. The band structures of molecular organic compounds are less information-rich than those of inorganic materials because the bands tend to be very narrow and bear a one to one correspondence with the molecular orbital of the isolated molecule. For this reason, while the band computations are useful to extract the effective masses, the essence of the electronic structure of an organic solid is usually better described by a very short list of symmetry independent hopping integrals [65]. With the recent experimental evaluations of anisotropic mobility [106–108] it will be possible to evaluate under what circumstances Eqs. (3) and (4) offer a reasonable estimate of the mobility tensor. The observation made above on the band structure of molecular organic semiconductor is not valid for polymeric crystalline semiconductors, which have been the first to be investigated by first principle methods [109–112], and are characterized by a much larger band dispersion.

## *3.2 Local Electron–Phonon Coupling*

Neglecting the effect of the surrounding dielectric environment, the total reorganization energy $\Lambda$ and its component along the molecular normal modes can be obtained from a simple series of computations on isolated molecules. Coropceanu et al. provided a valuable example of these computations having evaluated the local electron phonon coupling on a series of oligoacene molecules and compared the results with experimental gas phase ultraviolet photoelectron spectroscopy (UPS) [113, 114]. The total internal reorganization energy (for the hole) can be expressed as

$$\Lambda = E^{+}\left(\mathrm{M}^{+}\right) - E^{+}\left(\mathrm{M}\right) + E\left(\mathrm{M}\right) - E\left(\mathrm{M}^{+}\right) \tag{13}$$

where $E$ or $E^{+}$ indicate the total energy of the neutral molecule or the cation and the symbol in the parenthesis indicates if the computation is done in the optimized geometry of the neutral (M) or cation $\left(\mathrm{M}^{+}\right)$ molecule. The reorganization energy can be then partitioned into the normal modes of the molecule $\{Q_l\}$ as

$$\Lambda = \sum_l \Lambda_l = \sum_l \tfrac{1}{2}\hbar\omega_l \Delta Q_l^2 \tag{14}$$

The matrix element of Eq. (11d) can be evaluated from $\Lambda_l = \hbar\omega_l g^2_{jj,\mathbf{q}l}$, if the orbital $j$ is identified with the HOMO of the isolated molecule, and the optical phonons are assumed to be dispersionless (this is a good approximation because the most important modes have relatively high frequency and their crystal environment is known to influence them negligibly [115]). The procedure of [114] yields excellent agreement with the high resolution UPS spectra which can be interpreted as the overlap of different Frank–Condon progressions whose shape and relative intensity is determined by the $\Lambda_l$. This robust validation allows one to treat with confidence the computed local electron phonon couplings.

The correlation between reorganization energy and high mobility can be verified with a series of very similar compounds for which the other electronic factors can be considered approximately equivalent [116]. Mas-Torrent et al. [117] presented a nice series of tetrathiafulvalene derivatives whose field effect mobility correlates very well with the computed reorganization energy.

In contrast to the hopping integral, the reorganization energy follows a somewhat predictable trend among classes of similar compounds. Considering a heterogeneous set of molecules, $\Lambda$ is approximately proportional to the inverse of the size of the molecule [118]. The inverse proportionality is followed more strictly for series of analogous compounds [113] while there is more variation among heterogenous compounds. Considering the hole transport, pentacene displays a particularly low reorganization energy for holes $(0.09\,\text{eV})$ [119], slightly higher values are reported for rubrene $(0.11\,\text{eV})$ [64] and hexabenzocoronene $(0.11\,\text{eV})$ [120], and much larger for hexathiophene $(0.32\,\text{eV})$ [121]. Chen and Chao studied systematically how the reorganization energy is influenced by chemical substitution finding that polar substituents increase the reorganization energy in polyacenes [122, 123]. Another systematic study of this type but based on a series of heterocyclic oligomers was presented by Hutchison et al. [124]. The window of computed values for large conjugated compounds is relatively narrow and, although the high mobility of pentacene is certainly due in part to its lower reorganization energy, the factors limiting the mobility go well beyond this simple parameter.

An additional component to the local electron phonon coupling is given by the so-called *external reorganization energy* which is related to the energy gained by the crystal because of the nuclear rearrangement of the molecules around a carrier. This component is intuitively very small because only small displacements are allowed in a crystal and it is the same process that is usually advocated for the formation of the Frölich polaron. However, this small term can be important, especially whenever the internal reorganization energies are very small. The initial estimates [125] have not been updated for the new materials and the only recent calculation to our knowledge is from Brochencko [126] who found the value of the lattice relaxation to be 15 meV. Newer evaluations of this quantity, more in line with the current computational capabilities, would be greatly beneficial to the field. Initial attempts are being made using QM/MM methods [127, 128] and semiempirical computations with large clusters of organic molecules [129].

### 3.3 Computational Data and Conventional Theories

The original aim of the computational studies described above was to link some of the formal theories of Sect. 2 to the available experiments. This result is evidently not achieved since it is still not possible to predict the mobility for a given material or to rank the mobility measured for series of analogous compounds. The reason does not lie with the computational inaccuracies (because of the extensive validation described in the past section) but with the lack of a robust theoretical description of

the transport mechanism. Through these computations, however, it was possible to identify specific limitations of the classical theoretical models and to stimulate again the work on the development of new theoretical models.

Before a proper evaluation of the matrix elements was available and before the new experimental results on ultrapure pentacene and rubrene were realized, Kenkre et al. [130] were able to fit the classical results of Karl [131] on the temperature dependence of the anisotropic mobility of pentacene with a three dimensional Holstein model. It now seems clear that the fitted parameters are not compatible with the computations (the hopping integral is about two orders of magnitude smaller than the typical value) and that the Holstein Hamiltonian is insufficient to capture the physics of organic semiconductors.

Another, possibly disappointing, consequence of the computational results is that the rate equation at Eq. (10) cannot be applied even if the transport takes place through individual hopping steps between neighboring molecules (with or without taking the high temperature limit). That model, in fact, requires that the hopping integral is small compared to the reorganization energy, a situation that seems to be extremely rare in organic semiconductors and certainly not applicable for the most conductive solids, which have very small reorganization energy (see also Fig. 5).

Computational models seemed to point to a more delocalized model of transport for the most conductive solids because of a small reorganization energy in comparison with the hopping integrals, but the delocalized mechanisms described in Sects. 2.1 and 2.2 are not tenable beyond 150 K because they imply a scattering length comparable with the intermolecular distances. The next two sections present several additional computational evidences that pointed toward a possible solution of the problem.

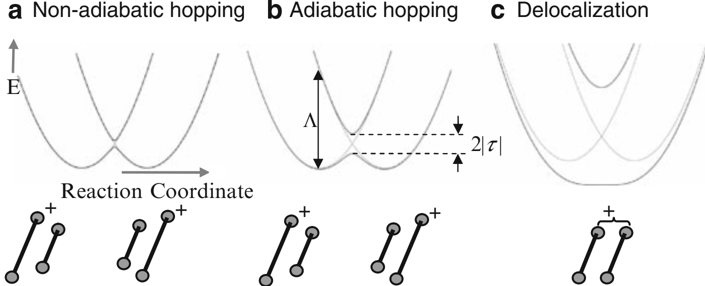


**Fig. 5** Potential energy surfaces for the hopping of a charge between two adjacent sites idealized as a diatomic molecule. The two parabolas in all panels represent the diabatic potential energy curves for the states where the charge is localized on each of the two sites deformed along the reaction coordinate. The thicker lines are the adiabatic (Born–Oppenhaimer) potential energy curves. The reorganization energy $\Lambda$ and hopping integrals $\tau$ are indicated in the central panel. Going from left to right the hopping integral $\tau$ is 0.03, 0.1, and 0.5 times the reorganization energy. Only for small $\tau/\Lambda$ can one use the nonadiabatic rate (Eq. 10), while, for large $\tau/\Lambda$ there are no localized states and the hopping rate is not defined. The computational results indicate that case (a) is rarely applicable to organic semiconductors

## 4 The Extreme Sensitivity of the Hopping Integral to the Intermolecular Geometry

HOMOs and LUMOs in organic semiconductors of common use have complex shapes with several nodal planes, and, consequently, the transfer integral between neighboring molecular orbitals is extremely sensitive to very small nuclear displacements. This sensitivity has been observed many times both theoretically and experimentally. An impressive experimental manifestation of this fact is the crystallochromy of perylene derivatives which was rationalized by Kazmaier and Hoffman in terms of the different intermolecular coupling between the perylene fragments using an extended Hückel computational approach [93]. A systematic study of Brédas and coworkers [132] quantified the importance of this effect for a series of tetracene derivatives.

This aspect is very well illustrated by several studies in the related study field of charge *transfer* in donor–bridge–acceptor systems. If the "bridge" is made by *covalently bonded atoms* (as in silicon) the coupling between donor and acceptor can be considered constant [133]. When the transfer takes place through *non-bonded molecules* (as in organic crystal), thermal motions cause a fluctuation of the donor–acceptor coupling that affects the charge transfer rate [134]. Examples of non-covalently bonded bridges that produce a strong fluctuation of the intermolecular coupling include, among others, the DNA base pairs [135], some proteins [136], or the solvent [137] in specially designed systems.

One important consequence of the subtle dependence of the intermolecular coupling on the relative position of the molecules is the very different band structure displayed by polymorphs of the same crystal. Polymorphism is a relatively common characteristic of organic solids and it has been studied intensively for the most important molecular semiconductors using pressure and temperature dependent Raman spectroscopy [115, 138, 139], together with the more straightforward crystallographic methods. Polymorphism is particularly frequent in thin films grown by vapor deposition, where the characteristics of the substrate and the growth conditions can be used to control the resulting polymorph [140–142]. Mattheus et al. found the conditions to grow reproducibly thin films of four crystal forms of pentacene and proposed a rationalization based on an empirical force field [140, 143]. These four pentacene polymorphs have very similar structures and belong to the same space group $\left(P\bar{1}\right)$. They have been labeled in [140] as I, II, III, and IV, corresponding to a distance between the crystal *ab* plane of 14.1, 14.4, 15.0, and 15.4 Å. The pentacene molecules with the largest intermolecular coupling are arranged in the *ab* plane (in a herringbone fashion) with their long axis roughly perpendicular to this plane. Going from polymorph I to polymorph IV the long axis of the pentacene approaches the perpendicular to the *ab* plane, the distance between these planes increases, and the neighboring molecules in one plane slide one with respect to the other. Similar results are reported by Datta and coworkers [144].

It is particularly important to establish how different are the hopping integrals (or, equivalently, the band structure) in these polymorphs of pentacene considering the

large number of papers which have measured the mobility in pentacene thin films without reporting the detail of the crystal structure. On one hand the experimental variability in reported mobility could be linked to the variability in electronic structure among polymorphs. On the other hand, one could identify a particular polymorph with better charge transport characteristics or even optimize the substrate to create high mobility thin film layers [145] as already done in the latest generation of silicon devices [146–148]. A band structure calculation of the four pentacene polymorphs was presented in [65], where a molecular orbital basis set and the B3LYP density functional have been used. Figure 6 shows the projection of the highest occupied band along the reciprocal space unit vectors $a^*$, $b^*$, and $c^*$ for the four polymorphs. It is immediately clear that the electronic structure is very different for the four considered cases, the bandwidth for polymorph IV being more than four times larger than for polymorphs I and II (for the highest occupied bands).

Even though we explained, in Sect. 2.1, why the simple band structure cannot be immediately related to transport characteristics in organic semiconductors, it is important to analyze the microscopic origin of the difference between the electronic structures of the polymorphs. The main advantage of using a molecular orbital basis set in the computation of the band structure is that the result can be discussed in

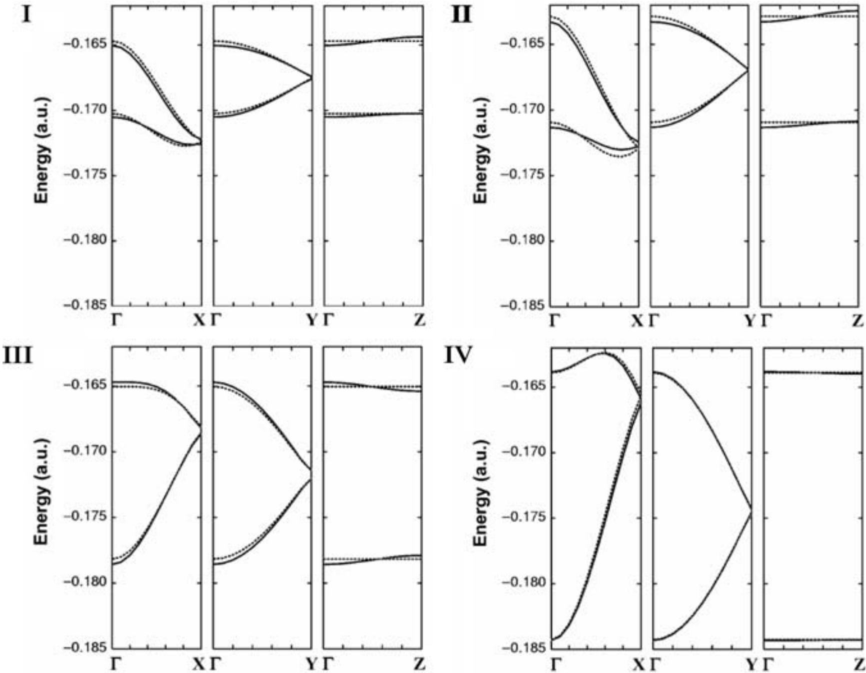


**Fig. 6** The two highest occupied bands resulting from the four pentacene polymorphs (there are two pentacene molecules in the unit cell). *Dashed lines* are computed including only the HOMO–HOMO interaction between nearest neighbors in the *ab* plane. Only four hopping integrals account for the electronic structure of the solid at $T = 0$ K. From [61]

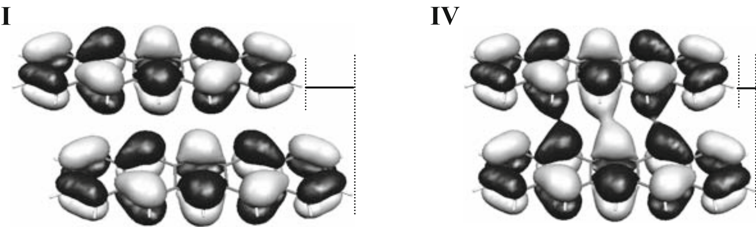


**Fig. 7** Representation of the two HOMO orbitals on two neighboring pentacene molecules along the a-axis in polymorph I and IV. The small sliding along the main axis of less than 0.9 Å is sufficient to change completely the overlap pattern between the two localized orbitals

terms of the individual hopping integrals. In this solid the two highest occupied bands are almost exclusively described by a linear combination of the HOMOs of the two molecules in the unit cell. Figure 7 shows the overlap between the HOMOs orbitals in polymorph I and IV for two pentacene molecules adjacent along the *a* crystallographic axis. The interaction is strongly antibonding in polymorph I (resulting in a coupling of 411 $\mathrm{cm}^{-1}$) and strongly bonding in polymorph IV (where the coupling is –715 $\mathrm{cm}^{-1}$). This major difference results from a displacement of one molecule with respect to the other of only 0.9 Å.

The observations described in this section are particularly relevant for the definition of the transport mechanism because they all hint to a major role of the non-local electron phonon coupling. If the intermolecular coupling is so sensitive to the relative position of the molecules, there must be vibrations that modulate very effectively the intermolecular coupling and these are described by the $V_{\mathrm{el-phon}}^{\mathrm{nonlocal}}$ term of the Hamiltonian in Eq. (11). The main effect of these vibrations is described in the next section.

# 5 The Effect of Thermal Motions on the Electronic Eigenfunction

## *5.1 Molecular Dynamics/Quantum Chemical Studies*

At temperatures higher than 150 K the charge transport in organic semiconductors cannot be explained by conventional transport mechanisms. The observations of Sect. 4 and the analogy with other weakly bound systems [135] indicate that it is possible that thermal motions of the bulk crystal have sufficiently large amplitude to modulate considerably the intermolecular coupling. The existence of (relatively) large amplitude motions inside organic crystals due to the weak intermolecular interactions can be verified from crystallographic measures [149–152] and unusually large motions have also been identified in pentacene [153]. One natural way

to address this effect computationally is to run a classical molecular dynamics (MD) simulation of the solid using quantum chemical (QC) methods to evaluate the hopping integrals at different snapshots of the trajectory [135, 154].

Deng and Goddard [155] provided the first MD/QC study of an organic solid (pentacene) but they used the MD snapshots only to obtain a better average of the hopping integral $\tau$ and assumed the validity of Marcus theory. Another computation focusing more on the effects of the hopping integral fluctuation of the charge transport mechanism was presented in [156] where the dynamics of a $3\times2\times2$ supercell of pentacene was studied with periodic boundary conditions employing the MM3 force field. The hopping integral at Eq. (12) between HOMO orbitals of 18 pairs of neighboring molecules was computed for snapshots taken every 30 fs in a trajectory of 100 ps (the INDO/S Hamiltonian [84] was used for this task). The large fluctuation of the hopping integrals vs time and the distribution function of the hopping integral at various temperatures are shown in Fig. 8. While the average coupling among different pairs varies between 440 and $1,100\,\text{cm}^{-1}$ the standard deviation of this coupling due to the thermal fluctuation at 300 K is between 37% and 56% of the average coupling value (Kwiatkowski et al. extended this concept to compute the coupling fluctuation due to zero-point motions [157]). This effect can hardly be considered a minor correction and it has a major influence on the way we should describe the charge dynamics in crystalline organic solids.

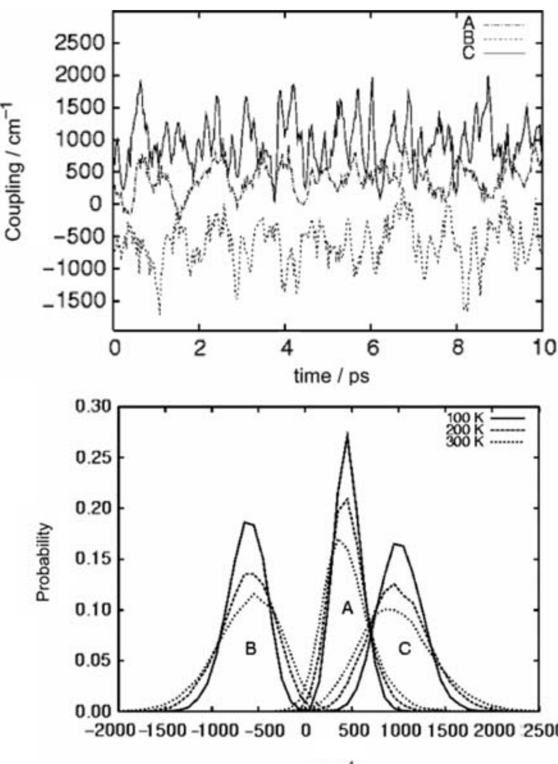


**Fig. 8** (*Top*) Time dependency of the HOMO–HOMO hopping integral among three inequivalent pairs of pentacene molecules (denoted as A, B and C) computed using a MD/QC approach. (*Bottom*) The probability density distribution of the coupling indicates clearly that the standard deviation of the hopping integral is of the same order of magnitude of its absolute value. From [151]

### 5.2 Dynamic Localization Effects

An uncorrelated modulation of the hopping integral is equivalent to the presence of *disorder* in the electronic structure and its main effect is the *localization* of the hole wavefunction [158–160]. The localization of the eigenfunctions (in the frozen conformation at a given time) of a system characterized by a given fluctuation of the hopping integral can be evaluated numerically by computing the eigenfunctions of a large supercell. The hopping integrals can be assigned to the adjacent molecular pairs according to the computed distributions (it was found computationally that the disorder in the hopping integral can be considered uncorrelated). Figure 9 shows how at 300 K the eigenfunctions of the electronic Hamiltonian are localized within few unit cells. The localization decreases as the temperature decreases because smaller disorder is associated to a smaller degree of localization.

A convenient way to evaluate the time scale of the hopping integral fluctuation is by computing the Fourier transform of the autocorrelation function $\langle \delta\tau(0)\,\delta\tau(t)\rangle$ [134] (the deviation from the average transfer integral is defined as $\delta\tau(t) = \tau(t) - \langle \tau(t)\rangle$ ). This computation for several solids shows that the majority of the phonon modes that modulate the coupling have energy around $40\,\mathrm{cm}^{-1}$ and that the contribution of modes above $160\,\mathrm{cm}^{-1}$ is negligible. Since only low frequency modes play a role in the modulation of the transfer integral, the semiclassical description adopted here can be considered valid at room temperature and at least plausible above 150 K (vibrations can be treated classically if their frequency $\omega$ is such that $\hbar\omega \ll k_{\mathrm{B}}T$). The other important point is that the dynamic disorder of organic crystals has a very long correlation time: $\tau(0)$ and $\tau(t)$ are correlated for times longer than the MD simulation length (in such cases the correlation time is not precisely determinable). The long correlation distinguishes these systems from liquid metals or liquid crystals [161, 162].

The function $\delta\tau(t)$ bears the same information of the non-local electron phonon coupling. The time dependent representation offers the advantage of a more compact look to the effect of this coupling and can be used to build simpler models

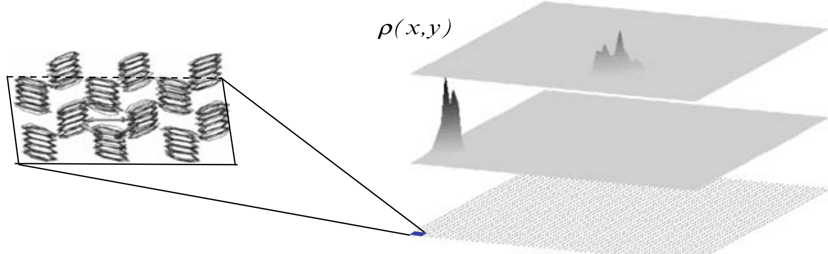


**Fig. 9** Localization of 2D wavefunctions due to the fluctuation of the hopping integral illustrated by a numerical example [61]. The electronic Hamiltonian of a supercell containing 3,200 molecules was built using the known disorder in the hopping integral at 300 K. The localized density distribution $\rho(x,y) = |\psi(x,y)|^2$ is shown for two eigenfunctions of such a disordered Hamiltonian

that capture the physics of this many-body problem. There are, in fact, $3N$ phonon modes for a unit cell with $N$ atoms, meaning that, for pentacene, a very long table of 216 matrix elements per adjacent pair should be compiled if we want to retain the representation of the Hamiltonian in Eq. (11). The detailed table of non-local electron phonon coupling (built with some simplifications, e.g., in [83] and [139]) does not convey immediately the notion that the fluctuation of the off-diagonal hopping integrals is of the same magnitude of the average hopping integral. This latter observation is crucial for the development of a transport model which is fully consistent with the experiment.

### *5.3 Rationalization*

The fluctuation of the hopping integral is not a unique characteristic of pentacene. The solids for which similar results have been reported also include rubrene [163], hexathiophene [164], and a series of 5–14 pentacene silylethynyl derivatives synthesized by J. Anthony [165, 166]. This latter class of compounds gives the best possible demonstration of the universality of the phenomenon. Although a number of these pentacene derivatives have been reported, all of them form crystal structures that fall into three general classes denoted by the authors as *slipped-stack*, 1*D columnar stack* and 2*D segregated-stacking* (illustrated in Fig. 10$a_1$, $a_2$ and $a_3$ respectively) [167]. For all these derivatives, unlike pristine pentacene, the adjacent pentacene fragments are all parallel to one another. The hopping integral and its fluctuations were computed for unequivalent pairs of molecules using a method similar to that adopted for pentacene.

Because of the particularly simple (coplanar) intermolecular arrangement it was possible in this case to rationalize the values of the average hopping and to illustrate more visually the effect of thermal motions on the modulation of the coupling. A map of the HOMO–HOMO coupling between two coplanar pentacene molecules as a function of their relative displacement was built (see Fig. 10b). As in the experimental crystal structure, the axes of the molecules are parallel one to another. The position in the map of five distinct couples of cofacial pentacene fragments found in three considered materials is indicated by the points labeled **a–e.** The map can be used to rank the coupling from the strongest to the weakest but it also shows very clearly that all five pentacene pairs are in a mutual position that corresponds to a point close to the nodal plane of the hopping integral map. The reason for this positioning is easily understandable in terms of rigid sphere packing: if we model the pentacene as a collection of 22 rigid spheres centered on the carbon atoms, the best coplanar packing requires an offset of the atom layers (the face to face packing of two pentacene molecules can be considered akin to that of two adjacent planes of graphite). The map illustrates that the energetically most favorable packing brings the molecules to a more unfavorable position for the hopping integral. From another perspective, since the relative position of the molecules is such that they are far from the maxima and minima of the hopping integral, they are

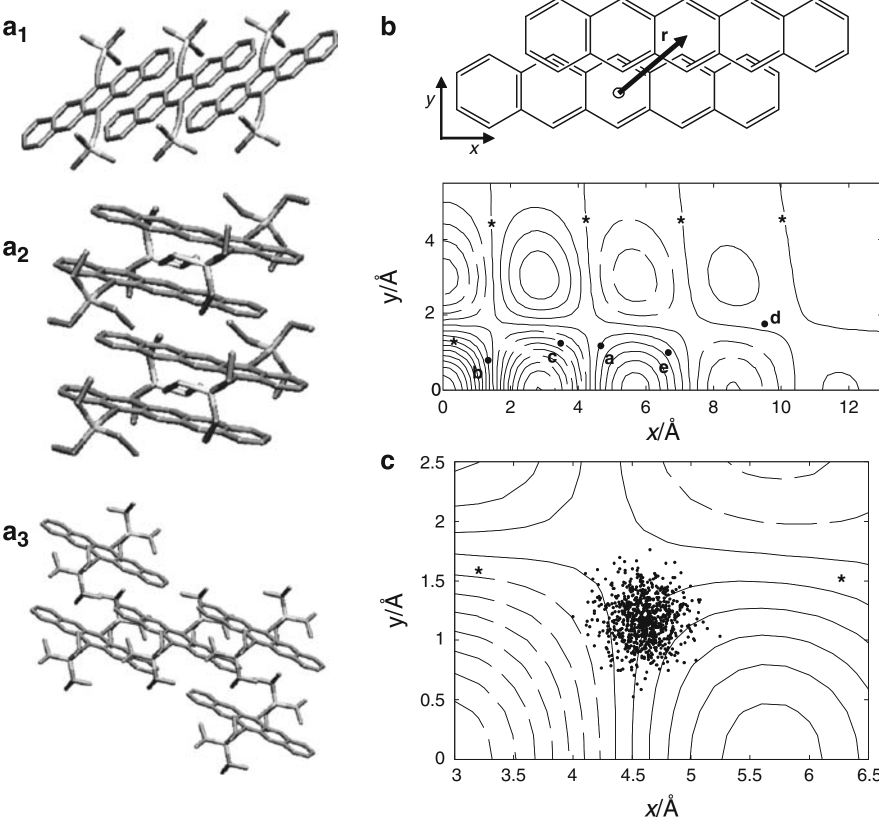


**Fig. 10** **a** Different packing motifs adopted by a class of pentacene derivatives (see text). **b** Map of the hopping integral between coaxial pentacene molecules sliding one with respect to the other in two parallel planes distant 3 Å. *Contour lines* are plotted at interval of 700 $cm^{-1}$ (*dashed lines* are negative contour lines, the contour lines with null coupling are indicated by *asterisk*). The labeled points *a–e* indicate the actual position of the pentacene pairs as found in the material. **c** The *black dots* in a smaller region of the same map represent the relative position of the pentacene pairs *a* sampled during a short MD simulation at 300 K

positioned in such a way that small geometric distortions cause the largest change in the hopping integral. This fact is illustrated by Fig. 10c which shows the relative position of the pentacene centers of mass in 400 snapshots of the simulation (for one of the solids at 300 K). Obviously, while the map was built using rigid molecules that kept their relative orientation, the thermal motions also cause slight deformation of the molecules and changes in their relative orientation. This analysis shows more graphically how the limited conformational space explored at room temperature is large enough to produce a considerable variation in the intermolecular coupling.

# 6 Models for the Charge Transport in the Presence of Strong Nonlocal Electron Phonon Coupling

The computational results in Sect. 5 clearly indicate that the standard transport mechanisms outlined in Sect. 2 are missing an important ingredient when applied to organic solids: the thermal fluctuation of the hopping integral (or, equivalently, the strong nonlocal electron phonon coupling). This term cannot be treated with one of the standard approximation techniques. The small polaron transformation and band renormalization are useful as long as the delocalized nature of the carrier is preserved, but this is not the case here because localization is produced by thermal disorder. The average intermolecular coupling is too strong compared to the local and nonlocal coupling to use simple hopping theories. However, it is possible to study the dynamics of a charge carrier in a system with dynamic disorder using a simplified model system and a "brute force" evaluation of the charge carrier dynamics.

## *6.1 Elementary Semiclassical Model: Diffusion Limited by Thermal Off-Diagonal Disorder*

The minimalist model which mimics the essential features derived by the computational studies on realistic systems is made by a one dimensional stack of planar conjugated molecules (Fig. 11), with one molecular orbital per molecule (for example the HOMO in case of hole transport). Each molecule $j$, associated with the orbital $|j\rangle$, has mass $m$ and can be displaced transversally by a length $u_j$ from its equilibrium position around which it oscillates with frequency $\omega$. The transfer integral $\tau$ between the consecutive orbitals $|j\rangle$ and $|j+1\rangle$ is modulated linearly by the term $a\alpha\left(u_{j+1}-u_j\right)$ with $\alpha$ the electron–phonon coupling constant. The semiclassical Hamiltonian for this system reads

$$H=\sum_j\left(-\tau+\alpha\left(u_{j+1}-u_j\right)\right)\left(|j\rangle\langle j+1|+|j+1\rangle\langle j|\right)+\sum_j\tfrac{1}{2}m\dot{u}_j^2+\sum_j\tfrac{1}{2}m\omega^2u_j^2 \tag{15}$$

It can be seen as the combination of a quantum Hamiltonian for the electron, whose off-diagonal elements are modulated by the nuclear positions $\left\{u_j\right\}$:

$$H^{\mathrm{el}}=\sum_j\left(-\tau+\alpha\left(u_{j+1}-u_j\right)\right)\left(|j\rangle\langle j+1|+|j+1\rangle\langle j|\right) \tag{16}$$

and a classical Hamiltonian for the nuclei, whose potential energy is determined by the electronic wavefunction $\psi(t)$:

$$H^{\mathrm{nucl}}=\sum_j\tfrac{1}{2}m\dot{u}_j^2+\sum_j\tfrac{1}{2}m\omega^2u_j^2+\left\langle\psi(t)\middle|H^{el}\middle|\psi(t)\right\rangle \tag{17}$$

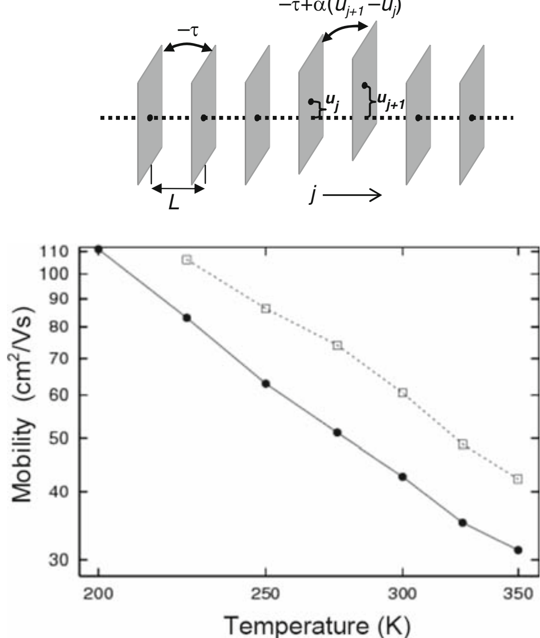


**Fig. 11** (*Top panel*) Illustration of the minimalist model of Eq. (15) (see text). (*Lower panel*) Temperature dependent mobility computed numerically for the model in Eq. (22) with (*full circles*) and without (*squares*) the effect of local electron–phonon coupling. The parameters of this model were chosen to mimic those computed for rubrene [143], i.e., $\tau = 1{,}150\,\mathrm{cm}^{-1}$, $\lambda^{(1)} = 21{,}200\,\mathrm{cm}^{-1}\,\text{Å}^{-1}$, $\omega^{(1)} = 1{,}400\,\mathrm{cm}^{-1}$, $m^{(1)} = 6\,\mathrm{amu}$, $\alpha^{(2)} = 3{,}980\,\mathrm{cm}^{-1}\,\text{Å}^{-1}$, $\omega^{(2)} = 50\,\mathrm{cm}^{-1}$, $m^{(2)} = 532\,\mathrm{amu}$

All the parameters of this Hamiltonian can be taken from the computations of the type presented in Sect. 5.1 with the average hopping integral $\tau$ and its standard deviation $\sigma_\tau$ being related to $\alpha$ as $\sigma_\tau = \alpha\sqrt{2k_\mathrm{B}T/m\omega^2}$. An important parameter is the frequency of the oscillations $\omega$ which must be set to a value deduced from the Fourier transform of $\langle\delta\tau(0)\,\delta\tau(t)\rangle$ (40–50 cm$^{-1}$ seems to be appropriate for most solids).

The numerical integration of Eq. (15) can be performed for example as indicated in [168]. Given the set of positions $u_j$, velocities $\dot{u}_j$ and wavefunction $\psi(t)$ at a time $t$, and an integration timestep $\Delta t$:

(1) The classical accelerations are computed as

$$m\ddot{u}_j(t) = -m\omega^2 u_j(t) - \frac{\partial}{\partial u_j}\left\langle \psi(t)\left| H^\mathrm{el} \right| \psi(t)\right\rangle \tag{18}$$

(2) The wavefunction is updated as ($\hbar = 1$)

$$\psi(t+\Delta t) = \psi(t) - iH^\mathrm{el}\psi(t)\Delta t - \tfrac{1}{2}i\left(H^\mathrm{el}(t)\,\dot{\psi}(t) + \dot{H}^\mathrm{el}(t)\,\psi(t)\right)\Delta t^2 \tag{19}$$

(3) The positions are updated with the Verlet algorithm as

$$u_j(t+\Delta t) = 2u_j(t) - u_j(t-\Delta t) + \ddot{u}_j(t)\Delta t^2 \tag{20}$$

Equation (19) is obtained expanding $\psi(t+\Delta t) = \psi(t) + \dot{\psi}(t)\Delta t + \frac{1}{2}\ddot{\psi}(t)\Delta t^2$ and using the Schrödinger equation $\dot{\psi}(t) = -iH^{\mathrm{el}}(t)\psi(t)$ and its time derivative $\ddot{\psi}(t) = -i\left(H^{\mathrm{el}}(t)\dot{\psi}(t) + \dot{H}^{\mathrm{el}}(t)\psi(t)\right)$. The time derivative of the electronic Hamiltonian is $\dot{H}^{\mathrm{el}} = \sum_j \left(\alpha\left(\dot{u}_{j+1} - \dot{u}_j\right)\right)\left(|j\rangle\langle j+1| + |j+1\rangle\langle j|\right)$. The charge carrier diffusion is monitored quantitatively from

$$R_n^2(t) \equiv \left\langle \psi_n(t)\left|r^2\right|\psi_n(t)\right\rangle - \left\langle \psi_n(t)\left|r\right|\psi_n(t)\right\rangle^2 \tag{21}$$

which measures the time dependent spread of the wavefunction. $R_n^2(t)$ is Boltzmann averaged for different initial wavefunctions $\psi_n(t=0)$ (and energy $E_n$) to give $\left\langle R^2(t)\right\rangle$. The diffusion constant is evaluated from $D = \lim_{t\to\infty}\left\langle R^2(t)\right\rangle/2t$ and the mobility from the Einstein relation $\mu = eD/k_{\mathrm{B}}T$.

The procedure leads to a real space representation of the charge dynamics as opposed to the reciprocal space representation needed to study band transport in inorganic semiconductors. Maybe surprisingly, the procedure provides absolute values of mobility (which are in good agreements with the experiments) because the model in Eq. (15) contains all the elements that determine the charge mobility in the material, i.e., it assumes that the carrier mobility is limited by the off-diagonal disorder in the electronic Hamiltonian. As shown in Fig. 11, the mobility computed with this method decreases with temperature in a way that could be described as a power law ($\mu \propto T^{-\alpha}$). Although, this behavior has often been interpreted as a clear signature of band transport, this model shows that it is also entirely consistent with a localized transport where the carriers are localized by thermal disorder. Band transport is inapplicable at temperatures greater than 100 K because the translational symmetry of the electronic Hamiltonian is completely destroyed and the wavevector $k$ ceases to be a good quantum number of the system.

As the temperature decreases the carrier becomes more delocalized and, in the opposite limit of $\mathrm{T} \to 0\,\mathrm{K}$, the best description of the transport becomes the delocalized band transport. Since for both the $\mathrm{T} \to 0\,\mathrm{K}$ limit and the $100\,\mathrm{K} < \mathrm{T} < 350\,\mathrm{K}$ range the mobility decreases with temperature, the simple model of Eq. (15) (analyzed with a semiclassical method at high temperature) is able to explain why the transport appears to be "band-like" when the apparent mean free path is also of the order of the intermolecular distance. It is somewhat intuitive that this transport mechanism named *diffusion limited by thermal disorder* (DLTS) can be thought of as if the charge carrier is scattered at each molecule and the interval between two scattering events is given by the oscillation period of the modes that modulate the hopping integrals. It is currently not possible to cover in a consistent way the temperature range between 0 K and 350 K because the classical treatment of the nuclear modes cannot be extended toward low temperatures. Moreover, as the charge carriers become more delocalized at low temperature, the size of the system to be considered for the numerical integration of Eq. (15) needs to be extended and the simulation time increases. It is not surprising that, in the low temperature limit, the real space representation of the wavefunction becomes less convenient than the reciprocal space representation.

### 6.2 Generalized Semiclassical Model

The model of Eq. (15) is meant to capture the essential differences between the transport in molecular semiconductors and the conventional band transport mechanism. However, it neglects completely the effect of local electron phonon coupling (Eqs. 1e and 11d) and it is convenient to consider a model where this approximation is not made in order to achieve a more robust comparison with the experiment. A generalized version of the model Hamiltonian is

$$
\begin{aligned}
H = & \sum_j \left( \varepsilon + \sum_k \lambda^{(k)} u_j^{(k)} \right) |j\rangle \langle j| + \sum_j \left( -\tau + \sum_k \alpha^{(k)} \left( u_{j+1}^{(k)} - u_j^{(k)} \right) \right) \\
& (|j\rangle \langle j+1| + |j+1\rangle \langle j|) + \sum_k \left( \sum_j \tfrac{1}{2} m^{(k)} \left( \dot{u}_j^{(k)} \right)^2 + \sum_j \tfrac{1}{2} m^{(k)} \left( \omega^{(k)} u_j^{(k)} \right)^2 \right)
\end{aligned}
\tag{22}
$$

This model includes more modes per site (labeled by the index $k$), the effect of the local electron phonon coupling term $\lambda^{(k)} u_j^{(k)} |j\rangle \langle j|$, and it can be regarded as the semiclassical version of Eq. (11). The spirit of the model is to capture the essence of the transport mechanism, keeping to a minimum the number of parameters. For this reason, even if all the parameters are computable from first principles, it is more convenient to identify one effective mode with local electron–phonon coupling and one effective mode with nonlocal coupling so that the number of parameters is kept under control and the numerical results can be better understood in the reduced parameter space. The calculation of the mobility using Eq. (22) was presented in [163] for rubrene. The reorganization energy $\Lambda$, computed for rubrene in [64], was used to evaluate the effective local electron–phonon coupling using the relation $\lambda^{(1)} = \omega^{(1)} \sqrt{m^{(1)} \Lambda}$. The computation of the nonlocal electron–phonon coupling followed the same procedure presented in Sect. 5.1 based on the combination of quantum chemical and classical MD simulations. The plot in Fig. 11 shows the comparison between mobility computed with and without the effect of the local electron phonon coupling and it is therefore a measure of how important the effect of $\lambda^{(1)}$ is on the computed mobility. It is found that, although the role of reorganization energy is quantitatively important (it causes a reduction of the mobility due to an increase of localization), for materials with low $\lambda$ (as rubrene or pentacene), its inclusion does not change the regime of transport.

The computed absolute value of $\mu$ is two to three times larger than the available experimental data, an agreement that is to be considered very good for the field of charge transport theory [54, 169, 170]. In particular, the temperature dependent measurement of Hall mobility performed by Podzorov et al. (Fig. 2) [54] shows, as the semiclassical computation, a decrease of the mobility by a factor of two as the temperature increases between 200 and 300 K. The model is currently limited to one dimension and the high frequency modes with local electron–phonon coupling might display significant quantum effects, ignored by the model. On the other hand,

the agreement with the experiments in terms of absolute mobility values and temperature dependence is so good that further improvement of the model requires data from new types of experiments.

## *6.3 Revised Polaronic Band Models*

Very important progress toward the incorporation of all types of electron–phonon couplings using a realistic Hamiltonian was achieved by Hannewald et al. [83, 171]. The matrix elements of the Hamiltonian in Eq. (11), have been computed with the DFT-LDA method implemented in the solid state program VASP [98]. The number of modes included in the calculation was reduced by adopting a rigid molecule approximation and ultimately considering the libration modes of the molecules as dispersionless optical phonons. The possibility of separating intra- and intermolecular modes have been extensively explored by the group of Dalla Valle and Girlando [115], who performed several Raman spectroscopic studies and analyzed the results studying how the intramolecular modes are affected by the crystal environment. The evaluations of the nonlocal electron phonon coupling of [139] and [83] agree on the greater importance of modes around 15 meV with the strongest $g_{ij,\mathbf{q}l}$ in the 0.3–1.1 range (in good agreement with the semiclassical analysis of [172]).

Hannewald et al. continued their analysis, applying a canonical transformation similar to that of Eq, (6) to the Holstein–Peierls Hamiltonian, achieving a very important generalization with respect to the available theories (a similar attempt was also made by Munn and Silbey [173, 174], when the matrix elements were not computationally available, and followed very closely by Wang et al. [175, 176]). In the same spirit of the theory described in Sect. 2.2.2, the authors assumed that the transport takes place in delocalized polaronic band (see Fig. 12). The work of [172], however, suggests that the delocalized picture ceases to be valid at temperatures above ∼150 K, since the variance of the intermolecular coupling is large compared to its average value. A similar upper limit for the validity of band transport is found

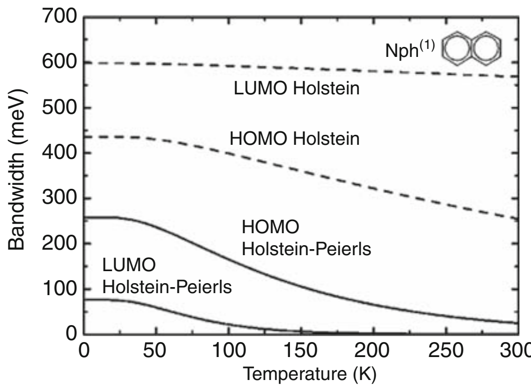


**Fig. 12** Band narrowing computed for the naphthalene solid with (Holstein–Peierls) and without (Holstein) the effect of nonlocal electron–phonon coupling using the canonical transformation methods. From [78]

by analyzing the mean free path of charge carrier in [81]. Since the semiclassical diffusion limited by thermal off-diagonal disorder (DLTD) approach cannot be applied towards the low temperature limit, the polaronic band and DLTD approaches can be seen as complementary, being optimal in two different transport regimes. A more recent attempt based on a temperature dependent polaron transformation was presented in [177].

From the combined consideration of [83] and [172] it emerges that the inclusion of the nonlocal electron phonon coupling considerably modifies the Holstein picture. Contrary to what is expected in a pure Holstein model, there is no abrupt change in transport mechanism between delocalized transport and activated transport. The polaronic band mechanism, appropriate at least until 100 K, gives way to the DLTD mechanism until $\sim 300$ K without approaching the hopping limit. Since both mechanisms result in a similar temperature dependence of the mobility $\left(\mu \sim aT^{-2}\right)$ they can both be extended beyond their "correct" limit of applicability, making it relatively easy to interpolate between them (or extrapolate each of them).

### 6.4 Localization Theory Models

Recent work that investigates further the possible analytical approaches to describe the charge mobility in the regime of dynamic disorder was presented by Picon et al. [178] who also identified in the work of Gosar and Choi [179] a predecessor of their idea. They clarify that only fast motions (with respect to the charge carrier) can be averaged out in the form of renormalized Hamiltonians like the one in Eqs. (6)–(9), while slower degrees of freedom have to be included explicitly in the Hamiltonian [180]. They built a model where the disorder is due to thermal fluctuations in the polarization energy but they showed how the fluctuation of the hopping integral [172] can be included without dramatic modifications. To evaluate the mobility, they first used the transfer matrix formalism [181, 182] to calculate the localization length of the carrier. Second, they assumed that acoustic phonons are coupled to the motion of the charge proposing for the mobility the following expression:

$$\mu = \frac{ev_{\mathrm{s}}L}{4k_{\mathrm{B}}T} \tag{23}$$

where $L$ is the localization length and $v_{\mathrm{s}}$ the sound velocity in the solid. This model might require some improvement for the evaluation of the diffusion property of the localized carrier but it shows clearly that an updated version of Anderson localization theory [183, 184] can provide the best framework for an analytic evaluation of the mobility in the presence of dynamic disorder.

## 6.5 Extension to Polymers and Liquid Crystals

Just for simplicity we have discussed the evolution of the understanding of charge transport mechanism in organic materials, limiting ourselves to molecular crystals. The work on highly ordered polymers and liquid crystals [185] has proceeded essentially in parallel and similar paradigms have been followed (Fig. 13). In an analogous way, the role of dynamic disorder has been included only in the most recent years but, as easily seen, the dynamic characterization of polymeric and liquid crystalline phases is more involved than simple crystals. We outline in this section only the points of this research area connected to our previous discussion, while an extensive review focusing more on "soft" semiconductors will be published elsewhere [186].

As in the case of molecular crystal, many electronic structure computations have been performed on crystalline organic semiconductors using computational methods ranging from semiempirical to DFT [110, 187, 188]. Many authors have studied oligomers of increasing length to extrapolate the properties of the full polymer [189, 190]. This approach was largely justified by the availability of the quick and reasonably accurate semiempirical method ZINDO which could be employed also for the study of the optical properties of these polymers. The difficulty in making

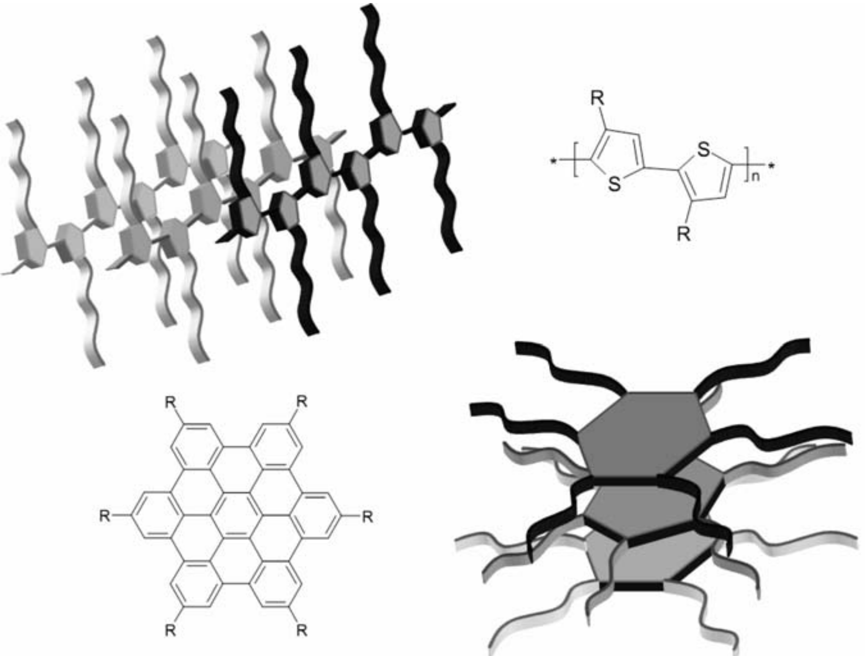


**Fig. 13** Chemical formula and schematic representation of the condensed phase morphology of the P3HT polymer (*top*) and the hexabenzacoronene molecule (HBC, *bottom*)

a straightforward extrapolation from the oligomer to the polymer was discussed theoretically in [191], while [192] also reviews the available experimental optical data relevant for the same problem.

The calculation of the local electron–phonon coupling in polymer was also largely based on oligomeric models [193, 194]. However, the oligomer model chosen to compute the electron–phonon coupling influences the results quite dramatically (the reorganization energy decreases with the increase of the size of the oligomer [195]). The localization due to the local electron–phonon coupling is coupled with the localization induced by the conjugation breaking related to the dynamics of the polymer at finite temperature [196–198] so that, in contrast with the molecular crystal case, there are no evaluations of the reorganization energy for polymers which can be validated by independent experimental methods. Recent works show that it is possible to identify a localized polaron in a long oligothiophene chain whose extension does not increase with increasing the length of the chain [193]. The situation is further complicated by the likely formation of bipolarons at higher charge density [199].

It is not surprising that, also in the case of polymers, the connection between the Hamiltonian parameters and the computation of the mobility is not straightforward. Band-like mobility was never observed for these systems and that has led to a preference for the hopping transport mechanism [31, 200]. However is it not possible to compute the charge transport along the chain in the absence of an independent evaluation of the localization length which is in turn determined by the dynamic disorder of the polymer. A semiclassical approach (where the structural degrees of freedom are treated classically and the single electronic degree of freedom is treated quantum mechanically) was adopted by Hultell and Stafstrom [201] and by Prins et al. [202, 203] to study the mobility in PPV (a related model with more adjustable parameters was proposed earlier [204]). It is possible with this approach to incorporate in the modeling the complexity of the chain conformation or the effect of the electric field. Moreover, the quality of the semiclassical Hamiltonian can be increased systematically and the approach can be in principle generalized to any semiconducting polymer.

A similar evolution from a quasistatic to a dynamic picture of the electronic structure was followed in the study of charge transport in semiconducting liquid crystals (hexabenzocoronene or triphenylene derivatives are among the most studied molecules in this class). The assumption of hopping transport between individual molecules led to several studies focusing on the determination of the parameters for the computation of the rate according to Eq. (10) (sometimes including the effect of static diagonal disorder) [205–208]. However, as we have seen in Sect. 4, the hopping integral is extremely sensitive to the relative molecular position [208] and to evaluate properly the distribution of the hopping integral it is necessary to couple extensive MD simulations with the quantum chemical evaluation of the coupling. This computationally demanding task was presented by Kirkpatrick et al. [120] and is the first step toward the quantitative understanding of the interplay between slow and very slow degrees of freedom in liquid crystal with the relatively fast electronic degree of freedom.

Outside the scope of this review but strongly related from the computational and theoretical points of view is the charge transport along DNA chains [209]. The experiments are still quite difficult and very heterogeneous (ranging from photoinduced charge transfer in solution [210] to current–voltage measurements in solid phase [211]). Essentially, all the models discussed in this review (polaronic band [212], hopping [213], disorder-based [135, 154]) have been proposed for DNA. There is good evidence [214] that the interplay between static and dynamic disorder (which include the motion of the counter ions [215]) has an important effect in the dynamic of the charge in DNA but the gradual refinement of the model is made difficult by the absence of a few benchmark measurements reproduced in different research labs.

## 7 Recent Experimental Evidence of Relevance to the Transport Mechanism

The experimental measures of the temperature dependent mobility can be fitted equally well using different theoretical models, which can be more or less consistent with the available computational data or with other experimental evidence. To make progress toward the understanding of the transport mechanism, it is very important to consider different experiments, beyond simple mobility measurements, which provide complementary information on the interaction between nuclear and electronic motions in the crystal.

Koch et al. used angle and energy dependent photoelectron spectroscopy to study the electronic structure of a pentacene thin film on graphite [216]. The technique is normally used to retrieve experimental information on the band structure of the valence electron [217–220] so that the results were analyzed in the framework of band theory. The authors reported an unexpected temperature dependence of the band structure which exhibits a width of 190 meV at room temperature and 240 meV at 120 K. The measurement revealed that it requires less energy to extract an electron from the crystal at room temperature. These results can be justified qualitatively in terms of localization induced by thermal disorder: at high temperatures the carriers are more localized (i.e., they have higher energy) and they are easier to ionize.

Lang et al. have analyzed the tail of the density of states using optical (photocurrent) and electrical (FET) methods [221]. They considered various existing models that describe the tail of the density of states and they concluded that their observation is consistent with the presence of some residual disorder which is not due to impurities (they used ultrapure crystals). The band tails are similar to those observed in amorphous inorganic solid, in agreement with the model of [172] which predicts that, from the electronic point of view, the pentacene crystal at room temperature can be seen as a disordered material.

Another important experiment was performed by Calhoun et al. [222] who were able to introduce, in a controlled way based on photo-induced charge transfer, shallow traps (both negative and positive) in the conduction channel of tetracene based

FET. The effect of trapping by impurities is extremely important for applications of organic FET and the authors provided a means of measuring the dependence of the field effect mobility on the density of the traps. Even if the role of charge carrier traps is not the main focus of this review, these authors observed an effect relevant for the understanding of the transport mechanism: while the introduction of negative traps decreases the apparent mobility of the holes, the introduction of positive traps leaves unchanged the measured mobility. The first observation is obviously due to the fact that the holes can be trapped by negative impurities. Their second observation, however, implies that the mobility of the holes is not affected by increasing the concentration of extrinsic scatterers. This can be only consistent with the view that the main scattering events in the transport are entirely intrinsic, i.e., due to phonons. It is therefore understandable why the assumption that low frequency scatterers dominate the transport can lead to computed mobility in the appropriate experimental range. It can be further argued that the absolute hole mobility of ultrapure crystals in the low temperature regime can be predicted by evaluating the scattering probability by phonons and ignoring the possible effect of impurities [223].

An interesting experimental observation was reported by Hulea et al. [170], who studied the temperature dependent field-effect mobility of rubrene, changing the dielectric material in contact with the conduction channel. The authors find that the mobility evolves from being "band-like" $(\mathrm{d}\mu/\mathrm{d}T < 0)$ to "hopping-like" $(\mathrm{d}\mu/\mathrm{d}T > 0)$ as the dielectric constant of the gate insulator increases. A device was also built with the crystal suspended in vacuum and mobilities similar to those of bulk samples have been recorded. This work stresses once again the importance of the interface for the understanding of the charge mobility [224–227] and provides a means to extend the model developed for bulk material to the interface [228]. In fact, the data are quantitatively explained assuming that a two-dimensional Frölich polaron (see Sect. 2.2.1) is formed at the interface, and the binding energy of the polaron is related to the known static and optical dielectric constant of the dielectric material. Interestingly, Frölich polaron models had not been used in organic electronics because of the nonpolar nature of these materials and the consequently small external reorganization energy in the bulk. The analysis of band narrowing at the interface due to polarization effects was also described theoretically by Houili et al. [229]. The difference between in-crystal and surface charge transport was recently measured simultaneously by Takeya and coworkers [230].

Frequency dependent conductivity measurements are another important source of information thanks especially to the recent possibility of exploring the THz region of the electromagnetic field [231–234]. Band-like conductance has been reported for example by Hegmann and coworkers [235]. The technique should offer the unique opportunity to probe the effect of the soft modes (in the 0.8–1.6 THz region) which affect the charge carrier dynamics more strongly. A particularly relevant result for the definition of the charge transport in organic solids was presented by Laarhoven et al. [236], who measured the transient photoconductivity of a pentacene sample. The measurement revealed that, in the presence of photogenerated holes and electrons, the sample absorbs radiation in the 0.9–1.1 THz range, i.e., the

same frequency range of the modes (described in Sect. 5.2) which cause dynamic localization. This was the first spectroscopic evidence of the coupling between low frequency vibrations and charge carrier dynamics, a characteristic that strongly supports the transport model based on dynamic localization.

Further indirect information on the transport mechanism can be obtained by spectroscopic investigations. Venuti et al., using Raman spectroscopy in conjunction with lattice dynamics calculation, found evidence of an efficient coupling between the lattice vibrations and low energy intramolecular modes [237]. Information of an even more indirect nature is provided by analyzing the field effect transistor characteristics which allow one to estimate the tail of the density of states of the semiconductor [238]. Interestingly, it is possible to compare quantitatively the tail of the density of states evaluated experimentally with the theoretical value obtained from MD/QC procedure [239].

Marumoto et al. [240] recently demonstrated the use of EPR to investigate the localization length of the charge carrier in an organic TFT. In some agreement with the theoretical estimate, they found that the holes are localized within about ten molecules at room temperature (a related measurement was also carried out by Matsui et al. [241]). It was also shown recently that, using time resolved microscopic optical second-harmonic generation, it is possible to visualize real carrier motion in organic materials [242]. Since the localization length of the carrier can be dependent on the typical timescale of the technique, the task of the theory in the following years is to develop a comprehensive model able to explain the full set of experimental observations.

## 8 Conclusion

The understanding of charge transport in ordered organic semiconductors has undergone profound changes in the past few years thanks to novel experiments, improved computational methods, and revised theories. The initial transport theories for this class of materials were dominated by the analogy with inorganic semiconductors, which provided an apparently solid ground for the development of models for organic electronics. The limitation of this analogy became apparent when the attempt to understand the experiments more quantitatively failed due to numerous inconsistencies. The difficulty of describing the charge transport in organic crystals in some familiar fashion led to uncertainty in the rationalization of the experiments and even in the language to be used. For example, the expression "band-like transport" was used instead of "band transport" because only part of the observations could be explained by the standard band transport theories.

A major contribution to overcome the impasse was given by a set of computational studies, which provided a realistic description of the Hamiltonian of the organic semiconductor and helped the definition of the most appropriate approximation schemes. Traditionally, computational studies follow from more formal and phenomenological theories and are used to connect the latter to the realistic systems.

However, formal theories cannot be built without an intuitive understanding of the process and several aspects of the charge dynamics in organic solids had eluded intuition until a few years ago. Electronic structure and electron–phonon coupling calculations have reached reassuring levels of accuracy and any acceptable transport theory should be consistent with the experiment *and* the computations. These computations revealed that the reorganization energy is too low to justify the use of a nonadiabatic charge transfer model in most cases and probably also too low to localize the charge in the most promising materials like pentacene and rubrene. On the other hand, the importance of off-diagonal electron–phonon coupling was discovered by several different computational studies which indicated also that thermal fluctuations of the hopping integral are sufficient to cause charge localization in organic solids.

The development of suitable transport theories taking into account these new computations is still in progress but several promising proposals have been put forward. These include semiclassical simulations, Holstein–Peierls polaron models, and dynamic localization theories. In the meantime, the experimental community is providing novel sets of spectroscopic and electric measures which reveal new aspects of the charge carrier dynamics and demand new explanations. The challenge for the next generation of charge transport theories is therefore greater than before: they should be able to predict the mobility of different materials *and* to interpret a variety of optical and electric measurements.

The greater understanding of charge transport in the bulk is likely to stimulate theoretical and computational investigations in other fundamental areas of organic electronics including the transport at the semiconductor–insulator interface and the charge injection process.

**Acknowledgements** The author is very grateful to Giorgio Orlandi, Jack Sleigh and David McMahon for their comments on this manuscript. This work was supported by EPRSC (UK).

## References

1. Pope M, Swenberg CE (1999) Electronic processes in organic crystals and polymers, 2nd edn. Oxford University Press, New York
2. Burroughes JH, Bradley DDC, Brown AR, Marks RN, Mackay K, Friend RH, Burns PL, Holmes AB (1990) Nature 347:539
3. Sheats JR, Antoniadis H, Hueschen M, Leonard W, Miller J, Moon R, Roitman D, Stocking A (1996) Science 273:884
4. Baldo MA, O'Brien DF, You Y, Shoustikov A, Sibley S, Thompson ME, Forrest SR (1998) Nature 395:151
5. Cao Y, Parker ID, Yu G, Zhang C, Heeger AJ (1999) Nature 397:414
6. Burroughes JH, Jones CA, Friend RH Nature (1988) 335:137
7. Horowitz G, Fichou D, Peng XZ, Xu ZG, Garnier F (1989) Sol State Commun 72:381
8. Kagan CR, Mitzi DB, Dimitrakopoulos CD (1999) Science 286:945
9. Dimitrakopoulos CD, Purushothaman S, Kymissis J, Callegari A, Shaw JM (1999) Science 283:822

10. Someya T, Kato Y, Sekitani T, Iba S, Noguchi Y, Murase Y, Kawaguchi H, Sakurai T (2005) Proc Natl Acad Sci U S A 102:12321
11. Hoppe H, Sariciftci NS (2004) J Mater Res 19:1924
12. Granstrom M, Petritsch K, Arias AC, Lux A, Andersson MR, Friend RH (1998) Nature 395:257
13. Eckert JF, Nicoud JF, Nierengarten JF, Liu SG, Echegoyen L, Barigelletti F, Armaroli N, Ouali L, Krasnikov V, Hadziioannou G (2000) J Am Chem Soc 122:7467
14. Peumans P, Uchida S, Forrest SR (2003) Nature 425:158
15. Mutolo KL, Mayo EI, Rand BP, Forrest SR, Thompson ME (2006) J Am Chem Soc 128:8108
16. Carrasco-Orozco M, Tsoi WC, O'Neill M, Aldred MP, Vlachos P, Kelly SM (2006) Adv Mater 18:1754
17. Katz HE (2004) Chem Mater 16:4748
18. Dimitrakopoulos CD, Malenfant PRL (2002) Adv Mater 14:99
19. Sirringhaus H (2005) Adv Mater 17:2411
20. Chang JF, Sun BQ, Breiby DW, Nielsen MM, Solling TI, Giles M, McCulloch I, Sirringhaus H (2004) Chem Mater 16:4772
21. Zaumseil J, Sirringhaus H (2007) Chem Rev 107:1296
22. Bassler H (1993) Phys Status Solidi B 175:15
23. Novikov SV, Dunlap DH, Kenkre VM, Parris PE, Vannikov AV (1998) Phys Rev Lett 81:4472
24. Vissenberg M, Matters M (1998) Phys Rev B 57:12964
25. Pasveer WF, Cottaar J, Tanase C, Coehoorn R, Bobbert PA, Blom PWM, de Leeuw DM, Michels MAJ (2005) Phys Rev Lett 94:206601
26. Mott NF (1962) Philos Mag 19:835
27. Baranovski SE (2006) Charge transport in disordered solids with applications in electronics. Wiley, West Sussex
28. Salleo A, Chen TW, Volkel AR, Wu Y, Liu P, Ong BS, Street RA (2004) Phys Rev B 70:115311
29. Limketkai BN, Jadhav P, Baldo MA (2007) Phys Rev B 75:113203
30. Li L, Meller G, Kosina H (2007) Microelectron J 38:47
31. Athanasopoulos S, Kirkpatrick J, Martinez D, Frost JM, Foden CM, Walker AB, Nelson J (2007) Nano Lett 7:1785
32. Kreouzis T, Poplavskyy D, Tuladhar SM, Campoy-Quiles M, Nelson J, Campbell AJ, Bradley DDC (2006) Phys Rev B 73:235201
33. Watkins PK, Walker AB, Verschoor GLB (2005) Nano Lett 5:1814
34. Grozema FC, Siebbeles LDA (2008) Int Rev Phys Chem 27:87
35. Cheung DL, Troisi A (2008) Phys Chem Chem Phys 10:5941
36. Sirringhaus H, Brown PJ, Friend RH, Nielsen MM, Bechgaard K, Langeveld-Voss BMW, Spiering AJH, Janssen RAJ, Meijer EW, Herwig P, de Leeuw DM (1999) Nature 401:685
37. Wang GM, Swensen J, Moses D, Heeger AJ (2003) J Appl Phys 93:6137
38. Kline RJ, McGehee MD, Toney MF (2006) Nat Mater 5:222
39. Facchetti A, Yoon MH, Stern CL, Katz HE, Marks TJ (2003) Angew Chem Int Ed 42:3900
40. Yoon MH, Facchetti A, Stern CE, Marks TJ (2006) J Am Chem Soc 128:5792
41. Locklin J, Ling MM, Sung A, Roberts ME, Bao ZN (2006) Adv Mater 18:2989
42. Briseno AL, Miao Q, Ling MM, Reese C, Meng H, Bao ZN, Wudl F (2006) J Am Chem Soc 128:15576
43. Tang ML, Okamoto T, Bao ZN (2006) J Am Chem Soc 128:16002
44. Lu J, Ho DM, Vogelaar NJ, Kraml CM, Bernhard S, Byrne N, Kim LR, Pascal RA (2006) J Am Chem Soc 128:17043
45. Kim DH, Lee DY, Lee HS, Lee WH, Kim YH, Han JI, Cho K (2007) Adv Mater 19:678
46. Paraskar AS, Reddy AR, Patra A, Wjjsboom YH, Gidron O, Shimon LJW, Leitus G, Bendikov M (2008) Chem Eur J 14:10639
47. Anthony JE (2008) Angew Chem Int Ed 47:452
48. Lin Y-Y, Gundlach DJ, Nelson SF, Jackson TN (1997) IEEE Trans Electron Dev 44:1325
49. Klauk H, Gundlach DJ, Nichols JA, Jackson TN (1999) IEEE Trans Electron Dev 46:1258
50. Jurchescu OD, Baas J, Palstra TTM (2004) Appl Phys Lett 84:3061

51. Ostroverkhova O, Cooke DG, Hegmann FA, Anthony JE, Podzorov V, Gershenson ME, Jurchescu OD, Palstra TTM (2006) Appl Phys Lett 88:162101
52. Podzorov V, Sysoev SE, Loginova E, Pudalov VM, Gershenson ME (2003) Appl Phys Lett 83:3504
53. Podzorov V, Menard E, Borissov A, Kiryukhin V, Rogers JA, Gershenson ME (2004) Phys Rev Lett 93:086602
54. Podzorov V, Menard E, Rogers JA, Gershenson ME (2005) Phys Rev Lett 95:226601
55. Warta W, Karl N (1985) Phys Rev B 32:1172
56. Karl N, Marktanner J, Stehle R, Warta W (1991) Synth Met 42:2473
57. Kostin AK, Savelev VV, Vannikov AV (1978) Phys Stat Solidi B 87:255
58. Ashcroft NW, Mermin D (1976) Solid state physics. Holt, Reinhart, and Winston, New York
59. de Wijs GA, Mattheus CC, de Groot RA, Palstra TTM (2003) Synth Met 139:109
60. Hutchison GR, Zhao YJ, Delley B, Freeman AJ, Ratner MA, Marks TJ (2003) Phys Rev B 68:035204
61. Doi K, Yoshida K, Nakano H, Tachibana A, Tanabe T, Kojima Y, Okazaki K (2005) J Appl Phys 98:113709
62. Koh SE, Delley B, Medvedeva JE, Facchetti A, Freeman AJ, Marks TJ, Ratner MA (2006) J Phys Chem B 110:24361
63. Kim EG, Coropceanu V, Gruhn NE, Sanchez-Carrera RS, Snoeberger R, Matzger AJ, Bredas JL (2007) J Am Chem Soc 129:13072
64. da Silva DA, Kim EG, Bredas JL (2005) Adv Mater 17:1072
65. Troisi A, Orlandi G (2005) J Phys Chem B 109:1849
66. Jacoboni C, Reggiani L (1983) Rev Mod Phys 55:645
67. Gnani E, Reggiani S, Rudan M (2002) Phys Rev B 66:195205
68. Duncan A, Ravaioli U, Jakumeit J (1998) IEEE Trans Electron Dev 45:867
69. Mahn GD (1990) Many-particle physics. Plenum, New York
70. Mahan GD (2000) Many-particle physics, 3rd edn. Plenum, New York
71. Holstein T (1959) Ann Phys 8:325
72. Lang IJ, Firsov YA (1962) Sov Phys JETP 16:1301
73. Marcus R (1956) J Chem Phys 24:979
74. Jortner J (1976) J Chem Phys 64:4860
75. Newton MD (1999) Electron transfer-from isolated molecules to biomolecules, pt 1, vol 106. Wiley, New York
76. Nitzan A (2001) Annu Rev Phys Chem 52:681
77. Fratini S, Ciuchi S (2003) Phys Rev Lett 91:256403
78. Loos J, Hohenadler M, Fehske H (2006) J Phys Cond Matt 18:2453
79. Kornilovitch PE (2007) J Phys Cond Matt 19:255213
80. Feynmann R (1955) Phys Rev 97:660
81. Cheng YC, Silbey RJ, da Silva Filho DA, Calbert JP, Cornil J, Bredas JL (2003) J Chem Phys 118:3764
82. Gershenson ME, Podzorov V, Morpurgo AF (2006) Rev Mod Phys 78:973
83. Hannewald K, Stojanovic VM, Schellekens JMT, Bobbert PA, Kresse G, Hafner J (2004) Phys Rev B 69:075211
84. Bredas JL, Beljonne D, Coropceanu V, Cornil J (2004) Chem Rev 104:4971
85. Coropceanu V, Cornil J, da Silva DA, Olivier Y, Silbey R, Bredas JL (2007) Chem Rev 107:926
86. Leach AR (1996) Molecular modelling: principles and applications. Addison Wesley, Essex
87. Jensen F (1999) Introduction to computational chemistry. Wiley, Chichester
88. Troisi A, Orlandi G (2001) Chem Phys Lett 344:509
89. Sancho-Garcia JC, Perez-Jimenez AJ (2008) J Chem Phys 129
90. Valeev EF, Coropceanu V, da Silva DA, Salman S, Bredas JL (2006) J Am Chem Soc 128:9882
91. Lipparini F, Mennucci B (2007) J Chem Phys 127:144706
92. Hutchison GR, Ratner MA, Marks TJ (2002) J Phys Chem A 106:10596
93. Kazmaier PM, Hoffmann R (1994) J Am Chem Soc 116:9684

94. Haddon RC, Chi X, Itkis ME, Anthony JE, Eaton DL, Siegrist T, Mattheus CC, Palstra TTM (2002) J Phys Chem B 106:8288
95. Margetis D, Kaxiras E, Elstner M, Frauenheim T, Manaa MR (2002) J Chem Phys 117:788
96. Endres RG, Fong CY, Yang LH, Witte G, Woll C (2004) Comput Mater Sci 29:362
97. Huang J, Kertesz M (2004) Chem Phys Lett 390:110
98. Hafner J (2007) Comput Phys Commun 177:6
99. Huang JS, Kertesz M (2005) J Chem Phys 122:234707
100. Hutchison GR, Ratner MA, Marks TJ (2005) J Phys Chem B 109:3126
101. Yang YT, Geng H, Yin SW, Shuai ZG, Peng JB (2006) J Phys Chem B 110:3180
102. Ortmann F, Hannewald K, Bechstedt F (2007) Phys Rev B 75:195219
103. Puschnig P, Ambrosch-Draxl C (1999) Phys Rev B 60:7891
104. Hummer K, Puschnig P, Ambrosch-Draxl C (2003) Phys Rev B 67
105. Tiago ML, Northrup JE, Louie SG (2003) Phys Rev B 67
106. Lee JY, Roth S, Park YW (2006) Appl Phys Lett 88:252106
107. Mannsfeld SCB, Locklin J, Reese C, Roberts ME, Lovinger AJ, Bao Z (2007) Adv Funct Mater 17:1617
108. Ostroverkhova O, Cooke DG, Hegmann FA, Tykwinski RR, Parkin SR, Anthony JE (2006) Appl Phys Lett 89:192113
109. Vogl P, Campbell DK (1989) Phys Rev Lett 62:2012
110. Dacosta PG, Dandrea RG, Conwell EM (1993) Phys Rev B 47:1800
111. Ambroschdraxl C, Majewski JA, Vogl P, Leising G (1995) Phys Rev B 51:9668
112. Bussi G, Ruini A, Molinari E, Caldas MJ, Puschnig P, Ambrosch-Draxl C (2002) Appl Phys Lett 80:4118
113. Coropceanu V, Malagoli M, da Silva Filho DA, Gruhn NE, Bill TG, Bredas JL (2002) Phys Rev Lett 89:275503
114. Malagoli M, Coropceanu V, da Silva DA, Bredas JL (2004) J Chem Phys 120:7490
115. Della Valle RG, Venuti E, Farina L, Brillante A, Masino M, Girlando A (2004) J Phys Chem B 108:1822
116. Zade SS, Bendikov M (2008) Chem Eur J 14:6734
117. Mas-Torrent M, Hadley P, Bromley ST, Ribas X, Tarres J, Mas M, Molins E, Veciana J, Rovira C (2004) J Am Chem Soc 126:8546
118. Devos A, Lannoo M (1998) Phys Rev B 58:8236
119. Gruhn NE, da Silva DA, Bill TG, Malagoli M, Coropceanu V, Kahn A, Bredas JL (2002) J Am Chem Soc 124:7918
120. Kirkpatrick J, Marcon V, Nelson J, Kremer K, Andrienko D (2007) Phys Rev Lett 98:227402
121. da Silva DA, Coropceanu V, Fichou D, Gruhn NE, Bill TG, Gierschner J, Cornil J, Bredas JL (2007) Philos Trans R Soc Math Phys Eng Sci 365:1435
122. Chen HY, Chao I (2005) Chem Phys Lett 401:539
123. Chen HY, Chao I (2006) ChemPhysChem 7:2003
124. Hutchison GR, Ratner MA, Marks TJ (2005) J Am Chem Soc 127:2339
125. Vilfan I (1973) Phys Stat Sol B 59:351
126. Brovchenko IV (1997) Chem Phys Lett 278:355
127. Norton JE, Bredas JL (2008) J Am Chem Soc 130:12377
128. Torras J, Bromley S, Bertran O, Illas F (2008) Chem Phys Lett 457:154
129. Castet F, Aurel P, Fritsch A, Ducasse L, Liotard D, Linares M, Cornil J, Beljonne D (2008) Phys Rev B 77:115210
130. Kenkre VM, Andersen JD, Dunlap DH, Duke CB (1989) Phys Rev Lett 62:1165
131. Warta W, Karl N (1985) Phys Rev B 32:1172
132. Bredas JL, Calbert JP, Da Silva Filho DA, Cornil J (2002) Proc Natl Acad Sci U S A 99:5804
133. Jordan KD, Paddon-Row MN (1992) Chem Rev 92:395
134. Troisi A, Nitzan A, Ratner MA (2003) J Chem Phys 119:5782
135. Troisi A, Orlandi G (2002) J Phys Chem B 106:2093
136. Balabin IA, Onuchic JN (2000) Science 290:114
137. Troisi A, Ratner MA, Zimmt MB (2004) J Am Chem Soc 126:2215
138. Della Valle RG, Venuti E, Brillante A, Girlando A (2006) J Phys Chem A 110:10858

139. Della Valle RG, Brillante A, Farina L, Venuti E, Masino M, Girlando A (2004) Mol Cryst Liq Cryst 416:145
140. Mattheus CC, Dros AB, Baas J, Oostergetel GT, Meetsma A, de Boer JL, Palstra TTM (2003) Synth Met 138:475
141. Siegrist T, Besnard C, Haas S, Schiltz M, Pattison P, Chernyshov D, Batlogg B, Kloc C (2007) Adv Mater 19:2079
142. Kakudate T, Yoshimoto N, Saito Y (2007) Appl Phys Lett 90:081903
143. Mattheus CC, de Wijs GA, de Groot RA, Palstra TTM (2003) J Am Chem Soc 125:6323
144. Datta A, Mohakud S, Pati SK (2007) J Chem Phys 126
145. Hu WS, Weng SZ, Tao YT, Liu HJ, Lee HY, Fan LJ, Yang YW (2007) Langmuir 23:12901
146. Lee ML, Fitzgerald EA, Bulsara MT, Currie MT, Lochtefeld A (2005) J Appl Phys 97:011101
147. Liu CW, Maikap S, Yu CY (2005) IEEE Circuits Dev 21:21
148. Nabok D, Puschnig P, Ambrosch-Draxl C, Werzer O, Resel R, Smilgies DM (2007) Phys Rev B 76
149. Harada J, Ogawa K (2001) J Am Chem Soc 123:10884
150. Harada J, Ogawa K (2004) J Am Chem Soc 126:3539
151. Moorthy JN, Venkatakrishnan P, Savitha G, Weiss RG (2006) Photochem Photobiol Sci 5:903
152. Murugan NA (2005) J Chem Phys 123:094508
153. Haas S, Batlogg B, Besnard C, Schiltz M, Kloc C, Siegrist T (2007) Phys Rev B 76:205203
154. Senthilkumar K, Grozema FC, Guerra CF, Bickelhaupt FM, Lewis FD, Berlin YA, Ratner MA, Siebbeles LDA (2005) J Am Chem Soc 127:14894
155. Deng WQ, Goddard WA (2004) J Phys Chem B 108:8614
156. Allinger NL, Li F, Yan L, Tai JC (1990) J Comput Chem 11:868
157. Kwiatkowski JJ, Frost JM, Kirkpatrick J, Nelson J (2008) J Phys Chem A 112:9113
158. Anderson PW (1958) Phys Rev 109:1492
159. Lee PA, Ramakrishnan TV (1985) Rev Mod Phys 57:287
160. Unge M, Stafstrom S (2003) Synth Met 139:239
161. Pecchia A, Lozman OR, Movaghar B, Boden N, Bushby RJ, Donovan KJ, Kreouzis T (2002) Phys Rev B 65:104204
162. Palenberg MA, Silbey RJ, Malagoli M, Bredas JL (2000) J Chem Phys 112:1541
163. Troisi A (2007) Adv Mater 19:2000
164. Troisi A (2006) Mol Simul 32:707
165. Troisi A, Orlandi G, Anthony JE (2005) Chem Mat 17:5024
166. Kim DH, Lee DY, Lee HS, Lee WH, Kim YH, Han JI, Cho K (2007) Adv Mater 19:678
167. Anthony JE (2006) Chem Rev 106:5028
168. Ness H, Fisher AJ (1999) Phys Rev Lett 83:452
169. Sundar VC, Zaumseil J, Podzorov V, Menard E, Willett RL, Someya T, Gershenson ME, Rogers JA (2004) Science 303:1644
170. Hulea IN, Fratini S, Xie H, Mulder CL, Iossad NN, Rastelli G, Ciuchi S, Morpurgo AF (2006) Nat Mater 5:982
171. Ortmann F, Hannewald K, Bechstedt F (2008) Appl Phys Lett 93
172. Troisi A, Orlandi G (2006) J Phys Chem A 110:4065
173. Munn RW, Silbey R (1985) J Chem Phys 83:1843
174. Munn RW, Silbey R (1985) J Chem Phys 83:1854
175. Wang LJ, Peng Q, Li QK, Shuai Z (2007) J Chem Phys 127:044506
176. Wang LJ, Li QK, Shuai Z (2008) J Chem Phys 128
177. Cheng YC, Silbey RJ (2008) J Chem Phys 128
178. Picon JD, Bussac MN, Zuppiroli L (2007) Phys Rev B 75:235106
179. Gosar P, Choi SI (1966) Phys Rev 18:49
180. Houili H, Picon JD, Zuppiroli L, Bussac MN (2006) J Appl Phys 100:023702
181. Pendry JB (1994) Adv Phys 43:461
182. Eilmes A, Romer RA, Schreiber M (1998) Eur Phys J B 1:29
183. Anderson PW (1978) Rev Mod Phys 50:191
184. Lee PA, Ramakrishnan TV (1985) Rev Mod Phys 57:287
185. O'Neill M, Kelly SM (2003) Adv Mater 15:1135

186. Cheung D, Troisi A (2008) Phys Chem Chem Phys 10:5942
187. Tobita M, Hirata S, Bartlett RJ (2001) J Chem Phys 114:9130
188. Ferretti A, Ruini A, Molinari E, Caldas MJ (2003) Phys Rev Lett 90:086401
189. Wang JF, Feng JK, Ren AM, Liu XD, Ma YG, Lu P, Zhang HX (2004) Macromolecules 37:3451
190. Johansson E, Larsson S Synth Met (2004) 144:183
191. Hutchison GR, Zhao YJ, Delley B, Freeman AJ, Ratner MA, Marks TJ (2003) Phys Rev B 68
192. Gierschner J, Cornil J, Egelhaaf HJ (2007) Adv Mater 19:173
193. Geskin VM, Dkhissi A, Bredas JL (2003) Int J Quant Chem 91:350
194. Moro G, Scalmani G, Cosentino U, Pitea D (2000) Synth Met 108:165
195. Bromley ST, Illas F, Mas-Torrent M (2008) Phys Chem Chem Phys 10:121
196. Zade SS, Bendikov M (2007) Chem Eur J 13:3688
197. Westenhoff S, Beenken WJD, Yartsev A, Greenham NC (2006) J Chem Phys 125:154903
198. Breza M, Lukes V, Vrabel I (2001) J Mol Struct Theochem 572:151
199. Geskin VM, Bredas JL (2003) ChemPhysChem 4:498
200. Kreouzis T, Donovan KJ, Boden N, Bushby RJ, Lozman OR, Liu Q (2001) J Chem Phys 114:1797
201. Hultell M, Stafstrom S (2007) Phys Rev B 75:104304
202. Prins P, Grozema FC, Galbrecht F, Scherf U, Siebbeles LDA (2007) J Phys Chem C 111:11104
203. Prins P, Grozema FC, Siebbeles LDA (2006) Mol Simul 32:695
204. Yu ZG, Smith DL, Saxena A, Martin RL, Bishop AR (2000) Phys Rev Lett 84:721
205. Cornil J, Lemaur V, Calbert JP, Bredas JL (2002) Adv Mater 14:726
206. Lemaur V, Da Silva Filho DA, Coropceanu V, Lehmann M, Geerts Y, Piris J, Debije MG, Van de Craats AM, Senthilkumar K, Siebbeles LDA, Warman JM, Bredas JL, Cornil J (2004) J Am Chem Soc 126:3271
207. van de Craats AM, Siebbeles LDA, Bleyl I, Haarer D, Berlin YA, Zharikov AA, Warman JM (1998) J Phys Chem B 102:9625
208. Senthilkumar K, Grozema FC, Bickelhaupt FM, Siebbeles LDA (2003) J Chem Phys 119:9809
209. Endres RG, Cox DL, Singh RRP (2004) Rev Mod Phys 76:195
210. Murphy CJ, Arkin MR, Jenkins Y, Ghatlia ND, Bossmann SH, Turro NJ, Barton JK (1993) Science 262:1025
211. Porath D, Cuniberti G, Di Felice R (2004) In: Schuster GB (ed) Long-range charge transfer in DNA, vol 237. Springer, Berlin Heidelberg New York
212. Conwell EM (2005) Proc Natl Acad Sci U S A 102:8795
213. Berlin YA, Kurnikov IV, Beratan D, Ratner MA, Burin AL (2004) In: Schuster GB (ed) Long-range charge transfer in DNA, vol 237. Springer, Berlin Heidelberg New York
214. O'Neill MA, Barton JK (2004) J Am Chem Soc 126:11471
215. Joy A, Schuster GB (2005) Chem Commun 2778
216. Koch N, Vollmer A, Salzmann I, Nickel B, Weiss H, Rabe JP (2006) Phys Rev Lett 96:156803
217. Azuma Y, Hasebe T, Miyamae T, Okudaira KK, Harada Y, Seki K, Morikawa E, Saile V, Ueno N (1998) J Synchrotron Radiat 5:1044
218. Fukagawa H, Yamane H, Kataoka T, Kera S, Nakamura M, Kudo K, Ueno N (2006) Phys Rev B 73:245310
219. Koch N, Salzmann I, Johnson RL, Pflaum J, Friedlein R, Rabe JP (2006) Org Electron 7:537
220. Jaeckel B, Sambur JB, Parkinson BA (2007) Langmuir 23:11366
221. Lang DV, Chi X, Siegrist T, Sergent AM, Ramirez AP (2004) Phys Rev Lett 93:086802
222. Calhoun MF, Hsieh C, Podzorov V (2007) Phys Rev Lett 98:096402
223. Kalb WL, Mattenberger K, Batlogg B (2008) Phys Rev B 78
224. Chua LL, Zaumseil J, Chang JF, Ou ECW, Ho PKH, Sirringhaus H, Friend RH (2005) Nature 434:194
225. Jurchescu OD, Popinciuc M, van Wees BJ, Palstra TTM (2007) Adv Mater 19:688
226. Lee CA, Park DW, Jung KD, Kim BJ, Kim YC, Lee JD, Park BG (2006) Appl Phys Lett 89:262120

227. Ruiz R, Papadimitratos A, Mayer AC, Malliaras GG (2005) Adv Mater 17:1795
228. Vazquez H, Flores F, Kahn A (2007) Org Electron 8:241
229. Houili H, Picon JD, Zuppiroli L, Bussac MN (2006) J Appl Phys 100
230. Takeya J, Kato J, Hara K, Yamagishi M, Hirahara R, Yamada K, Nakazawa Y, Ikehata S, Tsukagoshi K, Aoyagi Y, Takenobu T, Iwasa Y (2007) Phys Rev Lett 98:196804
231. Hegmann FA, Tykwinski RR, Lui KPH, Bullock JE, Anthony JE (2002) Phys Rev Lett 89
232. Thorsmolle VK, Averitt RD, Chi X, Hilton DJ, Smith DL, Ramirez AP, Taylor AJ (2004) Appl Phys Lett 84:891
233. Ostroverkhova O, Cooke DG, Hegmann FA, Tykwinski RR, Parkin SR, Anthony JE (2006) Appl Phys Lett 89:122103
234. Koeberg M, Hendry E, Schins JM, van Laarhoven HA, Flipse CFJ, Reimann K, Woerner M, Elsaesser T, Bonn M (2007) Phys Rev B 75
235. Ostroverkhova O, Cooke DG, Shcherbyna S, Egerton RF, Hegmann FA, Tykwinski RR, Anthony JE (2005) Phys Rev B 71:035204
236. Laarhoven HAV, Flipse CFJ, Koeberg M, Bonn M, Hendry E, Orlandi G, Jurchescu OD, Palstra TTM, Troisi A (2008) J Chem Phys 129:5
237. Venuti E, Bilotti I, Della Valle RG, Brillante A, Ranzieri P, Masino M, Girlando A (2008) J Phys Chem C 112:17416
238. Pernstich KP, Rossner B, Batlogg B (2008) Nat Mater 7:321
239. Sleigh J, McMahon D, Troisi A (2008) App Phys A doi: 101007/s00339
240. Marumoto K, Kuroda S, Takenobu T, Iwasa Y (2006) Phys Rev Lett 97:256603
241. Matsui H, Hasegawa T, Tokura Y (2008) Phys Rev Lett 100:126601
242. Manaka T, Lim E, Tamura R, Iwamoto M (2007) Nat Photonics 1:581

Adv Polym Sci (2010) 223: 301–323
DOI:10.1007/12_2009_14
© Springer-Verlag Berlin Heidelberg 2009
Published online: 26 August 2009

# Charge Transport in Organic Semiconductor Devices

**Ling Li and Hans Kosina**

**Abstract** In this chapter, we investigate the charge transport properties in organic semiconductor materials and devices, in the frame of variable range hopping theory. We discuss the dependences of mobility on temperature, carrier concentration, doping and trapping. We also present the charge transport model in organic light-emitting diodes.

**Keywords** Hopping transport · Organic semiconductor · Percolation theory

## Contents

1 Introduction . . . 302
2 Organic Semiconductor Physics . . . 302
3 Carrier Concentration-Dependent Mobility Model . . . 304
4 Doping and Trapping Model for Organic Semiconductors . . . 309
5 Charge Injection and Transport Model in Organic Light-Emitting Diodes . . . 315
5.1 Diffusion Controlled Injection Model . . . 315
5.2 Device Model for Unbipolar Organic Light-Emitting Diodes . . . 319
6 Conclusion . . . 321
References . . . 321

L. Li (✉) and H. Kosina
TU Wien, Gußhausstraße 27–29/E360, 1040, Wien, Austria
e-mail:li@iue.tuwien.ac.at;lingli@imec.be

L. Li
IMEC, Kapeldreef 75, 3001, Leuven, Belgium

## 1 Introduction

For the past 50 years, inorganic semiconductors have represented the standard material of microelectronics. Experiments with highly doped polyacetylene in the year 1977 [1], however, proved that polymers can conduct electric currents as well – a discovery which led to a huge research effort on conjugated organic materials. At the beginning, performance and stability of "plastic semiconductors" remained at a rather poor level. However, in the past two decades [2], due to drastic improvements in the synthesis and processing of new semiconducting hydrocarbon compounds, the prospects of commercial applications like organic light-emitting diodes (OLEDs) [3], field-effect transistors (OFETs) and solar cells are now greater than ever. In fact, Philips, Kodak and Sony introduced novel consumer electronics during the past few years featuring OLED-based display technology [4]. The applications range from digital cameras to electric shavers to a prototype OLED TV [4]. Simplicity in manufacturing and lower costs of organic devices have been the primary reasons driving these devices towards commercialization.

## 2 Organic Semiconductor Physics

In inorganic crystalline semiconductors, the strong coupling between the lattice-constituting ions and their periodic long-range order leads to delocalized electron states and the formation of valence and conduction bands, separated by forbidden energy gaps. For the most relevant materials, thermal activation lies in the same magnitude as these energy gaps and thus generates free carriers in the conduction band, leaving behind positively charged, freely moving holes in the valence band. The technologically most relevant *organic* semiconductors, however, are processed in their amorphous or polycrystalline phase, where microscopic obstacles like chemical impurities or topological and morphological defects inhibit free carrier propagation. Depending on the specific microscopic structure, the motion of a single carrier in an amorphous, hydrocarbon-based semiconductor resembles a thermally activated random walk among chains, chain strands, molecule stacks, or single molecules. This incoherent motion is typically described by a sequence of consecutive "hops," i.e. phonon-assisted tunneling events surpassing the potential barriers between, e.g., spatially separated molecules or chain strands separated by kinks or cross-links. Between two hops, a certain amount of "trapping time" elapses till the absorption of a sufficiently energetic phonon facilitates the next jump. The corresponding retardation thus reflects the barrier heights, the bulk temperature, and, last but not least, the electron–phonon coupling strength, which describes, metaphorically speaking, the frequency of escape attempts undertaken by the trapped carrier. Most models describing the hopping transport in disordered organic semiconductors are derived from the classical Miller–Abrahams expression, which originated from the theory of impurity band conduction in doped *inorganic* semiconductors [5].

In this model, the barrier between two localized states $i$ and $j$ separated by a distance $R_{ij}$ is simply determined by the corresponding work function difference $E_j$–$E_i$. The equilibration probability of this energy difference via phonon absorption is given by the Boltzmann factor, whereas the reverse transition from the higher energetic level to the lower one occurs with probability 1. The electron–phonon coupling strength is condensed into a model parameter $\nu_0$ labeled as "attempt-to-escape frequency" and is typically assigned the value $10^{14}\,\mathrm{s}^{-1}$ in the literature. Elastic tunneling between thermally equilibrated localized transport levels is governed by an overlap-dependent transmission rate between localized, i.e., exponentially decaying states of "size" $a$ and shape $\Psi(r) = e^{-r/a}$ [6]. The carrier transition rate from state $i$ to state $j$ thus finally decomposes into a product of three factors:

$$\omega_{ij} = \nu_0 \begin{cases} \exp\left(-2\alpha R_{ij} - \frac{E_j - E_i}{k_\mathrm{B}T}\right), & E_j > E_i \\ \exp\left(-2\alpha R_{ij}\right), & E_j < E_i \end{cases} \tag{1}$$

Thereby, $\alpha = 1/a$ denotes the so-called "inverse localization length" or synonymously, the "wave function overlap." Typically, in an organic semiconductor, $R \approx 0.5\,\mathrm{nm}$ and $2\alpha R_{ij} \approx 10$ holds true.

Provided that each state is capable of holding exactly one electron, the temporal evolution of the occupation probability $f_i$ of state $i$ can be described by a master equation:

$$\frac{\mathrm{d}f_i}{\mathrm{d}t} = \sum_{j \neq i} f_i(t)\left(1 - f_j(t)\right)\omega_{ij} - \sum_{j \neq i} f_j(t)\left(1 - f_i(t)\right)\omega_{ji} + \lambda_i f_i(t). \tag{2}$$

$\lambda_i$ describing the decaying processes ($\lambda = 0_i$ in case of charge carriers). The occupation probability of state $i$ with chemical potential $\mu_i$ is given by the Fermi–Dirac distribution:

$$f_i = \frac{1}{1 + \exp\left(\frac{E_i - \mu_i}{k_\mathrm{B}T}\right)}. \tag{3}$$

Assuming uncorrelated occupation probabilities for different localized states, the balance equation for the steady-state net current between two sites reads as

$$I_{ij} = q\left(f_i(t)\left(1 - f_j(t)\right)\omega_{ij} - f_j(t)\left(1 - f_i(t)\right)\omega_{ji}\right). \tag{4}$$

Substituting the Miller–Abrahams rate (1) into (4), the following expression for the current results:

$$I_{ij} = \frac{q\nu_0 \exp\left(-2\alpha R_{ij} - \frac{\left|E_i - E_j\right|}{2k_\mathrm{B}T}\right)\sinh\left(\frac{\mu_i - \mu_j}{2k_\mathrm{B}T}\right)}{\cosh\left(\frac{E_i - \mu_i}{2k_\mathrm{B}T}\right)\cosh\left(\frac{E_j - \mu_j}{2k_\mathrm{B}T}\right)}. \tag{5}$$

In the case of low electric fields and therefore small voltage drops over a single hopping distance ($\Delta\mu = \mu_j - \mu_i \ll k_B T$), the following conductance follows:

$$\sigma_{ij} = \frac{I_{ij}}{\Delta\mu} \propto \exp\left(-2\alpha R_{ij} - \frac{|E_i - \mu| + |E_j - \mu| + |E_i - E_j|}{2k_B T}\right). \tag{6}$$

Here $\mu_i \approx \mu_j \approx \mu$. Equation (6) has an important implication. Even in the case of moderately spread energy distributions, the exponential dependence of $\sigma_{ij}$ on the energies leads to very broadly spread conductivities. Consequently, in a network numerous negligible conductivities exist, reducing the computations of the effective network properties to that of a so-called "reduced network."

The hopping conductivity $G$ of reduced networks was first calculated by Miller and Abrahams in connection with doped inorganic semiconductors [5]. They assumed that the statistical distribution of the resistances only depends on the $R_{ij}$, but not on the site energies. This assumption was justified by experimental data for some (inorganic) semiconductors, indicating a well-defined activation energy for impurity conduction. Mott, however, pointed out that the exponential dependency of the resistances on the site energies cannot be ignored in many cases. When a carrier close to the Fermi energy hops away over a distance $R$ with an energy $\Delta E$, it has $\frac{4}{3}\pi R^3 \rho \Delta E$ sites to choose from, where $\rho$ is the site density (a constant $\rho$ is assumed here). In general, the carrier will jump to a site for which $\Delta E$ is as small as possible. The constraint to find a site within a range $(R, \Delta E)$ is given by $\frac{4}{3}\pi R^3 \rho \Delta E \approx 1$. Substituting this relation into (6) yields

$$G \propto \exp\left(-2\alpha R - \frac{1}{k_B T\,(4/3)\,\pi R^3 \rho}\right). \tag{7}$$

The optimum conductance is obtained by maximizing $G$ with respect to the hopping distance $R$ as

$$G \propto \exp\left(-\left(T_1/T\right)^{1/4}\right). \tag{8}$$

## 3 Carrier Concentration-Dependent Mobility Model

The carrier mobility of organic semiconductors has been improved tremendously over the past few years. A field-effect mobility as high as $0.1\,\mathrm{cm^2\,V^{-1}\,s^{-1}}$ has recently been measured in region-regular poly(thiophenes). Since the microscopic structure of the polymer depends on the processing conditions, it is not uncommon to find widely differing mobilities for one and the same polymer in literature. In this section, a carrier-concentration dependent mobility model based on the variable range hopping theory (VRH) is presented [7].

Noncrystalline organic solids, such as molecularly doped crystals, molecular glasses, and conjugated polymers, are characterized by small mean free paths for

carriers. The crucial transport mechanism is the charge transfer between adjacent charge transporting elements. According to Bässler's celebrated Gaussian disorder model, the polarization energies depend on a variety of mutually independent, randomly dispersed parameters, thus making the central limit theorem applicable to the density of (localized) states [8]:

$$g(E) = \frac{N_t}{\sqrt{2\pi}\sigma_v} \exp\left(-\frac{E^2}{2\sigma_v^2}\right), \tag{9}$$

Thereby, $E$ is the energy measured relatively to the center of the density of states and $\sigma_v$ is the standard deviation of the Gaussian distribution mirroring the degree of energetic disorder. Using the Gaussian energy distribution, we can express the carrier concentration as

$$n = \frac{N_t}{\sqrt{2\pi}\sigma_v} \int_{-\infty}^{\infty} \frac{\exp\left(-E^2/2\sigma_v^2\right)}{1+\exp\left(\frac{E-E_F}{k_B T}\right)}. \tag{10}$$

This expression cannot be integrated analytically. The majority of hopping transport takes place around the Fermi energy. Thus, when the carrier concentration is low, the Fermi energy resides in the tail of the Gaussian, where the exponential function can be viewed as an approximation [9]:

$$n = \frac{N_t}{k_B T_0} \int_{-\infty}^{0} \frac{\exp\left(E/k_B T_0\right)}{1+\exp\left(\frac{E-E_F}{k_B T}\right)} = N_t\, \Gamma_F \exp\left(\frac{E_F}{k_B T_0}\right). \tag{11}$$

Thereby, $T_0$ denotes the width of exponential distribution function and $\Gamma_F = \Gamma(1-T/T_0)\Gamma(1+T/T_0)$ ($\Gamma$ indicates the gamma function).

If the carrier concentration is very low, most of the carriers are trapped, and consequently no electric current exists. With increasing carrier concentration, however, several conduction clusters emerge (Fig. 1). Ambegaokar and coworkers argued that an accurate estimate of $G$ is the critical percolation conductance $G_c$ [10], which is the largest value of the conductance such that the subnet of the network with $G_{ij} > G_c$ still contains a conducting sample-spanning cluster. At the onset of percolation, the critical number $B_c$ can be written as

$$B_c = \frac{N_b}{N_S}. \tag{12}$$

$B_c = 2.8$ for a three-dimensional amorphous system and $N_b$ and $N_s$ are, respectively, the density of bonds and density of sites in a percolation system, and can be calculated as [9]

$$N_b = \int d\vec{R}_{ij} dE_i dE_j g(E_i) g(E_j) \theta(s_c - s_{ij}) \left(\frac{\pi}{2} - \theta\right) \tag{13}$$

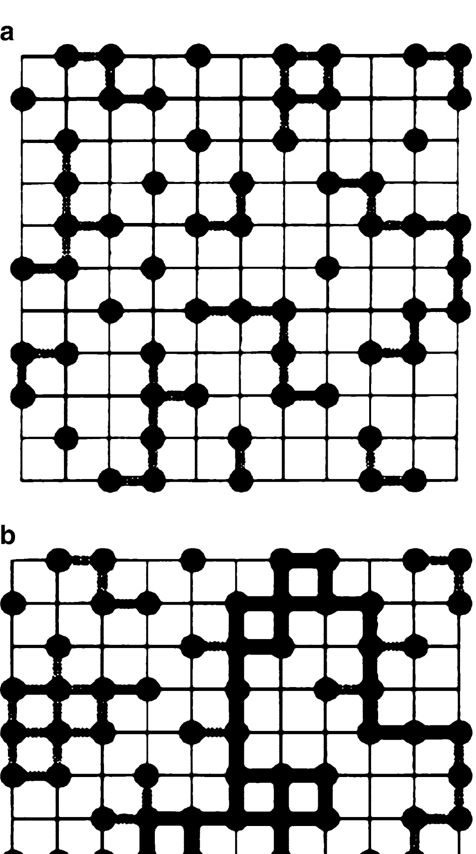


**Fig. 1** The emergence of a conducting ("*open*") path across the disordered system. The corresponding percolation current in the random environment of an amorphous organic semiconductor is distributed quite inhomogeneous

and

$$N_{\mathrm{s}} = \int \mathrm{d}E g(E) \theta (s_{\mathrm{c}} k_{\mathrm{B}} T - |E - E_{\mathrm{F}}|) . \tag{14}$$

Here $\vec{R}_{ij}$ denotes the distance vector between sites $i$ and $j$, $s_{\mathrm{c}}$ is the exponential conductance given in the relation [9]

$$\sigma = \sigma_0 \exp(-s_{\mathrm{c}}) , \tag{15}$$

and $\theta$ is step function. Substituting (11), (13), and (14) into (12), we obtain [9]

$$\sigma = \sigma_0 \left( \frac{\pi \delta N_{\mathrm{t}} (T_0/T)^3}{(2\alpha)^3 B_{\mathrm{c}} \Gamma (1 - T/T_0) \Gamma (1 + T/T_0)} \right)^{T_0/T} . \tag{16}$$

Here $\delta$ is the fraction of occupied states, defined as

$$\delta \cong \exp\left(\frac{E_{\mathrm{F}}}{k_{\mathrm{B}}T}\right)\Gamma\left(1-T/T_0\right)\Gamma\left(1+T/T_0\right). \tag{17}$$

Then the expression for the mobility as a function of carrier concentration $n$ can be calculated as

$$\mu\left(n,T\right)=\frac{\sigma_0}{q}\left(\frac{\left(T_0/T\right)^4\sin\left(\pi T/T_0\right)}{\left(2\alpha\right)^3 B_{\mathrm{c}}}\right)^{T_0/T} n^{T_0/T-1}. \tag{18}$$

However, this expression cannot account for situations where the carrier concentration is very low like, e.g., in the LED regime [11]. In order to solve this problem, we derive another mobility model assuming a Gaussian DOS as well as the applicability of the VRH. In this model, the DOS of (9) is reformulated as

$$g\left(E\right)=\frac{N_{\mathrm{t}}}{\sqrt{\pi}k_{\mathrm{B}}T_\sigma}\exp\left(-\left(E/k_{\mathrm{B}}T_\sigma\right)^2\right), \tag{19}$$

where $T_\sigma$ indicates the width of the DOS. At low carrier concentrations, the carrier gas is not degenerated [12]. Then we can obtain the Fermi energy by substituting (19) into (10):

$$E_{\mathrm{F}}=-\frac{k_{\mathrm{B}}T_\sigma^2}{4T}+k_{\mathrm{B}}T\ln\delta. \tag{20}$$

Combining (19), (20), (13), (14), and (15), the new percolation criterion takes the following form:

$$B_{\mathrm{c}}\approx\frac{2N_{\mathrm{t}}\left(\sqrt{2}+1\right)\sqrt{\pi}}{\left(2\alpha T/T_\sigma\right)^3}\left(\frac{E_{\mathrm{F}}+k_{\mathrm{B}}Ts_{\mathrm{c}}}{k_{\mathrm{B}}T_\sigma}\right)^2\exp\left(-\left(\frac{E_{\mathrm{F}}+k_{\mathrm{B}}Ts_{\mathrm{c}}}{k_{\mathrm{B}}T_\sigma}\right)^2\right). \tag{21}$$

Equation (21) is solved for $s_{\mathrm{c}}$ and the mobility is calculated as

$$\mu=\frac{\sigma_0}{qN_{\mathrm{t}}}\exp\left(\eta\right), \tag{22}$$

with

$$\eta=-\frac{T_\sigma}{T}\sqrt{-W\left(-\frac{B_{\mathrm{c}}\left(2\alpha T/T_\sigma\right)^3}{2\pi N_{\mathrm{t}}\left(1+\sqrt{2}\right)}\right)}-\frac{T_\sigma^2}{4T^2}, \tag{23}$$

where $W$ is the Lambert function [13]. Equation (23) is obtained assuming:

- The site positions are randomly distributed
- The energy barrier for the critical hopping is large
- The carrier concentration is very low

Using the model described above, we discuss the temperature dependence of the mobility first, as shown in Fig. 2. Here we can see that the agreement between the model (22) and the empirical equation $\mu \propto \exp\left(-(C\sigma_v/k_B T)^2\right)$ is quite good. The fitting parameter $C \approx 0.71$, which is close to $C \approx 0.69$ in [14] and 0.64 in [15].

The mobility as a function of the carrier concentration is presented in Fig. 3, where $T_\sigma/T$ is in the range 1.5–9.0, corresponding to some typical values for organic semiconductors. The mobility stays constant until a certain threshold value of the carrier occupation. Above this threshold, the mobility increases about four orders of magnitude at $T_\sigma/T = 9$. These effects have been observed in experimental work in [16].

Combining (18) and (22), we compare the model and the experimental data from [16]. The results are shown in Fig. 4.

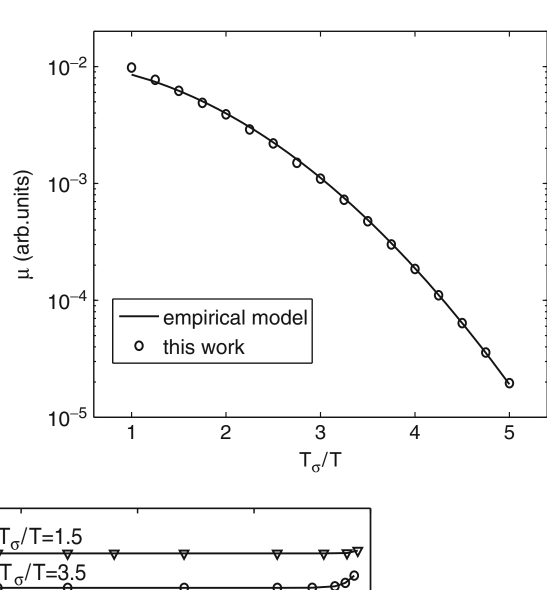


**Fig. 2** Comparison between our work and empirical model $\mu \propto \exp\left(-(C\sigma_v/k_B T)^2\right)$ at different temperatures

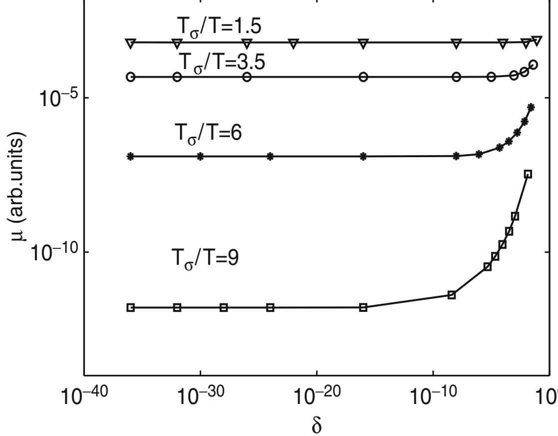


**Fig. 3** The calculated mobility vs carrier occupation at different temperatures

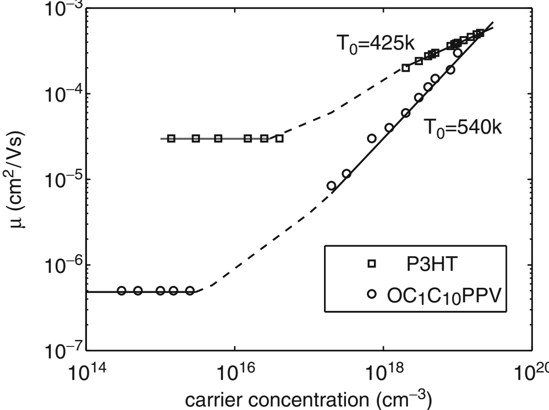


**Fig. 4** Comparison between calculation and typical experimental results [16]

## 4 Doping and Trapping Model for Organic Semiconductors

Earlier studies have shown that the molecular doping of organic semiconductors may increase the conductivity by many orders of magnitude. Other early studies have been devoted to the improvement of the photovoltaic behavior of doped thin films [17]. Although the doping process of organic semiconductors can largely be depicted by a standard model used for crystalline inorganic semiconductors, a general doping model still remains a challenge for organic semiconductors due to the weak intermolecular forces. At the same time, because of the bending or breaking of the high energy interaction bonds at crystalline defects, grain boundaries, and incorporated impurities, the traps within an organic semiconductor play an important role in charge transport. In the following, we present an analytical model for hopping transport in doped, disordered organic semiconductors based on VRH and percolation theory. This model can successfully explain the superlinear increase of conductivity with doping observed in several experimental data. Moreover, this model can also be used to describe the trapping characteristics in organic semiconductors [18, 19].

A double exponential density of states is assumed:

$$g(E) = \frac{N_t}{k_B T_0} \exp\left(\frac{E}{k_B T_0}\right) + \frac{N_d}{k_B T_1} \exp\left(\frac{E + E_d}{k_B T_1}\right), \quad (E < 0), \tag{24}$$

where $N_t$ and $N_d$ label the total concentration of the intrinsic and the dopant states, $T_0$ and $T_1$ are parameters indicating the width of the intrinsic and the dopant distribution, respectively, and $E_d$ is the Coulomb trap energy. For the double exponential DOS, the distribution of carriers, $\rho(E)$, is determined by the Fermi–Dirac distribution $f(E)$ as follows:

$$\rho(E) = g(E) f(E) = \frac{g(E)}{1 + \exp\left(\frac{E - E_F}{k_B T}\right)}. \tag{25}$$

The Fermi energy of this system is fixed by the equation for carrier concentration $n$ as

$$n = \int \frac{g(E)}{1+\exp\left(\frac{E-E_{\mathrm{F}}}{k_{\mathrm{B}}T}\right)} dE = n_{\mathrm{t}} + n_{\mathrm{d}}. \tag{26}$$

where

$$n_{\mathrm{t}} = N_{\mathrm{t}} \exp\left(\frac{E_{\mathrm{F}}}{k_{\mathrm{B}}T_0}\right) \Gamma(1-T/T_0)\,\Gamma(1+T/T_0)$$

and

$$n_{\mathrm{d}} = N_{\mathrm{d}} \exp\left(\frac{E_{\mathrm{F}}}{k_{\mathrm{B}}T_1}\right) \Gamma(1-T/T_1)\,\Gamma(1+T/T_1).$$

Substituting (24) and (26) into (13), (14), and (15), we obtain

$$B_{\mathrm{c}} = \frac{\pi N_{\mathrm{t}}^2 \varphi^3 \exp(2\eta) + \pi N_{\mathrm{d}}^2 \xi^3 \exp(2\gamma)}{N_{\mathrm{t}} \exp(\eta) + N_{\mathrm{d}} \exp(\gamma)} \tag{27}$$

with

$$\eta = \frac{E_{\mathrm{F}} + k_{\mathrm{B}}T s_{\mathrm{c}}}{k_{\mathrm{B}}T_0},\ \gamma = \frac{E_{\mathrm{F}} - E_{\mathrm{d}} + k_{\mathrm{B}}T s_{\mathrm{c}}}{k_{\mathrm{B}}T_1},\ \varphi = \frac{T_0}{4\alpha T},\ \xi = \frac{T_1}{4\alpha T}.$$

The parameter $s_{\mathrm{c}}$ is calculated by a numerical solution of (27) and the conductivity is obtained from (15).

Figure 5 illustrates the temperature dependence of the conductivity for different doping concentrations. The parameters are: $\alpha^{-1} = 0.37\,\text{Å}$, $E_{\mathrm{d}} = 0.5\,\mathrm{eV}$, $T_0 = 800\,\mathrm{K}$ and $T_1 = 400\,\mathrm{K}$. An Arrhenius-like temperature dependence $\log\sigma \propto -E_{\mathrm{A}}/k_{\mathrm{B}}T$ can be observed, where $E_{\mathrm{A}}$ is activation energy.

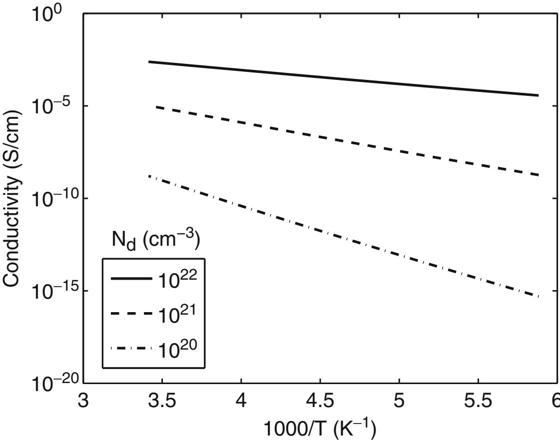


**Fig. 5** Temperature dependence of the conductivity at different doping concentration

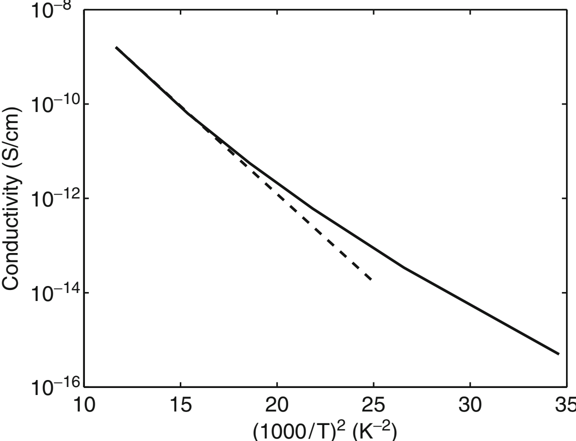


**Fig. 6** Temperature dependence of the conductivity in organic semiconductors, plotted as $\log \sigma$ vs $T^{-2}$. The *dashed line* is a guide to the eye

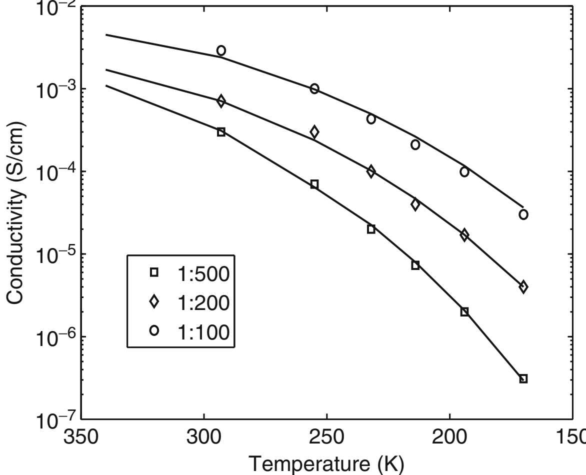


**Fig. 7** Conductivity of doped ZnPc at various doping ratios as a function of temperature. The *lines* represent the analytical model, the experimental values (*symbols*) are from [20]

In Fig. 6, we plot the graph $\log \sigma$ vs $T^{-2}$, which is observed to deviate slightly from a straight line (dashed in Fig. 6). This is because, at higher temperature, almost all the carriers occupy the intrinsic states; therefore the dopants do not change the trap-free relation $\log \sigma \propto T^{-2}$.

In Fig. 7, we compare the measured conductivities at room temperature with the theoretical values based on our model. The agreement is quite good. The fitting parameters are the same as in Fig. 5. From Figs. 5–7 we can deduce that the conductivity increases considerably with the dopant concentration, especially in the lower

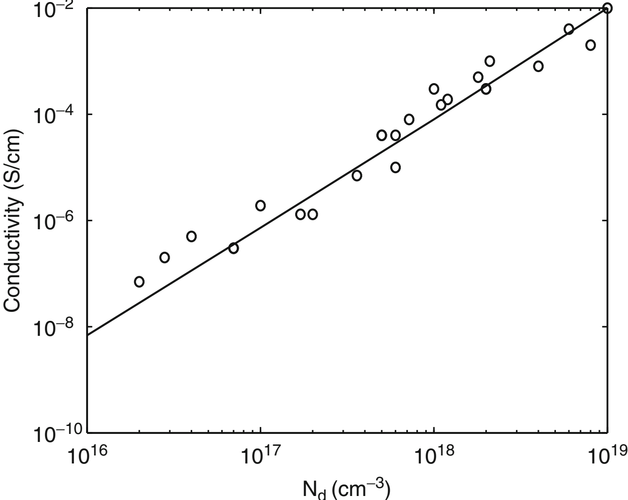


**Fig. 8** Conductivity of PPEEB films vs the dopant concentration. The *line* represents the analytical model. Experiments (*symbols*) are from [24]

temperature regime. The superlinear dependence of the conductivity on the doping concentration has been investigated by several groups [21, 22], where the empirical formula

$$\sigma \propto N_{\mathrm{d}}^{\gamma}$$

has been used. Using our model, the superlinear increase of the conductivity can be predicted successfully. We show this relation in Fig. 8 with the same parameters as in Fig. 5. Our model gives $\gamma = 4.9$ for $T = 250\,\mathrm{K}$ and $\gamma = 3.9$ for $T = 200\,\mathrm{K}$. Note that these choices are consistent with those in [23], where $\gamma$ is chosen in the range 3–5. In Fig. 8, we compare the predictions of our model with the experimental data of doped PPEEB [24]. The parameters are $\alpha^{-1} = 6\,\text{Å}$, $E_{\mathrm{d}} = 0.6\,\mathrm{eV}$, $T_0 = 1000\,\mathrm{K}$, and $T_1 = 500\,\mathrm{K}$. The predictions fit the experimental data very well.

In Fig. 9, we plot the relation between the conductivity and doping ratio $N_{\mathrm{d}}/(N_{\mathrm{t}} + N_{\mathrm{d}})$ for different temperatures with parameters $T_0 = 1000\,\mathrm{K}$ and $T_1 = 500\,\mathrm{K}$, $E_{\mathrm{d}} = 0.5\,\mathrm{eV}$ and $\sigma_0 = 1 \times 10^7\,\mathrm{S\,cm^{-1}}$. We can see that the conductivity increases with both the temperature and the doping ratio.

More specifically, there is a transition in the increase of the conductivity of organic semiconductor upon doping, which is manifested by a change in the slope of the curve, as shown in Fig. 10. The parameters are the same as in Fig. 9. There we can see that the conductivity increases linearly for low, and superlinearly for high doping levels. This transition has been interpreted in [25] in terms of the broadening of the transport manifold due to the enhanced disorder from the dopant.

With the model described above, we investigate the trapping characteristics of organic semiconductors. In Fig. 11 we compare the analytical model with experimental data reported in [26]. Parameters are the relative trap concentration

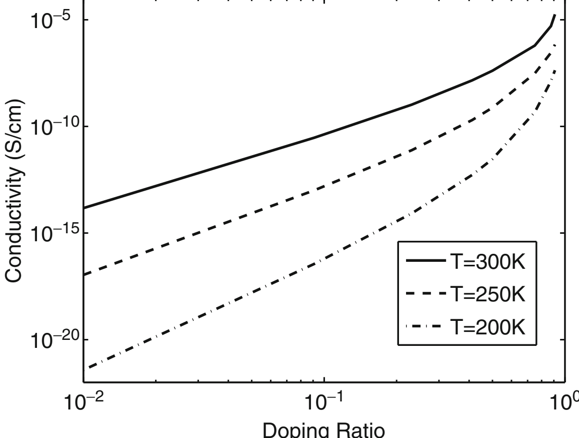


**Fig. 9** Conductivity as a function of the doping ratio with temperature as parameter

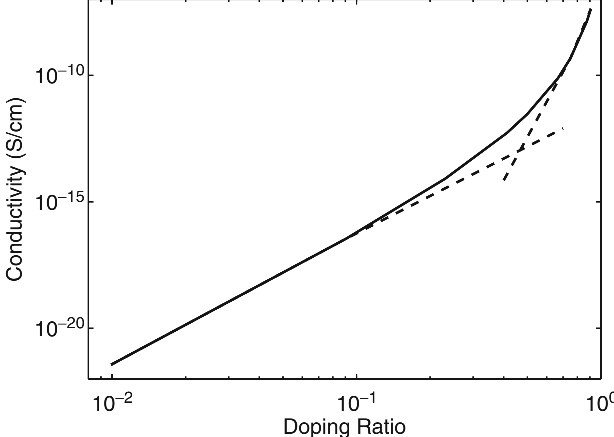


**Fig. 10** Conductivity at $T = 200\,\mathrm{K}$ as a function of the doping ratio. The *dashed line* is a guide to the eye

$c_t = N_d/N_t = 1 \times 10^{-2}$, $T_0 = 1{,}200\,\mathrm{K}$, $T_1 = 400\,\mathrm{K}$, $E_d = -0.15\,\mathrm{eV}$, $\alpha = 6\,\mathrm{nm}^{-1}$, and $\sigma_0 = 4.2 \times 10^8\,\mathrm{S\,m}^{-1}$. The data is for TTA with doping DAT.

The relation between the conductivity and the trap concentration is shown in Fig. 12. The numerical values of the occurring parameters are $N_t = 10^{22}\,\mathrm{cm}^{-3}$, $T_0 = 1{,}000\,\mathrm{K}$, $T_1 = 500\,\mathrm{K}$, $E_d = -0.2\,\mathrm{eV}$, $\alpha = 6\,\mathrm{nm}^{-1}$, the temperature is $T = 400\,\mathrm{K}$, and $\sigma_0 = 1 \times 10^4\,\mathrm{S\,m}^{-1}$. At a critical trap concentration, the conductivity has a minimum. This has been verified by experiments [27] as well as Monte-Carlo simulations [28]. The minimum is due to the onset of inter-trap transfer that alleviates thermal detrapping of carriers, which is a necessary step for charge transport. We can also see that a small trap concentration has virtually no effect on the conductivity.

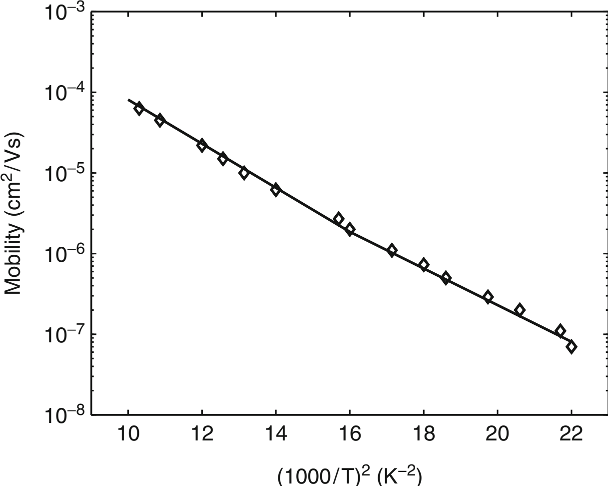


**Fig. 11** Temperature dependence of the zero-field mobility for TTA with trap DAT. *Symbols* represent experimental data from [26]

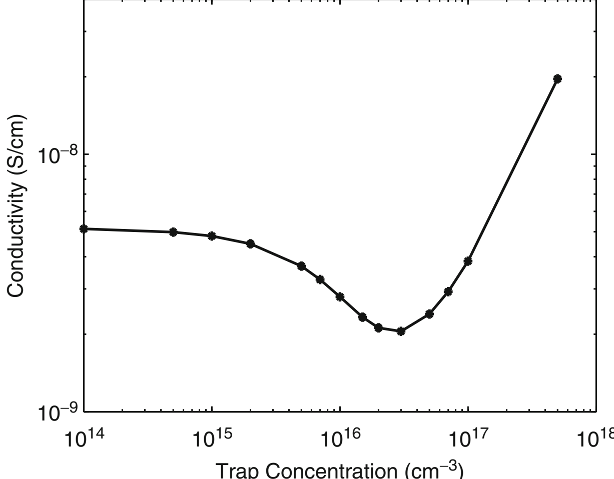


**Fig. 12** The dependence of the conductivity on the trap concentration

At higher trap concentration, however, the activation energy for the conductivity decreases. The traps themselves can serve as an effective hopping transport band. So the effect of traps on the charge conductivity is qualitatively similar to that caused by a high carrier concentration. It is interesting that such transition has also been observed in thermally stimulated luminescence measurements [29].

## 5 Charge Injection and Transport Model in Organic Light-Emitting Diodes

This section is concerned with injection-limited conduction at high electric fields. The textbook models describing injection into semiconductors are the Fowler–Nordheim (FN) model for tunneling injection and the Richardson–Schottky (RS) model for thermionic emission [30]. The FN model ignores image charge effects and assumes tunneling of electrons from a metal contact through a triangular barrier into a continuum of states. The injection current density reads as

$$j(F) = BF^2 \exp\left(-\frac{4\left(2m_{\mathrm{eff}}\right)^{1/2}\Delta^{3/2}}{3\hbar qF}\right),$$

and exhibits no temperature dependence. Here, $\Delta$ is the barrier height in the absence of both an external field and the image charge effect, $q$ is the elementary charge, $F$ is the external field, and $m_{\mathrm{eff}}$ is the effective mass of the carriers in the semiconductor. The RS model is based on the assumption that an electron from the metal can be injected once it has acquired a thermal energy sufficient to cross the potential maximum that results from the superposition of the external and the image charge potential. The injection current density $j(F)$ is predicted as

$$j(F) = CT^2 \exp\left(-\Delta + \left(\frac{q^3F}{4\pi\varepsilon\varepsilon_0}\right)^{1/2}\right)/k_{\mathrm{B}}T.$$

These two models, however, are insufficient to handle disordered organic materials, where the DOS is a Gaussian distribution, with localized carriers and discrete hopping within a distribution of energy states. Arkhipov presented an analytical model based on hopping theory [31] and Wolf preformed detailed Monte-Carlo simulations of hopping injection from a metal into an organic semiconductor [32]. Here we will present two injection models: one is based on drift–diffusion theory and the other on the master equation.

### 5.1 *Diffusion Controlled Injection Model*

Due to the low mobility in organic semiconductors, diffusion transport is also very important for the charge injection process. Therefore, an analytical diffusion controlled charge injection model particularly suited for OLEDs has been developed [33]. This model is based on drift–diffusion and multiple trapping theory. The latter can also be used to describe hopping transport in organic semiconductors [34].

The potential barrier, $q\varphi(x)$, formed at the metal/semiconductor interface, is a superposition of an external electric field and a Coulomb field binding the carrier on the electrode [35]:

$$q\varphi(x) = \Delta - \frac{q^2}{16\pi\varepsilon\varepsilon_0 x} - qFx. \tag{28}$$

Here, $x$ is the distance between the position of interest and the metal/organic layer interface. Since the rapid variation of the potential (28) takes place within $x_d$ in front of the electrode, the field $F$ can be regarded as being nearly constant.

Using drift–diffusion theory, the hole current $J$ can be written as

$$-J = k_B T\mu \left( \frac{q}{k_B T} p_e(x) \frac{d\varphi(x)}{dx} + \frac{dp_e(x)}{dx} \right), \tag{29}$$

where $\mu$ is the mobility. On taking $J$ and $\mu$ as constant, and solving for $n$, we obtain

$$p_e(x) = \left( N - \frac{J}{k_B T\mu} \int_0^x \exp\left( \frac{q\varphi(y')}{k_B T} \right) dy' \right) \exp\left( -\frac{q\varphi(x)}{k_B T} \right). \tag{30}$$

where $N$ is the carrier concentration at $x = 0$. In multiple trapping theory [36], the total carrier concentration is given by the sum of the carrier concentrations in the extended states $p_e(x)$ and the localized states:

$$p(x) = p_e(x) + \int_0^\infty g(E) f(E, E_F) dE. \tag{31}$$

Here $f(E)$ is the Fermi–Dirac distribution, and $E_F$ can be written as [36]

$$E_F(x) = k_B T \ln\left( \frac{v_0 \tau_0 N_t}{p_e(x)} \right),$$

where $\tau_0$ denotes the carrier-lifetime and $v_0$ labels the attempt-to-escape frequency.

In the injection regime, all traps within the vicinity of the contact are filled. Moreover, the carrier concentration in the extended states is much higher than that in the trapped states. As noted by Arkhipov et al. [36], the majority of carriers far away from the injecting electrode occupy localized states. So we propose here the concept of critical distance $x_d$, where the carrier concentration in the extended states is equal to the carrier concentration in localized states, i.e.,

$$p_e(x_d) = \int_0^\infty g(E, x_d) f(E, E_F) dE. \tag{32}$$

Substituting (28), (31), and (32) into the Poisson equation

$$\frac{d^2(q\varphi)}{dx^2} = -\frac{q}{\varepsilon\varepsilon_0} p(x), \tag{33}$$

the critical distance $x_\mathrm{d}$ can be calculated as

$$1 = \int_0^\infty \frac{16\pi x_\mathrm{d}^3 g\left(E - q\varphi\left(x_\mathrm{d}\right)\right)}{1 + 16\pi x_\mathrm{d}^3 v_0 \tau_0 N_\mathrm{t} \exp\left(-\frac{E}{k_\mathrm{B}T}\right)}. \tag{34}$$

The DOS in this model is assumed to be a Gaussian.

Solving (34) numerically, we can obtain the critical distance $x_\mathrm{d}$. The free carrier concentration at $x_\mathrm{d}$ is calculated by (32).

Ultimately, the injection current can be calculated as

$$J = k_\mathrm{B} T \mu \frac{\left(N - p_e\left(x_\mathrm{d}\right)\exp\left(\frac{q\varphi(x_\mathrm{d})}{k_\mathrm{B}T}\right)\right)}{\int_0^{x_\mathrm{d}} \exp\left(\frac{q\varphi(x)}{k_\mathrm{B}T}\right)\mathrm{d}x}. \tag{35}$$

The barrier height $\Delta$ plays an important role in injection efficiency. We calculate the relation between the injection current and the electric field for different values for $\Delta$, as shown in Fig. 13. The parameters are $N_\mathrm{t} = 1 \times 10^{18}\,\mathrm{cm}^{-3}$, $T = 300\,\mathrm{K}$, $v_0 = 10^{11}\,\mathrm{s}^{-1}$, $\tau_0 = 10^{-11}\,\mathrm{s}$, and $\mu = 1 \times 10^{-9}\,\mathrm{cm}^2\,\mathrm{V}^{-1}\,\mathrm{s}^{-1}$. As intuitively expected, the injection current increases with increasing electric field, and decreasing $\Delta$. The slope of $\log J$ vs $\log F$, however, is not constant. Figure 14 shows the temperature dependence of the injection current for the case $\Delta = 0.3\,\mathrm{eV}$. Thereby, the other parameters are the same as in Fig. 13. The temperature coefficient decreases strongly with increasing electric fields. As observed in [32] theoretically, the coefficient reverses its sign in the high field regime.

A comparison between this model prediction and experimental data [32] is shown in Fig. 15 with $\Delta = 0.3\,\mathrm{eV}$ and $\Delta = 0.5\,\mathrm{eV}$. The fitting parameters

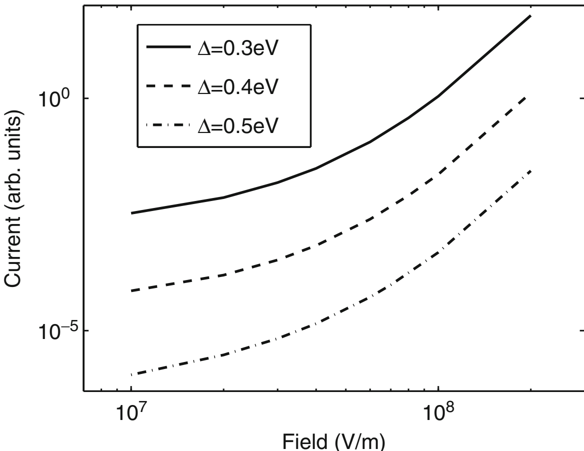


**Fig. 13** Dependence of injection current on the barrier height

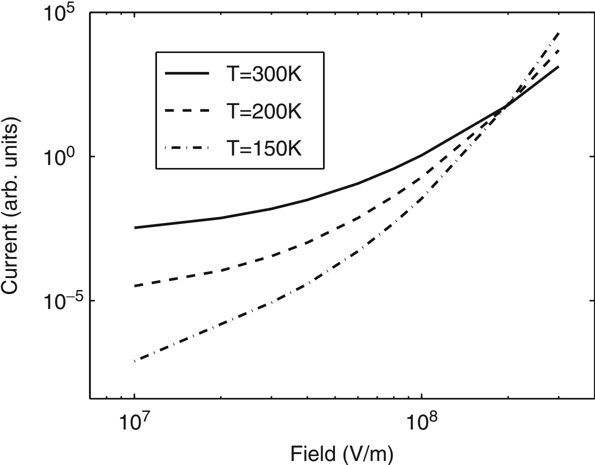


**Fig. 14** Temperature dependence of injection current

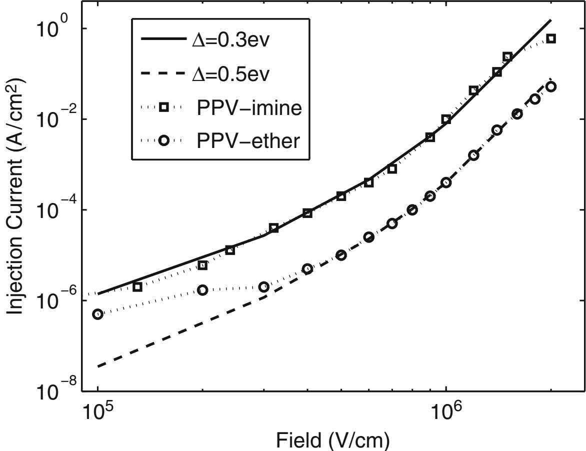


**Fig. 15** Comparison between the presented model and experimental data

are $N_t = 1 \times 10^{17}\,\text{cm}^{-3}$, $\mu = 2.56 \times 10^{-11}\,\text{cm}^2\,\text{V}^{-1}\,\text{s}^{-1}$ for PPV-ether and $2.51 \times 10^{-9}\,\text{cm}^2\,\text{V}^{-1}\,\text{s}^{-1}$ for PPV-imine, respectively. The other parameters are the same as Fig. 13.

Next, we compute the effect of the field-dependent mobility on the charge injection current. The mobility in organic semiconductor depends on the local electric field $F$ as [37]

$$\mu(F) = \mu_0 \exp\left(\gamma\sqrt{F}\right). \tag{36}$$

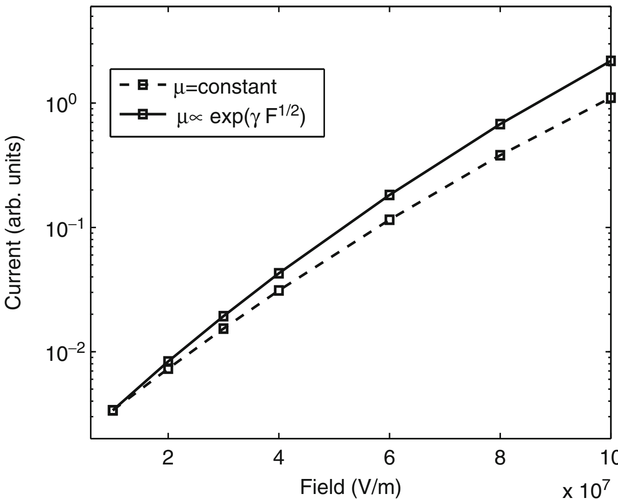


**Fig. 16** Comparison between injection current for field dependent mobility and constant mobility

Here, $\mu_0$ denotes the zero-field mobility and $\gamma$ is a parameter. We first re-calculate the carrier concentration as

$$p_e(x) = \left( N - \frac{J}{k_B T \mu_0 \exp\left(\gamma\sqrt{F}\right)} \int_0^x \exp\left(\frac{q\varphi(y)}{k_B T}\right) dy \right) \exp\left(-\frac{q\varphi(x)}{k_B T}\right). \quad (37)$$

Then, by connecting (34), (35), (36), and (37), we obtain the injection current with field-dependent mobility. Figure 16 illustrates the relation between injection current and electric field with field-dependent and constant mobility, with $\mu_0 = 7.3\times10^{-6}\,\mathrm{cm}^{-2}\mathrm{V}^{-1}\,\mathrm{s}^{-1}$, $\gamma = 1\times10^{-4}\left(\mathrm{m\,v}^{-1}\right)^{1/2}$, and $\Delta = 0.3\,\mathrm{eV}$.

### *5.2 Device Model for Unbipolar Organic Light-Emitting Diodes*

In order to analyze the interplay between charge injection and bulk conductivity, one must use specific models for both injection and charge transport in bulk. Here we treat the charge injection as diffusion-controlled and the transport is multiple trapping theory.

In this section we present a unified model for unbipolar OLEDs which includes charge injection, transport, and space charge effects in organic materials [38].

In the injection regime ($x < x_d$), we use the model described in the previous section. However, in the transport regime the potential expression (28) does not hold true any more. It can be calculated as

$$\frac{d^2\varphi(x)}{dx^2} = -\frac{dF}{dx} = -\frac{q}{\varepsilon\varepsilon_0} p(x). \quad (38)$$

The total carrier concentration $p(x)$ is

$$p(x) = p_e(x) + \int_0^\infty g(E) f(E, E_F) dE, \quad (x > x_d). \tag{39}$$

The Fermi energy is

$$E_F(x) = k_B T \ln\left(\frac{v_0 \tau_0 N_t}{p_e(x)}\right), \quad (x > x_d) \tag{40}$$

and the voltage is calculated as

$$V = F x_d + \int_{x_d}^{L} F(x) dx. \tag{41}$$

Here, $L$ is the thickness of the organic layer in the organic light-emitting diode. The $J - V$ characteristics of OLEDs is obtained by solving (38)–(41) numerically. The boundary conditions are $\varphi(0) = \varphi(x_d)$, $F(0) = F$, and $J = J_{inj}(F)$, where $\varphi(x_d)$ is calculated according to (28), $F$ denotes the electric field in the injection regime, and $J_{inj}(F)$ is calculated by (35).

With his model, we calculate the device characteristics of an unipolar OLED at different barrier heights $\Delta$, as shown in Fig. 17. The input parameters are $T = 300\,K$, $\sigma_v = 0.08\,eV$, $N_t = 1 \times 10^{16}\,cm^{-3}$, $v_0 = 10^{11}\,s^{-1}$, $\tau_0 = 10^{-11}\,s$, $\mu = 1 \times 10^{-4}\,cm^{-2}V^{-1}\,s^{-1}$, and the device length is 100 nm. The comparison between our work and experimental data of hole only ITO/NPB/Al [39] is plotted in Fig. 18 with $\Delta = 0.1\,eV$, $\mu = 2.9 \times 10^{-1}\,cm^{-2}V^{-1}\,s^{-1}$, and device length 65 nm. The other parameters are the same parameters as in Fig. 17.

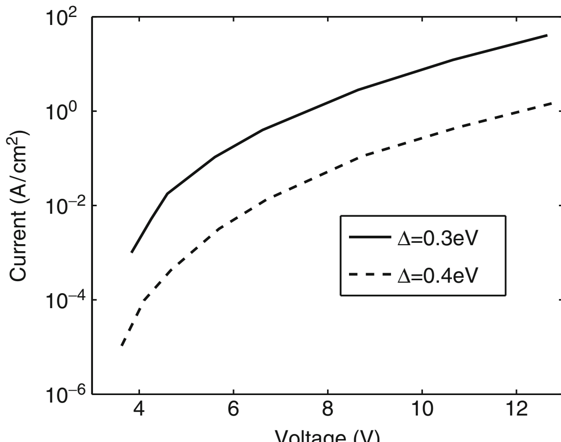


**Fig. 17** Barrier height dependence of the $J - V$ characteristics of organic light-emitting diodes (OLEDs)

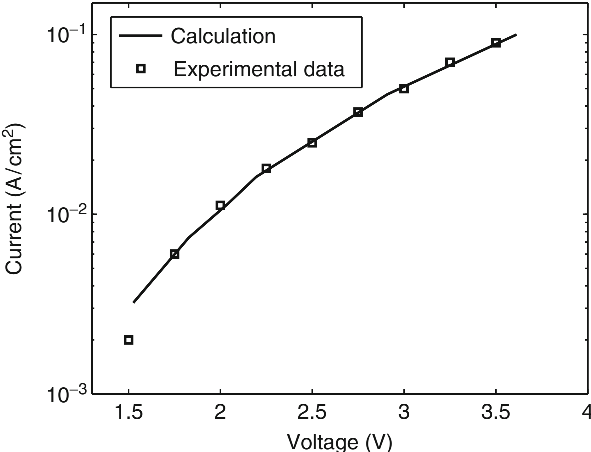


**Fig. 18** Comparison between the presented model and experimental data

## 6 Conclusion

We investigated a series of outstanding problems related to charge injection and transport in organic semiconductors and organic semiconducting devices. Our first contribution is to model the carrier concentration-dependent mobility. We showed that the shape of the density of states is an important factor for the relation between carrier concentration and mobility. The exponential DOS is not entirely reliable for the low carrier concentration regime. Following this, we proceeded to develop an analytical model describing the doping and the trapping characteristics in organic semiconductors. This model can explain the superlinear increase of conductivity upon the dopant concentration and reproduces the relation between trapping concentration and conductivity successfully.

Despite the successful application of the FN injection mechanism or the RS model on some experimental organic device data, it is very important to take into account the role of diffusion transport and backflow current in the connection with current injection model for organic devices. For this goal, we present an injection model based on multiple trapping theory. In the next step, we investigate the DC characteristics of unbipolar OLEDs by connecting this injection model and a space charge model for an organic material.

## References


1. Chiang CK, Fincher CR, Parker JYW, Heeger AJ, Shirakawa H, Louis EJ, Gau SC, MacDiamid AG (1977) Electrical conductivity in doped polyacetylene. Phys Rev Lett 39(17):1098–1101
2. Shaw JM, Seidler PF (2001) Organic electronics: introduction. IBM J Res Dev 45(1):3–10
3. Scott JC, Malliaras GG (1999) In conjugated polymers. Wiley, Germany

4. Deboer C (2004) Organic LED display. www.audioholics.com
5. Miller A, Abrahams E (1960) Impurity conduction at low concentrations. Phys Rev 120(3):745–755
6. Horowitz G (2000) Physics of organic field-effect transistors. Semiconducting Polymers. Wiley, Weinheim, pp 463–514
7. Li L, Meller G, Kosina H (2007) Carrier concentration dependence of the mobility in organic semiconductors. Synth Met 157:243–246
8. Bässler H (1993) Charge transport in disordered organic photoconductors. Phys Stat Sol(b) 175:15–55
9. Vissenberg MCJM, Matters M (1998) Theory of the field-effect mobility in amorphous organic transistors. Phys Rev B 57(20):12964–12967
10. Ambegaokar V, Halperlin BI, Langer JS (1971) Hopping conductivity in disordered systems. Phys Rev B 4(8):2612–2620
11. Coehoorn R, Pasveer WF, Bobbert PA, Michels MAJ (2005) Charge-carrier concentration dependence of the hopping mobility in organic materials with Gaussian disorder. Phys Rev B 72:1552061–1552063
12. Zvyagin IP, Plyukhin AV (1990) Low temperature relaxation in disordered organic semiconductors. Mos Univ Phys Bull 45:84–88
13. Corless RM, Gonner GH, Hare DEG (1996) On the lambert W function. Adv Comput Math 5(1):329–359
14. Bässler H (1990) Hopping and related phenomena: advances in disordered semiconductors. World Scientific, Singapore
15. Movaghar B, Grunewald M, Bässler H, Wurtz D (1986) Diffusion and relaxation of energy in disordered organic and inorganic materials. Phys Rev B 33(8):5545–5554
16. Tanase C, Meijer EJ, Blom PWM, de Leeuw DM (2003) Unification of the hole transport in polymeric field-effect transistors and light-emitting diodes. Phys Rev Lett 91(21):216601–216604
17. Leempoel P, Acuna MC, Fan FF, Bard AJ (1982) Semiconductor electrodes. 43. The effect of light intensity and iodine doping on the stabilization of n-silicon by phthalocyanine films. J Phys Chem 86:1396–1400
18. Li L, Meller G, Kosina H (2007) Analytical conductivity model for doped organic semiconductors. J Appl Phys 101:033716, 1–4
19. Li L, Meller G, Kosina H (2007) Influence of traps on charge transport in organic semiconductors. Solid State Electron 51:445–448
20. Maennig B, Pfeiffer M, Nollau A, Zhou X, Leo K, Simon P (2001) Controlled p-doping of polycrystalline and amorphous organic layers: self-consistent description of conductivity and field-effect mobility by a microscopic percolation model. Phys Rev B 64:195208
21. de Leeuw DM (1993) Stable solutions of doped thiophene oligomers. Synth Met 57:3597–3602
22. Maitrot M, Boudjema B, Andre JJ, Simon J (1986) Molecular material-based junctions: formation of a Schottky contact with metallophthalocyanine thin films doped by the cosublimation method. J Appl Phys 60:2396–2400
23. Jarrett CP, Friend RH, Brown AR, de Leeuw DM (1995) Field effect measurements in doped conjugated polymer films: assessment of charge carrier mobilities. J Appl Phys 77:6289–6294
24. Gregg BA, Chen SG, Branz HM (2004) On the superlinear increase in conductivity with dopant concentration in excitonic semiconductors. Appl Phys Lett 84:1707–1709
25. Shen Y, Diest K, Wong MH, Hsieh BR, Dunlap DH, Malliaras GG (2005) Charge transport in doped organic semiconductors. Phys Rev B 68:0812041–0812044
26. Borsenberger PM, Gruenbaum WT, Wolf U, Bässler H (1998) Hole trapping in tri-p-tolylamine-doped poly(styrene). Chem Phys 234:277–284
27. Pai DM, Yanus JF, Stolka M (1984) Trap-controlled hopping transport. J Phys Chem 88:4714–4717
28. Wolf U, Bässler H, Borsenberger PM, Gruenbaum WT (1997) Hole trapping in molecularly doped polymers. Chem Phys 222:259–267
29. Fishchuk II, Bässler H (2002) Nondispersive charge-carrier transport in disordered organic materials containing traps. Phys Rev B 66:20520801–20520812

30. Weissmantel C, Hamann C (1981) Grundlagen der Festköperphysik. Deutscher Verlag der Wissenschften, Germany
31. Arkipov VI, Emellianova EV, Tak YH, Bässler H (1998) Charge injection into light-emitting diodes: theory and experiment. J Appl Phys 84(2):848–856
32. Wolf U, Arkipov VI, Bässler H (1999) Current injection from a metal to a disordered hopping system. I. Monte carlo simulation. Phys Rev B 59(11):7507–7513
33. Li L, Meller G, Kosina H (2007) Diffusion-controlled charge injection model for organic light-emitting diodes. Appl Phys Lett 91(17):1–3
34. Pope M, Swenberg CE (1979) Electronic processes in noncrystalline materials. Oxford University Press, UK
35. Sze SM (1981) Physics of semiconductor devices. Wiley, USA
36. Arkhipov VI, Heremans P, Emelianova EV, Adriaenssens GJ (2001) Space-charge-limited currents in materials with Gaussian energy distributions of localized states. Appl Phys Lett 79(25):4154–4156
37. Pai DM (1970) Transient photoconductivity in poly(N-vinylcarbazole). J Phys Chem 52(5):2285–2291
38. Li L (2008) Charge transport in organic semiconductor materials and devices. Reviewer: Kosina H, Süss D, Institut für Mikroelektronik. Oral examination, 02–08–2008
39. Brütting W, Berlerb S, Muckl AG (2001) Device physics of organic light-emitting diodes based on molecular materials. Org Electron 2:1–36

# Index


Arrhenius temperature dependence 63
Averaging of hopping rates 46

Bardeen's model 140
Benzocyclobutene (BCB) 128, 162
Bias-stress 96, 105
  trapping 108
Bioelectric phenomena 189
BioFETs 189
  transient response 208
BioLEDs 189
Biomolecular electronics 189
Bio-organic optoelectronic devices, DNA 189
Bottom contact (BOC) 156
Brillouin–Wigner perturbation 266

Ca film 233
Carrier concentration-dependent mobility 304
Chalcogenides 3
Channel charge buildup 105
Channel formation 107
Channel length dependence 102
  submicrometer, undercutting 165
Charge carrier injection 213
Charge carrier transport/mobility 29, 50, 213
Charge carriers, hopping motion 31
Charge extraction by linearly increasing voltage (CELIV) 76
Charge photogeneration, Onsager concept 5
Charge transfer (CT) state 6
Charge transport 30, 73, 113
  molecular crystals 264
CMOS 213, 217
CMOS inverters 240
  ambipolar 245
  dielectric interface modification 247
  $SiO_2$ passivation 244
Complementary metal oxide semiconductor *see* CMOS
Conjugated polymers 1
Contact potential difference (CPD) 140
Contact resistance 113, 133
  unipolar devices 238
Contact structures 172
Copper phthalocyanine (CuPC) 32
Cr/Au 171, 205
Cyanoethylpullulan (CYEPL) 127, 200

Delay 107
Delocalized transport, polaronic band 266
  simple electronic band 265
Density of states (DOS) 4, 30, 47, 102, 122, 158, 229, 291, 309
2,4-Dichlorobenzenethiol 93
Dielectric constants 3, 7, 15, 17, 77
Dielectric materials 113
  organic transistors 126
Dielectric permittivity 24
Dielectrics 90, 105, 127, 200, 223
  high k 91
  inorganic 91
  polymers 89
  PVP 92, 102
$N,N'$-Diphenyl-$N,N'$-bis(1-naphthyl)-1, 1$'$-biphenyl–4,4$'$-diamine ($\alpha$-NPD) 32
Disorder 259
Disordered organic semiconductors (DOS) 46
  exponential, dispersive transport 54
  Gaussian 55

Dispersive/non-dispersive transport 55
Displacement current 106
Divinyltetramethyldisiloxane-bis(benzocyclobutene) (BCB) 200, 236
DNA–CTMA, films in nonlinear optics 195
  optoelectronic material 193
  organic field effect transistors 199
  organic light emitting diodes 195
  thin films, dielectric spectroscopy 205
DNA–surfactant cation complexes 202
Drain contacts 237
Drain current 116
Drift velocity, pulse voltage method 88
Drift–diffusion theory 315
Dynamic localization effects 280

Effective oxide thickness (EOT) 91
Electrode–semiconductor interface 133
Electron affinity (EA) 216
Electron blocking layer (EBL), DNA–CTMA 195
Electron transport 259
Electron–hole pair 1
Electron–phonon coupling 273
Electronic eigenfunction, thermal motions 278
Electrons, energy relaxation 54, 55
Ethylene, HOMO/LUMO 272
eTOF 74, 76
Exciton 1
  dissociation 13

Field dependence 100
Field-effect transistors (FETs) 2, 74, 213
Fokker–Planck equation 55
Fowler–Nordheim (FN) model, tunneling injection 315

Gate insulator 90
  surface-modified 175
Gated four-probe technique 133
Gaussian disorder model (GDM) 261
Gaussian DOS, electron energy relaxation 55
  hopping transport 23
Germanium, amorphous 47

Hexa-benzo-coronene, alkyl-substituted 12
Hexadecafluoro copper-phthalocyanine 74
Hexadecyltrimethylammonium chloride (CTMA) 193
Hexamethyldisilazane (HMDS) 93, 157
Hole field-effect mobility 216
Hole injection layer (HIL), PSS 199
HOMO/LUMO 11, 32, 138, 199, 216
Hopping integral, band structure 271
  intermolecular geometry 276
Hopping transport 1, 46, 268, 301

Induced density of interface state (IDIS) 142
Inkjet printing 218
Insulator surface, electronic states 229
Insulators 227
  dielectric properties 228
Insulator–semiconductor interface 125, 129
ITO/PhPPV:PDI/Al 13

Kelvin probe 140
Kohn–Sham–Fock operator 271

Laddertype polyphenylene (LPPP) 7
Large polaron theories 266
Localization theory 288
Long-channel approximation 81

Maxwell–Wagner effect 205
MEH–PPV 146
Metal phthalocyanine 261
Metal–insulator–metal (MIM) 201, 205
Metal–insulator–semiconductor (MIS) 201, 205
Miller–Abrahams rate model, phonon-assisted tunneling 32
Mobility 58, 73
  percolation models, low electric fields 31
Mobility extraction 75
Molecular crystals 259
  optical/electrical properties 3
Molecular dynamics/quantum chemical studies 278
Mott–Schottky (MS) limit 138
Multiple trapping model 261

Naphthalene 262
Nitrobenzenethiol 93

$OC_1C_{10}$-PPV 12, 245
Octadecanethiol 93
Octadecyltrichlorosilane (OTS) 93, 176

Octyltrichlorosilane 93
OFETs (organic field effect transistors) 2, 92, 155, 189, 213, 218, 302
  ambipolar 223
  CMOS inverters 240
  contacts 93
  DNA-CTMA 199
  field-effect mobility 92
  models 219
  short-channel 162
  unipolar 224
OLEDs 2, 30, 144, 189, 215, 302
  charge injection/transport model 315
  diffusion-controlled injection model 315
  TV 302
  unbipolar, device model 319
Oligothiophenes 74
Organic electronics 189
Organic field-effect transistors (OFETs) 155, 189, 213, 218
Organic photovoltaic cells (OPCs) 260
Organic photovoltaics (OPVs) 31
Organic semiconductors 73, 213, 301
  charge transport 119
  doping/trapping 309
  physics 302
Organic thin-film transistors (OTFTs) 114

Parameters extraction 113, 117
Pentacene 74, 89, 129, 145, 201, 228, 259, 261
  hole field-effect mobility 217
  thin-film phase 129
  transient response 97
Percolation 51
  models/theory 30, 31, 301
Perylene diimide 216
(6,6)-Phenyl $C_{61}$-butyric acid methyl ester (PCBM) 11, 245
Photocarrier yield, temperature dependence 23
Photoelectron spectroscopy 139
Photogeneration 1
  doped/blended conjugated polymers 11
  neat conjugated polymers 7
Photonic devices 189
Photoreceptors 3
Photovoltaic cells (PVs) 1, 2, 144, 216, 260
Pillow effect 143
Plastic electronics 189
PMMA (polymethyl-methacrylate) 200, 235
Polaron 259, 266
Polaronic band 266
  models 287
Poly(allyloxyphenylene) 178
Polyaniline (PANI) 128
Poly(2,5-bis(3-tetradecylthiophen-2yl)thieno[3,2-b]thiophene) 90, 98
Polycarbonate (PC) 235
Poly(3,9-di-*tert*-butylindeno[1,2-*b*]fluorene) (PIF) 246
Poly(9,9-di-*n*-octyl-fluorene-*alt*-benzothiadiazole) 223
Polyhexylthiophene 157, 260
  regio-regular (rr-P3HT) 10, 147
Polyimide (PI), gate insulator 127
Poly(2-methoxy-5-(3′,7′dimethyl-octyloxy))-*p*-phenylene vinylene (MDMO-PPV):PCBM 11
Poly(α-methylstyrene) 200
Polyphenylenevinylene (PPV) 7
Polystyrene (PS) 200, 235
Polystyrenesulfonate-doped polyethyleneoxythiophene (PEDOT:PSS) 128, 144
Polythiophene 10, 74, 90, 156, 176, 215
Polyvinyl carbazole 199
Poly(4-vinylphenol) (P4VP) 91, 200, 236
Poly-*p*-xylylene (parylene) 128
Poole Frenkel descriptions 30, 75
Pulse voltage method 75
PVA (polyvinyl alcohol) 127, 200
PVC (polyvinylchloride) 200
PVDF (polyvinylidenfluoride) 127, 200

Quantum chemistry 259

Radio frequency identification (RFID) 215
Random organic materials, charge carrier transport 51
Random organic semiconductors, charge carrier transport 50
Random organic solids, optical/electrical properties 3
Rationalization 281
Rayleigh–Schrödinger perturbation 266
Reactive ion etching (RIE) 167
Relaxation time 58
Richardson–Schottky (RS) model, thermionic emission 315
Rubrene 217, 261, 294

Saturation effects 60
Scaling 157
Schottky contact 172

Self-assembled monolayers (SAMs) 113, 128, 163, 228
  modified electrodes 146
Semiconductors 73, 119, 213, 301
  ambipolar 132
  complementary metal oxide (CMOS) 213
  disordered organic (DOS) 46
  electrode interface 133
  insulator interface 125, 129
  morphology 228
  random organic 50
Short-channel effects 155
  simulation 163
Short-channel OFETs 162
Short-channel transistor 155
Silicon, amorphous 47
Silicon dioxide 91, 98, 100
  passivation 244
Stilbene 262
Strong electron–phonon coupling theory 267
SU8 178
Superyellow 12
Surface potential microscopy/Kelvin probe force microscopy (KPFM) 135

Tantalum oxide 91, 97, 99
Temperature models 34
Tetrathiafulvalenes 261
Thermal off-diagonal disorder 283
Thin-film phase 129
Thin-film silicon transistor 199
Thin-film transistors 114, 215, 260
  threshold voltage 184
Time scale, extension 105
Time-of-flight 73
TPD(4M)–MEH–PPV 175, 176
Transfer line method (TLM) 134
Transport, simulation 85
Transport energy 14, 51, 52
Trapped charge limited (TCL) model 30
Trapping time 302
Triarylamines 131
Tris(8-hydroxyquinoline) aluminum ($AlQ_3$) 29
Tunnelling transitions (hopping) 46

Ultraviolet photoelectron spectroscopy (UPS) 139
Underetching 155

van der Waal's forces, weak 30
Variable-range-hopping (VRH) 46, 122, 304, 307

Wannier-like excitons 3
Weak electron–phonon coupling theory 266